Title
Computational Modeling of Ground-Bridge Seismic Response and Liquefaction Scenarios

Author
Qiu, Zhijian

Publication Date
2020

Peer reviewed|Thesis/dissertation

UNIVERSITY OF CALIFORNIA SAN DIEGO

Computational Modeling of Ground-Bridge Seismic Response and Liquefaction Scenarios

A dissertation submitted in partial satisfaction of the
requirements for the degree of Doctor of Philosophy

in

Structural Engineering

by

Zhijian Qiu

Committee in charge:

Professor Ahmed Elgamal, Chair
Professor Benson Shing
Professor Gilberto Mosqueda
Professor Jiun-Shyan (JS) Chen
Professor Kevin Brown

2020

The Dissertation of Zhijian Qiu is approved, and it is acceptable in quality and form for publication on microfilm and electronically:

Chair

University of California San Diego

2020

Dedication

To my wife Yilin Chu and my daughter Shirley

Epigraph

"*Life is more than the tedium before us; there's also poetry, and the faraway*."

-Gao Xiaosong

Table of Contents

List of Figures

List of Tables

Acknowledgements

I would like to express my sincere gratitude to my advisor Prof. Ahmed Elgamal for the continuous support of my Ph.D study and related research, for his patience, motivation, and immense knowledge. His guidance helped me throughout the time of this research. I could not have imagined having a better advisor and mentor for my Ph.D study.

I would like to thank all my committee members, Prof. Benson Shing, Prof. Gilberto Mosqueda, Prof. Jiun-Shyan (JS) Chen and Prof. Kevin Brown for their time and helpful suggestions on my research. In addition, my gratitude to my friends in the research group and our department for their support and advice: Mr. Muhammed Zayed, Dr. Kyungtae Kim, Mr. Athul Prabhakaran, Dr. John Li, Dr. Ahmed Ebeido, Dr. Abdullah Almutairi, Ms. Lan Luo, Dr. Wenyong Rong and Dr. Lei Su. I will always be grateful for your friendship and all the great times we shared.

Special thanks to i) Dr. Jinchi Lu for his great contribution to the computational aspects and soil constitutive plasticity models; ii) Prof. Geoffrey R. Martin of USC for proving insightful comments and advice; and iii) Dr. Fadel Alameddine of Caltrans for the valuable technical suggestions, comments, and contributions.

I am also grateful for the kind invitation by Professors Majid T. Manzari, Mourad Zeghal Bruce L. Kutter and Kyoheito Ueda to participate in LEAP-UCD-2017 at the University of California Davis, LEAP-Asia-2019 at Osaka, Japan, and the virtual workshop LEAP-RPI-2020.

I would like to express my deepest gratitude to my family members: i) My mom who gives me endless love and support throughout my whole life; ii) My elder sisters Lingling, Jingjing and Fenfen who give me unconditional support and enormous encouragement; iii) My parents-in-law who are the nicest people on the planet and give me so much support; and (iv) My beloved father who taught me to be a man in his limited life span (slightly over 50 years). You have been in my

dreams every night since you passed away 2 months after I started my Ph.D study in 2015. I miss you so much and I wish you rest in peace.

Above all, I would like to thank my wonderful wife Yilin Chu who has been extremely supportive of me throughout this entire process and has made countless sacrifices to help me get to this point. I would not be able to finish my Ph.D journey without her support. She resigned from her job in Orange County, CA and stayed with me since 2018, when I was going through some particularly challenging times. Her continuous support and encouragement took me through the darkness into a new life full of light and joy. I will never forget the days we shared together, and I will spend the rest of my life keeping our pledge: "I love you. North, south, east, and west. You are the one I love the best".

At this moment, I want to acknowledge my daughter (Shirley) who was born one month before my Ph.D defense. You complete me and make me the happiest person. Because of you and your mom, the world is beautiful, and life has meaning.

This thesis contains a mix of material published in technical papers, reports, conference papers, and new content being prepared for publication. A summary of this work is given below.

Chapter 2, in part, has been published as it appears in the following paper (The dissertation author was the primary investigator and author of this paper):

Qiu, Z., Lu, J., Elgamal, A., Su, L., Wang, N. and Almutairi, A. (2019). "OpenSees Three-Dimensional Computational Modeling of Ground-Structure Systems and Liquefaction Scenarios." Computer Modeling in Engineering & Sciences, 120(3), 629-656.

Chapter 3, in part, has been published as it appears in the following paper (The dissertation author was the primary investigator and author of this paper):

Qiu, Z. and Elgamal, A. (2020). "Three-Dimensional Modeling of Strain-Softening Soil Response for Seismic-Loading Applications." Journal of Geotechnical and Geoenvironmental Engineering, 146(7), 04020053.

Chapter 4, in full, has been published as it appears in the following paper (The dissertation author was the primary investigator and author of this paper):

Qiu, Z. and Elgamal, A. (2020). "Numerical Simulations of LEAP Centrifuge Tests for Seismic Response of Liquefiable Sloping Ground." Soil Dynamics and Earthquake Engineering, 139, 106378.

Chapter 4, in part, is a reprint of material as it appears in the following conference publication (The dissertation author was the primary investigator and author of this paper):

Qiu, Z. and Elgamal, A. (2020). "Numerical Simulations of LEAP Dynamic Centrifuge Model Tests for Response of Liquefiable Sloping Ground." In Model Tests and Numerical Simulations of Liquefaction and Lateral Spreading, 521-544. Springer, Cham.

Chapter 5, in full, is currently being prepared for submission for publication of the material as it may appear in the following journal publication (The dissertation author was the primary investigator and author of this paper):

Qiu, Z. and Elgamal, A. "Seismic Response of a Sheet-Pile Retaining Structure Supporting Liquefiable Soils: Numerical Simulations of LEAP Centrifuge Tests."

Chapter 6, in full, has been published as it appears in the following paper (The dissertation author was the primary investigator and author of this paper):

Qiu, Z., Ebeido, A., Almutairi, A., Lu, J., Elgamal, A., Shing, P.B. and Martin, G. (2020). "Aspects of Bridge-Ground Seismic Response and Liquefaction-Induced Deformations." Earthquake Engineering & Structural Dynamics, 49(4), 375-393.

Chapter 6, in part, is a reprint of material as it appears in the following paper (The dissertation author was the primary investigator and author of this paper):

Qiu, Z., Ebeido, A., Almutairi1, A., Lu, J., Elgamal, A. and Martin, G. (2019). "Bridge-Ground Seismic Response and Liquefaction-Induced Deformations." Earthquake Geotechnical Engineering for Protection and Development of Environment and Constructions, Rome, Italy, ISBN 978-0-367-14328-2.

Chapter 7, in full, has been submitted for publication of the material as it may appear in the following conference publication (The dissertation author was the primary investigator and author of this paper):

Qiu, Z. and Elgamal, A. (Manuscript accepted, 2020). "Three-Dimensional Bridge-Ground Liquefaction-Induced Deformations." 16th International Conference of IACMAG International Association for Computer Methods and Advances in Geomechanics, Torino, Italy. 3-4 May.

Chapter 8, in full, is currently being prepared for submission for publication of the material as it may appear in the following journal publication (The dissertation author was the primary investigator and author of this paper):

Qiu, Z., Lu, J., Ebeido, A., Elgamal, A., Uang, C. M. and Martin, G. "Bridge in Narrow Canyon: Seismic Response and Liquefaction-induced Deformations."

Chapter 9, in full, is currently being prepared for submission for publication of the material as it may appear in the following journal publication (The dissertation author was the primary investigator and author of this paper):

Qiu, Z., Elgamal, A. and Ebeido, A. "Arch Bridge Configuration for Mitigation of Liquefaction-Induced Lateral Deformations."

Chapter 10, in full, is currently being prepared for submission for publication of the material as it may appear in the following journal publication (The dissertation author was the primary investigator and author of this paper):

Qiu, Z. and Elgamal, A. "Canyon Effects on Seismically-Induced Liquefaction and Lateral Deformations."

Chapter 11, in full, is currently being prepared for submission for publication of the material as it may appear in the following journal publication (The dissertation author was a primary investigator and author of this paper):

Elgamal, A., Qiu, Z. and Luo, L. "Liquefaction-Induced Excess Pore Pressure beyond Vertical Effective Stress and Potential Consequences."

Chapter 12, in part, has been submitted for publication of the material as it may appear in the following conference publication (The dissertation author was the primary investigator of this paper):

Elgamal, A., Chen, J., Qiu, Z., Huang T., Wei, H. and Lu, J. (2020). "Meshfree Framework for Seismic Response of Earth Systems." In 16th International Conference of IACMAG International Association for Computer Methods and Advances in Geomechanics, Torino, Italy. 3-4 May.

Vita

06/2012	Bachelor of Engineering in Civil Engineering Nanchang Institute of Technology, Nanchang, China.
06/2015	Master of Science in Structural Engineering Xiamen University, Xiamen, China.
10/2020	Doctor of Philosophy in Structural Engineering University of California San Diego, La Jolla, USA.

Publications

Qiu, Z., Lu, J., Elgamal, A., Su, L., Wang, N. and Almutairi, A. (2019). "OpenSees Three-Dimensional Computational Modeling of Ground-Structure Systems and Liquefaction Scenarios." *Computer Modeling in Engineering & Sciences*, 120(3), 629-656.

Qiu, Z., Ebeido, A., Almutairi, A., Lu, J., Elgamal, A., Shing, B. and Martin, G. (2020). "Aspects of Bridge-Ground Seismic Response and Liquefaction-Induced Deformations." *Earthquake Engineering &Structural Dynamic*s, 49(4), 375-393.

Qiu, Z. and Elgamal, A. (2020). "Three-Dimensional Modeling of Strain Softening Soil Response for Seismic Loading Applications". *Journal of Geotechnical and Geoenvironmental Engineering*, 146(7), 04020053.

Qiu, Z. and Elgamal, A. (2020). "Numerical Simulations of LEAP Centrifuge Tests for Seismic Response of Liquefiable Sloping Ground." *Soil Dynamics and Earthquake Engineering*, 139, 106378.

Qiu, Z., Ebeido, A., Almutairi1, A., Lu, J., Elgamal, A. and Martin, G. (2019). "Bridge-Ground Seismic Response and Liquefaction-Induced Deformations." *Earthquake Geotechnical*

Engineering for Protection and Development of Environment and Constructions, Rome, Italy, ISBN 978-0-367-14328-2.

Qiu, Z. and Elgamal, A. (2020). "Numerical Simulations of LEAP Dynamic Centrifuge Model Tests for Response of Liquefiable Sloping Ground." *In Model Tests and Numerical Simulations of Liquefaction and Lateral Spreading*, 521-544. Springer, Cham.

Li, Y., Huang, S., Lin, C., Gu, Q. and **Qiu, Z.** (2017). "Response Sensitivity Analysis for Plastic Plane Problems Based on Direct Differentiation Method." *Computers & Structures*, 182, 392-403.

Gao, Y., Gu, Q., **Qiu, Z.** and Wang, J. (2016). "Seismic Response Sensitivity Analysis of Coupled Dam-Reservoir-Foundation Systems." *Journal of Engineering Mechanics*, 142(10), 04016070.

Gu, Q., **Qiu, Z.** and Huang, S. (2015). "A Modified Multi-Yield-Surface Plasticity Model: Sequential Closest Point Projection Method." *Computers and Geotechnics*, 69, 378-395.

Zayed, M., Ebeido, A., Prabhakaran, A., **Qiu, Z.** and Elgamal, A. (2020). "Asymmetric Input Motion for Accumulation of Ground Deformation in Laminar Container Shake Table Testing." *Canadian Geotechnical Journal*. (ja)

Zayed, M., Ebeido, A., Prabhakaran, A., Kim, K., **Qiu, Z.** and Elgamal, A. (2020). "Shake Table Testing: A High-Resolution Vertical Accelerometer Array for Tracking Shear Wave Velocity." *Geotechnical Testing Journal*, 44(4).

Prabhakaran, A., Kim, K., Orang, M.J., **Qiu, Z.** Ebeido, A., Zayed, M., Boushehri, R., Motamed, R., Elgamal, A. and Frazao, C. (2020). "Polymer Injection and Liquefaction-Induced Foundation Settlement: a Shake Table Test Investigation." *In Geo-Congress 2020: Geotechnical Earthquake Engineering and Special Topics (1-9)*. Reston, VA: American Society of Civil Engineers.

Elgamal, A., Chen, J., **Qiu, Z.**, Huang T., Wei, H. and Lu, J. (2020). "Meshfree framework for Seismic Response of Earth Systems." *In 16th International Conference of IACMAG International Association for Computer Methods and Advances in Geomechanics*, Torino, Italy. 3-4 May.

Elgamal, A., **Qiu, Z.**, Lu, J. and Almutairi, A. (2020). "Nonlinear Seismic Response of Ground-Structure Systems: Developments and Challenges." *In 16th International Conference of IACMAG International Association for Computer Methods and Advances in Geomechanics*, Torino, Italy. 3-4 May.

Qiu, Z., Elgamal, Z., Adalier, K. and Luo, J. (2021). "Mechanism of Post Liquefaction Settlement in Stratified Ground." *In Proceeding 17th World Congress on Earthquake Engineering (17th WCEE)*. Sendai International Center, Miyagi Prefecture, Japan.

Qiu, Z. and Elgamal, A. (2020). "Three-Dimensional Bridge-Ground Liquefaction-Induced Deformations." *In 16th International Conference of IACMAG International Association for Computer Methods and Advances in Geomechanics*, Torino, Italy. 3-4 May.

Qiu, Z., Lu, J., Ebeido, A., Elgamal, A., Uang, C. M. and Martin, G. (In preparation). "Bridge in Narrow Canyon: Seismic Response and Liquefaction-induced Deformations."

Qiu, Z., Elgamal., A. and Ebeido, A. (In preparation). "Arch Bridge Configuration for Mitigation of Liquefaction-Induced Lateral Deformations."

Elgamal, A., **Qiu, Z.** and Luo, L. (In preparation). "Liquefaction-Induced Excess Pore Pressure beyond Vertical Effective Stress and Potential Consequences."

Qiu, Z. and Elgamal, A. (In preparation). "Seismic Response of a Sheet-Pile Retaining Structure Supporting Liquefiable Soils: Numerical Simulations of LEAP Centrifuge Tests."

Qiu, Z. and Elgamal, A. (In preparation). "Canyon Effects on Seismically-Induced Liquefaction and Lateral Deformations."

Abstract of the Dissertation

Computational Modeling of Ground-Bridge Seismic Response and Liquefaction Scenarios

by

Zhijian Qiu

Doctor of Philosophy in Structural Engineering

University of California San Diego, 2020

Professor Ahmed Elgamal, Chair

Considerable bridge-ground interaction effects are involved in evaluating the consequences of liquefaction-induced deformations. Due to seismic excitation, liquefied soil layers may result in substantial accumulated permanent deformation of sloping ground near the abutments. Ultimately, global response is dictated by the bridge-ground interaction as an integral system. Generally, a holistic assessment of such response requires a highly demanding full three-

dimensional (3D) Finite Element (FE) model of the bridge and surrounding ground. As such, in order to capture a number of the salient involved mechanisms, this study focuses on the liquefaction-induced seismic response of integral bridge-ground systems motivated by details of actual existing bridge-ground configurations. In these 3D FE models, realistic multi-layer soil profiles are considered with interbedded liquefiable/non-liquefiable strata. Effect of the resulting liquefaction-induced ground deformation is explored. Attention is given to overall deformation of the bridge structure due to lateral spreading in the vicinity of the abutments. The derived insights indicate a need for such global analysis techniques, when addressing the potential hazard of liquefaction and its consequences.

In order to reproduce the salient response characteristics of soils, three plasticity constitutive models were developed and implemented into the employed computational framework OpenSees including: (1) A pressure-dependent sand model with the Lade-Duncan failure criterion as the yield function to provide a more accurate representation of shear response for gravel, sand and silt, incorporating liquefaction effects, (2) A 3D model for simulating the strain softening behavior of soil materials such as sensitive clays, cemented, over-consolidated, very dense, or frozen soils among others, and (3) A practical 3D model for simulating the cyclic softening behavior of soil materials, as might emanate from pore-pressure build-up, among other stiffness and strength degradation mechanisms.

An opportunity to investigate liquefaction-induced lateral spreading and its effects on sheet pile was permitted by availability of large sets of experimental data. The underlying mechanisms of ground failure and damage to sheet pile were further explored by FE numerical simulations of a series of experiments as follows: (1) A total of 17 centrifuge tests on a liquefiable sloping ground, and (2) A total of 11 centrifuge tests on a sheet pile retaining wall system supporting liquefiable

soils. The overall measurements were reasonably captured by the conducted FE simulations, demonstrating that the employed constitutive models as well as the overall computational framework have the potential to realistically evaluate the performance of ground-structure systems when subjected to seismically-induced liquefaction.

Overall, the primary findings may be summarized as: (1) Response is highly dependent on the bridge-ground system as an integral global entity. Connectivity provided by the bridge deck, soil profile variability along the bridge length, and geometric configuration of the slopes are all factors that can significantly influence the outcome, (2) The bridge structure and its foundations may exert a significant restraining effect on lateral ground deformations. Such restraining effects partially stem from the bridge-ground global connectivity characteristics, which can be of considerable influence, (3) Incorporation of strain softening where applicable, is an important consideration for a wide range of ground scenarios involving sensitive clays, cemented, over-consolidated, very dense, or frozen soils among others, and (4) Strength and stiffness degradation due to strain softening mechanisms might play a substantial role in terms of accumulated deformations and its effect on the resulting ground acceleration and extent of permanent displacement.

Chapter 1. Introduction and Literature Review

1.1. OpenSees UC San Diego Computational Modeling of Ground-Structure Systems: A Brief Overview

With the recent developments in material modeling techniques and high-speed computing, three-dimensional (3D) nonlinear Finite Element (FE) simulations are becoming increasingly feasible for geotechnical earthquake engineering applications (Elgamal et al. 2008; Kwon and Elnashai 2008; Asgari et al. 2013; Torabi and Rayhani 2014; McGann and Arduino 2014, 2015; Rayamajhi et al. 2013, 2016a, b; Su et al. 2017; Qiu et al. 2019, 2020). Calibration, on the basis of data from field case histories as well as centrifuge and shake table experiments, is gradually allowing for more accurate computational modeling efforts (e.g., Lu et al. 2011; Chang et al. 2013; Karimi and Dashti 2015, 2016; He et al. 2017; Su et al. 2018). As such, calibrated FE simulations are increasingly providing a reliable environment for modeling geotechnical earthquake problems, such as soil liquefaction, soil-structure interaction (SSI), and ground modification.

Particularly suited to seismic applications, the open-source computational platform OpenSees (Mazzoni et al. 2009; McKenna 2011) provides such 3D simulation capabilities. Implemented in OpenSees (Yang 2000; Yang and Elgamal 2002) is an analysis framework for saturated soil response as a two-phase material following the *u-p* formulation of Chan (1988) and Zienkiewicz et al. (1990), where *u* is displacement of the soil skeleton, and *p* is pore pressure. As such, the soil domain (in 3D) is represented by effective-stress solid-fluid fully coupled brick elements (Parra 1996; Yang 2000; Lu 2006; Yang et al. 2008) to describe the solid translational degrees of freedom (DOFs) and the fluid pressure (e.g., OpenSees 20_8_BrickUP element, brickUP and bbarBrickUP elements).

The OpenSees framework also includes a number of pressure-independent and pressure-dependent soil constitutive models (Parra 1996; Yang and Elgamal 2002; Elgamal et al. 2003; Yang et al. 2003; Yang et al. 2008), developed based on the multi-surface-plasticity theory (Mroz 1967; Iwan 1967; Prevost 1977, 1978, 1985). The pressure-independent models (Elgamal 2008; Yang et al. 2008; Lu et al. 2011) simulate the nonlinear cyclic hysteresis material response (e.g., undrained clay-type loading conditions). The pressure-dependent material models (typically used with the above mentioned solid-fluid fully coupled brick elements) mainly aim at simulating the liquefaction-induced shear strain accumulation mechanism in cohesionless soils (Yang and Elgamal 2002; Elgamal et al. 2003; Yang et al. 2003, 2008). Currently, the above modeling tools have been used by researchers worldwide in numerous reported studies (e.g., Elgamal et al. 2008, 2009; Zhang et al. 2008; Kwon and Elnashai 2008; Aygün et al. 2009, 2010; Ilankatharan and Kutter 2008, 2010; Atik and Sitar 2010; Lu et al. 2011; Asgari et al. 2013; Chang et al. 2013; Torabi and Rayhani 2014; McGann and Arduino 2014, 2015; Hashash et al. 2015; Tang et al. 2015; Rayamajhi et al. 2013, 2016a, b; Karimi and Dashti 2015, 2016; He et al. 2017; Su et al. 2017, 2018; Qiu et al. 2019, 2020).

In order to facilitate the OpenSees analysis pre- and post-processing phases, the graphical user interfaces OpenSeesPL (Lu et al. 2006; Elgamal and Lu 2009), BridgePBEE (Mackie et al. 2012) and MSBridge (Elgamal et al. 2014) were developed and employed. OpenSeesPL allows for execution of push-over and seismic SSI pile-ground simulations (Lu et al. 2006; Elgamal and Lu 2009). In addition, various ground modification scenarios may be studied in OpenSeesPL by appropriate specification of the material within the pile zone. BridgePBEE is a user-interface for conducting performance-based earthquake engineering (PBEE) studies for 2-span single-column bridge-ground systems (Mackie et al. 2012). MSBridge focuses on efficiently conducting

nonlinear FE studies for a wide range of multi-span bridge systems (Elgamal et al. 2014), with a recently added PBEE analysis option (Elgamal et al. 2017; Almutairi et al. 2018).

Overall, the earlier studies (as mentioned above) aim to illustrate the potential for further reliance on computer simulation in the assessment of nonlinear SSI response. Challenges in calibration and in high fidelity modeling are being gradually overcome. With careful attention to the involved modeling details, effective insights may be gleaned for a wide range of practical applications.

1.2. Soil Liquefaction and Its Consequences

Soil liquefaction (Figure 1.1) occurs when a saturated granular soil substantially loses strength and stiffness and becomes easier to deform (National Academies of Sciences, Engineering, and Medicine, 2016). Large regions of the United States are highly susceptible to strong earthquake shaking (Figure 1.2) that can cause liquefaction when saturated soils are present. Consequences of liquefaction include: 1) Sand boils, 2) Settlements, 3) Loss of lateral support, 4) Loss of bearing capacity, 5) Flotation of light structures, 6) Increased lateral pressures against retaining structures, 7) Lateral spreading of soils, and 8) Lateral flows (National Academies of Sciences, Engineering, and Medicine, 2016).

1.3. Case Histories of Spreading-Induced Damage to Bridge Foundations

Large bridge overcrossings with high ground water table are particularly vulnerable to liquefaction-induced lateral spreading and loss of pile foundation capacity (Youd 1993; Hamada et al. 1996; Tokimatsu and Asaka 1998; Berrill et al. 2001). Damage to such bridges has been observed in a large number of reconnaissance investigations, including the Llacolén Bridge (Figure 1.3) during 2010 Maule earthquake of Chile (Arduino et al. 2010; Bray and Frost 2010; Verdugo 2012; Ledezma et al. 2012), the San Felipito Bridges (Figure 1.4) during 2010 El Mayor-Cucapah

earthquake of Mexico (Turner et al. 2013, 2016), and the South Brighton Bridge (Figure 1.5) during the 2010-2011 Canterbury earthquakes (Cubrinovski et al. 2011, 2014; Wotherspoon et al 2011).

1.4. One-g Shake Table Tests: Liquefaction and Pile Response

Physical modelling (1-g) shake table tests using rigid (Tokida et al. 1970; Hamada 2000) and laminar containers (Tokimatsu and Suzuki 2004; Cubrinovski et al. 2006; He et al. 2009; Chang and Hutchinson 2013; Motamed et al. 2013) provided insight and increased our understanding of the mechanisms of pile response due to liquefaction and lateral spreading. More recently, Ebeido et al. 2019 investigated the pile and pile-group response to liquefaction-induced lateral spreading in four large-scale 1-g shake-table experiments (Figure 1.6).

1.5. Numerical Analysis of Bridge-Ground Systems

Investigators have been increasingly studying the entire bridge and the surrounding ground response within an integral framework. Different approaches to the representation of ground response at the location of each bridge bent, and effects on the entire bridge were presented (Boulanger et al. 2007; Ashford et al. 2009, 2011; Aygün et al. 2009; Ledezma and Bray 2010; Padgett et al. 2013; Turner et al. 2013, 2016; Cubrinovski et al. 2014; Wang et al. 2013a, b; McGann and Arduino 2015; Ghofrani et al. 2016; Soltanieh et al. 2019). Aygün et al. 2011 presents a relatively simple approach for analysis of coupled bridge-soil-foundation systems that combines nonlinear FE models of a three-dimensional bridge system with a 2D soil domain via a set of *p-y* curves (Figure 1.7).

Alternatively, using two-dimensional (2D) plane-strain FE continuum models to represent the ground and canyon configuration, the bridge model and its foundations were idealized and connected to the ground using soil spring formulations (Bowers 2007; Zhang et al. 2008; Kwon et

al. 2009). Shin et al. 2007, 2008 performed the global seismic analysis of a typical highway bridge subjected to liquefaction-induced lateral spreading (Figure 1.8).

Results of these studies show that consideration of the entire bridge-ground system provides a more realistic distribution of force and displacement demands. As such, it is indicated that global analysis is paramount in realistically evaluating the performance of liquefaction-induced lateral spreading and its consequences (Qiu et al. 2020).

1.6. Research Objectives

To increase our understanding of liquefaction-induced seismic response of integral bridge-ground systems, this dissertation provides a wide range of studies about soil constitutive modeling and calibration by experiments, and computational simulation of large-scale bridge-ground systems during liquefaction. Main objectives of this research are summarized as follows:

1. Implementation in OpenSees of a 3D multi-surface cyclic plasticity sand model with Lode Angle effect to reproduce salient characteristics of laboratory sample test data.

2. Development of a 3D multi-surface plasticity model for simulating the strain softening behavior of soil materials such as sensitive clays, cemented soils, over-consolidated clays, very dense sands, and frozen soils among others.

3. Development of a practical 3D plasticity model for simulating the cyclic softening behavior of soil materials, as might emanate from pore-pressure build-up, among other stiffness and strength degradation mechanisms.

4. Calibrations of 2D FE models using a series of LEAP centrifuge tests on a liquefiable sloping ground and a sheet-pile retaining wall supporting liquefiable soils.

5. Development of full 3D FE models to investigate a number of salient features associated with liquefaction-induced seismic response of integral bridge-ground systems including multi-

span bridges, short-span bridges in narrow canyon, and a newly proposed arch bridge configuration.

6. Development of 2D FE plane strain simulations to investigate liquefaction-induced canyon effects on the resulting seismic response and corresponding slope deformations.

7. Implementation of the 3D plasticity strain-softening model into a large deformation framework (RKPM2D) to study the earthquake-induced deformation of a simple idealized earth dam configuration.

1.7. Outline

This dissertation consists of 13 chapters, organized as follow:

- *Chapter 1: Introduction and Literature Review*. This chapter gives a brief overview of the motivation behind the research program and a brief summary of earlier related work.
- *Chapter 2: Pressure-Dependent Multi-surface Plasticity Models Incorporating Liquefaction Effects.* This chapter presents brief descriptions of the OpenSees UC San Diego pressure-dependent multi-surface models, including PressureDependMultiYield02, PressureDependMultiYield03, and LadeDuncanMultiYield.
- *Chapter 3: Three-Dimensional Modeling of Strain-Softening Soil Response for Seismic-Loading Applications.* This chapter presents a new 3D incremental plasticity constitutive model for simulating the strain softening behavior of soil materials including sensitive clays, cemented soils, over-consolidated clays, very dense sands, and frozen soils among others.
- *Chapter 4: Numerical Simulations of LEAP Centrifuge Tests for Seismic Response of Liquefiable Sloping Ground.* This chapter presents numerical simulations of a liquefiable sloping ground related to LEAP-UCD-2017 and LEAP-Asia-2019 dynamic centrifuge tests

(Kutter et al. 2018b; Ueda 2018).

- *Chapter 5: Seismic Response of a Sheet-Pile Retaining Structure Supporting Liquefiable Soils: Numerical Simulations of LEAP Centrifuge Tests.* This chapter presents numerical simulations of a sheet-pile retaining structure under liquefaction-induced lateral loading related to LEAP-2020 dynamic centrifuge tests (Zeghal et al. 2019).
- *Chapter 6: Aspects of Bridge-Ground Seismic Response and Liquefaction-Induced Deformations.* This chapter focuses on the longitudinal seismic performance of an idealized bridge-ground configuration, motivated by details of an existing multi-span bridge-ground system, in order to capture a number of the salient involved mechanisms. A realistic multi-layer soil profile is considered with interbedded liquefiable/non-liquefiable strata. Effect of the resulting liquefaction-induced ground deformation is explored. Attention is given to overall deformation of the bridge structure due to lateral spreading in the vicinity of the abutments.
- *Chapter 7: Three-Dimensional Bridge-ground Liquefaction-induced Deformations.* This chapter extends the work presented in chapter 6, with a full 3D FE analysis. Similarities and differences in the results of these two chapters are highlighted.
- *Chapter 8: Bridge in Narrow Canyon: Seismic Response and Liquefaction-Induced Deformations.* This chapter investigates longitudinal seismic performance of an overall short-span bridge-ground system. Of particular interest is the scenario of narrow canyons where interaction between lateral deformations at both ends of the bridge plays a major role.
- *Chapter 9: Arch Bridge Configuration for Mitigation of Liquefaction-Induced Lateral Deformations.* This chapter proposes an arch bridge configuration as a structural system to

mitigate the consequences of potential liquefaction-induced lateral deformations. Where applicable in terms of the underlying canyon geometry, such a configuration might offer beneficial outcomes as discussed in this study. For that purpose, a full 3D FE computational simulation is conducted to highlight these benefits.

- *Chapter 10: Liquefaction-Induced Canyon Effects on Seismic Response of Sloping Ground.* This chapter investigates the liquefaction-induced canyon effects in terms of the involved mechanisms and their consequences. For reference, the presented results are compared with those obtained from the corresponding traditional one-dimensional soil column representation.
- *Chapter 11: Liquefaction-Induced Excess Pore Pressure beyond Vertical Effective Stress and Potential Consequences.* This chapter discusses a potential mechanism of liquefaction-induced excess pore pressure that can far exceed the initial effective vertical stress, referred to herein as super-liquefaction. The mechanism is presented, along with representative idealized experimental and numerical simulations.
- *Chapter 12: Meshfree Framework for Seismic Response of Earth Systems.* This chapter makes an effort to bring the capabilities and advantages of the meshfree method within a dedicated open-source framework RKPM2D (Huang et al. 2019) for use in earthquake engineering applications. For illustration, initial results of an idealized earth embankment configuration subjected to seismic loading are presented and discussed.
- *Chapter 13: Summary and Conclusions*. This chapter summarizes the main contributions and findings from the research reported herein. Areas of potential future research are discussed as well.

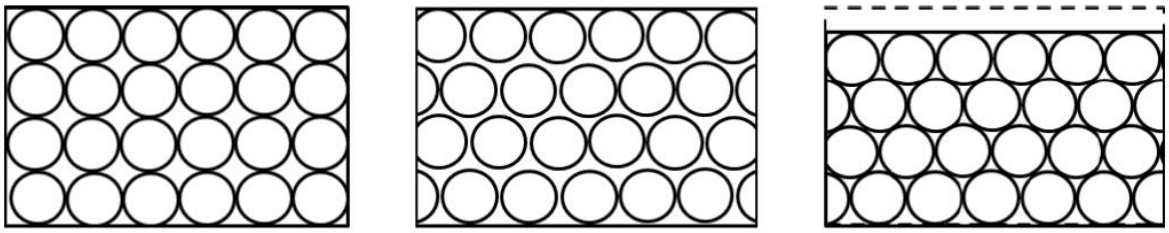

Figure 1.1 Soil liquefaction mechanism (National Academies of Sciences, Engineering, and Medicine, 2016)

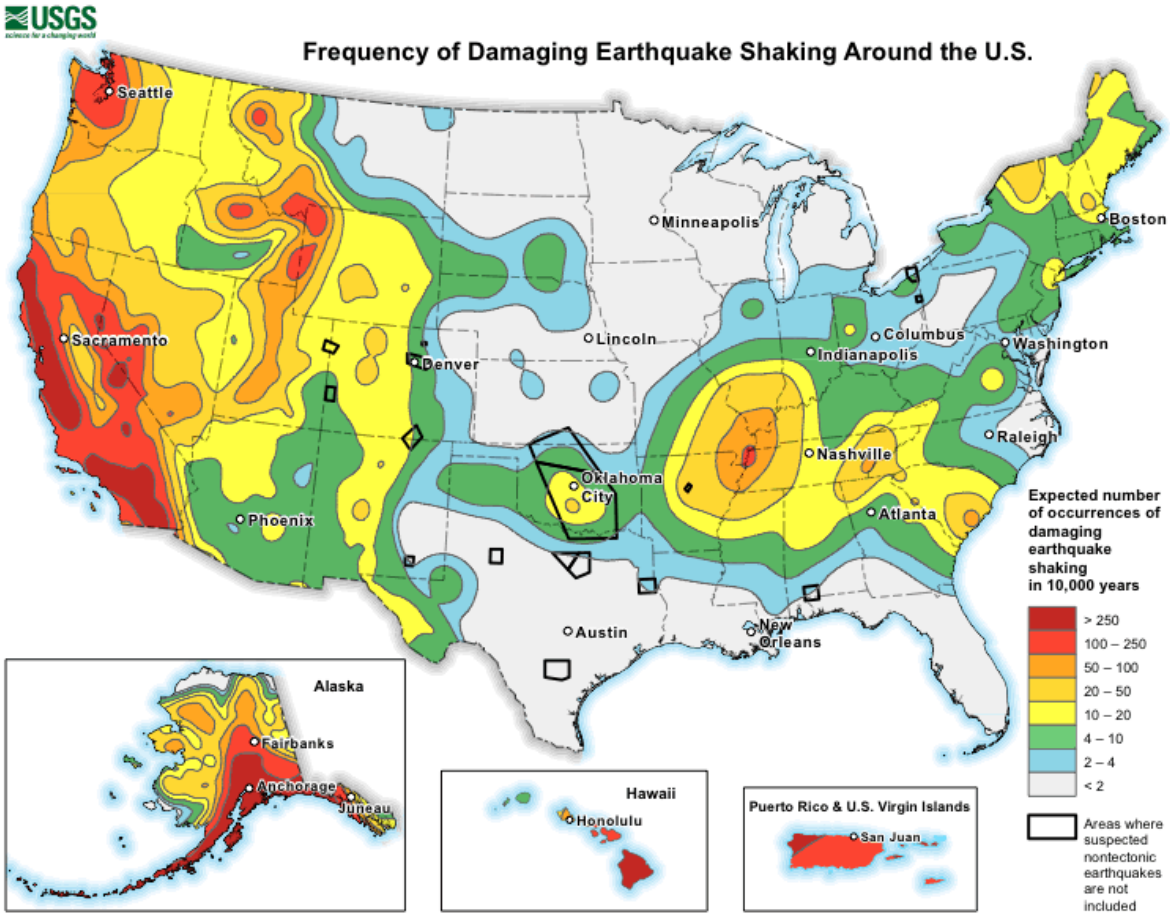

Figure 1.2 Vulnerable locations in the US (USGS, https://www.usgs.gov/media/images/frequency-damaging-earthquake-shaking-around-us)

(a)

(b)

Figure 1.3 The Llacolén Bridge during 2010 Maule earthquake of Chile: (a) Damaged region; (b) Deck unseating due to lateral spreading (after Ledezma et al. 2012)

Figure 1.4 The San Felipito Bridges during 2010 El Mayor-Cucapah earthquake of Mexico (after Turner et al. 2013, 2016)

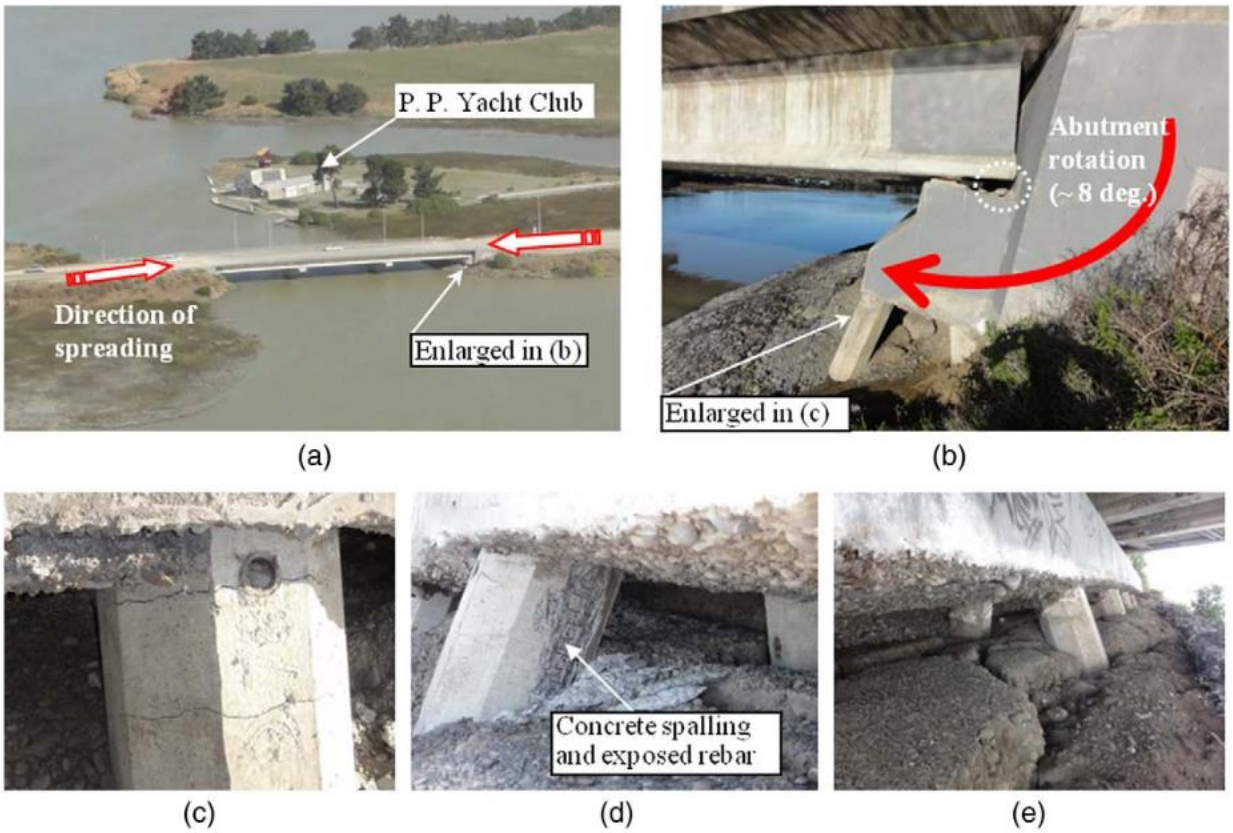

Figure 1.5 The South Brighton Bridge during 2011 Christchurch earthquake of New Zealand (after Cubrinovski et al. 2011, 2014)

(a)

(b)

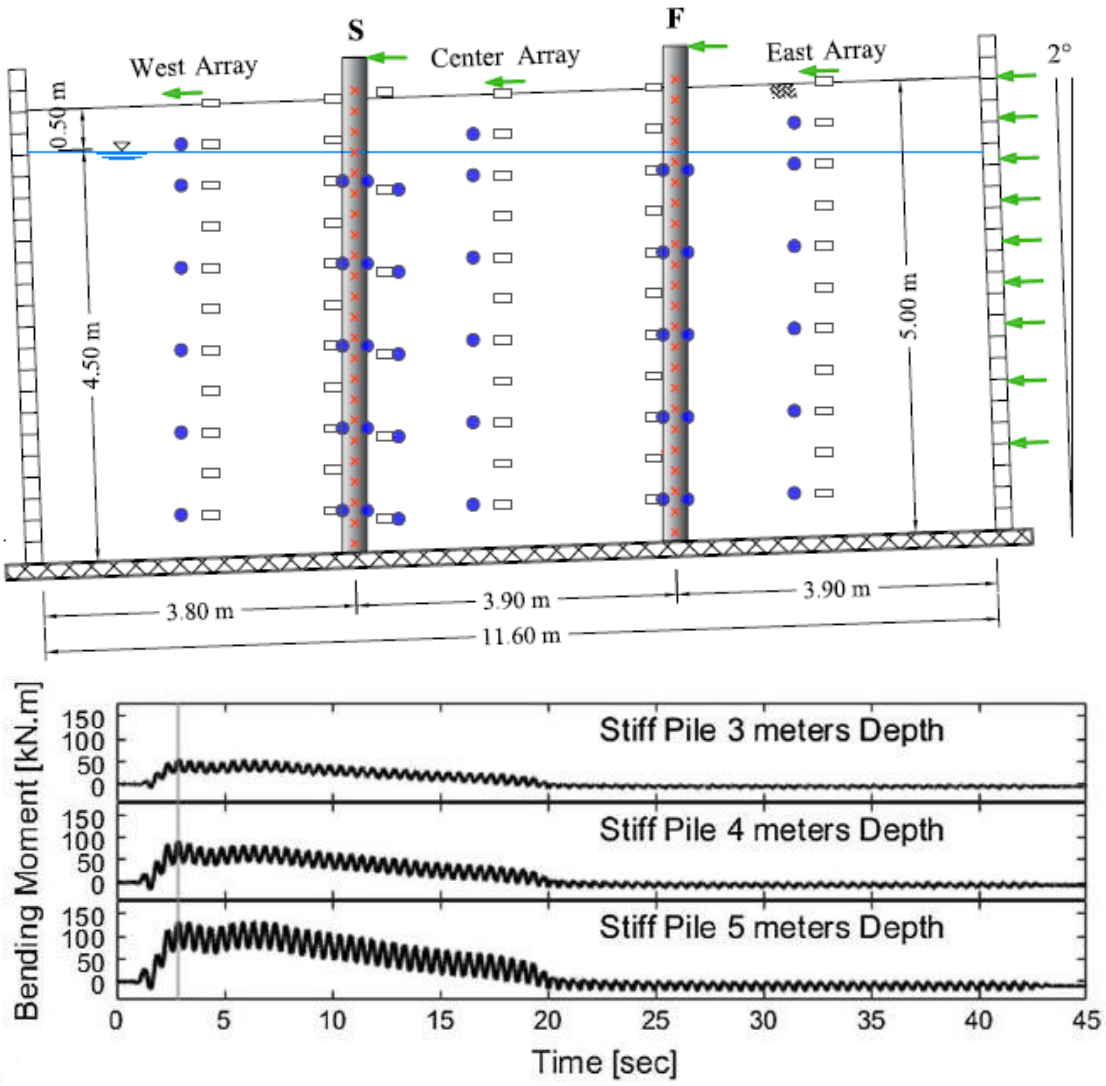

Figure 1.6 Large laminar-box shaking table experiment: (a) Schematic representation; (b) Moment of stiff and flexible piles (after Ebeido et al. 2019)

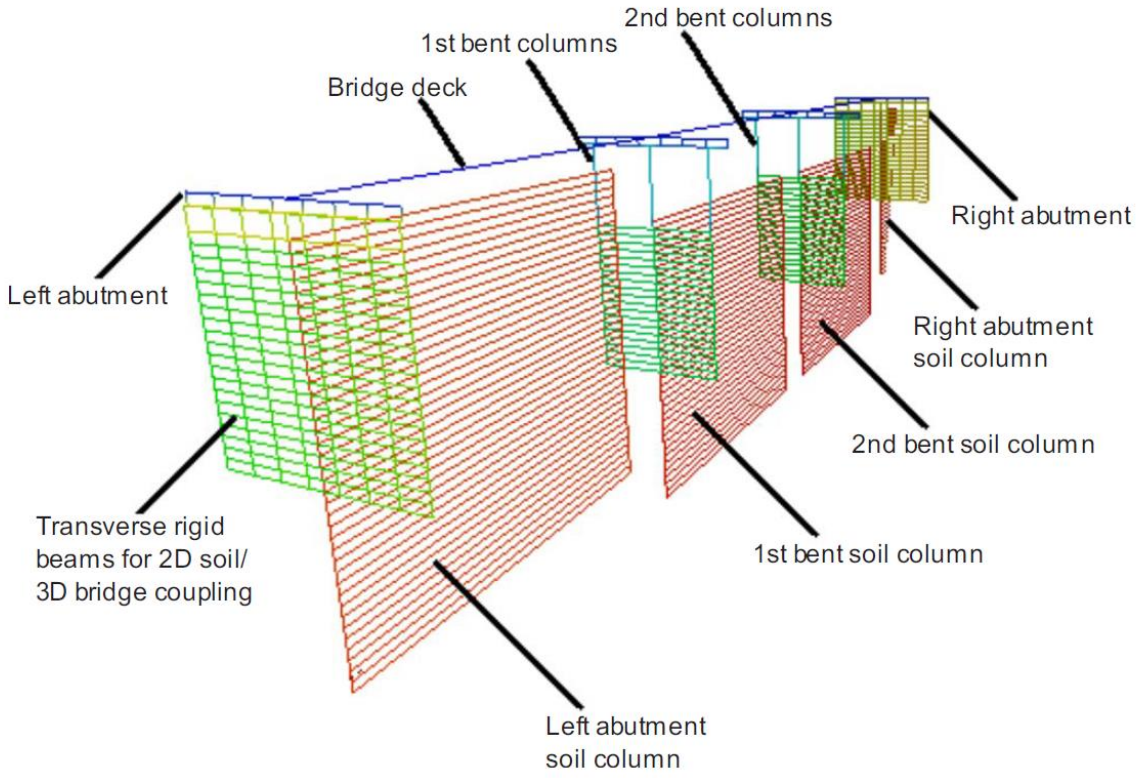

Figure 1.7 Coupled 3D bridge and 2D soil model with 1D *p-y* curves for 1D site response and liquefaction simulation (after Aygün et al. 2011)

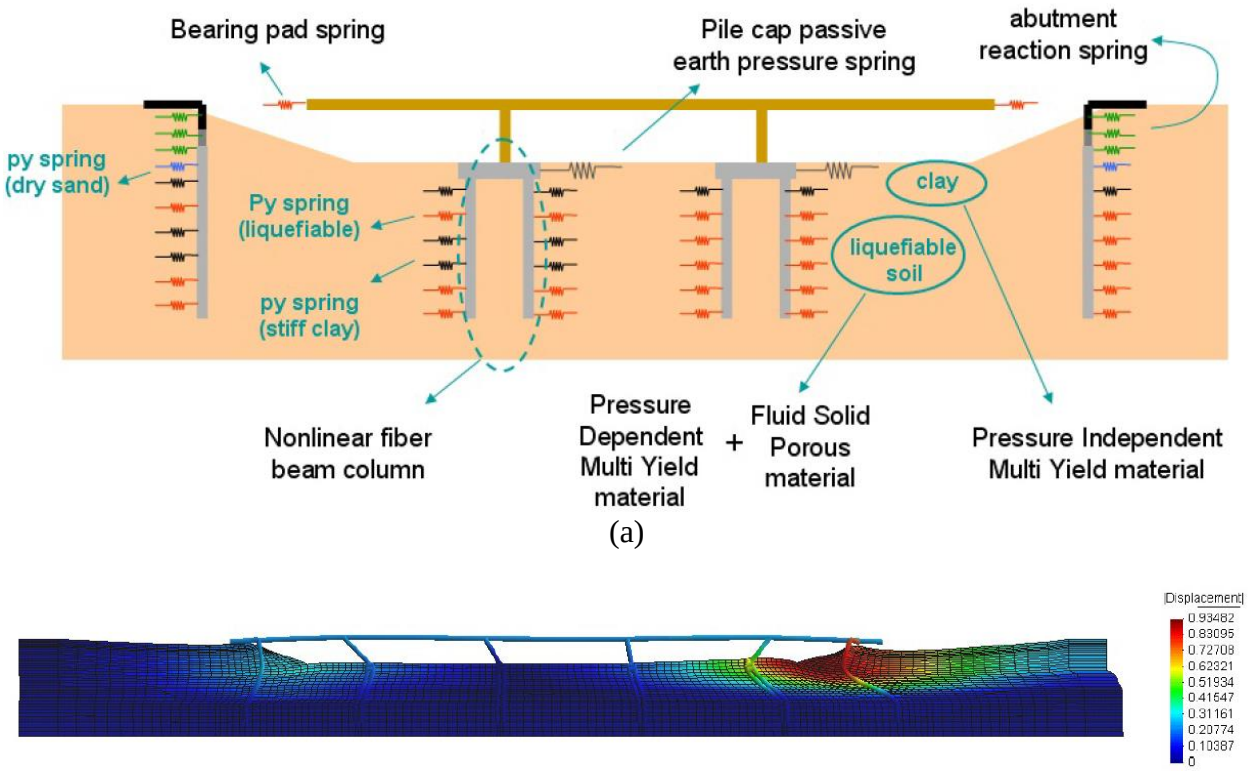

Figure 1.8 A typical highway bridge underlain by liquefiable soil susceptible to lateral spreading: (a) Modeling of soil-structure interaction in OpenSees; (b) Deformed FE mesh (after Shin et al. 2007, 2008)

Chapter 2. UC San Diego Pressure-Dependent Multi-Surface Plasticity Models Incorporating Liquefaction Effects

2.1. Introduction

These pressure-dependent soil constitutive models were developed based on the multi-surface plasticity theory (Parra 1996; Yang 2000; Yang and Elgamal 2002; Elgamal et al. 2003; Yang et al. 2003; Khosravifar et al. 2018). In these soil constitutive models, the shear-strain backbone curve may be simply represented by the hyperbolic relationship. The low-strain shear modulus is computed using the equation $G = G_0(p'/p'_r)^n$, where p' is effective confining pressure, p'_r is a reference effective confining pressure, and G_0 is shear modulus at p'_r. The dependency of shear modulus on confining pressure (n) is typically taken as 0.5. The constant M_f (failure surface size) relating deviator shear and confinement (triaxial compression scenario) is related to the friction angle φ (Chen and Mizuno 1990) as defined by $M_f = 6sin\varphi/(3 - sin\varphi)$. As such, soil is simulated by the implemented OpenSees materials PressureDependMultiYield (Parra 1996; Yang 2000; Yang and Elgamal 2002; Elgamal et al. 2003), PressureDependMultiYield02 (Yang et al. 2003), PressureDependMultiYield03 (Khosravifar et al. 2018), and LadeDuncanMultiYield (Yang and Elgamal 2008; Qiu et al. 2019).

2.2. PressureDependMultiYield02 Material

The PressureDependMultiYield02 material (Figure 2.1 and Figure 2.2) has mechanisms to simulate the dilatancy and cyclic mobility of pressure sensitive soils (Elgamal et al. 2003; Yang et al. 2003). Calibration was performed based on a series of laboratory and centrifuge tests, and the model parameters were provided for sands with different relative densities (Elgamal et al. 2003; Yang et al. 2003). Brief descriptions of this soil constitutive model are included below. A large

number of numerical studies employing the OpenSees PressureDependMultiYield02 material have been conducted for simulating large-scale seismic soil-structure interaction and liquefaction scenarios (Shin et al 2007, 2008; Zhang et al 2008; McGann and Arduino 2014, 2015; Karimi and Dashti 2015; He et al. 2017; Su et al. 2018).

2.2.1. Yield Function

The yield function is defined as a conical surface in principal stress space (Prevost 1985; Lacy 1986; Yang and Elgamal 2002):

$$f = \frac{3}{2}\left(\boldsymbol{s} - \left(p' + p'_0\right)\boldsymbol{a}\right) : \left(\boldsymbol{s} - \left(p' + p'_0\right)\boldsymbol{a}\right) - M^2\left(p' + p'_0\right)^2 = 0 \qquad (2\text{-}1)$$

where, $\boldsymbol{s} = \boldsymbol{\sigma}' - p'\boldsymbol{\delta}$, is the deviatoric stress tensor, $\boldsymbol{\sigma}'$ is the effective Cauchy stress tensor, $\boldsymbol{\delta}$ is the second-order identity tensor, p' is mean effective stress, p'_0 is a small positive constant (Figure 2.1) such that the yield surface size remains finite at $p' = 0$ for numerical convenience, $\boldsymbol{a}$ is a second-order deviatoric tensor defining the yield surface center in deviatoric stress subspace, *M* defines the yield surface size, and ":" denotes doubly contracted tensor product.

2.2.2. Contractive Phase

Shear-induced contraction occurs inside the phase transformation (PT) surface ($\eta < \eta_{PT}$), as well as outside ($\eta > \eta_{PT}$) when $\dot{\eta} < 0$, where, η is the stress ratio and η_{PT} is the stress ratio at phase transformation surface (Figure 2.2). The contraction flow rule is defined as:

$$P" = (1 - \frac{\dot{\boldsymbol{n}} : \dot{\boldsymbol{s}}}{||\dot{\boldsymbol{s}}||}\frac{\eta}{\eta_{PT}})^2(c_1 + c_2\gamma_c)(\frac{p'}{p_a})^{c_3} \qquad (2\text{-}2)$$

where c_1, c_2 and c_3 are non-negative calibration constants, γ_c is octahedral shear strain accumulated during previous dilation phases, p_a is atmospheric pressure for normalization purpose, and $\dot{\boldsymbol{s}}$ is the deviatoric stress rate. The $\dot{\boldsymbol{n}}$ and $\dot{\boldsymbol{s}}$ tensors are used to account for general 3D loading scenarios,

where, $\dot{\boldsymbol{n}}$ is the outer normal to a surface (Yang et al. 2003). The parameter c_3 is used to represent the dependence of pore pressure buildup on initial confinement (i.e., K_σ effect).

2.2.3. Dilative Phase

Dilation appears only due to shear loading outside the PT surface ($\eta > \eta_{PT}$ with $\dot{\eta} > 0$), and is defined as:

$$P'' = (1 - \frac{\dot{\boldsymbol{n}}:\dot{\boldsymbol{s}}}{||\dot{\boldsymbol{s}}||}\frac{\eta}{\eta_{PT}})^2(d_1 + (\gamma_d)^{d_2})(\frac{p'}{p_a})^{-d_3} \quad (2\text{-}3)$$

where d_1, d_2 and d_3 are non-negative calibration constants, and γ_d is the octahedral shear strain accumulated from the beginning of a particular dilation cycle (such as, stage 1-2 or 5-6 in Figure 2.2) as long as there is no significant load reversal. Subsequently, dilation rate increases as the shear strain accumulates in a particular cycle (Yang et al. 2003). Furthermore, a significant unloading (such as stage 6-8 in Figure 2.2) will reset γ_d to zero. Parameter d_3 in Equation (2-3), reflects the dependence of pore pressure buildup on initial confinement (i.e., K_σ effect).

2.2.4. Neutral Phase

When the stress state approaches the PT surface ($\eta = \eta_{PT}$) from below, a significant amount of permanent shear strain may accumulate prior to dilation, with minimal changes in shear stress and confinement (implying $P'' = 0$). For simplicity, $P'' = 0$ is maintained during this highly yielded phase until a boundary defined in deviatoric strain space is reached, and then dilation begins. This yield domain will enlarge or translate depending on load history. In deviatoric strain space, the yield domain (Figure 2.2) is a circle with the radius γ defined as (Yang et al. 2003):

$$\gamma = (\gamma_s + \gamma_{rv})/2$$

$$\gamma_s = y_1 \langle \frac{p'_{max} - p'_n}{p'_{max}} \rangle^{0.25} \int_0^t d\gamma_c \tag{2-4}$$

$$\gamma_{rv} = y_2 \langle \frac{p'_{max} - p'_n}{p'_{max}} \rangle^{0.25} oct(\boldsymbol{e} - \boldsymbol{e}_p)$$

where, y_1 (non-negative) is used to define the accumulated permanent shear strain γ_s as a function of dilation history $\int_0^t d\gamma_c$ and allow for continuing enlargement of the domain, p'_{max} is maximum mean effective confinement experienced during cyclic loading, p'_n is mean effective confinement at the beginning of current neutral phase, and $\langle\ \rangle$ denotes MacCauley's brackets (i.e., $\langle a \rangle = max\ (a, 0)$). The y_2 (non-negative) parameter is mainly used to define the biased accumulation of permanent shear strain γ_{rv} as a function of load reversal history and allows for translation of the yield domain during cyclic loading. In Equation (2-4), $oct(\boldsymbol{e} - \boldsymbol{e}_p)$ denotes the octahedral shear strain of tensor $\boldsymbol{e} - \boldsymbol{e}_p$, where $\boldsymbol{e}$ is current deviatoric shear strain, and $\boldsymbol{e}_p$ is pivot strain obtained from previous dilation on load reversal point.

2.3. PressureDependMultiYield03 Material

In order to more closely capture the established guidelines concerning triggering of liquefaction (Idriss and Boulanger 2008), the PressureDependMultiYield02 material has been recently updated (PressureDependMultiYield03 in Khosravifar et al. 2018). The model parameters were calibrated with established guidelines on the liquefaction triggering logic (Idriss and Boulanger 2008), i.e., cyclic stress ratio versus number of equivalent uniform loading cycles in undrained shear loading to cause single-amplitude shear strain of 3 % (Khosravifar et al. 2018). Figure 2.3 depicts the calibration results of PressureDependMultiYield03 for shear loading tests at a vertical consolidation stress of 1 atm and lateral earth pressure coefficients K_o = 0.5 (Figure

2.3a) and K_o = 1.0 (Figure 2.3b), along with those of the PM4Sand model (Boulanger and Ziotopoulou 2015) response for comparison.

2.4. LadeDuncanMultiYield Material

To allow for further accuracy in capturing 3D shear response, the OpenSees material PressureDependMultiYield03 has been extended to incorporate the Lode angle effect (Figure 2.4) by employing the Lade-Duncan failure criterion as the yield function (Lade and Duncan 1975; Yang and Elgamal 2008; Qiu et al. 2019). This failure criterion is represented by (Chen and Mizuno 1990):

$$J_3 - \frac{1}{3} I_1 J_2 + \left(\frac{1}{27} - \frac{1}{k_1}\right) I_1^3 = 0 \tag{2-5}$$

where, I_1 is volumetric stress, J_2 and J_3 are second and third deviatoric stress invariants, respectively, parameter k_1 (> 27) is related to soil shear strength (or friction angle ϕ). A typical yield surface f_m (Figure 2.4) is defined by Yang and Elgamal 2008:

$$f_m = \bar{J}_3 - \frac{1}{3}(\eta_m I_1)\bar{J}_2 + a_1(\eta_m I_1)^3 = 0 \tag{2-6}$$

where η_m is normalized yield surface size ($0 < \eta_m < 1$) and $a_1 = \frac{1}{27} - \frac{1}{k_1}$ (Yang and Elgamal 2008). In Equation (2-6), $\bar{J}_2 = \frac{1}{2}\bar{\boldsymbol{s}}:\bar{\boldsymbol{s}}$ and $\bar{J}_3 = \frac{1}{2}(\bar{\boldsymbol{s}}\cdot\bar{\boldsymbol{s}}):\bar{\boldsymbol{s}}$, where, $\bar{\boldsymbol{s}} = \boldsymbol{s} - p'\boldsymbol{\alpha}$ and $\boldsymbol{s} = \boldsymbol{\sigma} - p'\boldsymbol{\delta}$, $\boldsymbol{\delta}$ is the second-order identity tensor, $p' = \frac{1}{3}I_1$ is mean effective stress ($I_1 = 3p'$), deviatoric tensor $\boldsymbol{\alpha}$ is back stress (yield surface center), and the operators "·"and ":" denote single and double contraction of two tensors, respectively.

To more closely capture the established guidelines on the liquefaction triggering logic (Idriss and Boulanger 2008), the contraction rule of LadeDuncanMultiYield material is improved:

$$P"_{new} = b_1 \left(b_2 \left(\frac{\eta}{\eta_{PT}} - b_3 \right) \left(\frac{\eta}{\eta_{PT}} - b_3 \right) + b_4 \right) P'' \quad (2\text{-}7)$$

where, P'' is defined in Equation (2-2), and b_1, b_2, b_3, b_4 are non-negative calibration parameters. Figure 2.5 shows the cyclic stress ratio to trigger liquefaction versus the number of loading cycles in undrained cyclic shear simulations. The results are shown for sands with $(N_1)_{60}$ values of 5, 15 and 25 (corresponding to relative densities D_r = 35 %, 55 % and 75 %) under confining effective stress of 1 atm. The calibrated LadeDuncanMultiYield model parameters are listed in Table 2.1. Each curve in Figure 2.5 is fitted with a power function ($CSR = aN^{-b}$) and the b-value is shown ranging from 0.27 to 0.34.

For illustration, the LadeDuncanMultiYield material was calibrated using cyclic laboratory test data in which an Ottawa F-65 sand (Kutter et al. 2018b) was employed. Figure 2.6 displays the experimental (Kutter et al. 2018b) and computed results for a consolidated, stress-controlled undrained cyclic triaxial test. It can be seen that the soil gradually loses its effective confinement during cyclic triaxial loading, and the axial strain accumulates after liquefaction on a cycle-by-cycle basis (Figure 2.6) with a strong dilation tendency and associated regain in shear stiffness.

2.5. Summary and Conclusions

Pressure-dependent models implemented with the characteristics of dilatancy, cyclic mobility and associated shear deformation are presented, including PressureDependMultiYield02, PressureDependMultiYield03, and LadeDuncanMultiYield materials. To allow for further accuracy in capturing 3D shear response, the PressureDependMultiYield03 material employs the Lade-Duncan failure criterion (LadeDuncanMultiYield material) as the yield function. Salient features of the model performance are presented based on the calibration of laboratory undrained triaxial cyclic test data for Ottawa F-65 sand, where the yield function provides a more accurate representation of nonlinear shear response. Finally, in order to more closely capture the established

guidelines concerning triggering of liquefaction (Idriss and Boulanger 2008), the PressureDependMultiYield02 material (PressureDependMultiYield03 in Khosravifar et al. 2018) and the LadeDuncanMultiYield material have been recently updated (Qiu et al. 2019).

2.6. Acknowledgements

Chapter 2, in part, has been published as it appears in the following paper (The dissertation author was the primary investigator and author of this paper):

Qiu, Z., Lu, J., Elgamal, A., Su, L., Wang, N. and Almutairi, A. (2019). "OpenSees Three-Dimensional Computational Modeling of Ground-Structure Systems and Liquefaction Scenarios." Computer Modeling in Engineering & Sciences, 120(3), 629-656.

Table 2.1 LadeDuncanMultiYield model parameters (Khosravifar et al. 2018)

Sand Model Parameters		Loose	Medium	Dense
$(N_1)_{60}$		5	15	25
Relative density, D_r		35 %	55 %	75 %
Reference mean effective pressure, p'_r (kPa)		101	101	101
Mass density, ρ (t/m^3)		1.94	1.99	2.03
Maximum shear strain at reference pressure, $\gamma_{max,r}$		0.1	0.1	0.1
Shear modulus at reference pressure, G_r (MPa)		46.9	73.7	94.6
Stiffness dependence coefficient n, $G = G_r(\frac{P'}{P'_r})^n$		0.5	0.5	0.5
Poisson's ratio, v		0.33	0.33	0.33
Shear strength at zero confinement, c (kPa)		2	2	2
Friction angle ϕ, with resulting shear strength defined as $p'\sin\phi$		30°	35°	40°
Phase transformation angle, ϕ_{PT}		30°	28°	35°
Contraction coefficient, c_1		0.1	0.035	0.02
Contraction coefficient, c_2		5.0	3.0	3.0
Contraction coefficient, c_3		0.05	0.2	0.4
Dilation coefficient, d_1		0.1	0.15	0.2
Dilation coefficient, d_2		3.0	3.0	3.0
Dilation coefficient, d_3		0.05	0.2	0.4
y_1		1.0	1.0	1.0
y_2		0.0	0.0	0.0
Additional contraction parameters (calibration for K_0 = 1)	b_1	2.0	1.0	0.6
	b_2	30	30	20
	b_3	0.0	0.0	0.05
	b_4	0.001	0.001	0.001

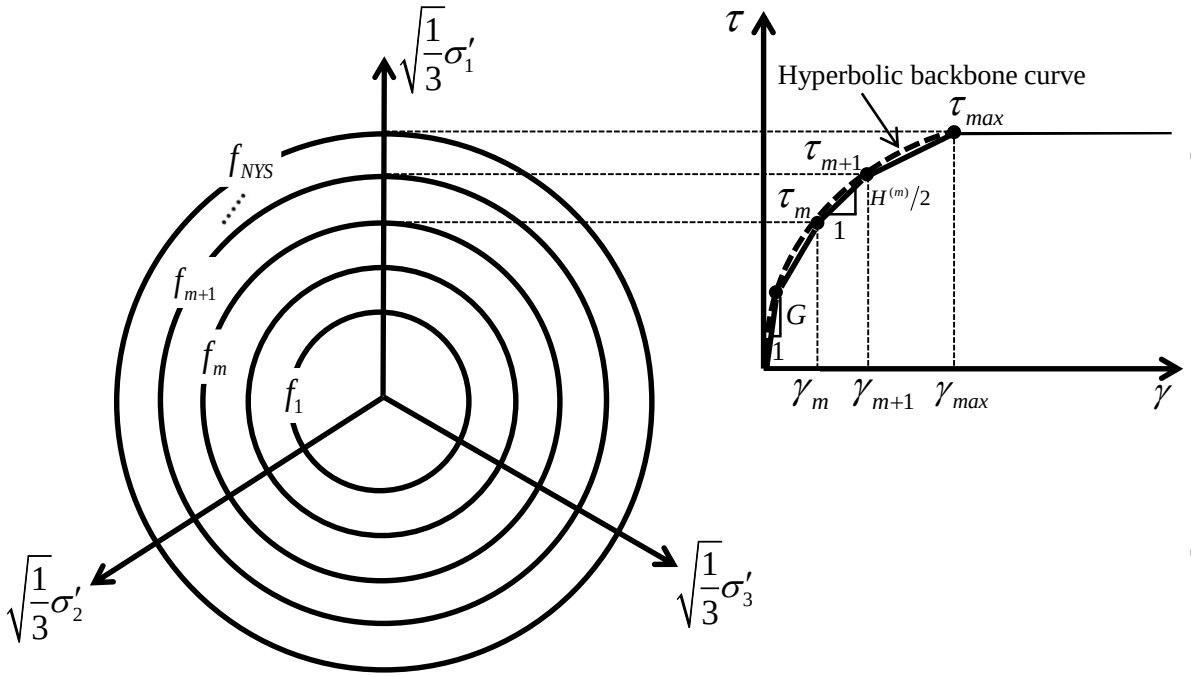

(a)

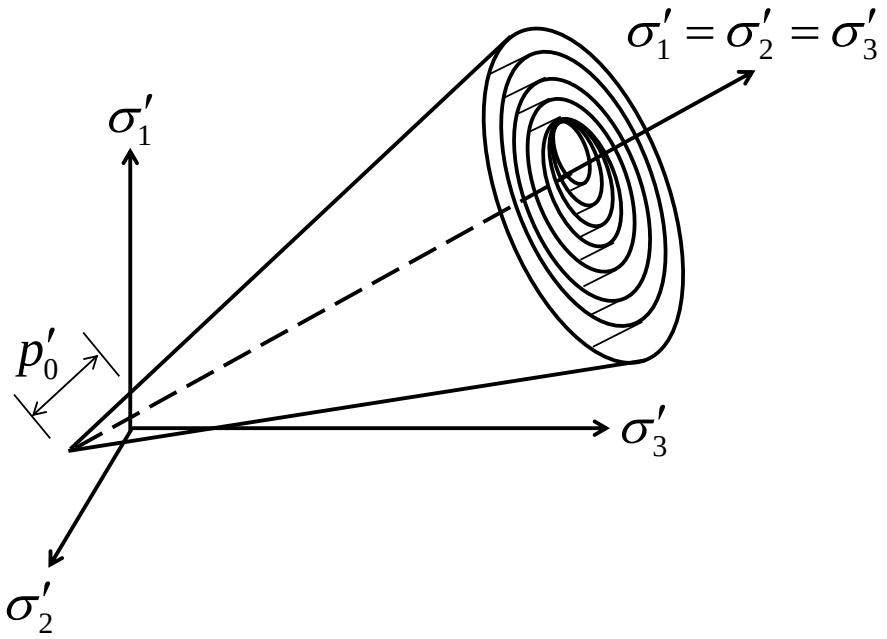

(b)

Figure 2.1 Pressure-dependent multi-surface plasticity model: (a) In deviatoric plane and octahedral shear stress and strain; (b) In stress space (after Yang et al. 2003)

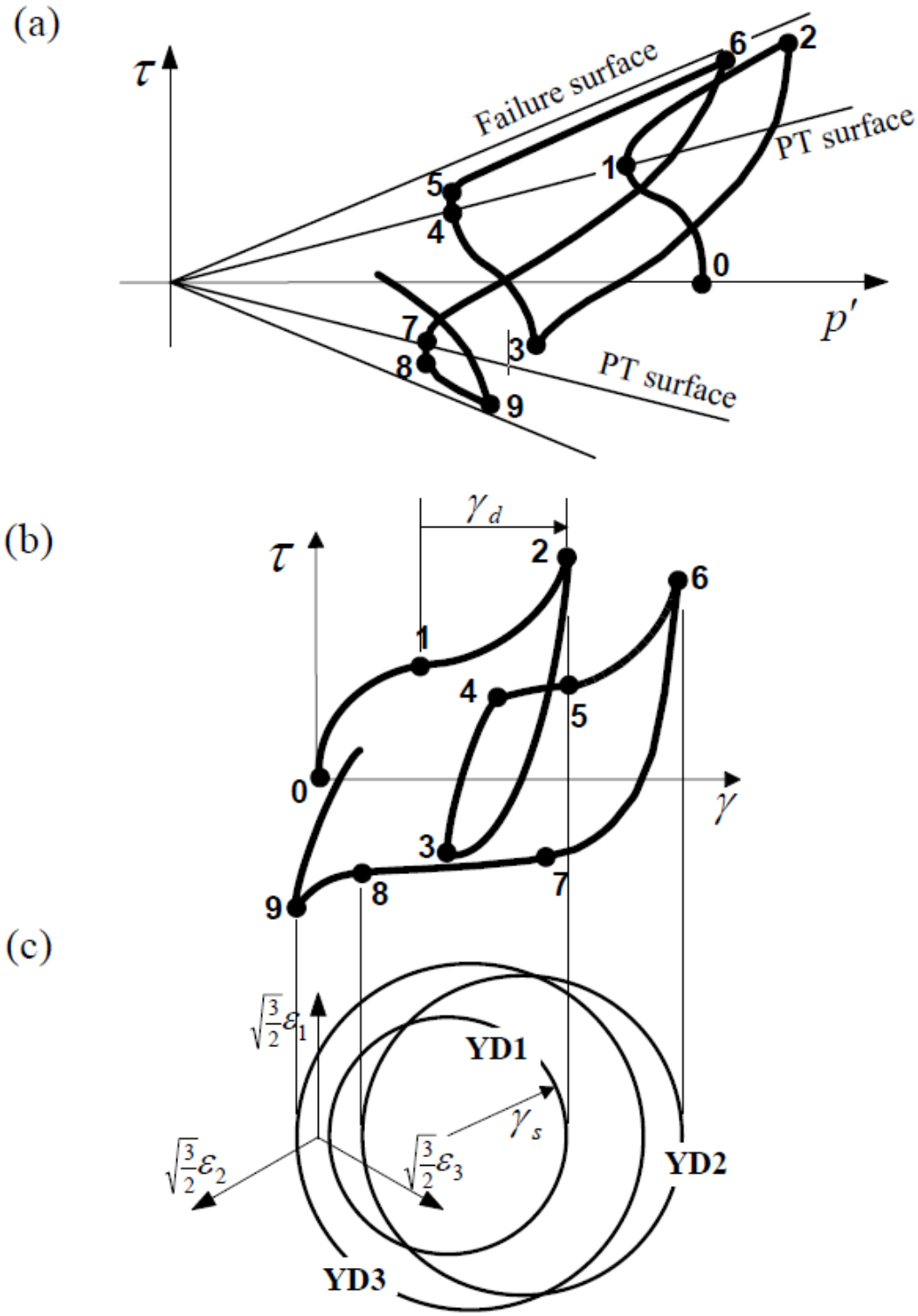

Figure 2.2 Schematic of constitutive model response: (a) Octahedral stress-effective confinement response; (b) Octahedral shear stress-strain response; (c) Configuration of yield domain (after Yang et al. 2003)

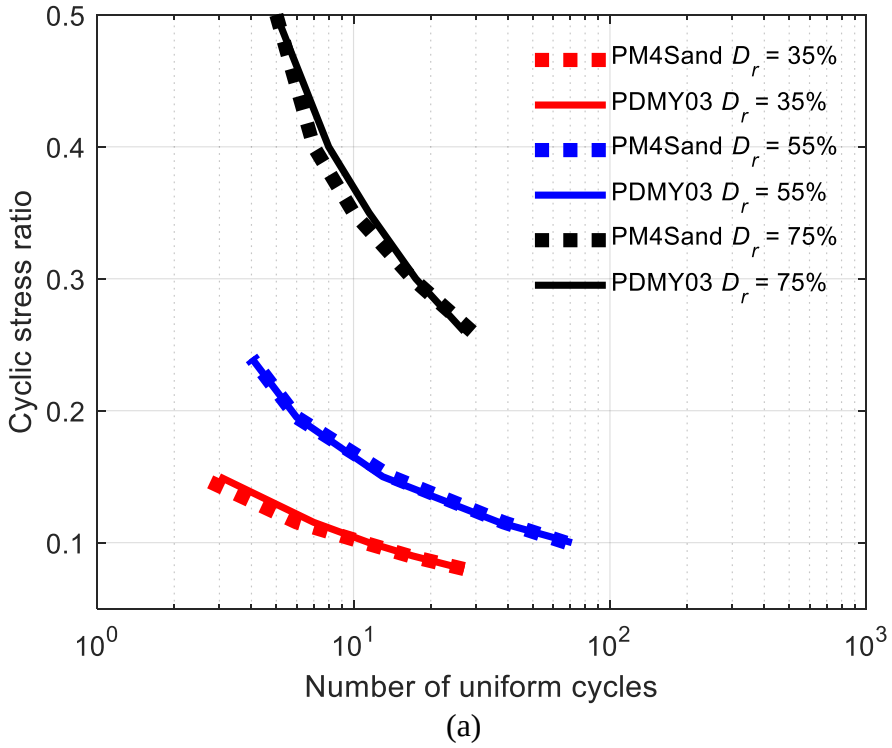

(a)

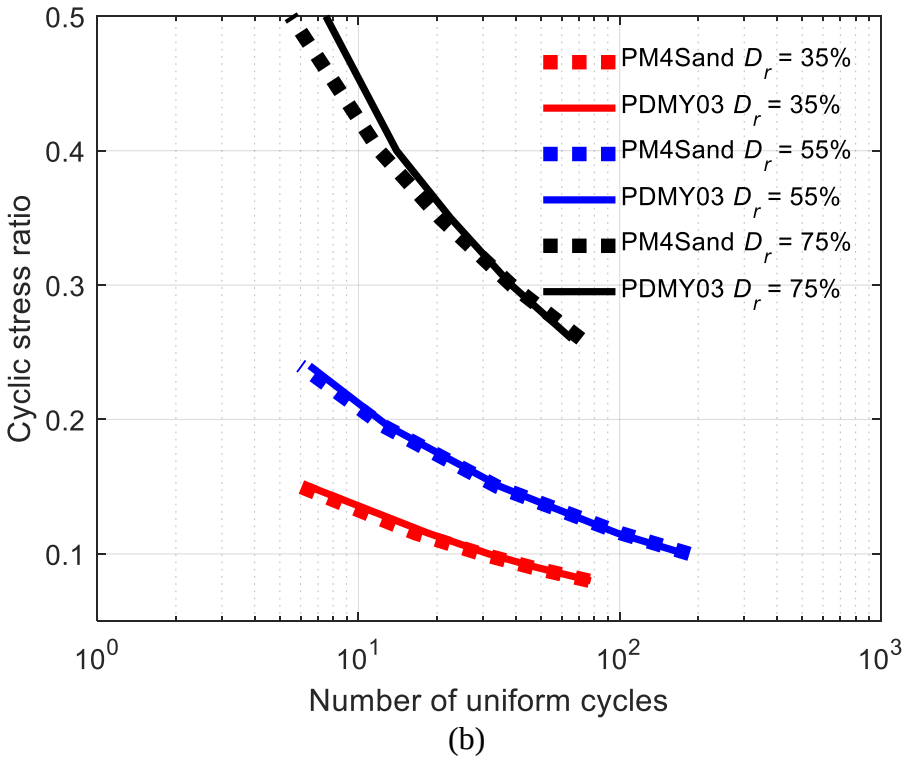

(b)

Figure 2.3 Calibration of PressureDependMultiYield03 material (after Khosravifar et al. 2018): (a) Lateral earth pressure coefficient K_o = 0.5; (b) K_o = 1.0

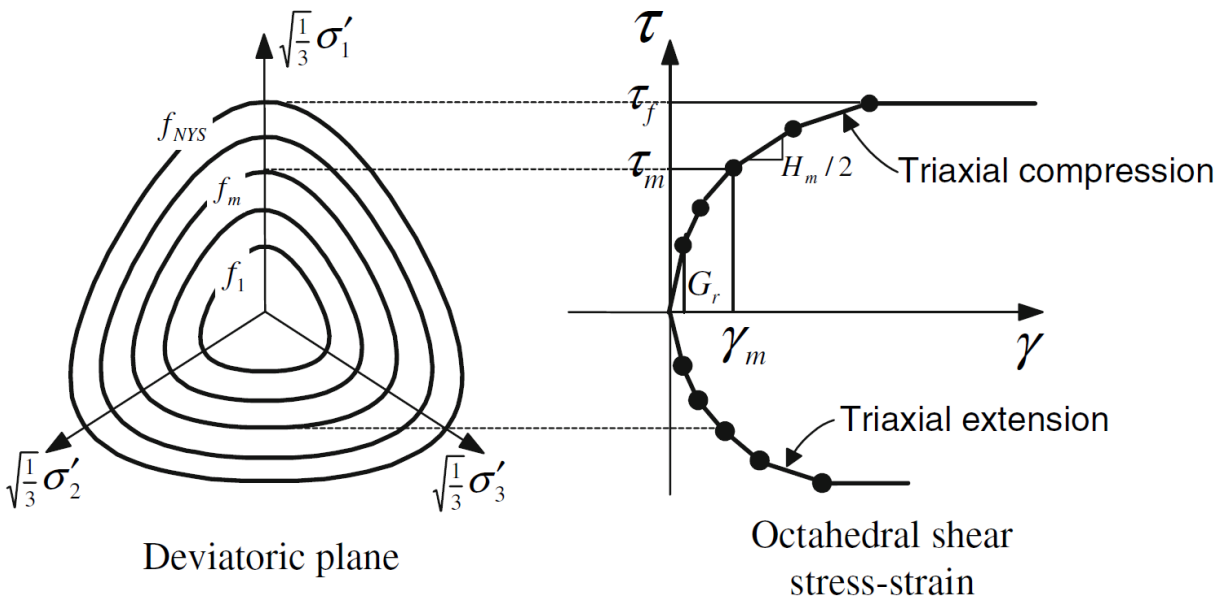

(a)

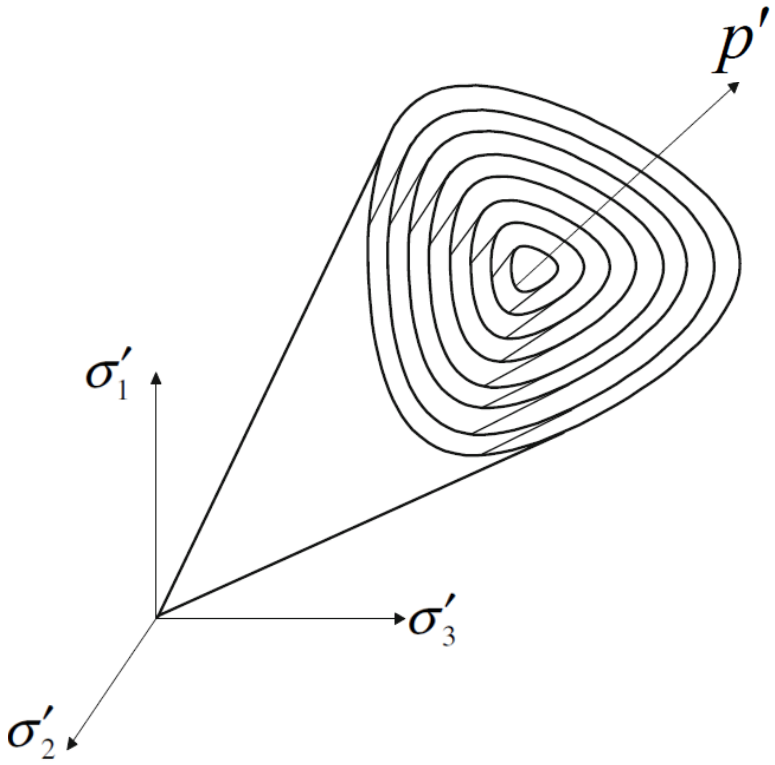

(b)

Figure 2.4 LadeDuncanMultiYield model: (a) In deviatoric plane and octahedral shear stress and strain; (b) In stress space (after Yang and Elgamal 2008)

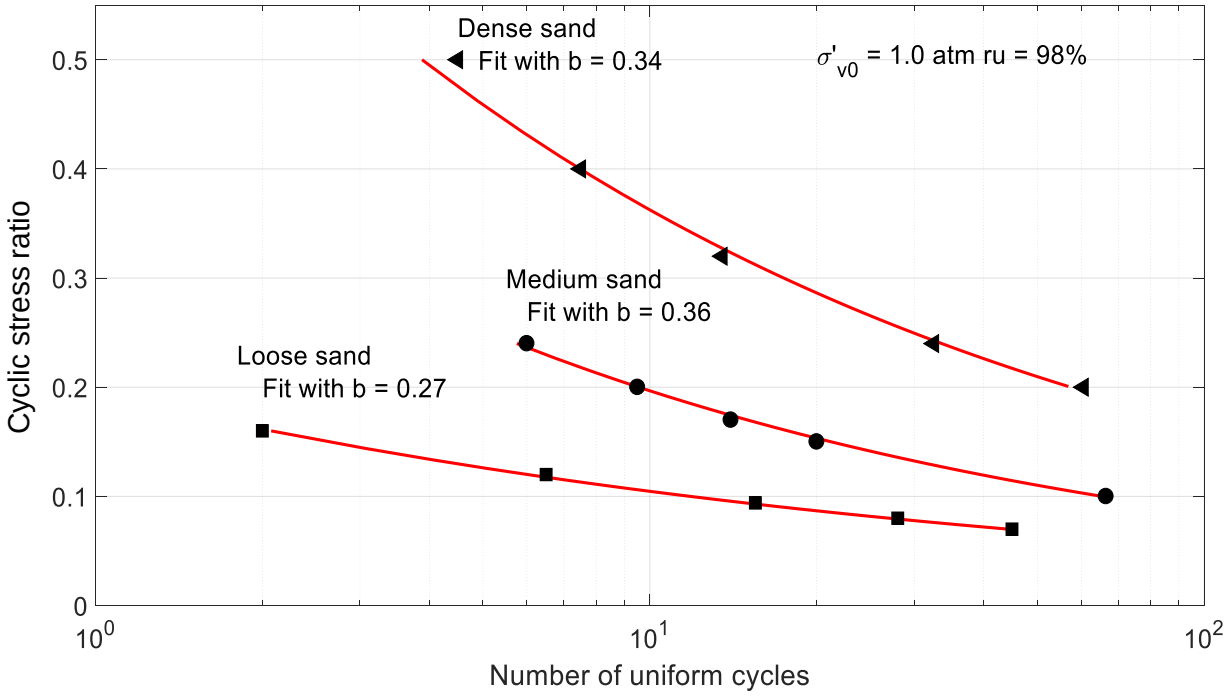

Figure 2.5 Cyclic stress ratios versus number of equivalent uniform loading cycles

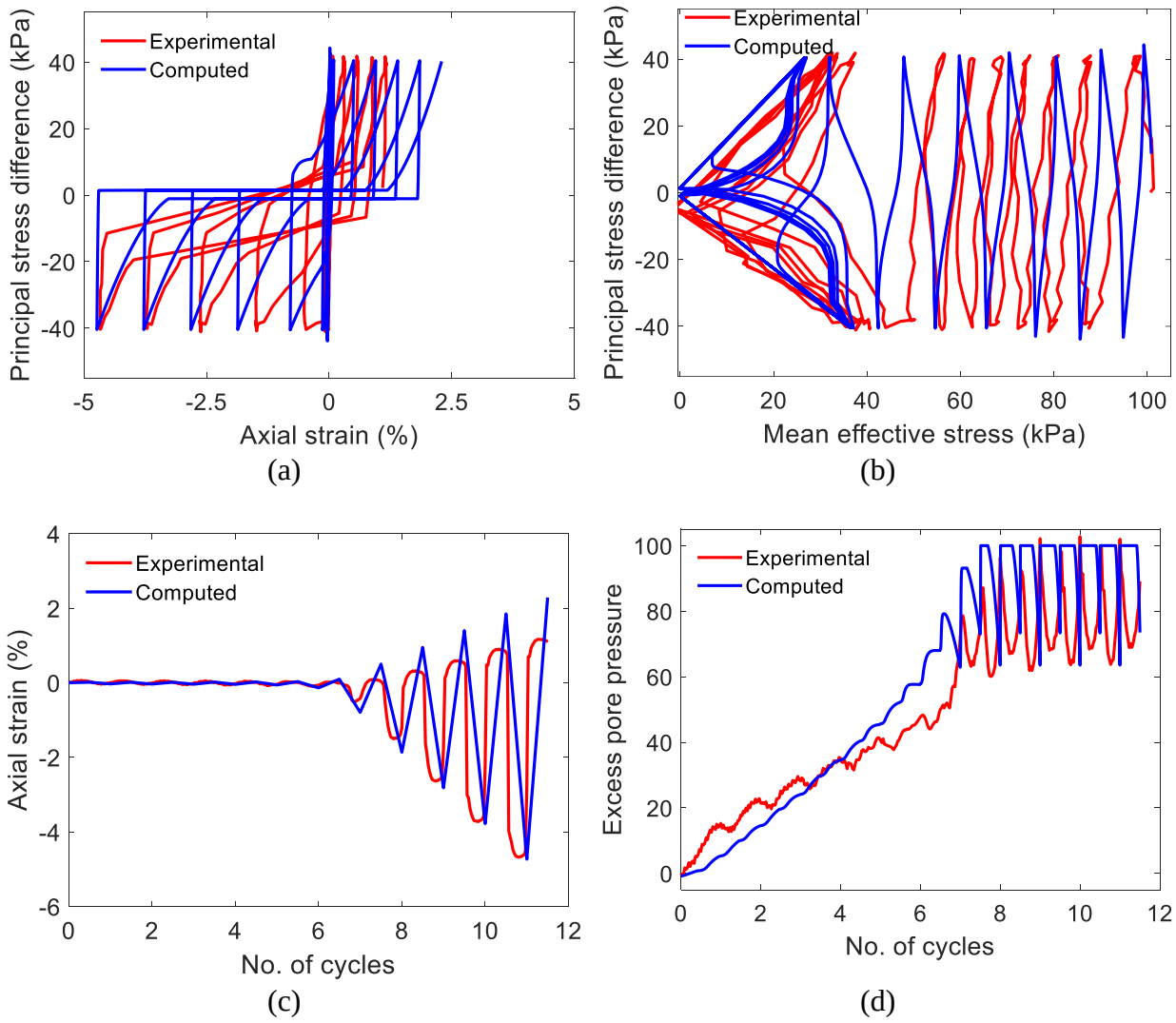

Figure 2.6 Computed and laboratory results of an undrained cyclic triaxial test on Ottawa F-65 sand (data from Kutter et al. 2018b): (a) Axial strain-deviator stress; (b) Mean effective stress-deviator stress; (c) Axial strain; (d) Excess pore pressure

Chapter 3. Three-Dimensional Modeling of Strain-Softening Soil Response for Seismic-Loading Applications

3.1. Abstract

A three-dimensional (3D) incremental plasticity constitutive model is developed for simulating the strain softening behavior of soil materials. The constitutive model extends an existing multi-yield surface (MYS) plasticity formulation with a new strain softening logic. Formulation of the model is presented, and calibration is undertaken to match an available data set. Implementing the model into OpenSees, Finite Element (FE) simulations are conducted to highlight the underlying response mechanisms. Strength and stiffness degradation due to the strain softening mechanism is shown to play a substantial role in terms of accumulated deformation and influence on the resulting ground accelerations. For that purpose, computed results with and without the strain softening effect are compared and discussed. As such, incorporation of strain softening is an important consideration for a wide range of scenarios involving sensitive clays, cemented, over-consolidated, very dense, or frozen soils among others. Overall, the derived insights are of significance for seismic loading in such soil formations.

3.2. Introduction

Strain softening behavior (Figure 3.1) exhibited by materials such as cemented soils, dense sands, over-consolidated clays, frozen soils, structured clays, and sensitive clays (Lee and Seed 1967; Zhu and Carbee 1984; Burland 1990; Anagnostopoulos et al. 1991; Burland et al. 1996; Terzaghi et al. 1996; Horpibulsuk et al. 2004; Abuhajar et al. 2010; Shelman et al. 2014; Gylland et al. 2014; Yang et al. 2015; Zhang et al. 2017; Das 2019) might play an important role during seismic excitation. For such soils, degradation of stiffness and strength with the increase in shear strain may cause detrimental consequences such as slope failure and landslide hazard (Crawford

1968; Geertsema and Torrance 2005; Bagheri and Naggar 2015). For instance, failures in sensitive clays under static loading have been reported and discussed (Gregersen 1981; Longva et al. 2003; Andersson et al. 2005; L'Heureux 2012; Solberg et al. 2016; Locat et al. 2017). Furthermore, a number of large-scale landslides triggered by earthquake loading have been observed in sensitive clay slopes (Seed and Wilson 1967; Kerr and Drew 1968; Keefer 1984; Lefebvre et al. 1992; Rodriguez 1999; Brooks 2013; Perret et al. 2013; Demers et al. 2014). All these investigations highlight the need for modeling the soil strain softening mechanism and its effect on overall performance of the ground system.

To simulate the monotonic-loading strain softening behavior, a number of plasticity constitutive models have been developed (Prevost and Hoeg 1975; Whittle and Kavvadas 1994; Kasama et al. 2000; Kavvadas and Amorosi 2000; Liu and Carter 2002; Lee et al. 2004; Lai et al. 2009; Horpibulsuk et al. 2010; Suebsuk et al. 2011; Yao et al. 2012; Nguyen and Fatahi 2016; Park and Kutter 2016; Loria et al. 2017; Fei and Yang 2019). Using such models, static Finite Element (FE) analyses of slopes with strain softening soil deposits have been reported (Kvalstad et al. 2005; Troncone 2005; Conte et al. 2010; Gylland and Jostad 2010; Kovacevic et al. 2007; Quinn et al. 2011, 2012; Locat et al. 2013; Mohammadi and Taiebat 2013; Troncone et al. 2014; Dey et al. 2015, 2016; Wang et al. 2016).

Currently, FE analyses for seismic response, with consideration of strain softening in the ground are rather limited (Kourkoulis et al. 2010; Chen and Qiu 2014; Islam et al. 2018). Kaynia (2012) and Kaynia and Saygili (2014) developed the one-dimensional (1D) dynamic slope stability QUIVER code. Zhou et al. (2017) implemented an additional soil disturbance dependent constitutive model into QUIVER and performed 1D seismic response analyses for mild infinite-slope submarine sensitive clays. In the realm of 2D FE dynamic analysis, Taiebat et al. (2010)

implemented the SANICLAY (Dafalias et al. 2006) constitutive model with a strain softening formulation into FLAC and performed numerical simulations for a structured clay slope.

Calibration of the employed constitutive model in these studies was done based on the generally scarce availability of post-peak strain softening cyclic loading data, particularly as pertains to degradation of the soil stiffness (e.g., limited insights are discussed for a cemented soil in works of Sharma and Fehey 2003a, b and 2004).

Following in the footsteps of the above pioneering efforts, full 3D modeling of seismic response in strain softening strata remains as an area of interest. To address this concern, a 3D plasticity constitutive model for simulating the seismic strain softening behavior in soils is developed. This model extends an existing multi-yield surface (MYS) plasticity formulation (Prevost 1977; Elgamal et al. 2008; Lu et al. 2011; Gu et al. 2009, 2013, 2015) with a newly developed strain softening logic. For the purposes of this study, the strain softening model (SSM) was calibrated based on laboratory sample test data for quick Tiller clay (Gylland et al. 2014). The model's salient response mechanism is illustrated first via 1D site response simulations. For that purpose, behavior of the FE model with and without the strain softening effect is compared and discussed. Thereafter, a 3D slope is systematically studied to highlight the influence of strain softening on the underlying response mechanisms.

The following sections of this chapter present: 1) the strain softening constitutive model formulation, 2) model calibration, 3) computational framework, 4) application examples and computed response, and 5) insights derived from this study. Finally, a number of conclusions are summarized and discussed.

3.3. Constitutive Model Formulation

The constitutive model incorporates a new strain softening logic into an existing MYS associative J_2-plasticity formulation (Prevost 1977; Elgamal et al. 2008; Lu et al. 2011; Gu et al. 2009, 2013, 2015). In the π-plane, it is of the Drucker-Prager type, and does not consider the Lode angle effect. This section briefly describes the basic MYS model framework including yield function and backbone curve. Further details and model implementation specifics are provided in Gu et al. (2009, 2013, 2015).

3.3.1. Multi-Yield Surface Formulation

In the context of MYS J_2-plasticity (Figure 3.2), yield surfaces are defined in deviatoric stress space by:

$$f_m = \left\{\frac{3}{2}\left(\boldsymbol{\tau} - \boldsymbol{\alpha}^{(m)}\right) : \left(\boldsymbol{\tau} - \boldsymbol{\alpha}^{(m)}\right)\right\}^{\frac{1}{2}} - K^{(m)} = 0, (m = 1, 2, 3, \dots, NYS) \tag{3-1}$$

where $\boldsymbol{\tau}$ denotes the deviatoric stress tensor, m denotes the yield surface number beginning from 1 to NYS (the total number of yield surfaces), and $\boldsymbol{\alpha}^{(m)}$ and $K^{(m)}$ represent the back-stress tensor and the size of the m^{th} yield surface, respectively. Nonlinear shear response before softening can be described by a stress-strain backbone curve as shown in Figure 3.2b, represented by the hyperbolic formula as:

$$\tau = \frac{G\gamma}{1 + \gamma/\gamma_r} \tag{3-2}$$

where τ and γ denote the octahedral shear stress and shear strain, respectively, G is the low-strain shear modulus, and γ_r is the reference shear strain computed as $\gamma_r = \frac{\gamma_{max}\tau_{max}}{G\gamma_{max} - \tau_{max}}$, where τ_{max} is the shear strength that corresponds to the shear strain γ_{max} (Figure 3.2b).

The stress-strain points used to describe the piecewise linear approximation of the originally smooth backbone curve (Figure 3.2b) are defined such that their projections on the τ

axis are uniformly spaced:

$$\tau_m = \tau_{max}(m/NYS)$$
$$\gamma_m = \tau_{max}\frac{\tau_m \gamma_r}{G\gamma_r - \tau_m} \quad (3\text{-}3)$$

As such, the hyperbolic backbone curve [Equation (3-2)] is replaced by a piecewise linear approximation as shown in Figure 3.2b. Each line segment represents the domain of a yield surface $\{f_m = 0\}$ of size $K^{(m)} = 3\tau_m/\sqrt{2}$ characterized by an elasto-plastic shear modulus:

$$H^{(m)} = 2\left(\frac{\tau_{m+1} - \tau_m}{\gamma_{m+1} - \gamma_m}\right) \quad (3\text{-}4)$$

In general, for the specification of yield surface characteristics (sizes and elasto-plastic moduli), conventional shear modulus reduction curves (Seed 1970; Seed et al. 1986; Sun et al. 1988) may be employed as well.

For model initialization, peak (octahedral) shear strength τ_{max} (Figure 3.2) can be defined based on friction angle ϕ and cohesion c as a function of the initial static effective confinement p' as:

$$\tau_{max} = \frac{2\sqrt{2}sin\varphi}{3 - sin\varphi}p' + \frac{2\sqrt{2}}{3}c \quad (3\text{-}5)$$

As such, the stress-strain hyperbolic backbone relationship becomes $\tau = \frac{G_r(p'/p'_r)^d\gamma_{max}}{1+\gamma_{max}/\gamma_r}$, where p'_r and G_r are user-defined reference mean effective confining pressure and low-strain shear modulus, and *d* denotes pressure-dependence coefficient (*d* = 0.5 in this study).

As described in more detail (Prevost 1977; Elgamal et al. 2008; Lu et al. 2011), an associative flow rule is adopted to define the plastic strain direction. In addition, a purely kinematic hardening rule is employed to conveniently generate the desired hysteretic cyclic response. In the formulation, translation of the yield surface is governed by the consideration that no overlapping

is allowed between yield surfaces (Prevost 1977; Elgamal et al. 2008; Lu et al. 2011; Gu et al. 2009, 2013, 2015). As such; i) the active surface location is updated according to the logic described in Elgamal et al. (2003), and ii) all inner yield surface locations $\{f_1 = 0\}$, $\{f_2 = 0\}$, …, $\{f_{m-1} = 0\}$ are updated such that $\{f_1 = 0\}$ to $\{f_m = 0\}$ are tangent to each other at the current stress point $\boldsymbol{\tau}$ as shown in Figure 3.2d. Accordingly, translation of all inner yield surfaces is controlled by:

$$\frac{\boldsymbol{\tau}_n - \boldsymbol{a}^{(m)}}{K^{(m)}} = \frac{\boldsymbol{\tau}_n - \boldsymbol{a}^{(m-1)}}{K^{(m-1)}} = \cdots = \frac{\boldsymbol{\tau}_n - \boldsymbol{a}^{(1)}}{K^{(m)}} \tag{3-6}$$

3.3.2. Strain Softening Logic

A schematic of the strain softening logic (Qiu and Elgamal 2020a) is shown in Figure 3.3. Post τ_{max}^A, the strain softening curve (octahedral shear stress-strain) is simply defined by:

$$\tau = \begin{cases} ae^{k_1\gamma} + b, \gamma_{max}^A \leq \gamma \leq \dfrac{\gamma_{max}^A + \gamma_{res}}{2} \\ ce^{-k_2\gamma} + d, \dfrac{\gamma_{max}^A + \gamma_{res}}{2} \leq \gamma \leq \gamma_{res} \end{cases} \tag{3-7}$$

where, k_1 and k_2 are non-negative input calibration parameters. As such, the constants *a-d* in Equation (3-7) are calculated based on the user-defined peak (τ_{max}^A, γ_{max}^A) and residual states (τ_{res}, γ_{res}), and calibration constants (k_1 and k_2) as follows:

$$\begin{aligned} a &= \frac{\tau_{max}^A - \tau_{res}}{2\left[e^{k_1\gamma_{max}^A} - e^{k_1(\gamma_{max}^A + \gamma_{res})/2}\right]}, \; b = \frac{(\tau_{max}^A + \tau_{res})e^{k_1\gamma_{max}^A} - 2\tau_{max}^A e^{k_1(\gamma_{max}^A + \gamma_{res})/2}}{2\left[e^{k_1\gamma_{max}^A} - e^{k_1(\gamma_{max}^A + \gamma_{res})/2}\right]} \\ c &= \frac{\tau_{res} - \tau_{max}^A}{2\left[e^{k_2\gamma_{res}} - e^{k_2(\gamma_{max}^A + \gamma_{res})/2}\right]}, \; d = \frac{(\tau_{max}^A + \tau_{res})e^{k_1\gamma_{max}^A} - 2\tau_{max}^A e^{k_1(\gamma_{max}^A + \gamma_{res})/2}}{2\left[e^{-k_2\gamma_{res}} - e^{-k_2(\gamma_{max}^A + \gamma_{res})/2}\right]} \end{aligned} \tag{3-8}$$

In the above τ_{res} is defined by an expression similar to Equation (3-5), in which a residual friction angle ϕ_{res} and cohesion c_{res} are used. On this basis, the parameters of Equations (3-2) and (3-5) conveniently allow for modelling shear response as a function of confinement p', based on experimentation data sets when available.

Figure 3.4 depicts the model response under monotonic loading for different sets of calibration parameters k_1 and k_2. For $k_1 = k_2 = 0$, the strain softening segment is linear. For k_1=k_2, strain softening representative of thixotropic clay (Park and Kutter 2015, 2016) can be simulated. For $k_1 = 0$ and $k_2 > 0$, sudden decrease of shear strength for quick clays or cemented soils (Park and Kutter 2015, 2016) can be modeled.

As seen in Figure 3.3, the hyperbolic backbone curve before strain softening is O-A and the initial shear modulus is G. If the current deviatoric stress reaches peak point A and the octahedral shear strain is still increasing (until the residual point C in Figure 3.3 is reached): i) the stress state and size of all yield surfaces is gradually and permanently reduced by the ratio (τ/τ_{max}) according to the logic of Equation (3-7), and ii) using Equation (3-6), location of the inner surfaces $\boldsymbol{\alpha}$ is updated to maintain the tangency condition of Equation (3-6). In addition, the backbone curve [Equation (3-2)] is updated, where the attained instantaneous τ in Equation (3-7) replaces τ_{max} (Figure 3.3b). In this regard, the low-strain shear modulus *G* can be re-defined to match experimental observations when available. In this study, it is allowed to decrease by the ratio$(\tau/\tau_{max})^n$, where parameter n is a non-negative constant. Due to the scarcity of post-peak strain softening cyclic loading test data as relates to degradation of shear stiffness, this constant in the presented computational simulations below was taken as n = 0.5 (conventional value for pressure-dependent soil materials). As such: i) a new set of stress-strain points [Equation (3-3)] is defined describing the piecewise linear approximation of the updated smooth backbone and the elasto-plastic shear moduli are updated [Equation (3-4)]. Upon load reversal, the updated yield surface sizes, low-strain shear modulus, and elasto-plastic moduli are systematically employed (Figure 3.3).

3.4. Model Calibration and Performance

The SSM was calibrated by laboratory monotonic triaxial test data for quick Tiller clay (Gylland et al. 2014). The goal was to obtain a reasonable match of strain softening characteristics for this soil. With the modeling parameters of Table 3.1, the computed response (Figure 3.5a) reasonably follows the reported quick Tiller clay deviator stress-axial strain curve at the confining pressure of 73 kPa (Gylland et al. 2014).

Representative cyclic loading simulations using the calibrated quick Tiller clay model are shown in Figure 3.5b-e. Model response (confining pressure = 73 kPa) under strain-controlled cyclic shear loading (Figure 3.5b), shows degradation of strength and stiffness, eventually reaching the residual state (Figure 3.5c). Figure 3.5d and e display the model cyclic response (confining pressure = 73 kPa) for a scenario representative of a stress-state in a ground slope. For illustration, a biased strain-controlled cyclic strain history is applied (Figure 3.5d). Under this loading, the model reproduces the shown (Figure 3.5e) cycle-by-cycle degradation of shear strength, eventually reaching the residual state. Similar to the original MYS formulation (Prevost 1977; Elgamal et al. 2008; Lu et al. 2011; Gu et al. 2009, 2013, 2015), the SSM cyclic response may be seen (Figure 3.5b) to generate hysteresis damping of the Masing type (Masing 1926). In the softening range, this damping is dictated systematically by the updated hyperbolic backbone curve characteristics (Figure 3.3).

3.5. Computational Framework

The Open System for Earthquake Engineering Simulation (OpenSees, McKenna 2011, http://opensees.berkeley.edu) was employed to conduct the nonlinear seismic loading FE analyses presented below. OpenSees is developed by the Pacific Earthquake Engineering Research (PEER) Center and is widely used for simulation of structural and geotechnical systems under conditions

of static and seismic loading (Yang 2000; Yang and Elgamal 2002; Lu et al. 2011).

In conducting the dynamic computations, the FE matrix equation is integrated in time using a single-step implicit predictor multi-corrector scheme of the Newmark type (Chan 1988; Parra 1996) with integration parameters $\gamma = 0.6$, $\beta = 0.3025$ and a time step Δt of 0.01s. The equation is solved using the modified Newton-Raphson method with Krylov subspace acceleration (Carlson and Miller 1998; Mazzoni et al. 2009). Convergence for solving the nonlinear FE matrix equation is based on a displacement increment norm of 10^{-4}. Slight tangent stiffness-proportional viscous damping (Priestley et al. 2005; Petrini et al. 2008; Jehel et al. 2014) was used (coefficient = 0.003) to enhance the numerical system stability, with the main damping emanating from the soil nonlinear shear stress-strain hysteresis response.

Finally, it is noted that the strain softening mechanism in continuum damage mechanics can lead to mesh dependency, where the solution will highly depend on the finite element size. To address this type of mesh dependency and the strain localization issue, the gradient method (a regularization method) may be employed (Borst et al. 1995, 1996; Lasry and Belytschko 1988; Chen et al. 2007). To maintain focus in elucidating the soil model response characteristics, the FE studies below did not include any such regularization procedure.

3.6. Site Response and Permanent Deformation

Before presenting a 3D seismic response scenario, a mildly inclined infinite slope (Figure 3.6) with the calibrated quick Tiller clay model (Table 3.1) is employed to illustrate the salient soil strain-softening response characteristics. Representative shear behavior of the employed SSM is shown in Figure 3.6b, along with that of the corresponding MYS model for reference. As such, a 1D free-field ground response model is represented by ten brick elements (Figure 3.6a) at a 4^o inclination, in order to provide a static driving shear stress due to gravity (Elgamal et al. 2009; Lu

et al. 2019). The displacement degrees of freedom at any given depth are tied together both horizontally and vertically (to reproduce the desired 1D site response representation).

A base motion with a relatively high peak acceleration was employed, so as to trigger strain softening and induce significant accumulation of lateral ground deformation. For that purpose, this motion (Figure 3.6c) was simply taken as that of the 1994 Northridge earthquake Rinaldi Receiving Station record (Component S48W), scaled down to a peak amplitude of 0.4 g.

Figure 3.7 shows the computed shear stress-strain at the depths of 5 and 10 m, respectively. Due to the large fling-motion pulse in the base input acceleration (Figure 3.6c) and the static driving shear stress (4^o inclination), a significant level of accumulated permanent shear strain was incurred. In this figure, the SSM response clearly shows the strain softening effect, with shear stress reaching its residual value. As expected, the MYS response is noticeably different, with overall lower levels of permanent shear strain.

Accordingly, the SSM accumulated permanent ground displacement is seen to be greater (Figure 3.8a). This outcome is a consequence of the SSM reduction in soil strength and stiffness (Figure 3.7), resulting in a more compliant soil system. The acceleration and corresponding response spectrum are shown in Figure 3.8b and c, respectively. Significant differences are seen in the SSM time history and its frequency content compared to those of the MYS model. Specifically, during the softening phase: a) peak accelerations are markedly reduced in the negative direction, during the phases of downslope displacement accumulation (analogous to the classical Newmark 1965 sliding block response), and b) a corresponding marked decrease in peak spectral values is evident. As such, incorporation of strain softening where applicable, may significantly change the soil system response, in terms of acceleration at the ground surface, and magnitude of accumulated permanent displacement.

3.7. Three-Dimensional Ground Slope

Using the same soil properties (Table 3.1) and input ground motion (scaled down to a peak amplitude of 0.3 g), a 3D model of sloping ground is studied in this section. For that purpose, the FE mesh is configured to have a gradually varying slope inclination over a distance of 80 m (Figure 3.9), with the steepest being at 2H:1V (Horizontal: Vertical) at Z = 80 m and the mildest at 6H:1V from Z = 0 to 20 m. In this configuration, seismic excitation is imparted solely in the longitudinal X-direction. As such, the 3D FE model is 400 m long, and 80 m wide, with 10 m of overlying sloping ground. Based on the above, the FE mesh for the 3D ground slope was generated comprising 32,550 nodes, and 28,780 brick elements.

3.7.1. Boundary and Loading Conditions

The boundary and loading conditions are implemented in a staged fashion as follows (Figure 3.9):

1) Gravity was applied first to activate an initial static state with: i) linear elastic properties, ii) nodes along the left- and right-side mesh boundaries (X = 0 m and X = 400 m) fixed against longitudinal translation, iii) to generate a periodic boundary (Law and Lam 2001), nodes along the back and front longitudinal planes (Z = 0 m and Z = 80 m) fixed against transverse translation, and iv) fixed nodes along the FE model base (Y = 0 m).

2) Soil properties were switched from linear elastic to plastic (Table 3.1).

3) Dynamic analysis was conducted by applying the acceleration time history (Figure 3.6c) to the FE model base (Y = 0 m), scaled down to 0.3 g in peak value. During the shaking event, 2D plane strain soil columns of large depth (not shown) are included (Su et al. 2017) along the left- and right-side mesh boundaries (X = 0 m and X = 400 m). These columns have the same height and material properties as the adjacent soil profile on each side. Relative to the Z-direction 80 m

transverse dimension (Figure 3.9), the large depth conveniently enforces the desired free-field ground response, at an adequate distance away from the sloping zone of interest (to minimize boundary effects).

3.7.2. Deformation

The deformed FE mesh at end of shaking (colors depict the total accumulated 3D displacement) is shown in Figure 3.10. Large permanent ground deformation occurs reaching a peak of about 1.7 m near the steepest 2H:1V slope inclination (Figure 3.11a). Figure 3.12 and Figure 3.13 provide a clearer picture of the accumulated longitudinal, transverse, and vertical deformations. Arrows depicting the direction of 3D slope deformation are shown in Figure 3.11a. Due to the geometric features of the slope with various inclinations, transverse displacement of about 0.25 m is seen in Figure 3.11d. Peak slope settlements near the steepest section show slumping by as much as 0.82 m (Figure 3.11c).

To further illustrate the involved salient 3D deformation pattern, Figure 3.13 depicts the displacement profile along the slope top (from Z = 0 m to 80 m). For relatively mild inclinations from 4H:1V to 6H:1V, the longitudinal displacement peaks at about 3 seconds (Figure 3.12a and Figure 3.13), upon passage of the main shaking pulse (Figure 3.6c). Conversely, additional longitudinal displacement continues to accumulate in the relatively steep zone between the inclinations from 4H:1V to 2H:1V (Figure 3.12a and Figure 3.13).

For vertical displacement, a similar pattern (Figure 3.12b) was observed, and the maximum value reached about 0.82 m near the steepest inclination 2H:1V (Figure 3.13). Due to the variation of geometric configuration in this 3D slope, transverse displacement (Figure 3.12a and Figure 3.13) was also seen along the slope top, reaching a peak value of about 0.16 m in the zone near the inclination 3H:1V.

3.7.3. Three-Dimensional Shear Response

In accordance with the above 3D deformation pattern, Figure 3.14 depicts shear strain contours at end of shaking along a number of XY cross-sectional slices. It can be seen that the highest shear strains γ_{xy} occurred at the relatively steep inclinations from 4H: 1V to 2H:1V (Figure 3.14b). These large strains correspond to overall higher ground surface displacement at these locations (Figure 3.9-Figure 3.11).

Related to the influence of longitudinal displacement on transverse deformation, Figure 3.15 depicts the shear strain γ_{xz} contours along a number of XZ cross-sectional slices. As seen in this figure, peak γ_{xz} shear strain occurred within the slope, reaching a value of about 7.5 %.

Finally, the shear strain γ_{yz} in a number of YZ cross-sectional slices is displayed in Figure 3.16. The peak shear strain occurs within the plane boundaries defined by X = 200 m - 208 m, in accordance with the deformation pattern of this 3D slope (Figure 3.9-Figure 3.11).

The coupled mechanisms of 3D shear response are further highlighted in Figure 3.17. The dominant shear driven by longitudinal downslope deformation is seen to exceed its peak value at around 3 seconds. Thereafter, softening ensues with residual stress approached and with large accumulated strains (Figure 3.17a-c). Overall, it is seen that accumulation of shear strain occurs in all direction throughout the strong shaking duration.

3.7.4. Acceleration

Figure 3.18 displays representative acceleration response time histories. At the slope top, peak acceleration is amplified compared to that of the base input motion (0.3 g). In the longitudinal direction, it may be seen that lower negative peak accelerations prevail at the steep 2H:1V location, in accordance with occurrence of significant downslope deformations. In addition, it can be seen that significant vertical and transverse response appear as a consequence of the imparted

longitudinal excitation and resulting 3D slope deformations.

The variability in overall response is further illustrated by Figure 3.19, displaying the spectral response in all three directions. In the vertical direction, the highest values appear at the steep 2H:1V plane. Finally, transverse motion (Figure 3.19b) in the central section of the mesh (away from the front and back symmetry planes) is generated as well, with the slope undergoing a full 3D pattern of deformations.

3.7.5. Computed Response Using MYS model

To assess influence of strain softening effect, an additional numerical simulation of the above 3D slope was conducted using the MYS model (Figure 3.6b). Figure 3.20a shows the deformed mesh with a peak displacement of about 0.55 m near the steepest inclination 2H:1V. Compared to the SSM scenario (Figure 3.21a), this accumulated MYS permanent displacement is significantly lower. Similarly, the MYS shear strains are much reduced (Figure 3.22) compared to their SSM counterpart (Figure 3.17). In accordance with the response pattern of Figure 3.8, Figure 3.21b displays the corresponding response spectra with SSM being significantly lower over a wide frequency range.

3.8. Potential Application of SSM

In addition to post-peak stress softening, cyclic degradation exhibited by soils due to mechanisms such as pore pressure generation for instance (Idriss et al. 1978; Vucetic and Dobry 1988; Vucetic 1988; Zergoun and Vaid 1994; Matasović and Vucetic 1995; Ishihara 1996; Boulanger and Idriss 2006, 2007; Tsai et al. 2014) can be incorporated into the developed strain softening plasticity constitutive model.

As such, degradation can be defined based on mechanisms such as accumulated energy (Kokusho and Mimori 2015; Kokusho 2017), or accumulated plastic shear strain (Ishibashi et al.

1985; Elgamal 1991). In this section, degradation of shear stiffness and strength is defined based on the relatively simple mechanism described below. Other degradation logics (e.g., Elgamal 1991) may be implemented depending on the nature of the data at hand, and the intended scope of application (e.g., earthquake response versus low-strain repetitive cyclic loading).

In this section, the SSM was calibrated to represent the Cloverdale clay laboratory undrained test data (Figure 3.23) of Zergoun and Vaid (1994). For that purpose, the material parameters undrained shear strength S_u (τ_{max}) = 56 kPa, $\gamma_{max} = 10$ %, and G = 28 MPa closely match the monotonic undrained stress-strain behavior (Figure 3.23a). Degradation of shear strength $\Delta\tau$ is simply related to the accumulated shear strain γ by the relationship $\Delta\tau = a(\gamma)^b$ in which a and b are non-negative input calibration constants. Furthermore, the low-strain shear modulus and elasto-plastic moduli are decreased according to the factor $e^{-k\gamma}$, where k is an additional non-negative input calibration constant. On this basis, a, b, and k of 0.85, 0.2 and 3 respectively, provided a reasonable match to the reported data for the normalized cyclic stress ratios of τ_{cy}/S_u = 0.75 and 0.62 within the range of as many as 12 loading cycles (Figure 3.23b). As such, both the computed and laboratory results show similar cycle-by-cycle degradation in shear stiffness strength (Figure 3.23c and d), with potential application for an earthquake response scenario.

3.9. Cyclic Softening Model

This section extends the above practical 3D plasticity model to simulate the cyclic softening behavior of soil materials (Figure 3.24), as might emanate from pore-pressure build-up, among other potential stiffness and strength degradation mechanisms (Elgamal 1991). The relation which governs pore-pressure build-up based on experimental cyclic torsional strain-controlled testing of Ottawa sand (Ishibashi et al. 1985) is given by:

$$r_u = \frac{(\kappa/2)}{(c + \kappa/2)} \tag{3-9}$$

where r_u is pore-pressure ratio ($0.0 \leq r_u \leq 1.0$), c is a model parameter (controlling the rate of pore pressure build-up) to be specified by the user, and κ is related to γ in the following simple fashion:

$$\kappa = \langle \gamma - \gamma_{th} \rangle \tag{3-10}$$

$$\kappa(t) = \kappa(l) + \langle |\gamma(t) - \gamma_L| - \gamma_{th} \rangle$$

in which t is time step, γ_{th} represents a threshold strain (0.00005 for Ottawa sand, Elgamal 1991) below which no pore pressure is generated, γ_L denotes the octahedral shear strain when the last stress (or strain) reversal took place and $|\quad|$ is the absolute value. Variable $\mu(t)$ modifies the curve-fitting constants as follows:

$$\mu(t) = [1 - r_u(t)]/[1 - r_u(t-1)] \tag{3-11}$$

For the hyperbolic relation:

$$G(t) = \mu^{k_1} G(t-1) \tag{3-12}$$

$$\tau_{max}(t) = \mu^{k_2} \tau_{max}(t-1) \tag{3-13}$$

in which, parameters k_1 and k_2 are employed to represent the degradation of shear strength and stiffness, and the updated yield surface sizes and elasto-plastic moduli will be systematically defined (Figure 3.3), in terms of the updated low-strain shear modulus $G(t)$ and strength $\tau_{max}(t)$.

Representative cyclic loading simulations using this cyclic softening model are shown in Figure 3.25. As seen in this figure, model response under strain-controlled and stress-controlled cyclic shear loading (Figure 3.25a and b) clearly shows the degradation of strength and stiffness with the increase of excess pore pressure ratio. Figure 3.25c displays model response under a biased strain-controlled cyclic shear loading. It can be seen that the model reproduces the shown (Figure 3.25c) cycle-by-cycle degradation of shear strength and stiffness.

3.10. Summary and Conclusions

A three-dimensional (3D) incremental plasticity constitutive model for simulating cyclic strain softening behavior is developed. The constitutive model extends an existing multi-yield surface plasticity (MYS) formulation with a newly developed strain softening logic. Using the calibrated constitutive model, 1D and 3D Finite Element (FE) simulations are presented to highlight the underlying response mechanisms.

The main remarks may be summarized as:

1. Strength and stiffness degradation due to the strain softening mechanism might play a substantial role in terms of accumulated deformations and its effect on the resulting ground acceleration and extent of permanent displacement.

2. Incorporation of strain softening where applicable, is an important consideration for a wide range of ground scenarios involving sensitive clays, cemented, over-consolidated, very dense, or frozen soils among others.

3. Additional experimental data sets are needed in order to further quantify degradation of strength and stiffness due to cyclic loading (post-peak behavior). As such new data sets become available, the gained insights may be introduced into the presented softening framework.

3.11. Acknowledgements

Chapter 3, in part, has been published as it appears in the following paper (The dissertation author was the primary investigator and author of this paper):

Qiu, Z. and Elgamal, A. (2020). "Three-Dimensional Modeling of Strain-Softening Soil Response for Seismic-Loading Applications." Journal of Geotechnical and Geoenvironmental Engineering, 146(7), 04020053.

Table 3.1 Calibrated SSM model parameters for quick Tiller clay **(**Gylland et al. 2014**)**

Model parameters	Value
Reference pressure, p'_r (kPa)	100.0
Mass density, ρ (t/m^3)	2.0
Low-strain shear modulus, G (MPa)	8.0
Poisson's ratio, v	0.4
Cohesion, c (kPa)	6.0
Octahedral shear strain at peak strength, γ_{max} (%)	1.96
Residual cohesion, c_{res} (kPa)	3.0
Residual octahedral shear strain, γ_{res} (%)	25.46
Friction angle, ϕ	28.0
Residual friction angle, ϕ_{res}	11.0
Calibration parameter, k_1	0
Calibration parameter, k_2	20
Stiffness reduction ratio, n	0.5
Number of yield surfaces (NYS)	40

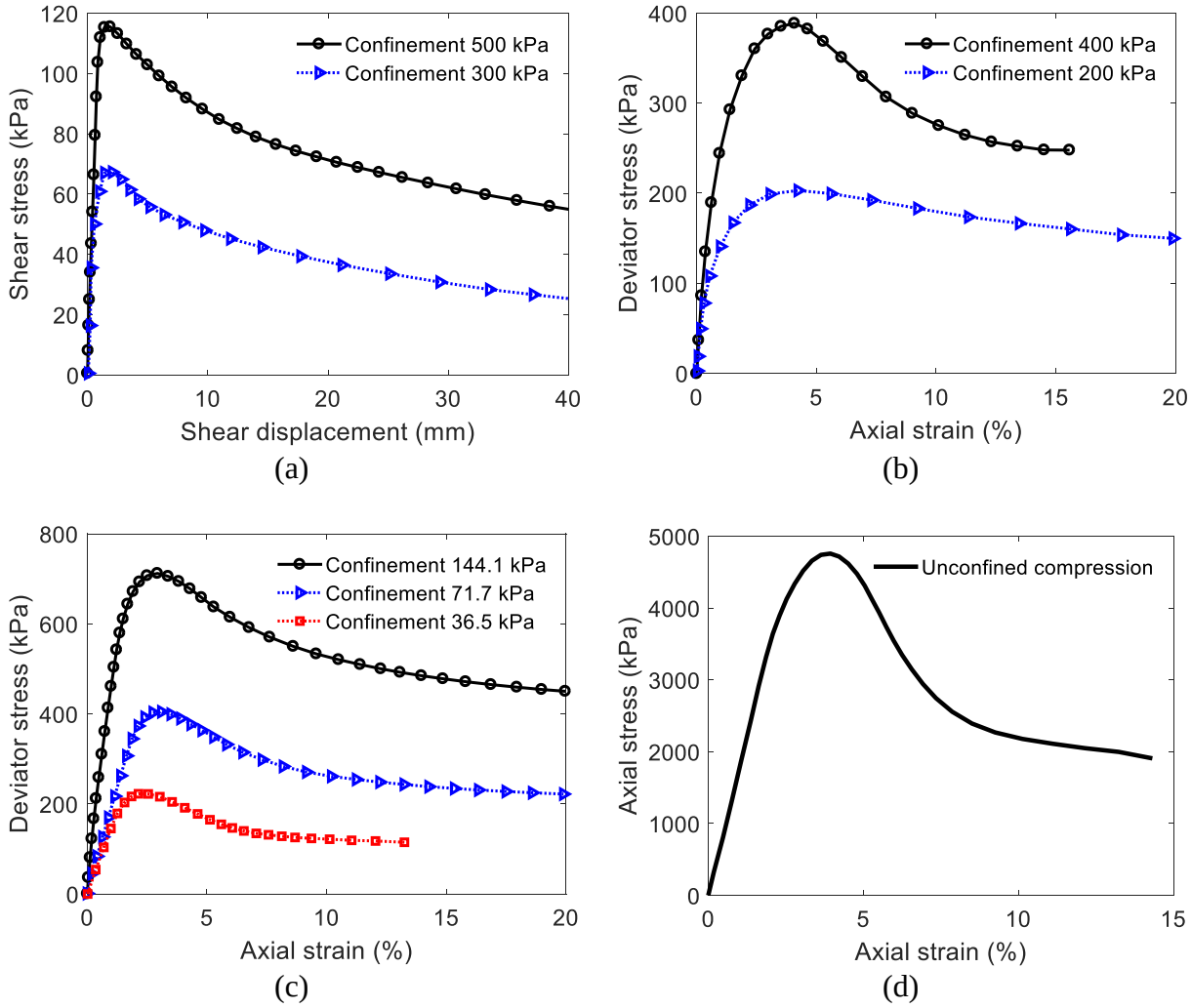

Figure 3.1 Strain softening behavior: (a) Sensitive clay (data from Stark and Contreras 1998); (b) Cemented clay (data from Horpibulsuk et al. 2004); (c) Dense sand (data from Wilson and Elgamal 2015); (d) Frozen soil (data from Shelman et al. 2014)

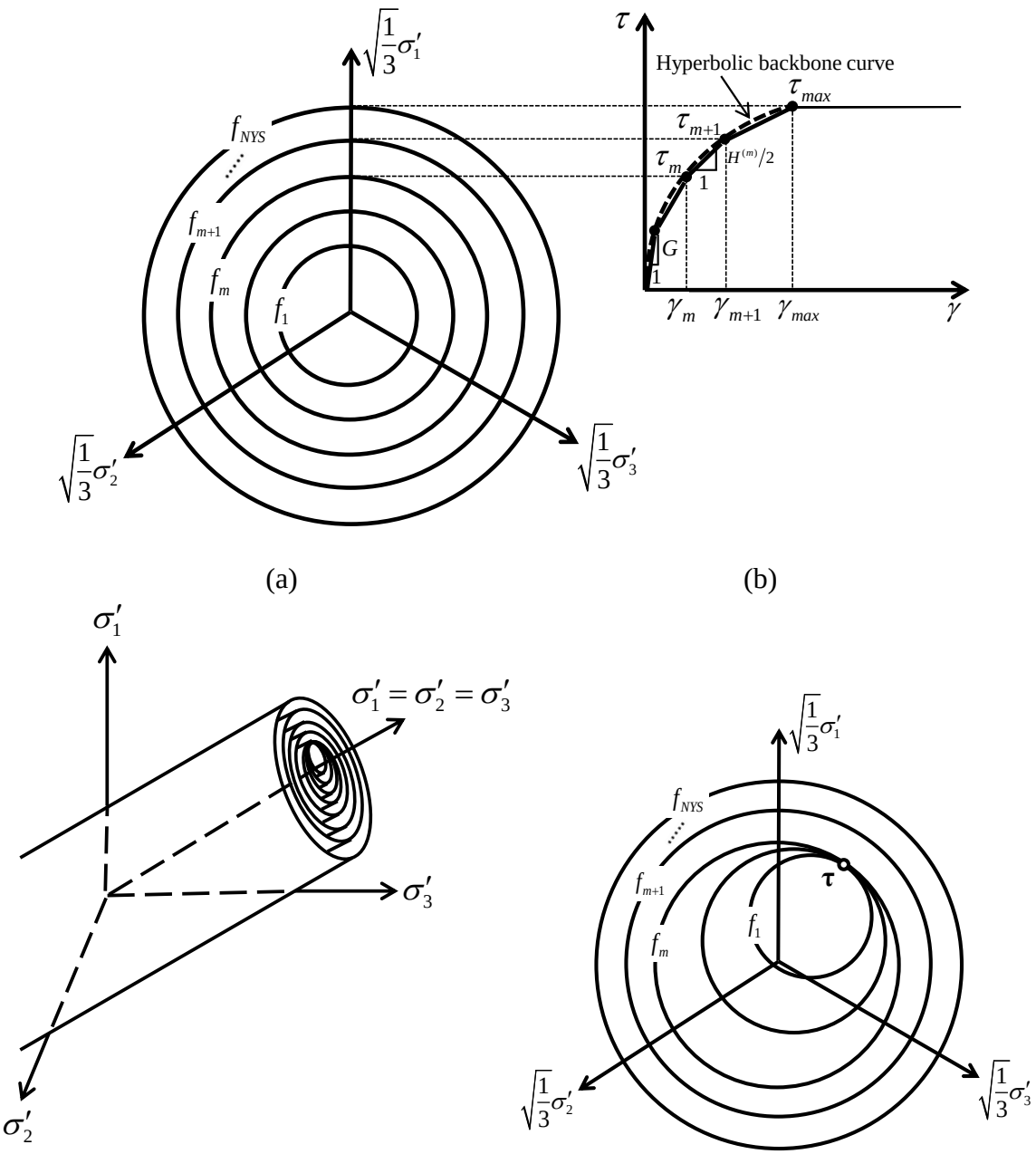

Figure 3.2 The multi-yield surface plasticity model: (a) In deviatoric plane and octahedral shear stress and strain; (b) In stress space; (d) Inner yield surface movements (after Elgamal et al. 2008; Lu et al. 2011)

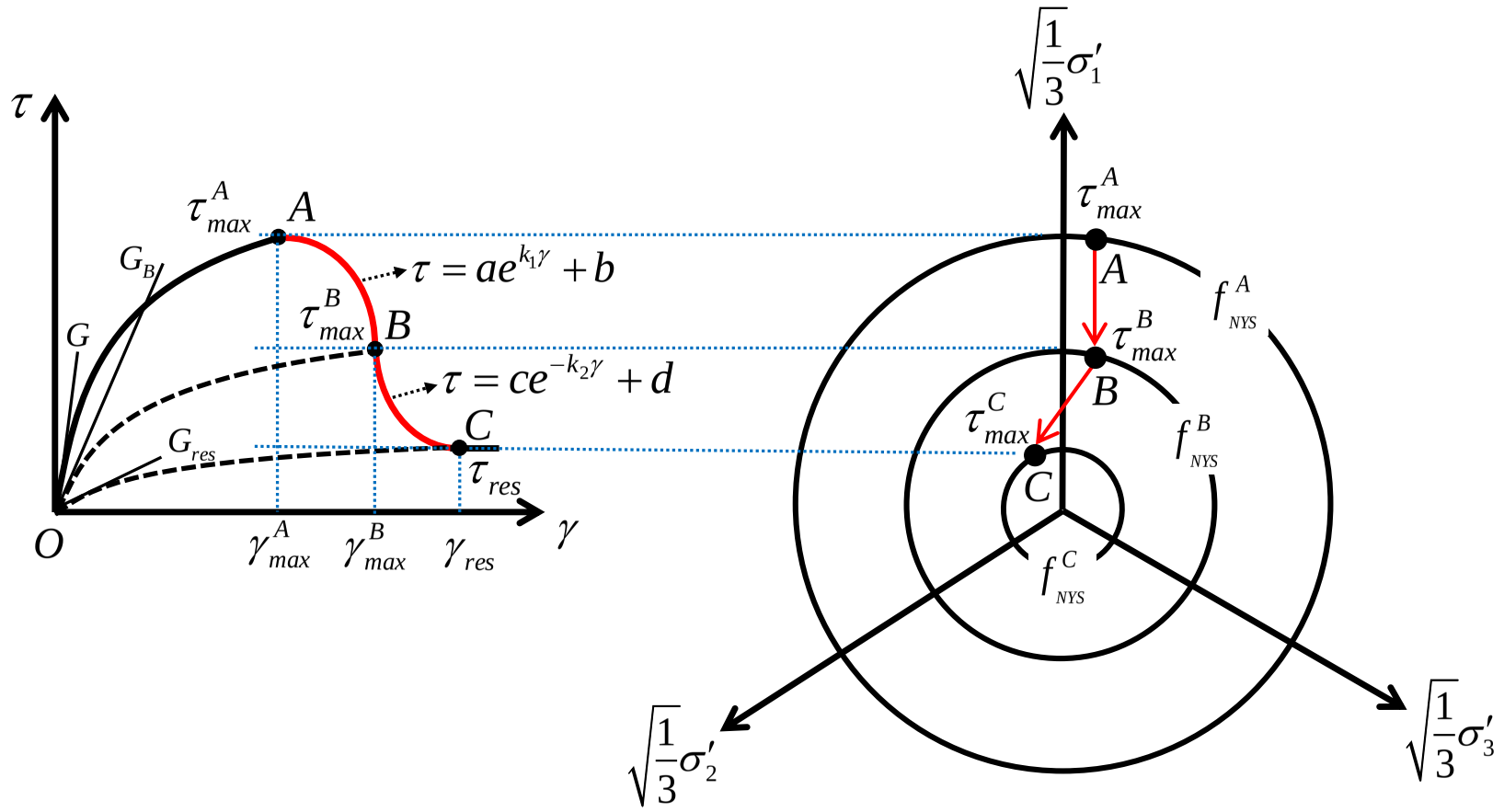

Figure 3.3 Schematic of strain softening logic: (a) Octahedral shear stress and strain; (b) In stress space (f_{NYS} depicts the outmost yield surface)

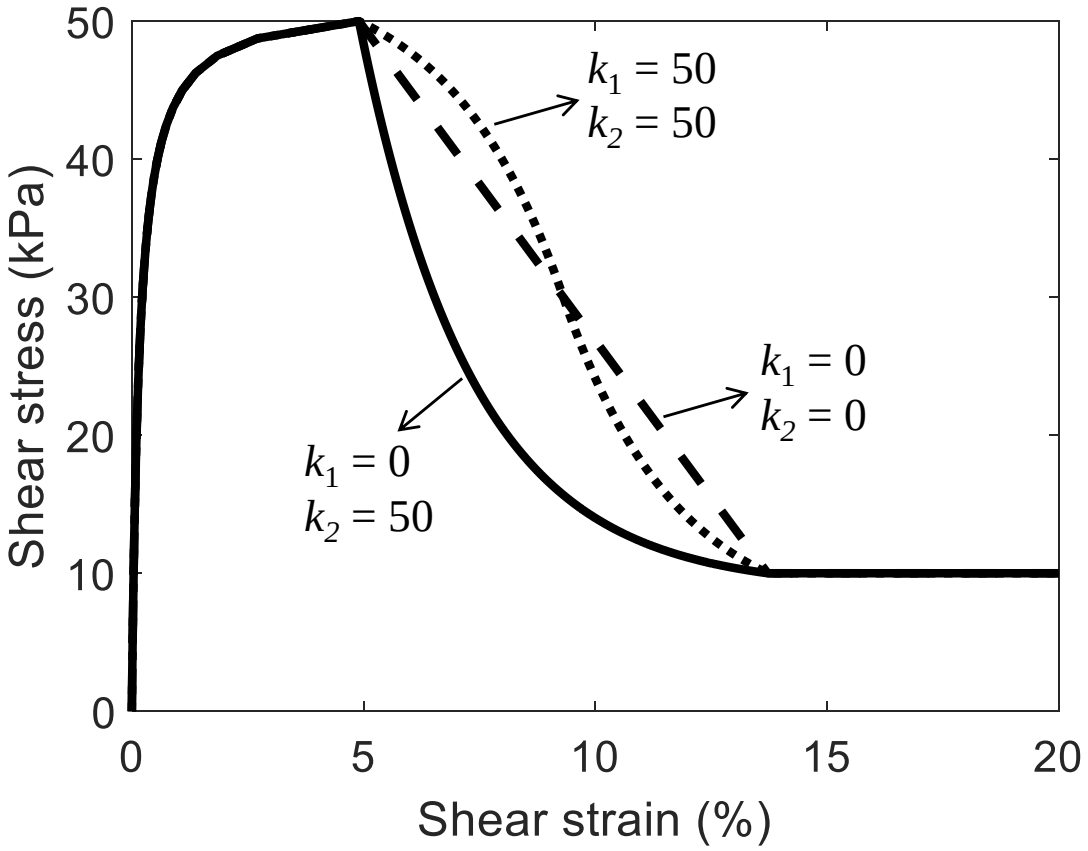

Figure 3.4 Effect of calibration constants k_1 and k_2

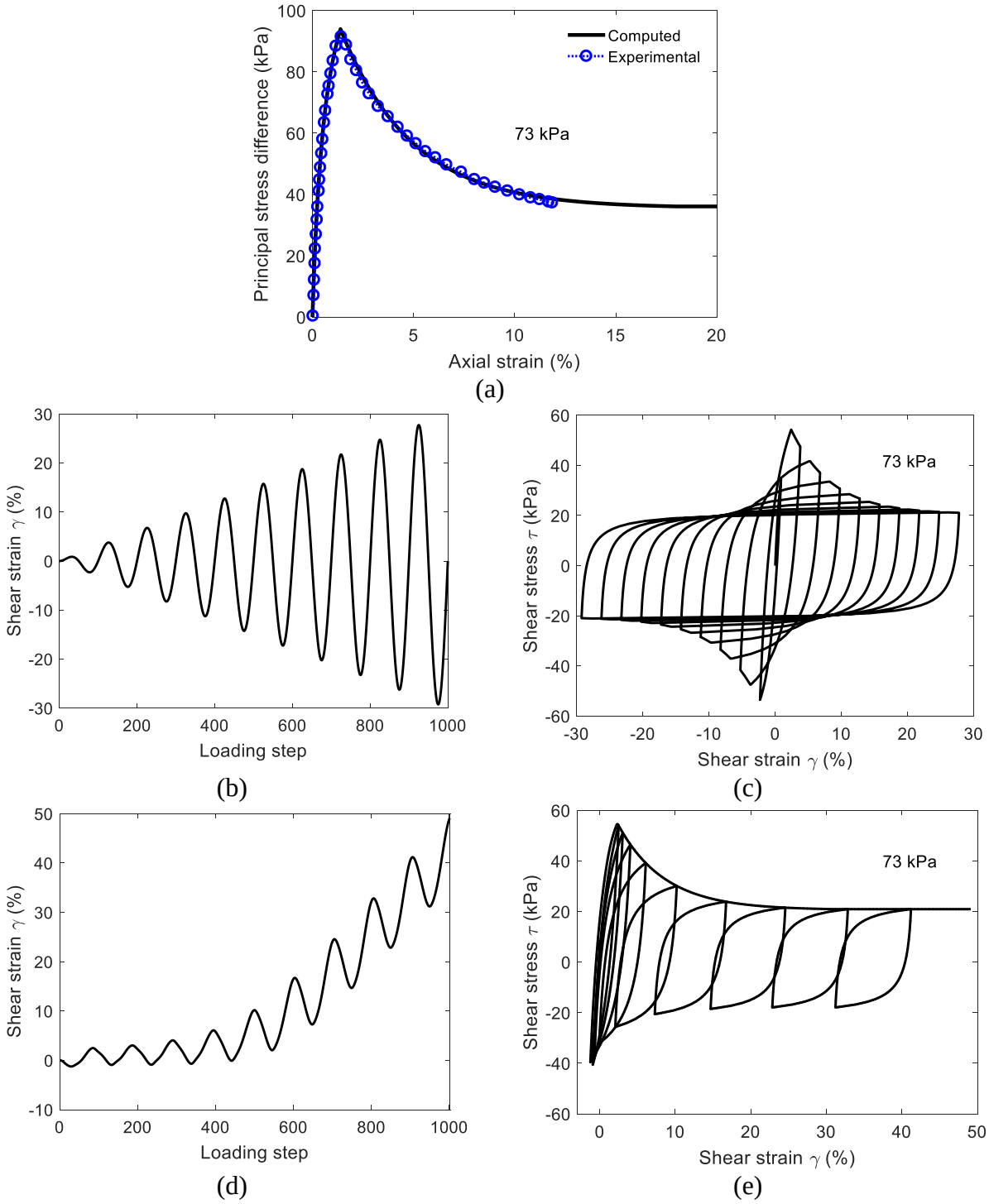

Figure 3.5 SSM Response (Isotropically consolidated at a mean effective pressure of 73 kPa): (a) Computed and laboratory data for Quick Tiller clay undrained triaxial compression test (Gylland et al. 2014); (b), (c) Under cyclic shear loading; (d), (e) Model response depicting accumulation of permanent shear strain

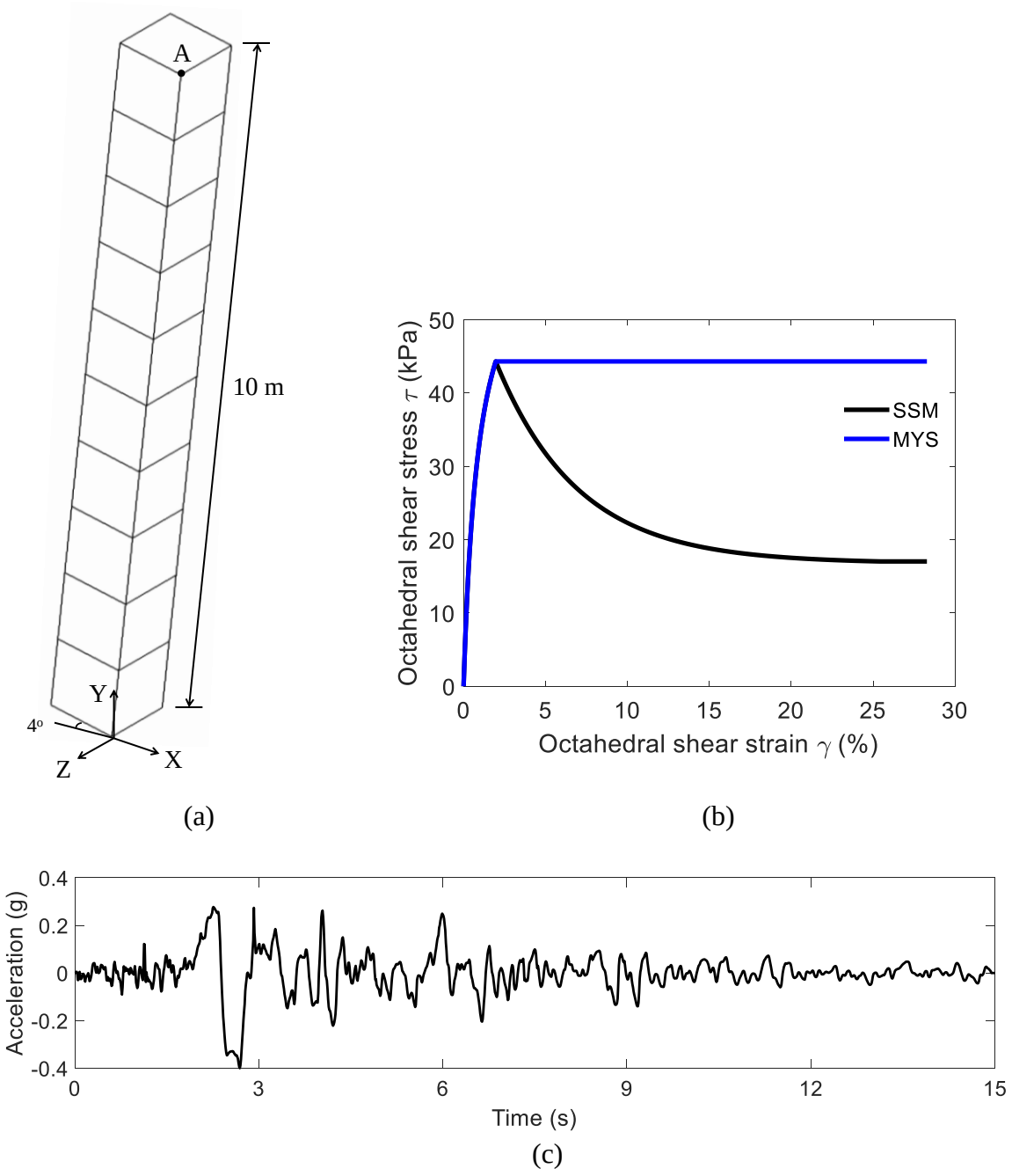

Figure 3.6 Infinite slope at 4° inclination: (a) FE model; (b) Octahedral shear stress-strain response of SSM and MYS models for quick Tiller clay at a mean effective confining pressure of 73 kPa; (c) Input motion

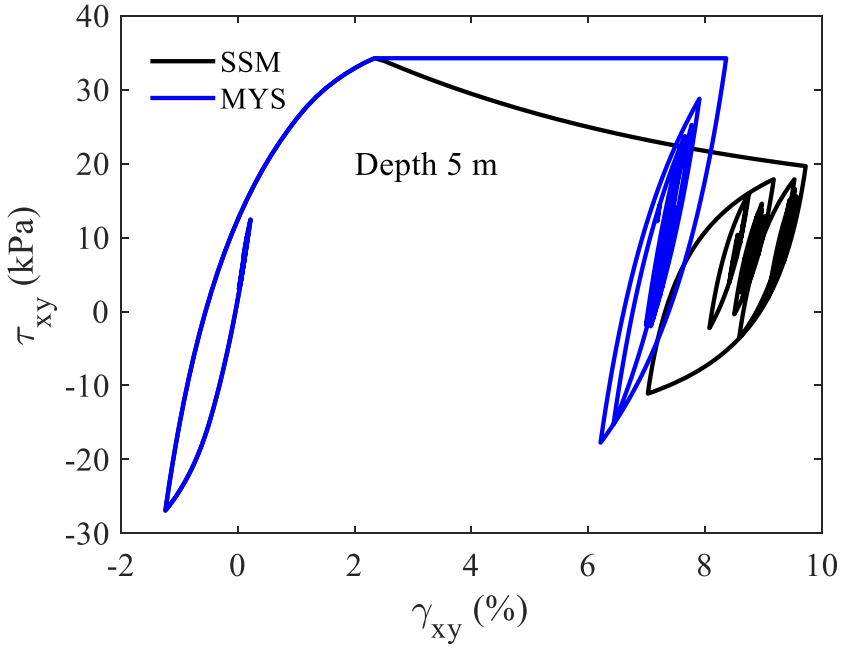

(a)

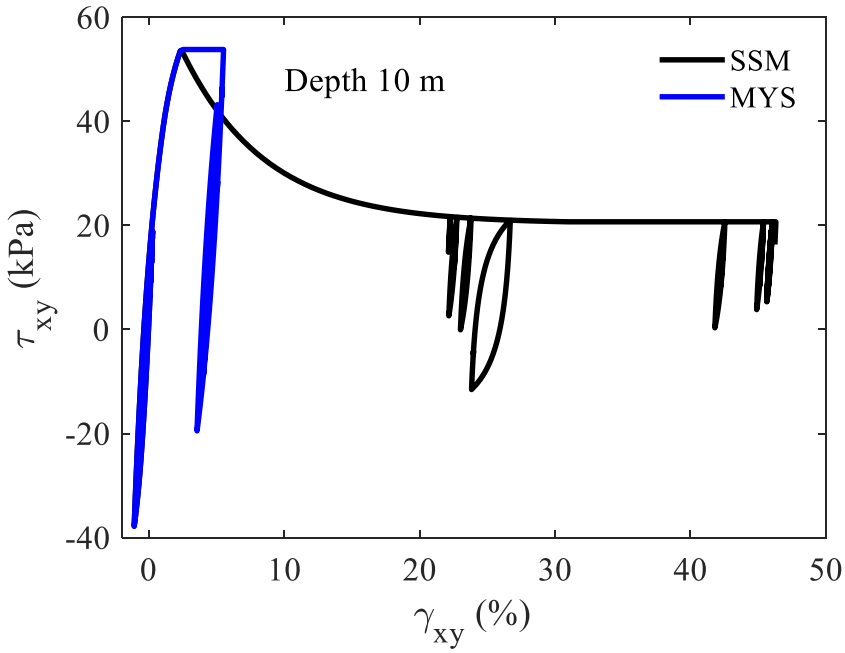

(b)

Figure 3.7 Shear stress-strain response: (a) Depth 5 m; (b) Depth 10 m

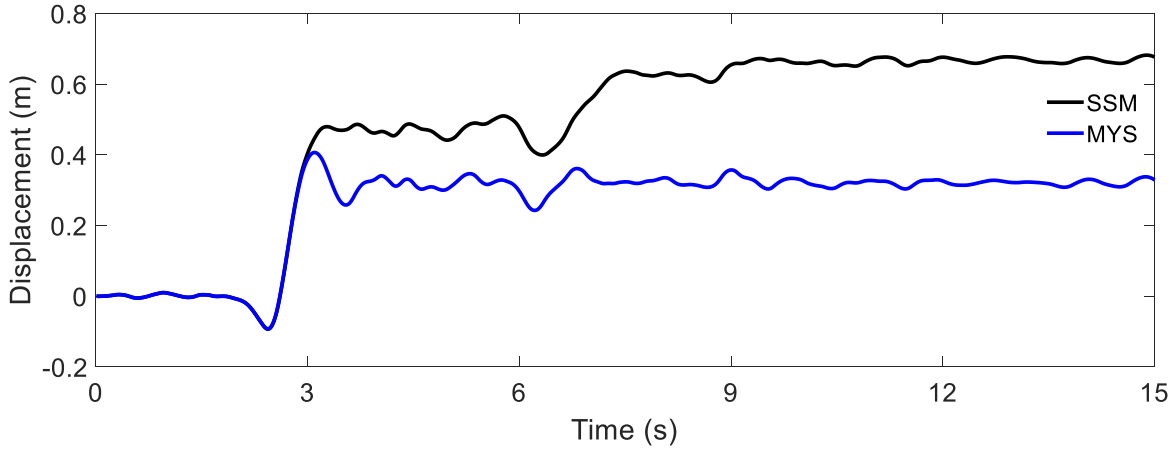

(a)

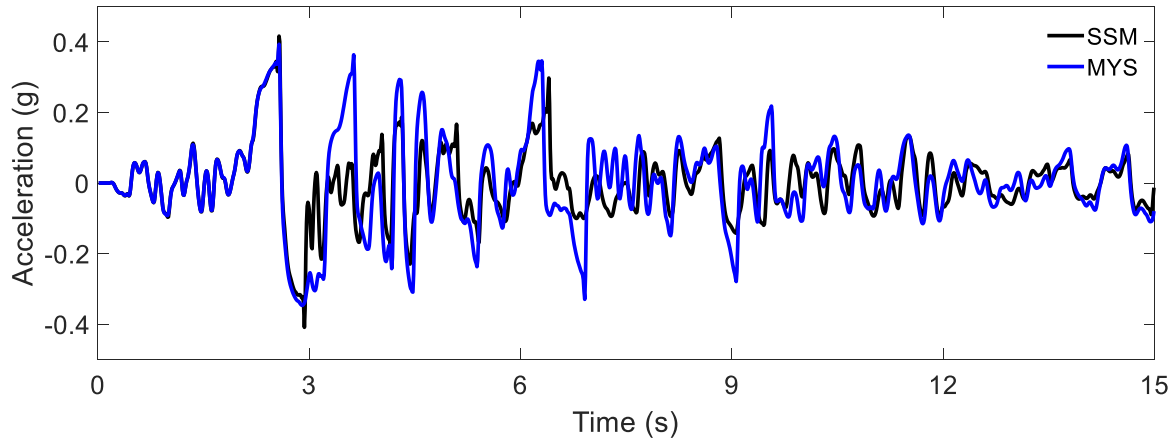

(b)

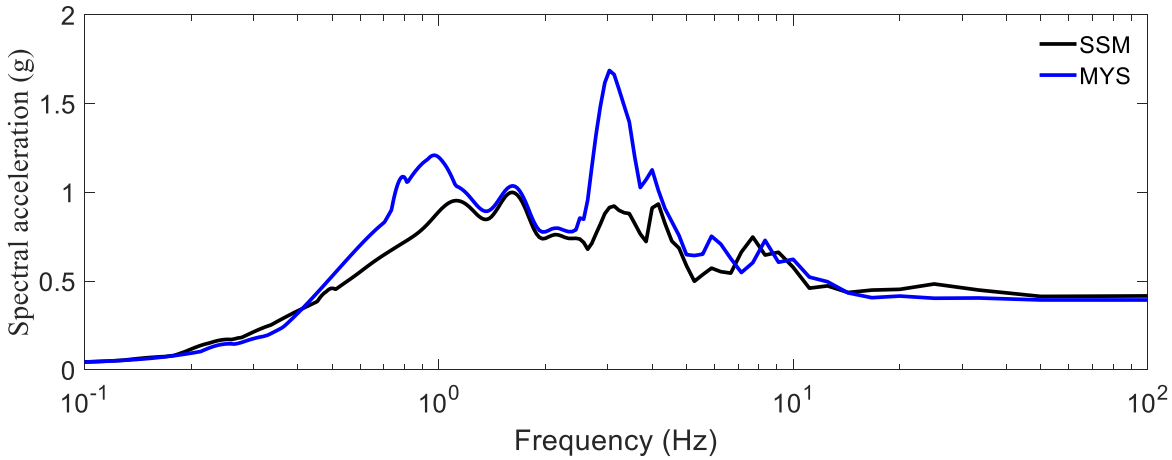

(c)

Figure 3.8 Computed response at point A (ground surface): (a) Displacement time history; (b) Acceleration time history; (c) Spectral acceleration

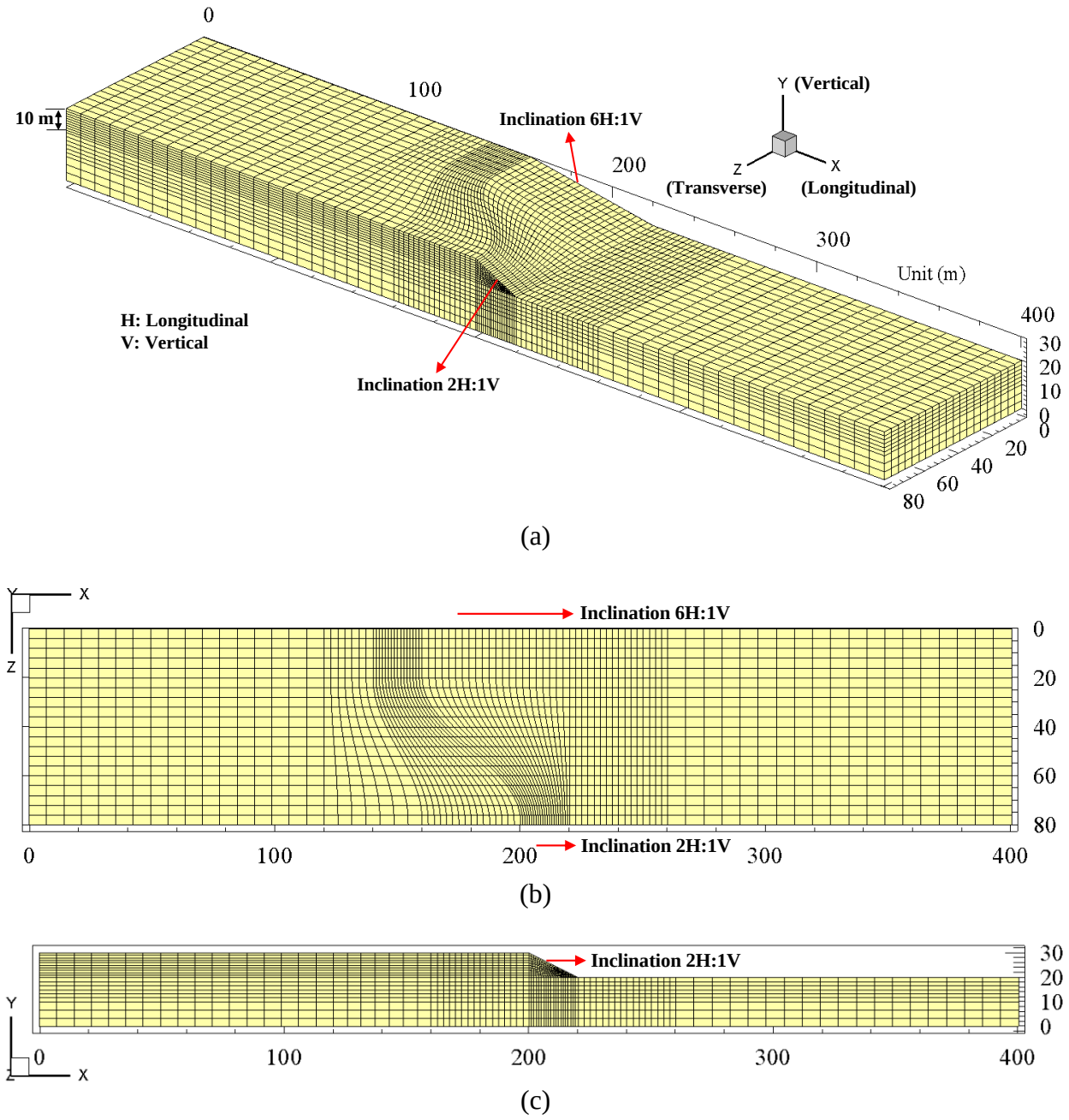

Figure 3.9 3D slope FE model: (a) Isometric view; (b) Plan view; (c) Side view (symmetry plane)

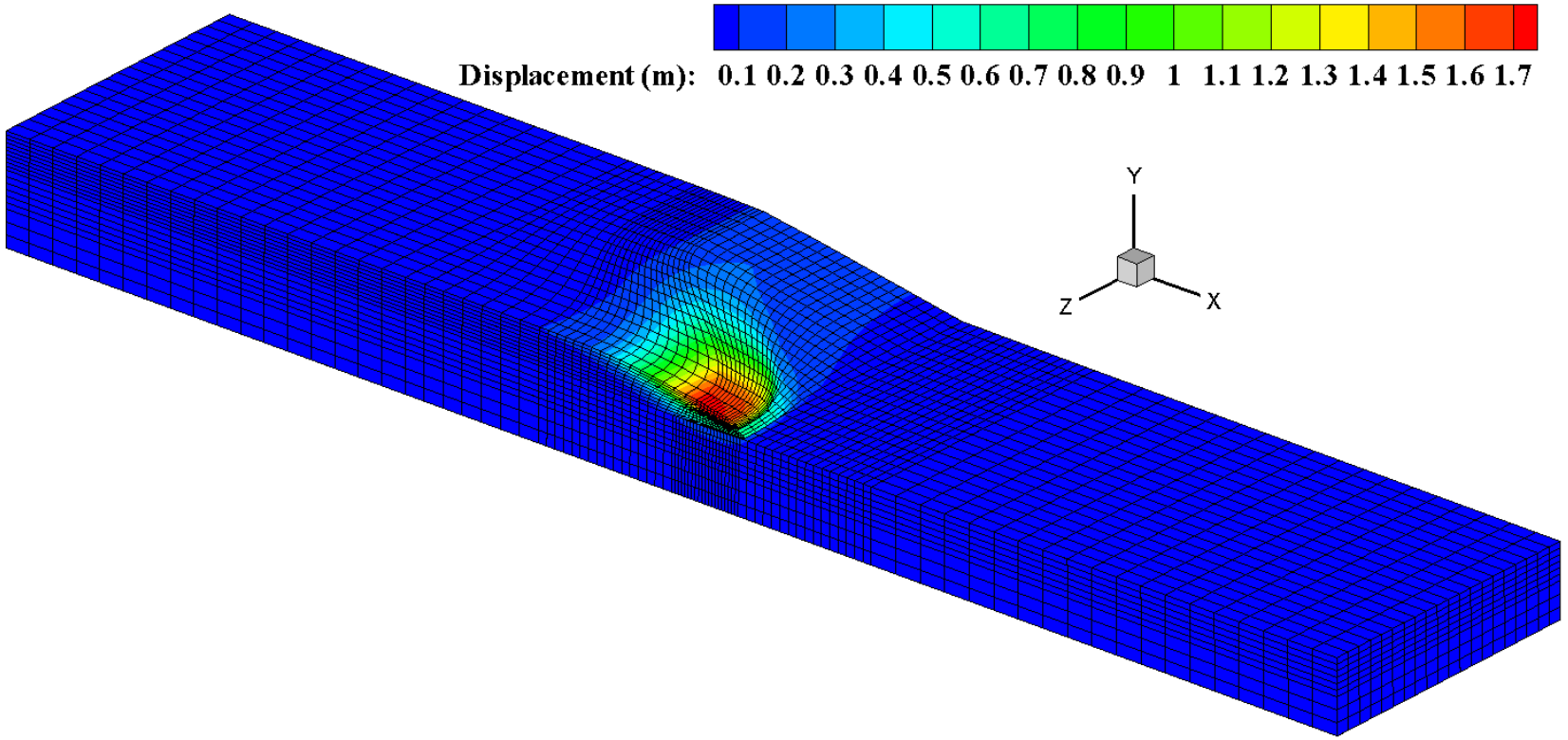

Figure 3.10 Deformed FE mesh at end of shaking (colors depict total relative displacement; factor = 5)

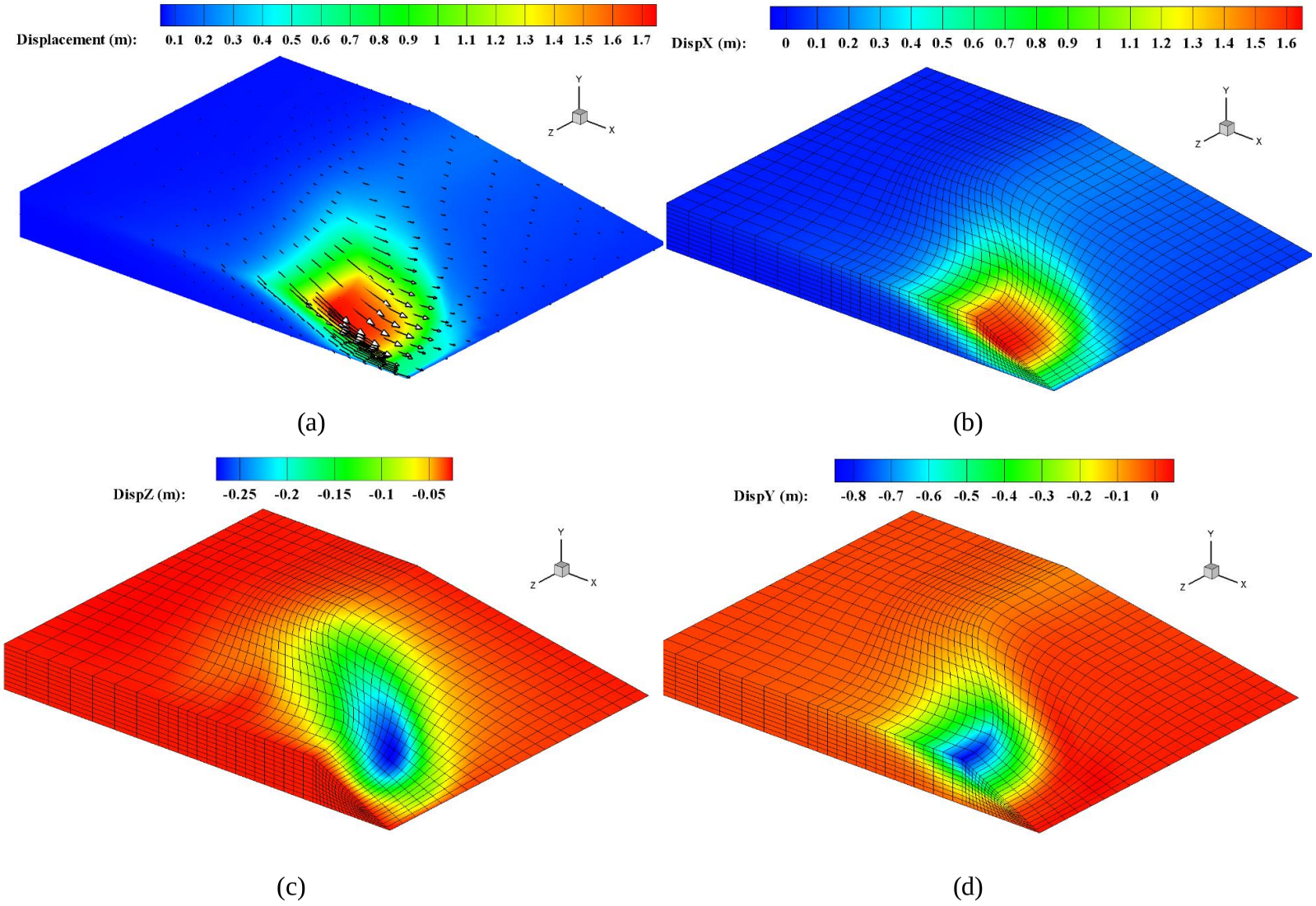

Figure 3.11 Computed displacement contours: (a) Arrows showing direction of ground movement; (b) Longitudinal X; (c) Vertical Y; (d) Transverse Z

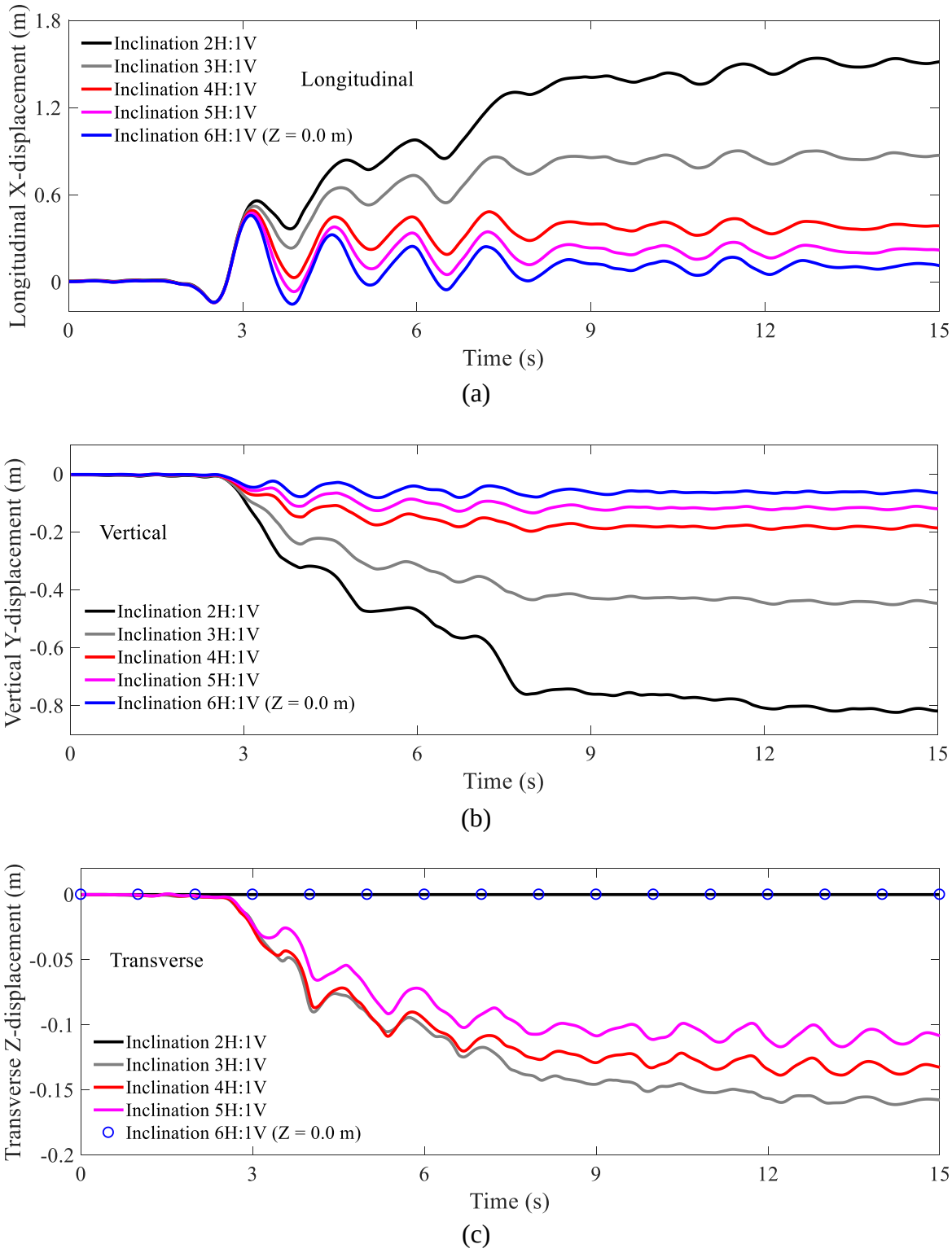

Figure 3.12 Displacement time histories of slope top along transverse Z direction: (a) Longitudinal; (b) Vertical; (c) Transverse

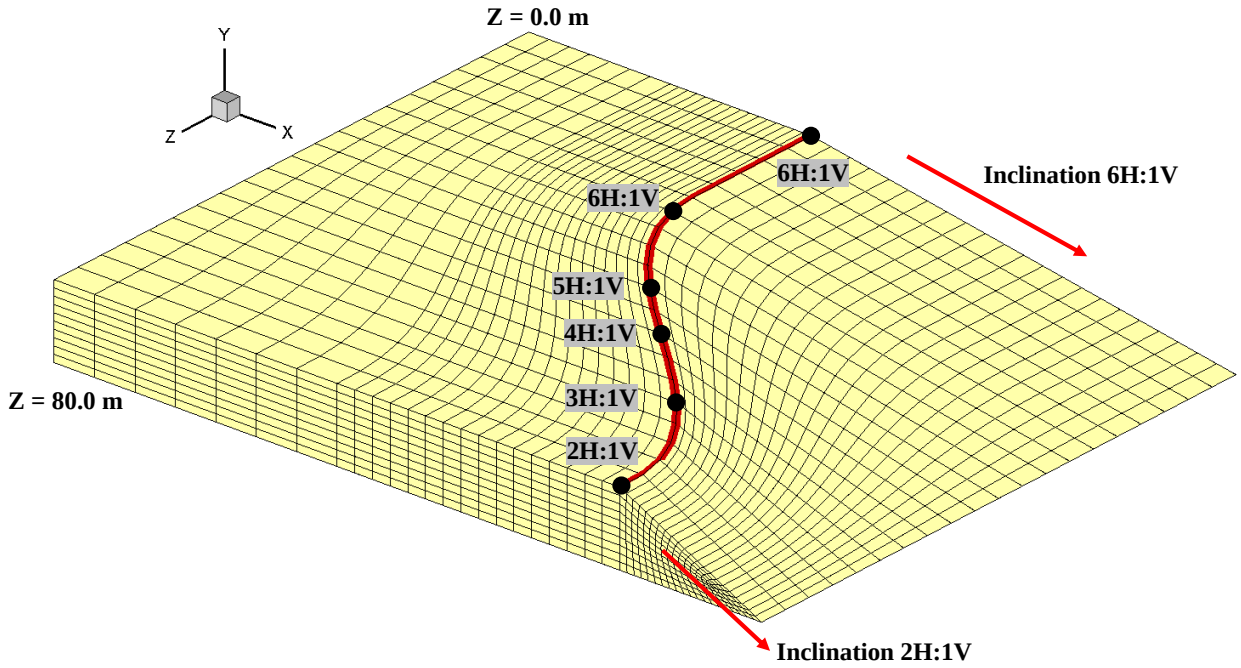

(a)

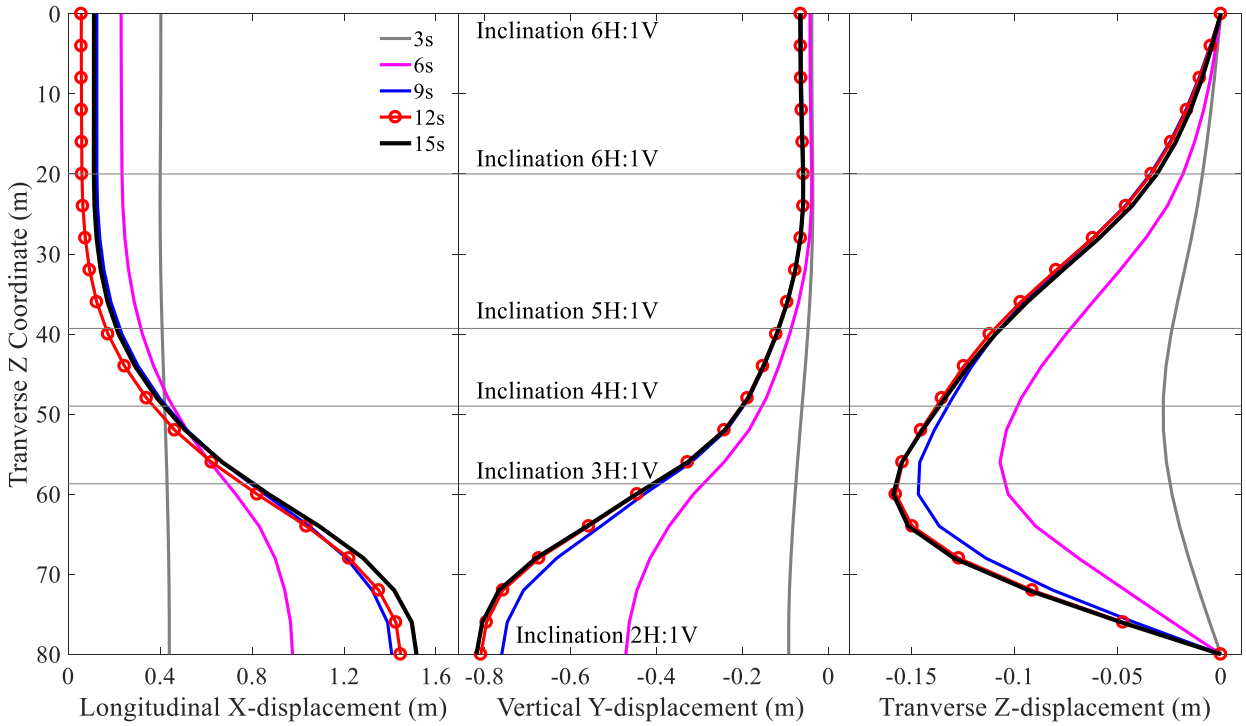

(b)

Figure 3.13 Displacement profile of slope top along transverse Z direction: (a) Isometric view; (b) At different time constants

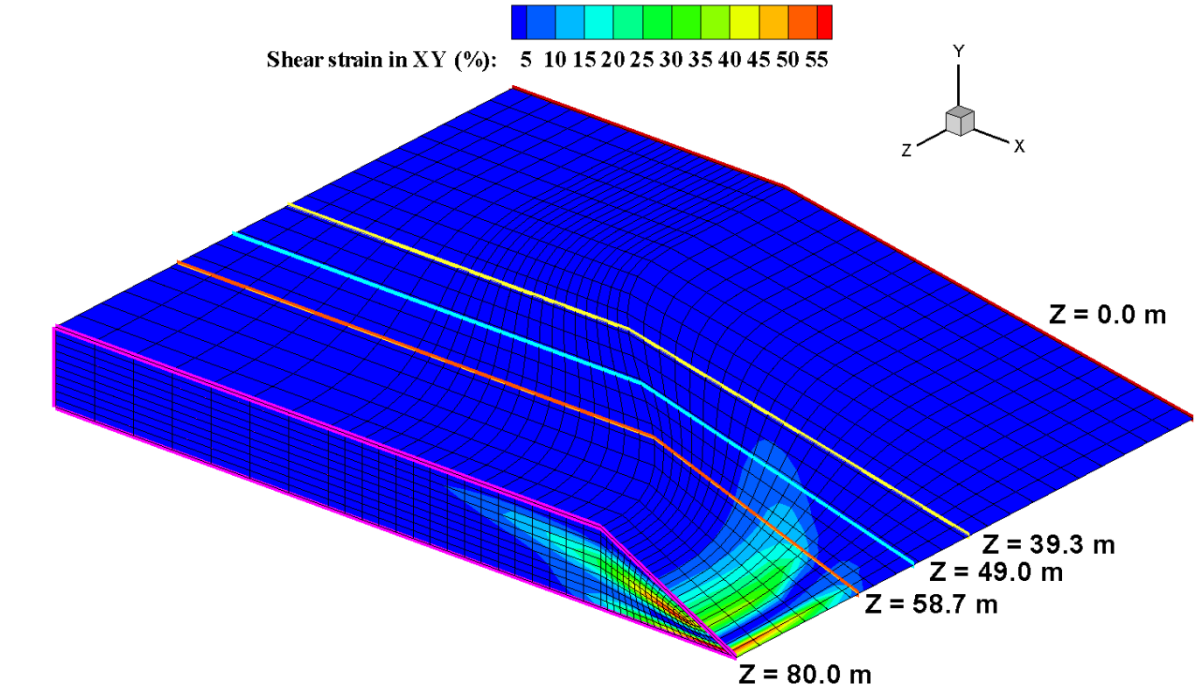

(a)

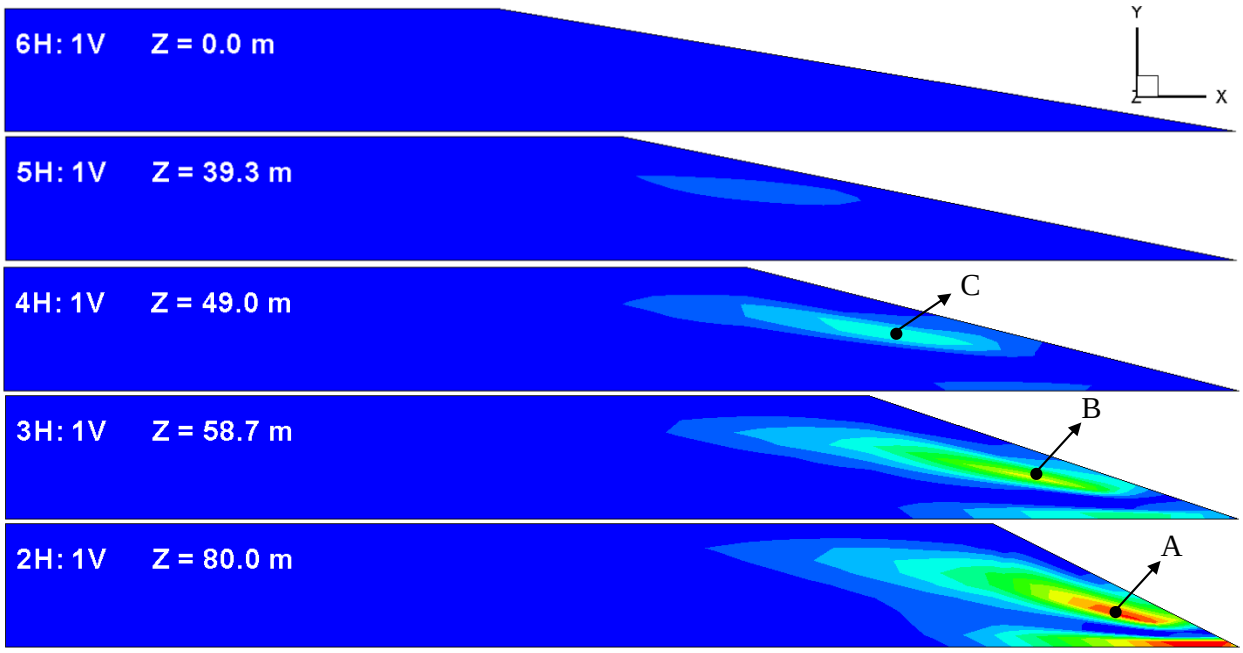

(b)

Figure 3.14 Shear strain γ_{xy}: (a) Contour with FE mesh; (b) Slices were taken at Z = 0.0 m, 39.3 m, 49.0 m, 58.7 m and 80.0 m

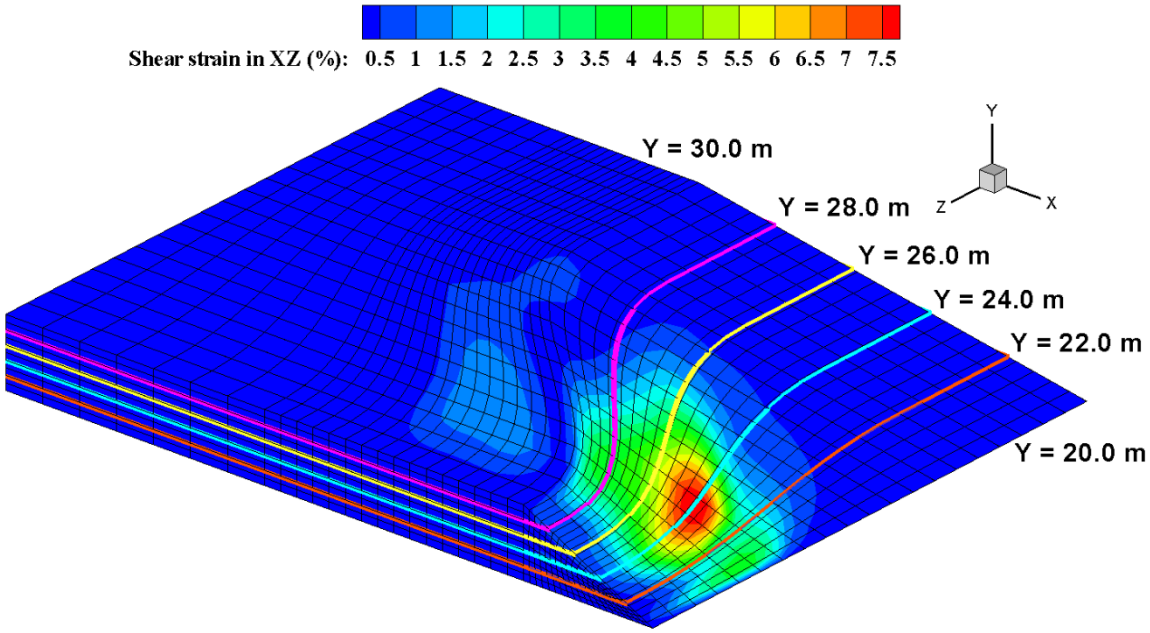

(a)

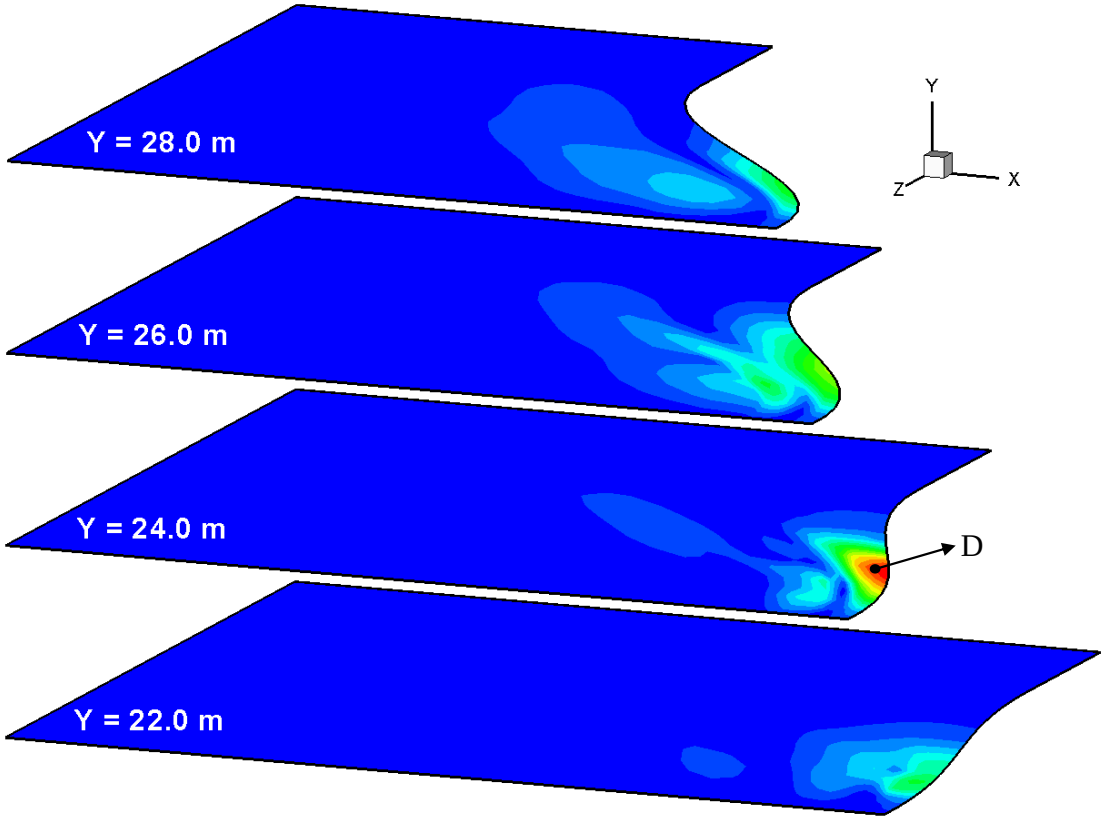

(b)

Figure 3.15 Shear strain γ_{xz}: (a) Contour with FE mesh; (b) Slices were taken at Y = 22 m, 24 m, 26 m and 28 m

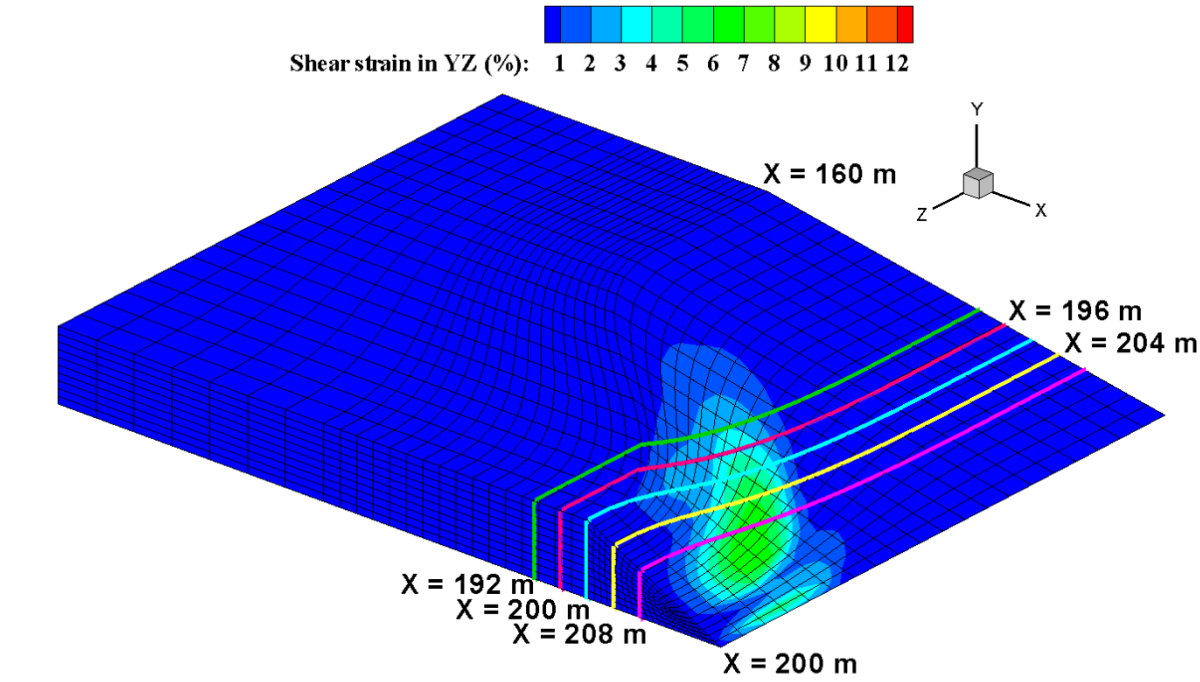

(a)

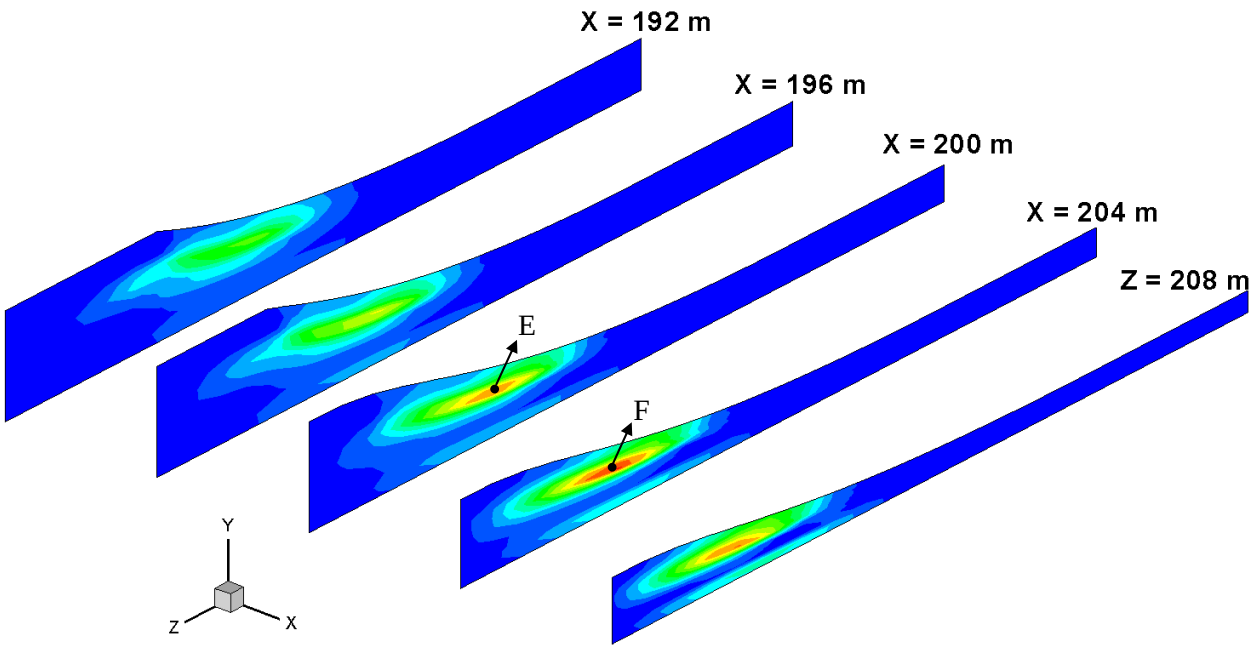

(b)

Figure 3.16 Shear strain γ_{yz}: (a) Contour with FE mesh; (b) Slices were taken at X = 192 m, 196 m, 200 m, 204 m and 208 m

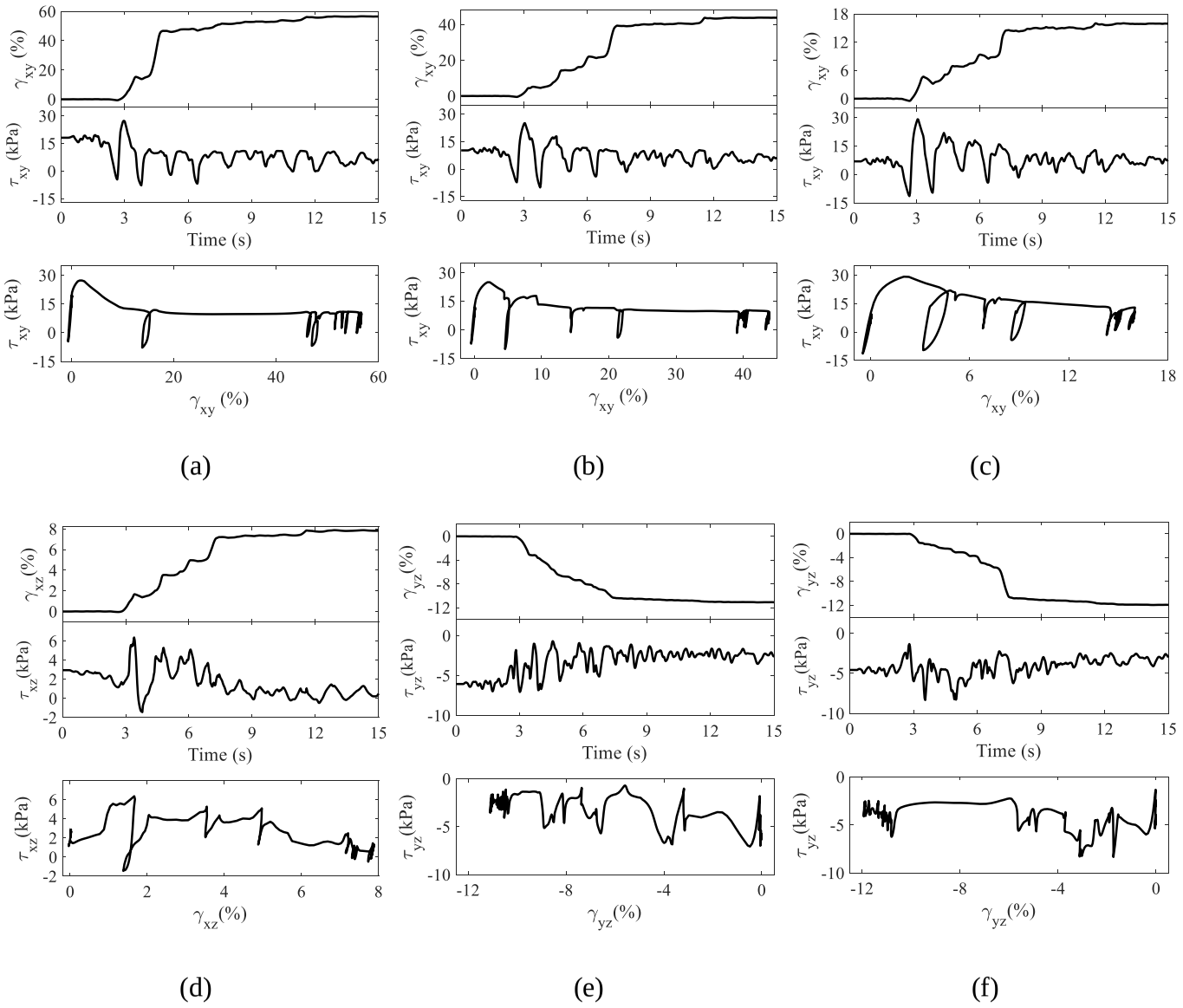

Figure 3.17 Shear stress and strain: (a)-(c) Points A-C (of Figure 3.14); (d) Point D (of Figure 3.15); (e), (f) Points E and F (of Figure 3.16)

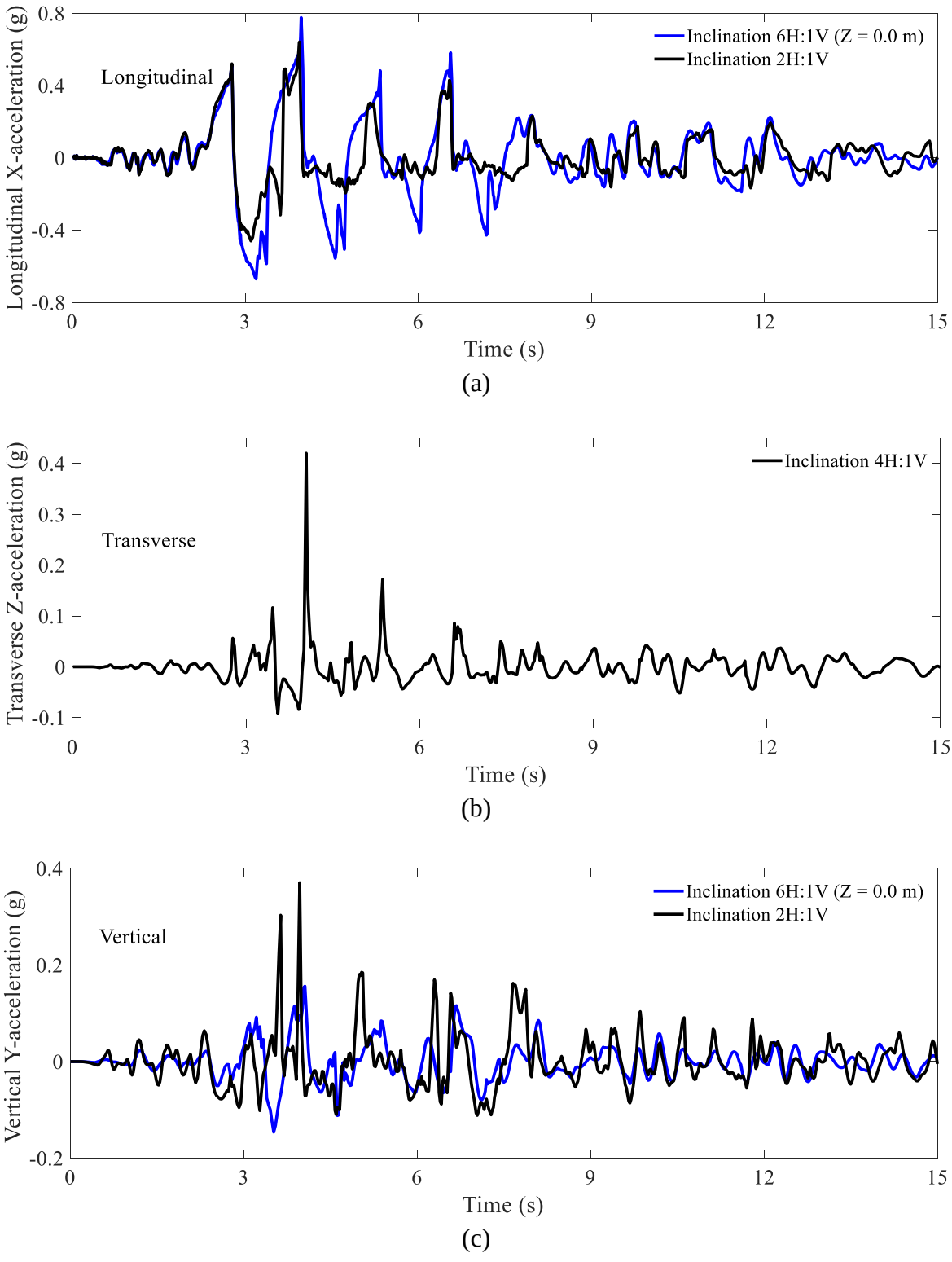

Figure 3.18 Acceleration time histories of slope top along transverse Z direction: (a) Longitudinal; (b) Transverse; (c) Vertical

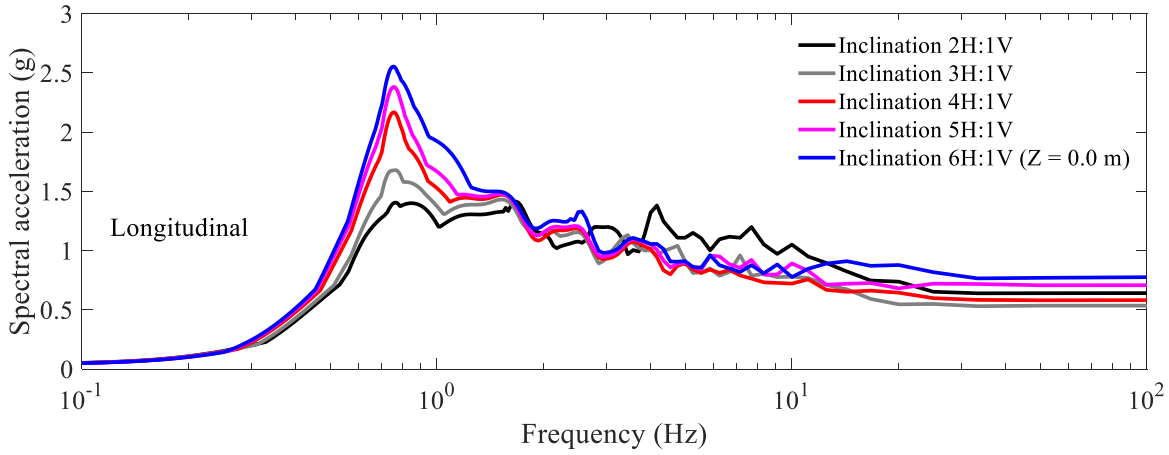

(a)

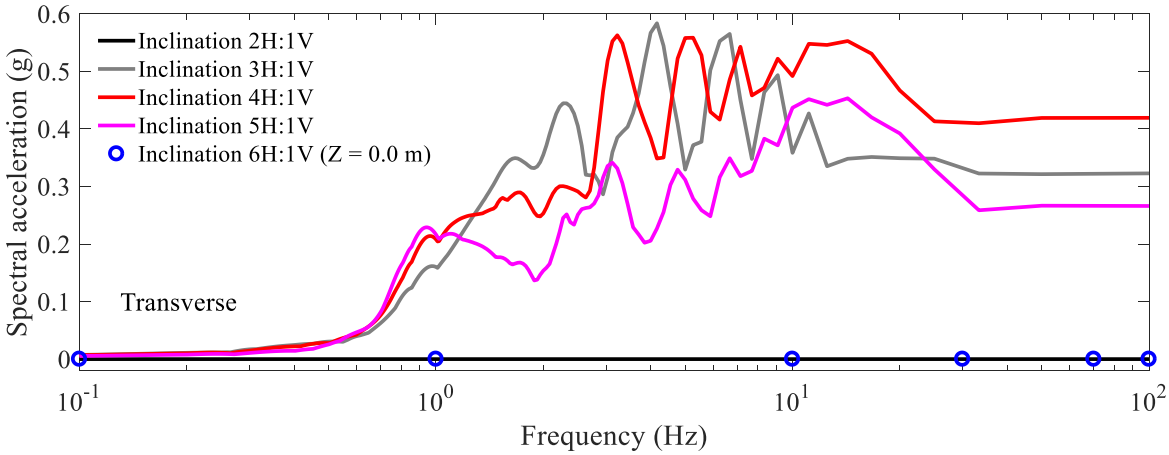

(b)

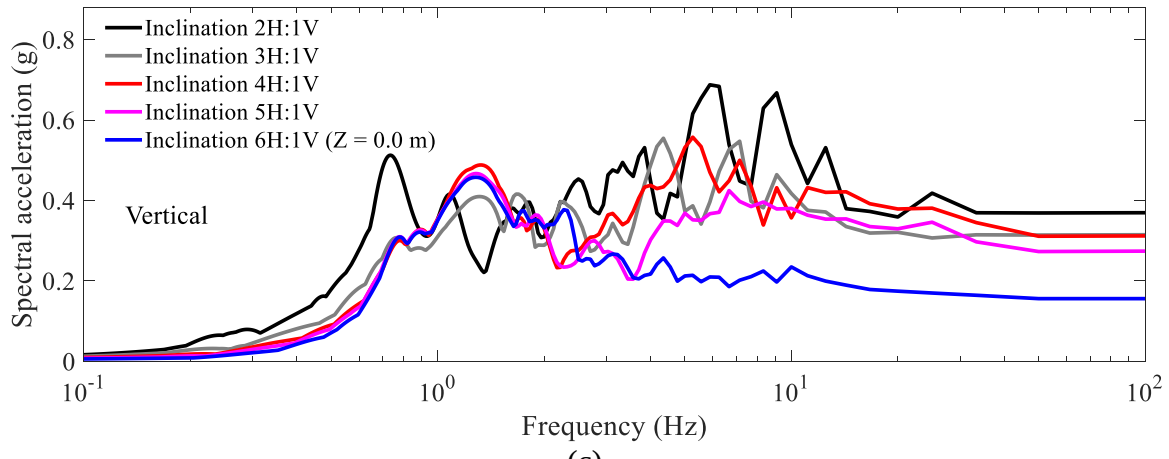

(c)

Figure 3.19 Acceleration response spectrum of slope top along transverse Z direction: (a) Longitudinal; (b) Transverse; (c) Vertical

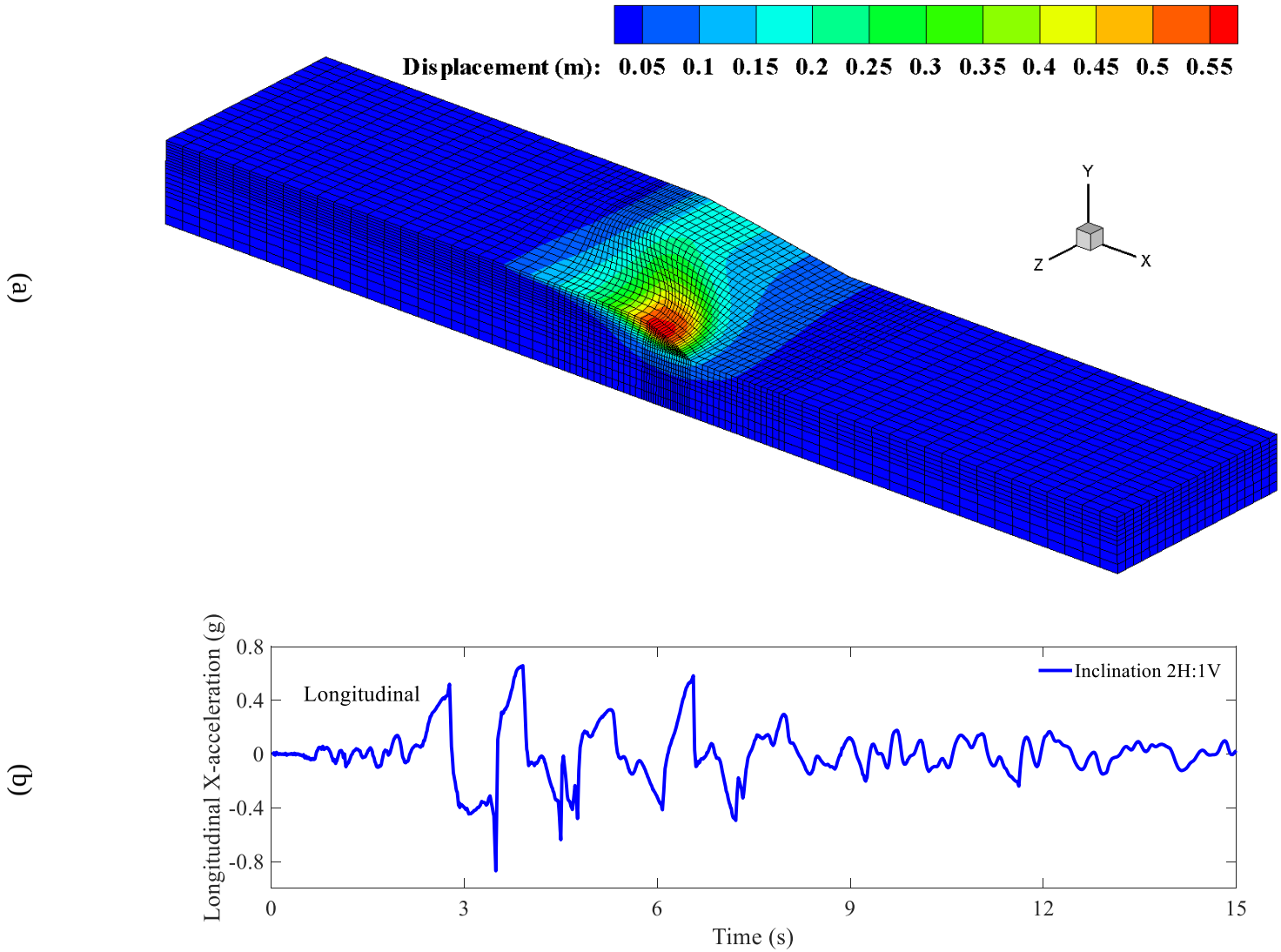

Figure 3.20 Computed response of MYS model: (a) Deformed FE mesh at end of shaking; (b) Acceleration time history of slope top at inclination 2H:1V (colors depict total relative displacement; factor = 5)

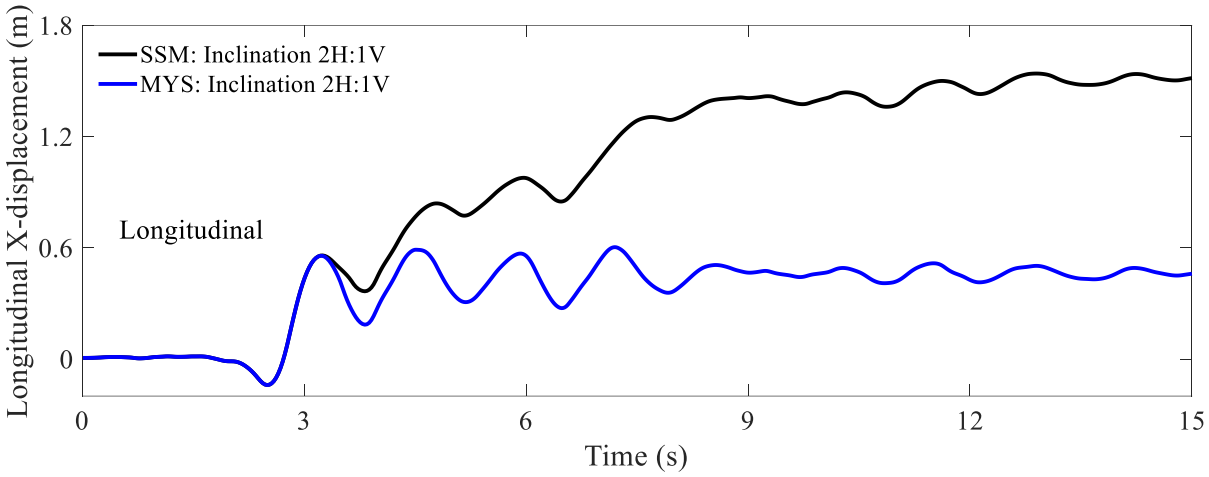

(a)

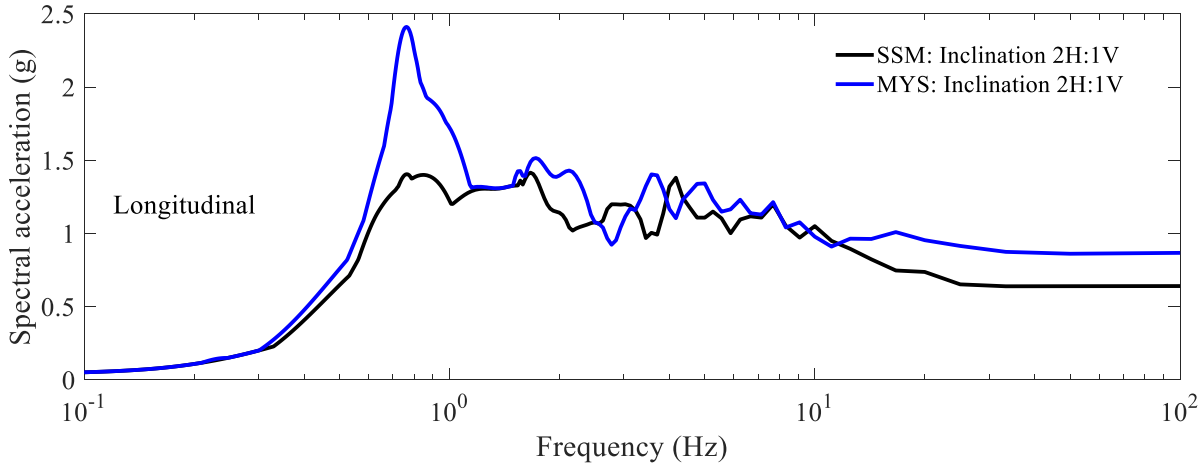

(b)

Figure 3.21 Comparison results of SSM and MYS models: (a) Displacement time history; (b) Spectral acceleration

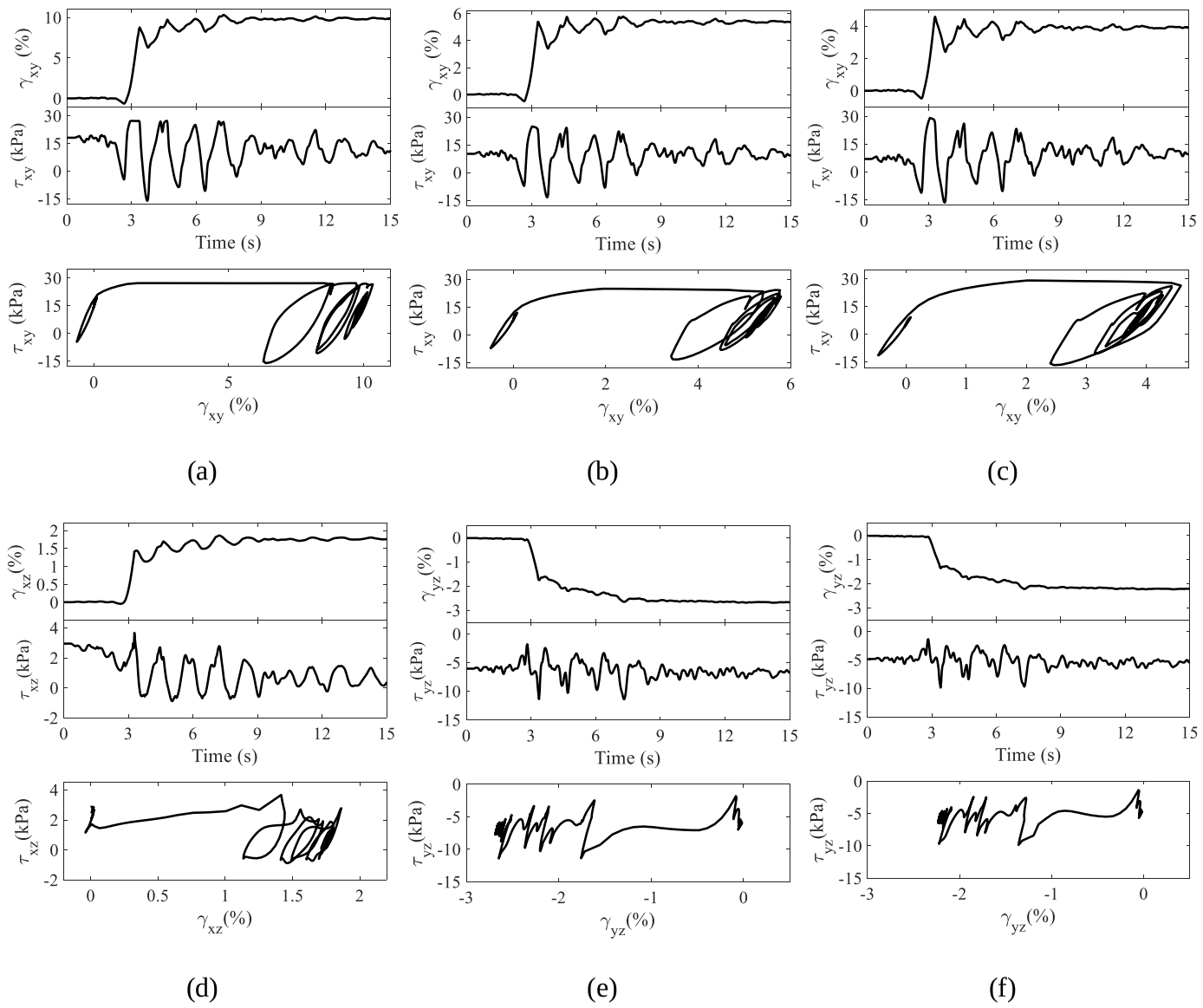

Figure 3.22 Shear stress and strain of MYS model: (a)-(c) Points A-C (of Figure 3.14); (d) Point D (of Figure 3.15); (e), (f) Points E and F (of Figure 3.16)

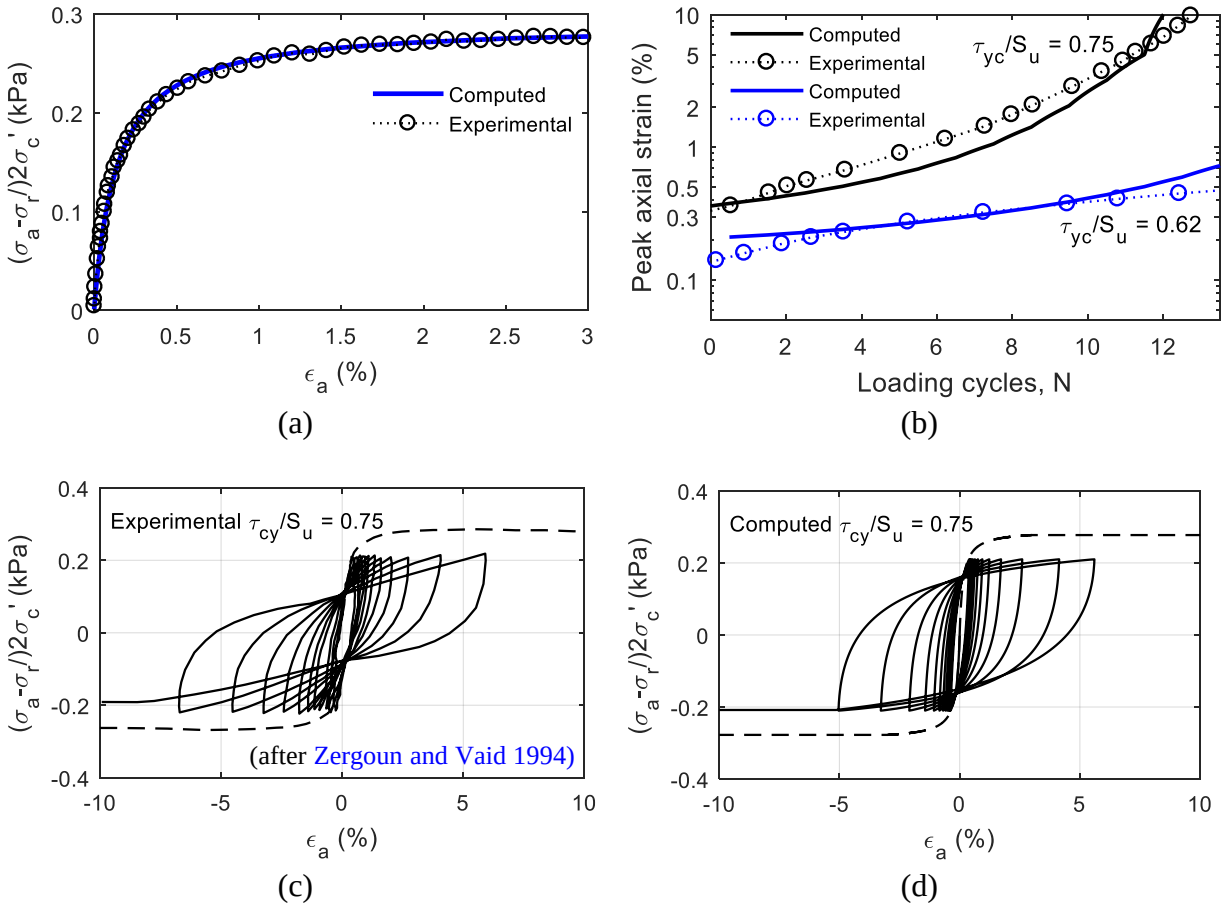

Figure 3.23 Computed and laboratory results of undrained triaxial test for Cloverdale clay: (a) Monotonic loading; (b) Peak axial strain versus number of loading cycles (after Zergoun and Vaid 1994); (c), (d) Cyclic loading with τ_{cy}/S_u = 0.75

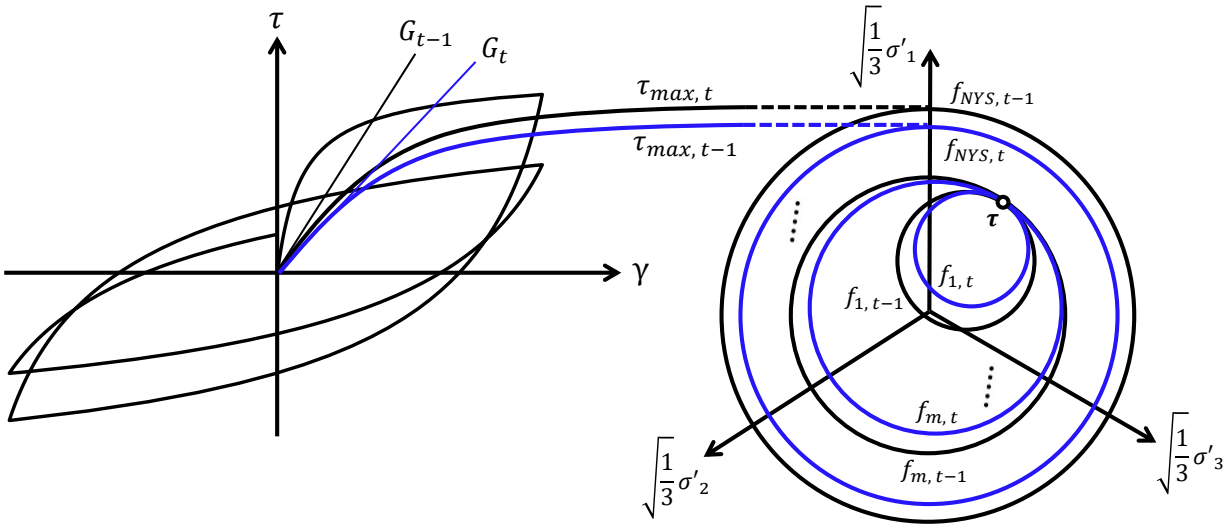

Figure 3.24 Schematic of cyclic softening logic

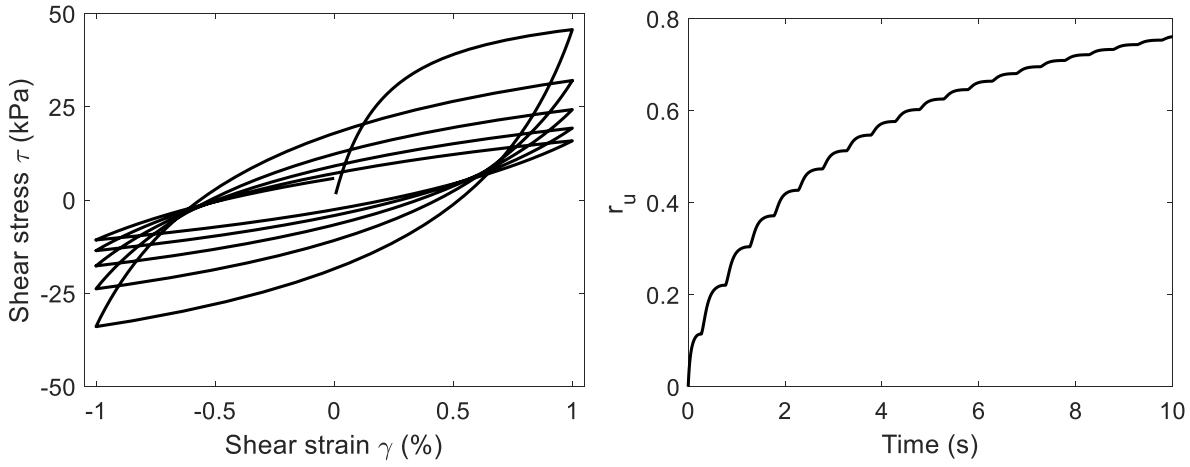

(a)

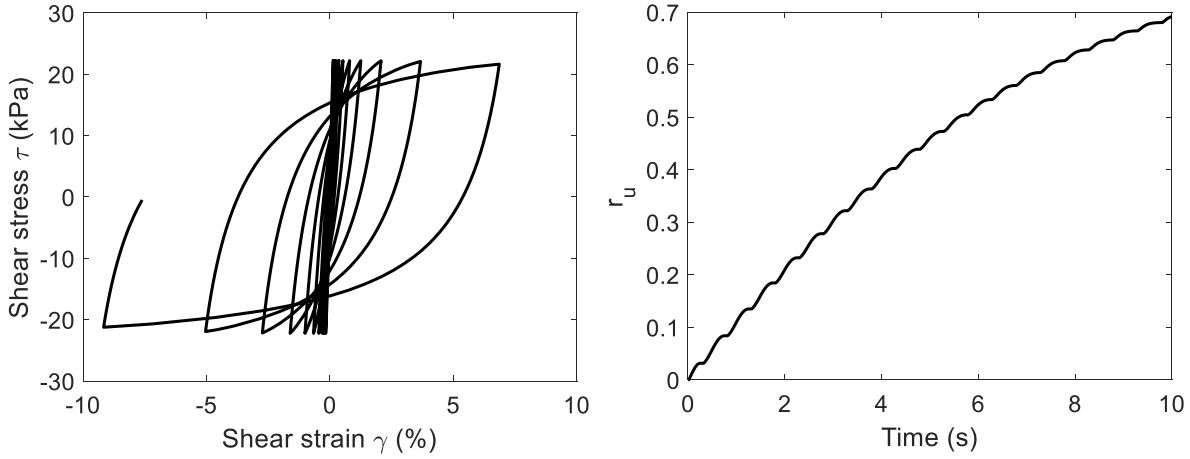

(b)

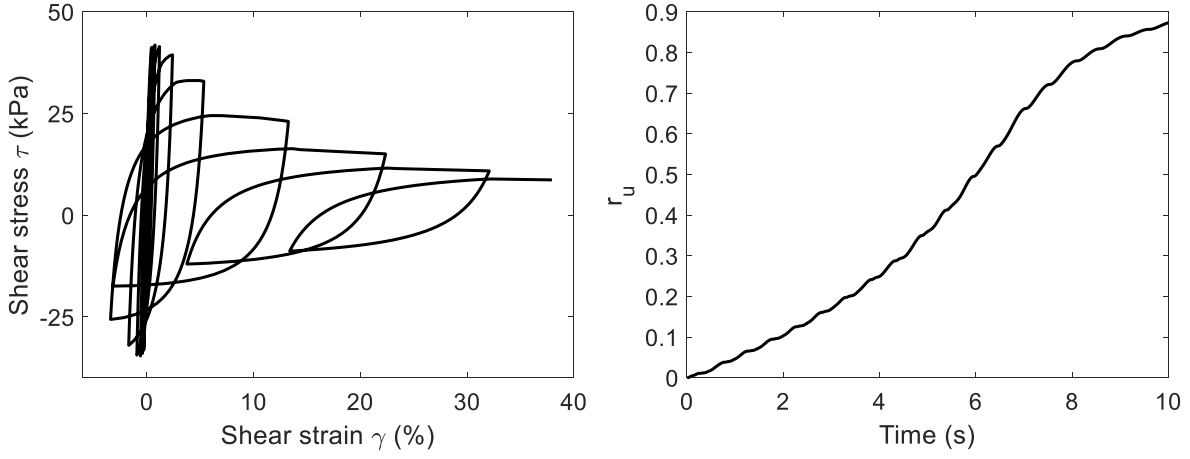

(c)

Figure 3.25 Cyclic softening model response under cyclic loading: (a) Strain controlled; (b) Stress controlled; (c) Biased accumulation of permanent shear strain

Chapter 4. Numerical Simulations of LEAP Centrifuge Tests for Seismic Response of Liquefiable Sloping Ground

4.1. Abstract

This chapter presents numerical simulations of a liquefiable sloping ground related to LEAP-UCD-2017 and LEAP-Asia-2019 (Liquefaction Experiments and Analysis Projects) dynamic centrifuge model tests (Type-C phase) conducted by various institutions. The numerical simulations are performed using a pressure-dependent constitutive model implemented with the characteristics of dilatancy, cyclic mobility and associated shear deformation. The soil parameters are determined based on a series of available stress-controlled cyclic triaxial and torsional shear tests for matching the liquefaction strength curves of Ottawa F-65 sand with relative densities D_r = 65 % and 60 % in calibration phase of LEAP-UCD-2017 and LEAP-Asia-2019, respectively. The computational framework for the dynamic response analysis is discussed and the computed results are presented for the selected centrifuge experiments during Type-C phase. Measured time histories (e.g., displacement, acceleration, and excess pore pressure ratio) of these experiments are reasonably captured. Comparisons between the numerical simulations and measured results showed that the pressure-dependent constitutive model as well as the overall employed computational framework have the potential to predict the response of the liquefiable sloping ground, and subsequently realistically evaluate the performance of an equivalent soil system subjected to seismically-induced liquefaction.

4.2. Introduction

LEAP (Liquefaction Experiments and Analysis Projects) is an effort to facilitate validation and verification of numerical procedures for liquefaction-induced lateral spreading analysis of a liquefiable sloping ground (Manzari et al. 2014; Kutter et al. 2014, 2015, 2018a). In order to obtain

a set of reliable centrifuge test data with high quality among different facilities, a centrifuge experiment was repeated at 6 facilities in LEAP-GWU-2015 (Manzari et al. 2018; Kutter et al. 2018a), as one project within LEAP. In addition, the associated numerical simulations conducted by several predictors (Armstrong 2018; Ghofrani and Arduino 2018; Ueda and Iai 2018; Zeghal et al. 2018; Ziotopoulou 2018) were compared with the measured response from the conducted experiments.

As part of the ongoing LEAP, i.e., LEAP-UCD-2017 (El Ghoraiby et al. 2017, 2020; Kutter et al. 2020a-d; Manzari et al. 2020a, b; Qiu and Elgamal 2020b, c) and LEAP-Asia-2019 (Ueda 2018; Qiu and Elgamal 2020b, c), a new set of dynamic centrifuge tests have been performed to simulate the liquefaction induced lateral spreading phenomenon in a fully saturated sloping ground. The test results of LEAP-UCD-2017 and LEAP-Asia-2019 are available in DesignSafe-CI (Kutter et al. 2018b; Ueda 2018).

On this basis, the results of numerical simulations for these dynamic centrifuge tests during Type-C phase in LEAP-UCD-2017 and LEAP-Asia-2019 are presented in this chapter. All the Finite Element (FE) simulations are performed using a pressure-dependent constitutive model (Parra 1996; Yang 2000; Yang and Elgamal 2002; Elgamal et al. 2003; Yang et al. 2003; Khosravifar et al. 2018) implemented with the characteristics of dilatancy, cyclic mobility and associated shear deformation. The soil parameters in LEAP-UCD-2017 and LEAP-Asia-2019 are determined based on a series of stress-controlled cyclic triaxial and torsional shear tests provided in the calibration phase for matching the liquefaction strength curves of Ottawa F-65 sand with relative densities D_r = 65 % and 60 %, respectively. To better capture the overall dynamic response of each selected centrifuge test in Type-C phase, two contraction parameters c_4 and c_5 controlling

the rate of pore pressure build-up were adjusted based on observations from selected centrifuge test results.

The following sections of this chapter outline: 1) computational framework, 2) specifics and calibration processes, 3) details of the employed FE modeling techniques, and 4) computed results of the selected centrifuge tests. Finally, a number of conclusions are presented and discussed.

4.3. Brief Summary of the Centrifuge Tests in LEAP-UCD-2017 and LEAP-Asia-2019

A schematic representation of the centrifuge tests (El Ghoraiby et al. 2020) is shown in Figure 4.1. The soil specimen is a sloping layer of Ottawa F-65 sand with 5° slope (target relative density D_r = 65 % in LEAP-UCD-2017 and D_r = 60 % in LEAP-Asia-2019). The soil layer has a length of 20 meters (in prototype scale) and a height of 4 meters (in prototype scale) at the center. The specimen is built in a container with rigid walls. Three arrays of accelerometers and pore pressure transducers are placed in the central section and at 3.5 meters away from the side walls on the upslope and downslope of the centrifuge model. In the vertical direction, the sensors are 0.5 meters apart. The sensors in the central section are required sensors and those of side arrays (away from central section) are recommended for all centrifuge facilities. All centrifuge models were subjected to a target motion of ramped, 1 *Hz* sine wave base motion with amplitude 0.15 g. Figure 4.2 shows the achieved motions for all selected centrifuge experiments with various relative densities in LEAP-UCD-2017 (Kutter et al. 2018b) and LEAP-Asia-2019 (Ueda 2018), respectively.

4.4. Finite Element Model

A two-dimensional FE mesh (Figure 4.3) is created to represent the centrifuge model, comprising 4961 nodes and 4800 quadrilateral elements (maximum size = 0.2 m). All numerical

simulations for the selected centrifuge experiments during Type-C phase of LEAP-UCD-2017 and LEAP-Asia-2019 are performed using the computational platform OpenSees. The Open System for Earthquake Engineering Simulation (OpenSees, McKenna 2011, http://opensees.berkeley.edu) developed by the Pacific Earthquake Engineering Research (PEER) Center, is an open source, object-oriented finite element platform. Currently, OpenSees is widely used for simulation of structural and geotechnical systems (Yang 2000; Yang and Elgamal 2002) under static and seismic loading.

Quadrilateral Four-node plane-strain elements with two-phase material following the *u-p* (Chan 1988) formulation were employed for simulating saturated soil response, where *u* is the displacement of the soil skeleton and *p* is the pore water pressure. Implementation of the *u-p* element is based on the following assumptions: 1) small deformation and rotation; 2) solid and fluid density remain constant in time and space; 3) porosity is locally homogeneous and constant with time; 4) soil grains are incompressible; 5) solid and fluid phases are accelerated equally. Hence, the soil layers represented by effective stress fully coupled *u-p* elements (quadUP in OpenSees) are capable of accounting for soil deformations and the associated changes in pore water pressure.

4.4.1. Soil Constitutive Model

The employed soil constitutive model (Parra 1996; Yang 2000; Yang and Elgamal 2002; Elgamal et al. 2003; Yang et al. 2003; Khosravifar et al. 2018) was developed based on the multi-surface-plasticity theory (Prevost 1978, 1985). In this employed soil constitutive model (Figure 4.4), the shear-strain backbone curve was represented by the hyperbolic relationship with the shear strength based on simple shear (reached at an octahedral shear strain of 10 %). The low-strain shear modulus under a reference effective confining pressure p'_r is computed using the equation

$G = G_0(p'/p'_r)^n$, where p' is effective confining pressure and G_0 is shear modulus at pressure p'_r. The dependency of shear modulus on confining pressure is taken as n = 0.5. The critical state frictional constant M_f (failure surface) is related to the friction angle ϕ (Chen and Mizuno 1990) and defined as $M_f = 6\sin\phi/(3-\sin\phi)$. As such, the soil is simulated by the implemented OpenSees material PressureDependMultiYield03 (Khosravifar et al. 2018). It is noted that PressureDependMultiYield03 includes recent modifications to more closely capture the established guidelines on liquefaction triggering (Idriss and Boulanger 2008). Brief descriptions of this soil constitutive model are included below.

4.4.2. Yield Function

The yield function is defined as a conical surface in principal stress space (Prevost 1985; Lacy 1986; Yang and Elgamal 2002):

$$f = \frac{3}{2}\left(\boldsymbol{s} - \left(p' + p'_0\right)\boldsymbol{a}\right) : \left(\boldsymbol{s} - \left(p' + p'_0\right)\boldsymbol{a}\right) - M^2\left(p' + p'_0\right)^2 = 0 \qquad (4\text{-}1)$$

where, $\boldsymbol{s} = \boldsymbol{\sigma}' - p'\boldsymbol{\delta}$, is the deviatoric stress tensor, $\boldsymbol{\sigma}'$ is the effective Cauchy stress tensor, $\boldsymbol{\delta}$ is the second-order identity tensor, p' is mean effective stress, p'_0 is a small positive constant (0.3 kPa in this chapter) such that the yield surface size remains finite at $p' = 0$ for numerical convenience and to avoid ambiguity in defining the yield surface normal to the yield surface apex, $\boldsymbol{a}$ is a second-order deviatoric tensor defining the yield surface center in deviatoric stress subspace, M defines the yield surface size, and ":" denotes doubly contracted tensor product.

4.4.3. Contractive Phase

Shear-induced contraction occurs inside the phase transformation (PT) surface ($\eta < \eta_{PT}$), as well as outside ($\eta > \eta_{PT}$) when $\dot{\eta} < 0$, where, η is the deviatoric stress ratio defined as

$\sqrt{\frac{3}{2}\boldsymbol{s}:\boldsymbol{s}}/(p' + p'_0)$ and η_{PT} is the deviatoric stress ratio at phase transformation surface (Figure 4.4b). The contraction flow rule is defined as:

$$P'' = (1 - \frac{\dot{\boldsymbol{n}}:\dot{\boldsymbol{s}}}{||\dot{\boldsymbol{s}}||}\frac{\eta}{\eta_{PT}})^2(c_1 + c_2\gamma_c)(\frac{p'}{p_a})^{c_3}(c_4\eta_{rv})^{c_5}$$
$$\eta_{rv} = \frac{\sqrt{[(\sigma_{11} - \sigma_{22})^2 + (\sigma_{22} - \sigma_{33})^2 + (\sigma_{11} - \sigma_{33})^2]/2 + {\tau_{12}}^2 + {\tau_{23}}^2 + {\tau_{13}}^2}}{(p' + p'_0)} \quad (4\text{-}2)$$

where c_1, c_2, c_3, c_4 and c_5 are non-negative calibration constants, γ_c is octahedral shear strain accumulated during previous dilation phases, p_a is atmospheric pressure for normalization purpose, and $\dot{\boldsymbol{s}}$ is the deviatoric stress rate. In Equation (4-2), η_{rv} is the shear stress ratio on load reversal point during cyclic loading, essentially representing the effect of previous shear stress on the subsequent contractive behavior. The $\dot{\boldsymbol{n}}$ and $\dot{\boldsymbol{s}}$ tensors are used to account for general 3D loading scenarios, where, $\dot{\boldsymbol{n}}$ is the outer normal to a surface. The parameter c_3 is used to represent the dependence of pore pressure buildup on initial confinement (i.e., K_σ effect).

4.4.4. Dilative Phase

Dilation appears only due to shear loading outside the PT surface ($\eta > \eta_{PT}$ with $\dot{\eta} > 0$), and is defined as:

$$P'' = (1 - \frac{\dot{\boldsymbol{n}}:\dot{\boldsymbol{s}}}{||\dot{\boldsymbol{s}}||}\frac{\eta}{\eta_{PT}})^2(d_1 + {\gamma_d}^{d_2})(\frac{p'}{p_a})^{-d_3} \quad (4\text{-}3)$$

where d_1, d_2 and d_3 are non-negative calibration constants, and γ_d is the octahedral shear strain accumulated from the beginning of a particular dilation cycle (such as, stage 1-2 or 5-6 in Figure 4.4b) as long as there is no significant load reversal. Subsequently, dilation rate increases as the shear strain accumulates in a particular cycle. Furthermore, a significant unloading (such as stage

6-8 in Figure 4.4b) will reset γ_d to zero. Parameter d_3 in Equation (4-3), reflects the dependence of pore pressure buildup on initial confinement (i.e., K_σ effect).

4.4.5. Neutral Phase

When the stress state approaches the PT surface ($\eta = \eta_{PT}$) from below, a significant amount of permanent shear strain may accumulate prior to dilation, with minimal changes in shear stress and confinement (implying $P" = 0$). For simplicity, $P" = 0$ is maintained during this highly yielded phase until a boundary defined in deviatoric strain space is reached, and then dilation begins. This yield domain will enlarge or translate depending on load history. In deviatoric strain space, the yield domain (Figure 4.4b) is a circle with the radius γ defined as (Yang et al. 2003):

$$\gamma = \frac{\gamma_s + \gamma_{rv}}{2}$$

$$\gamma_s = y_1 \langle \frac{p'_{max} - p'_n}{p'_{max}} \rangle^{0.25} \int_0^t d\gamma_c \tag{4-4}$$

$$\gamma_{rv} = y_2 \langle \frac{p'_{max} - p'_n}{p'_{max}} \rangle^{0.25} oct(\boldsymbol{e} - \boldsymbol{e}_p)$$

where, y_1 (non-negative) is used to define the accumulated permanent shear strain γ_s as a function of dilation history $\int_0^t d\gamma_c$ and allow for continuing enlargement of the domain, p'_{max} is maximum mean effective confinement experienced during cyclic loading, p'_n is mean effective confinement at the beginning of current neutral phase, and $\langle\ \rangle$ denotes MacCauley's brackets (i.e., $\langle a \rangle = max\ (a, 0)$). Figure 4.5a shows the effect of y_1 on the evolution process of yield domain for an undrained cyclic loading simulation. As seen in this figure, larger y_1 will result in a higher level of cycle-by-cycle shear strain accumulation. The y_2 (non-negative) parameter is mainly used to define the biased accumulation of permanent shear strain γ_{rv} as a function of load reversal history and allows for translation of the yield domain during cyclic loading. Figure 4.5b investigates the effect

of y_2 on the translation of the yield domain on a cycle-by-cycle basis. It can be seen that the scenario with a larger value of y_2 will cause a higher level of slip strain γ_{rv} (Figure 4.5b). In Equation (4-4), $oct(\boldsymbol{e} - \boldsymbol{e}_p)$ denotes the octahedral shear strain of tensor $\boldsymbol{e} - \boldsymbol{e}_p$, where $\boldsymbol{e}$ is current deviatoric shear strain, and $\boldsymbol{e}_p$ is pivot strain obtained from previous dilation on load reversal point.

4.5. Boundary and Loading Conditions

The boundary and loading conditions for dynamic analysis of the liquefiable sloping ground (Figure 4.3) under an input motion are implemented in a staged fashion as follows:

1) Gravity was applied to activate the initial static state with: i) linear elastic properties (Poisson's ratio of 0.47 to lower the initial locked shear stress), ii) nodes on both side boundaries (vertical faces) of the FE model were fixed against longitudinal translation for complicity (i.e., no separation between container wall and soil), iii) nodes were fixed along the base against vertical translation only to avoid superfluous unrealistic initial locked shear stress at the model base (prototype scenario, nevertheless, it is noted that fixing horizontal translation as well, did not result in appreciable difference in the overall dynamic response in view of the relatively small 5° slope and the resulting low initial states of shear stress), iv) water table was specified with related water pressure and nodal forces specified along ground surface nodes (initial hydrostatic values of pore water pressures were fixed at the ground surface nodes), and flow of water was restricted to across the container boundaries. At the end of this step, the static soil state was imposed and displacements under own-weight application were re-set to zero using the OpenSees command InitialStateAnalysis.

2) Nodes were fixed along the base against longitudinal translation.

3) Soil properties were switched from elastic to plastic (Table 4.1) and the internal variables of PressureDependMultiYield03 constitutive model were adjusted to this stress state (Figure 4.6 before shaking).

4) Dynamic analysis is conducted by applying an acceleration time history to the base of the FE model.

The FE matrix equation is integrated in time using a single-step predictor multi-corrector scheme of the Newmark type with integration parameters $\gamma = 0.6$ and $\beta = 0.3025$ presented in early studies (Chan 1988; Parra 1996). The equation is solved using the modified Newton-Raphson method, i.e., Krylov subspace acceleration (Carlson and Miller 1998) for each time step. For the convergence criterion, a test of energy increment is used with 10^{-6} and maximum number of iterations of 50. Furthermore, the constraints are imposed using Transformation method in OpenSees. Finally, a relatively low-level of initial stiffness proportional damping (coefficient = 0.003 leading to 1 % damping ratio at frequency = 1 *Hz*) with the main damping emanating from the soil nonlinear shear stress-strain hysteresis response (Parra 1996) was used to enhance numerical stability of the liquefiable sloping system.

4.6. Calibration Phase: Determination of Soil Model Parameters

4.6.1. LEAP-UCD-2017

To predict dynamic response of centrifuge tests in LEAP-UCD-2017, the employed soil constitutive model parameters are calibrated for matching the liquefaction strength curve of the Ottawa F-65 sand with relative density D_r = 65 %, which will be further used in Type-C simulations. For that purpose, a total of 6 undrained stress-controlled cyclic triaxial tests are performed and the laboratory results are provided in calibration phase (Vasko 2015; Bastidas 2016; Vasko et al. 2018; El Ghoraiby et al. 2020). The parmeability of the Ottawa F-65 sand is about

1.1×10^{-4} m/s determined from El Ghoraiby et al. 2020. The internal friction angle, defined in $\sin\phi = (3+M_f)/(6+M_f)$, is obtained by matching the critical state frictional constant M_f of test data (Kutter et al. 2018b). On this basis, the calibrated soil model parameters for the Ottawa F-65 sand of D_r = 65 % are presented in Table 4.1.

Figure 4.7a shows the plot of liquefaction strength curves achieved from the FE simulations and experimental measurements. The data plotted in Figure 4.7a is composed of the number of cycles until a 2.5% single amplitude of strain is achieved versus the applied cyclic stress ratio (*CSR*). It can be seen that a comparatively good match is reached between simulation results and laboratory data. For illustration, an example of undrained cyclic triaxial stress-controlled test with *CSR* = 0.2 is displayed in Figure 4.7b-e. As seen in these figures, the computed response reasonably matches the stress path and maximum axial strain. It is noted that the yield surface of PressureDependMultiYield03 material is conical in principal stress space (Figure 4.4), such that the computed deviatoric stress versus axial strain curve is symmetric (Figure 4.7b). As a result, the simulations generate a higher material damping (measured as the area enclosed by the stress-strain loops from Kramer 1996) compared to the experimental data.

4.6.2. LEAP-Asia-2019

A total of 4 undrained stress-controlled torsional shear tests for Ottawa F-65 sand of relative density D_r = 60 % are performed in LEAP-Asia-2019 and the test results are available in DesignSafe-CI (Ueda 2018). Figure 4.8a shows the comparison result of computed and experimental liquefaction strength curves. The data plotted in Figure 4.8a is composed of the number of cycles until a 7.5 % double amplitude (i.e., 3.75 % single amplitude) of strain is achieved versus the applied cyclic stress ratio. It can be seen that the computed results are in good agreement with the laboratory data. An example of undrained stress-controlled torsional shear test

with *CSR* = 0.2 is illustrated in Figure 4.8b-e. The computed results reasonably match the stress path and shear stress-strain response of laboratory test (Ueda 2018), indicating that the material damping may be captured to a reasonable accuracy as well.

4.7. Computed Results of Type-C Simulations in LEAP-UCD-2017

The simulation results of selected 9 centrifuge tests in Type-C phase are presented (experimental data is available in DesignSafe-CI, Kutter et al. 2018b). The achieved base input motions of centrifuge tests with different relative densities at various facilities are shown in Figure 4.2a. The model parameters are calibrated primarily for matching the liquefaction strength curve (Figure 4.7a) and listed in Table 4.1.

Although the computed results and measurements are in good agreement in calibration phase, it was found that the simulations were unable to successfully capture the overall response of selected centrifuge tests in Type-C phase. In order to better capture the dynamic response of all centrifuge tests, UCD-3 is selected as the calibration basis for adjusting the material parameters (i.e., c_4 and c_5 controlling the rate of pore pressure build-up). As such, the contraction parameter c_4 = 5.2 and c_5 = 3.0 obtained in calibration phase (Table 4.1) are adjusted to 1.0 and 0.5, respectively, based on observations from test results of UCD-3 (D_r = 64.2 %) in Type-C phase. Thereafter, the following numerical simulations for other centrifuge tests are performed based on the adjusted parameters c_4, c_5 and the rest of material properties in calibration phase (Table 4.1).

4.7.1. Acceleration

Figure 4.9 depicts the computed and experimental acceleration time histories at the locations AH1-AH4 (middle array of accelerometers in Figure 4.1) for LEAP-UCD-2017. It can be seen that the computed acceleration at deeper depths (AH1-AH2) are in good agreement with those from the measurements (Figure 4.7). For shallower depths (AH3-AH4), both the computed

results and measurements showed a consistent trend for acceleration spikes due to dilation. Since the material parameters c_4 and c_5 are adjusted primarily for matching the experimental results of UCD-3, it might be inappropriate for calibrations of other centrifuge tests with different relative densities (Figure 4.2a). As seen in Figure 4.9, the experimental accelerations at AH4 were not captured successfully in KAIST-1, KAIST-2, NCU-3, and KyU-3. All these experimental results showed very high acceleration spikes due to strong dilation. However, in calibrations of CU-2 and Ehime-2, the computed results displayed much higher dilation spikes in contrast to measurements. It can be stated that these unintended inconsistencies in test results are mainly due to the different relative densities in centrifuge experiments conducted at various facilities.

4.7.2. Excess Pore Pressure Ratio

Figure 4.10 illustrates the time histories of excess pore pressure ratio $r_u = u_e/\sigma'_v$ in LEAP-UCD-2017, where u_e is excess pore pressure and σ'_v denotes initial mean effective stress. The soil liquefaction is conventionally defined by the value of r_u reaching a maximum of 1.0. As such, the r_u in simulations are compared with measurements (Figure 4.10) for the middle array of pore pressure transducers P1-P4 (Figure 4.1). In general, the computed r_u reasonably matches with those from measurements, such as UCD-3, KyU-3, CU-2, NCU-3 KAIST-1 and ZJU-3. Both the computed results and measurements showed a consistent trend of negative spikes due to dilation, in accordance with the acceleration (Figure 4.9). However, there are significant discrepancies in P3 and P4 between the simulations and measurements in Ehime-2 and KAIST-2. It can be seen clearly that the values of r_u exceeded 1.0 by a large margin in P3 and P4 in experimental results of Ehime-2 and KAIST-2 (Figure 4.9). This might be due to the actual locations of P3 and P4 are deeper than the planned locations in centrifuge tests (Figure 4.1). In addition, soils at deeper depths of UCD-1 are not fully liquefied, such that the peak values of r_u are overpredicted by numerical

simulations. These inconsistencies of experimental results achieved from various facilities are hindering such comparisons with the numerical simulations.

4.7.3. Displacement

Figure 4.11 displays the computed horizontal displacement time histories and experimental measurements at the midpoint of the ground surface. It can be seen that the computed results of UCD-3 and Ehime-2 are in good agreement with those from measurements. However, there are some discrepancies for other tests, such as the horizontal displacements of CU-2, NCU-3, KAIST-2, ZJU-2 are underpredicted, and UCD-1, KAIST-1, KyU-3 are overpredicted, mainly due to the different relative densities in centrifuge experiments conducted at various facilities. These inconsistencies indeed make it challenge to achieve a perfect match between the experimental measurements and numerical simulations for all selected centrifuge tests. As such, material parameter y_2 controlling the cycle-by-cycle shear strain accumulation is suggested to be adjusted to better capture the permanent displacement in measurements (as discussed below).

4.7.4. Computed Response of UCD-3

To investigate the overall response of the liquefiable sloping ground, computed results of UCD-3 is presented in Figure 4.12-Figure 4.15. The deformed FE mesh at end of shaking (Figure 4.12) showed a maximum horizontal displacement occurred near the ground surface in the middle of slope, reaching about 0.11 m. Furthermore, Figure 4.12b shows the horizontal displacement contour with arrows displaying the direction of ground movement. It can be seen that the horizontal displacements of soil ground at deeper depths are also high due to the liquefaction of underlying soil layers (Figure 4.10). Vertical displacement contour at end of shaking is illustrated in Figure 4.12c. As seen in this figure, the upslope soil settled about 0.06 m and ground heave in downslope reached about 0.025 m.

Figure 4.13 shows the displacement profile along depth in the middle of slope. After 6 seconds, the soil displacement starts accumulating due to the pore pressure build-up (Figure 4.10). Upon liquefaction (about 12 seconds), the permanent displacement is accumulating much faster until the end of shaking about 20 seconds (Figure 4.11 and Figure 4.13).

In accordance with the ground deformation contours (Figure 4.12), Figure 4.14 illustrates the shear strain in xy plane with a peak value of about 4 % in the middle of slope. In upslope side, the horizontal strain reached about positive 2.5 %, indicating that soil is moving away from the rigid container wall. In downslope side, soil compression is observed with negative horizontal strain of a value about 2 %. The vertical strain contour is displayed in Figure 4.14, with a similar ground deformation pattern as observed in Figure 4.12c.

Figure 4.15 depicts the computed shear stress versus mean effective stress, and shear stress versus shear strain for integration points near the locations of pore pressure transducers (P1-P4). In Figure 4.15a, a cycle-by-cycle accumulation of shear deformations is observed, and the spikes in shear stress are consistent with the pore pressure dips due to dilation (Figure 4.10).

4.8. Computed Results of Type-C Simulations in LEAP-Asia-2019

This section presents the simulation results of selected 8 centrifuge tests in Type-C phase of LEAP-Asia-2019 (Ueda 2018). The achieved input motions of centrifuge tests with different relative densities at various facilities are displayed in Figure 4.2b. The material parameters (Table 4.1) are calibrated primarily for matching the liquefaction strength curve of Ottawa F-65 sand with D_r = 60 % in calibration phase. To better capture the overall dynamic response of centrifuge tests of RPI-A-A1-1, RPI-A-B1-1, UCD-A-A1-1 and UCD-A-A2-1, the contraction parameters c_4 = 7.0 and c_5 = 4.0 obtained in calibration phase (Table 4.1) are adjusted to 0.6 and 0.1, respectively. The experimental results of RPI-A-A1-1 (D_r = 64 %) are selected as the calibration basis for adjusting

the material parameters c_4 and c_5. As such, the numerical simulations of RPI-A-B1-1, UCD-A-A1-1 and UCD-A-A2-1 are performed based on the material properties from calibration phase (Table 4.1) with the adjusted parameters c_4 and c_5 obtained in calibration of RPI-A-A1-1.

As observed from the four centrifuge test results of KyU, the pore pressure transducers are not providing consistent results with those from RPI and UCD. As such, contraction parameters c_4 and c_5 are further adjusted to 0.2 and 0.1, respectively, to better capture the much slower pore pressure build-up rate in these centrifuge tests of KyU. In the following results, numerical simulations of four KyU centrifuge tests are performed based on the material properties from calibration phase (Table 4.1) with the newly adjusted parameters c_4 and c_5.

4.8.1. Acceleration

Figure 4.16 depicts the computed and experimental acceleration time histories at the locations AH1-AH4 in LEAP-Asia-2019. It can be seen that the computed accelerations reasonably match those from the measurements in RPI-A-A1-1, UCD-A-A2-1, KyU-A-A2-1 and KyU-A-B2-1 (Figure 4.16). Both the computed results and measurements showed a consistent trend of acceleration spikes due to dilation. However, there are significant differences in rest of simulations compared to the experimental data. As seen in Figure 4.16, the accelerations spikes are overpredicted in RPI-A-B1-1, UCD-A-A1-1, and are underpredicted in KyU-A-A1-1, KyU-A-B1-1, mainly due to the different relative densities at various facilities.

4.8.2. Excess Pore Pressure Ratio

Figure 4.17 illustrates the time histories of excess pore pressure ratio r_u in LEAP-Asia-2019. As seen in figure, the computed excess pore pressure reasonably matches with those from the centrifuge tests of RPI-A-A1-1, RPI-A-B1-1, and UCD-A-A2-1. However, in calibration of UCD-A-A1-1, the computed results showed a relatively faster pore pressure build-up compared to

the measurements. In four tests of KyU, the much slower pore pressure build-up rate exhibited in measurements is well captured by further adjusting contraction parameters c_4 and c_5 (as discussed above) in simulations. As such, both the computed results and measurements (Figure 4.17) showed a consistent trend of negative spikes due to dilation. In addition, the dissipation of computed pore pressure generally following the trend of measurements after shaking.

4.8.3. Displacement

Figure 4.18 displays the computed horizontal displacement time histories and measurements at the midpoint of the ground surface. It can be seen that the computed results of RPI-A-A1-1, UCD-A-A2-1 and the four tests of KyU are in good agreement with those from measurements. However, some discrepancies are seen between the simulation results and experimental measurements in tests of RPI-A-B1-1 and UCD-A-A1-1. This higher amount of experimental permanent displacement of RPI-A-B1-1 can be better captured by further adjusting the parameter y_2 in numerical simulation (as discussed below).

4.8.4. Computed Response of RPI-A-B1-1 Test

An additional numerical simulation is performed to better capture the horizontal permanent displacement of RPI-A-B1-1. In this scenario, parameter $y_2 = 0$ (Table 4.1) is adjusted to 1.0, in order to reproduce a higher accumulation of shear deformation during earthquake loading. For comparison purposes, the computed results with material parameters $y_2 = 0$ and 1.0 are displayed in one figure (Figure 4.19 and Figure 4.20). From Figure 4.19a, it can be seen that the computed permanent displacement ($y_2 = 1$) is accumulating faster than that of scenario $y_2 = 0$ after 11 seconds, and eventually matches the experimental result (about 0.3 m) at end of shaking. In accordance with the deformation contour, Figure 4.19c shows the shear strain γ_{xy} contour with a peak value of about 12 % at deeper depth of the liquefiable sloping ground.

Figure 4.20 depicts the computed shear stress versus mean effective stress, and shear stress versus shear strain for integration points near the locations of pore pressure transducers (P1-P4). As seen in Figure 4.20a, the computed results with adjusted parameter y_2 = 1.0 reproduces a larger cycle-by-cycle accumulation of shear deformation in downslope direction than that of scenario y_2 = 0.

4.9. Summary and Conclusions

The simulation results of centrifuge model tests (Type-C phase) conducted by various facilities in LEAP-UCD-2017 and LEAP-Asia-2019 for a liquefiable sloping ground are presented. All the numerical simulations are performed using a calibrated pressure-dependent constitutive model (PressureDependMultiYield03) implemented with the characteristics of dilatancy, cyclic mobility and associated shear deformation. The soil parameters are determined based on a series of available stress-controlled cyclic triaxial and torsional shear tests (provided in the calibration phase) for matching the liquefaction strength curves of Ottawa F-65 sand with relative density D_r = 65 % in LEAP-UCD-2017 and D_r = 60 % in LEAP-Asia-2019. The computational framework and staged analysis procedure are presented as well. The primary conclusions can be drawn as follows:

(1) Determination of soil model parameters in calibration phase showed that the pressure-dependent model, i.e., PressureDependMultiYield03 material, generally resonably captured the liquefaction strength curves of Ottawa F-65 sand with relative densities D_r = 65 % and 60 %, respectively. Although the computed deviatoric stress versus axial strain curve in LEAP-UCD-2017 is symmetric due to the yield surface is conical in principal stress space, the soil model still can resonably capture the stress path, maximum axial strain of the undrained stress-controlled cyclic triaxial test.

(2) The unintended inconsistencies of centrifuge test results in Type-C phase may indeed hinder the comparisons between numerical simulations and measurements. To better capture the overall dynamic response of selected centrifuge tests, contraction parameters c_4 and c_5 (controlling the pore pressure build-up rate) are suggested to be adjusted to simulate the inconsistent contractive behavior exhibited by Ottawa F-65 sand of various relative densities.

(3) Although the centrifuge tests conducted by various institutions are not providing completely consistent results, measured time histories are reasonably captured by the numerical simulations in LEAP-UCD-2017 and LEAP-Asia-2019, using the same soil constitutive model parameters. The good agreement between computed and measured results for each centrifuge test demonstrated that the PressureDependMultiYield03 soil model as well as the overall employed computational methodology have the potential to predict the response of liquefiable sloping ground, and subsequently realistically evaluate the performance of analogous soil systems subjected to seismically-induced liquefaction.

(4) Permanent deformations of the liquefiable sloping ground are captured to a reasonable level. However, further adjustment of damage parameters y_1 and y_2 is much helpful to quantify the permanent displacement. As such, additional experimental data sets are needed related to large post-liquefaction shear deformation accumulation. As such new data sets become available, damage parameters y_1 and y_2 of the PressureDependMultiYield03 material can be better calibrated and applied in the prediction of liquefaction-induced lateral spreading.

4.10. Acknowledgements

Chapter 4, in full, has been published as it appears in the following paper (The dissertation author was the primary investigator and author of this paper):

Qiu, Z. and Elgamal, A. (2020). "Numerical Simulations of LEAP Centrifuge Tests for Seismic Response of Liquefiable Sloping Ground." Soil Dynamics and Earthquake Engineering, 139, 106378.

Chapter 4, in part, is a reprint of material as it appears in the following conference publication (The dissertation author was the primary investigator and author of this paper):

Qiu, Z. and Elgamal, A. (2020). "Numerical Simulations of LEAP Dynamic Centrifuge Model Tests for Response of Liquefiable Sloping Ground." In Model Tests and Numerical Simulations of Liquefaction and Lateral Spreading, 521-544. Springer, Cham.

Table 4.1 Model parameters (PressureDependMultiYield03) in calibration phase and Type-C simulations

Model Parameters	LEAP-UCD-2017	LEAP-Asia-2019
Relative density, D_r	65 %	60 %
Reference mean effective pressure, p'_r (kPa)	101	101
Mass density ρ (t/m^3)	2.04	2.0
Maximum shear strain at reference pressure, $\gamma_{max,r}$	0.1	0.1
Shear modulus at reference pressure, Go (MPa)	25	23
Stiffness dependence coefficient d, $G = Go(\frac{P'}{P'_r})^d$	0.5	0.5
Poisson's ratio v (for dynamics)	0.4	0.4
Shear strength at zero confinement, c (kPa)	0.3	0.3
Friction angle, ϕ	36°	30°
Phase transformation angle, ϕ_{PT}	22°	20°
Contraction coefficient, c_1	0.015	0.015
Contraction coefficient, c_2	3.0	3.0
Contraction coefficient, c_3	0.15	0.15
Contraction coefficient, c_4	5.2/1.0*	7.0/0.6**/0.2***
Contraction coefficient, c_5	3.0/0.5*	4.0/1.0**/0.1***
Dilation coefficient, d_1	0.08	0.06
Dilation coefficient, d_2	3.0	3.0
Dilation coefficient, d_3	0.2	0.2
Damage parameter, y_1	2.0	0.6
Damage parameter, y_2	0.0	0.0
Permeability (m/s)	1.1×10^{-4}	1.1×10^{-4}
Number of yield surfaces	20	20

*Adjusted for all LEAP-UCD-2017 centrifuge tests.

**Adjusted for RPI-A-A1-1, RPI-A-B1-1, UCD-A-A1-1 and UCD-A-A2-1.

***Adjusted for KyU-A-A1-1, KyU-A-A2-1, KyU-A-B1-1 and KyU-A-B2-1.

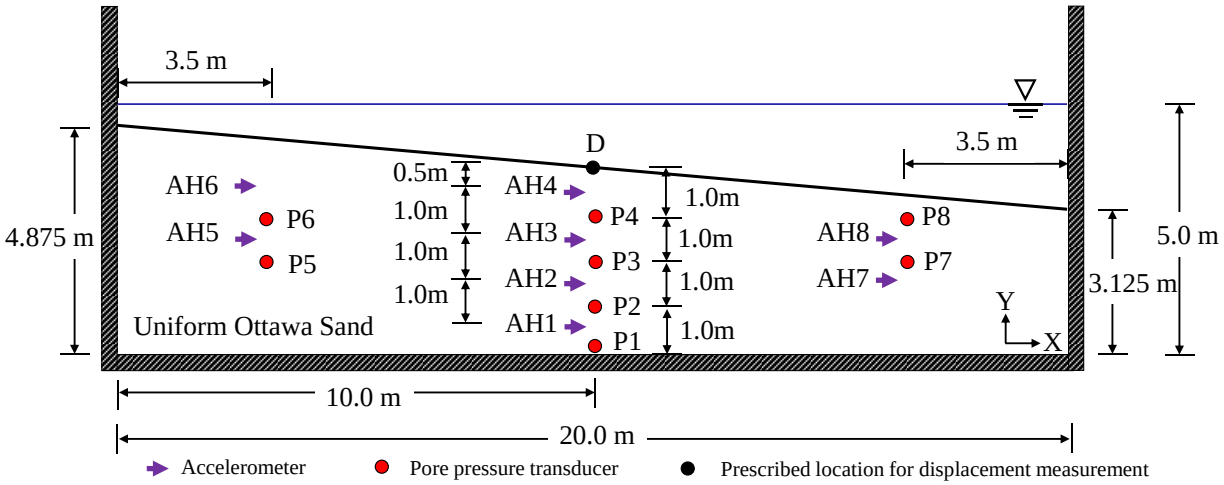

Figure 4.1 Schematic representation of the centrifuge test layout (after El Ghoraiby et al. 2020)

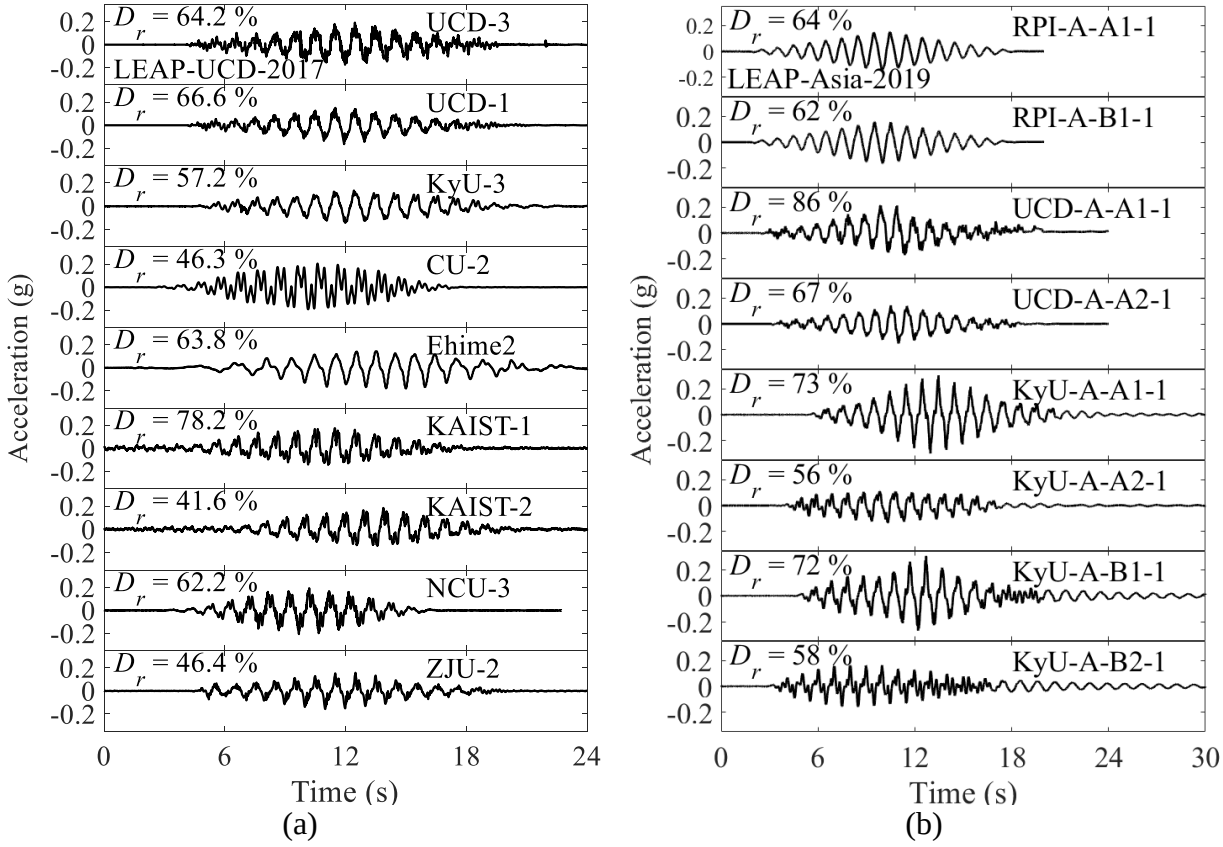

Figure 4.2 Selected base input motions (Kutter et al. 2018b; Ueda 2018): (a) LEAP-UCD-2017; (b) LEAP-Asia-2019

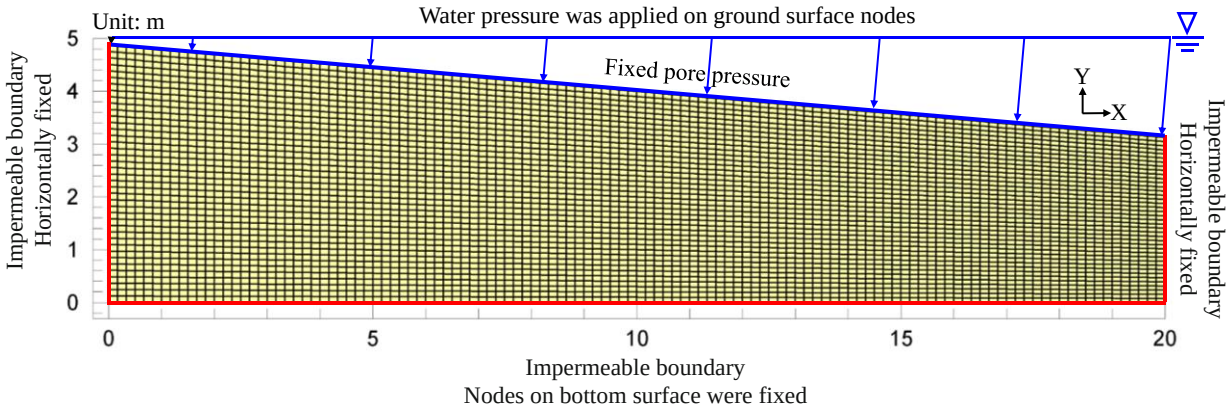

Figure 4.3 Finite Element mesh (maximum size = 0.2 m)

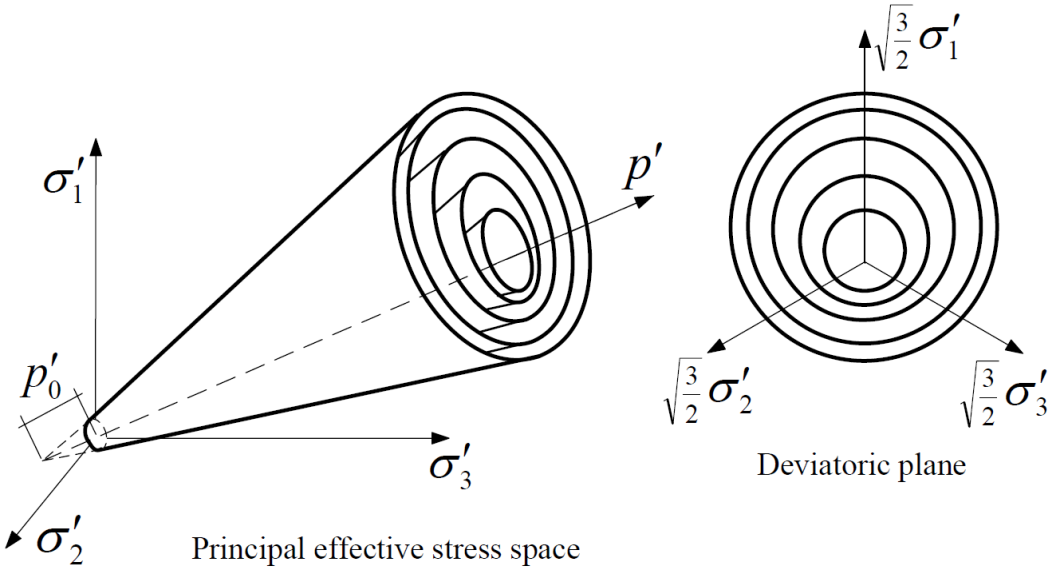

(a)

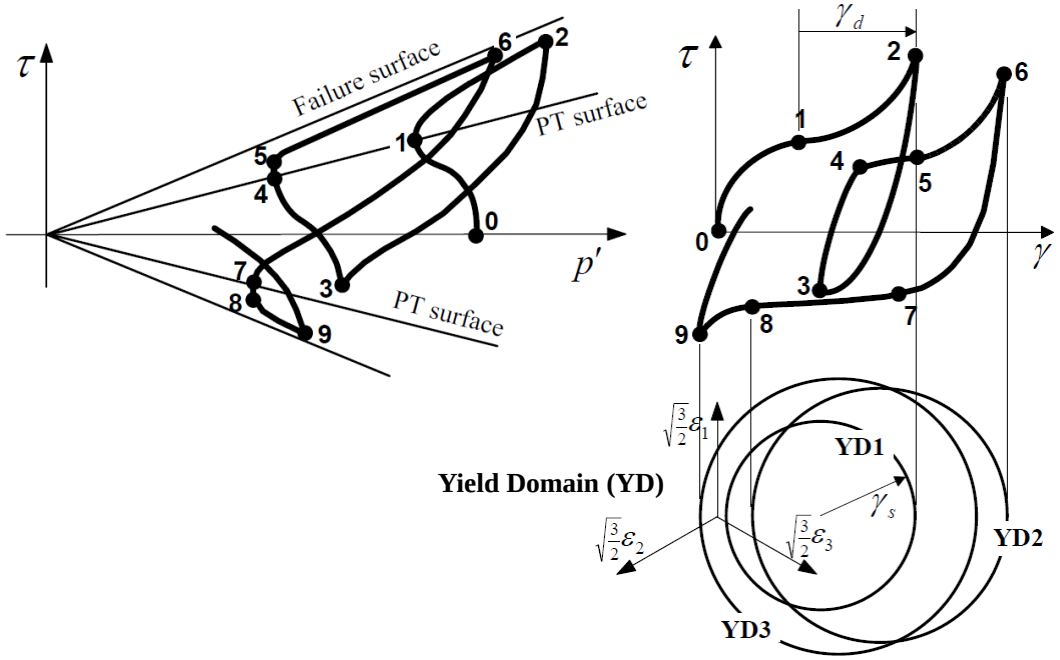

(b)

Figure 4.4 PressureDependMultiYield03 material: (a) Conical yield surfaces in principal stress space and deviatoric plane; (b) Schematic of constitutive model response and configuration of yield domain (after Yang and Elgamal 2002; Elgamal et al. 2003; Yang et al. 2003)

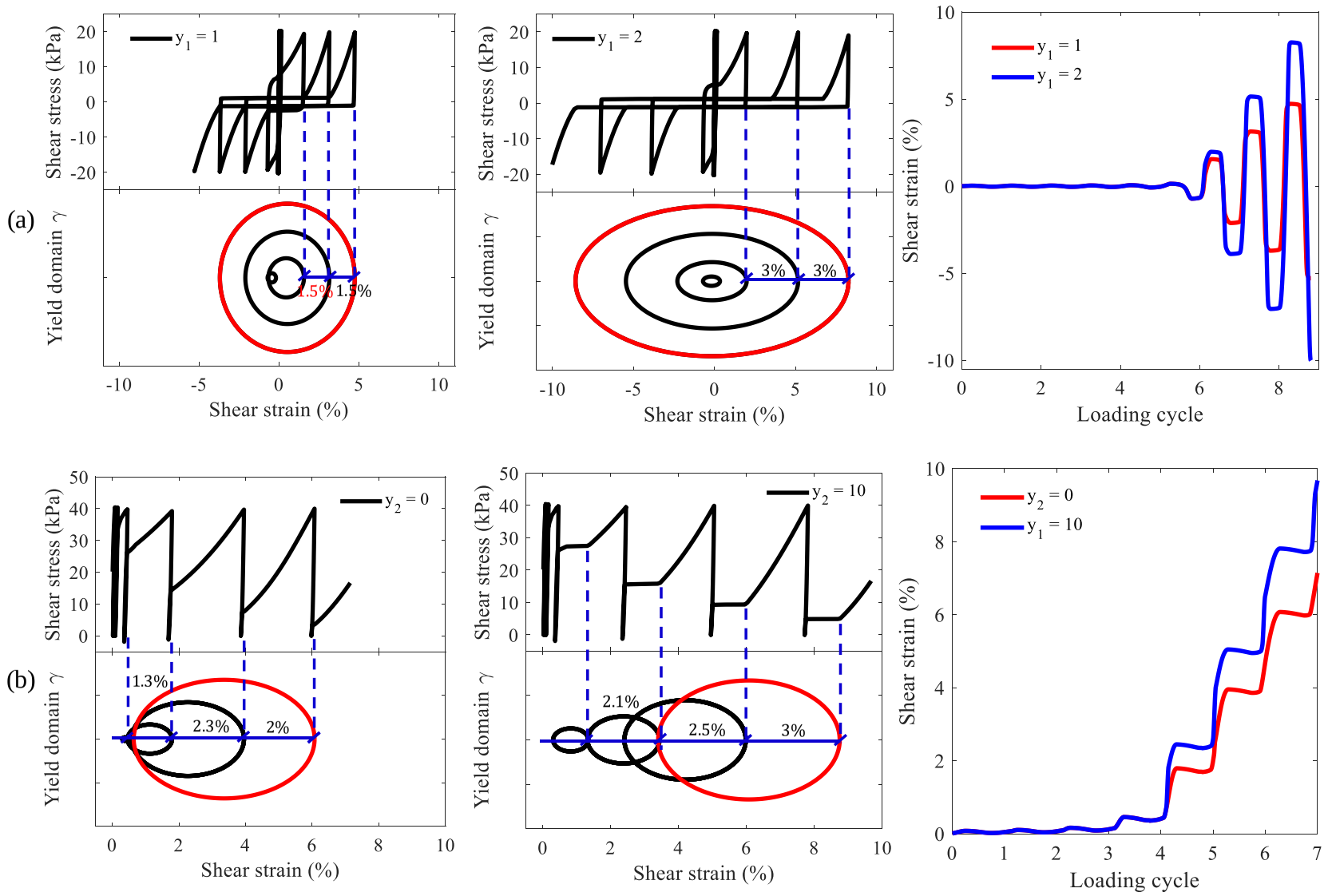

Figure 4.5 Large post-liquefaction shear strain accumulation (yield domain γ is not scaled): (a) Effect of y_1 at $y_2 = 0$; (b) Effect of y_2 at $y_1 = 1$

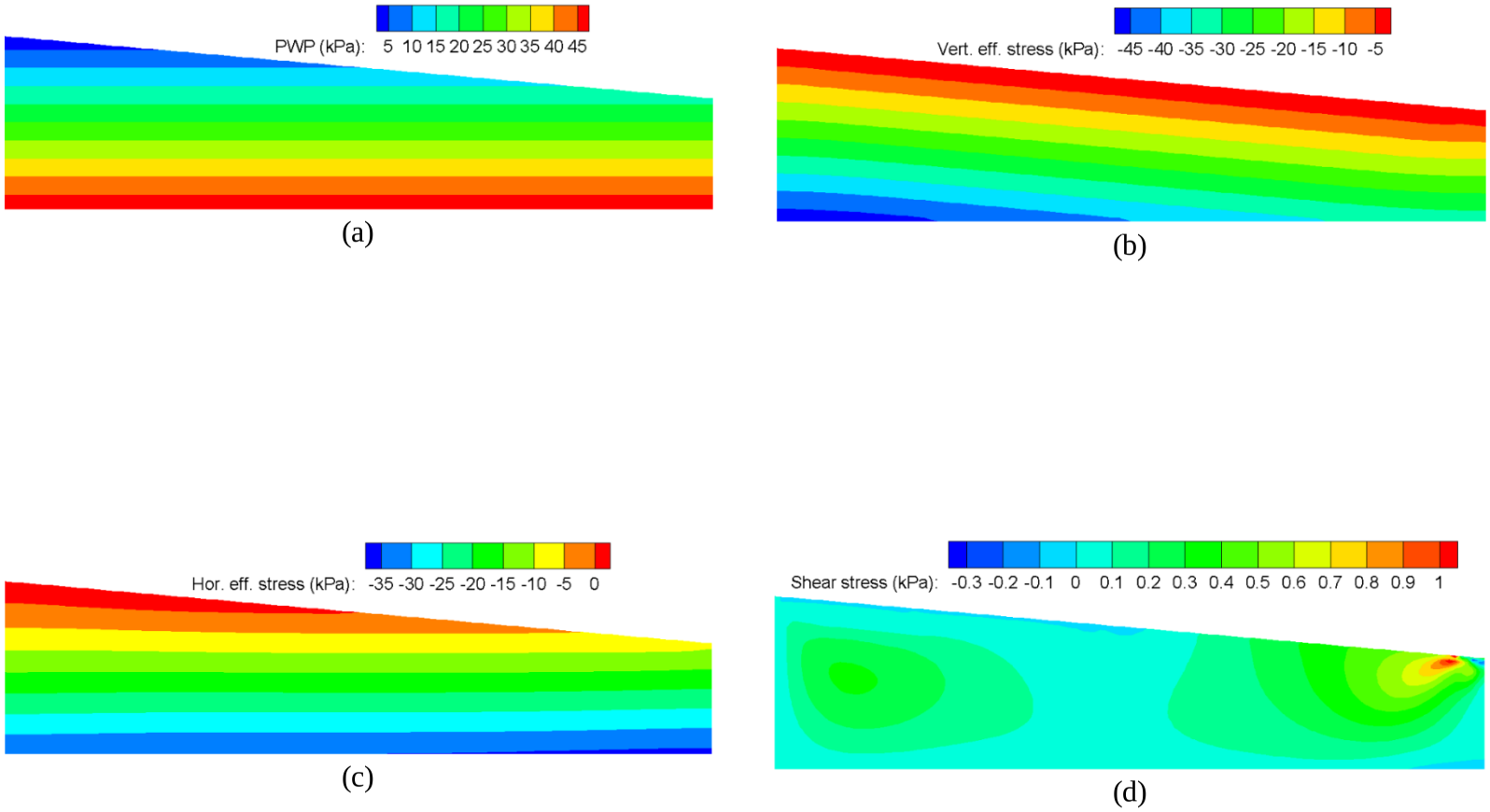

Figure 4.6 Initial state of soil due to gravity (before shaking): (a) Pore water pressure; (b) Vertical effective stress σ'_{yy}; (c) Horizontal effective stress σ'_{xx}; (d) Shear stress τ_{xy}

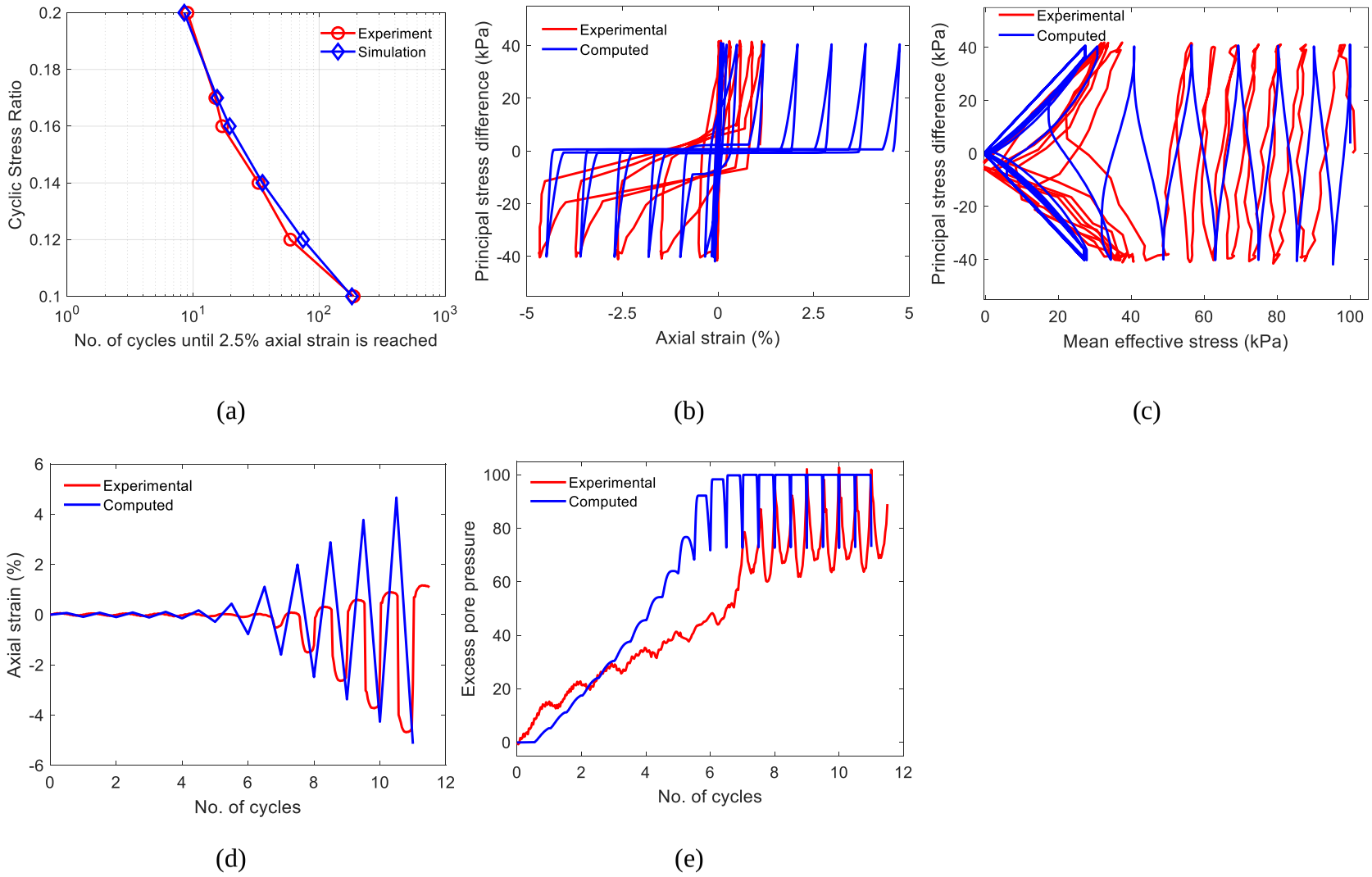

Figure 4.7 LEAP-UCD-2017 triaxial tests in calibration phase: (a) Liquefaction strength curve; (b)-(e) Undrained stress-controlled cyclic soil response with *CSR* = 0.2

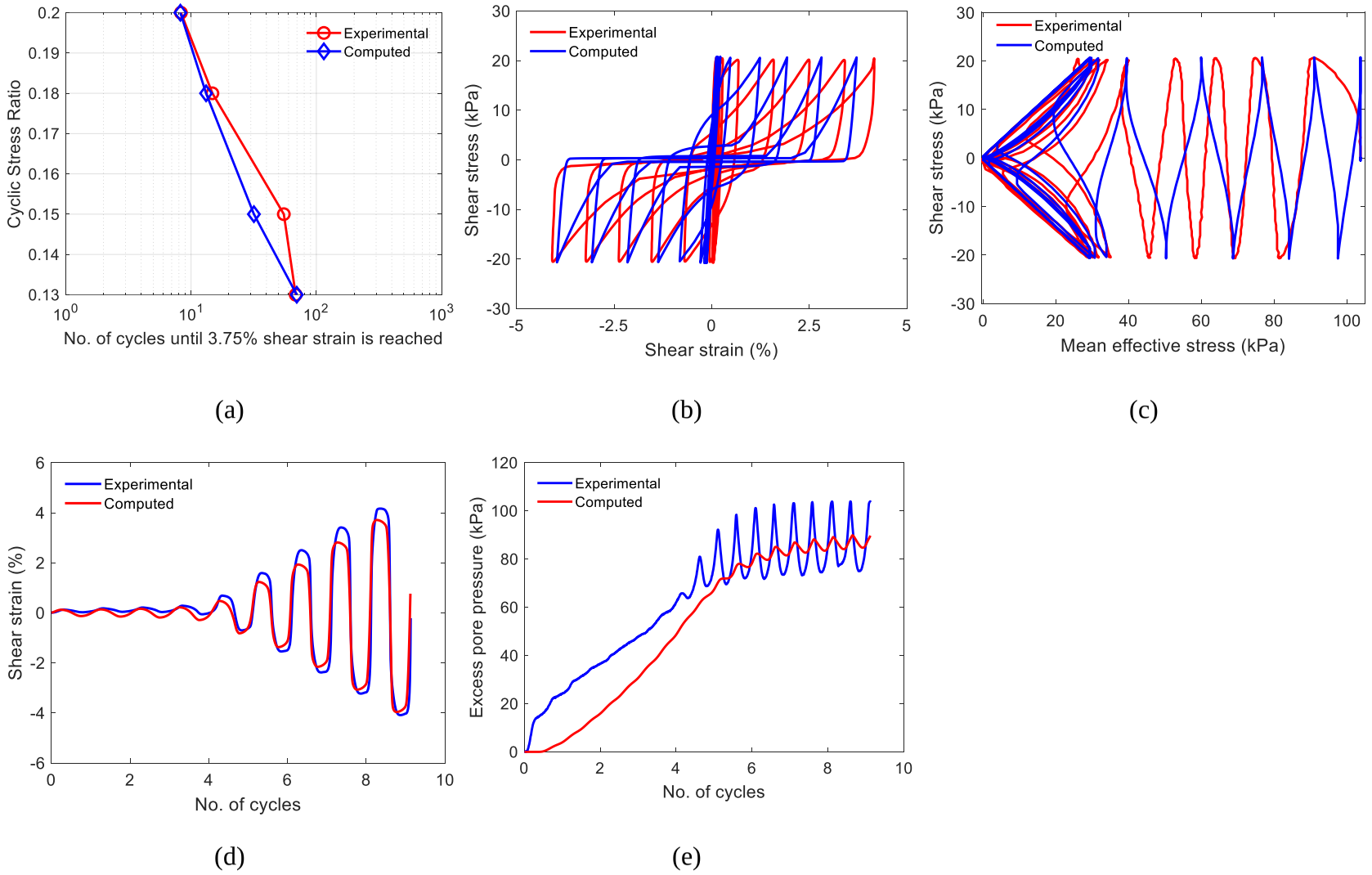

Figure 4.8 LEAP-Asia-2019 torsional shear tests in calibration phase: (a) Liquefaction strength curve; (b)-(e) Undrained stress-controlled cyclic soil response with *CSR* = 0.2.stress-controlled cyclic soil response with *CSR* = 0.2

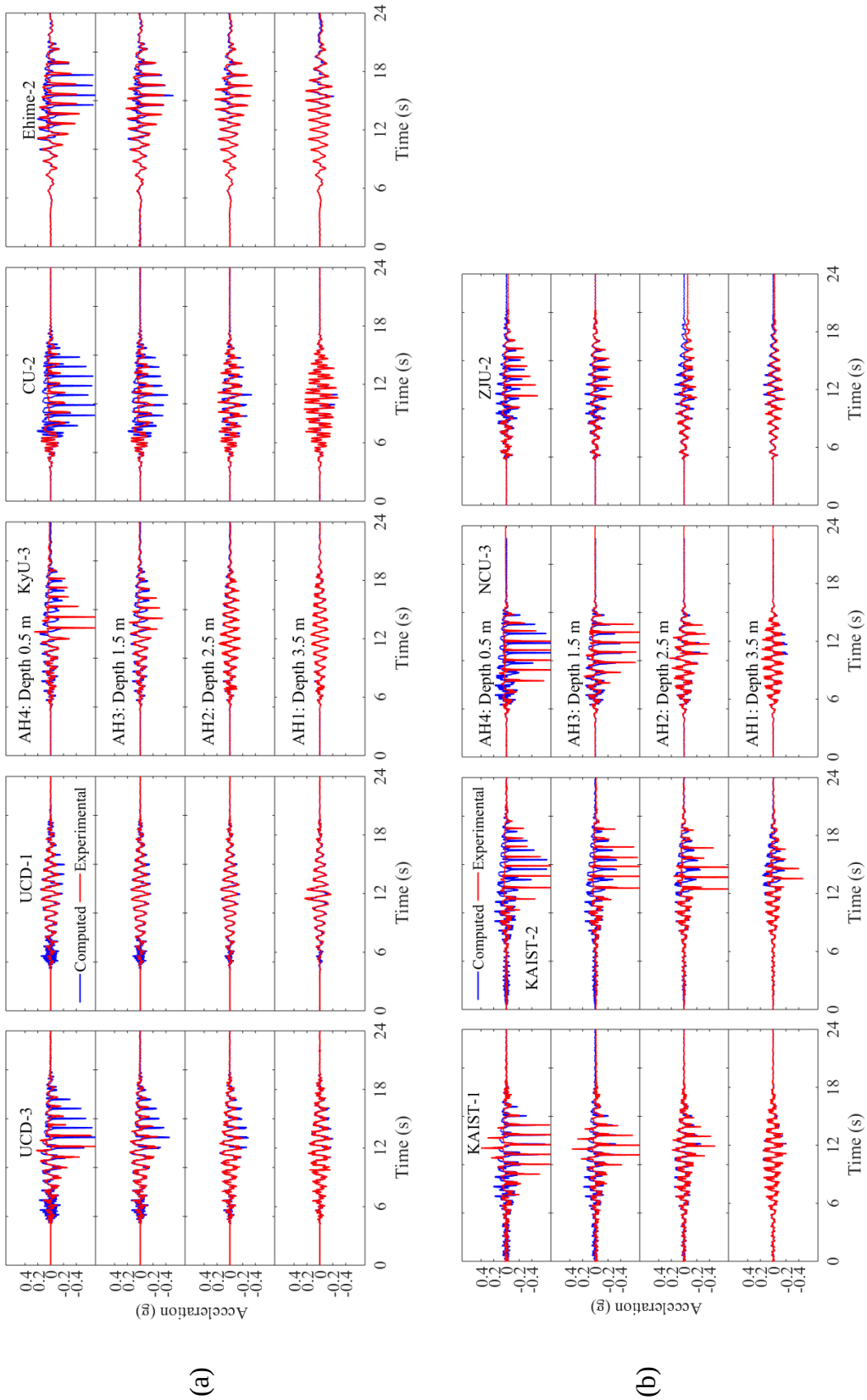

Figure 4.9 LEAP-UCD-2017: measured and computed acceleration time histories

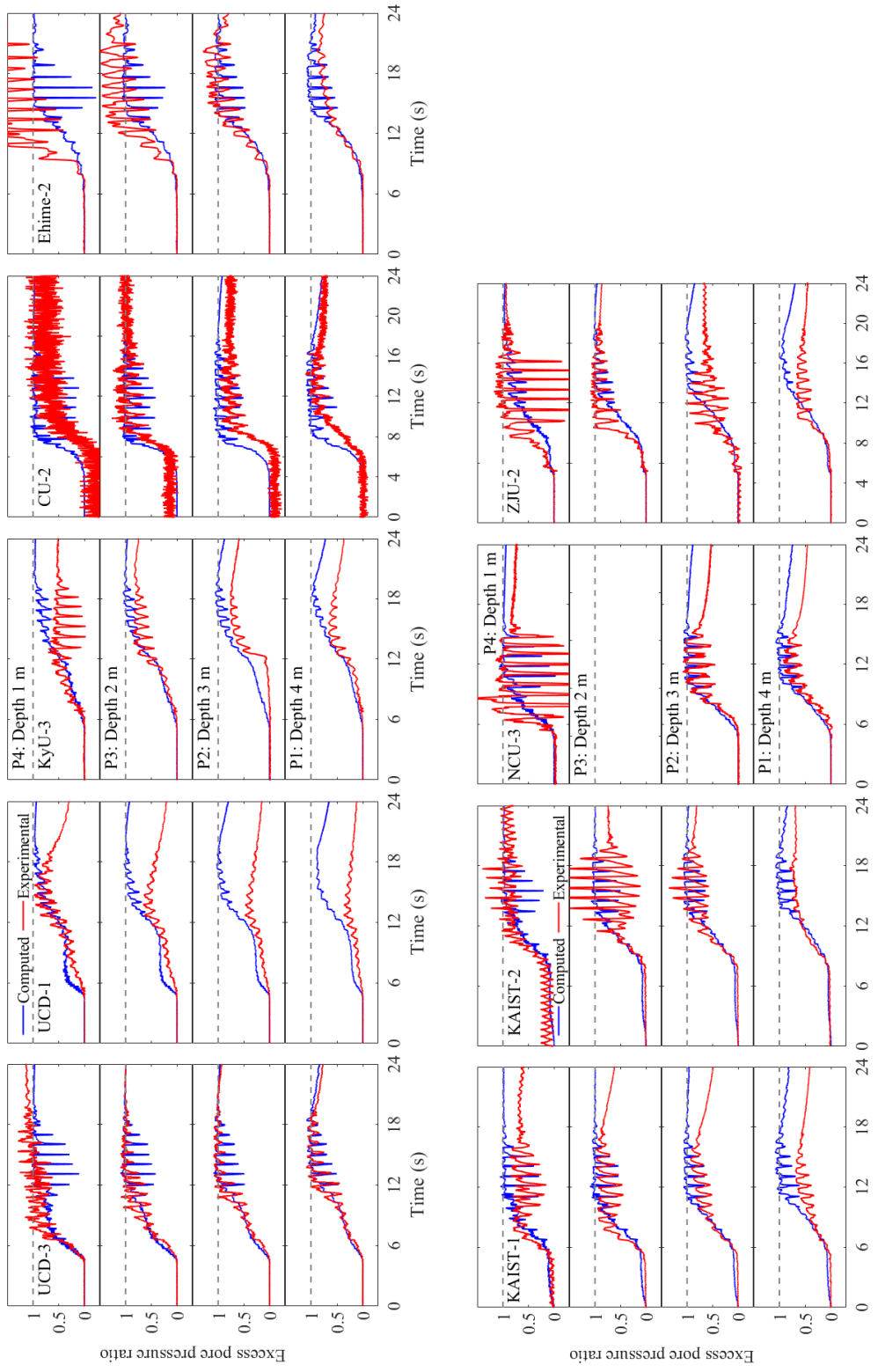

Figure 4.10 LEAP-UCD-2017: measured and computed time histories of excess pore pressure ratio

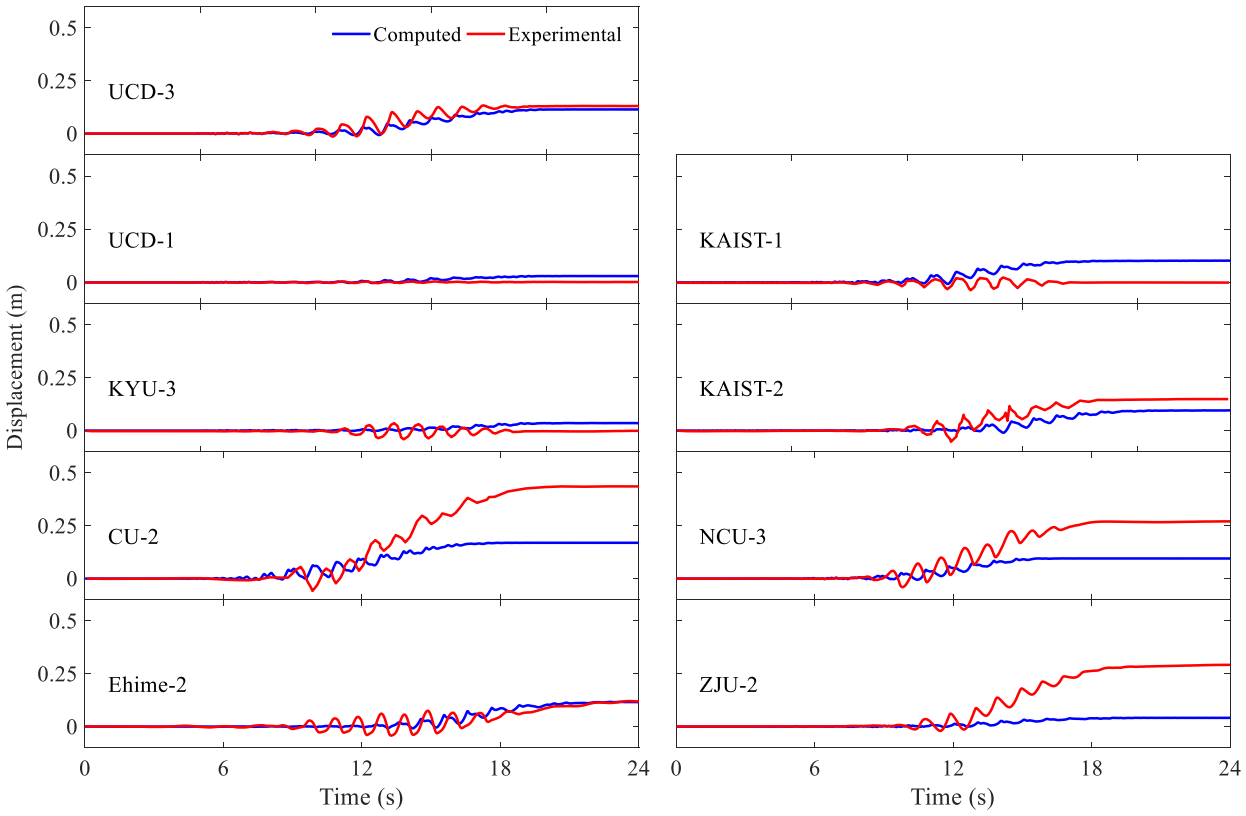

Figure 4.11 LEAP-UCD-2017: measured and computed displacement time histories

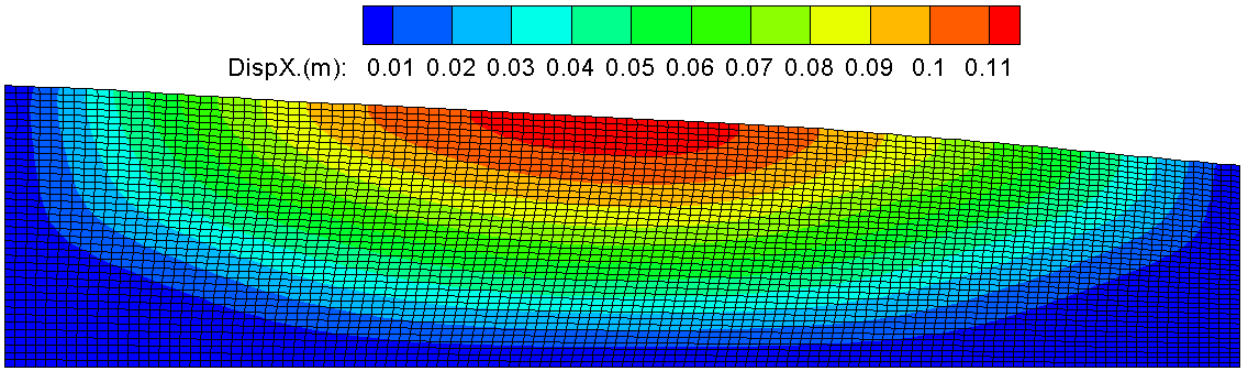

(a)

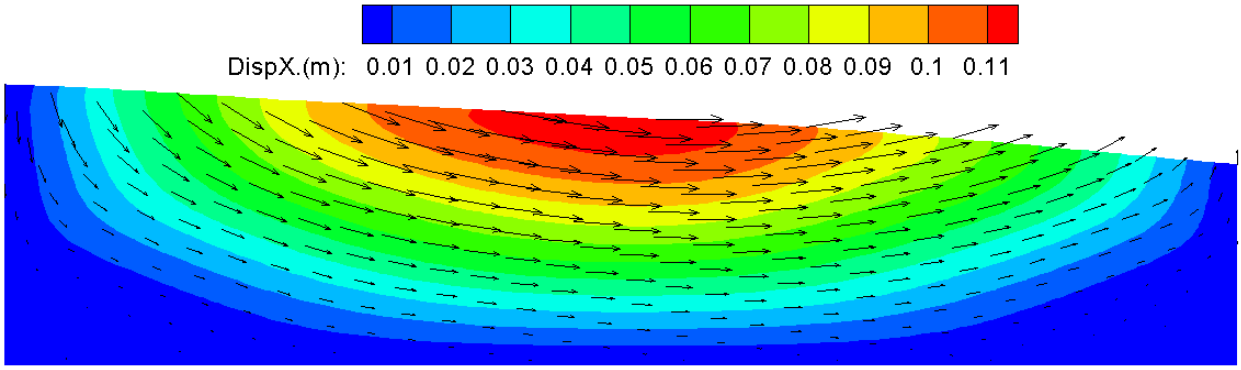

(b)

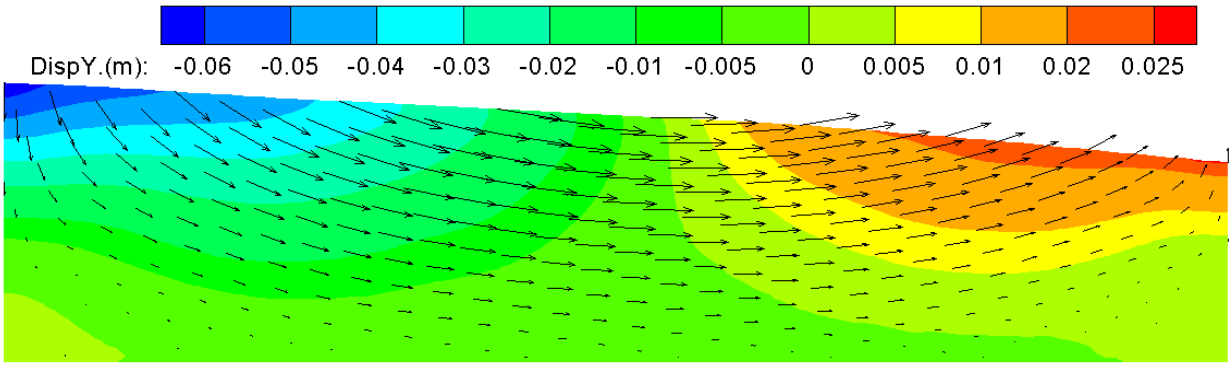

(c)

Figure 4.12 Computed deformation at end of shaking in UCD-3 of LEAP-UCD-2017: (a) Deformed FE mesh; (b) Horizontal displacement contour; (c) Vertical displacement (arrows display direction of ground movement; factor = 5)

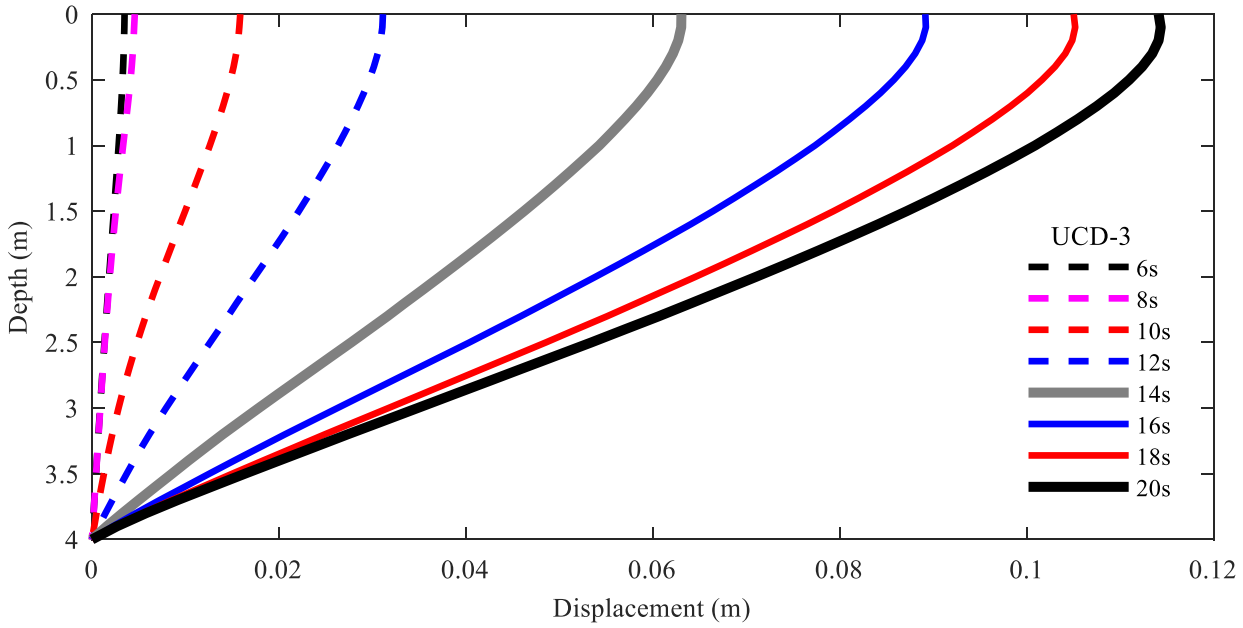

Figure 4.13 Displacement profile along depth in the middle of slope in UCD-3 of LEAP-UCD-2017

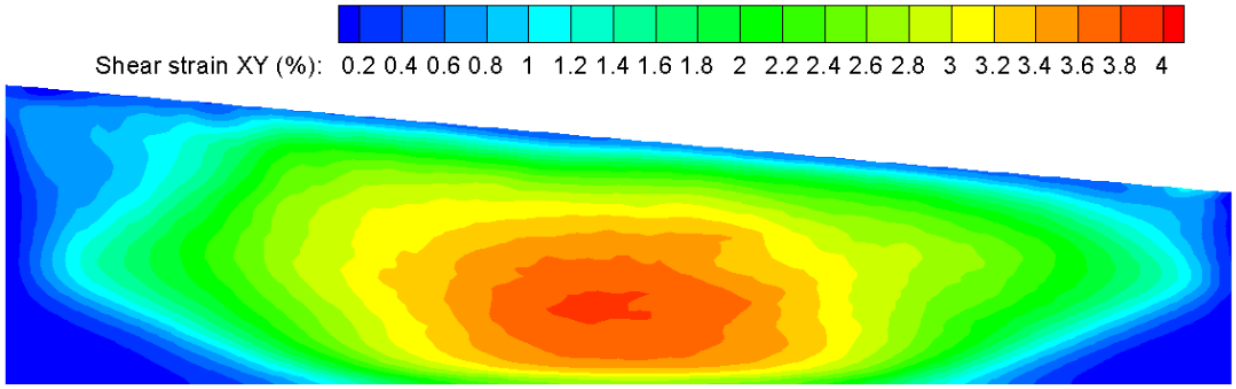

(a)

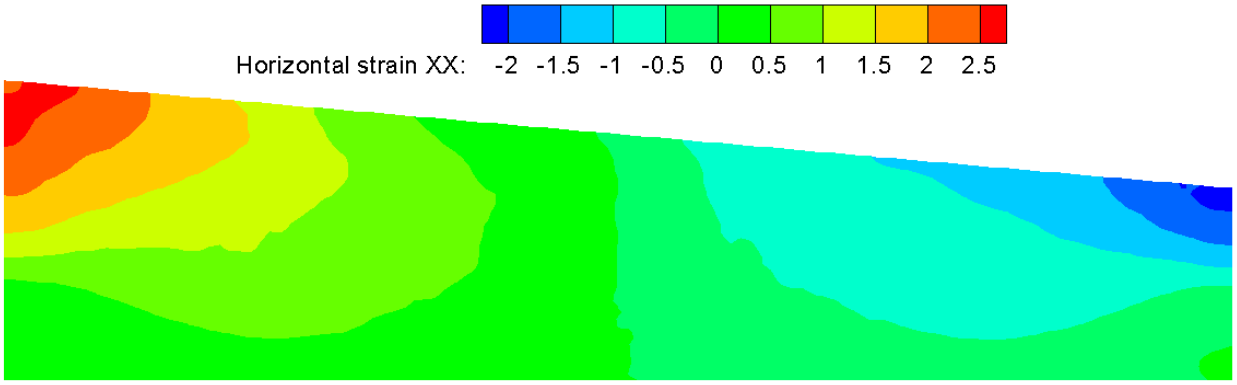

(b)

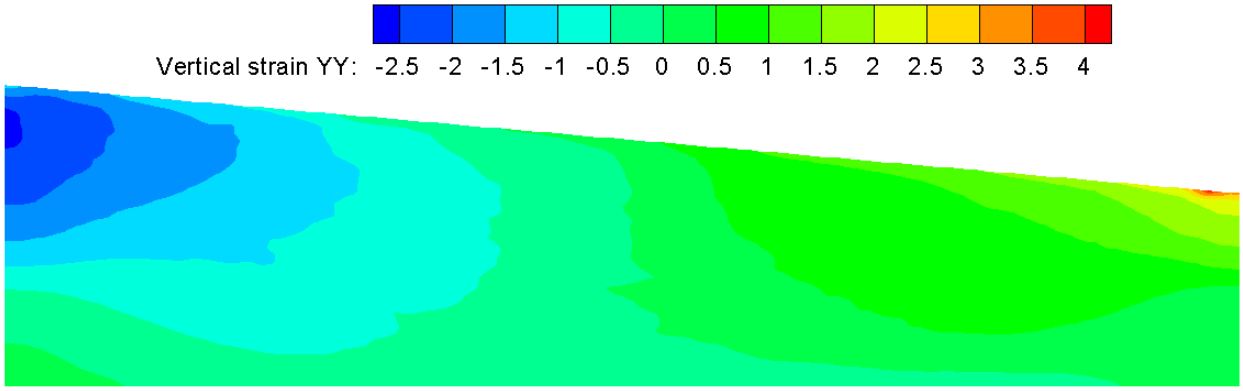

(c)

Figure 4.14 Computed strain contours at end of shaking in UCD-3 of LEAP-UCD-2017: (a) Shear strain γ_{xy}; (b) Horizontal strain ε_{xx}; (c) Vertical strain ε_{yy}

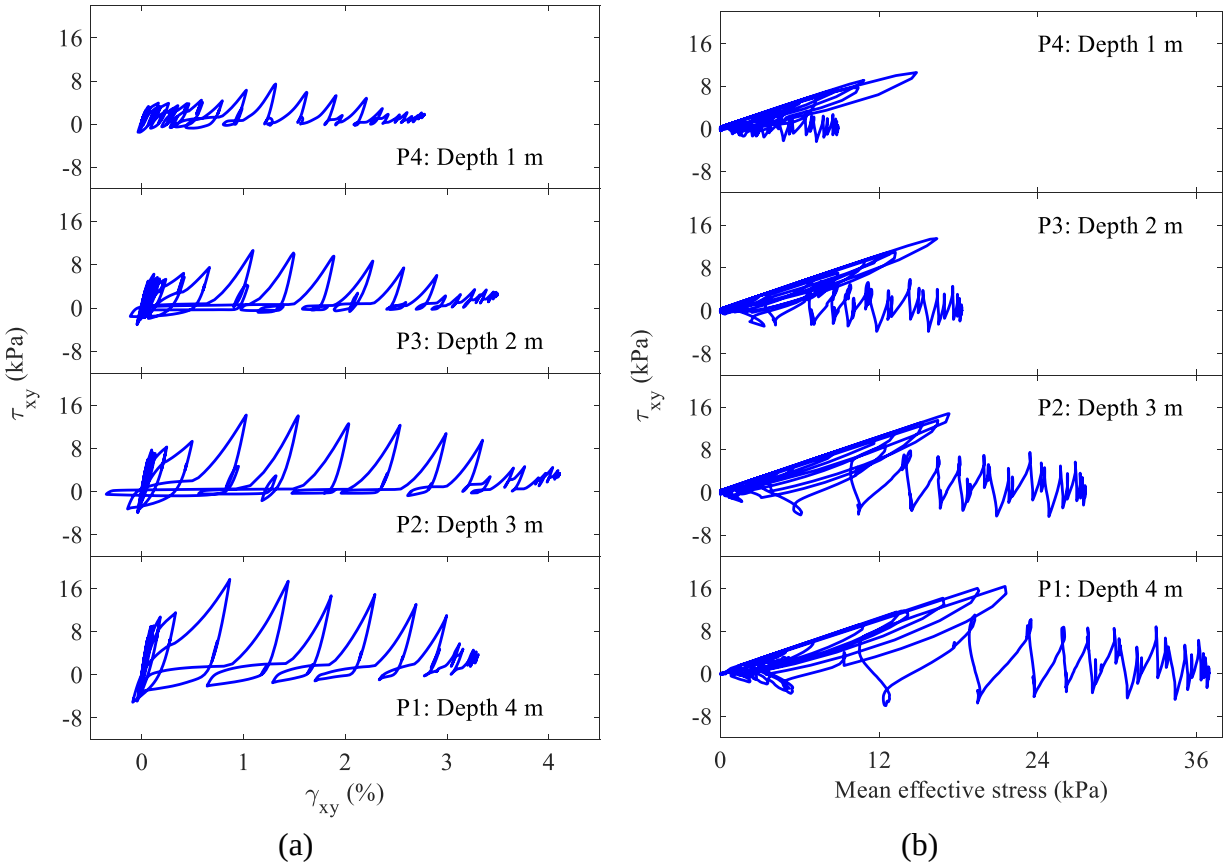

Figure 4.15 Computed soil response in UCD-3 of LEAP-UCD-2017: (a) Shear stress-strain; (b) Mean effective stress-shear stress

(a)

(b)

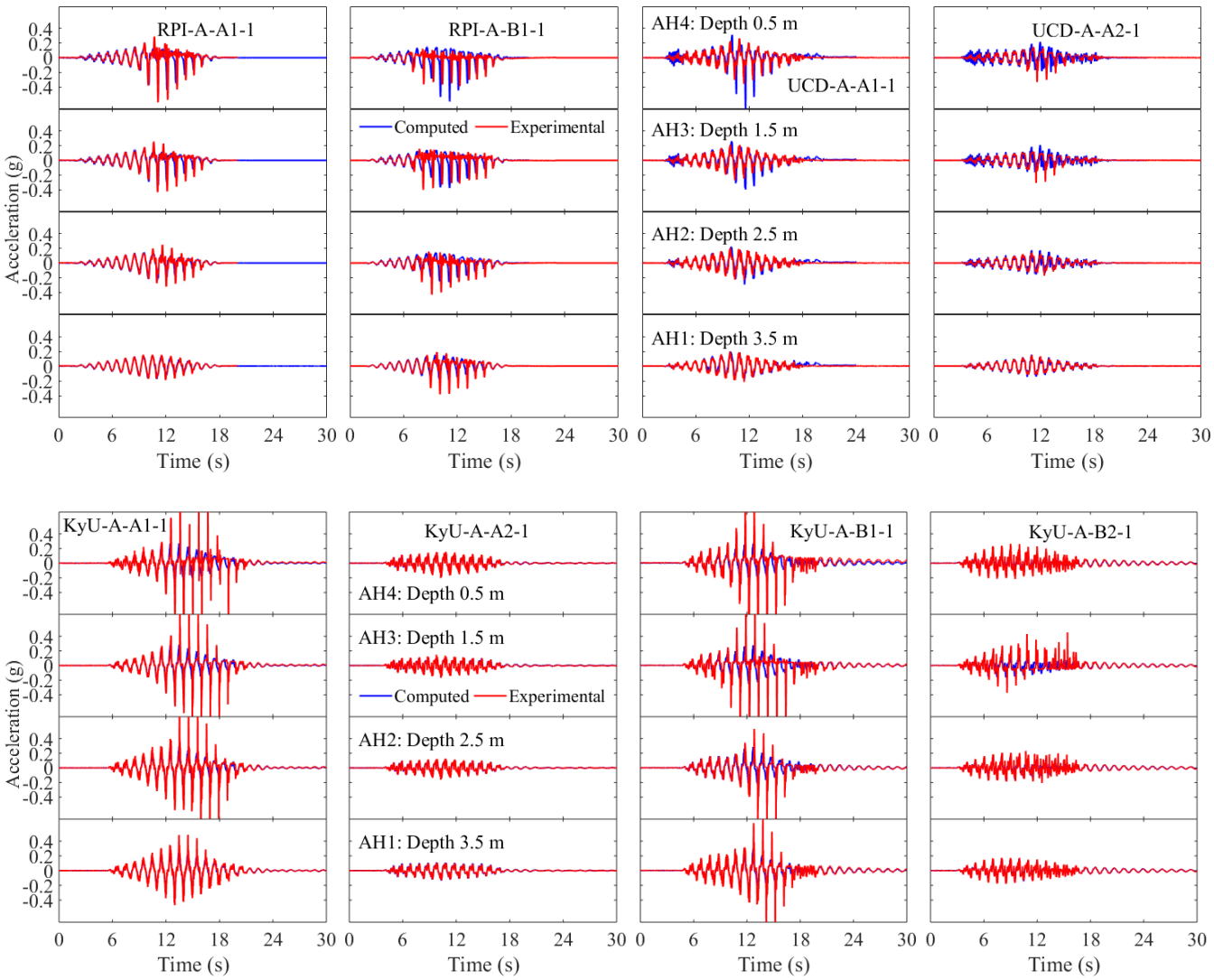

Figure 4.16 LEAP-Asia-2019: measured and computed acceleration time histories

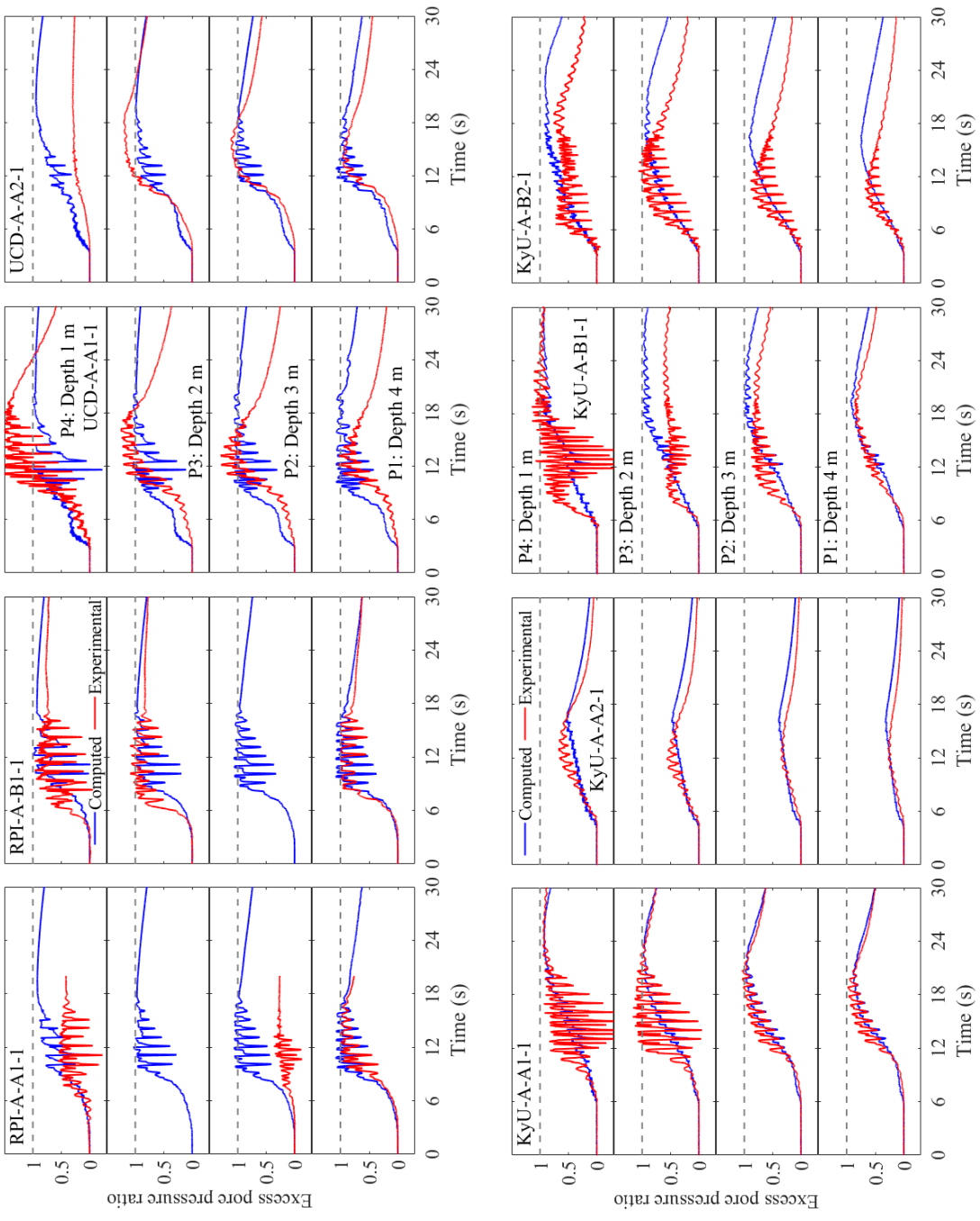

Figure 4.17 LEAP-Asia-2019: measured and computed time histories of excess pore pressure ratio

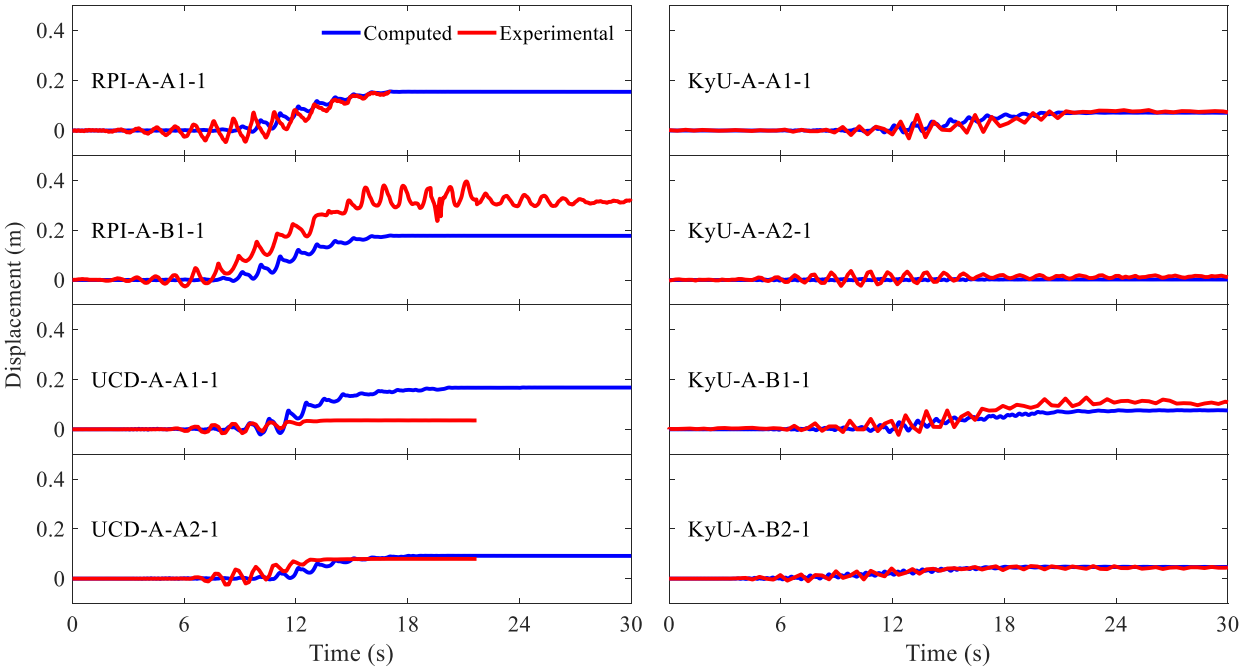

Figure 4.18 LEAP-Asia-2019: measured and computed displacement time histories

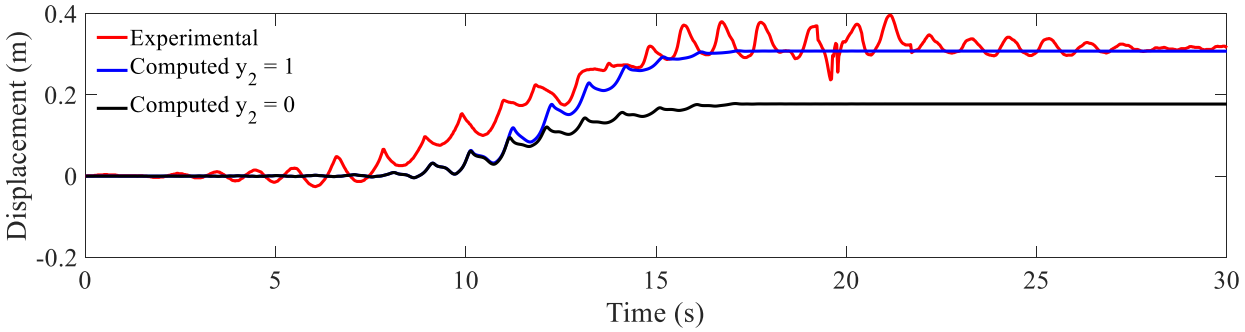

(a)

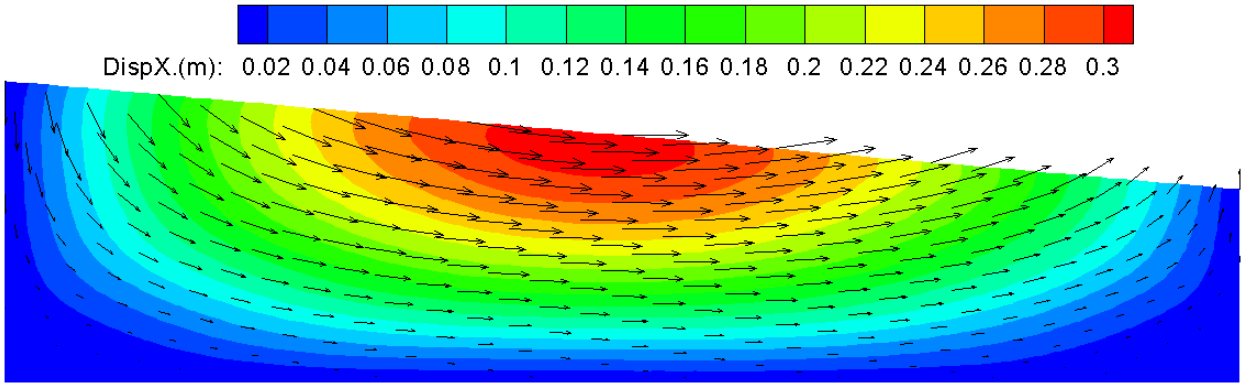

(b)

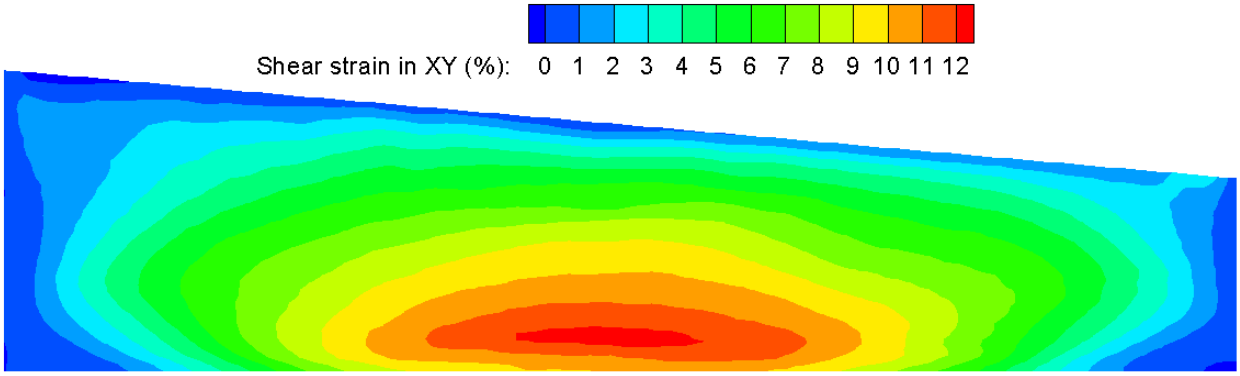

(c)

Figure 4.19 Adjusted parameter y_2 = 1.0 to capture horizontal permanent deformation of RPI-A-B1-1 in LEAP-Asia-2019: (a) Displacement time history; (b) Contour; (c) Shear strain γ_{xy} contour (arrows display direction of ground movement)

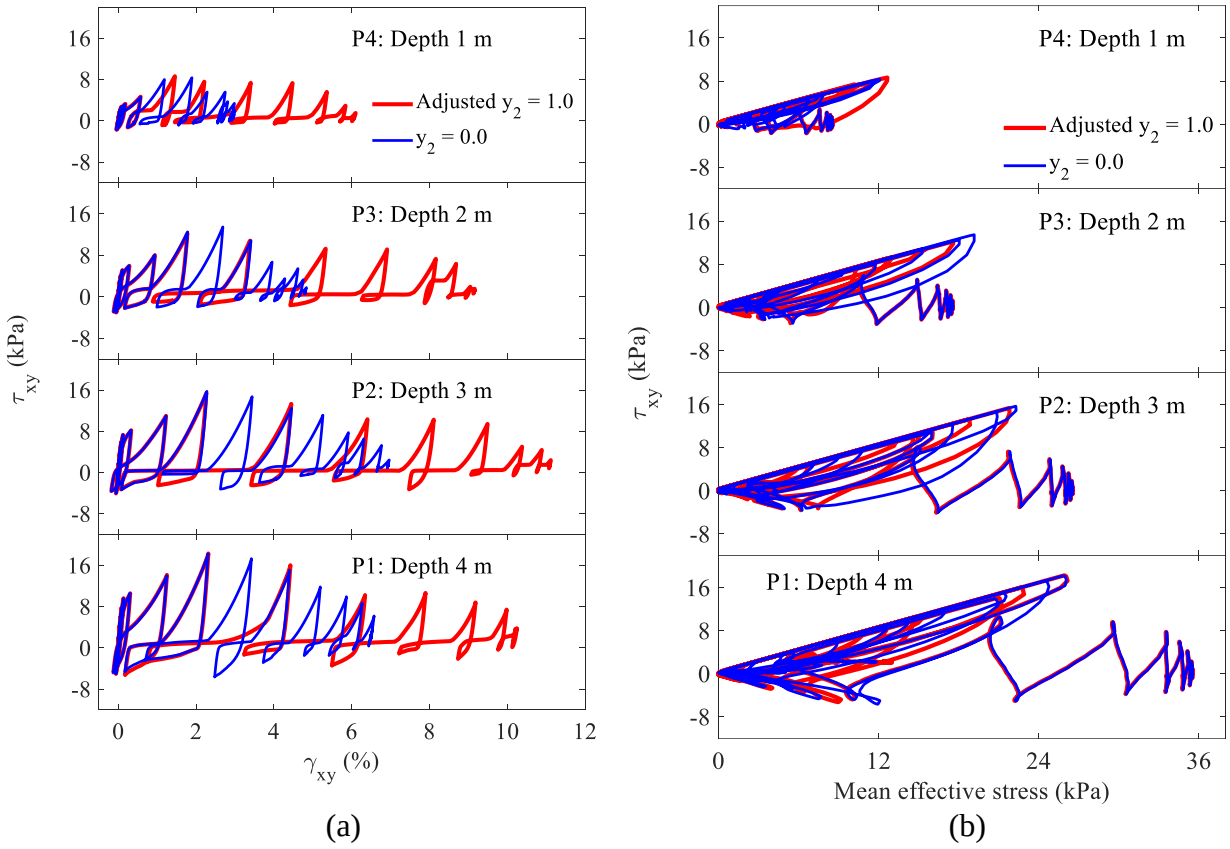

Figure 4.20 Adjusted parameter y_2 to capture horizontal permanent deformation in RPI-A-B1-1 of LEAP-Asia-2019: (a) Shear stress-strain; (b) Mean effective stress-shear stress

Chapter 5. Seismic Response of a Sheet-Pile Retaining Structure Supporting Liquefiable Soils: Numerical Simulations of LEAP Centrifuge Tests

5.1. Abstract

This chapter presents the numerical simulations of a sheet-pile retaining structure under liquefaction-induced lateral loading related to LEAP-2020 (Liquefaction Experiments and Analysis Projects) dynamic centrifuge model tests conducted by various institutions. The numerical simulations are performed using a pressure-dependent constitutive model implemented with the characteristics of dilatancy, cyclic mobility and associated shear deformation. The soil parameters are determined based on a series of available stress-controlled direct simple shear tests for matching the liquefaction strength curves of Ottawa F-65 sand with relative density D_r = 67 % in calibration phase. The computational framework for the dynamic response analysis is discussed and the computed results are presented for the selected centrifuge experiments during Type-C phase. Measured time histories (e.g., displacement, acceleration, and excess pore pressure ratio) of these experiments are reasonably captured. Comparisons between the numerical simulations and measured results showed that the pressure-dependent constitutive model as well as the overall employed computational framework have the potential to predict the seismic response of a sheet-pile retaining structure supporting liquefiable soils, and subsequently realistically evaluate the performance of an equivalent soil-pile-structure system subjected to seismically-induced liquefaction.

5.2. Introduction

As part of the ongoing LEAP (Zeghal et al. 2019), a new series of centrifuge experiments have been performed at different centrifuge facilities across the world to investigate the seismic response of a sheet-pile retaining structure supporting liquefiable soils. Liquefaction Experiments and Analysis Projects (LEAP) is an effort to facilitate validation and verification of numerical procedures for liquefaction-induced lateral spreading analysis (Manzari et al. 2014; Kutter et al. 2014, 2015, 2018a; Qiu and Elgamal 2020b, c). In order to obtain a set of reliable centrifuge test data with high quality among different centrifuge facilities, a centrifuge experiment was repeated at 6 centrifuge facilities in LEAP-GWU-2015 (Manzari et al. 2018; Kutter et al. 2018a) for a liquefiable sloping ground, as one project within LEAP. The associated numerical simulations conducted by several predictors (Armstrong 2018; Ghofrani and Arduino 2018; Ueda and Iai 2018; Zeghal et al. 2018; Ziotopoulou 2018) were compared with the measured response from the experiments. In addition, LEAP-UCD-2017 and LEAP-Asia-2019 continued to provide more reliable centrifuge test data achieved from various facilities for the same model. The test results of LEAP-UCD-2017 and LEAP-Asia-2019 are available in DesignSafe-CI (Kutter et al. 2018b; Ueda 2018).

On this basis, the results of numerical simulations for these dynamic centrifuge tests during Type-C phase are presented in this chapter. All the Finite Element (FE) simulations are performed using a pressure-dependent constitutive model (Parra 1996; Yang 2000; Yang and Elgamal 2002; Elgamal et al. 2003; Yang et al. 2003; Khosravifar et al. 2018) implemented with the characteristics of dilatancy, cyclic mobility and associated shear deformation. The soil parameters in LEAP-2020 are determined based on a series of cyclic stress-controlled simple shear tests provided in the calibration phase (Type-A) for matching the liquefaction strength curves of Ottawa F-65 sand with

relative density D_r = 67 % at confining stress = 40 kPa and 100 kPa, respectively. Using the same soil constitutive model parameters obtained from Type-A, numerical simulations are performed for the selected centrifuge tests and the computed results are compared with the experimental data during the Type-C phase.

The following sections of this chapter outline: 1) computational framework, 2) specifics and calibration processes, 3) details of the employed FE modeling techniques, and 4) computed results of the selected centrifuge tests. Finally, a number of conclusions are presented and discussed.

5.3. Brief Summary of the Centrifuge Tests in LEAP-2020

A schematic representation of the centrifuge tests (Zeghal et al. 2019) is shown in Figure 5.1. The LEAP-2020 centrifuge experiments are focused on the dynamic response of sheet-pile retaining structures supporting liquefiable layer of Ottawa F-65 sand. The total length of the model is about 20 m. Behind the sheet pile (landside), the liquefiable soil layer has a thickness of 4 m and a length of about 13 m in prototype scale. In front of the sheet pile (waterside), the layer has a thickness of 1 m and a length of about 7 m. The reference relative density for liquefiable layer (green in Figure 5.1) will range from D_r = 55 % to 75 %. This soil layer is underlain by a very dense sand of D_r = 90 % with 1 m thickness (yellow in Figure 5.1). In addition, the sheet-pile tip is initially located at mid-depth of the dense layer (elevation = 0.5 m) before shaking.

The specimen is built in a container with rigid walls. In the liquefiable layer, three arrays of sensors are used to monitor the soil response behind the sheet-pile and two arrays are used for the soil in front of the wall. The left array of sensors (close to the left boundary of the container and the farthest from the sheet pile) is optional in terms of presenting the numerical simulation results (i.e., AB1-AB3 and PB1-PB3). The middle array of sensors (i.e., AM1-AM3 and PM1-

PM3) are located with the aim of capturing the response close to the boundary of the failure prism behind the wall. The "W" arrays of sensors (i.e., AW1-AW3 and PW1-PW3) are intended to capture the soil-structure interaction response. In front of the sheet pile, two vertical arrays of sensors are installed including AFW, PFW close to the wall and AFWB, PFWB away from the sheet-pile (optional in terms of presenting the numerical results).

The selected ground motion is a ramped sine wave with dominant frequency of 1 *Hz* with 5 consecutive uniform cycles at the same PGA. In addition to the 1 *Hz* components of the motion, the majority of base excitations include higher frequency harmonics (3 to 6 *Hz*) that are either included intentionally in the target motion, or obtained as a result of the dynamic characteristics of the shaking system. As such, Figure 5.2 shows the achieved motions for all selected centrifuge experiments. Primary interests of these tests are the lateral displacement of soil surface behind the wall, deflection of the sheet-pile and general dynamic response of the deposit.

5.4. Finite Element Model

A two-dimensional (2D) FE mesh (Figure 5.3) is created to represent the centrifuge model, comprising 1362 nodes and 1265 quadrilateral elements (maximum size = 0.2 m). All numerical simulations of the selected centrifuge experiments are performed using the computational platform OpenSees during LEAP-2020 Type-C phase. Quadrilateral Four-node plane-strain elements with two-phase material following the *u-p* (Chan 1988) formulation were employed for simulating saturated soil response (quadUP in OpenSees).

The sheet-pile is modeled by linear elastic beam-column elements with material properties (Zeghal et al. 2019) listed in Table 5.2. In order to represent the geometric space occupied by the pile in the soil domain, rigid beam-column links ($EI = 10^5$ times the linear EI of the pile) are used normal to the vertical axis of the pile. As such, the 2D quadUP elements representing the soil are

connected to the pile geometric configuration at the outer nodes of these rigid links using the equalDOF constraint in OpenSees. In this FE model, pile nodes embedded in the dense layer are rigidly connected to the corresponding soil nodes for both lateral and vertical translations. For simplicity, pile nodes in the liquefiable layer are connected only laterally to the soil nodes, such that the upper soil layer can slide smoothly along the sheet-pile wall.

5.4.1. Soil Constitutive Model

The employed soil constitutive model (Parra 1996; Yang 2000; Yang and Elgamal 2002; Elgamal et al. 2003; Yang et al. 2003; Khosravifar et al. 2018) was developed based on the multi-surface plasticity theory (Prevost 1978, 1985). In this employed soil constitutive model, the shear-strain backbone curve was represented by the hyperbolic relationship with the shear strength based on simple shear (reached at an octahedral shear strain of 10 %). The low-strain shear modulus is computed using the equation $G = G_0(p'/p'_r)^n$, where p' is effective confining pressure, p'_r is a reference effective confining pressure, and G_0 is shear modulus at p'_r. The dependency of shear modulus on confining pressure is typically taken as n = 0.5. The constant M_f (failure surface size) relating deviator shear and confinement (triaxial compression scenario) is related to the friction angle φ (Chen and Mizuno 1990) as defined by $M_f = 6sin\varphi/(3 - sin\varphi)$. As such, the soil is simulated by the implemented OpenSees material PressureDependMultiYield03 (Khosravifar et al. 2018).

5.4.2. Contractive Phase

Shear-induced contraction occurs inside the phase transformation (PT) surface ($\eta < \eta_{PT}$), as well as outside ($\eta > \eta_{PT}$) when $\dot{\eta} < 0$, where, η is the deviatoric stress ratio defined as $\sqrt{\frac{3}{2}\boldsymbol{s}:\boldsymbol{s}}/(p' + p'_0)$ and η_{PT} is the deviatoric stress ratio at phase transformation surface (Figure 5.4). The contraction flow rule is defined as:

$$P'' = (1 - \frac{\dot{\boldsymbol{n}}:\dot{\boldsymbol{s}}}{||\dot{\boldsymbol{s}}||}\frac{\eta}{\eta_{PT}})^2(c_1 + c_2\gamma_c)(\frac{p'}{p_a})^{c_3}(c_4\eta_{rv})^{c_5}$$
$$\eta_{rv} = \frac{\sqrt{{\tau_{12}}^2 + {\tau_{23}}^2 + {\tau_{13}}^2}}{(p' + {p'}_0)} \quad (5\text{-}1)$$

where c_1, c_2, c_3, c_4 and c_5 are non-negative calibration constants, γ_c is octahedral shear strain accumulated during previous dilation phases, p_a is atmospheric pressure for normalization purpose, and $\dot{\boldsymbol{s}}$ is the deviatoric stress rate. In Equation (5-1), η_{rv} is the shear stress ratio on load reversal point during cyclic loading, essentially representing the effect of previous shear stress on the subsequent contractive behavior. The $\dot{\boldsymbol{n}}$ and $\dot{\boldsymbol{s}}$ tensors are used to account for general 3D loading scenarios, where, $\dot{\boldsymbol{n}}$ is the outer normal to a surface. The parameter c_3 is used to represent the dependence of pore pressure buildup on initial confinement (i.e., K_σ effect).

5.4.3. Boundary and Loading Conditions

The boundary and loading conditions for dynamic analysis of the sheet-pile retaining wall system (Figure 5.3) under an input motion are implemented in a staged fashion as follows:

1) Gravity was applied to activate the initial static state with: i) linear elastic properties (Poisson's ratio of 0.47 to lower the initial locked shear stress), ii) nodes on both side boundaries (vertical faces) of the FE model were fixed against longitudinal translation for complicity (i.e., no separation between container wall and soil), iii) nodes were fixed along the base against both longitudinal and vertical translations, iv) water table was specified with related water pressure and nodal forces specified along ground surface nodes on waterside (initial hydrostatic values of pore water pressures were specified), and nodes on landside have a fixed pore water pressure (flow of water was restricted to across the container boundaries, Figure 5.3). At the end of this step, the static soil state was imposed and displacements under own-weight application were re-set to zero using the OpenSees command InitialStateAnalysis.

2) The linear elastic beam-column elements of sheet-pile wall were added (Table 5.2). The pile nodes were connected to the soil nodes via the rigid link elements as described above. Thereafter, self-weight of the structure was applied.

3) Soil properties were switched from elastic to plastic (Table 5.1 and Figure 5.5) and the internal variables of PressureDependMultiYield03 consitutive model were adjusted to this stress state (before shaking).

4) Dynamic analysis is conducted by applying an acceleration time history to the base of the FE model.

The FE matrix equation is integrated in time using a single-step predictor multi-corrector scheme of the Newmark type with integration parameters $\gamma = 0.6$ and $\beta = 0.3025$ presented in early studies (Chan 1988; Parra 1996). The equation is solved using the modified Newton-Raphson method, i.e., Krylov subspace acceleration (Carlson and Miller 1998) for each time step with. For the convergence criterion, a test of energy increment is used with 10^{-5} and maximum number of iterations of 20. Furthermore, the constraints are imposed using Transformation method in OpenSees. Finally, a relatively low-level of initial stiffness proportional damping (coefficient = 0.003 leading to 1 % damping ratio at frequency = 1 *Hz*) with the main damping emanating from the soil nonlinear shear stress-strain hysteresis response (Parra 1996) was used to enhance numerical stability of the liquefiable sloping system.

5.5. Calibration Phase: Determination of Soil Model Parameters

To predict dynamic response of centrifuge tests in LEAP-2020, the employed soil constitutive model parameters are calibrated for matching the liquefaction strength curves of the Ottawa F-65 sand with relative density $D_r = 67$ % at vertical stress of 100 and 40 kPa respectively. For that purpose, a total of 11 undrained stress-controlled cyclic direct simple shear tests are

conducted and the laboratory results are provided in the calibration phase (ElGhoraiby and Manzari 2020). The parmeability of the Ottawa F-65 sand is about 1.1×10^{-4} m/s as determined by El Ghoraiby et al. (2020). On this basis, the calibrated soil model parameters for the Ottawa F-65 sand of D_r = 67 % are presented in Table 5.1. Figure 5.6 shows the plot of liquefaction strength curves achieved from the FE simulations and experimental measurements. The data plotted in Figure 5.6 is composed of the number of cycles until a 7.5 % double amplitude (i.e., 3.75 % single amplitude) of strain is achieved versus the applied cyclic stress ratio (*CSR*). It can be seen that a reasonaby good match is reached between simulation results and laboratory data at two different confining stress levels. For illustration, examples of undrained cyclic stress-controlled tests with *CSR* = 0.16 at confinement = 100 kPa and *CSR* = 0.17 at confinement = 40 kPa are displayed in Figure 5.7 and Figure 5.8, respectively. As seen in these figures, the computed results reasonably match the stress path and shear stress-strain response of laboratory tests at two different confining stress levels (i.e., 40 kPa and 100 kPa).

During the calibration phase, additional numerical simulations of cyclic simple shear tests with a specified non-uniform stress input and an initial shear stress are performed (Figure 5.9). The non-uniform shear stress input is in the form of a ramped sinusoidal wave that reaches a maximum cyclic stress ratio (CSR_{max}) and then ramps down to zero (Figure 5.9a). For illustration, two examples of non-uniform cyclic stress-controlled tests with CSR_{max} = 0.38, initial shear stress = 3.5 kPa at confinement = 40 kPa and CSR_{max} = 0.42, initial shear stress = 2.6 kPa at confinement = 30 kPa are depicted in Figure 5.9. It can be seen that the model reproduces a cycle-by-cycle permanent shear strain accumulation pattern during non-uniform cyclic loading.

5.6. Computed Results of Type-C Simulations

Simulation results will be presented for the selected 11 centrifuge tests of Type-C phase (data from Zeghal et al. 2019). The achieved base input motions of these centrifuge tests at various facilities are shown in Figure 5.2. In the calibration phase, the model parameters (Table 5.1) are defined by matching the liquefaction strength curves (Figure 5.6). As such, numerical simulations of the selected centrifuge tests are performed based on these material properties from the calibration phase, and the computed results are compared with those from the measurements directly.

5.6.1. Acceleration

Figure 5.10-Figure 5.13 depict the computed and experimental acceleration time histories at all locations (Figure 5.1) for LEAP-2020. It can be seen that the computed acceleration time histories at deeper depths (such as, AB1-AB2, AM1-AM2, AW1-AW2, AD and AFWW) are in good agreement with those from the measurements. For shallower depths (AB3, AM3, AW3 and AFWB), both the computed results and measurements generally showed a consistent trend for acceleration spikes due to dilation. However, the measurements displayed much higher dilation spikes in contrast to the computed results.

5.6.2. Excess Pore Pressure

Figure 5.14-Figure 5.17 illustrate the time histories of excess pore pressure in LEAP-2020. In general, the computed excess pore pressures reasonably match those from measurements for the back and middle sensor arrays (PB1-PB3 and PM1-PM3). Both the computed results and measurements showed a consistent trend of negative spikes due to dilation, in accordance with the acceleration (Figure 5.10-Figure 5.13). However, there are some discrepancies near the wall sensor arrays (Figure 5.16 and Figure 5.17), such as PW1-PW3, PD, PFW and PFWB. As seen in Figure

5.16, the experimental data of RPI tests 9-13 showed less dilative pore pressure spikes compared to the computed results. However, in calibrations of other tests (such as UCD-1, ZJU-1, and KyU-3), the experimental results displayed much higher negative dilation spikes in contrast to the simulations. These unintended inconsistencies in test results are considered to be mainly due to the different relative densities of centrifuge experiments conducted at various facilities. Furthermore, soil-structure interaction effects near the sheet-pile wall add complexity in terms of comparing the experimental data to the numerical simulations.

5.6.3. Displacement

Figure 5.18 displays the computed longitudinal displacement time histories and experimental measurements at the top of the sheet-pile wall. It can be seen that the computed results of UCD-1, EU-2, KyU-3, RPI-9, 10 and 13 are in good agreement with those from the measurements. However, there are some discrepancies for other tests, such as the longitudinal displacements of ZJU-1, KAIST-2, RPI-11 which are over-predicted, and KyU-1, RPI-12 which are under-predicted, mainly due to the different relative densities of centrifuge experiments conducted at the various facilities. These inconsistencies indeed make it challenging to achieve a perfect match between the experimental measurements and numerical simulations for all selected centrifuge tests.

5.6.4. Computed Response of RPI-9 Test

To investigate the overall response of the sheet-pile retaining wall system, computed results of test RPI-9 is presented in Figure 5.19-Figure 5.21. The deformed FE mesh at end of shaking (Figure 5.19) showed a maximum horizontal displacement that occurred near the sheet-pile wall ground surface landside, reaching about 0.4 m. Furthermore, Figure 5.19b shows the horizontal displacement contour with arrows displaying the direction of ground movement. It can be seen

that the landside ground deformed laterally toward to the waterside due to the soil liquefaction. Vertical displacement contours at end of shaking are illustrated in Figure 5.19c. As seen in this figure, the landside soil settled about 0.18 m and ground heave on the waterside reached about 0.04 m.

In accordance with the ground deformation contours, Figure 5.20 illustrates the shear strain in the *x-y* plane with a peak value of about 13 % at the bottom of the liquefiable layer. Representative soil response (i.e., shear stress versus mean effective stress and shear stress versus shear strain) for integration points near the locations of pore pressure transducers are presented in Figure 5.21. As seen in this figure, a cycle-by-cycle accumulation of shear deformations is observed, and the spikes in shear stress are consistent with the pore pressure dips due to dilation (Figure 5.14-Figure 5.17).

5.7. Summary and Conclusions

The numerical simulation results of centrifuge model tests (Type-C phase) conducted by various facilities in LEAP-2020 for a sheet-pile retaining structure under liquefaction-induced lateral loading are presented. All the numerical simulations are performed using a calibrated pressure-dependent constitutive model (PressureDependMultiYield03) implemented with the characteristics of dilatancy, cyclic mobility and associated shear deformation. The soil parameters are determined based on a series of available stress-controlled cyclic simple shear tests for matching the liquefaction strength curves of Ottawa F-65 sand with relative density D_r = 67 % at two different confining stress levels. The computational framework and staged analysis procedure are presented as well. Primary conclusions can be drawn as follows:

(1) The unintended inconsistencies of centrifuge test results in Type-C phase may indeed hamper the comparisons between numerical simulations and measurements. These inconsistencies

are mainly due to the different relative densities of the centrifuge experiments conducted at various facilities.

(2) Soil-structure interaction effects near the sheet-pile wall add challenges in achieving a satisfactory match between the experimental measurements and numerical simulations for all selected centrifuge tests. Further attention might be given to the interface between the soil and the structure. At this interface, numerical simulation of pore water pressure should be considered as well.

(3) Determination of soil model parameters in the calibration phase showed that the pressure-dependent model, i.e., PressureDependMultiYield03 material has captured resonably the liquefaction strength curves of Ottawa F-65 sand with relative density D_r = 67 % and the corresponding soil response of each undrained cyclic stress-controlled test.

(4) The dense sand layer may have a significant effect on the response of the sheet-pile wall system and its material parameters should be calibrated as well.

(5) Although the centrifuge tests conducted by various institutions are not providing completely consistent results, measured time histories are reasonably captured by the numerical simulations in LEAP-2020 using the same soil constitutive model parameters. The good agreement between computed and measured results for each centrifuge test demonstrated that the PressureDependMultiYield03 soil model as well as the overall employed computational methodology have the potential to predict the dynamic response of equivalent soil-pile-structure systems subjected to liquefaction-induced lateral loading.

(6) Additional experimental data sets might be needed related to post-liquefaction shear deformation accumulation due to presence of an initial shear stress basis. As such new data sets

become available, damage parameters y_1 and y_2 of the PressureDependMultiYield03 material can be better calibrated and applied in the prediction of liquefaction-induced lateral spreading.

5.8. Acknowledgements

Chapter 5, in full, is currently being prepared for submission for publication of the material as it may appear in the following journal publication (The dissertation author was the primary investigator and author of this paper):

Qiu, Z. and Elgamal, A. "Seismic Response of a Sheet-Pile Retaining Structure Supporting Liquefiable Soils: Numerical Simulations of LEAP Centrifuge Tests."

Table 5.1 Model parameters (PressureDependMultiYield03) in calibration phase and Type-C simulations

Model Parameters	D_r = 66.7 %	D_r = 90 %
Reference mean effective pressure, p'_r (kPa)	101.0	101.0
Mass density, ρ (t/m^3)	2.0	2.05
Maximum shear strain at reference pressure, $\gamma_{max,r}$	0.1	0.1
Shear modulus at reference pressure, G_r (MPa)	41.7	100.0
Stiffness dependence coefficient, n, $G = G_r(\frac{\boldsymbol{P'}}{\boldsymbol{P'_r}})^{\boldsymbol{n}}$	0.5	0.5
Poisson's ratio v for dynamics	0.4	0.4
Shear strength at zero confinement, c (kPa)	0.3	0.3
Friction angle, ϕ	30°	40°
Phase transformation angle, ϕ_{PT}	22°	22°
Contraction coefficient, c_1	0.08	0.05
Contraction coefficient, c_2	15	1.0
Contraction coefficient, c_3	0.2	0.2
Contraction coefficient, c_4	5.0	2.0
Contraction coefficient, c_5	7.0	2.0
Dilation coefficient, d_1	0.1	0.1
Dilation coefficient, d_2	3.0	3.0
Dilation coefficient, d_3	0.15	0.15
Damage parameter, y_1	1	1
Damage parameter, y_2	0.0	0.0
Permeability, (m/s)	$1.1\text{x}10^{-4}$	$1.1\text{x}10^{-4}$

Table 5.2 Sheet pile properties

Model Parameters	Value
Elastic modulus (GPa)	69
Mass density, ρ (t/m^3)	2.8
Poisson's ratio, v	0.31
Moment of inertia, I (m^4)	0.01

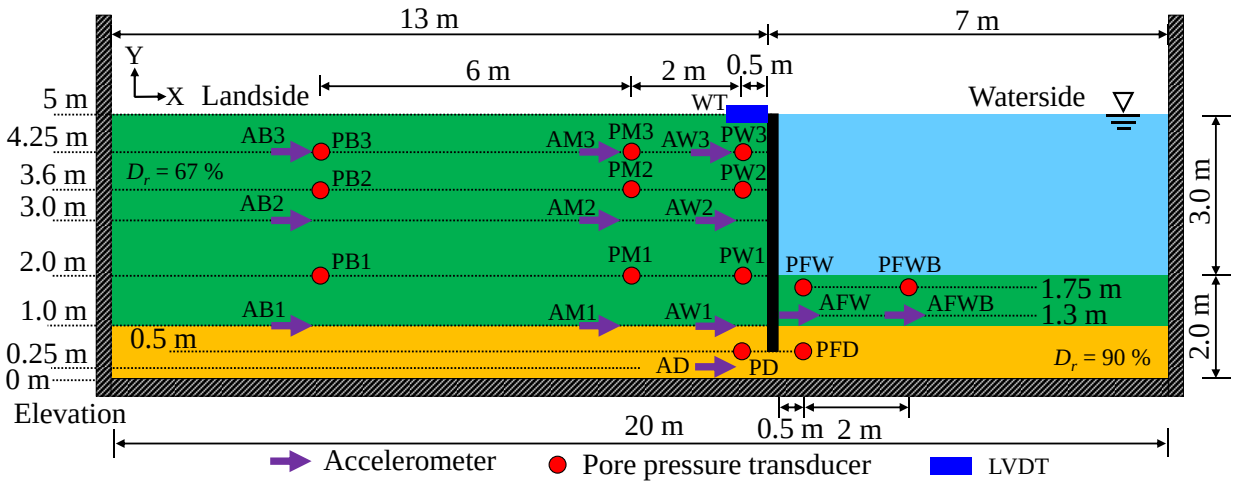

Figure 5.1 Schematic representation of the centrifuge test layout for LEAP-2020 simulations (after Zeghal et al. 2019)

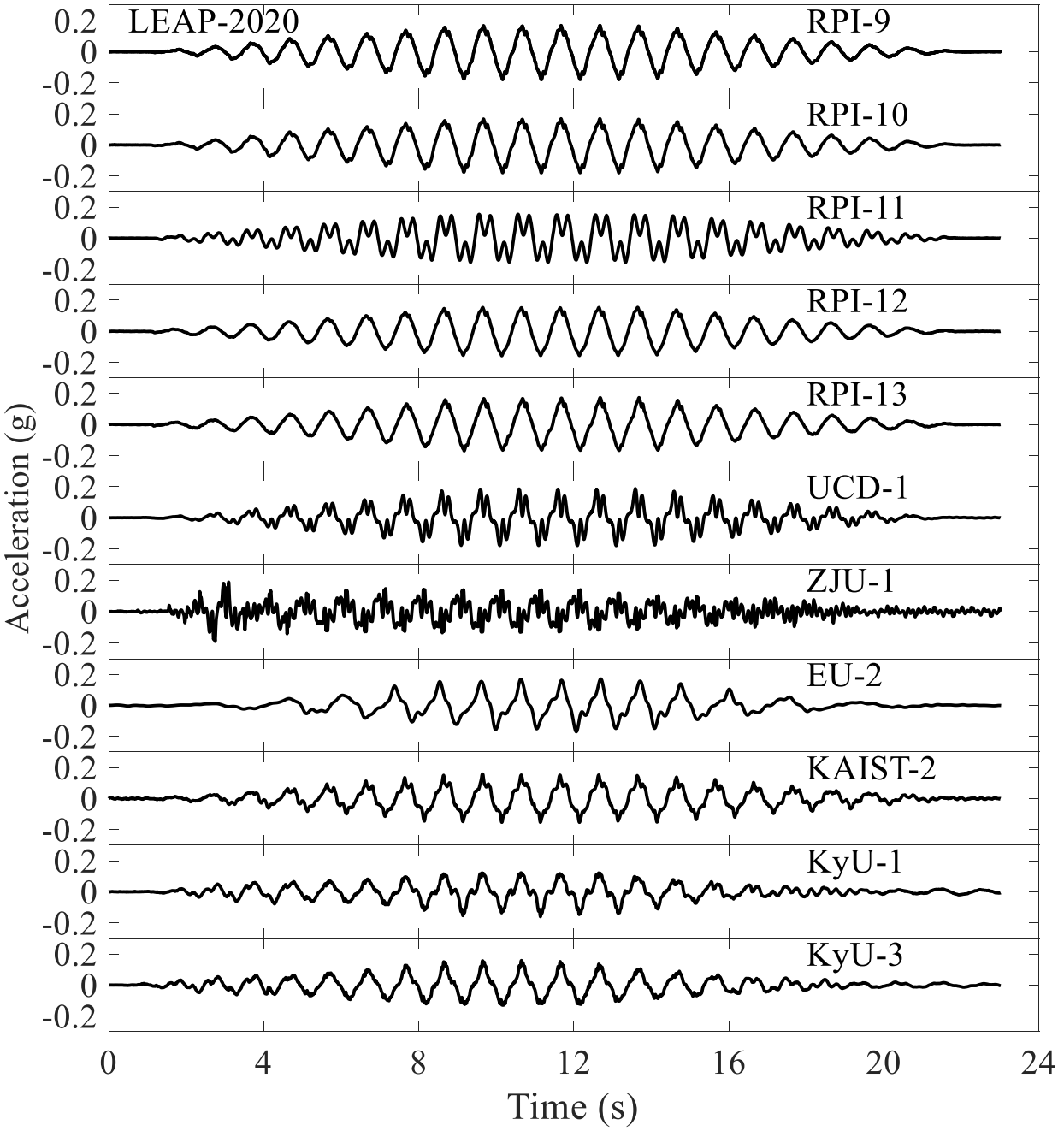

Figure 5.2 Base input motions (after Zeghal et al. 2019)

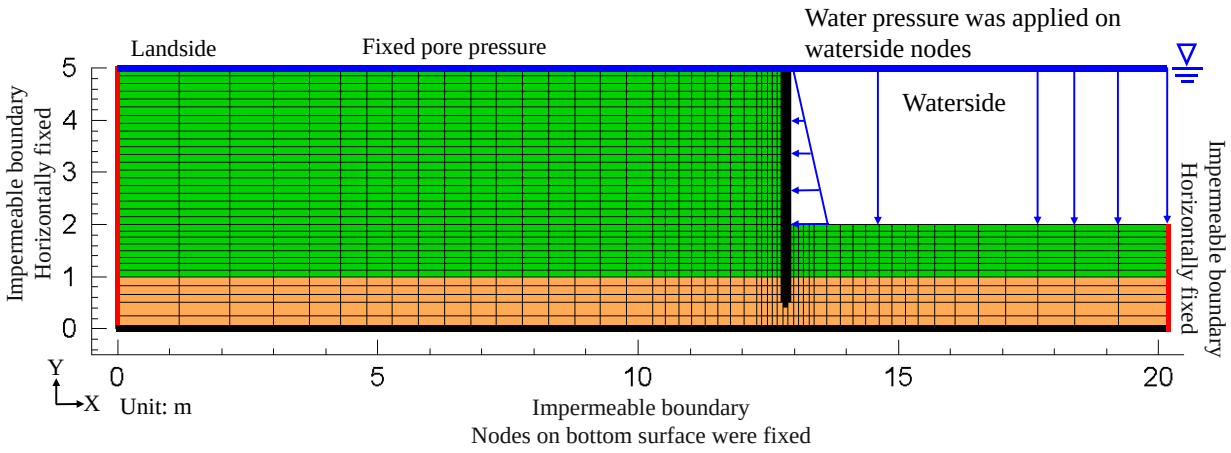

Figure 5.3 Finite Element mesh

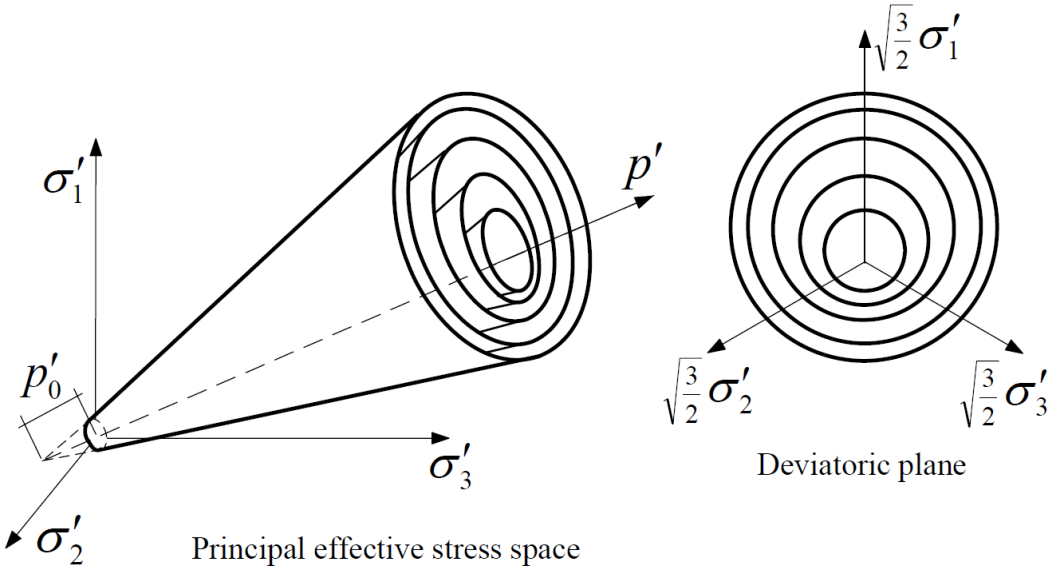

(a)

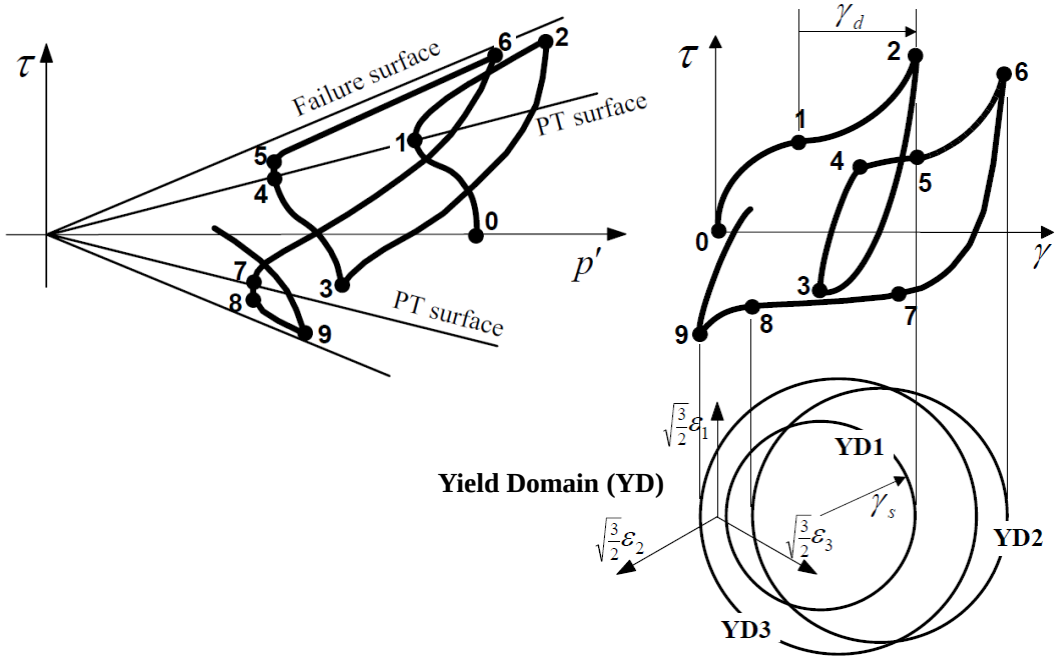

(b)

Figure 5.4 PressureDependMultiYield03 material: (a) Conical yield surfaces in principal stress space and deviatoric plane; (b) Schematic of constitutive model response and configuration of yield domain (after Yang et al. 2003)

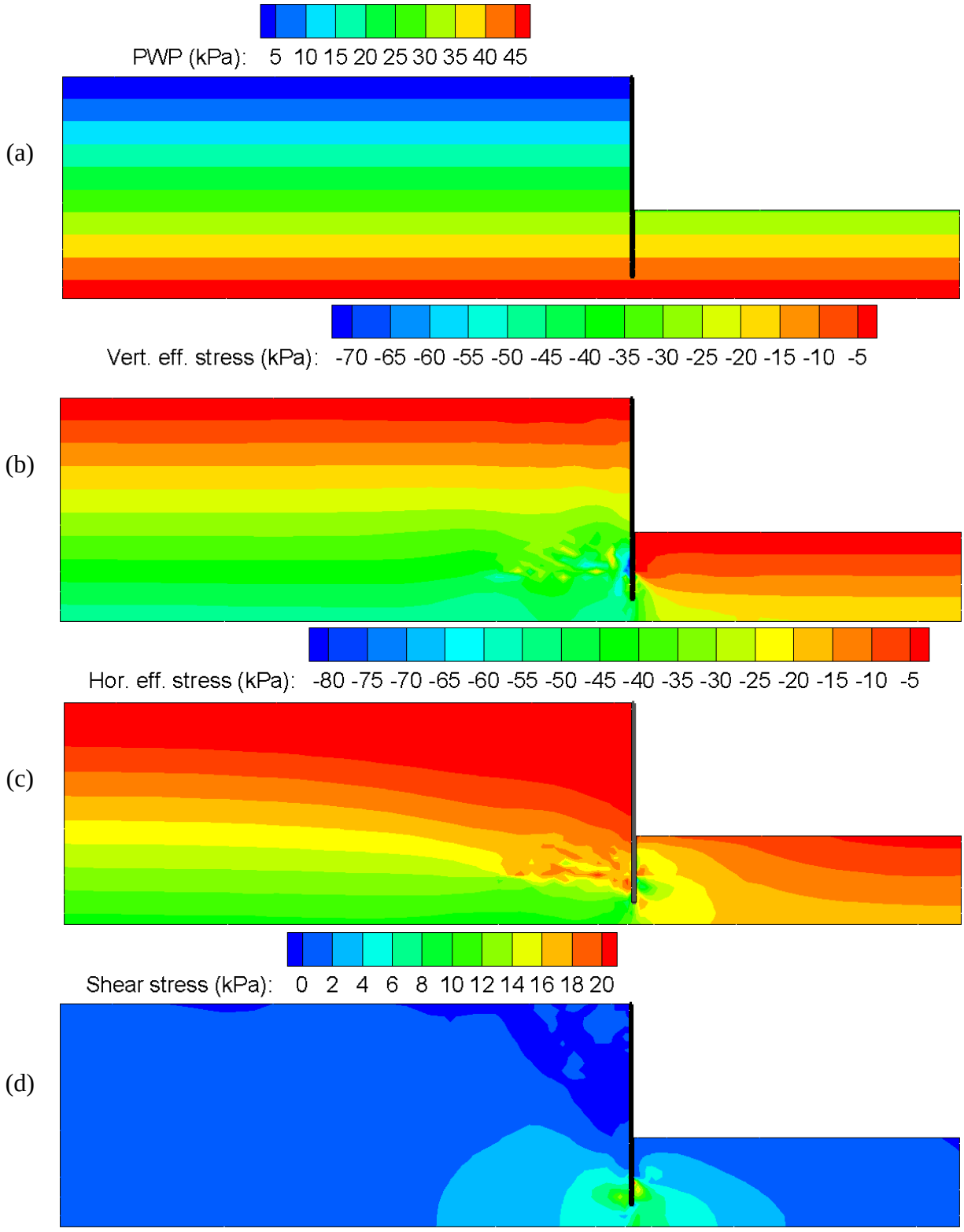

Figure 5.5 Initial state of soil due to gravity (before shaking): (a) Pore water pressure; (b) Vertical effective stress σ'_{yy}; (c) Horizontal effective stress σ'_{xx}; (d) Shear stress τ_{xy}

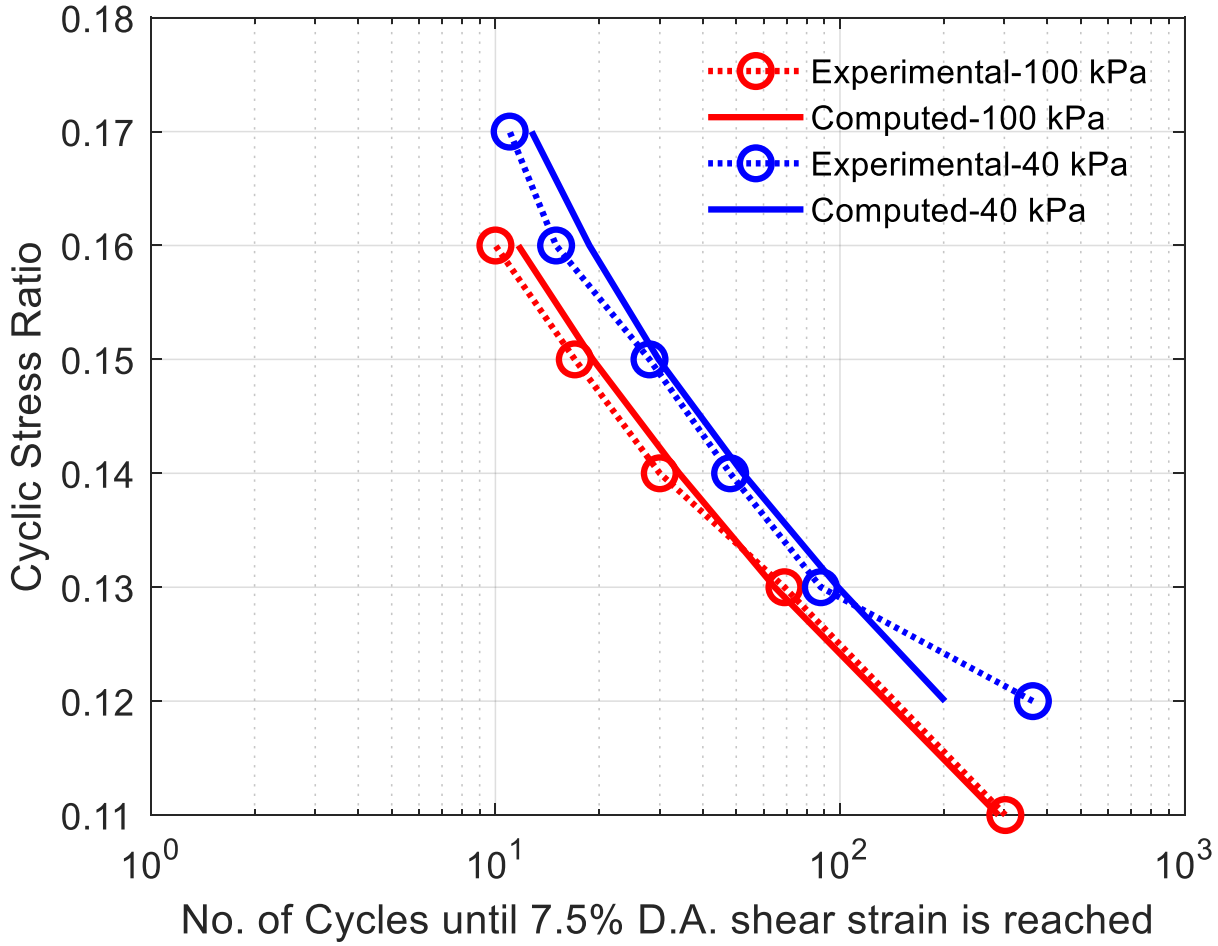

Figure 5.6 Liquefaction strength curve (data from Zeghal et al. 2019)

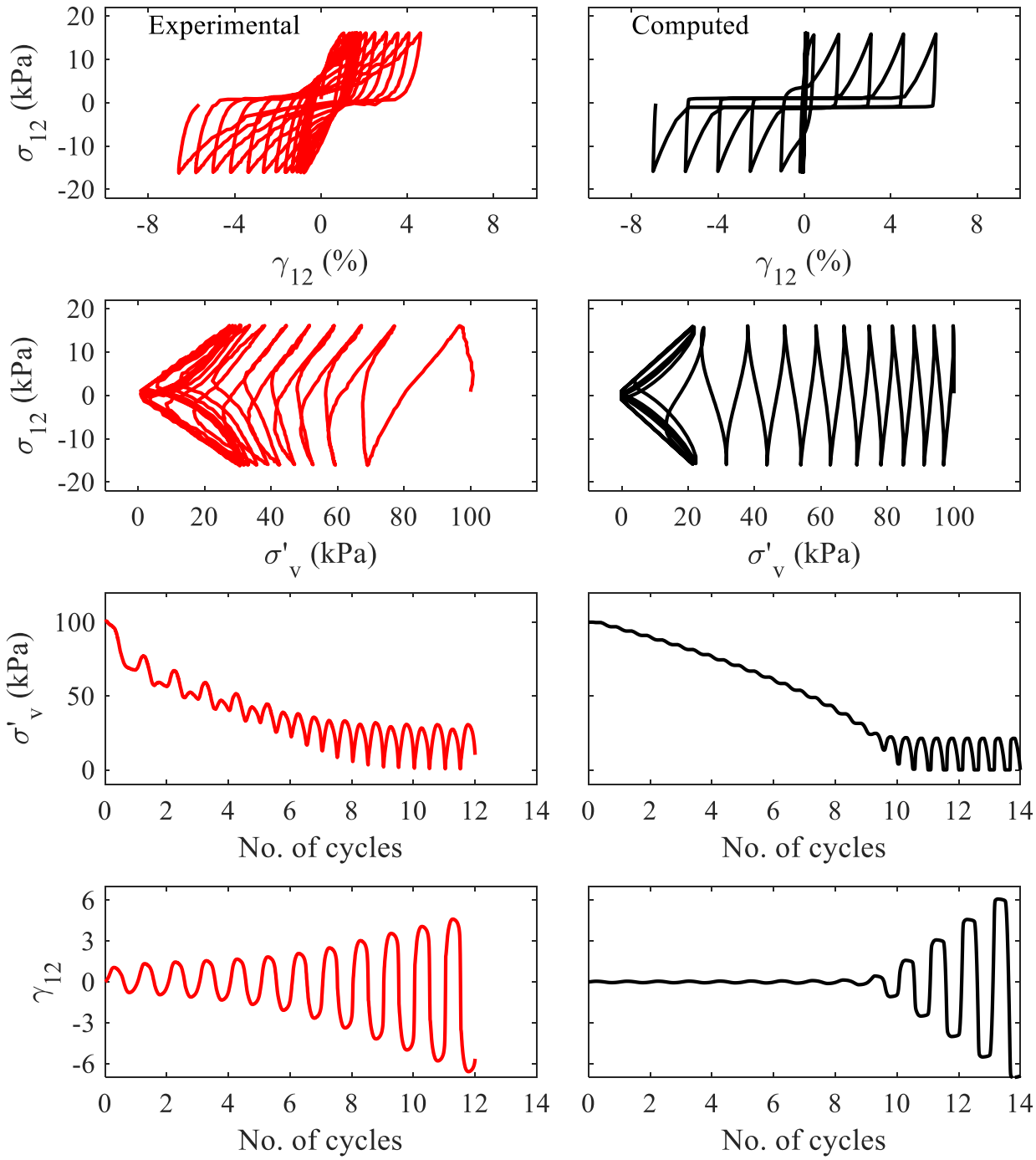

Figure 5.7 Soil response of undrained cyclic stress-controlled direct tests for *CSR* = 0.16 at a confinement of 100 kPa (data from Zeghal et al. 2019)

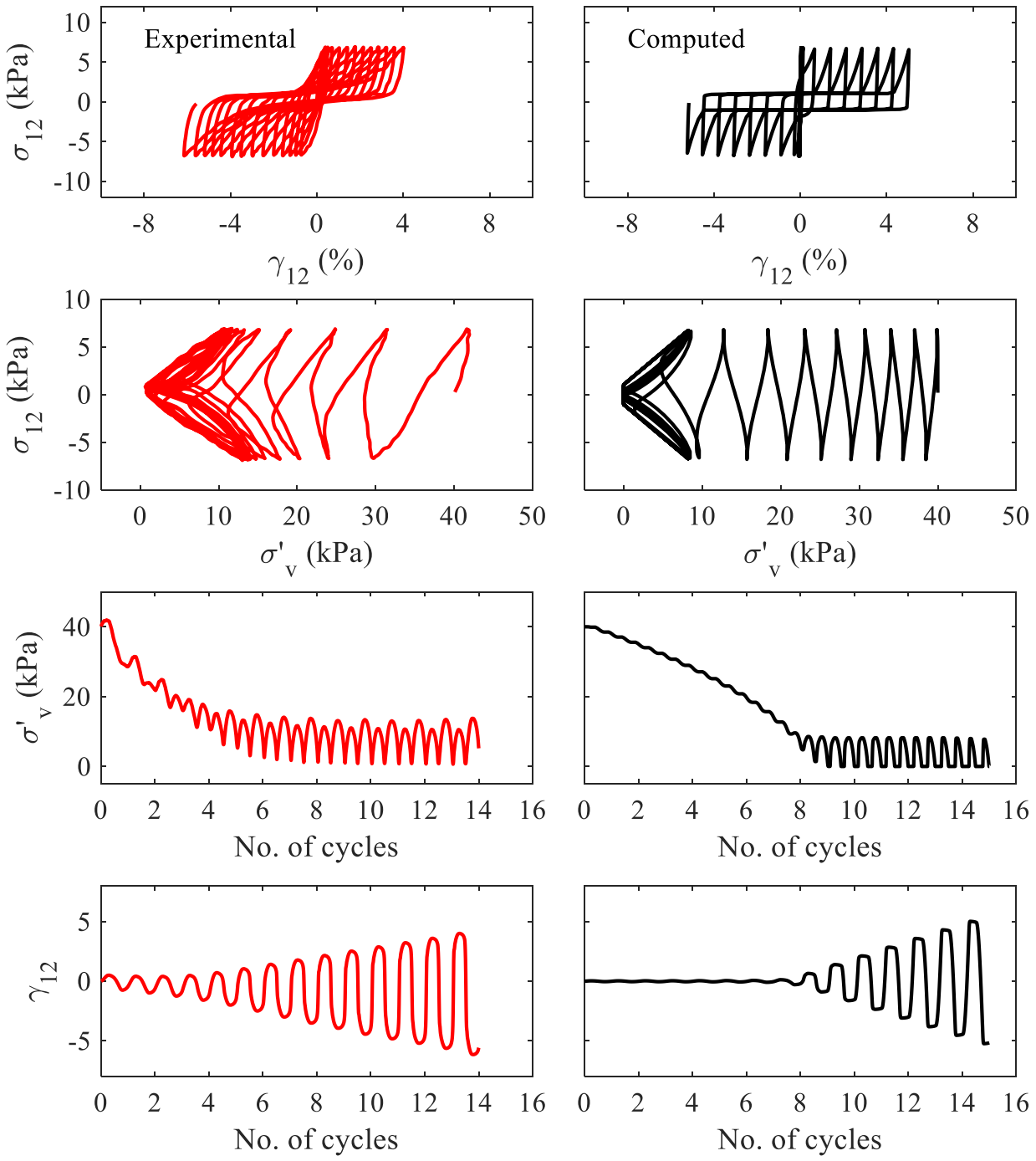

Figure 5.8 Soil response of undrained cyclic stress-controlled direct tests for *CSR* = 0.17 at a confinement of 40 kPa (data from Zeghal et al. 2019)

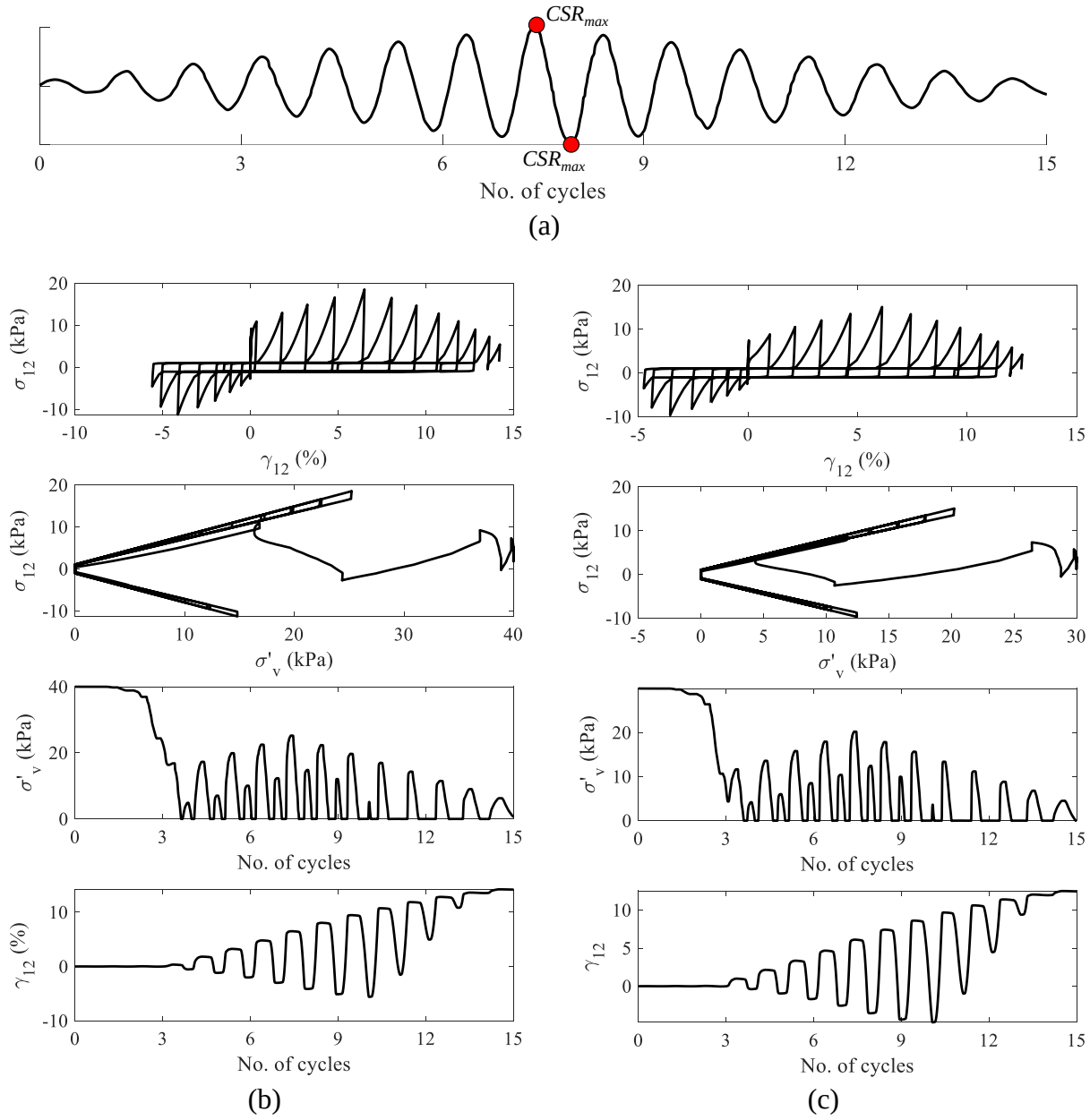

Figure 5.9 Computed soil response of non-uniform undrained cyclic stress-controlled direct simple shear tests: (a) Shear stress input; (b) CSR_{max} = 0.38 with initial shear stress bias of 3.5 kPa at confinement = 40 kPa; (c) CSR_{max} = 0.42 with initial shear stress bias of 2.6 kPa at confinement = 30 kPa (data from Zeghal et al. 2019)

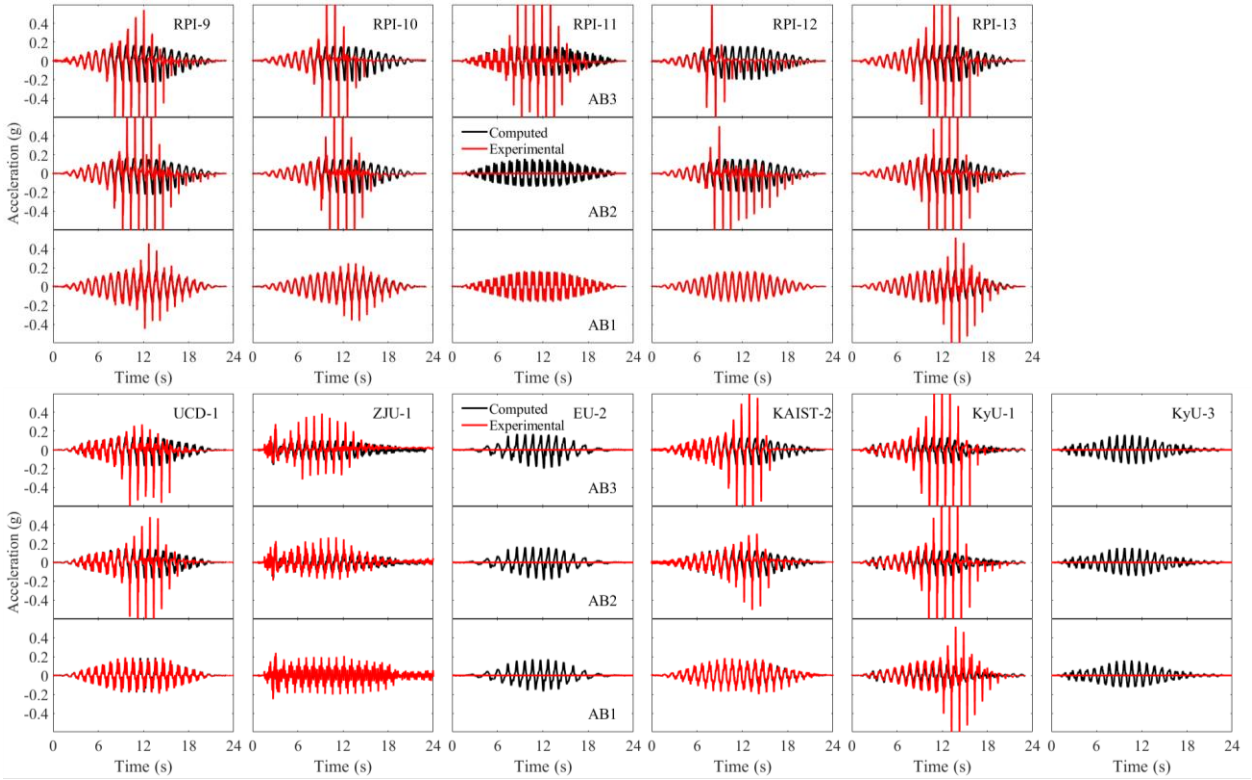

Figure 5.10 Measured and computed acceleration time histories for AB1, AB2, AB3

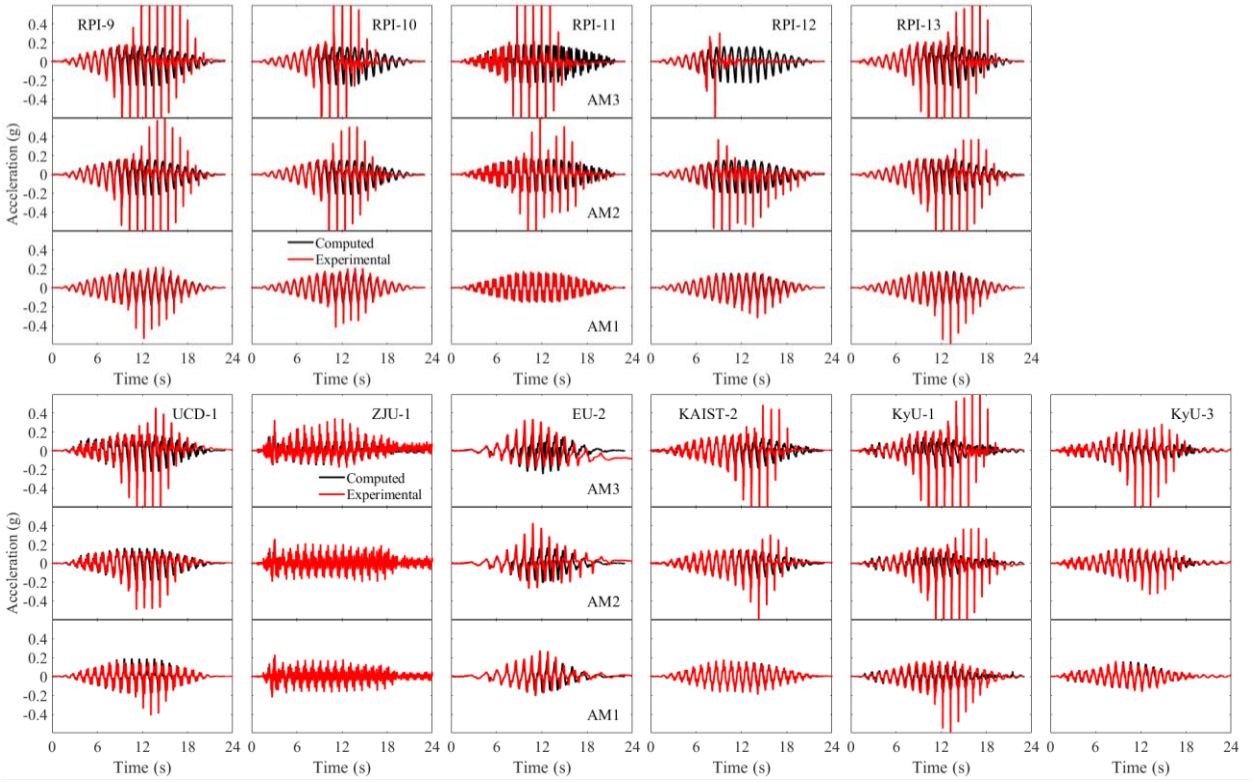

Figure 5.11 Measured and computed acceleration time histories for AM1, AM2, AM3

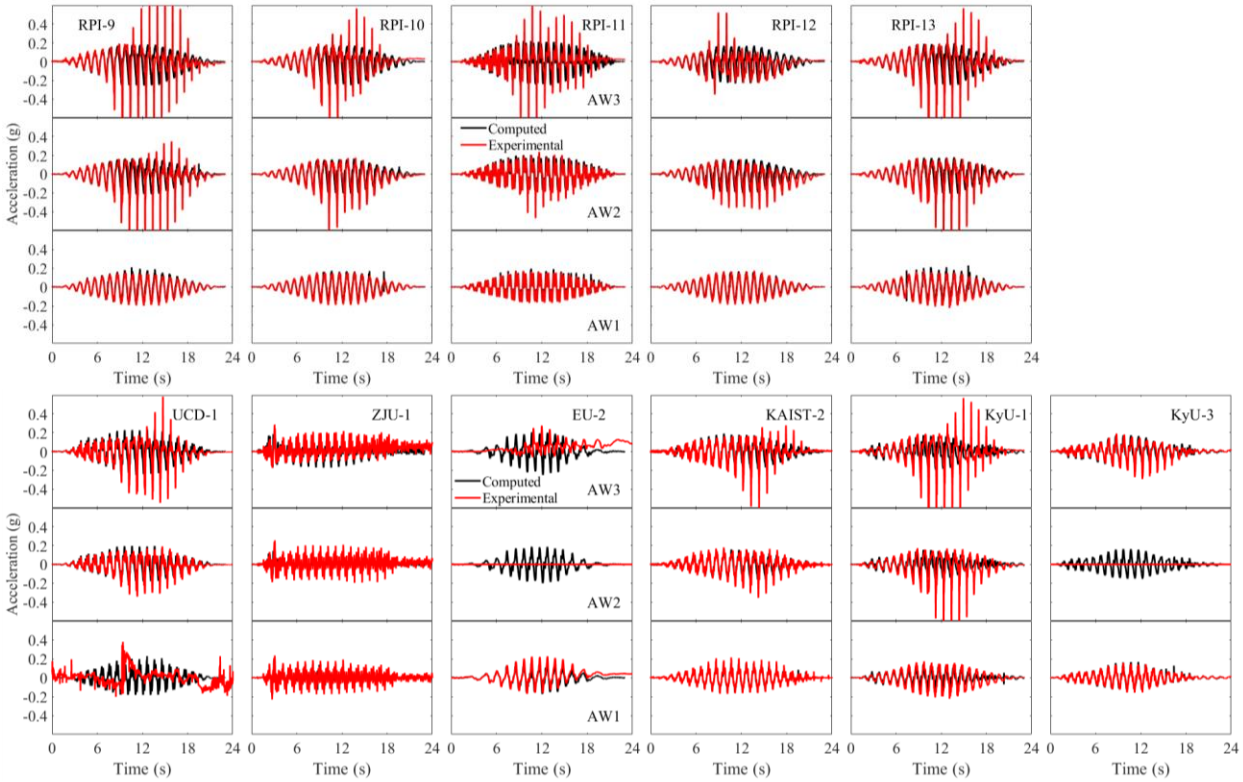

Figure 5.12 Measured and computed acceleration time histories for AW1, AW2, AW3

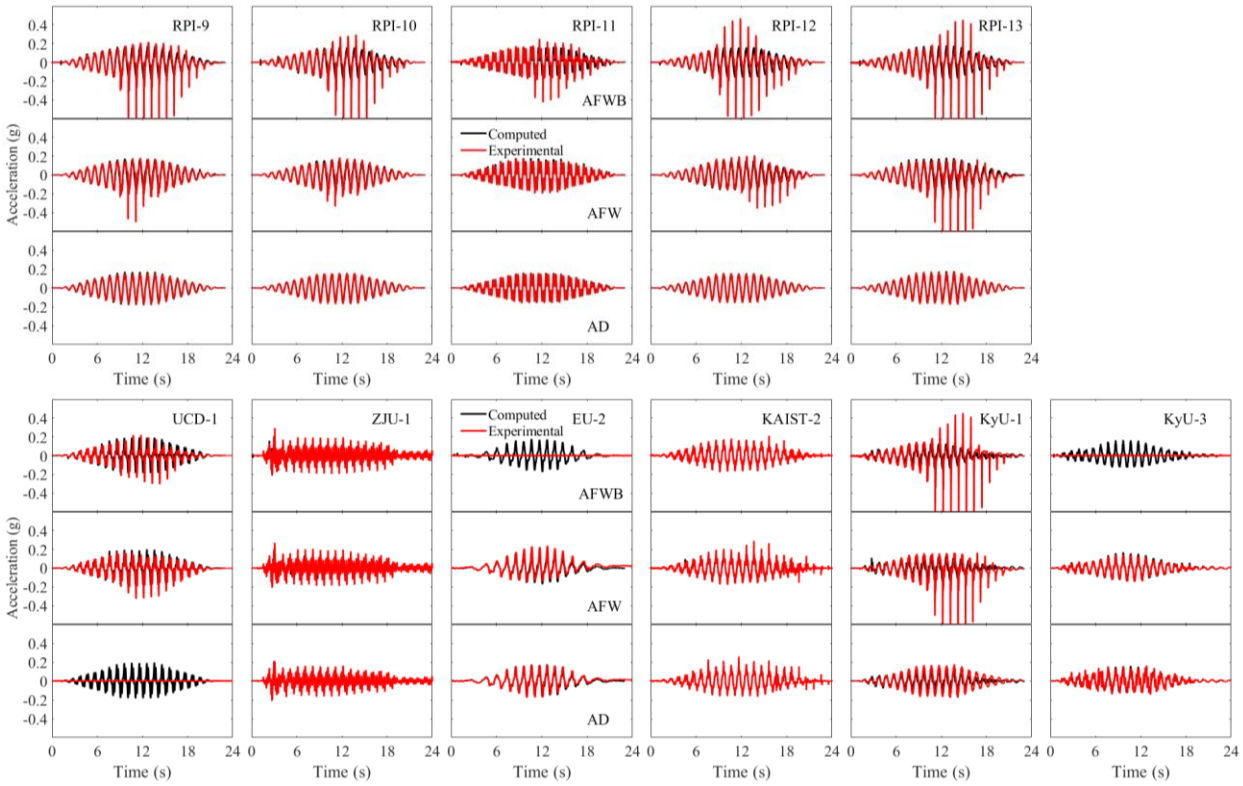

Figure 5.13 Measured and computed acceleration time histories for AD, AFW, AFWB

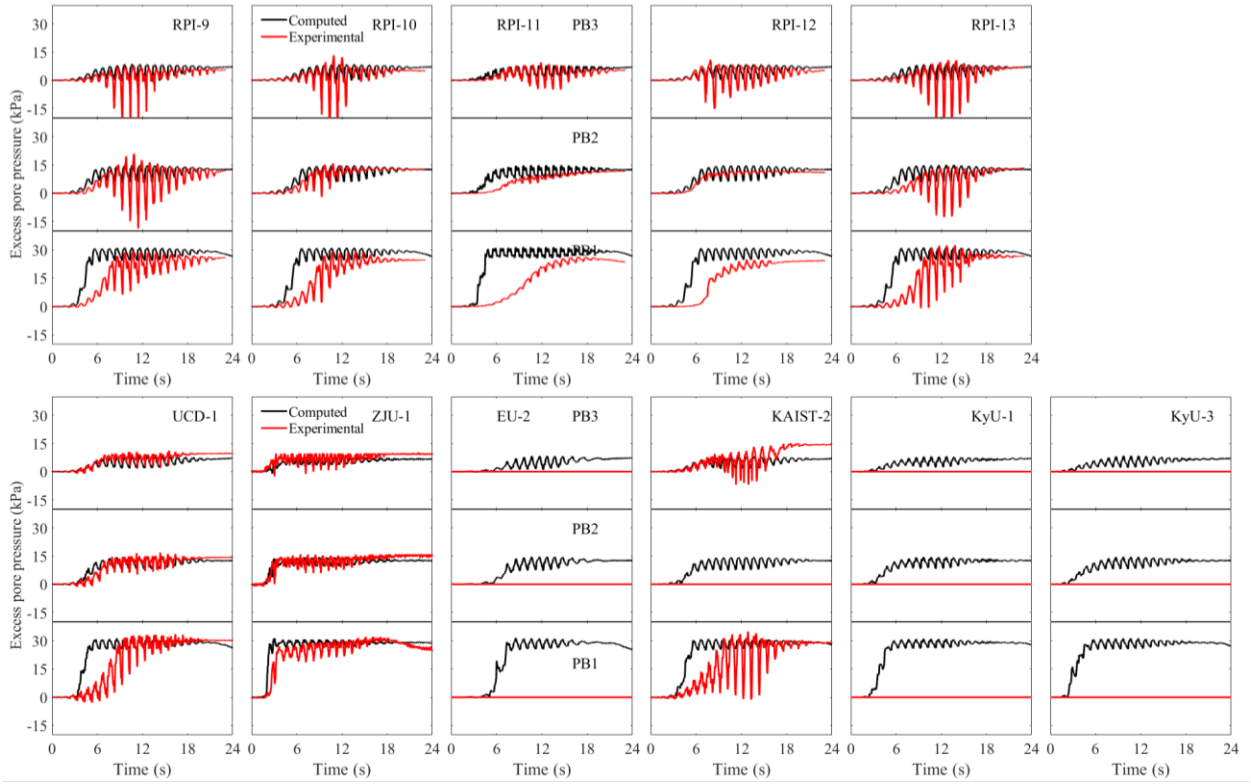

Figure 5.14 Measured and computed excess pore pressure for PB1, PB2, PB3

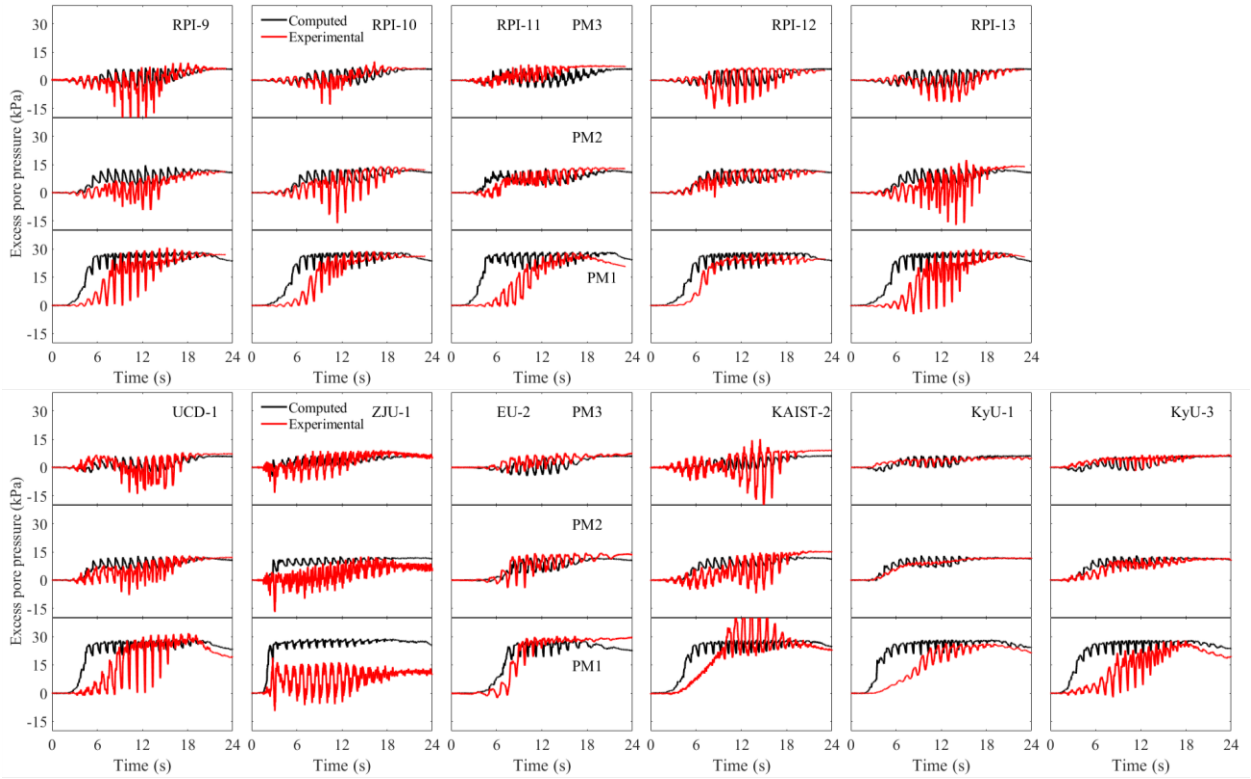

Figure 5.15 Measured and computed excess pore pressure for PM1, PM2, PM3

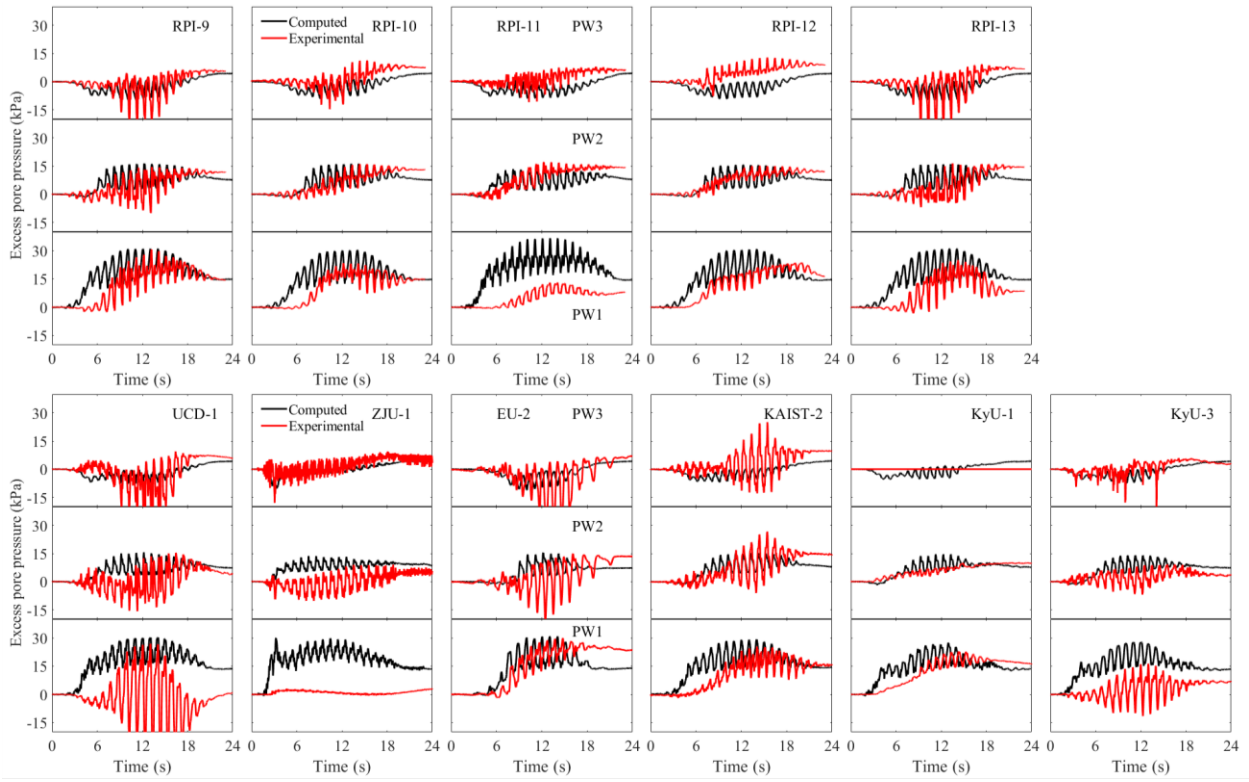

Figure 5.16 Measured and computed excess pore pressure for PW1, PW2, PW3

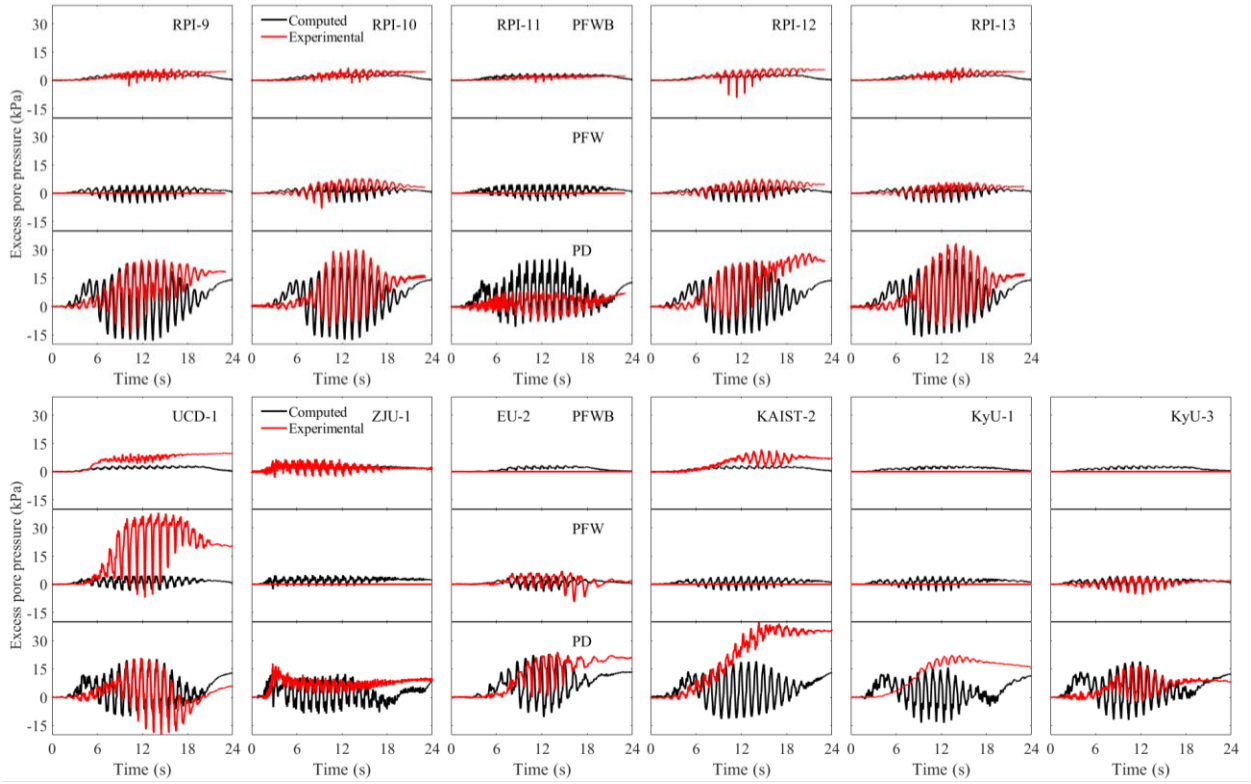

Figure 5.17 Measured and computed excess pore pressure for PD, PFW, PFWB

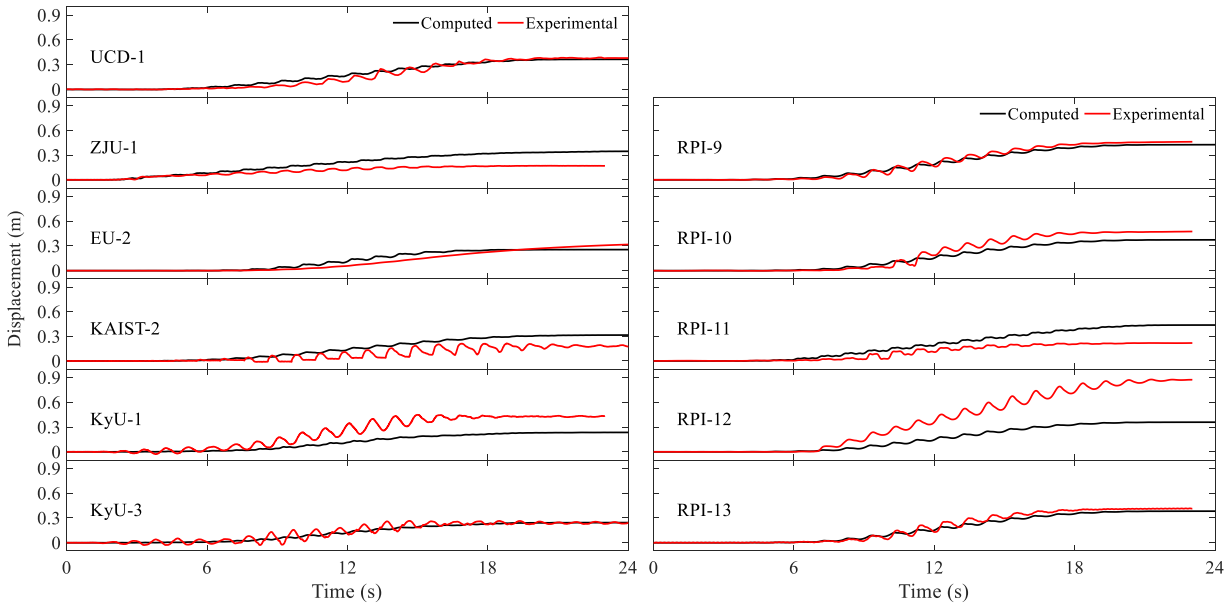

Figure 5.18 LEAP-2020: measured and computed displacement time histories

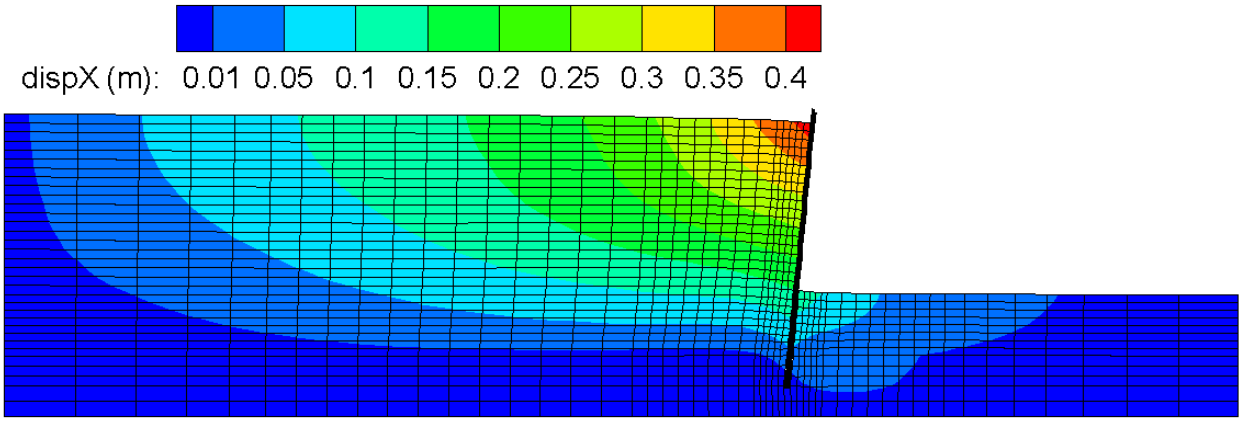

(a)

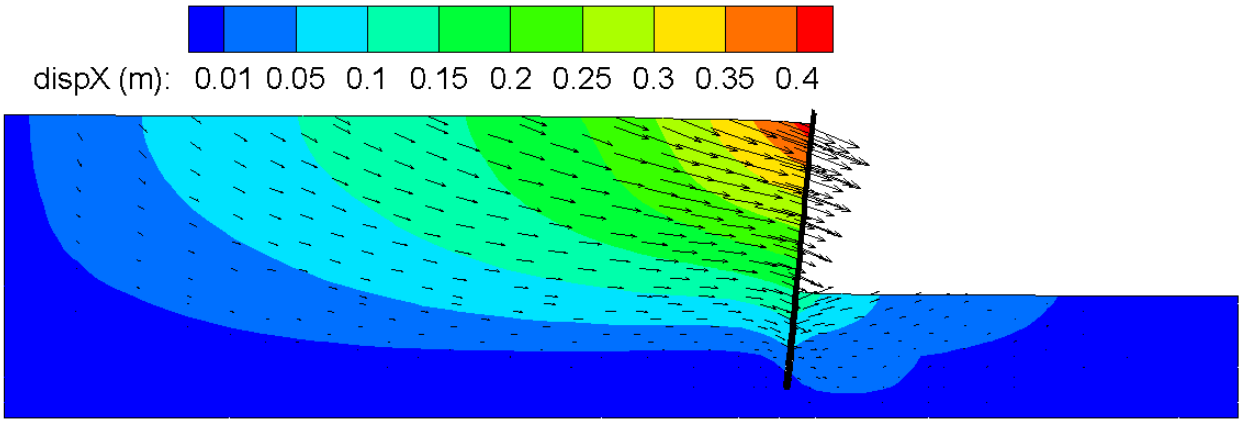

(b)

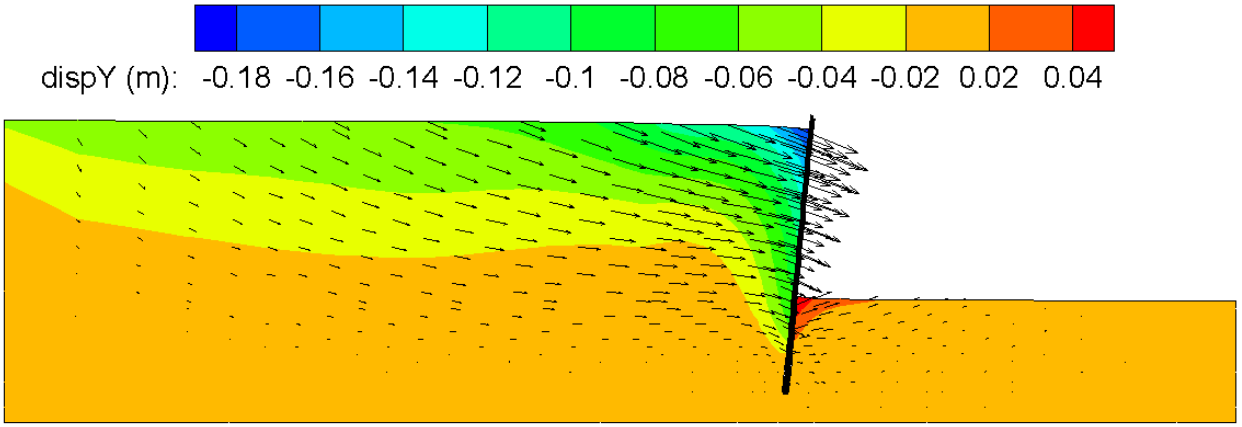

(c)

Figure 5.19 Computed deformation at end of shaking in test RPI-9: (a) Deformed FE mesh; (b) Horizontal displacement contour; (c) Vertical displacement (arrows display direction of ground movement; factor = 5)

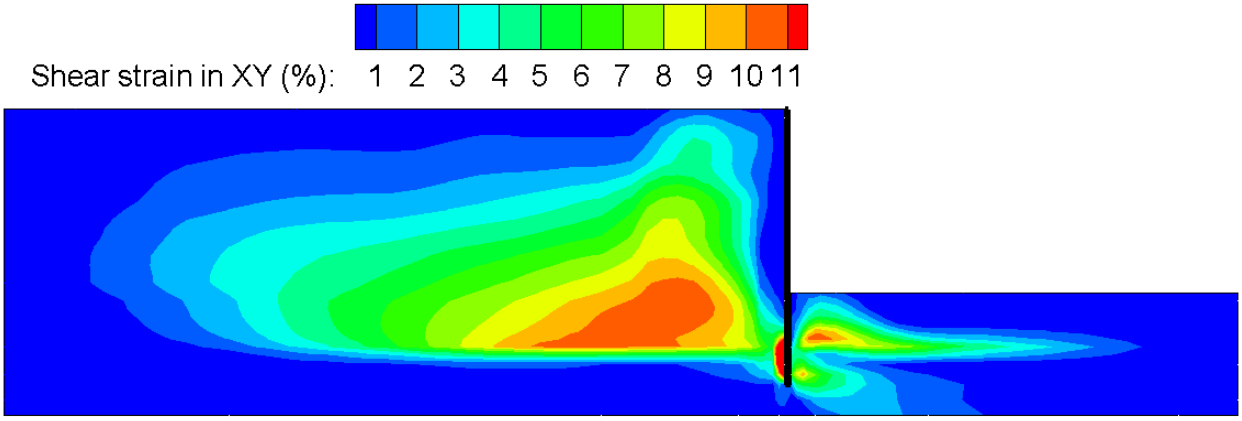

Figure 5.20 Computed shear strain contour at end of shaking in test RPI-9

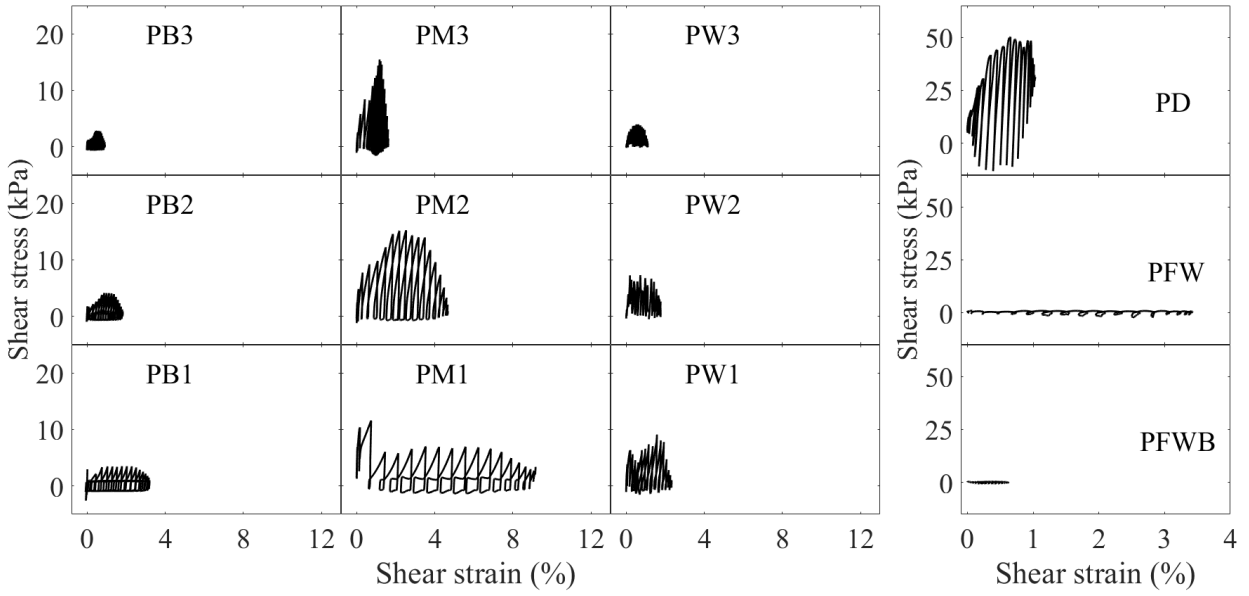

(a)

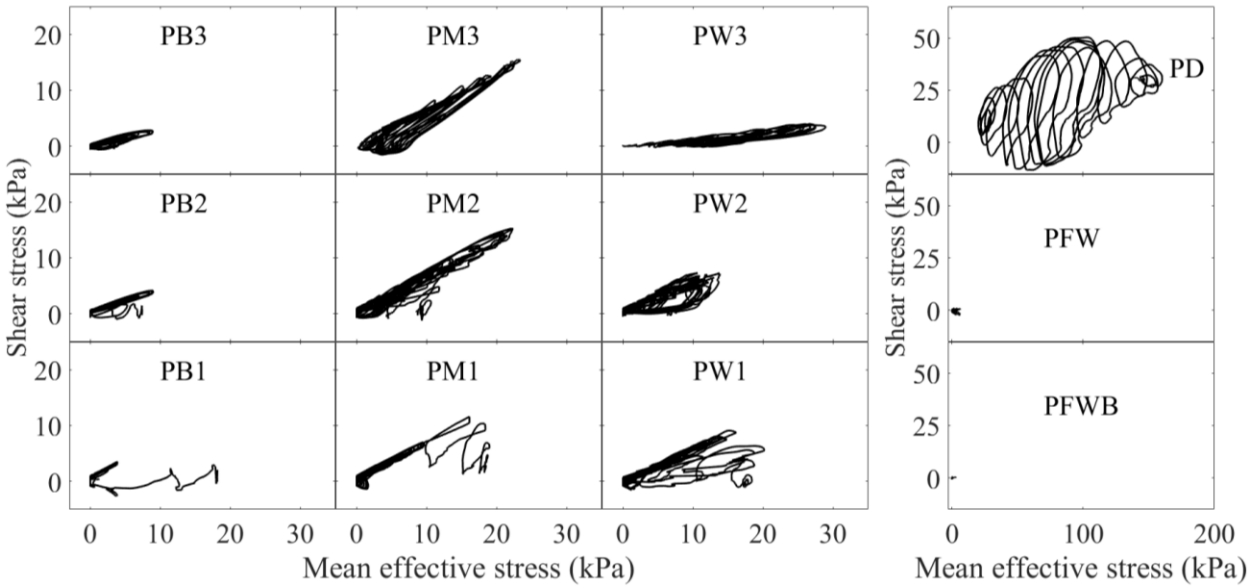

(b)

Figure 5.21 Computed soil response of test RPI-9: (a) Shear stress-strain; (b) Shear stress-mean effective stress

Chapter 6. Aspects of Bridge-Ground Seismic Response and Liquefaction-Induced Deformations

6.1. Abstract

Considerable bridge-ground interaction effects are involved in evaluating the consequences of liquefaction-induced deformations. Due to seismic excitation, liquefied soil layers may result in substantial accumulated permanent deformation of sloping ground near the abutments. Ultimately, global response is dictated by the bridge-ground interaction as an integral system. However, a holistic assessment of such response generally requires a highly demanding full three-dimensional (3D) model of the bridge and surrounding ground. As such, in order to capture a number of the salient involved mechanisms, this study focuses on the longitudinal seismic performance of a simpler idealized configuration, motivated by details of an existing bridge-ground configuration. In this model, a realistic multi-layer soil profile is considered with interbedded liquefiable/non-liquefiable strata. Effect of the resulting liquefaction-induced ground deformation is explored. Attention is given to overall deformation of the bridge structure due to lateral spreading in the vicinity of the abutments. The derived insights indicate a need for such global analysis techniques, when addressing the potential hazard of liquefaction and its consequences.

6.2. Introduction

Large bridge overcrossings with high ground water table are particularly vulnerable to liquefaction-induced lateral spreading and loss of pile foundation capacity during earthquakes (Youd 1993; Hamada et al. 1996; Tokimatsu and Asaka 1998; Berrill et al. 2001). Damage to such bridges has been observed in reconnaissance investigations, including the recent 2010 Maule (Arduino et al. 2010; Ledezma et al. 2012; Verdugo et al. 2012) and the 2011 Christchurch

earthquakes (Cubrinovski et al. 2011, 2014; Wotherspoon et al. 2011). From these investigations, observed response was often noted to be highly influenced by the global bridge-ground overall characteristics as an integral system.

As such, investigators have been increasingly studying the entire bridge and the surrounding ground response within an integral framework. Different approaches to the representation of ground response at the location of each bridge bent foundation, and effects on the entire bridge were presented (Boulanger et al. 2007; Ashford et al. 2009, 2011; Aygün et al. 2009, 2010; Ledezma and Bray 2010; Padgett et al. 2013; Turner et al. 2013, 2016; Wang et al. 2013a, b; McGann and Arduino 2015; Ghofrani et al. 2016; Soltanieh et al. 2019). Alternatively, using two-dimensional (2D) plane-strain Finite Elements (FE) continuum models to represent the ground and canyon configuration, the bridge model and its foundations were idealized and connected to the ground using soil spring formulations (Bowers 2007; Shin et al. 2007, 2008; Zhang et al. 2008; Kwon et al. 2009).

Results of these studies show that consideration of the entire bridge-ground system provides a more realistic distribution of force and displacement demands. As such, it is indicated that global analysis is paramount in realistically evaluating the performance of liquefaction-induced lateral spreading and its consequences.

On this basis, an idealized 3D FE model motivated by the details of an actual bridge-ground system (Caltrans 2017) was developed to investigate consequences of liquefaction-induced ground deformation on salient characteristics of the resulting structural response. In this model, a longitudinal slice of the bridge-ground system is represented and analyzed.

The following sections of this chapter outline the: 1) computational framework, 2) specifics and model properties of the bridge-ground system, 3) details of the employed FE modeling

techniques, 4) conducted numerical simulations and salient bridge system response mechanisms, and 5) insights derived from the study. Finally, a number of conclusions are presented and discussed.

6.3. Computational Framework

The Open System for Earthquake Engineering Simulation (OpenSees, http://opensees.berkeley.edu, McKenna 2011) framework was employed to conduct the nonlinear bridge-ground system analyses subjected to seismic excitation. OpenSees is developed by the Pacific Earthquake Engineering Research (PEER) Center and is widely used for simulation of geotechnical systems and soil-structure interaction applications (Yang and Elgamal. 2002; Lu et al. 2001; Su et al. 2017). The OpenSees elements and materials used in this FE model are briefly described below.

Three-dimensional solid-fluid brick elements following the *u-p* formulation (Chan 1988) were employed for simulating saturated soil response, where *u* is displacement of the soil skeleton and *p* is pore-water pressure. Implementation of this *u-p* element is based on the following assumptions: 1) small deformation and rotation; 2) solid and fluid density remain constant in time and space; 3) porosity is locally homogeneous and constant with time; 4) soil grains are incompressible; 5) solid and fluid phases are accelerated equally. Hence, the soil layers represented by these effective stress fully coupled elements account for deformations and changes in pore-water pressure during seismic excitation.

The employed soil constitutive models (Yang and Elgamal. 2002; Parra 1996; Yang 2000; Elgamal et al. 2003) were developed based on the multi-surface-plasticity theory (Iwan 1967; Prevost 1985). In these models, the shear stress-strain backbone curve is represented by the hyperbolic relationship. As such, soil is simulated by the implemented OpenSees materials

PressureDependMultiYield03 (Khosravifar et al. 2018) and PressureIndependMultiyield (PIMY). It is noted that PressureDependMultiYield03 has been calibrated in earlier studies (Yang and Elgamal. 2002; Parra 1996; Yang 2000; Elgamal et al. 2003) and includes recent modifications to more closely capture the established guidelines on liquefaction triggering (Idriss and Boulanger 2008).

The FE matrix equation of the bridge-ground system is integrated in time using a single-step predictor multi-corrector scheme of the Newmark type (Chan 1998; Parra 1996) with integration parameters $\gamma = 0.6$ and $\beta = 0.3025$. The equation is solved using the modified Newton-Raphson approach with Krylov subspace acceleration (Carlson and Miller 1998; McKenna 2011). A relatively low level of stiffness proportional viscous damping was used to enhance numerical stability (coefficient = 0.003), with the main damping emanating from the soil nonlinear shear stress-strain hysteresis response (Su et al. 2017).

6.4. Pile and Soil-Pile Interaction

Three-dimensional nonlinear force-based beam-column elements with fiber-section (Scott and Fenves 2006; Scott and Ryan 2013) were employed to represent the piles, for the purpose of this liquefaction-induced lateral spreading investigation (He et al. 2017; Elgamal and Lu 2009). In order to represent the geometric space occupied by the pile in the soil domain, rigid beam-column links ($EI = 10^4$ times the linear EI of the pile) are used normal to the vertical axis of the pile (Elgamal et al. 2008), effectively defining its surface for friction along its length and end bearing at its base. The 3D brick elements representing the soil are connected to the pile geometric configuration at the outer nodes of these rigid links (Law and Lam 2001) by using zerolength elements, zerolengthSection elements and the OpenSees equalDOF translation constraint (Elgamal et al. 2008). The zerolength and zerolengthSection elements are employed to axially connect the

rigid links to adjacent soil nodes and provide yield shear force in each link according to the soil-pile interface friction angle and adhesion. As such, the yield shear force is limited by $F = (c_A + \sigma' tan\delta) \cdot l \cdot h/N$, where l is the perimeter of the pile, h is center to center contributing height (according to the adjacent soil element heights), c_A is the soil-pile adhesion, δ is the soil-pile friction angle, σ' is the lateral effective stress and N is the number of zeroLengthSection elements along the pile perimeter (Su et al. 2017).

6.5. Finite Element Model

Figure 6.1 depicts the investigated bridge-ground configuration. This 18-span reinforced concrete bridge (Caltrans 2017) is approximately 197 m long and 9.9 m wide, composed of a reinforced concrete deck on vertical pier walls with pile groups (Piers 5-10), and on single piles (Abutment 1, 19 and Bents 2-4, 11-18). Cross sections of the bridge structural components are displayed in Figure 6.1b.

Along the bridge deck, two expansion joints (with a 0.05 m gap each) are located adjacent to Piers 5 and 10, respectively. Bilinear zerolength element abutment springs connect the deck to the adjacent soil nodes, with peak force defined to account for the available passive soil resistance at these locations.

In the transverse direction, a representative 2.0 m wide slice (Figure 6.1a) was taken to account for the bridge's geometric configuration (Su et al. 2017). On this basis, a 3D bridge-ground FE mesh is developed (Figure 6.2). While permitting a representation of the foundation center-to-center layout (Figure 6.1a), it does not capture all of the involved bridge-ground 3D response characteristics (McGann CR, Arduino 2015; Ghofrani et al. 2016; Elgamal et al. 2018) and associated potentially higher demands. For the purposes of this investigation, it integrates the overall global bridge-ground configuration, with seismic response addressed only in the

longitudinal direction. Missing effects such as three-dimensional shaking, and influence of lateral spreading outside the bridge's footprint, it mainly serves to elucidate salient characteristics of the system's global response as discussed in the following sections.

Based on the above, the FE mesh for the bridge-ground model (Figure 6.2a) was generated comprising 22,050 nodes, 17,415 brick elements, 464 nonlinear and 90 linear elastic beam-column elements, 1,856 rigid beam-column links, 1,856 zerolength elements and 1,856 zerolengthSection elements. Along both the West and East side mesh boundaries (Figure 6.2), soil columns of large size (not shown) are included (Nielsen 2014; Su et al. 2017). These soil columns, at an adequate distance (around 100 m) away from the bridge structure to minimize boundary effects (Løkke and Chopra, 2017, 2018), efficiently reproduce the desired free-field response at these locations.

6.5.1. Ground Configuration

The overall ground configuration is shown in Figure 6.3a, with the following main soil profiles (Figure 6.3b), based on existing boring data and site conditions (Caltrans 2017): East Embankment (near Location A), Channel Zone (between Locations B and E), and West Embankment (near Location F). In general, the site profiles consist of shallow, fine-grained soils, loose sand layers, underlain by medium dense to dense sands (Figure 6.3b). The water table was prescribed at an elevation of 30.5 m as shown in Figure 6.3a. Table 6.1 and Table 6.2 list the saturated sand and clay (PIMY in OpenSees) model parameters, respectively. For illustration, the soil model responses for sand and clay (Table 6.1 and Table 6.2) under undrained monotonic loading conditions (confinement = 100 kPa or 1 atmosphere) are presented in Figure 6.4. As shown in Figure 6.4a, the saturated loose sand (LS2) displays a contractive tendency, with loss of strength down to the residual shear strength of 2 kPa (Table 6.1). On the other hand, shear strength of the

saturated medium dense sand (MS2) and the dense sand (DS1 and DS2) increase under monotonic loading (due to the dilative tendency as defined in Table 6.1).

6.5.2. Bridge Structure

All structural components except for the reinforced concrete deck (modeled by linear elastic beam-column elements with self-weight q as shown in Figure 6.3a) were modeled using 3D nonlinear force-based beam-column elements with fiber-section. In this fiber section formulation (Shin et al. 2008; Zhang et al. 2008; Su et al. 2017; Elgamal et al. 2008), OpenSees Concrete01 Kent-Scott-Park model (Kent and park 1071; Mander et al. 1988) with degraded linear unloading/reloading stiffness was employed to simulate the nonlinear behavior of the cover and core concrete. The OpenSees ReinforcingSteel model (Chang and Mander 1994; Dodd and Restrepo 1995) with isotropic strain hardening and softening was used to simulate the reinforcement steel.

Geometry and fiber discretization of the bridge support cross-sections (Figure 6.1b) are shown in Figure 6.5a. Moment-curvature for each fiber section (Figure 6.5a) under different axial load levels is shown in Figure 6.5b. It can be seen that the flexural strength of Section 5 is rather low (Figure 6.5b), promoting the potential for damage at the corresponding locations of Bents 11-18 (Figure 6.1).

Axial force-strain response for each fiber section is shown in Figure 6.5c. In this regard, the Concrete01 material only displays strength in compression, with tension supported only by the reinforcing steel (Figure 6.5c).

6.5.3. Boundary and Loading Conditions

As mentioned above, both West and East lateral mesh boundaries are located away from the bridge structure (Figure 6.2 and Figure 6.3). Along the 2.0 m apart longitudinal symmetry

planes (Figure 6.2), no out of plane motion is allowed. Loading was implemented in a staged fashion as follows:

1) Gravity was applied to activate the initial static state for the soil domain only with: i) linear elastic properties (Poisson's ratio of 0.47 for all layers), ii) nodes on both lateral boundaries of the model were fixed against longitudinal translation, iii) nodes were fixed along the base against vertical translation, iv) water table was specified (Figure 6.3a) with related water pressure and nodal forces specified along the channel boundary. At the end of this step, the static soil state is imposed and displacements under own-weight application is re-set to zero using the OpenSees command InitialStateAnalysis.

2) Soil properties were switched from linear elastic to plastic (Table 6.1 and Table 6.2).

3) The nonlinear force-based beam-column elements of pile and elastic beam-column elements of reinforced concrete deck were added. The pile nodes were connected to the soil nodes via the rigid link, zerolength and zerolengthSection elements as described above. Thereafter, self-weight of the bridge structure was applied.

In this study, the base of the computational soil domain is located at a depth of 37.8 m from the ground surface (Figure 6.3a), about 20 m away from the bridge foundations. Lateral response of the soil strata below this 37.8 m depth was represented by the Lysmer-Kuhlemeyer (Lysmer and Kuhlemeyer 1969) dashpot boundary, applied along the base of the FE model (base V_s = 600 m/s, in the range of soft rock, slightly higher than stiffness of the overlying stratum), so as to avoid spurious wave reflections. As such, two dashpots are activated in the x and z directions at each node along the base, and the incident seismic wave excitation is defined by dynamic equivalent nodal forces (Zhang et al. 2008; Elgamal 2008).

For the shaking phase (purely in the longitudinal direction), seismic motion (Figure 6.6a) was simply taken as that of the 1994 Northridge earthquake ground surface Rinaldi Receiving Station record (Component S48W), scaled down to a peak amplitude of 0.4 g (Caltrans 2017). For the purpose of this study, deconvolution was employed as a simple approach (using Shake91 by Idriss and Sun 1993), to derive an incident earthquake motion (Figure 6.6a), imparted (Elgamal 2008) thereafter along the base of the FE model (elevation 0.0 in Figure 6.3a). In this representation, free-field motion along both the West and East side mesh boundaries is generated by the included soil columns mentioned above.

6.6. Computed Response

6.6.1. Free-Field Acceleration

Figure 6.6b shows the computed acceleration time histories along the East and West mesh boundaries, respectively. Due to nonlinear response and liquefaction (discussed below), peak ground surface acceleration was slightly lower compared to that of the base input motion. In addition, reduced higher frequency response is noted within and above the liquefiable strata (starting at elevation 28.5 m in Figure 6.6b).

6.6.2. Liquefaction and Permanent Shear Strain

Figure 6.7 shows time histories of effective confinement p' divided by the initial value p'_0 (before shaking) at locations A and F (Figure 6.3). The ratio p'/p'_0 reaching 0 indicates loss of effective confinement due to liquefaction. In this figure, it is noted that:

1. At the east side, in the loose sand layer (location A, Figure 6.7a), the ratio p'/p'_0 reached 0 at about 2.5 seconds, during the large input fling-motion pulse which reached its positive peak around 2.3 seconds (Figure 6.6b). Upon liquefaction, this loose stratum attains its low specified residual shear strength of 2 kPa (Table 6.1 and Figure 6.4).

2. On the west side (Figure 6.7b), the medium dense sand liquefied shortly thereafter at about 3.1 seconds, upon passage of the pulse. Subsequently, the shear response of this medium dense sand will be mainly influenced by its dilative tendency as depicted in Figure 6.4.

At the end of shaking, Figure 6.8 displays profiles of confinement reduction and accumulated lateral shear strain. With the loose and medium dense liquefied sands at the elevation range of about 25.9-30.5 m, it can be seen that:

1. At the east boundary, permanent westward shear strains of about 4 % in peak value were accumulated, mainly in the prevalent loose sand stratum at this zone.

2. At the west boundary, much lower levels of strain were observed, primarily due to absence of the loose stratum, and the higher shear strength afforded by dilative tendency (Figure 6.4) in the medium dense stratum at this zone.

3. In the east-side slopes (as indicated by locations B and C), additional westward (downslope) shear strains were accumulated, reaching peak values of about 14 %.

4. Conversely, the west-side slopes (locations D and E), are seen to accumulate lower levels of eastward (downslope) strain (about 4 %), partially because of the adjacent more stable medium dense sands on the west side of the bridge (Figure 6.3).

6.7. Deformation

6.7.1. Ground Deformation at End of Shaking

In accordance with the above shear strain profiles, Figure 6.9a and b depict the deformed mesh at end of shaking (colors show longitudinal displacement, i.e., x direction). Away from the bridge, lateral deformation above the liquefied strata was westward, about 0.15 m on the east-side and only 0.06 m on the west-side (Figure 6.10). Superposed on this global westward displacement pattern, local downslope deformations are seen on both sides of the bridge (Figure 6.10). Near the

abutments, additional downslope deformation relative to the surrounding ground (Figure 6.9b and Figure 6.10c, d) was about 0.2 m (east-side), and 0.12 m (west-side). These downslope displacements clearly continued to accumulate in the liquefied loose sand stratum well after occurrence of the strong shaking pulse (Figure 6.10c).

As such, the corresponding pattern of bridge deformation can be seen in Figure 6.9b. Due to the downslope deformations at both sides, the bridge deck through its piers and foundations acts as a strut that provides added restraint to the slope deformations on both sides. In light of this deformation mechanism, it can be seen in Figure 6.11b that both 0.05 m gap expansion joints (Figure 6.3a) became closed upon occurrence of the main permanent deformation westward lurch. Without the bridge (an additional FE run was conducted) and its restraining effect, it is observed that (Figure 6.9c) much increased slope deformations take place, superposed on the same global lateral ground deformation pattern.

6.7.2. Deformation at Maximum Deck Displacement

To recognize inertial effects of the bridge-ground system during the shaking phase, the time instant of maximum deck displacement (labeled as max time step) is selected for illustration (Figure 6.11a). In contrast to the end of shaking time step (Figure 6.9), the entire bridge-ground system is moving westward (Figure 6.12). The difference in west- and east-side ground displacement plays a role in dictating the overall picture of bridge deformation and seismic load as will be further discussed below. Incidentally, without the bridge, Figure 6.12c depicts noticeable localized east-side slope deformations already underway (in addition to the global pattern, local deformation of about 0.1 m).

6.7.3. Bridge Deck Loads

Figure 6.13 displays lateral displacement of the bridge structure and the deck axial force profiles at max time step and at end of shaking. At max time step, the entire bridge moves westward with peak displacement of about 0.28 m at east embankment, and with the expansion joint near Pier 5 completely closed (Figure 6.13a). As such, compressive axial forces were imposed on the deck (Figure 6.13b) generally increasing up to Pier 6, and gradually decreasing thereafter. No appreciable deck axial force is seen along Bent 11-Abut. 19 (only local inertial force) as the expansion joint near Pier 10 was not fully closed yet at this time instant (Figure 6.11b).

Figure 6.13c shows lateral displacement at end of shaking with a peak displacement of about 0.24 m. At this time step, both expansion joints were completely closed (Figure 6.11b). As discussed above, both east and west embankments moved downslope into the channel zone, such that the entire bridge deck was in a compressive state (Figure 6.13d). Since there was no inertial effect, the axial force along the deck is constant within each span. Change in axial force along the deck reflects shear force at the deck-pier connections as presented in the following sections.

6.8. Bridge Structure Response

Figure 6.14 depicts the axial forces before shaking, at maximum time step and at end of shaking. As a reference, Figure 6.14a shows the computed self-weight axial force, with all supporting elements in compression throughout (i.e., negative axial force). At maximum time step, east-side piles in pile groups 5-10 are under tension (positive axial force) and west-side piles are under compression. For this particular deformed configuration, peak compressive axial force has increased by about 4 times, with peak tensile axial force reaching about 200 kN. Nevertheless, all forces remained generally within the elastic capacity of the corresponding cross-sections as presented in Figure 6.5.

At end of shaking, most piles are in compression, except for the lower sections of the west-side piles, sustaining a relatively low tensile force of about 50 kN. In general, it is noted that presence of large tensile forces in bridge foundations, might be undesirable particularly when water is present, from the long-term serviceability point of view.

Figure 6.15 and Figure 6.16 show the corresponding shear forces and bending moments, respectively. Generally, it can be seen that the highest values occurred at: i) the interface between liquefied and non-liquefied soils, and ii) the Pier-deck connections. Seismic loading consequences due to these observed moments are addressed next in the form of ductility demand defined as the ratio of ultimate attained curvature ϕ_u to yield curvature ϕ_y corresponding to 0.75 of the yield moment (Park 1988). As such, Figure 6.17 shows the ductility demand profiles for the bridge structure (values < 1 are not shown for clarity). At max time step, peak values are attributed to: i) the east-side slope movement and resulting bridge deck translation (Abut.1-bent 3 and Abut. 19), ii) the relatively small translation of piles in the middle of the channel (Piers 7-10), and iii) the low Section 5 flexural strength at the column-deck connection (bent 18). At end of shaking, peak values are highly influenced by the local slope deformations (Abutments 1 and 19), and low flexural strength of Section 5 (bents 16-18) at the column-deck connection (Figure 6.5). Ductility demands throughout the entire shaking event (Figure 6.17a) generally show high values: i) at the middle of the bridge (where the foundations have not moved much, allowing for resistance to the lateral forces transmitted by the bridge deck), ii) at the west-side due to the low flexural section strength (Figure 6.6) and local downslope displacements, and iii) in the vicinity of the liquefied stratum. The attained peak values, reaching as much as 9.5 would generally be considered of concern and would warrant closer scrutiny.

6.9. Bridge-Ground System Response under Reverse Input Motion

In general, definition of expected earthquake shaking is an important matter that requires careful attention. To assess influence of input motion polarity (Todorovska and Trifunac 1997), an additional numerical simulation was conducted with sign of the Figure 6.6a excitation reversed. The fling motion pulse in this particular shaking record, which dictated a substantial level of the accumulated global site deformation (Figure 6.9 and Figure 6.10), motivated the investigation of this additional scenario. The results in terms of maximum deck displacement and end of shaking displacement are shown in Figure 6.18 Ductility demand is shown in Figure 6.19. In contrast to the original results, it can be seen that: i) the overall displacement of the entire bridge-ground system in Figure 18 (0.25 m for structure) is slightly lower when compared to those in Figure 6.12 and Figure 6.13 (0.28 m for structure), ii) ductility demand (Figure 19) was significantly lower, only reaching 3.1. Comparing these two shaking scenarios, it can be concluded that polarity of the employed input motion might have an important influence, mainly due to the loose soil being prevalent on the east-side of the bridge, with medium dense on the west-side (Figure 6.3). As such, larger permanent ground deformations occurred in the loose sand east-side slope when the higher inertial forces contributed constructively.

6.10. Retrofit Analyses

Strictly for the purpose of illustration, potential use of the numerical model to conduct retrofit studies is addressed briefly in this section. For that purpose, three additional numerical simulations were conducted: i) using a 6 mm steel jacket to strengthen the relatively weak column cross section 5 of bents 11-18 (Figure 6.1 and Figure 6.5), and ii) furthermore, adding external piles (one or two) at the Abutments 1 and 19, without more costly modifications within the water channel.

Under these scenarios, the ductility demand (Figure 6.20a-c) might be directly compared to that of the original bridge (Figure 6.17). As such, Figure 6.20a shows a peak ductility demand reduction from 9.3 down to 7.0. At the strengthened bents 11-17, the ductility demand fell below 1.0, indicating a clear and significant improvement.

With the additional abutment pile strengthening (Figure 6.20b and c), further decrease in peak ductility demand is observed, falling below 1.5 except for locations around the bridge's central section. Notably in these figures, the two-pile retrofit did not result in a substantially different outcome compared to the single pile scenario.

6.11. Summary and Conclusions

A FE analysis framework was presented to study a number of salient features associated with the liquefaction-induced seismic response of a bridge-ground system. For that purpose, an idealized FE model was developed, motivated by the details of an actual bridge-ground configuration. The bridge-ground system and details of the corresponding numerical analysis were discussed. Displacement, moment, shear, axial forces, and ductility demand of the structure, resulting from the liquefaction-induced ground deformations were explored. In addition, the bridge's restraining influence, effect of input motion polarity, and potential for retrofit studies were investigated. The numerical framework and the insights derived from this study are of general relevance to bridge-ground seismic response scenarios.

Specific observations and conclusions include:

1) As highlighted in earlier studies (Cubrinovski et al. 2014; McGann and Arduino 2015; Shin et al. 2008; Zhang et al. 2008), response is highly dependent on the bridge-ground system as an integral global entity. Connectivity provided by the bridge deck, soil profile variability along

the bridge length, and geometric configuration of the slopes are all factors that can significantly influence the outcome.

2) Particularly for pulse-type seismic motions, local slope deformations may be superposed on an overall global pattern of permanent lateral ground motion, which might contribute to higher demands due to the combined outcome of both.

3) The bridge structure and its foundations exerted a significant restraining effect on lateral ground deformations. Such restraining effects partially stem from the bridge-ground global connectivity characteristics, which can be of considerable influence.

4) Peak demands for some of the piers and/or piles might occur due to the combined inertial and kinematic load during the shaking event. In simplified analyses, both inertial as well as kinematic load cases should be considered.

5) Moments and curvatures in the piers depend on relative displacement between the deck and the pile foundations. In this regard, some of the observed peak demand values were near the center of the bridge, where the pile foundations did not move appreciably in either direction.

6) Significant tensile forces might evolve in pile group configurations, and further attention to potential consequences is suggested.

7) Polarity of the input motion may influence the outcomes, and further attention to this matter is warranted from the seismological point of view.

8) Further studies may be conducted to assess sensitivity of the numerical results to the salient modeling idealizations including the employed geometric configuration, material models and properties, as well as input motions and characteristics of the associated transmitting boundary. Higher demands resulting from full 3D modeling with 3D seismic excitation might be also explored, albeit requiring a significantly greater effort.

6.12. Acknowledgements

Chapter 6, in full, has been published as it appears in the following paper (The dissertation author was the primary investigator and author of this paper):

Qiu, Z., Ebeido, A., Almutairi, A., Lu, J., Elgamal, A., Shing, P.B. and Martin, G. (2020). "Aspects of Bridge-Ground Seismic Response and Liquefaction-Induced Deformations." Earthquake Engineering & Structural Dynamics, 49(4), 375-393.

Chapter 6, in part, is a reprint of material as it appears in the following paper (The dissertation author was the primary investigator and author of this paper):

Qiu, Z., Ebeido, A., Almutairi1, A., Lu, J., Elgamal, A. and Martin, G. (2019). "Bridge-Ground Seismic Response and Liquefaction-Induced Deformations." Earthquake Geotechnical Engineering for Protection and Development of Environment and Constructions, Rome, Italy, ISBN 978-0-367-14328-2.

Table 6.1 Sand PressureDependMultiYield03 model parameters (Khosravifar et al. 2018)

Model Parameters		LS2	MS2	DS1	DS2	VDS
Reference mean effective pressure, p'_r (kPa)		170*	210*	270	340	430
Mass density, ρ (t/m^3)		1.98*	2.03*	2.08	2.08	2.13
Maximum shear strain at reference pressure, $\gamma_{max,r}$		0.1*	0.1*	0.1	0.1	0.1
Low-strain shear modulus at reference pressure, G_r (MPa)		80.4*	118*	164	256	435
Stiffness dependence coefficient n, $G = G_r(\frac{\boldsymbol{p'}}{\boldsymbol{p'_r}})^{\boldsymbol{n}}$		0.5*	0.5*	0.5	0.5	0.5
Poisson's ratio v for dynamic analysis		0.4*	0.4*	0.4	0.4	0.4
Shear strength at zero confinement (kPa)		2.0*	2.0*	2.0	2.0	2.0
Friction angle ϕ, with resulting shear strength defined as $p' \sin\phi$		29°	31°	34°	36°	40°
Phase transformation angle, ϕ_{PT}		29°	27°	29°	31°	33°
Contraction coefficient, c_1		0.1	0.035	0.015	0.015	0.001
Contraction coefficient, c_2		5.0	3.0	1.0	1.0	0.0
Contraction coefficient, c_3		0.05	0.2	0.45	0.45	0.8
Dilation coefficients, d_1		0.1	0.15	0.2	0.2	0.6
Dilation coefficients, d_2		3	3	3	3	3
Dilation coefficient, d_3		0.05	0.2	0.45	0.45	0.5
Permeability (m/s)		10^{-5}	10^{-5}	10^{-5}	10^{-5}	10^{-5}
Additional contraction parameters	b_1	0.35	0.2	0.2	0.1	0.1
	b_2	30	30	15	10	10
	b_3	0.0	0.0	0.06	0.06	0.06
	b_4	0.001	0.001	0.001	0.001	0.001

Note: For each involved soil layer, the soil-pile friction angle δ and/or the soil-pile adhesion c_A are assumed equal to the corresponding friction angle and/or cohesion, respectively.
*Sands LS1 and MS1 (Figure 6.3) include the same model parameters as LS2 and MS2 except for friction angles, respectively.

Table 6.2 Soil model parameters

Model parameters (PressureIndependMultiYield)	SC	SC1	SC2
Mass density, ρ (t/m^3)	2.07	2.1	2.1
Low-strain shear modulus, G (MPa)	52.9	95.5	82.3
Poisson's ratio v for dynamic analysis	0.4	0.4	0.4
Cohesive strength, c_u (kPa)	24	96	48
Maximum shear strain at reference pressure, $\gamma_{max,r}$	0.1	0.1	0.1
Permeability (m/s)	10^{-9}	10^{-9}	10^{-9}

Note: For each involved soil layer, the soil-pile adhesion c_A is assumed equal to the corresponding cohesive strength.

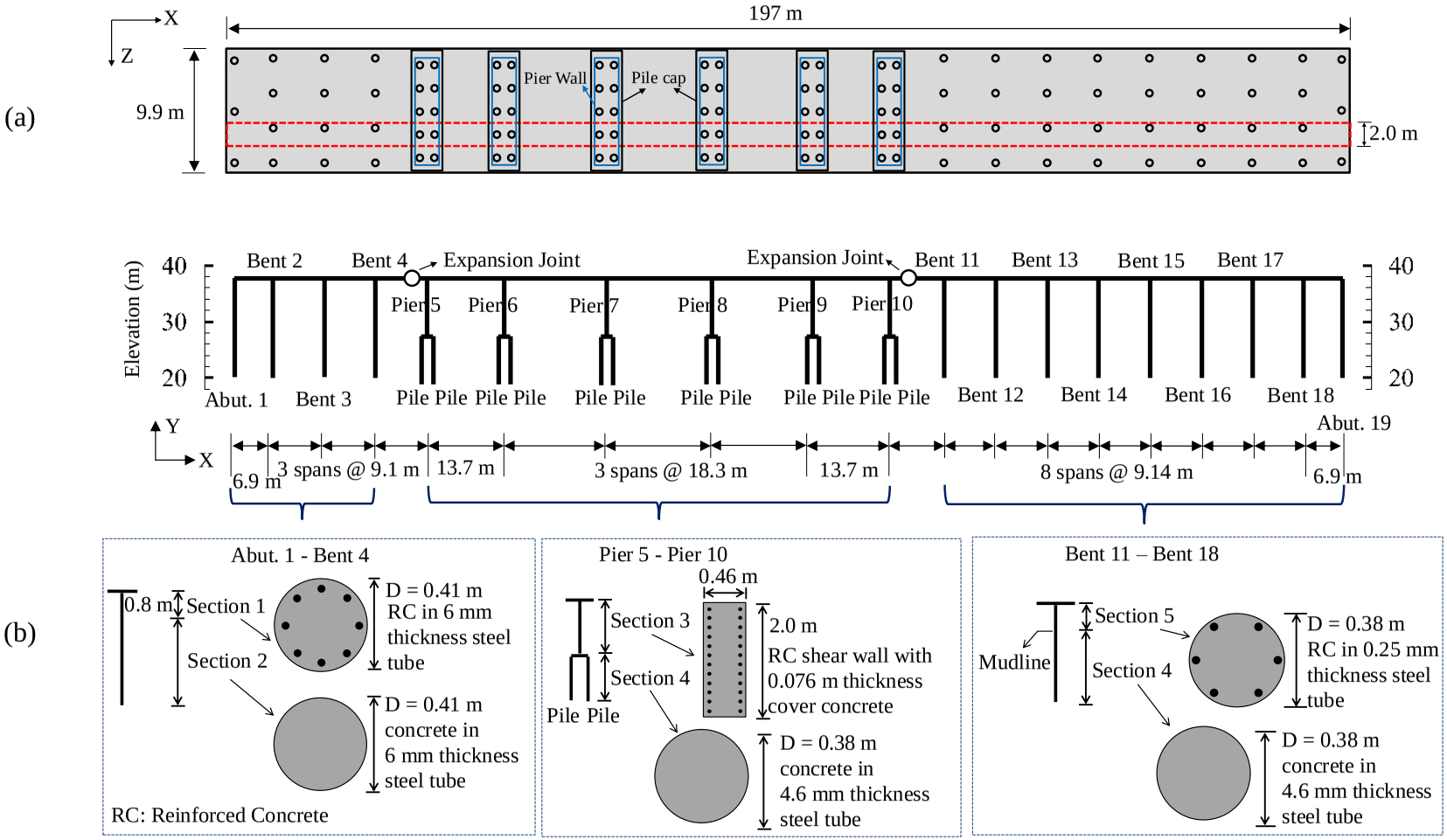

Figure 6.1 Bridge configuration: (a) Schematic plan view (not to scale); (b) Elevation view and cross sections

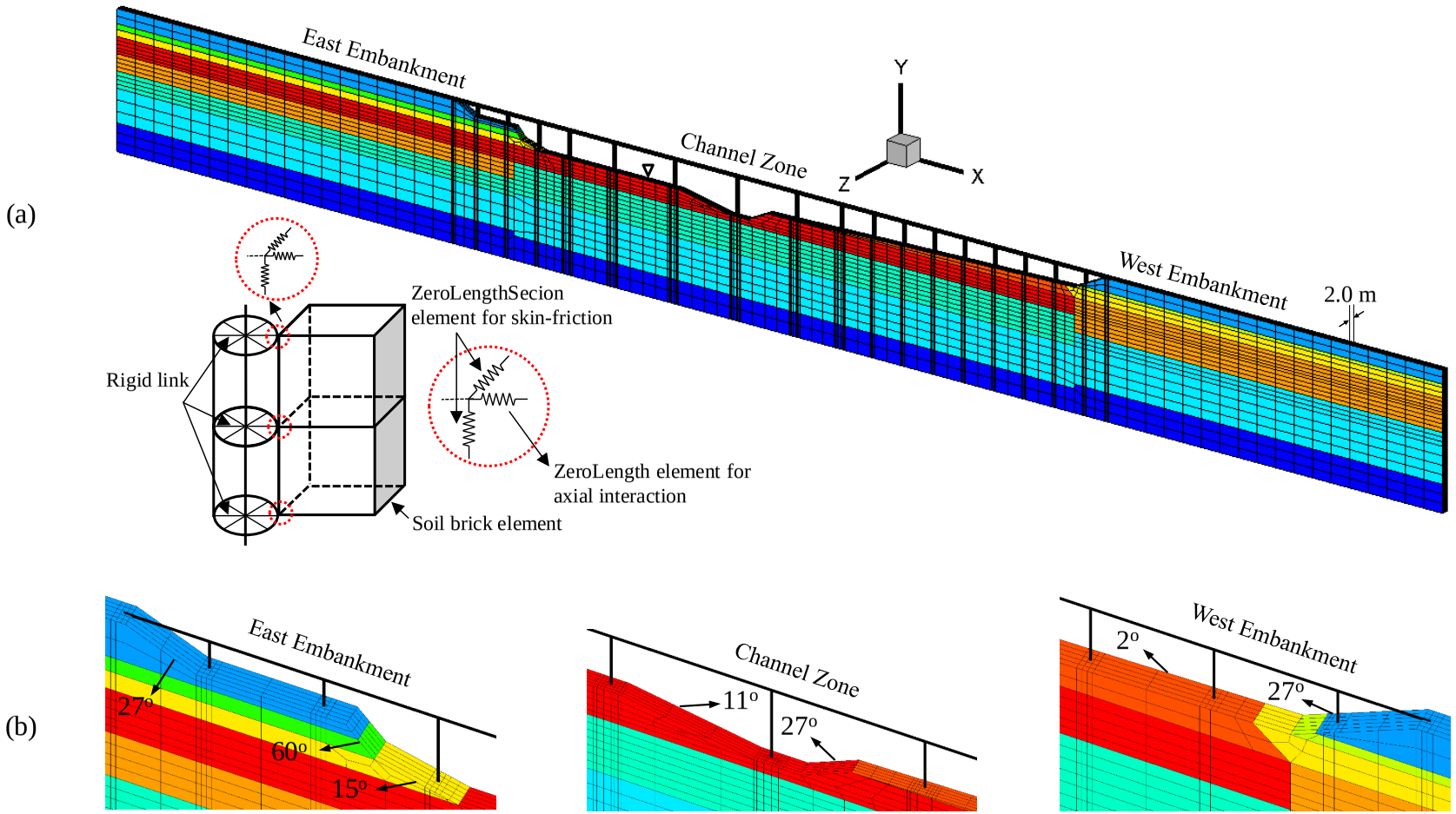

Figure 6.2 Finite element mesh of bridge: (a) Isometric view; (b) Local slopes

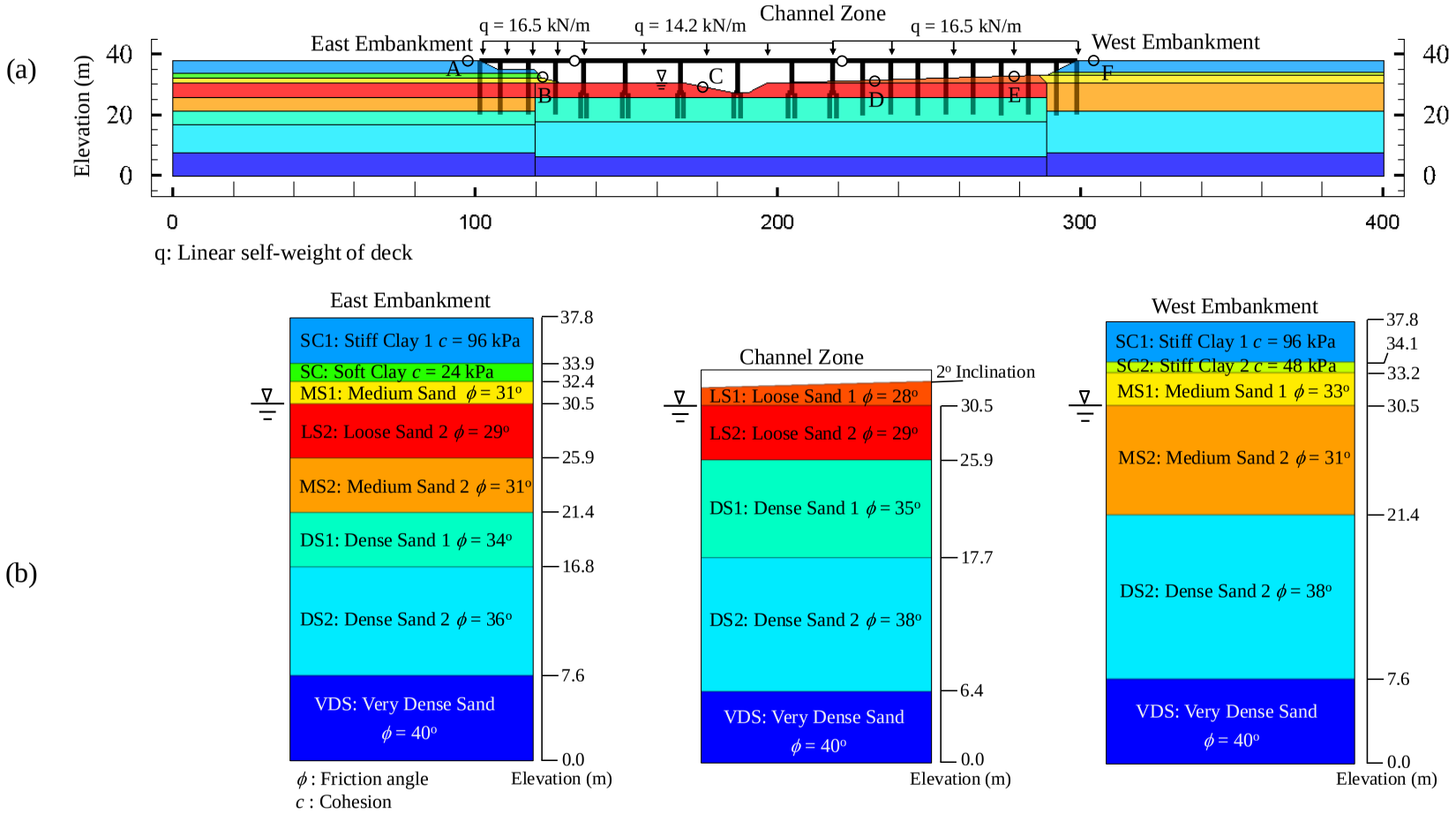

Figure 6.3 Ground configuration: (a) Elevation view; (b) Site soil profiles (Caltrans 2017)

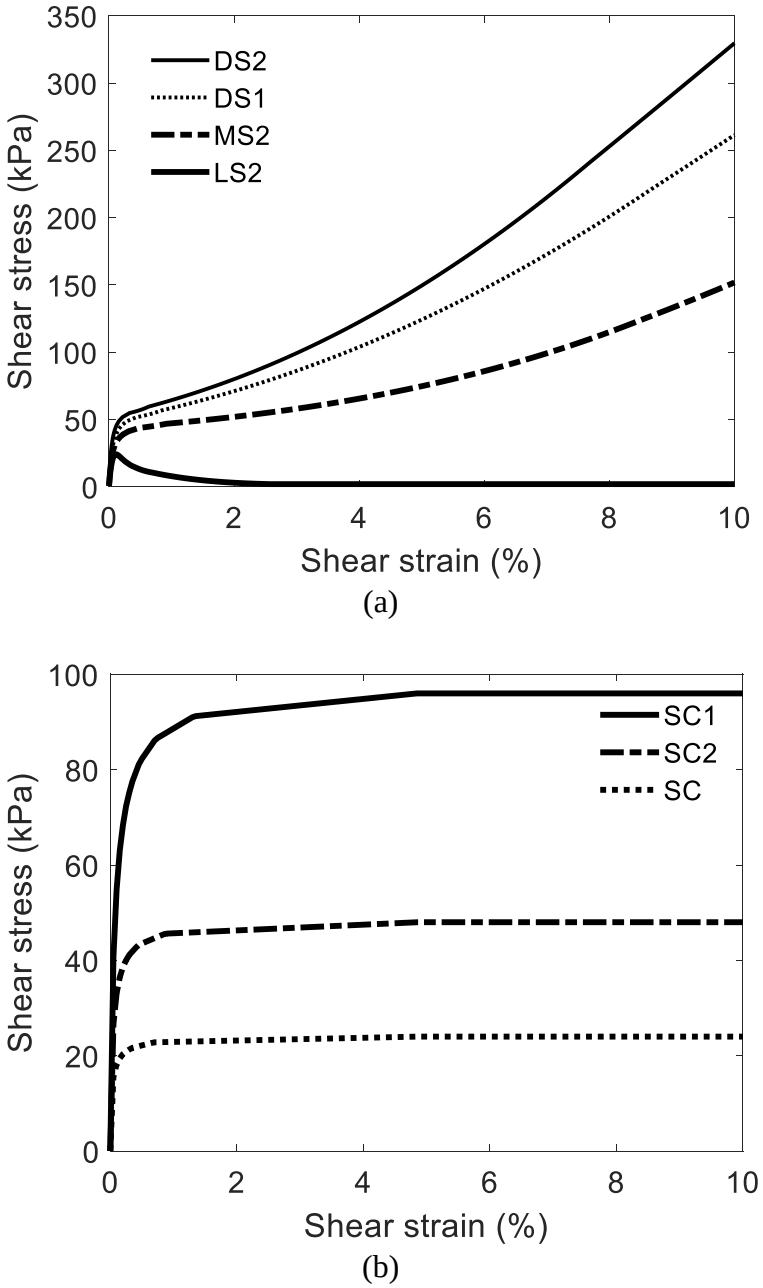

Figure 6.4 Soil model response: (a) Sand model under undrained condition; (b) Clay PIMY (Table 6.1)

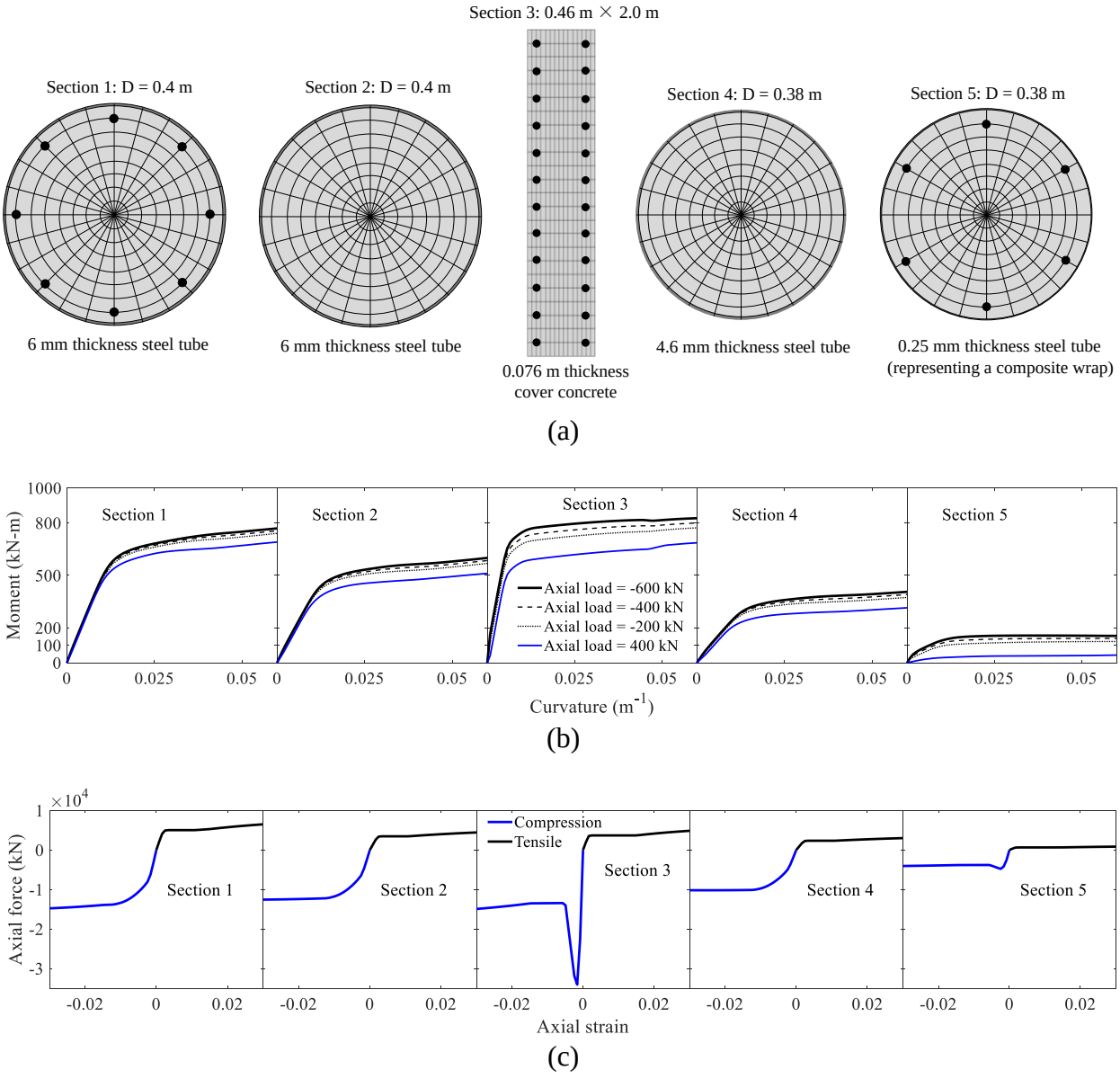

Figure 6.5 Fiber sections and response: (a) Fiber sections; (b) Moment-curvature; (c) Axial force-strain (D represents diameter)

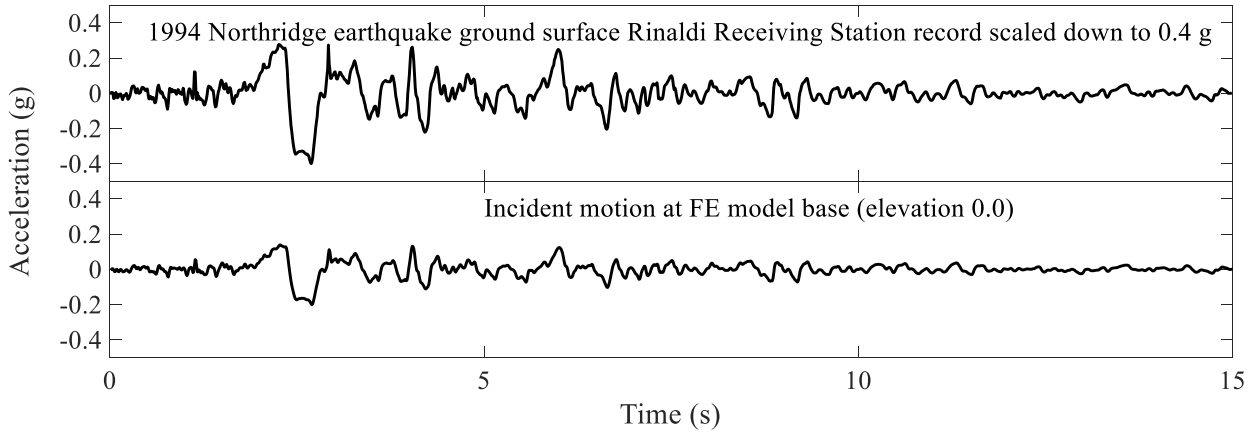

(a)

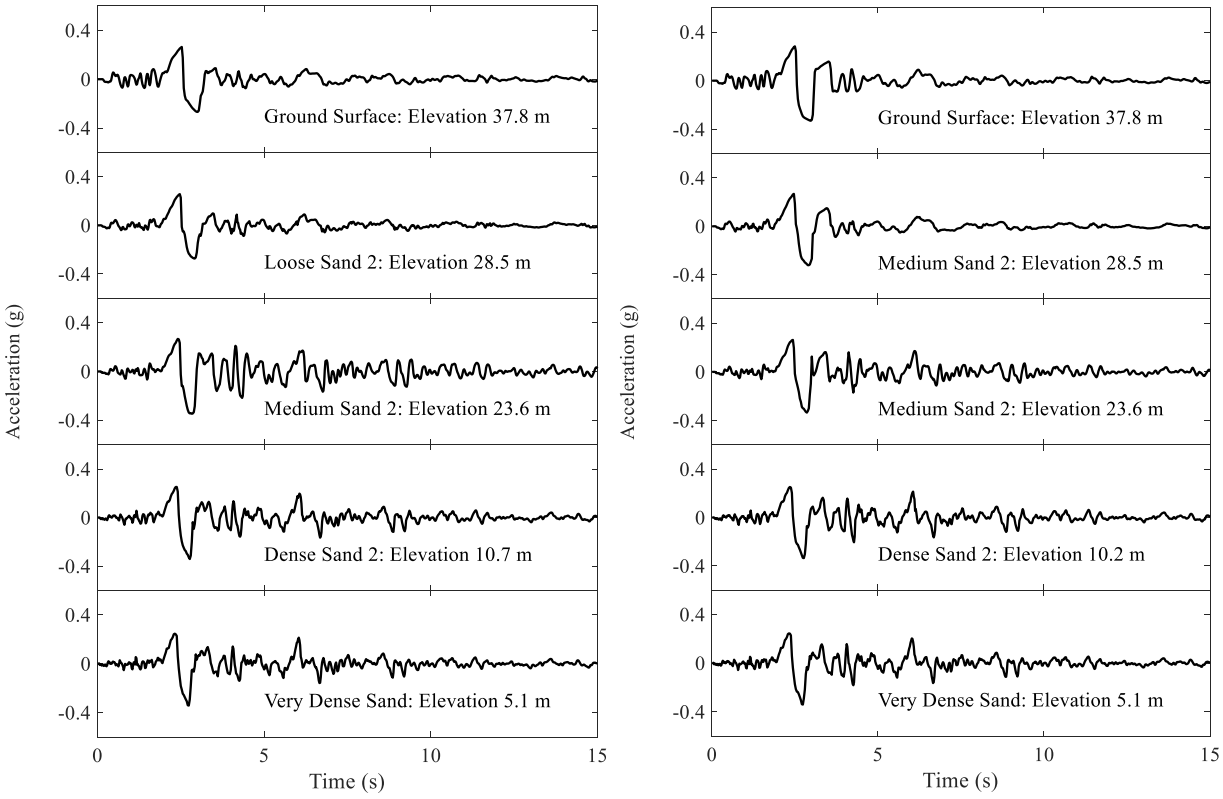

(b)

Figure 6.6 Input motion and computed time histories of acceleration: (a) Deconvolution; (b) Along East (left) and West (right) boundaries

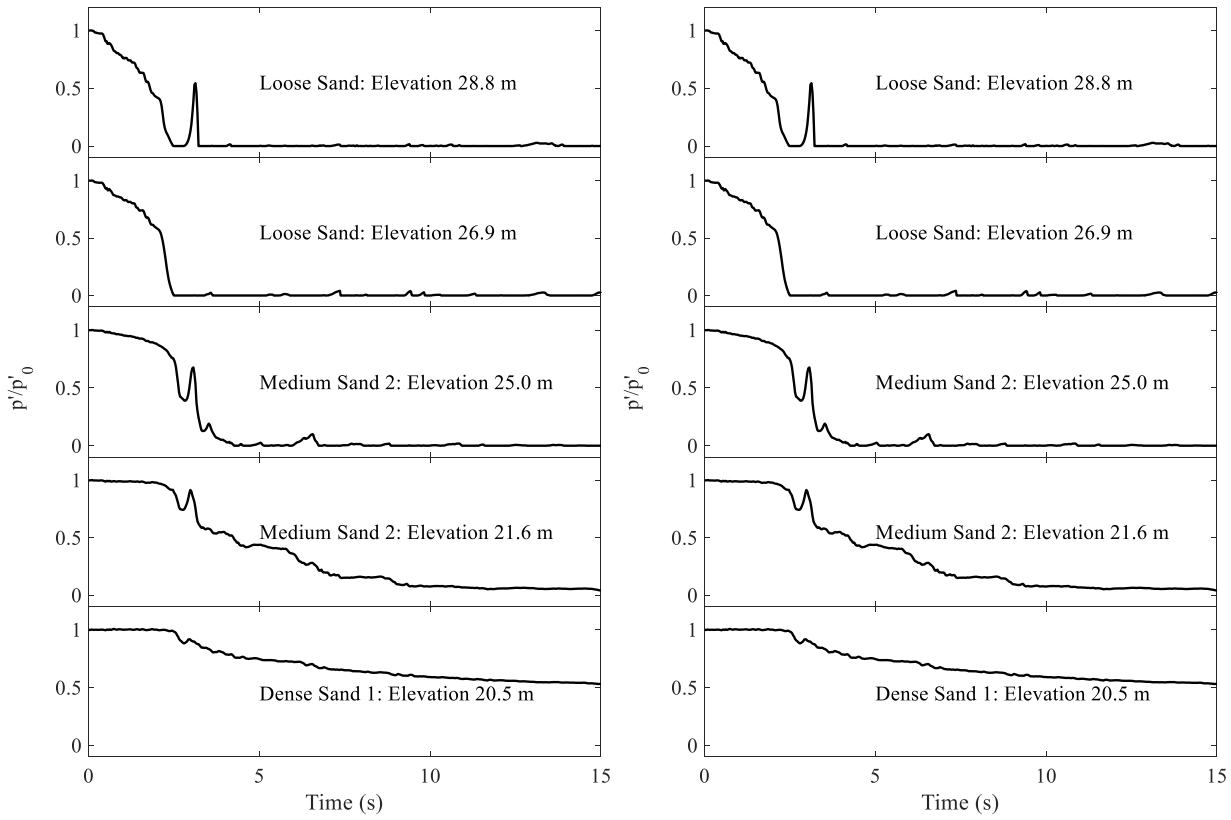

Figure 6.7 Ratio of confinement to initial confinement computed time histories: (a) Location A: (b) Location F (p' and p'_0 represent confinement and initial confinement, respectively)

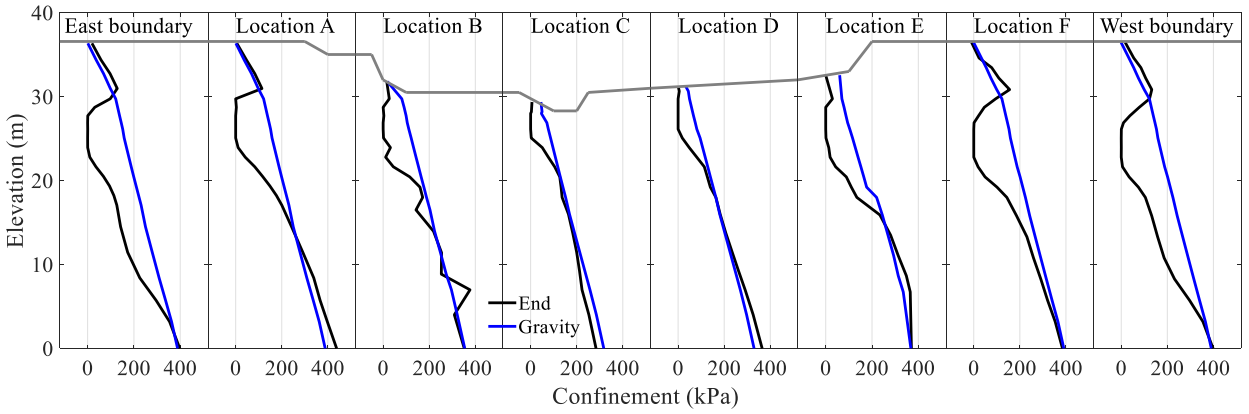

(a)

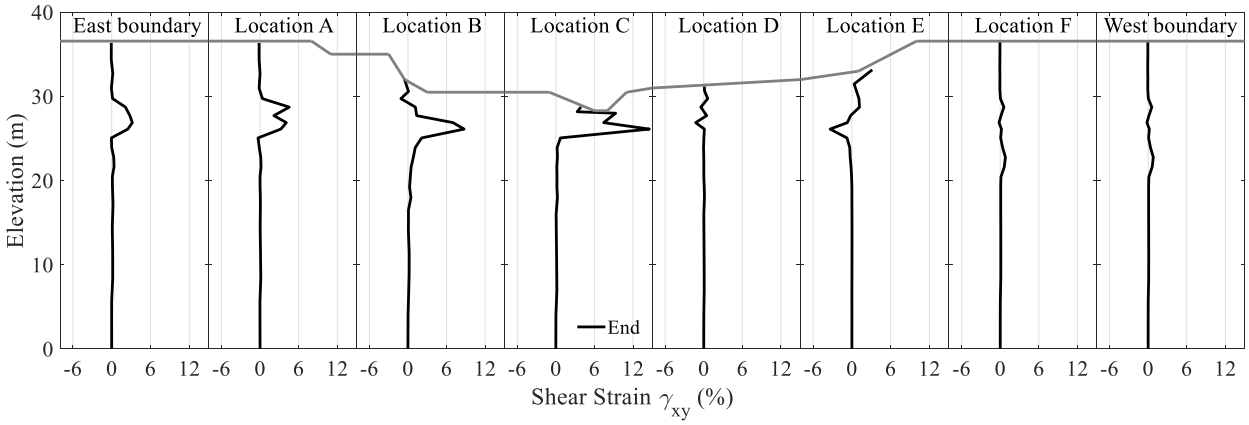

(b)

Figure 6.8 Computed response profiles at six locations A-F and two boundaries: (a) Confinement; (b) Shear strain

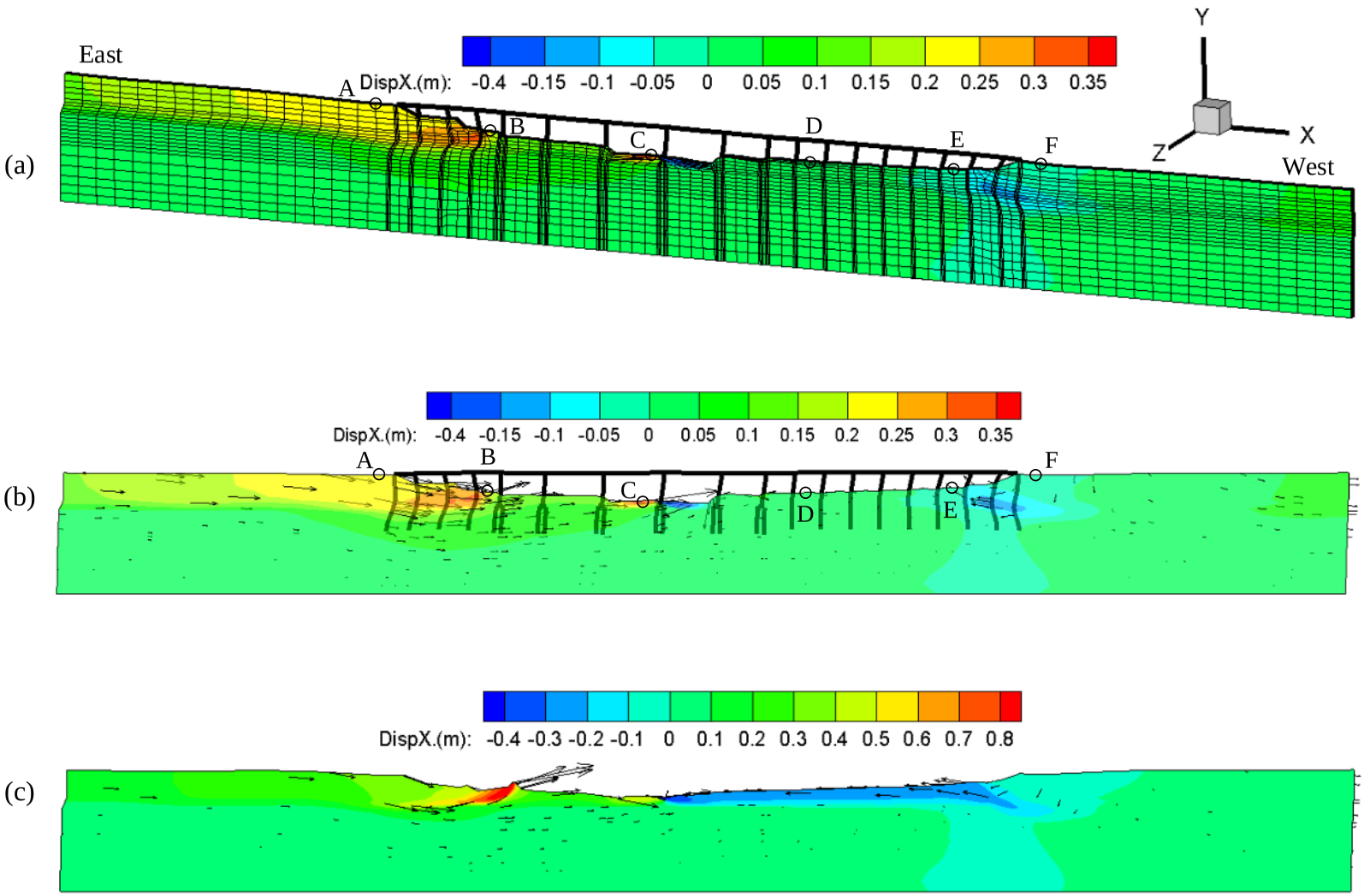

Figure 6.9 Deformed FE mesh at end of shaking: (a) Isometric view; (b) Elevation view; (c) Without bridge (contour fill shows the horizontal displacement; arrows display direction of ground movement; factor = 15)

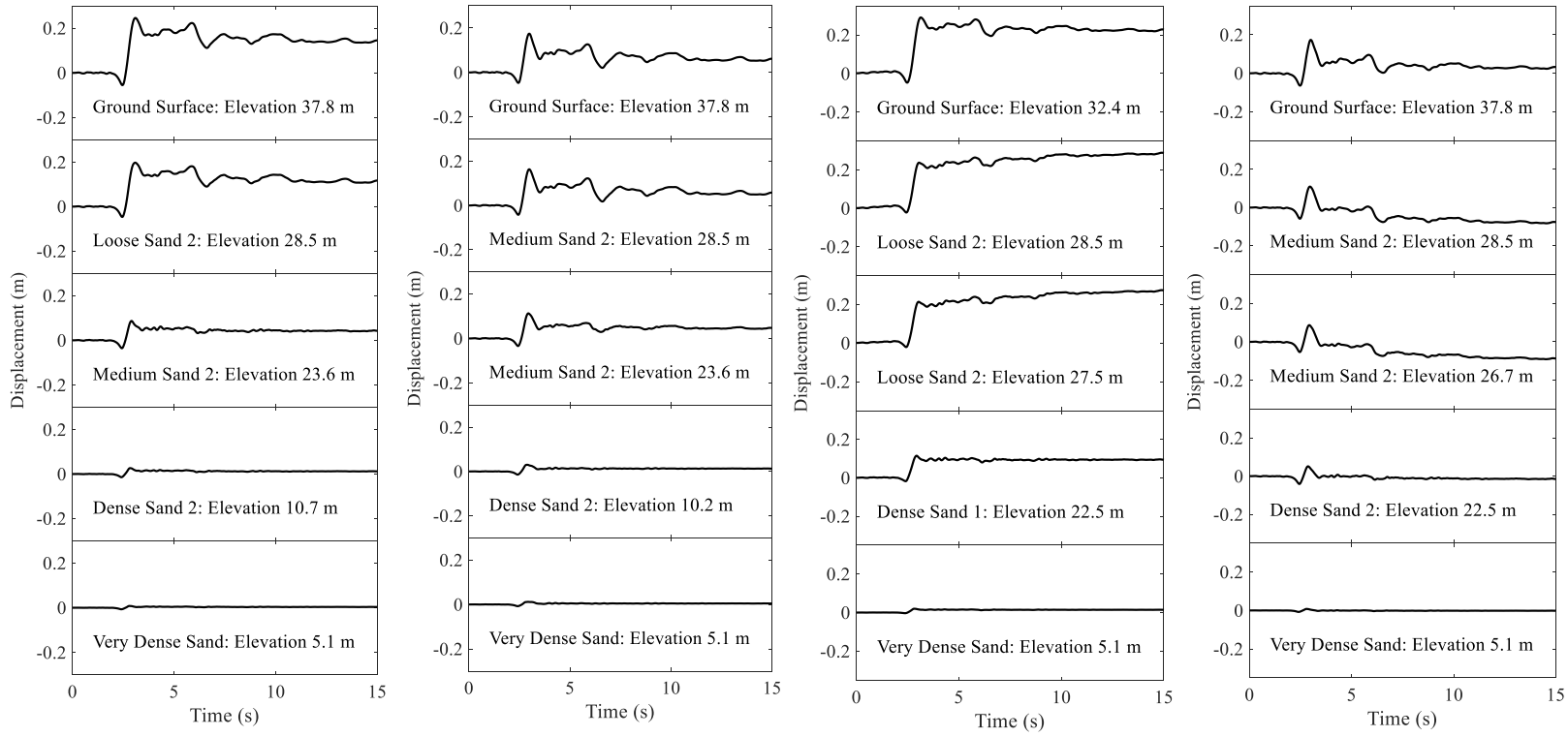

(a) (b) (c) (d)

Figure 6.10 Computed relative displacement: (a) East boundary; (b) West Boundary; (c) Location B; (d) Location F

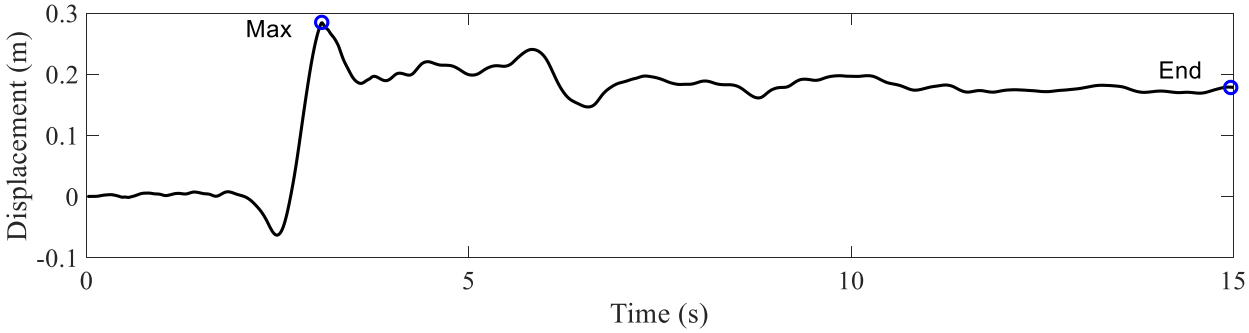

(a)

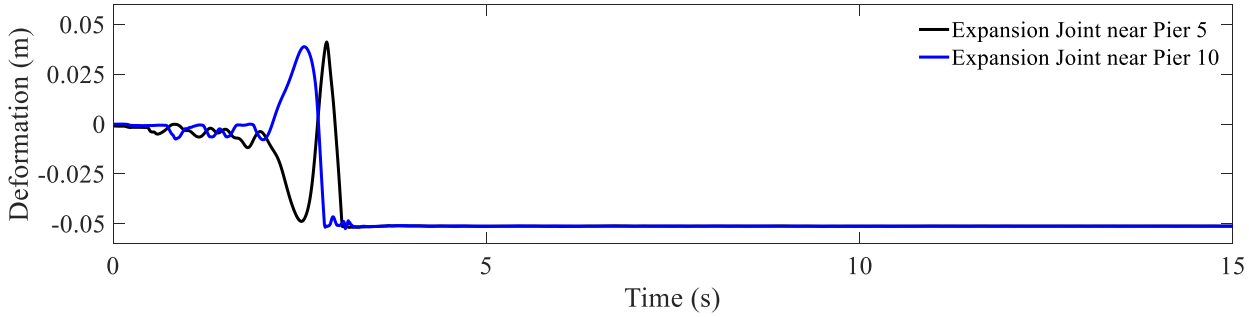

(b)

Figure 6.11 Computed relative displacement: (a) Deck; (b) Expansion Joints

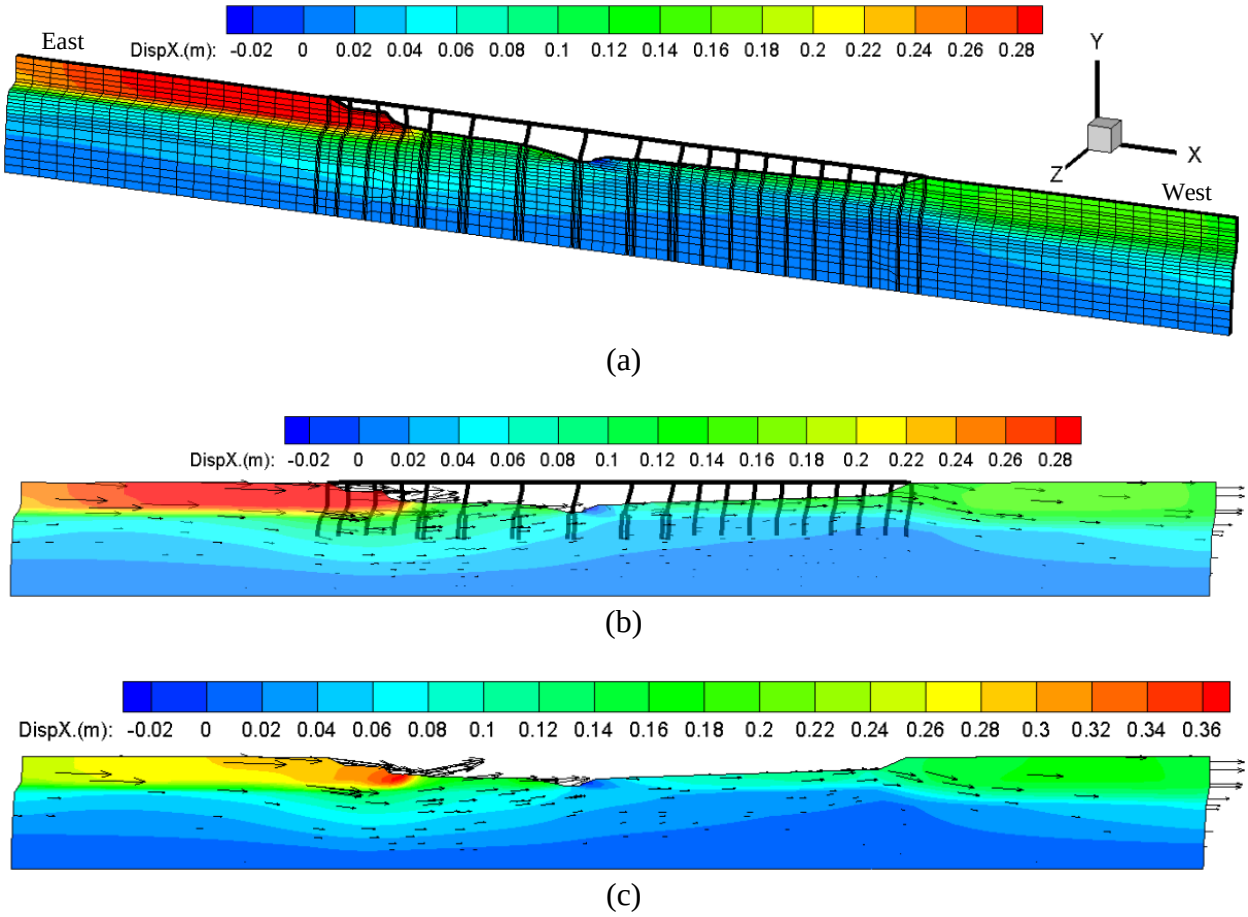

Figure 6.12 Deformed FE mesh at maximum deck displacement: (a) Isometric view; (b) Elevation view; (c) Without bridge (contour fill shows the horizontal displacement; arrows display direction of ground movement; factor = 15)

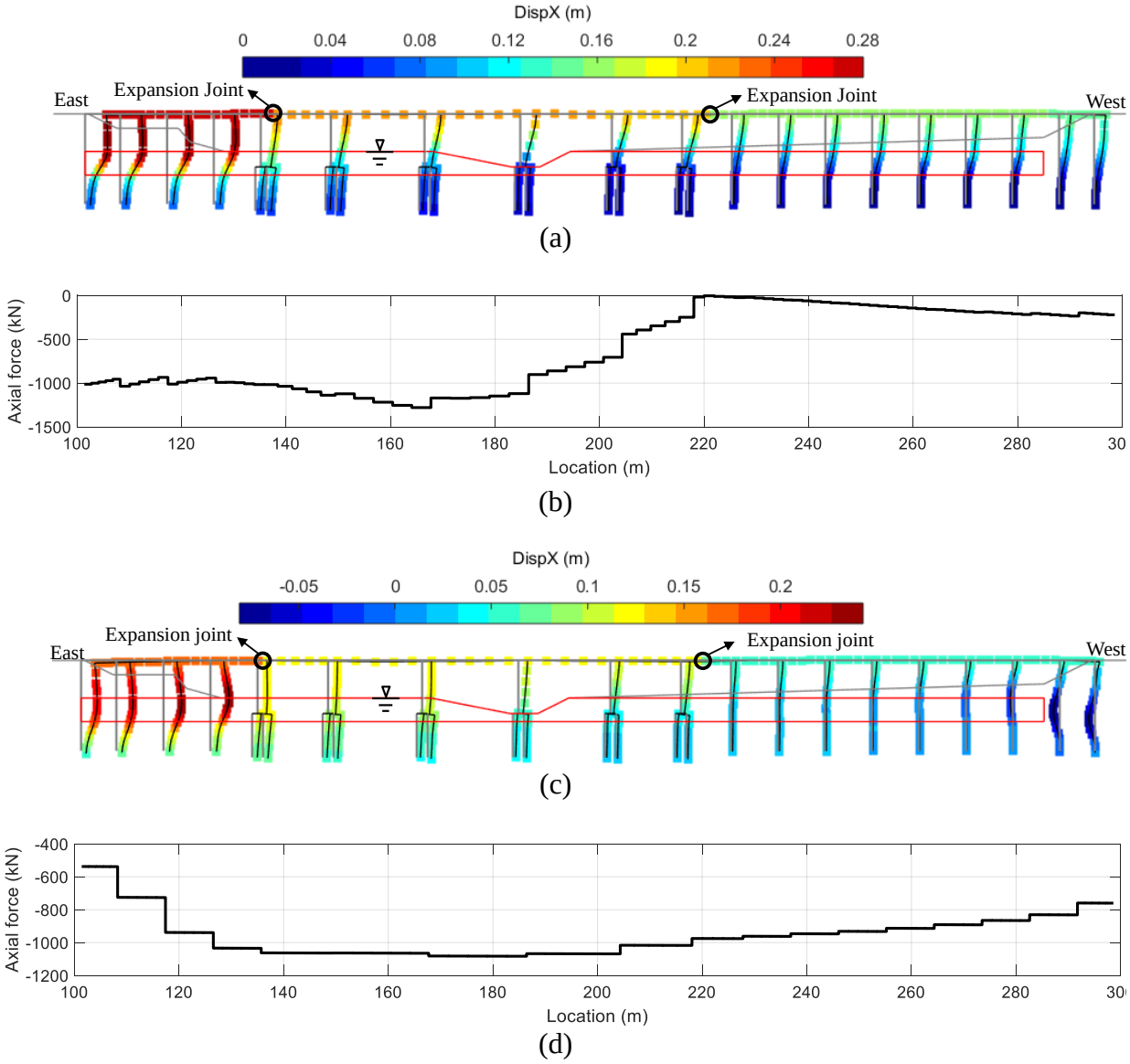

Figure 6.13 Deformed FE mesh of bridge and deck axial forces: (a), (b) At maximum deck displacement; (c), (d) At end of shaking (contour fill shows the horizontal displacement; red line represents outline of loose sand layer LS2; factor = 15)

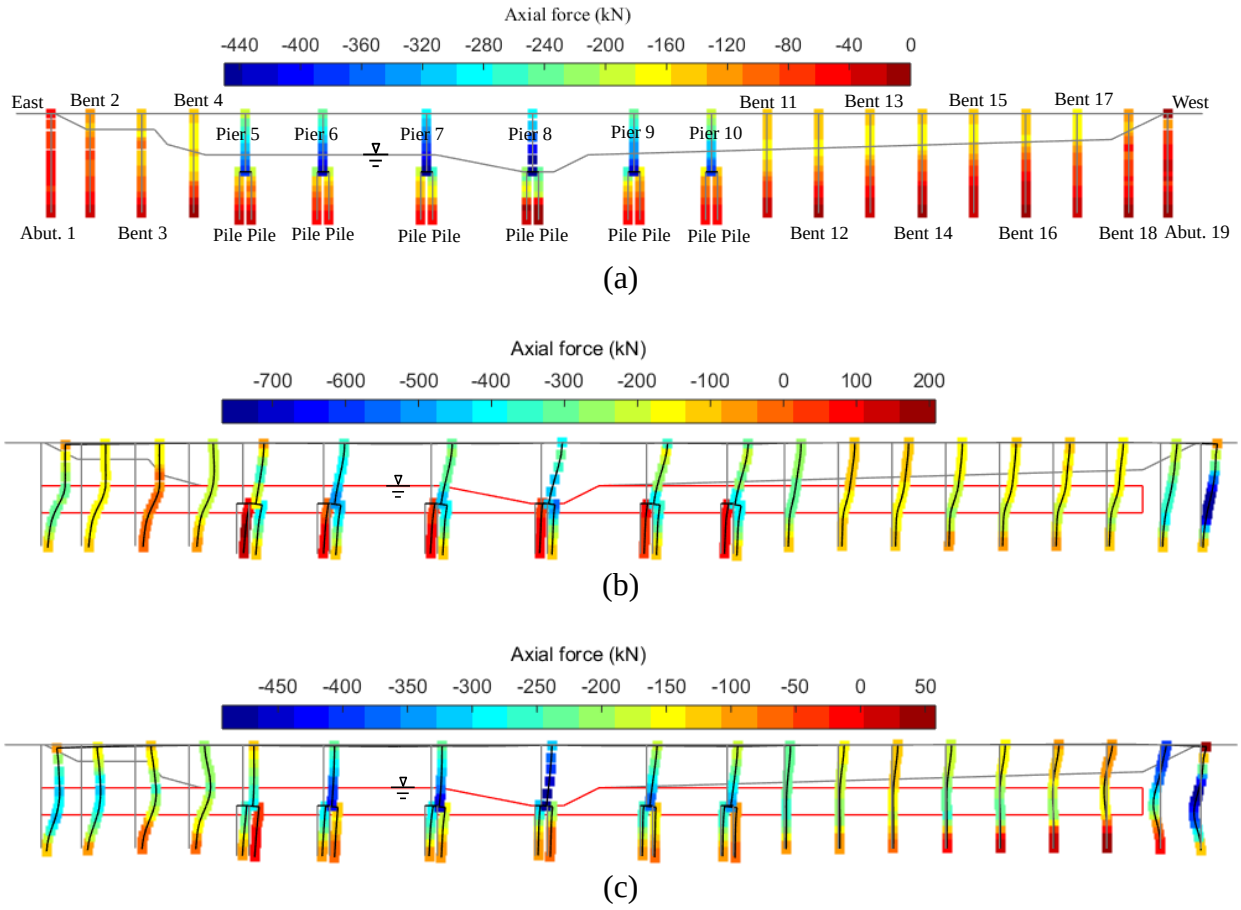

Figure 6.14 Bridge axial force: (a) Before shaking; (b) At maximum deck displacement; (c) At end of shaking (grey represents original configuration; red line represents outline of loose sand layer LS2; negative represents compression and positive represents tension; factor = 15)

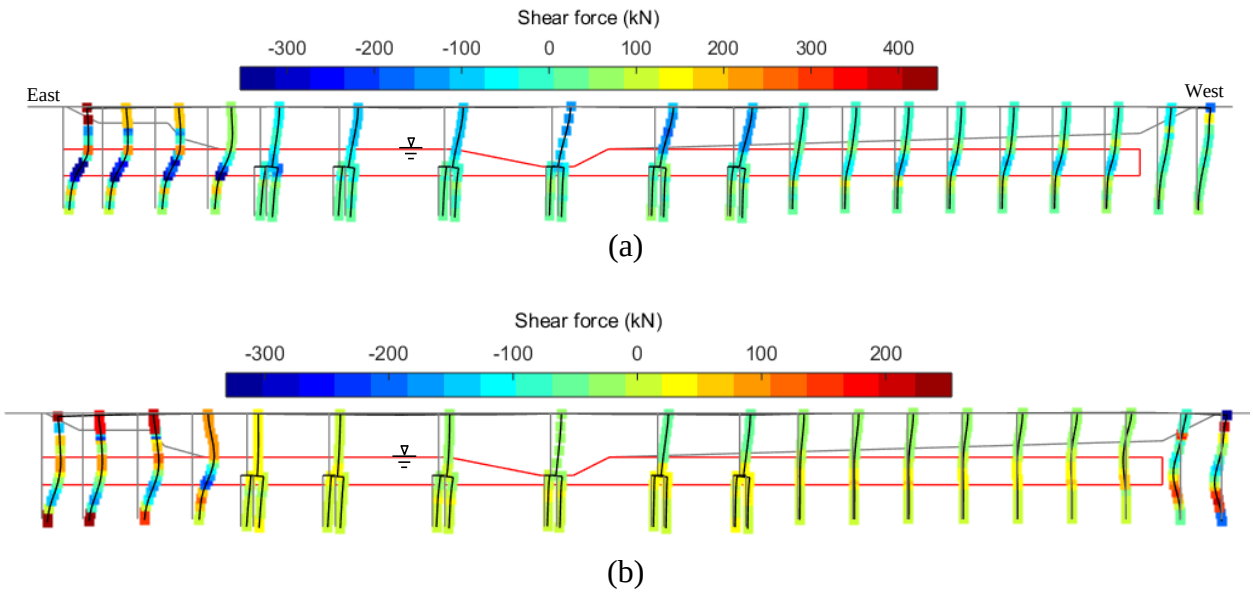

Figure 6.15 Bridge shear force: (a) At maximum deck displacement; (b) At end of shaking (grey represents original configuration; red line represents outline of loose sand layer LS2; factor = 15)

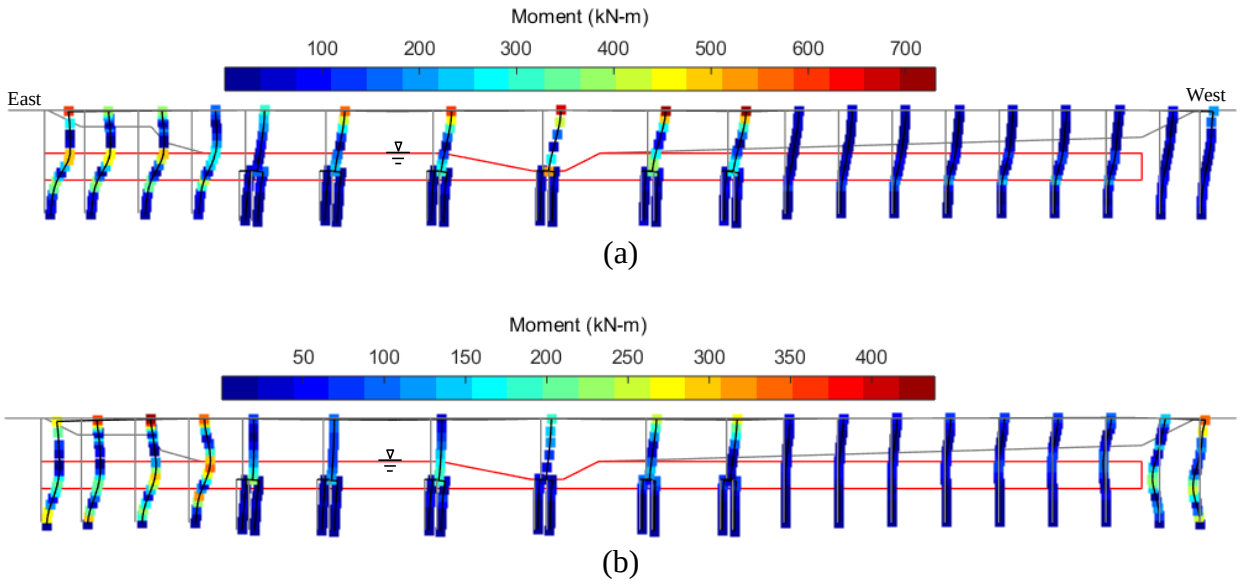

Figure 6.16 Bridge bending moment: (a) At maximum deck displacement; (b) At end of shaking (grey represents original configuration; red line represents outline of loose sand layer LS2; factor = 15)

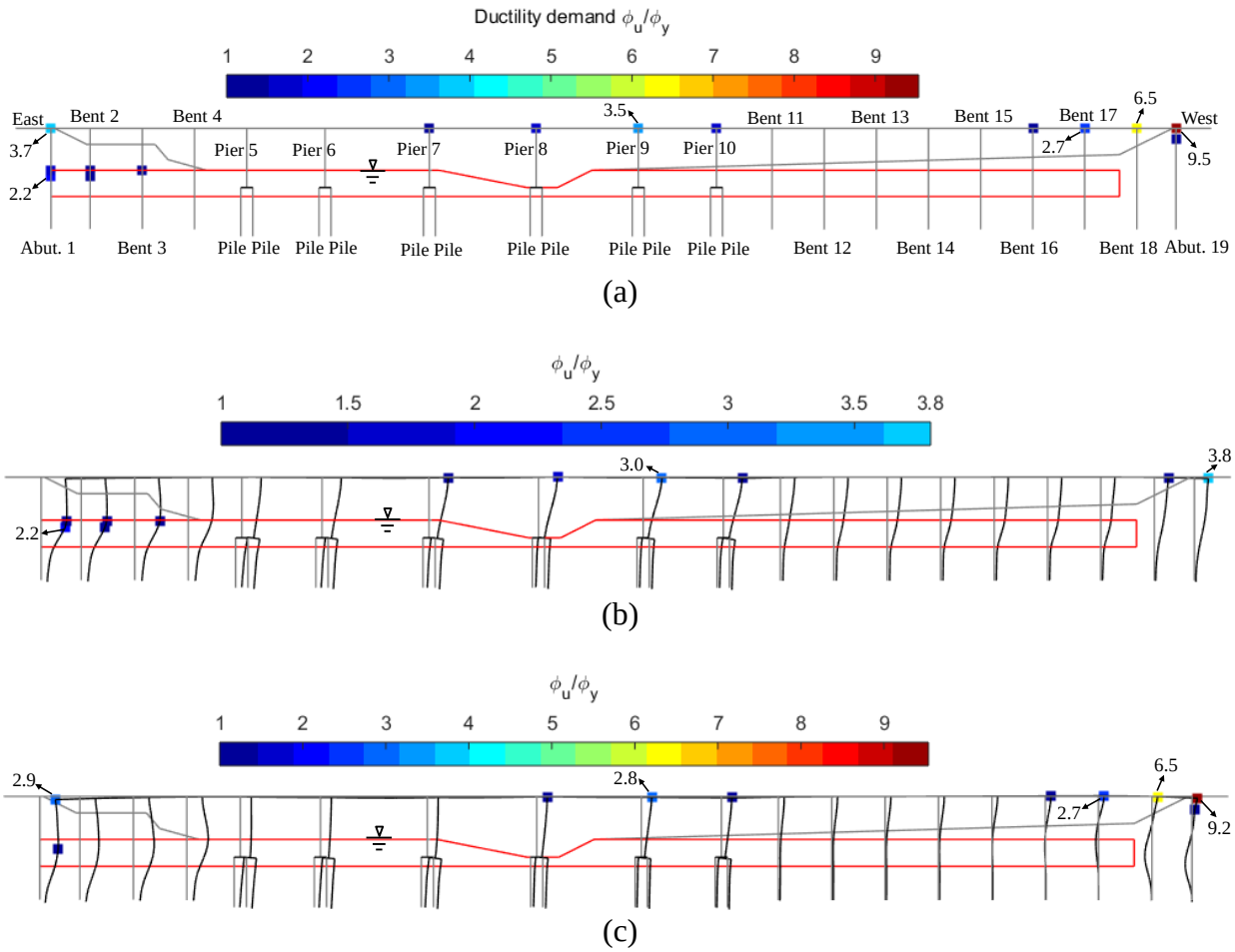

Figure 6.17 Bridge ductility demand: (a) Over entire shaking event; (b) At maximum deck displacement; (c) At end of shaking (grey represents original configuration; red line represents outline of loose sand layer LS2; values < 1 are not shown for clarity; factor = 15)

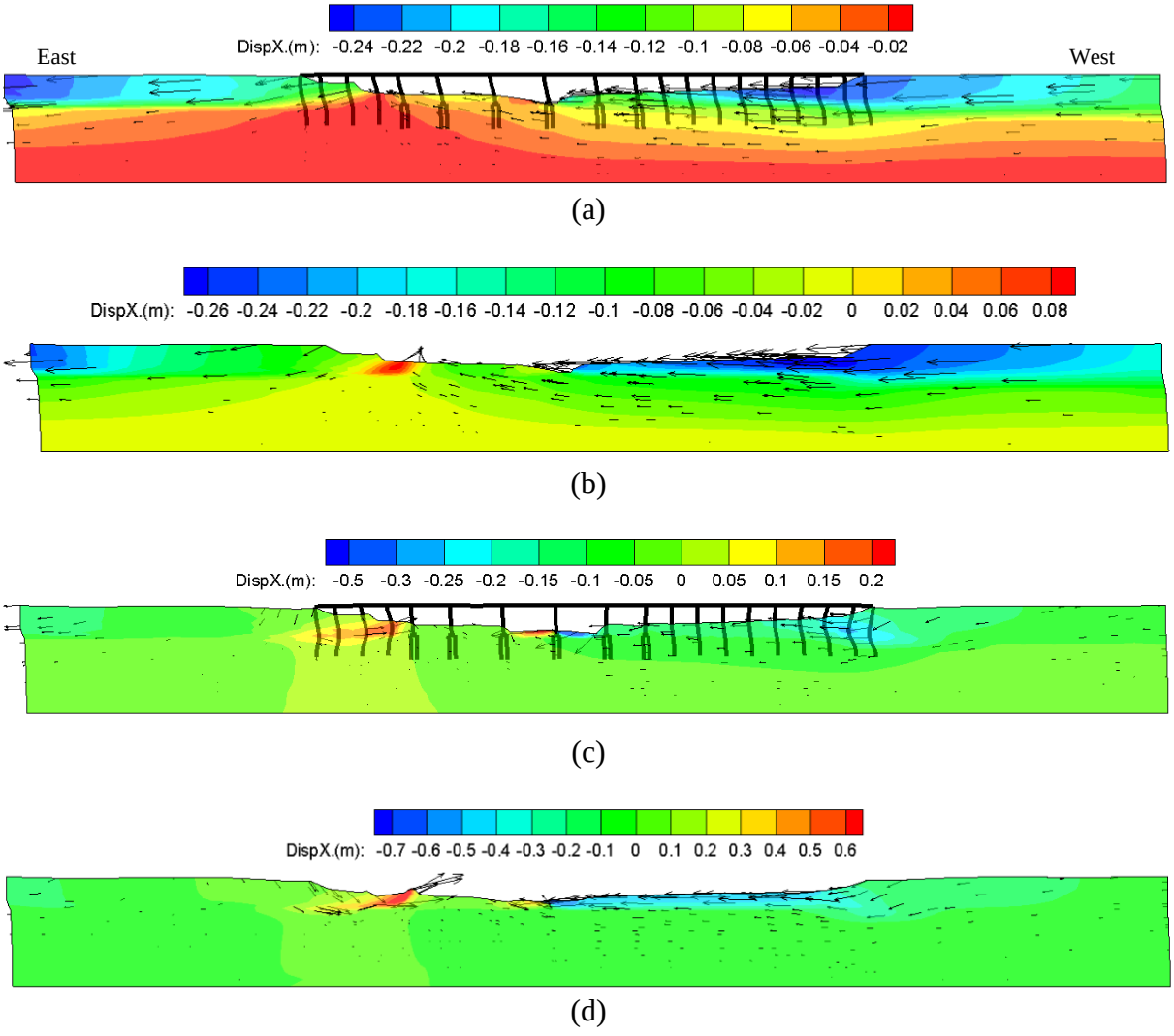

Figure 6.18 Deformed FE mesh under reverse Rinaldi motion with/without bridge: (a), (b) At maximum deck displacement; (c), (d) At end of shaking (contour fill shows the horizontal displacement; arrows display direction of ground movement; factor = 15)

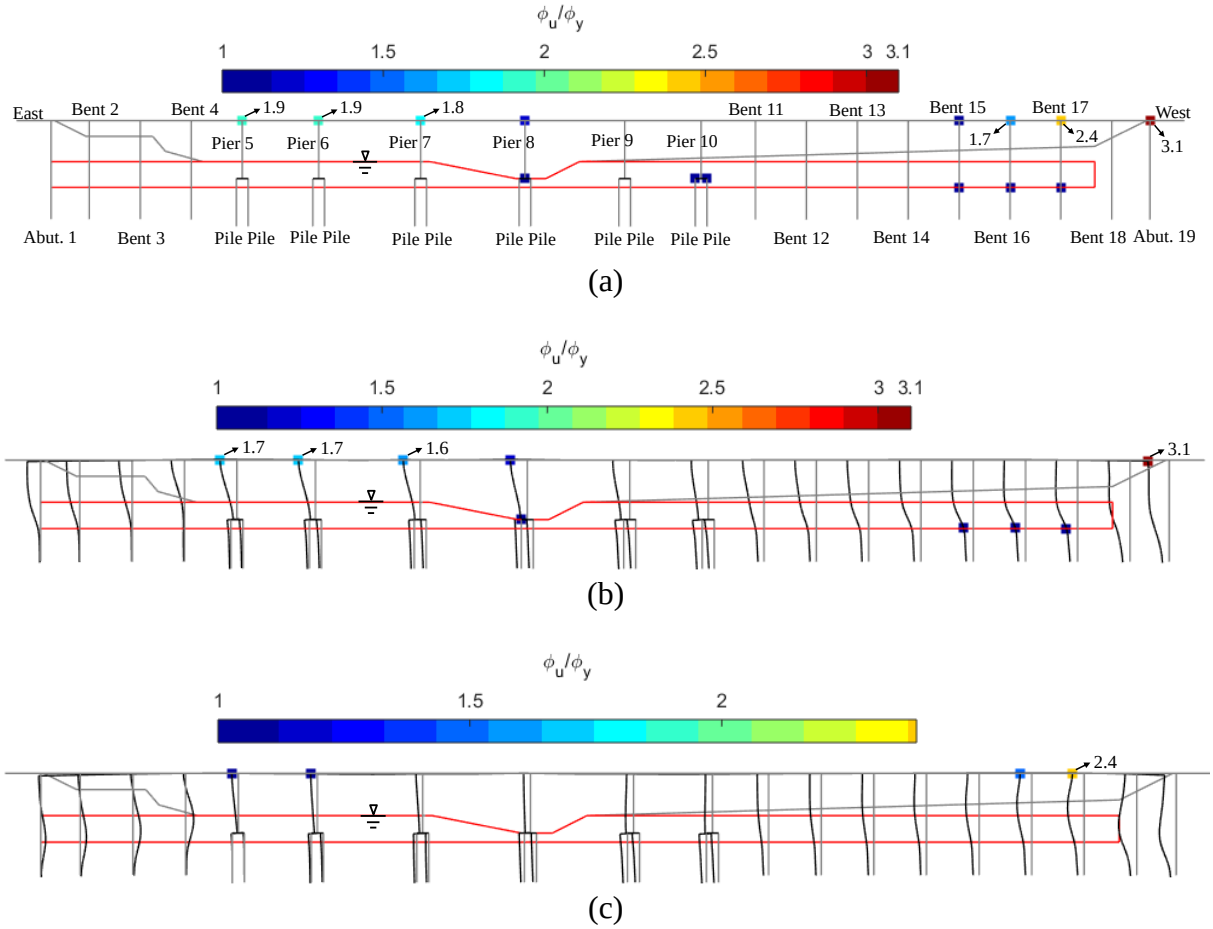

Figure 6.19 Bridge ductility demand under reverse Rinaldi motion: (a) Over entire shaking event; (b) At maximum deck displacement; (c) At end of shaking (grey represents original configuration; red line represents outline of loose sand layer LS2; values < 1 are not shown for clarity; factor = 15)

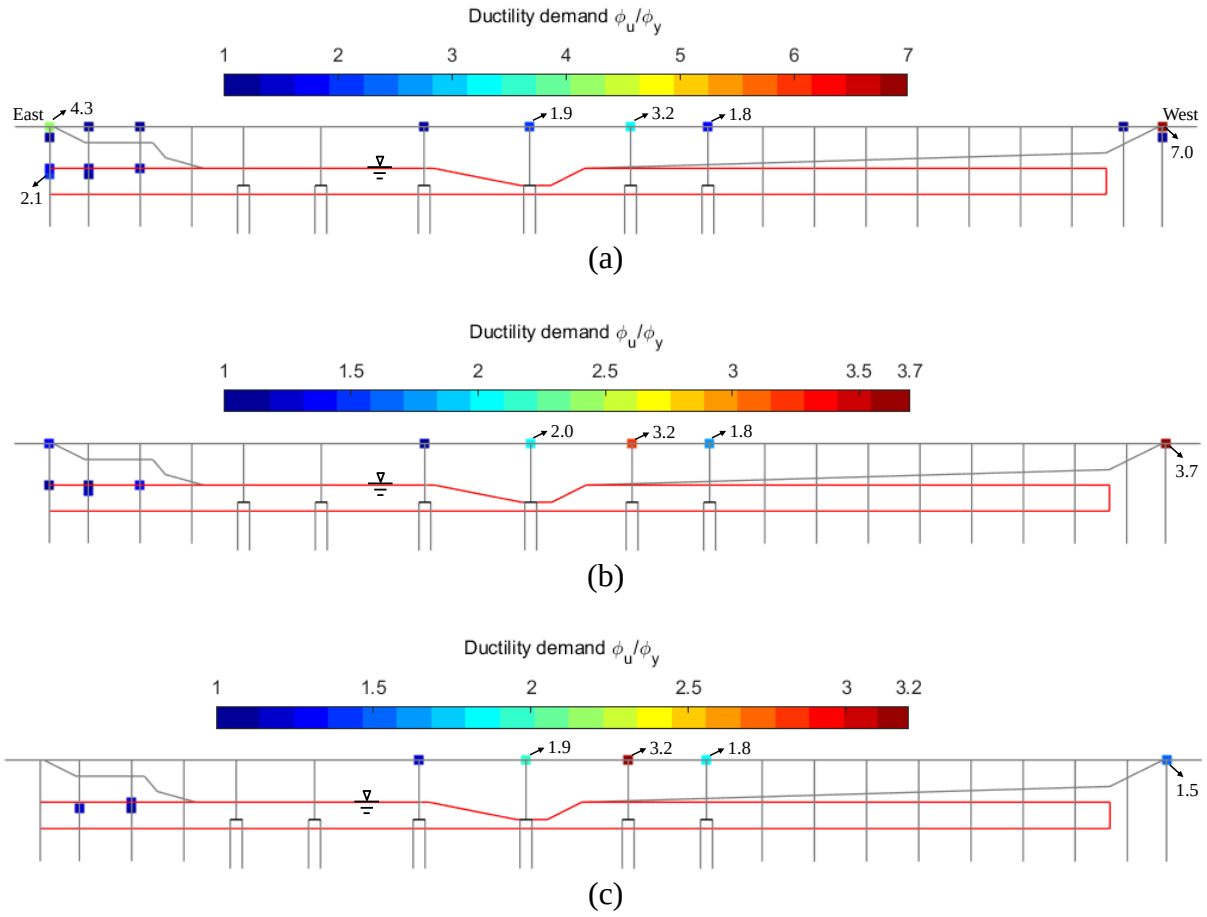

Figure 6.20 Retrofit Analyses: (a) Strengthening section 5 of bents 11-18 by a 6 mm steel jacket; (b) and (c), Furthermore, strengthening Abutments1 and 19 by adding one, and two piles, respectively (grey represents original configuration; red line represents outline of loose sand layer LS2; values < 1 are not shown for clarity)

Chapter 7. Three-Dimensional Bridge-Ground Liquefaction-Induced Deformations

7.1. Abstract

Global response of bridges is dictated by soil-structure interaction considerations of the entire bridge-ground system. In this study, the three-dimensional (3D) longitudinal response of such a bridge-ground system is numerically investigated. A realistic multi-layer soil profile is considered with interbedded liquefiable/non-liquefiable strata. Effect of the resulting liquefaction-induced ground deformation on the bridge-ground system is explored. The analysis techniques as well as the derived insights are of significance for general bridge-system configurations under liquefaction-induced ground deformation.

7.2. Introduction

Liquefaction and related damage to large bridges remained as a main concern in recent earthquakes, including the events of 2010 Maule (Arduino et al. 2010) and 2011 Christchurch (Cubrinovski et al. 2011, 2014). Generally, the observed response is highly influenced by the global bridge-ground overall characteristics as an integral system. As a consequence, investigators have been increasingly studying the entire bridge and the surrounding ground response within an integrated framework (Boulanger et al. 2007; Shin et al. 2008; Zhang et al. 2008; Ashford et al. 2009, 2011). Such studies indicated that global analysis is paramount in realistically evaluating the performance of liquefaction-induced lateral spreading and its consequences. On this basis, a three-dimensional (3D) finite element (FE) bridge-ground model was developed herein to capture salient characteristics of the involved response mechanisms. In developing this model, a realistic bridge geometric layout and ground stratification profile are represented. In the following sections, details of this modeling effort are presented and discussed.

7.3. Computational Framework

The Open System for Earthquake Engineering Simulation (OpenSees, McKenna 2011) framework was employed. Developed by the Pacific Earthquake Engineering Research (PEER) Center, OpenSees is widely used for simulation of geotechnical systems and soil-structure interaction applications (Qiu et al. 2020). The OpenSees elements and materials used in this study are briefly described below.

Three-dimensional solid-fluid *u-p* elements (Chan 1988) were employed for simulating soil response, where *u* is displacement of the soil skeleton and *p* is pore water pressure. Calibrated in a large number of earlier studies, the employed soil constitutive models (Parra 1996; Yang 2000; Yang and Elgamal 2002; Elgamal et al. 2003) were the PressureDependMultiYield03 and the PressureIndependMultiyield (PIMY). In these models, the shear stress-strain backbone curve is represented by the hyperbolic relationship with the shear strength based on simple shear. The PressureDependMultiYield03 (Khosravifar et al. 2018) includes new modifications to better capture the established guidelines on liquefaction triggering (Idriss and Boulanger 2008).

Details concerning the employed time integration scheme are described in Qiu et al. (2020). A relatively low level of stiffness proportional viscous damping was used to enhance numerical stability (coefficient = 0.003), with the main damping emanating from the soil nonlinear shear stress-strain hysteresis response (Qiu et al. 2020).

7.4. Bridge-Ground System

Figure 7.1 depicts the investigated bridge-ground configuration (Qiu et al. 2020). This 18-span reinforced concrete bridge is approximately 197 m long and 9.9 m wide, composed of a reinforced concrete deck on vertical pier walls with pile groups, and on single piles. Along the bridge deck, two expansion joints are located adjacent to the Piers (Figure 7.1b). In general, the

site soil profile consists of shallow, fine-grained soils underlain by medium dense to dense sands (Qiu et al. 2020 provides the material properties), with loose sand layers (red zone Figure 7.1b). The water table was prescribed at an elevation of 30.5 m (Figure 7.1b). Cross sections of the bridge structural components are presented in Qiu et al. (2020).

Based on the soil profiles (Qiu et al. 2020) and ground configuration (Figure 7.1), a 3D bridge-ground FE model is developed (Figure 7.2). Along both the West and East side mesh boundaries (Figure 7.2), soil columns of large size (not shown) are included (Qiu et al. 2020). These soil columns, at an adequate distance (around 100 m) away from the bridge structure to minimize boundary effects, efficiently reproduce the desired free-field response at these locations. Figure 7.2 shows the full 3D FE models (half mesh due to symmetry), comprising 58,801 nodes and 52,292 brick elements. In this model, seismic response is investigated only in the longitudinal direction, no out of plane motion is allowed. As such, loading was implemented in a staged fashion as follows:

1) Gravity was applied to activate the initial static state for the soil domain only with: i) linear elastic properties (Poisson's ratio of 0.47 for all layers), ii) nodes on both side planes of the model fixed against longitudinal translation, iii) nodes along the base fixed against vertical translation, iv) water table prescribed (Figure 7.2) with related water pressure and nodal forces specified along the canyon boundary. At the end of this step, the static soil state was imposed and displacements under own-weight application were re-set to zero using the OpenSees command InitialStateAnalysis.

2) Soil properties were switched from linear elastic to plastic.

3) Nonlinear force-based beam-column elements of pile and elastic beam-column elements of reinforced concrete deck were added. The pile nodes were connected to the soil nodes by rigid

links, zerolength and zerolengthSection elements as described in Qiu et al. (2020). Thereafter, self-weight of the bridge structure was applied.

In this study, the Lysmer-Kuhlemeyer 1969 boundary is applied along the base of the FE model (base V_s = 600 m/s, slightly higher than the stiffness of the overlying stratum), so as to avoid spurious wave reflections along this model boundary. For the shaking phase (purely in the longitudinal x-direction), seismic motion was simply taken as that of the 1994 Northridge earthquake ground surface Rinaldi Receiving Station record (Component S48W), scaled down to a peak amplitude of about 0.2 g (Figure 7.3). Via deconvolution (using Shake91 by Idriss and Sun, 1993), an incident earthquake motion (Figure 7.3) was derived and imparted (Elgamal et al. 2008) along the base of the FE model (elevation 0.0 in Figure 7.1). In this representation, free-field site response along both the side mesh boundaries is generated by the included 2D plane strain soil columns mentioned above.

7.5. Computed Response

Figure 7.3b displays the full 3D model lateral bridge deck displacement, along with that predicted by the slice approach of Qiu et al. (2020). Maximum displacement of the full 3D model is slightly higher than that of the slice model (0.13 m), reaching about 0.16 m. Post peak, permanent displacement of the full 3D model is significantly higher than that of the slice model by about 30 %. This makes sense in light of the additional imposed demands from lateral deformation of the large ground domain surrounding the bridge in the full 3D model simulation. Figure 7.4 displays the displacement contours of the two bridge-ground system models at end of shaking. For the slice model (Figure 7.4a), maximum displacement of the overall bridge-ground system reached about 0.15 m (in the vicinity of the bridge model). In Figure 7.4b, noticeable localized east-side slope deformations of the free-field (away from the bridge) is seen. In Figure 7.5, deformation of the

outer bents (Figure 7.1) is significantly higher than those of the inner bents, due to the large permanent downslope displacement of the surrounding sloping ground. Computed moment curvature of bents 1-4 and 17-19 (Figure 7.1) in the slice and full 3D models are displayed in Figure 7.6. It can be seen clearly that the outer piles in full 3D model sustain more loads than the inner piles. In addition, the loads of both outer and inner piles in the full 3D model are higher than the corresponding counterparts of the slice model.

7.6. Conclusions

A 3D FE analysis framework was presented to study the liquefaction-induced seismic response of bridge-ground systems as dictated by soil-structure interaction. For that purpose, results of two 3D FE models representing the same ground-bridge-foundation configuration were presented. Permanent deformation patterns resulting from the liquefaction-induced lateral spreading were explored. Comparison results of the two 3D models demonstrated that a holistic assessment of such response generally requires a highly demanding full three-dimensional (3D) model of the bridge and surrounding ground. In such a full 3D modeling representation, the outer piles of each bent will encounter higher demands than their corresponding inner piles, due to the larger imposed lateral deformations of the soil domain, transversally around the bridge's footprint.

7.7. Acknowledgements

Chapter 7, in full, has been submitted for publication of the material as it may appear in the following conference publication (The dissertation author was the primary investigator and author of this paper):

Qiu, Z. and Elgamal, A. (Manuscript accepted, 2020). "Three-Dimensional Bridge-Ground Liquefaction-Induced Deformations." 16th International Conference of IACMAG

International Association for Computer Methods and Advances in Geomechanics, Torino, Italy. 3-4 May.

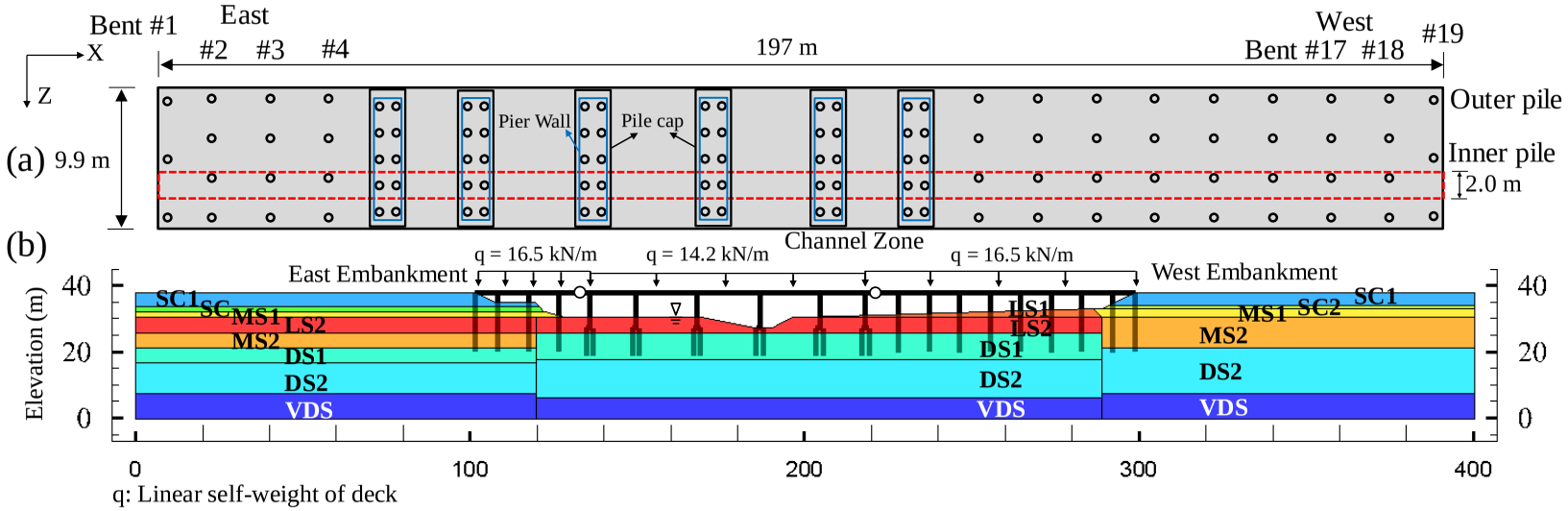

Figure 7.1 Bridge-ground system: (a) Schematic plan view (not to scale); (b) Ground configuration

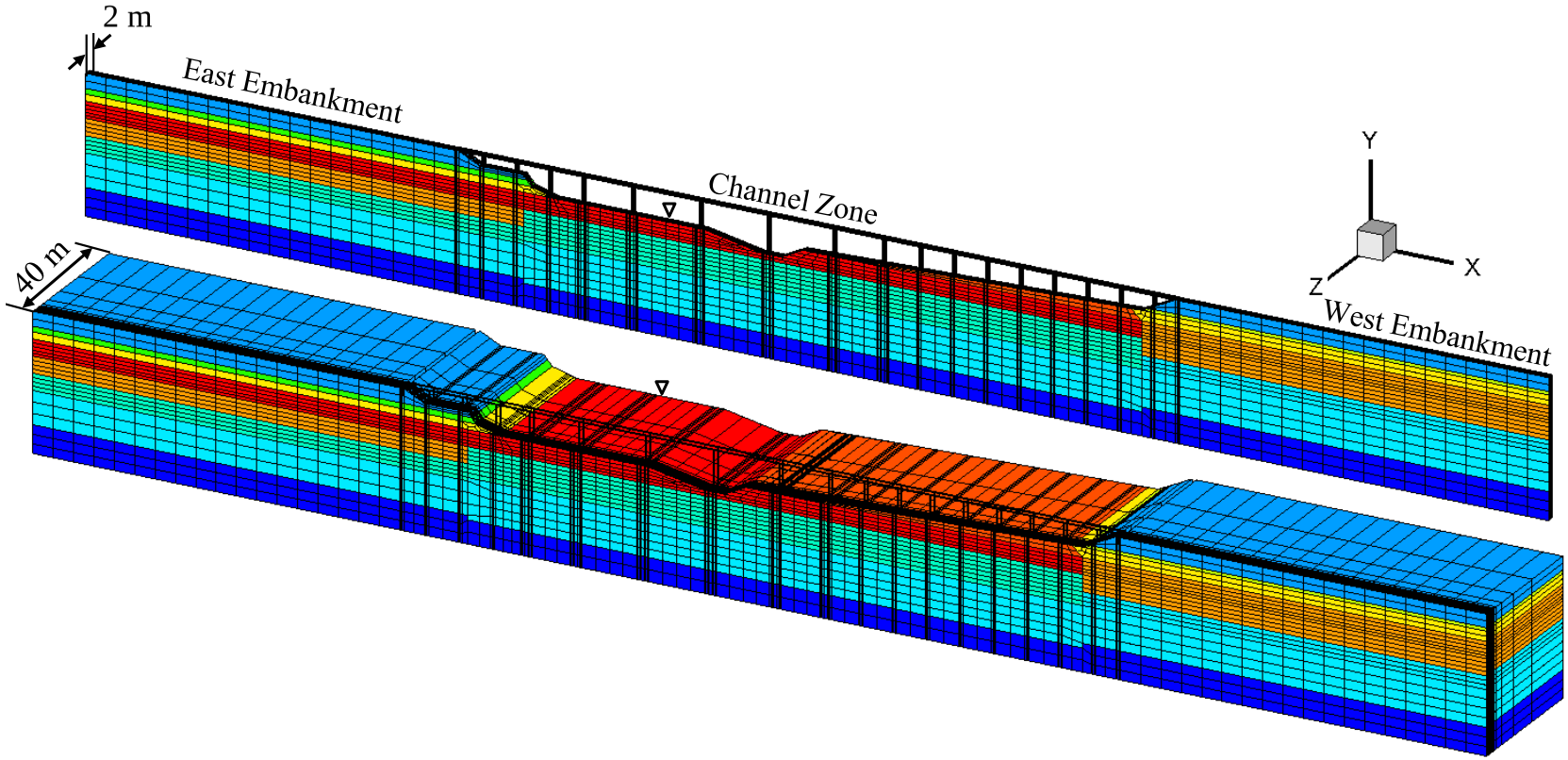

Figure 7.2 FE mesh: (a) Slice model; (b) Full 3D model shown below (half mesh due to symmetry)

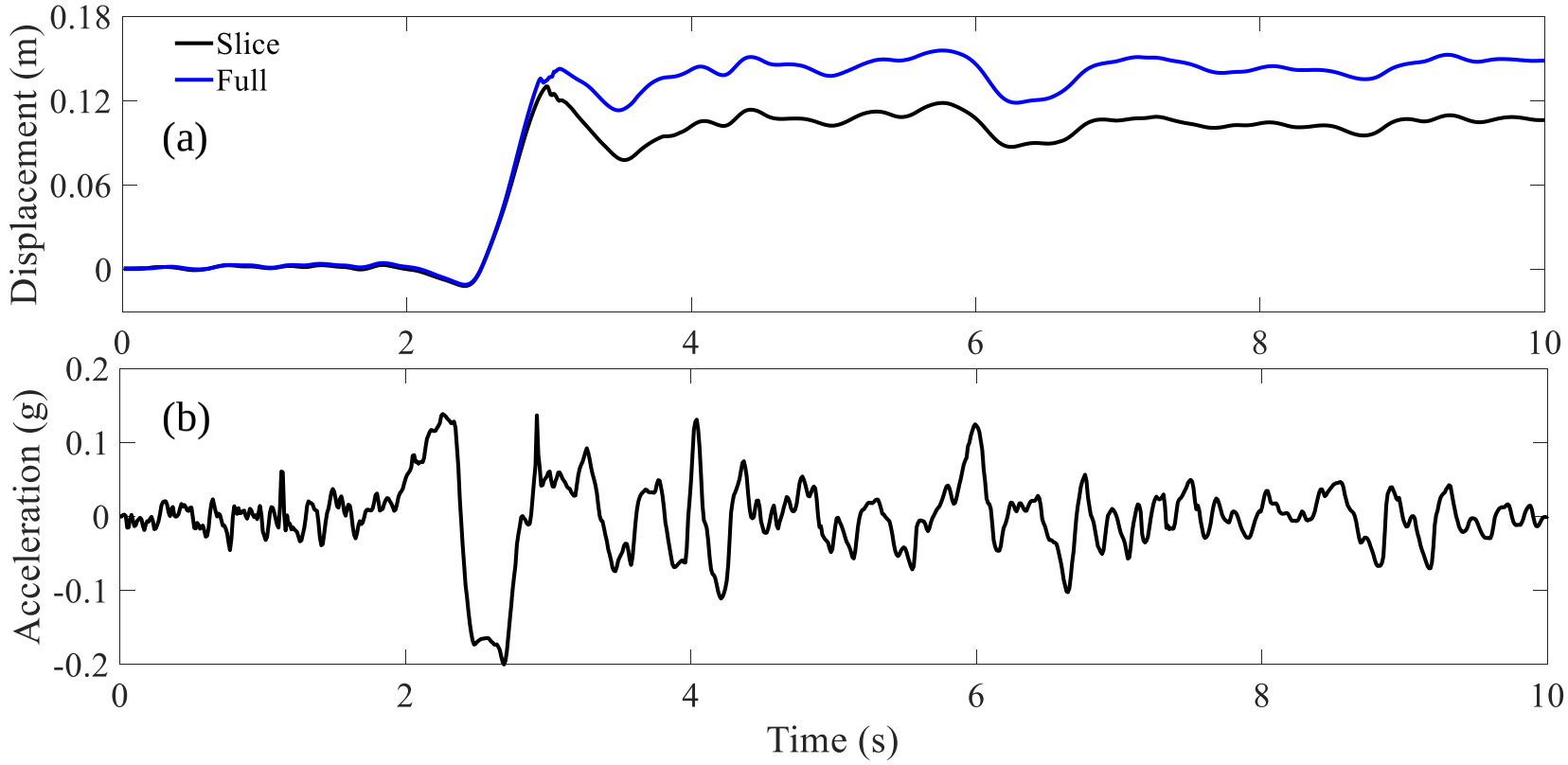

Figure 7.3 Incident input motion and computed bridge deck relative displacement time history

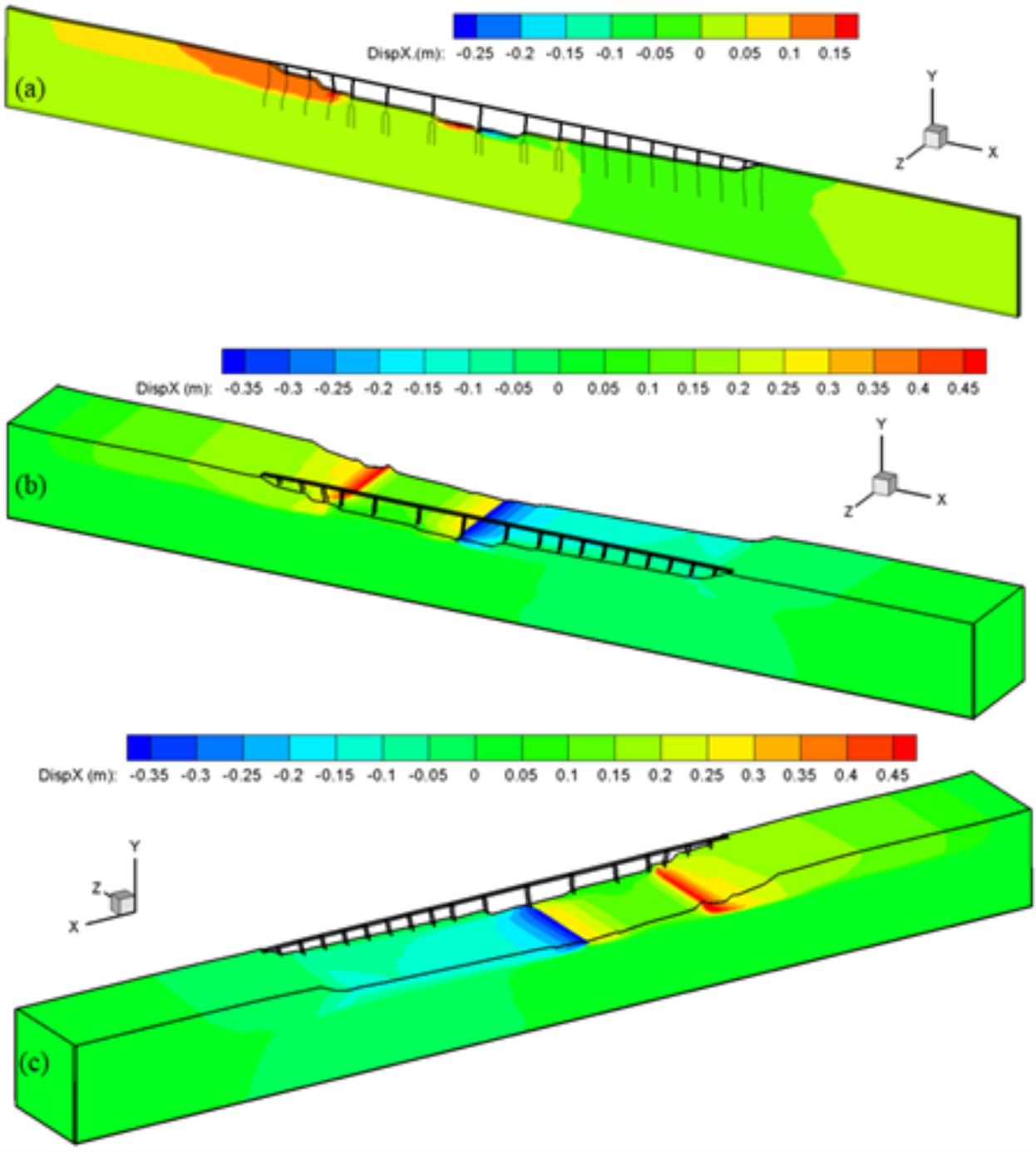

Figure 7.4 Displacement contours at end of shaking: (a) Slice model (Qiu et al. 2020); (b), (c) Full 3D model

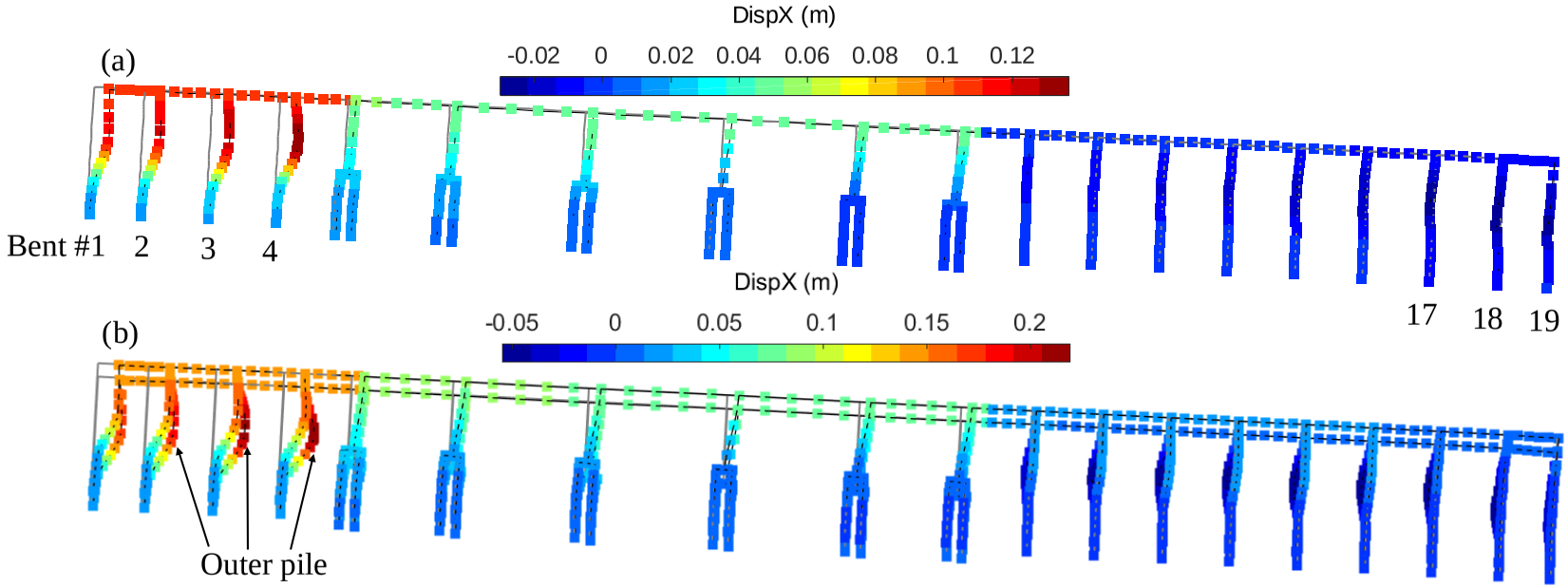

Figure 7.5 Deformed FE mesh of bridge at end of shaking: (a) Slice model; (b) Full 3D model

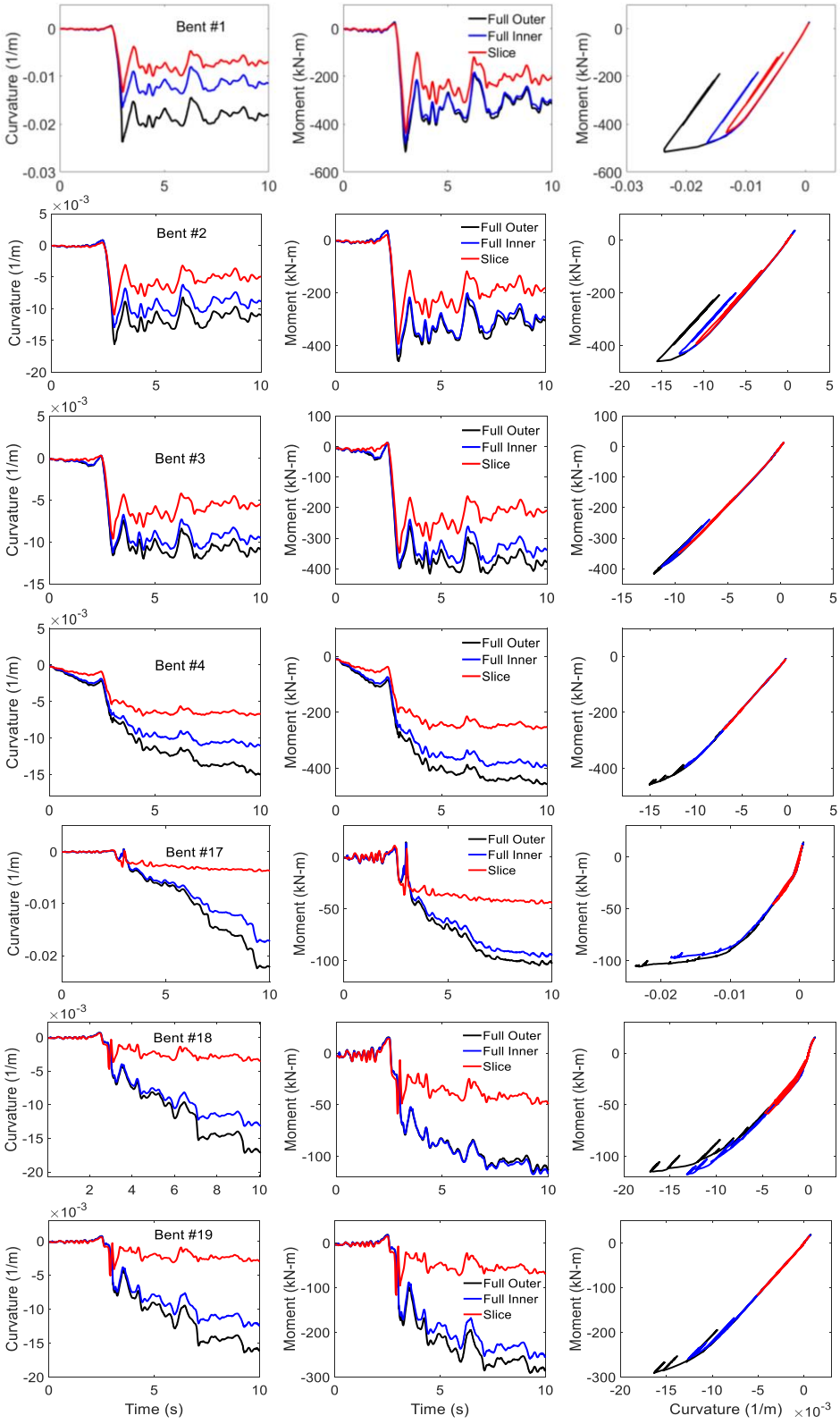

Figure 7.6 Computed maximum moment-curvature response of bents 1-4, 17-19 as shown in Figure 7.1

Chapter 8. Bridge in Narrow Canyon: Seismic Response and Liquefaction-Induced Deformations

8.1. Abstract

Considerable bridge-ground interaction effects are involved when evaluating the consequences of liquefaction-induced deformations. Due to seismic excitation, liquefied soil layers may result in substantial accumulated permanent deformation due to the sloping ground near the abutments. Ultimately, global response of the bridge is dictated by soil-structure interaction considerations of the entire bridge-ground system. Of particular interest is the scenario of narrow canyons where interaction between lateral deformations at both ends of the bridge takes place. In order to highlight the salient involved mechanisms, this study investigates the longitudinal response of an overall bridge-ground system. For that purpose, a full three-dimensional (3D) Finite Element (FE) model is developed, motivated by details of an existing narrow canyon bridge-ground configuration. As such, a realistic multi-layer soil profile is considered with interbedded liquefiable/non-liquefiable strata. Effects of the resulting liquefaction-induced ground deformation on the bridge-ground system are explored. Specific attention is given to global deformation of the bridge structure as an integral entity due to lateral spreading in the vicinity of the abutments. Generally, the analysis technique as well as the derived insights are of significance for the response of bridge-ground systems during liquefaction-induced ground deformations.

8.2. Introduction

Liquefaction-induced damage to bridge foundations has been observed frequently during earthquakes (Youd 1993; Hamada et al. 1996; Tokimatsu and Asaka 1998; Berrill et al. 2001), including the recent 2010 Maule (Arduino et al. 2010; Ledezma et al. 2012; Verdugo et al. 2012)

the 2011 Christchurch (Cubrinovski et al. 2011, 2014; Wotherspoon et al. 2011), and the El Mayor-Cucapah earthquakes (Turner et al. 2013, 2016). Figure 8.1 illustrates typical response for a short span bridge as discussed earlier by Cubrinovski et al. (2011, 2014).

To study the entire bridge and surrounding canyon within an integrated framework (Figure 8.1), different approaches to the representation of ground response at the location of each bridge foundation were presented by Boulanger et al. 2007, Ashford et al. 2009, 2011, Aygün et al. 2009, 2010, Ledezma and Bray 2010, Padgett et al. 2013, Turner et al. 2013, 2016, Wang et al. 2013a, b, McGann and Arduino 2015, Ghofrani et al. 2016, Soltanieh et al. 2019, and Qiu et al. 2020. Results of these studies show that consideration of the entire bridge-ground system provides a more realistic distribution of force and displacement demands.

Currently, 3D Finite Element (FE) analyses for seismic response of bridges, with consideration of soil liquefaction, are rather limited. For instance, McGann and Arduino 2014 conducted quasi static analysis of the Mataquito River Bridge abutment and foundation system subjected to liquefaction-induced lateral spreading. Similarly, McGann and Arduino 2015 and McGann 2020 conducted parametric studies to investigate the influence of 3D site geometry on seismic response of the bridge piles and abutments.

In view of the observed system response as depicted schematically in Figure 8.1, a full 3D bridge-ground FE investigation is undertaken herein. Focus is placed on a narrow canyon configuration, motivated by the details of an actual short-span bridge-ground system (Caltrans 2017).

As such, the following sections of this chapter outline the: 1) computational framework, 2) specifics and model properties of the bridge-ground system, 3) details of the employed FE

modeling techniques, and 4) computed response and insights derived from the study. Finally, a number of conclusions are presented and discussed.

8.3. Computational Framework

The Open System for Earthquake Engineering Simulation (OpenSees, McKenna 2011, http://opensees.berkeley.edu) framework was employed to conduct the nonlinear bridge-ground system analysis subjected to seismic excitation. OpenSees is developed by the Pacific Earthquake Engineering Research (PEER) Center, and it is widely used for simulation of geotechnical systems and soil-structure interaction applications (Yang and Elgamal 2002; Lu et al. 2011; Su et al. 2017). The OpenSees elements and materials used in this FE model are briefly described below.

Three-dimensional solid-fluid brick elements (i.e., bbarBrickUP element in OpenSees) following the *u-p* formulation (Chan 1988) were employed for simulating saturated soil response, where *u* is displacement of the soil skeleton and *p* is pore-water pressure. As such, the 3D soil domain is represented by effective-stress solid-fluid fully coupled brick elements (Parra 1996; Yang 2000; Lu 2006; Yang et al. 2008) to describe the solid translational degrees of freedom (DOFs) and the fluid pressure.

The OpenSees soil material PressureDependMultiYield03 (typically used with the solid-fluid fully coupled brick elements, Khosravifar et al. 2018) is employed to simulate the liquefaction-induced shear strain accumulation mechanism in cohesionless soils (Yang and Elgamal 2002; Elgamal et al. 2003; Yang et al. 2003, 2008). In order to more closely capture the established guidelines concerning triggering of liquefaction (Idriss and Boulanger 2008), the PressureDependMultiYield03 material has been recently updated (Khosravifar et al. 2018). In addition, the PressureIndependMultiYield material (Elgamal 2008; Yang et al. 2008; Lu et al. 2011) is employed for simulating elasto-plastic undrained clay-type shear response.

The FE matrix equation of the bridge-ground system is integrated in time using a single-step predictor multi-corrector scheme of the Newmark type (Chan 1988; Parra 1996) with integration parameters $\gamma = 0.6$ and $\beta = 0.3025$. The equation is solved using the modified Newton-Raphson approach with Krylov subspace acceleration (Carlson and Miller 1998; Mazzoni et al. 2009). A relatively low level of stiffness proportional viscous damping was used to enhance numerical stability (coefficient = 0.003), with the main damping emanating from the soil nonlinear shear stress-strain hysteresis response (Su et al. 2017; Qiu et al. 2020).

8.4. Pile and Soil-Pile Interaction

Three-dimensional nonlinear force-based beam-column elements with fiber-section (Scott and Fenves 2006; Scott and Ryan 2013) were employed to represent the piles, for the purpose of this liquefaction-induced lateral spreading investigation (Elgamal and Lu 2009; He et al. 2017). In order to represent the geometric space occupied by the pile in the soil domain, rigid beam-column links ($EI = 10^4$ times the linear EI of the pile) are used normal to the vertical axis of the pile (Su et al. 2017; Qiu et al. 2020) effectively defining its surface for friction along its length and end bearing at its base. Details of the calculation for this yield shear force can be found in Su et al. 2017 and Qiu et al. 2020.

8.5. Finite Element Model

Figure 8.2 depicts the investigated bridge-ground configuration. This three-span reinforced concrete bridge is approximately 96 m long (spans of equal length) and 11.4 m wide (Caltrans 2017), composed of reinforced concrete pier walls, seat-type abutments and wing walls founded on steel H-piles (Figure 8.2b). Four hinge-type connections (Figure 8.2b) are located along the bridge deck. Cross sections of the bridge structural components are displayed in Figure 8.2c.

For the purposes of this investigation, seismic excitation is applied only in the longitudinal direction (i.e., no transverse or vertical shaking is imparted), thus allowing for the use of a half-mesh configuration due to symmetry (Figure 8.3). In the transverse direction, an additional 34 m wide soil domain is included in order to capture the canyon response away from the bridge structure. On this basis, a 3D bridge-ground FE mesh (Figure 8.3) is generated comprising 65,714 nodes, 60,060 brick elements, 725 nonlinear and 30 linear elastic beam-column elements, 2988 rigid beam-column links, 2988 zerolength elements and 2988 zerolengthSection elements.

Along the left and right side mesh boundaries (Figure 8.3), 2D plane strain soil columns of large size and depth (not shown) are included (Qiu et al. 2020). These soil columns, at an adequate distance (around 100 m) away from the bridge structure to minimize boundary effects (Figure 8.3), efficiently reproduce the desired shear beam free-field response at these locations (Qiu et al. 2020).

8.5.1. Ground Configuration

The overall ground configuration based on existing boring data and site conditions (Caltrans 2017) is shown in Figure 8.4. Inclination angle of the slopes (2H:1V) is about 27 degrees, and water table is located at the elevation of 28.8 m, at the interface between Layers Q3a and Q3b. In this ground profile (Figure 8.4), Layers Q2 and Q4 are deemed to be potentially liquefiable, and Layer Q3b is a relatively weak soft clay. Table 8.1 and Table 8.2 list the sand and clay model parameters, respectively. For illustration, the soil model responses under undrained monotonic loading conditions for the clay and sand (initial confinement = 100 kPa) are presented in Figure 8.5. It can be seen that shear strength of the soft clay Q3b is comparatively low (Figure 8.5a), further promoting the potential of seismically-induced lateral spreading deformations. As shown in Figure 8.5b, shear strength of the saturated medium dense and dense sands (Q2 and Q4) depict

an increase with the increase in shear strain (undrained response, due to the prescribed dilative tendency as noted in Table 8.1).

8.5.2. Bridge Structure

All structural components except for the reinforced concrete deck (modeled by linear elastic beam-column elements with linear self-weight q as shown in Figure 8.4) were modeled using 3D nonlinear force-based beam-column elements with fiber-section. In this fiber section formulation, OpenSees uniaxial material Concrete01 (Kent and Park 1971; Mander et al. 1988) was employed to simulate the core and cover concrete, and Steel02 (Giuffrè A and Pinto 1970; Menegotto and Pinto 1973; Filippou et al. 1983) was used to simulate the reinforcement steel (Figure 8.5c and d). Geometry and fiber discretization of the bridge pile cross sections (Figure 8.2c) are shown in Figure 8.6. In this figure, moment-curvature for each fiber section under different axial load levels is displayed. It can be seen that the flexural strength of the steel HP 10×57 pile is comparatively low (Figure 8.6), promoting the potential for damage at the corresponding locations of A1-A11 and D1-D11 near the abutments (Figure 8.2).

In addition, axial force-strain response for each fiber section is shown in Figure 8.6. In this regard, the Concrete01 material only displays strength in compression, with tension supported by the reinforcing steel (Figure 8.6).

8.5.3. Boundary and Loading Conditions

As mentioned above, both lateral mesh boundaries (X = 0 m and X = 300 m) are located away from the bridge structure (Figure 8.2 and Figure 8.3). Along the longitudinal symmetry plane (Z = 40 m) of the model (Figure 8.2), no out of plane motion is allowed. Loading was implemented in a staged fashion following the steps outlined earlier in Su et al. 2017 and Qiu et al. 2020.

In this study, the base of the soil domain is located at a depth of 50 m from the ground surface (Figure 8.4), about 10 m away from the bridge foundations which were tipped into bedrock (layer TM). Lateral response of the soil strata below this 50 m depth was represented by the Lysmer-Kuhlemeyer (Lysmer and Kuhlemeyer 1969) dashpot boundary, applied along the base of the FE model (base V_s = 600 m/s, in the range of soft rock, slightly higher than stiffness of the overlying TM stratum), so as to avoid spurious wave reflections. As such, a dashpot is activated in the x-direction at each node along the base, and the incident seismic wave excitation is defined by dynamic equivalent nodal forces (details of this process are presented earlier in Zhang et al. 2008 and Elgamal et al. 2008).

For the shaking phase (purely in the longitudinal direction), seismic motion (Figure 8.7) was simply taken as that of the 1994 Northridge earthquake ground surface Rinaldi Receiving Station record (Component S48W), scaled down to a peak amplitude of 0.3 g. For the purpose of this study, deconvolution was employed as a simple approach (using Shake91 by Idriss and Sun 1993), to derive an incident earthquake motion (Figure 8.7), imparted (Elgamal et al. 2008) thereafter along the base of the FE model (elevation 0.0 in Figure 8.4). In this representation, free-field motion along both the left and right-side mesh boundaries (Figure 8.3) is generated by the included left and right boundary soil columns mentioned above.

8.6. Acceleration Time History

Figure 8.7 shows acceleration response at various locations of the bridge-ground configuration. In general, amplitudes are amplified closer to the ground surface. Motion along the ground surface appears to be rather similar, in view of the stiff TM ground formation that surrounds the canyon (Figure 8.3 and Figure 8.4). Since there is a larger extent of softer soils at the right-side slope compared to that at the left, peak spectral acceleration at R1 is slightly lower than that at L1.

Nevertheless, the relatively small difference in acceleration along the bridge deck and its abutments denotes influence of the connectivity exerted by the bridge structure.

8.7. Displacement

In the following, the computed results will be discussed at two specific time instants (Figure 8.8-Figure 8.12) during the shaking phase: i) the time step at maximum deck displacement (labeled as max time step, t = 2.9 s) to recognize inertial effects of the bridge-ground system, and ii) the time step at the end of shaking (labeled as final time step, t = 15 s) to investigate the permanent deformation.

8.7.1. Deformation at Maximum Deck Displacement

Figure 8.8 shows the longitudinal (i.e., X-direction) relative displacement contours at max deck displacement. It can be seen that the entire bridge-ground system is moving leftward (Figure 8.8) at this specific time instant, with displacement of the TM soil canyon on both side boundaries (X = 0 and X = 300 m) reaching about 0.07 m near the ground surface. Away from the bridge (Z = 0 m), slope crest displacements are significantly higher downslope (Location R0), and lower upslope (Location L0). At Z = 40 m, with the bridge deck connecting both sides, slope crest R1 displacement is lower than R0, restrained by resistance from the left side where L1 displacement became larger than L0.

8.7.2. Deformation at End of Shaking

Figure 8.9 depicts the longitudinal relative displacement contours at end of shaking. At the left and right boundaries, deformation of the TM soil canyon was minimal, only reaching about 0.01 m (Figure 8.9 and Figure 8.11). Within the canyon, the left and right downslope deformations are seen to interact, pushing against each other. Away from the bridge (Z = 0 m), downslope crest displacements were about -0.36 m at R0, compared to +0.03 m only at L0. At Z = 40 m, the bridge

through its deck and foundations acted as a strut that reduced deformations from the R0 -0.36 m to R1 of about -0.1 m, with resistance mobilized from the left side slope whose downslope deformation was reversed from the L0 of +0.03 m (downslope) to the L1 of -0.09 m (Figure 8.9 and Figure 8.11).

Figure 8.10 displays the vertical relative displacement contours at end of shaking. Peak settlement occurred near the right-side slope (location R2) and showed slumping of as much as 0.26 m (Figure 8.11). For this relatively narrow canyon geometry, the interaction of both slopes (Figure 8.10) resulted in the central section experiencing upward ground heave reaching of about 0.5 m (Figure 8.11). Finally, settlement is significantly lower at Z = 40 m, due to presence of the bridge's structural system (Locations R1, R3 compared to R0, R2).

It is worth noting that considerable interaction is taking place in terms of downslope permanent displacements of both slopes. In this regard, if unrestrained by the slope on the other side of this narrow canyon (based on conducted 2D plane-strain simulations, not shown), the right- and left-side slopes would experience much higher displacements of 5.0 m and 0.24 m, respectively (compared to the observed canyon-influenced 0.6 m, and 0.1 m).

8.7.3. Bridge Deck Response

Figure 8.12 displays relative displacement of the bridge deck, and pile caps B and C. Permanent displacement is initiated during the 2.4-2.9 s time interval due to the large fling motion pulse in the base input acceleration (Figure 8.7). The bridge lurches first slightly to the right in the downslope direction for pile cap B. Thereafter, pile cap C moves sharply to the left (downslope at this location) and continues to accumulate displacements throughout the remainder of the shaking phase. Along with these longitudinal displacements, vertical settlement (Figure 8.12b) is also seen to be much larger at the right embankment compared to its left counterpart. As discussed above,

this significant right-side downslope deformation has potentially helped to impede the corresponding left slope deformations, with pile cap B only exhibiting a permanent downslope value of +0.04 m. At the deck level, the large right-side downslope deformation forced the bridge to move leftwards, pushing into the left-side slope as an additional restraining mechanism.

8.7.4. Liquefaction and Accumulated Shear Strain

Figure 8.13 shows time histories of effective confinement p' divided by the initial value p'_0 (before shaking) at locations of M2 and M3. The ratio p'/p'_0 reaching 0 indicates loss of effective confinement due to liquefaction. With the medium dense Q2 sand at the elevation range of about 18.1-29.1 m, it is noted that the ratio p'/p'_0 at Z = 0.0 m decreased slightly faster than that at Z = 40 m closer to the bridge. Upon liquefaction, Q2 at both locations M2 and M3 attains its low specified residual shear strength of 2 kPa (Figure 8.13c and Table 8.1) at zero p'/p'_0. In light of the large deformations of the right-side slope (Figure 8.9), accumulated shear strains in this Q2 stratum and in the soft Q3b (Figure 8.14) are seen to be quite high. Away from the bridge (Z = 0 m), larger shear strains are noted within Q3b (Figure 8.15) and near the base of the liquefied Q2 (Figure 8.15b).

From the overall picture of shear strains γ_{xy} at the end of shaking (Figure 8.15), it may be noted that:

1. At the left and right boundaries of the ground domain, shear strain is relatively small reaching only about 0.5 %, mainly due to the high shear strength afforded by the stiff canyon AF, Q3a and TM strata (Figure 8.4 and Table 8.2).

2. At the right-side slope (Locations M2 and M3), downslope shear strains were accumulated, reaching peak values of about 14 % near the base of the liquefied sand Q2 layer. In this figure, the overall shear strain at Location M3 (Z = 40 m close to the structure) is lower than

that at Location M2 (Z = 0 m away from the bridge), due to restraining effects of the bridge structure and its local foundation.

8.8. Response of Bridge Structure

8.8.1. Axial Force

Figure 8.16 displays lateral displacement of the bridge structure and the deck axial force profiles at max time step and at end of shaking. At max time step, the entire bridge moves leftward with peak displacement of about 0.18 m at pile Cap C (Figure 8.16a). As such, compressive axial forces were imposed on the deck (Figure 8.16a).

Figure 8.16b shows lateral response at end of shaking with a peak displacement of about 0.5 m. As discussed above, both sides moved downslope towards the center of the narrow canyon, such that the entire bridge deck was in a compressive state (Figure 8.16b). Since there was no inertial effect, the axial force along the deck is constant within each span.

Figure 8.17 presents axial forces in the foundation piles before shaking, at max time step, and at end of shaking. As a reference, Figure 8.17a shows the computed self-weight axial force, with all supporting elements under compression throughout (i.e., negative axial force). At max time step, pile groups B1-B10, C1-C10 (below elevation 30 m) are under tension (positive axial force). For this particular deformed configuration, peak compressive axial force reached a high value of about 3200 kN in D1-D5 piles (yielding force being 3300 kN in Figure 8.6a) at the elevation range of about 21-35 m where the soft clay Q3b is encountered. These high values of axial forces in D1-D5 are attributed to ground settlement at the right-side slope which exerted additional downdrag forces on these piles. Nevertheless, all pile forces remained within the elastic capacity of the corresponding cross-sections (Figure 8.6). At end of shaking, most piles are in compression, except for sustaining a low level of tensile force (about 100 kN) at the lower zones

of C1-C10 (Figure 8.17). In general, it is noted that all pile forces remained within the elastic range (Figure 8.6) after shaking.

8.8.2. Bending Moment and Ductility Demand

Figure 8.18 depicts the bending moment profiles. Generally, it can be seen that the highest values occur at: i) the pier cap connection, ii) the interface between liquefied and non-liquefied soils, and iii) the pile-deck connections. Seismic loading intensity due to these moments is addressed below in the form of ductility demand defined as the ratio of ultimate attained curvature ϕ_u to yield curvature ϕ_y. As such, Figure 8.19 shows the ductility demand profiles for the bridge foundations (values < 1 are not shown for clarity). It can be seen that the highest values occurred at: i) the pile-deck connection for A, D piles, (ii) the interface between liquefied and non-liquefied soils, and iii) pile segments within the zone of the soft clay Q3b for D piles. The attained peak values, reaching as much as 30 would generally be considered of concern and would warrant closer scrutiny.

A note of considerable importance is that some of these highest values are occurring on the left side that experienced much lower downslope deformation. The reason being that the large downslope displacements of the right-side slope pushed the bridge structure leftwards causing these piles to experience significant lateral deformations away from the canyon. Due to the interaction of left and right-side slopes through the rigid bridge superstructure, substantial damage occurred at the pile-deck connections on both sides and interface between liquefied and non-liquefied soils.

8.9. Bridge-Ground System under Reverse Motion

To assess influence of input motion polarity, an additional numerical simulation was conducted reversing direction of the employed input motion (Figure 8.7a). The fling motion pulse

in this particular shaking record, which dictated a substantial level of the accumulated global site deformations (Figure 8.9), motivated investigation of this additional scenario. The results in terms of maximum deck displacement and end of shaking displacement are shown in Figure 8.20 and Figure 8.21. As might be expected, deformation at maximum deck displacement is quite different with the left side slope dominating (Figure 8.8 and Figure 8.20).

At end of shaking (Figure 8.21), it can be seen that the right-side slope displacement (0.55 m) is slightly lower when compared to that of Figure 8.9 (0.6 m). However, it is also seen that the left side downslope displacement became substantially higher.

The ductility demand at end of shaking is displayed in Figure 8.22. Despite the difference in the ground deformation pattern (Figure 8.9 and Figure 8.21), it appears that ductility demand ended up being rather similar in this case (Figure 8.19 and Figure 8.22).

8.10. Retrofit Analyses

Strictly for the purpose of illustration, potential use of the numerical model to conduct retrofit studies is addressed briefly in this section. For that purpose, two additional numerical simulations were conducted by adding concrete walls (linear elastic, with Young's modulus E = 30 GPa) around the abutment and wing-walls (Figure 8.23). In configuring this mitigation approach, attention was given to the option where retrofit is implemented at the abutments rather than within the canyon, where cost and effort would substantially increase. The conceptual mitigation mechanisms discussed below, would be implemented in practice by appropriate techniques to introduce equivalent stiffness and strength into the existing foundations.

The first scenario (Figure 8.23a and Figure 8.24) was introduced for direct comparison to the original results (Figure 8.19) by adding a concrete wall on the outer side of the wing-walls. As seen in Figure 8.24, the ductility demand was significantly decreased at the upper section of A, D

piles, only reaching about 18. Furthermore, the overall ductility demand values of D piles in soft clay Q3b were reduced to less than 1 (i.e., elastic range without any damage). In the second scenario (Figure 8.23b), one additional cement wall was placed behind the abutment to achieve a more effective solution of mitigation for the entire bridge. As seen in Figure 8.25, most ductility demand values were lower than 1 (elastic range) except for the pile-deck connections. In this regard, only relatively inexpensive repairs would be needed, close to the ground surface.

8.11. Summary and Conclusions

A full 3D FE analysis framework was presented to study a number of salient features associated with the liquefaction-induced seismic response of a bridge-ground system in a narrow canyon (Cubrinovski et al. 2014). For that purpose, an idealized 3D FE model was developed, motivated by the details of an actual bridge-ground configuration. The bridge-ground system and the corresponding numerical analysis details were discussed. Displacement, moment, axial forces, and ductility demand of the structure, resulting from the liquefaction-induced ground deformations were explored. In addition, the bridge's restraining influence, and effect of input motion direction were investigated. The numerical framework and the insights derived from this study are of general relevance to bridge-ground seismic response in narrow canyon scenarios.

Specific observations and conclusions include:

1) For relatively narrow canyon geometries, soil in the central sections might be experiencing a state of higher lateral confinement. This mechanism might have a significant influence on the liquefaction response at such locations. Furthermore, upward heave is likely to be an additional involved mechanism.

2) As highlighted in earlier studies (Shin et al. 2008; Zhang et al. 2008; Cubrinovski et al. 2014, McGann and Arduino 2015; Qiu et al. 2020), response is highly dependent on the soil

ground system as an integral global entity. Connectivity provided by the bridge deck, soil profile and its variation along the bridge length, and geometric configuration of the slopes and the underlying water channel are all factors that can significantly influence the outcome.

3) Pile damage mainly occurred at the pile-deck connection as observed in an actual short-span bridge and presented by Cubrinovski et al. 2014. In addition, the piles could incur damage at the interfaces between liquefiable and non-liquefiable or soft clay and stable soil strata.

4) The bridge structure and its foundations act as a strut that exerted a significant added restraint to the slope deformations on both sides. These restraining effects partially stem from the bridge's global connectivity and the corresponding abutment-to-abutment interaction, which can be of much influence.

5) Peak demands might occur due to the combined inertial and kinematic load during the shaking event. In a simplified analysis, both inertial as well as kinematic load cases should be considered.

6) Polarity of the input motion may influence the outcomes, and further attention to this matter is warranted from the seismological point of view.

8.12. Acknowledgements

Chapter 8, in full, is currently being prepared for submission for publication of the material as it may appear in the following journal publication (The dissertation author was the primary investigator and author of this paper):

Qiu, Z., Lu, J., Ebeido, A., Elgamal, A., Uang, C. M. and Martin, G. "Bridge in Narrow Canyon: Seismic Response and Liquefaction-induced Deformations."

Table 8.1 Sand (Figure 8.4) model parameters (Khosravifar et al. 2018)

Model Parameters (PressureDependMultiYield03)		Q2	Q4
Reference mean effective pressure, p'_r (atm)		2.0	2.7
Mass density, ρ (t/m^3)		1.89	1.92
Maximum shear strain at reference pressure, $\gamma_{max,r}$		0.1	0.1
Low-strain shear modulus at reference pressure, G_r (MPa)		73.8	104
Stiffness dependence coefficient d, $G = G_r(\frac{\boldsymbol{P'}}{\boldsymbol{P'_r}})^{\boldsymbol{d}}$		0.5	0.5
Poisson's ratio v for dynamics		0.4	0.4
Shear strength at zero confinement, c (kPa)		2.0	2.0
Friction angle ϕ, with resulting shear strength defined as $p'\sin\phi$		35°	37°
Phase transformation angle		29°	30°
Contraction coefficient, c_1		0.035	0.02
Contraction coefficient, c_2		3.0	3.0
Contraction coefficient, c_3		0.2	0.2
Dilation coefficient, d_1		0.15	0.2
Dilation coefficient, d_2		3.0	3.0
Dilation coefficient, d_3		0.2	0.2
Additional contraction parameters	b_1	0.2	0.15
	b_2	20	20
	b_3	0.0	0.0
	b_4	0.001	0.001

Note: For each involved soil layer, the soil-pile friction angle δ and/or the soil-pile adhesion c_A are assumed equal to the corresponding friction angle and/or cohesion, respectively.

Table 8.2 Clay model parameters (Figure 8.4)

Model parameters (PressureIndependMultiYield)	AF	Q1	Q3a	Q3b	TM
Mass density, ρ (t/m^3)	1.92	1.84	1.92	1.84	2.16
Shear modulus, G (MPa)	117	71	139.3	75.2	293.0
Poisson's ratio for dynamics, v	0.4	0.4	0.4	0.4	0.4
Shear strength (kPa)	80.0	40.0	108.0	53.0	400.0
Shear strain at maximum shear strength	0.1	0.1	0.1	0.1	0.1

Note: For each involved soil layer, the soil-pile adhesion c_A is assumed equal to the corresponding cohesive strength

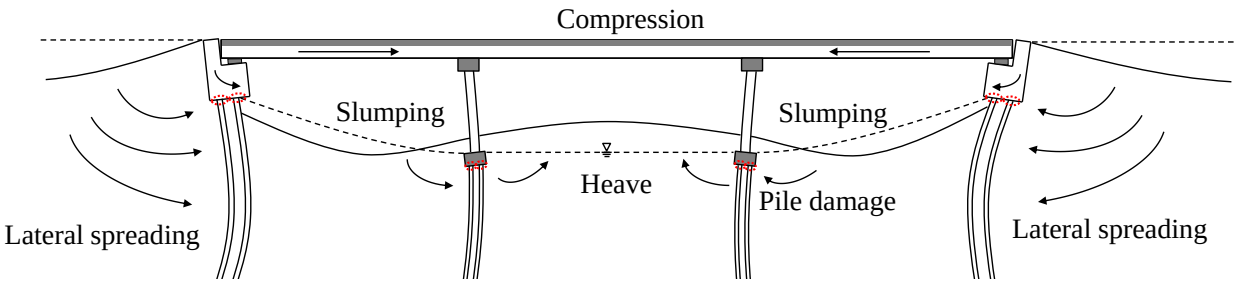

Figure 8.1 Schematic illustration of spreading-induced damage mechanism

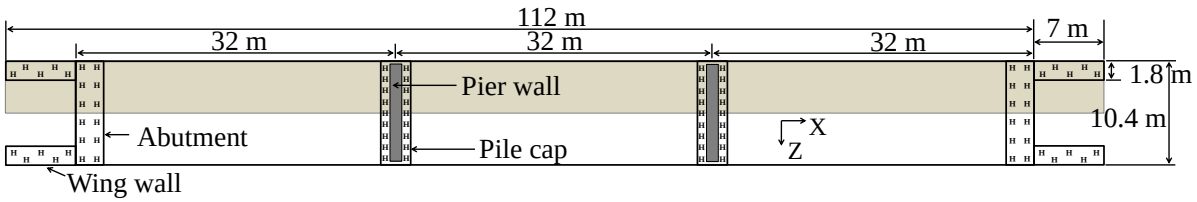

(a)

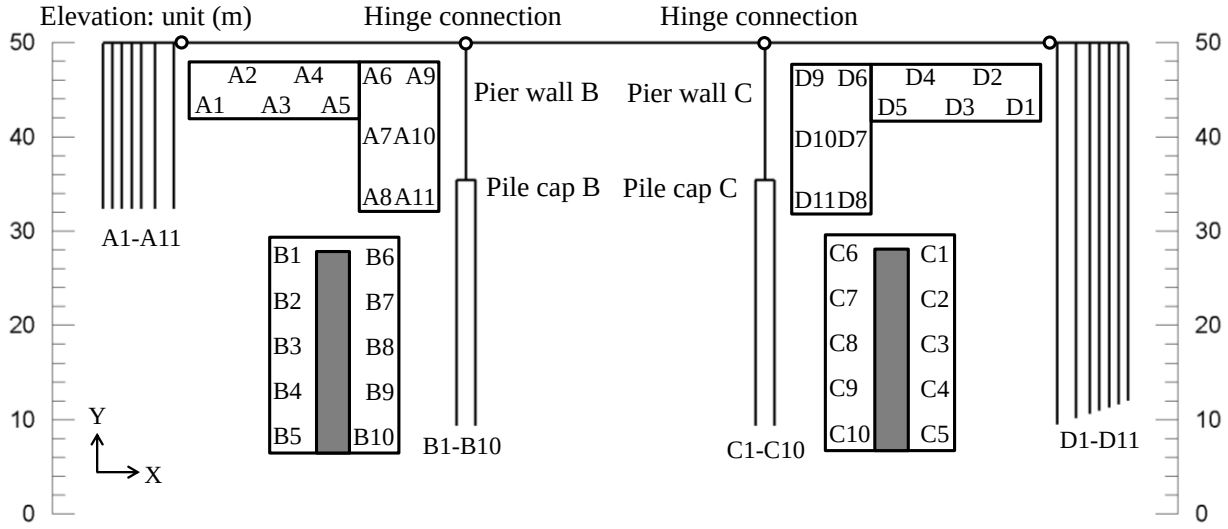

(b)

B, C reinforced concrete pier walls

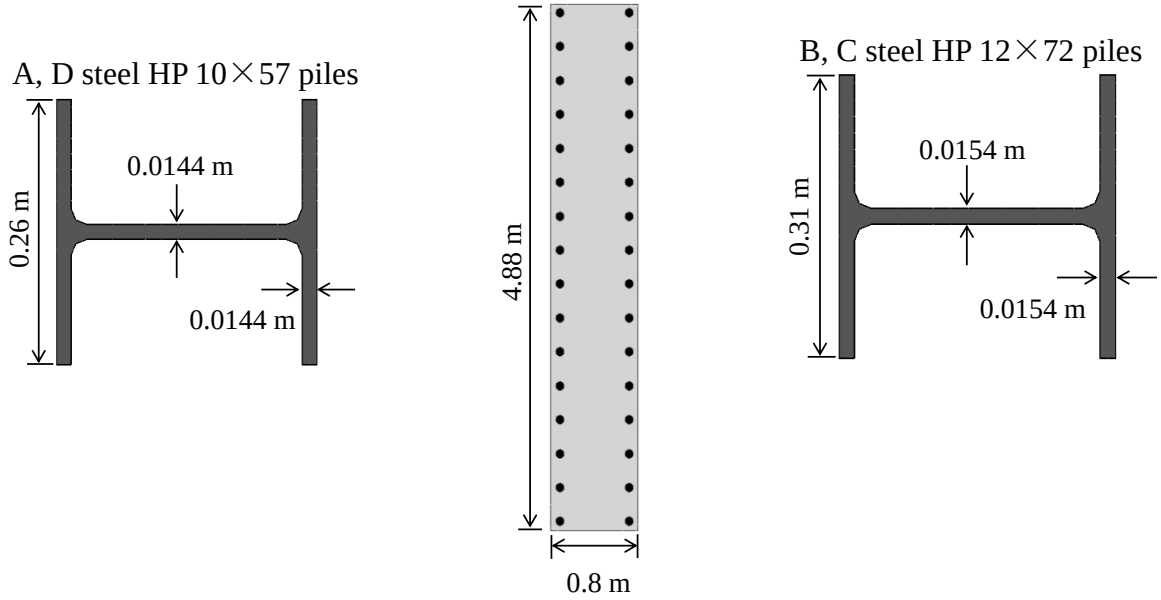

(c)

Figure 8.2 Bridge configuration: (a) Plan view (upper half of bridge is modeled in view of symmetry); (b) Elevation view of bridge and plan view of foundations systems; (c) Cross sections

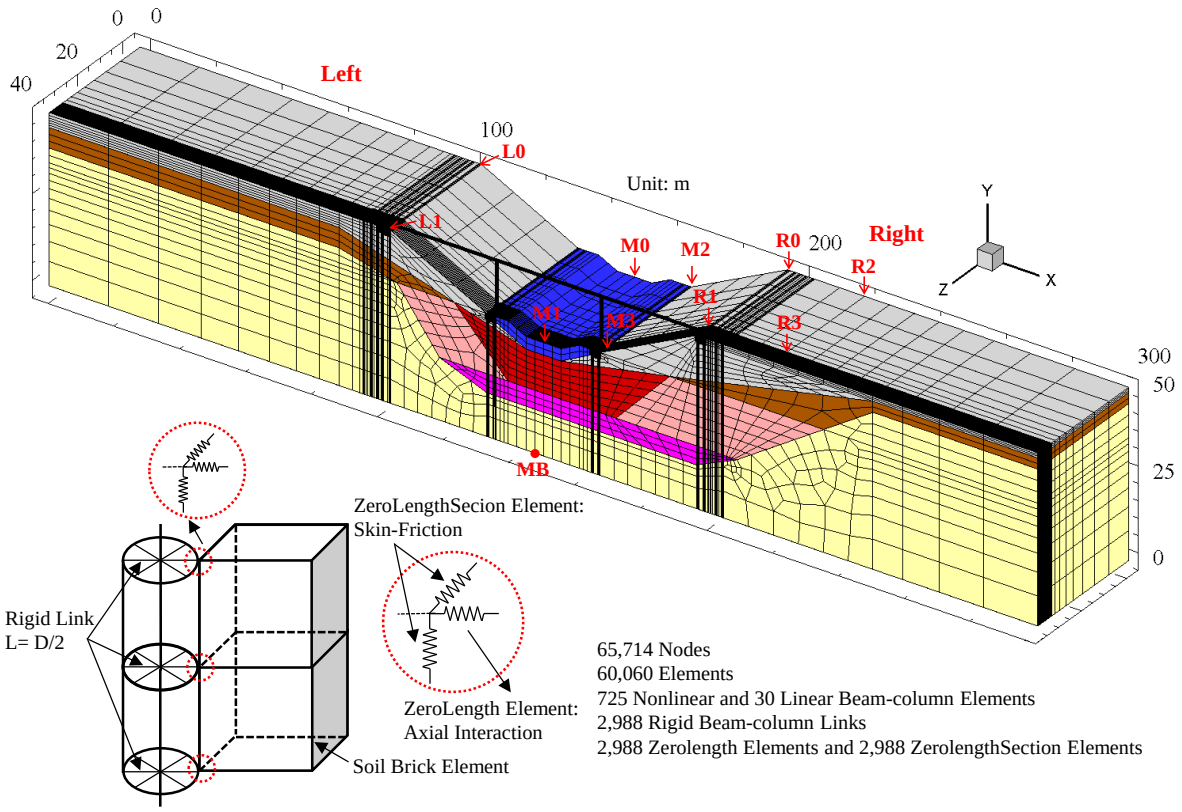

(a)

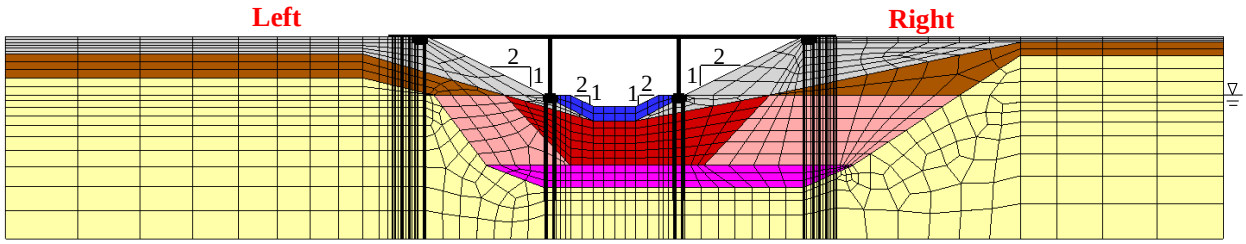

(b)

Figure 8.3 Finite element model of bridge-ground system (half mesh due to symmetry): (a) Isometric view; (b) Elevation view

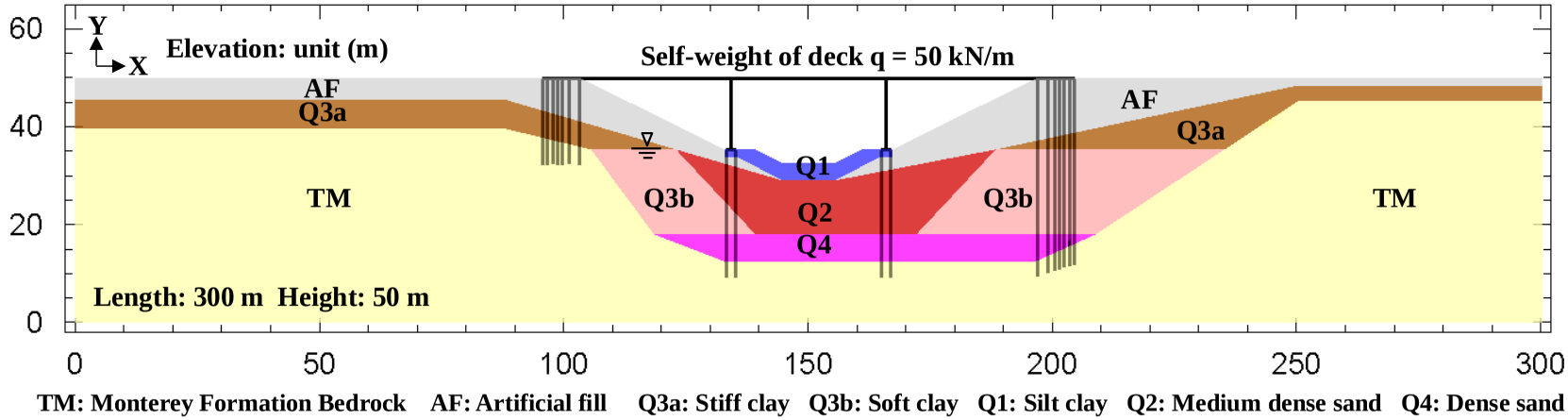

Figure 8.4 Ground configuration

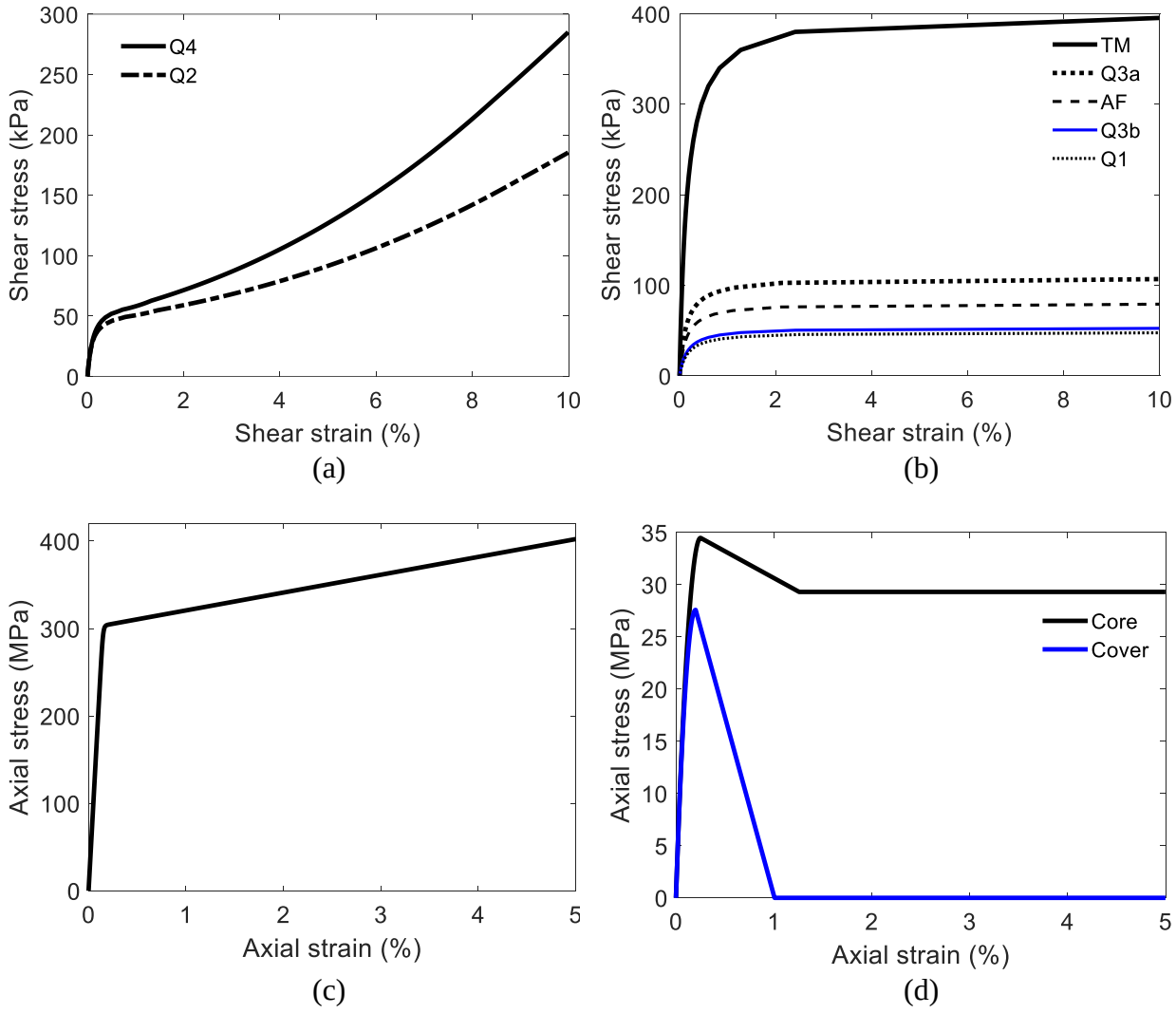

Figure 8.5 Material model response: (a) Sand model under undrained condition; (b) Clay (PIMY); (c) Steel02; (d) Concrete01

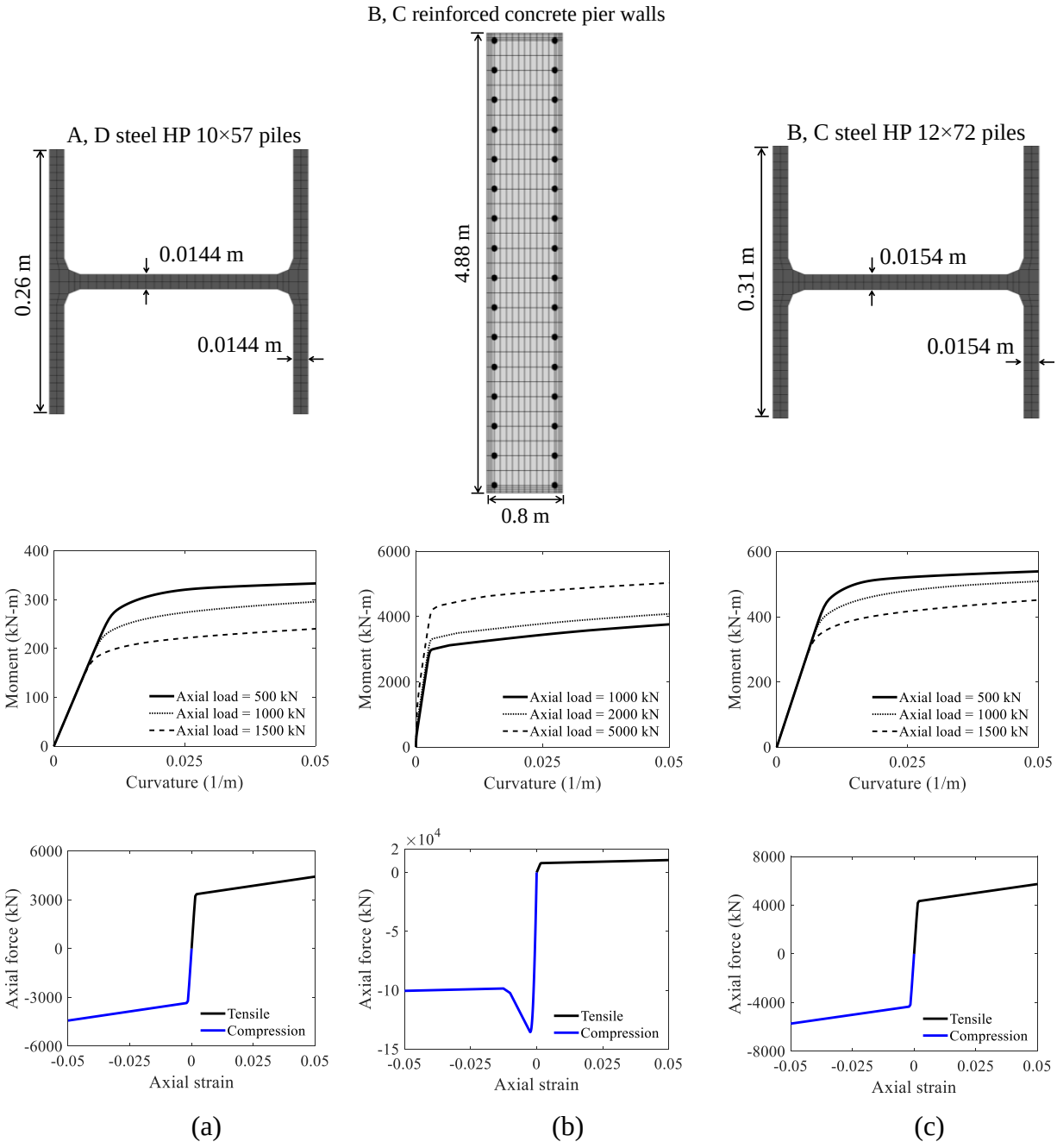

Figure 8.6 Fiber sections and response: (a) A, D piles; (b) B, C pier walls; (c) B, C piles

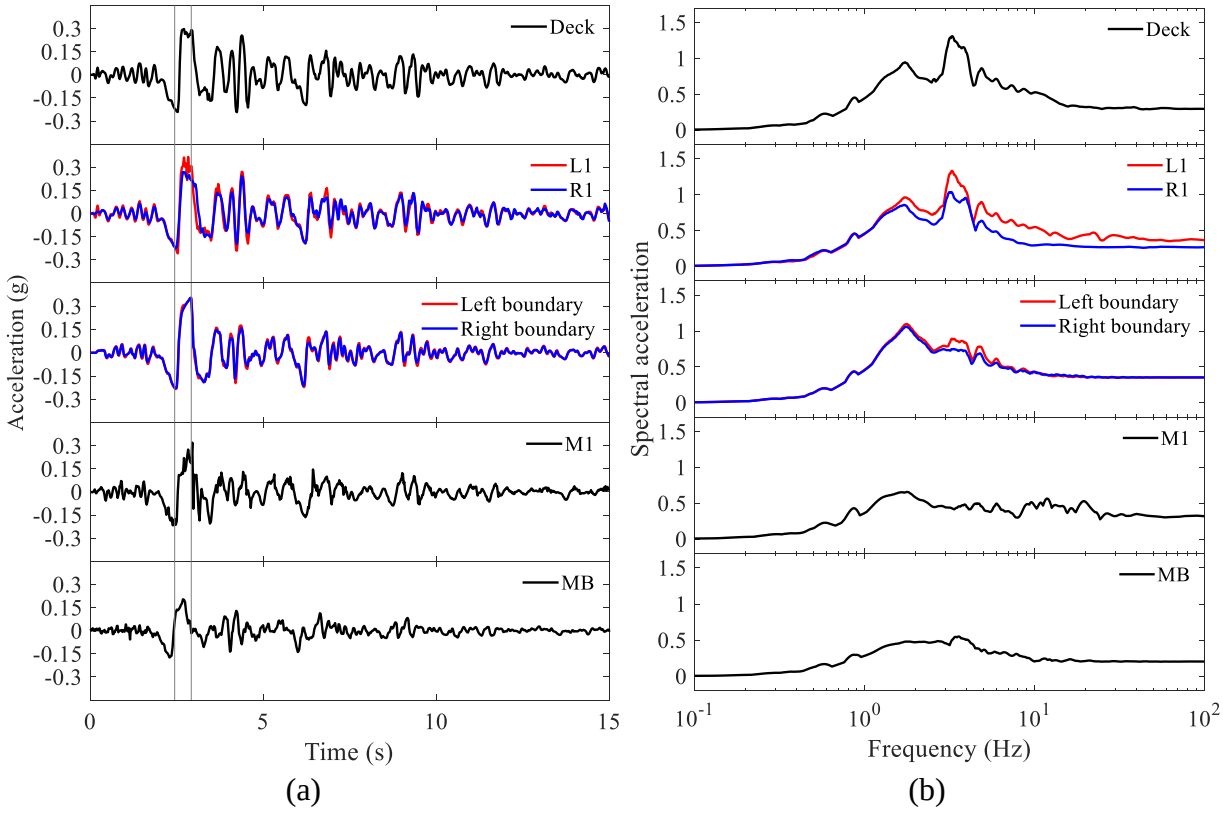

Figure 8.7 Acceleration response along the bridge-ground configuration (Figure 8.3): (a) Time histories; (b) Spectra (5 % damped)

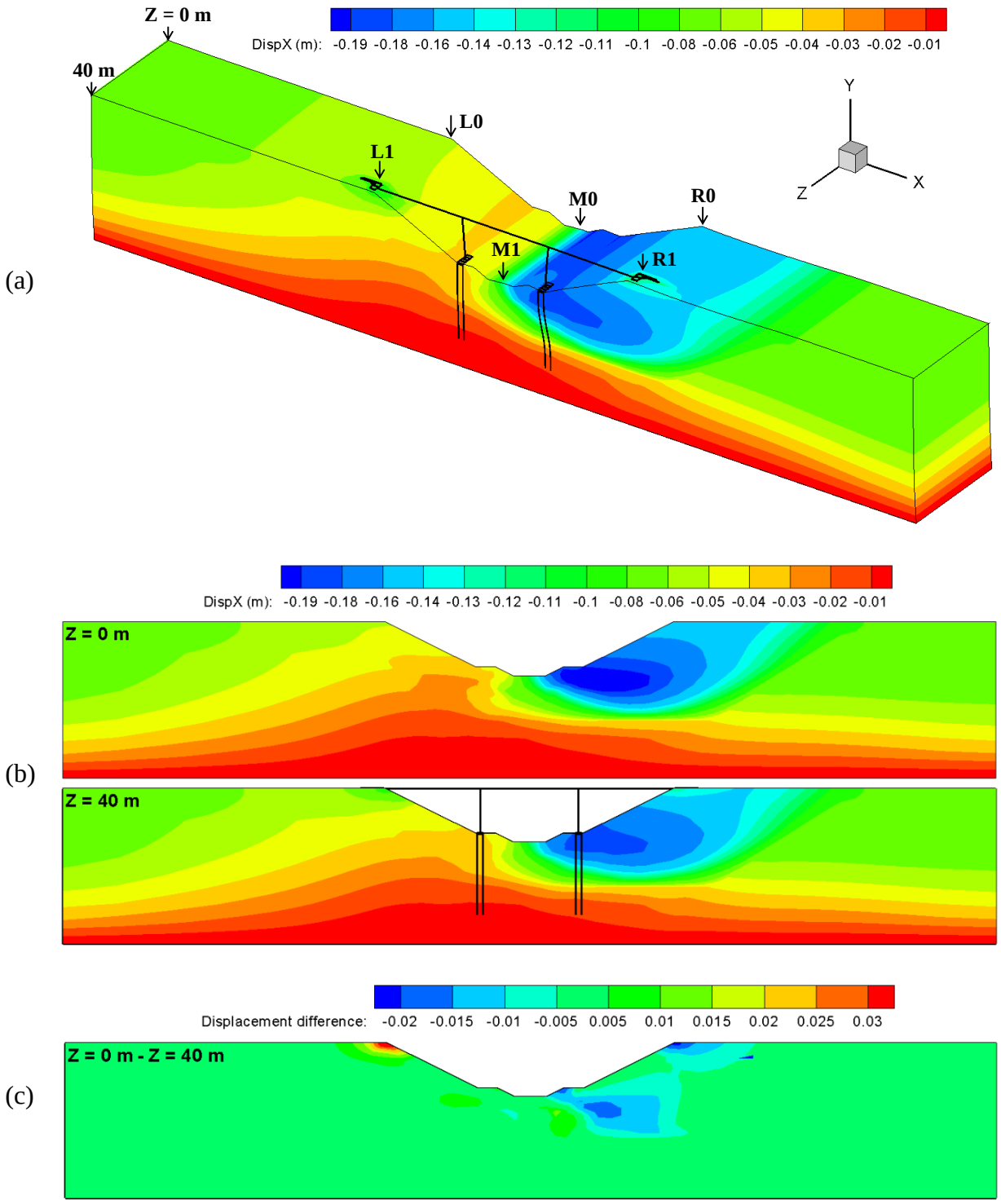

Figure 8.8 Longitudinal displacement contours at maximum deck displacement: (a) Isometric view; (b) Side views at Z = 0 m, 40 m (factor = 10); (c) Difference between Z = 0 and 40 m

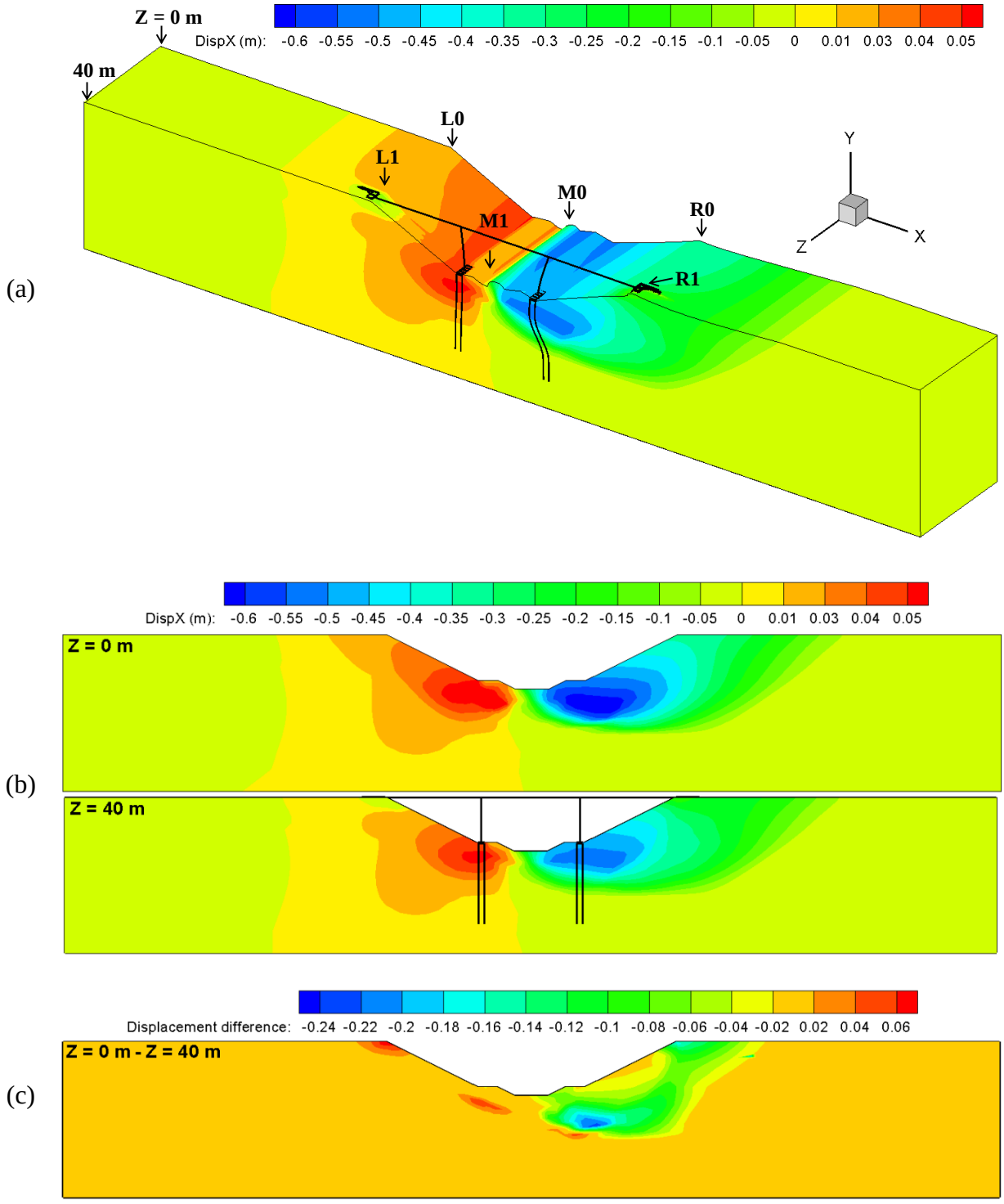

Figure 8.9 Longitudinal displacement contours at end of shaking: (a) Isometric view; (b) Side views at Z = 0 m, 40 m (factor = 10); (c) Difference between Z = 0 and 40 m

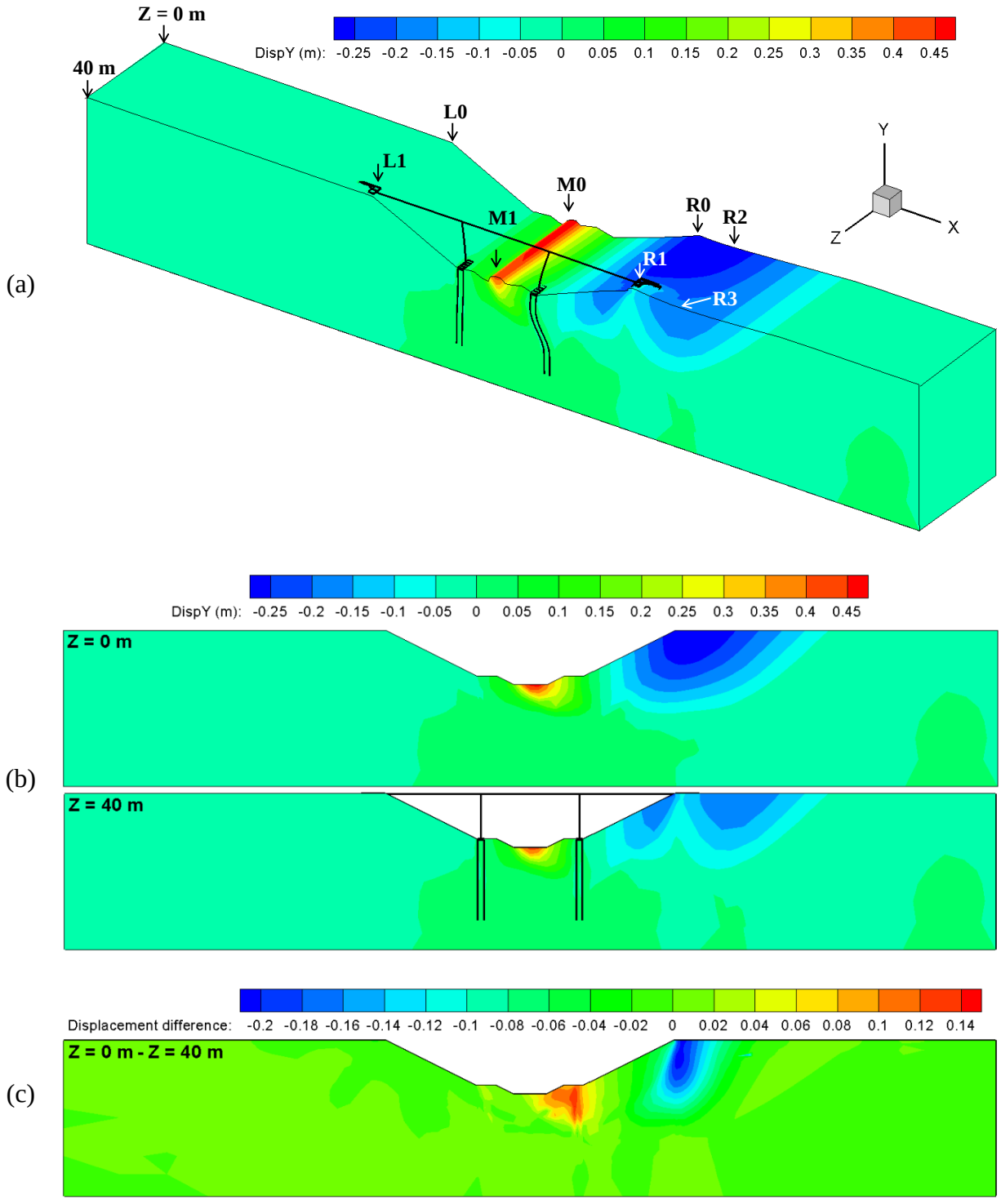

Figure 8.10 Vertical displacement contours at end of shaking: (a) Isometric view; (b) Side views at Z = 0 m, 40 m (factor = 10); (c) Difference between Z = 0 and 40 m

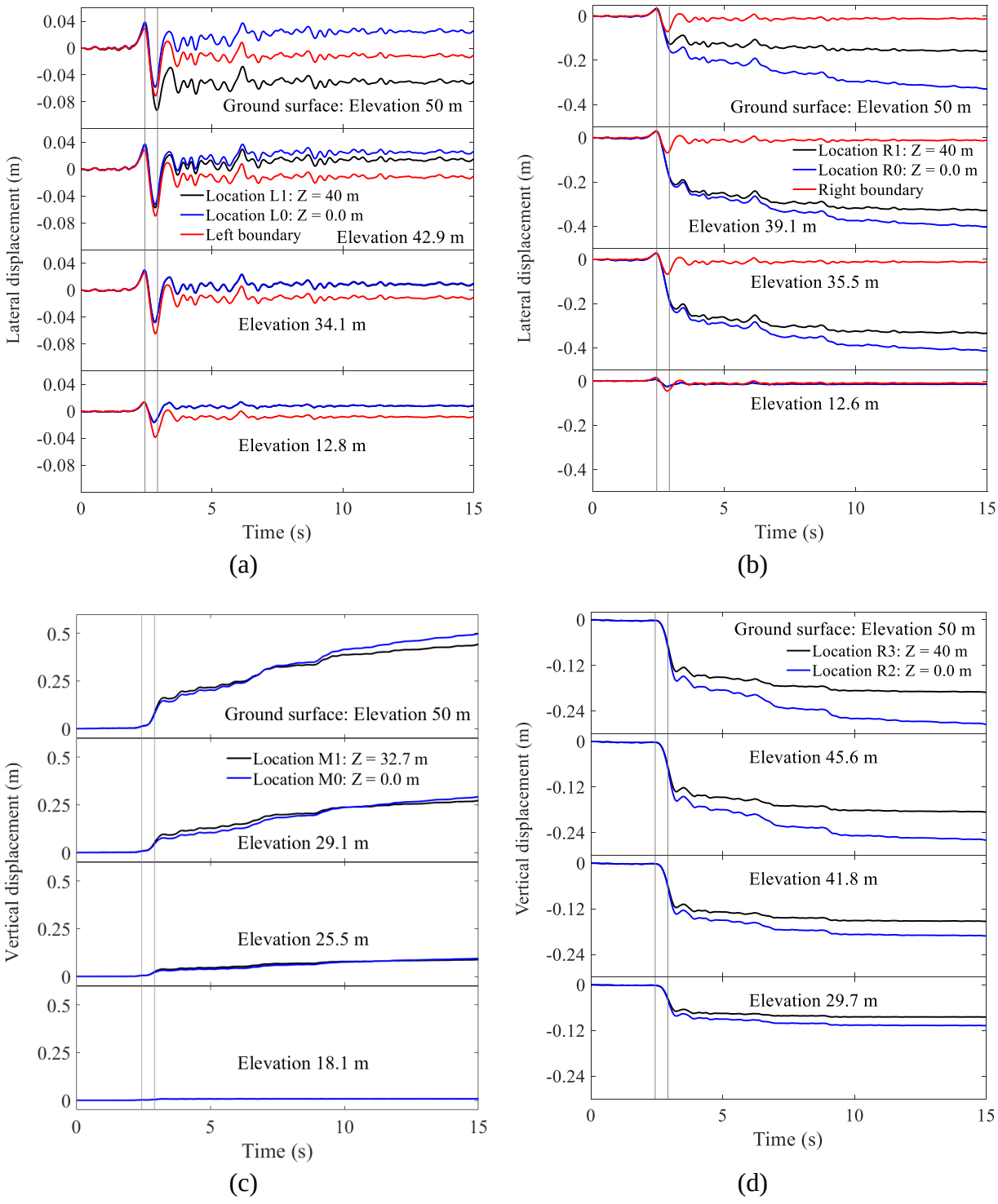

Figure 8.11 Ground displacement time histories: (a) Locations L0, L1; (b) Locations R0, R1; (c) Locations M0, M1; (d) Locations R2, R3

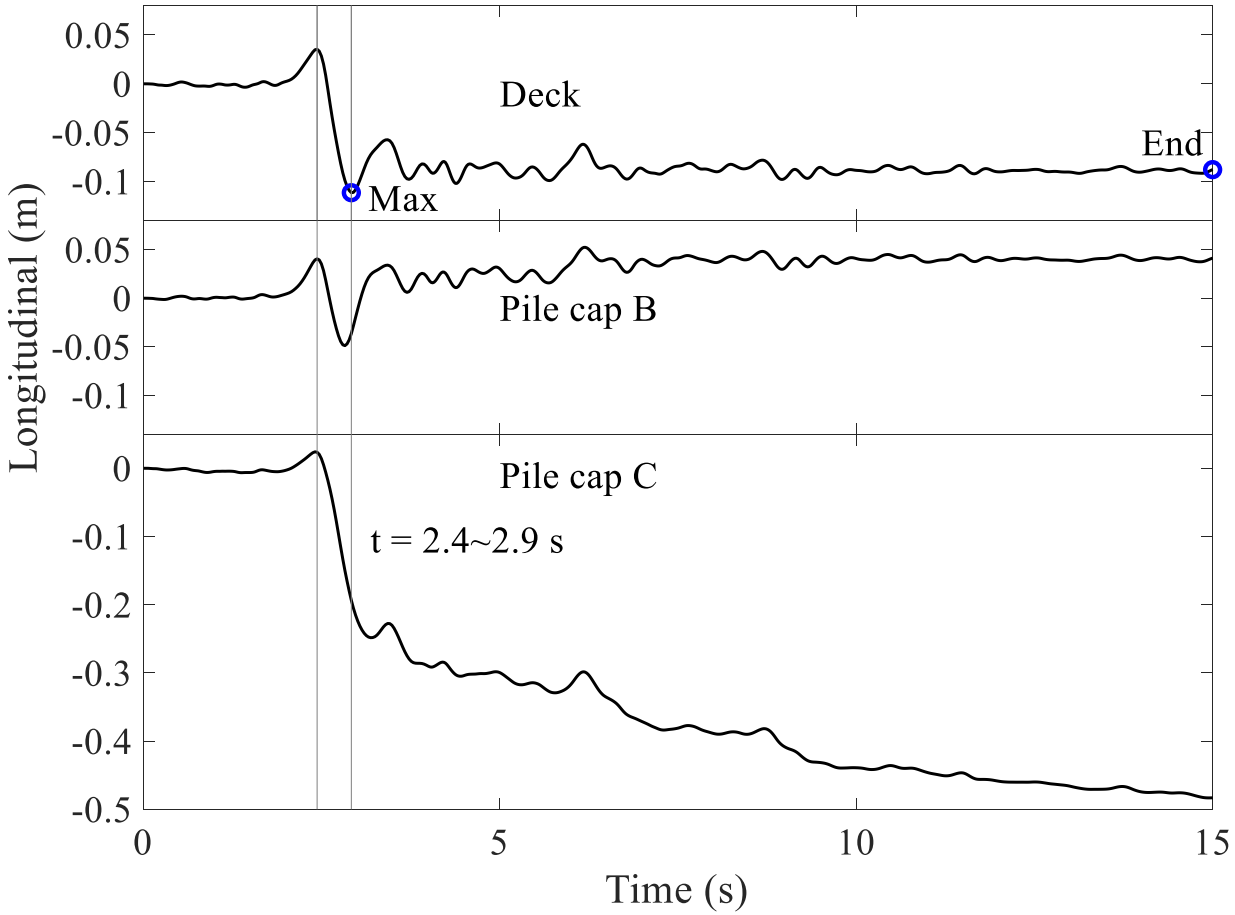

(a)

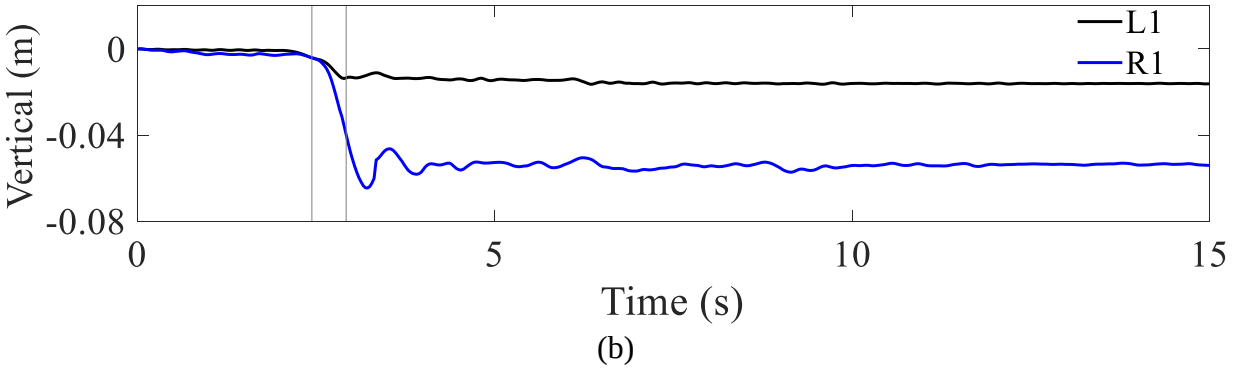

(b)

Figure 8.12 Bridge (Figure 8.2 and Figure 8.3) relative displacement time histories: (a) Longitudinal (positive towards the right and negative towards the left); (b) Vertical (negative is settlement)

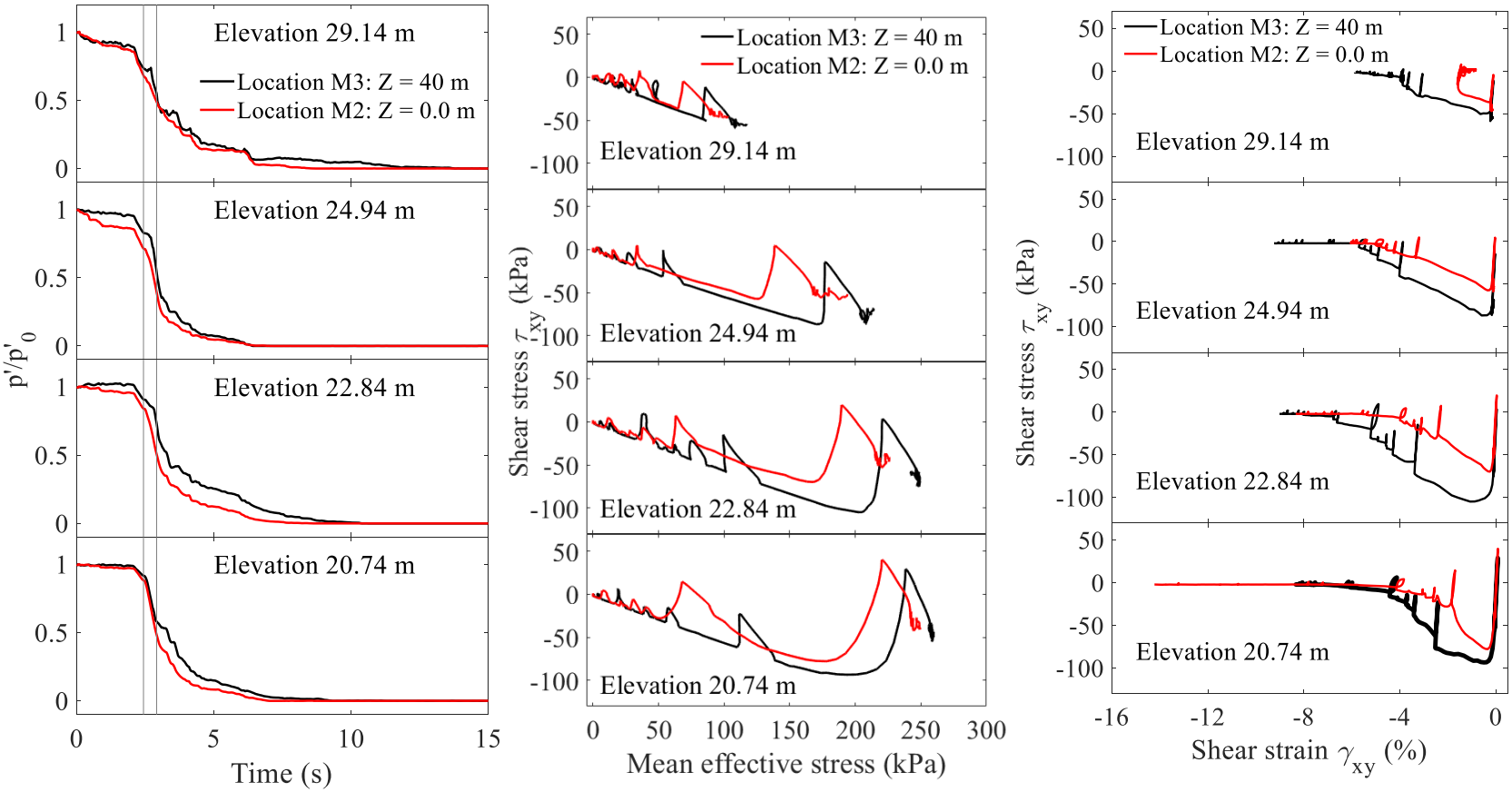

Figure 8.13 Soil response at Locations M2 and M3 (Figure 8.3): (a) Effective confinement ratio; (b) Mean effective stress-shear stress; (c) Shear stress-strain

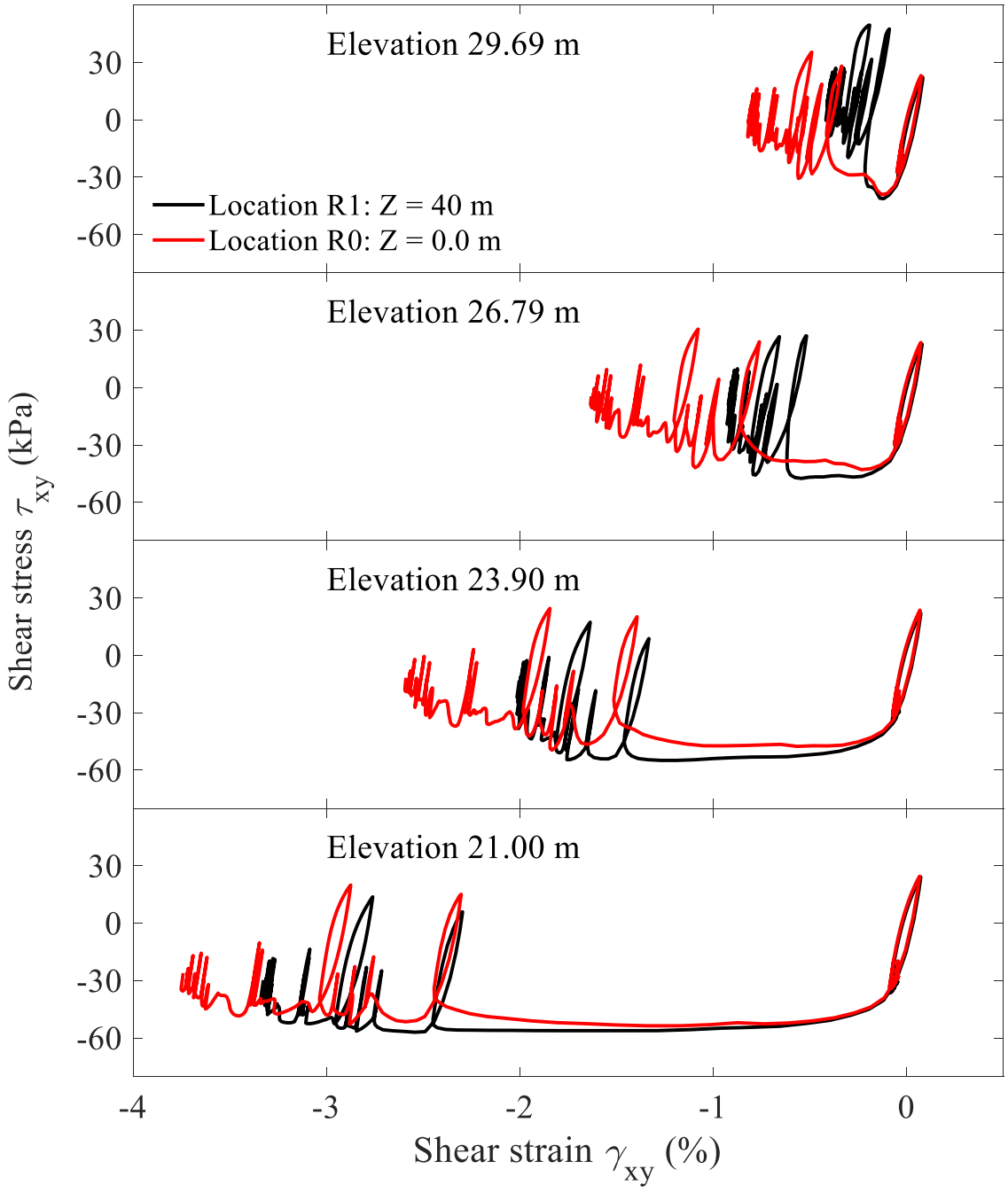

Figure 8.14 Shear stress-strain in Q3b clay layer at Locations R0, R1

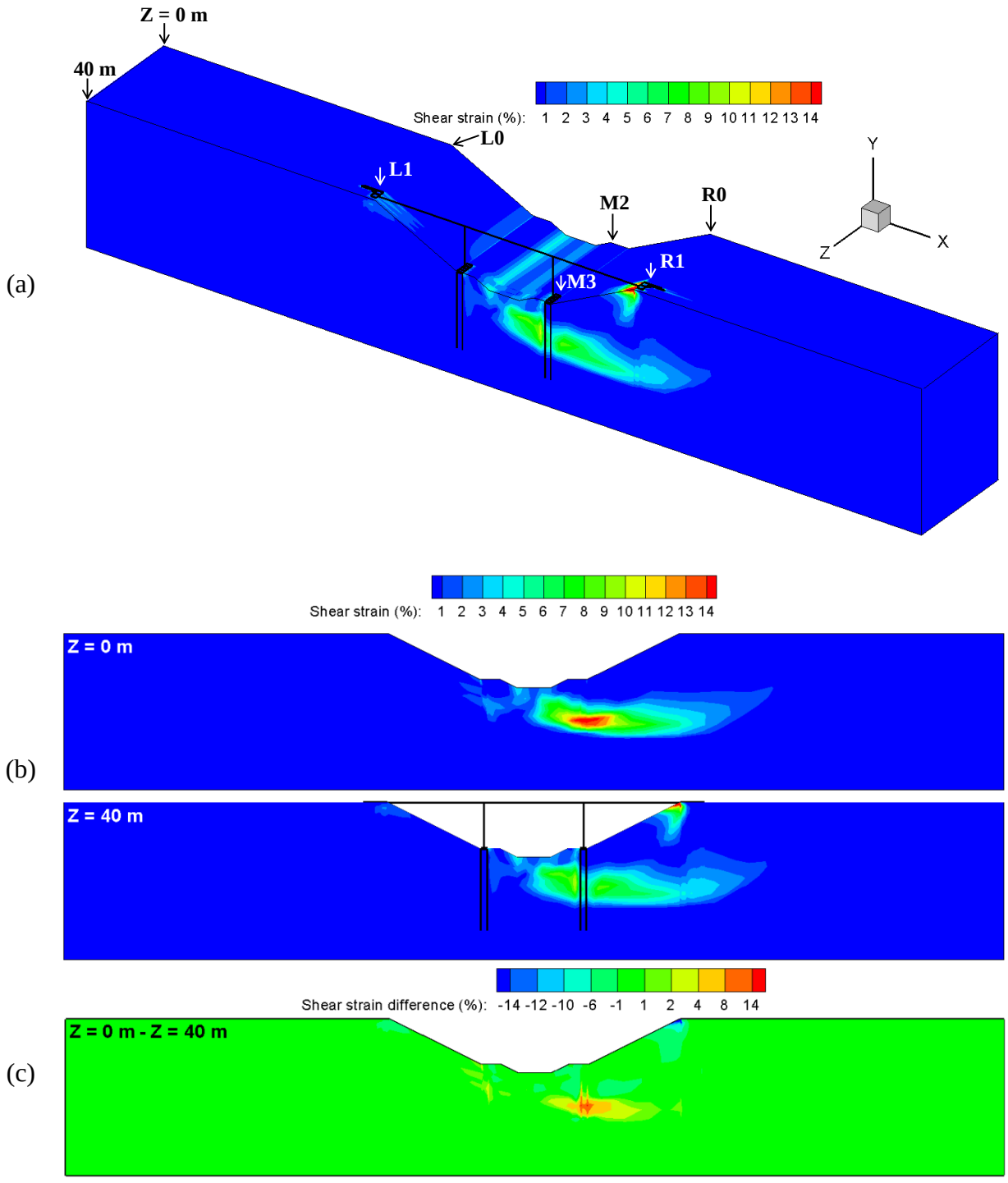

Figure 8.15 Contour of shear strain γ_{xy} at end of shaking: (a) Isometric view; (b) Side views at Z = 0 m, 40 m; (c) Difference between Z = 0 and 40 m

(a)

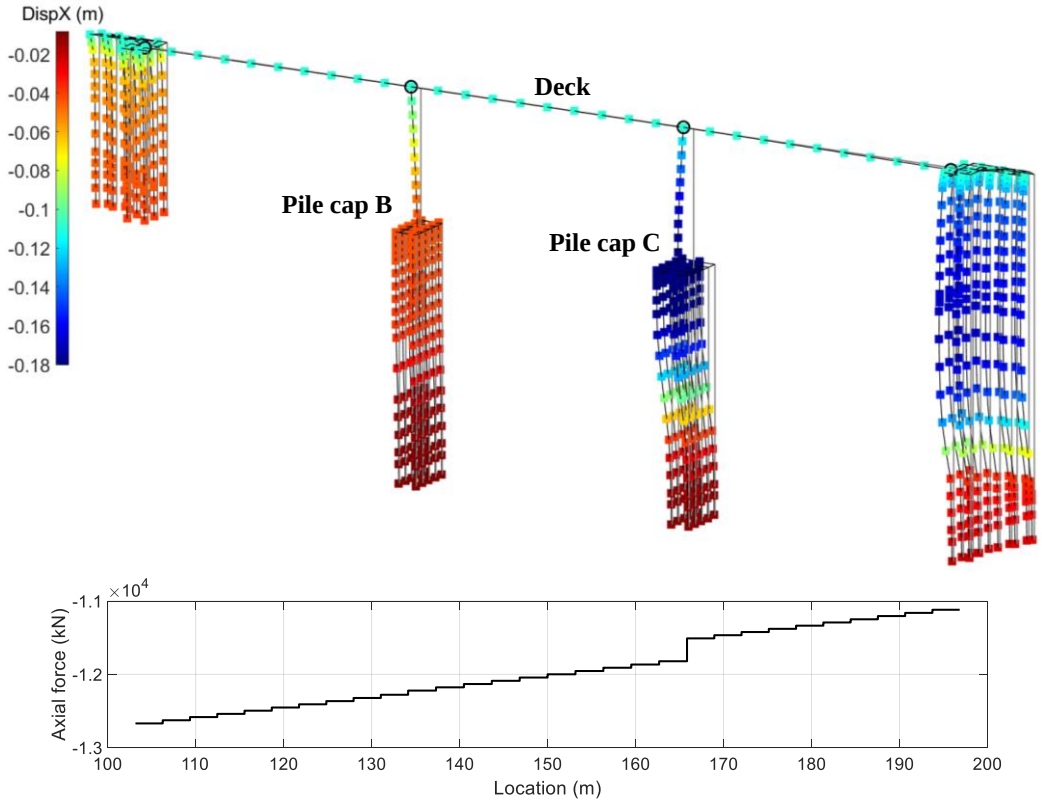

(b)

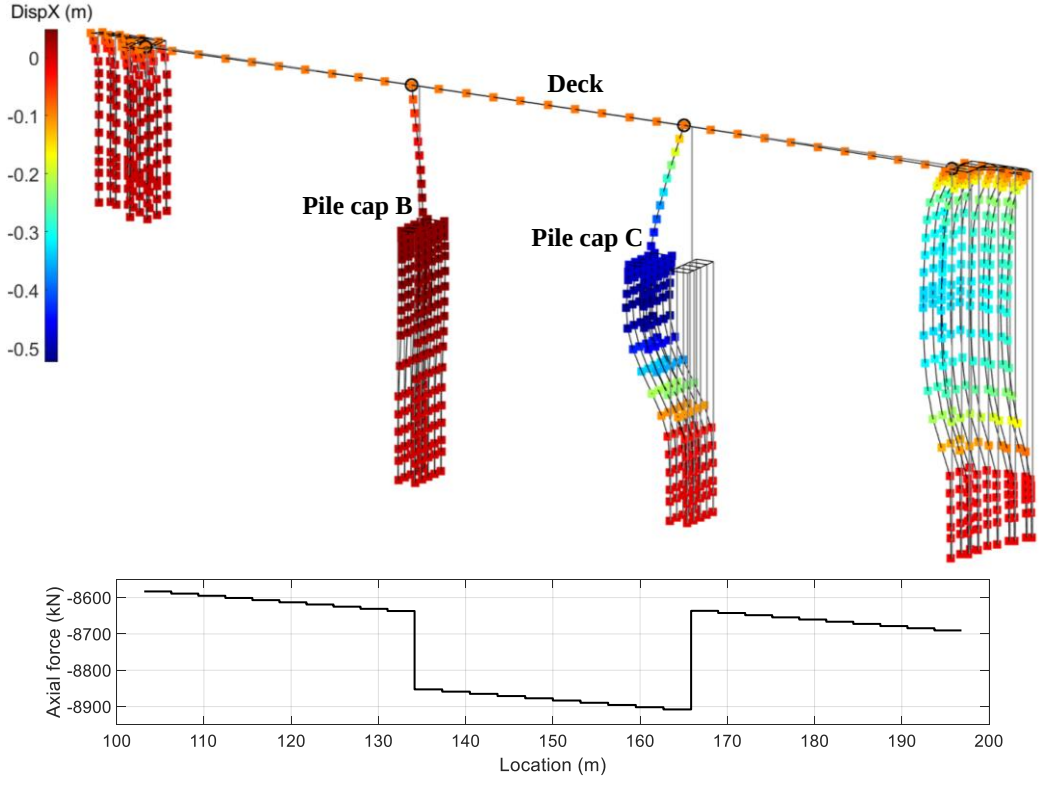

Figure 8.16 Deformed FE mesh of bridge and deck axial forces: (a) At maximum deck displacement; (b) At end of shaking (contour fill shows the horizontal displacement; factor = 10)

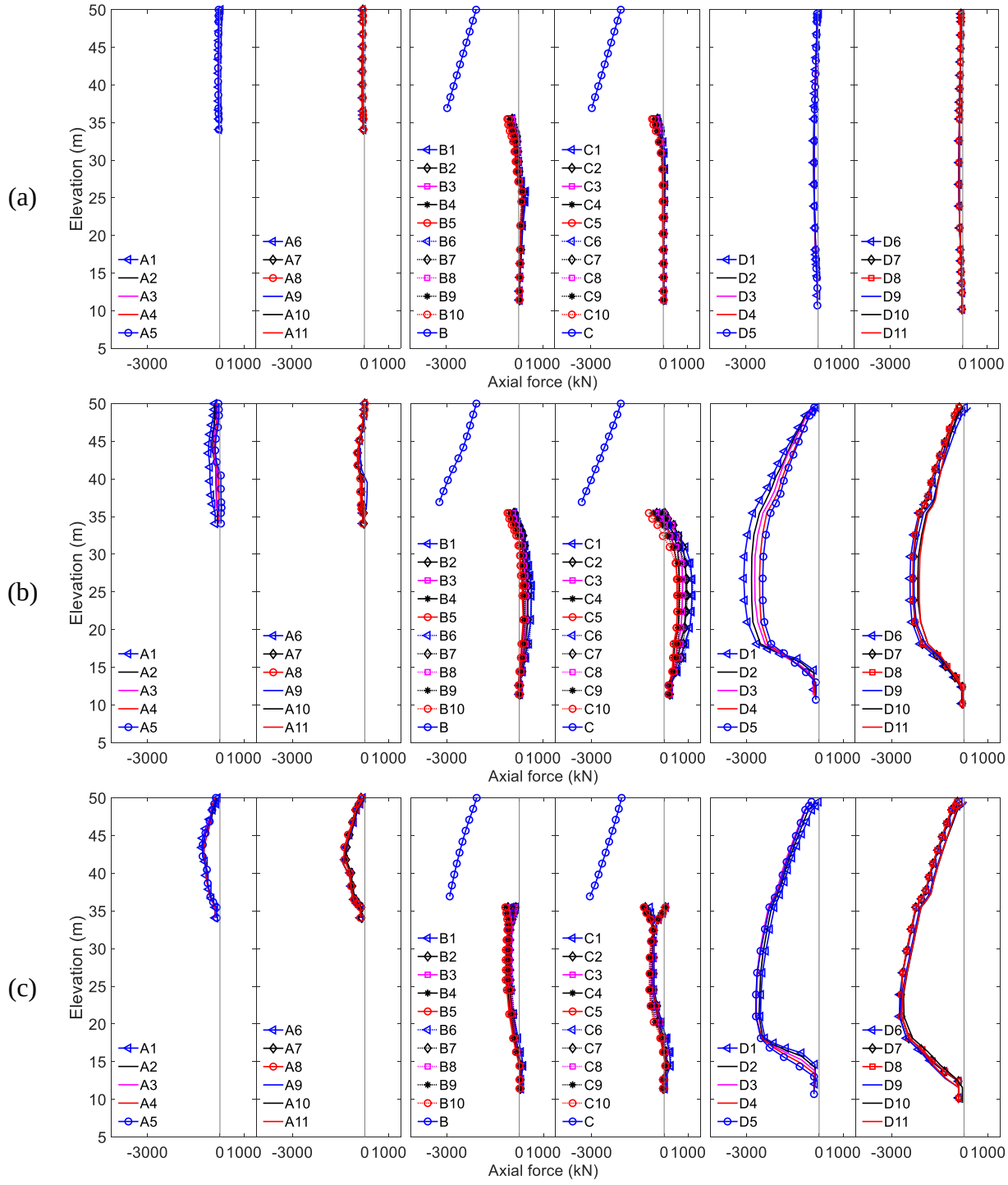

Figure 8.17 Axial force: (a) Before shaking; (b) At maximum deck displacement; (c) At end of shaking (negative represents compression and positive represents tension)

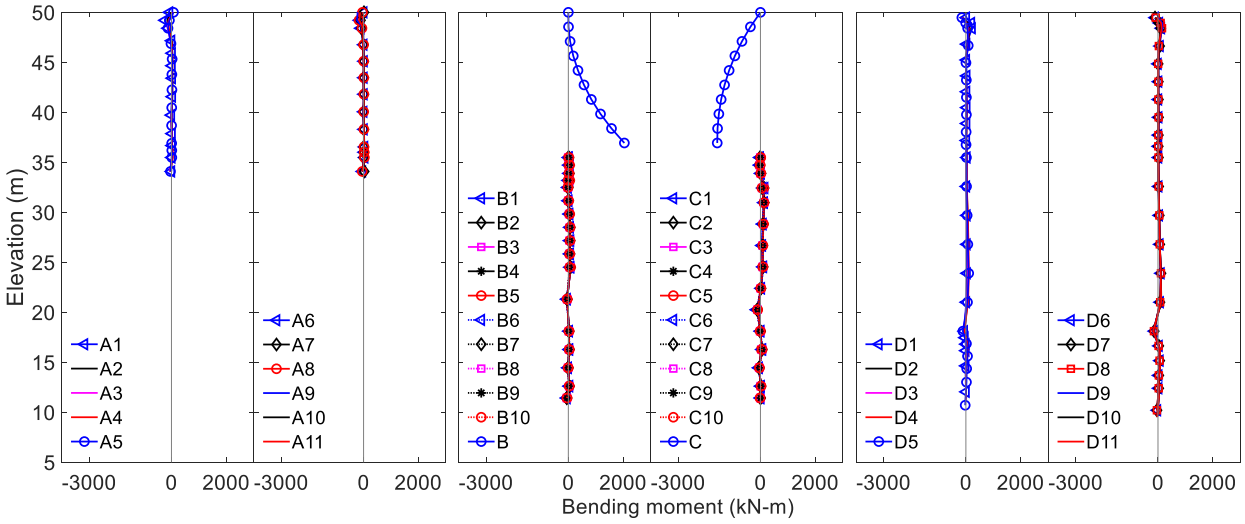

(a)

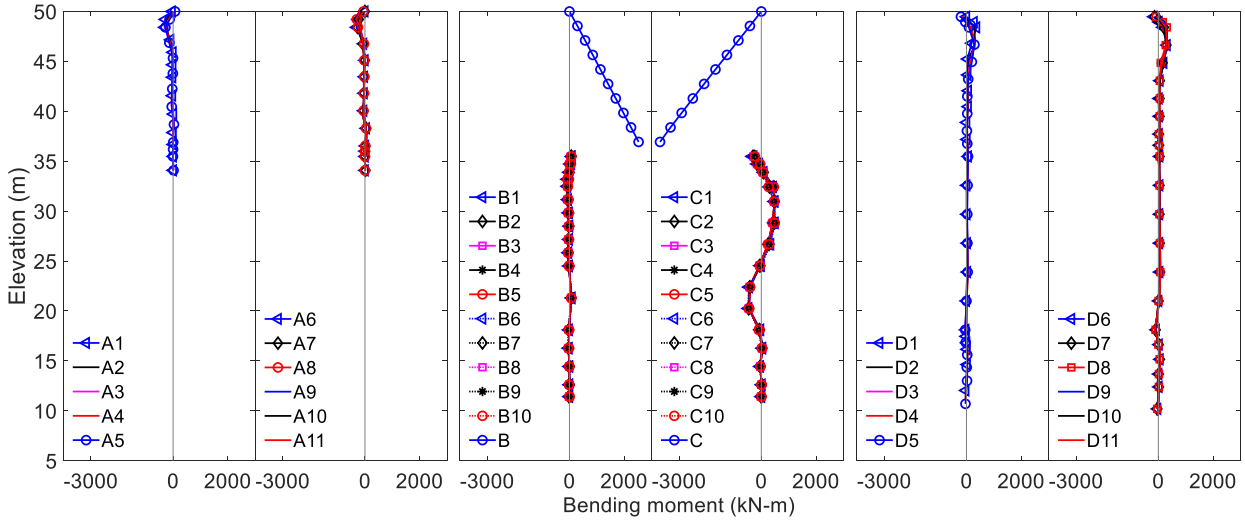

(b)

Figure 8.18 Bending moment: (a) At maximum deck displacement; (b) At end of shaking

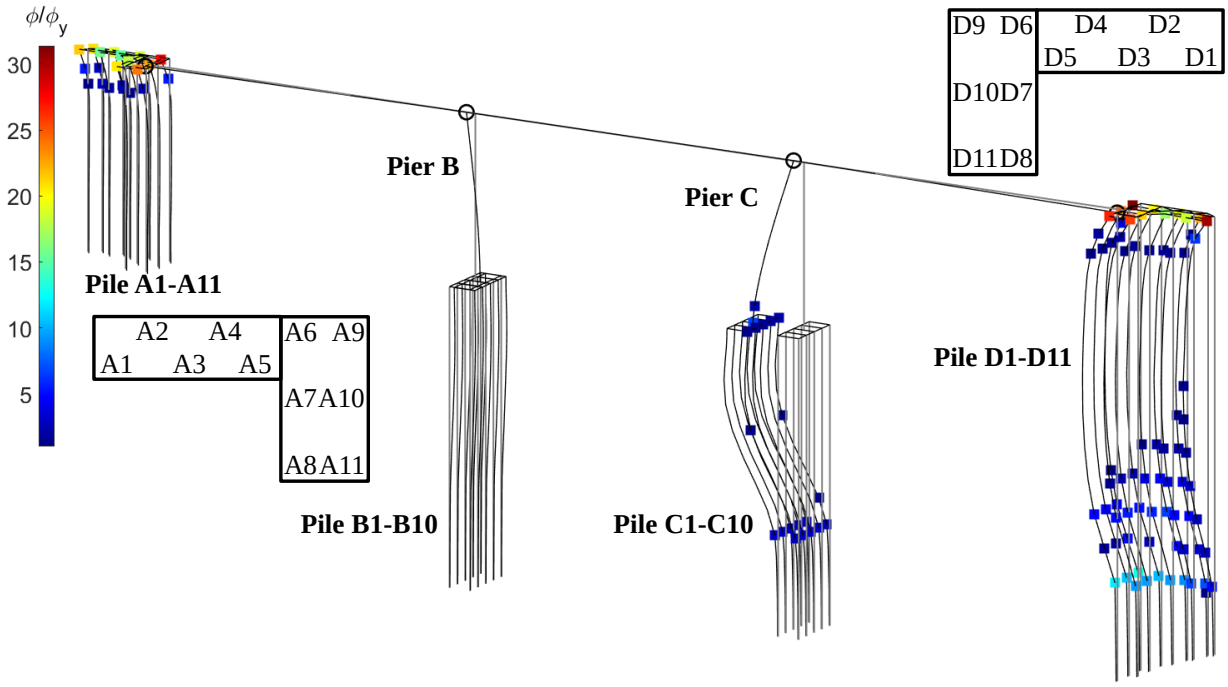

(a)

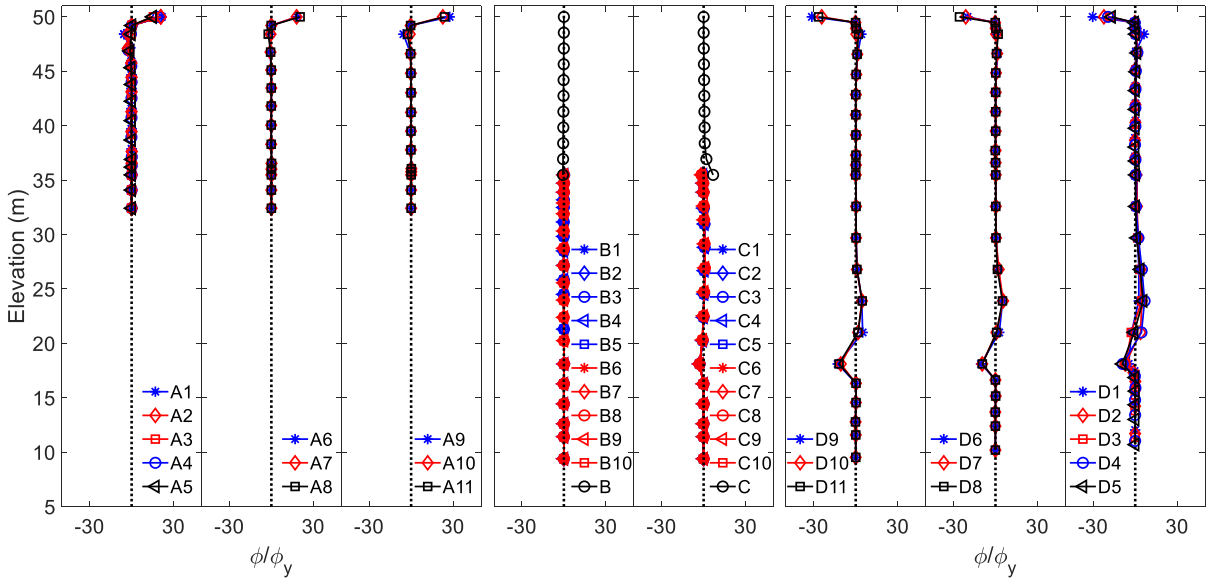

(b)

Figure 8.19 Ductility demand at end of shaking: (a) Ratio ϕ/ϕ_y; (b) Profile (grey represents original configuration; values < 1 are not shown for clarity; factor = 10)

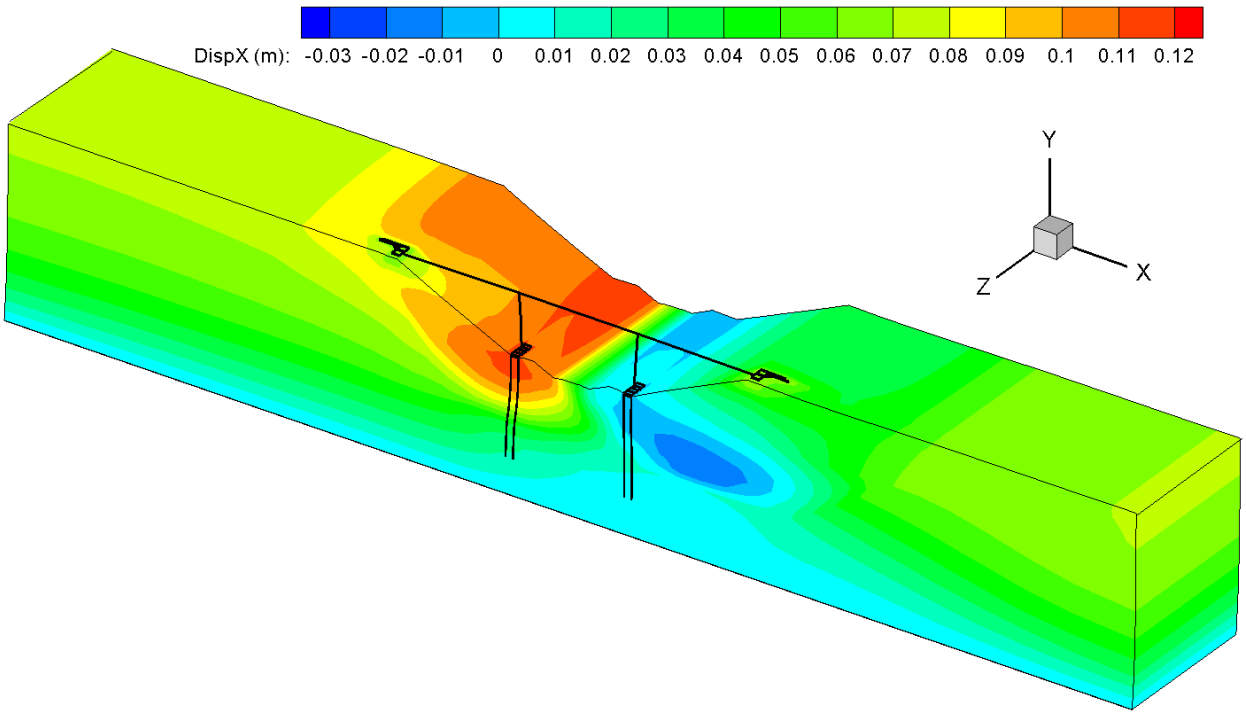

(a)

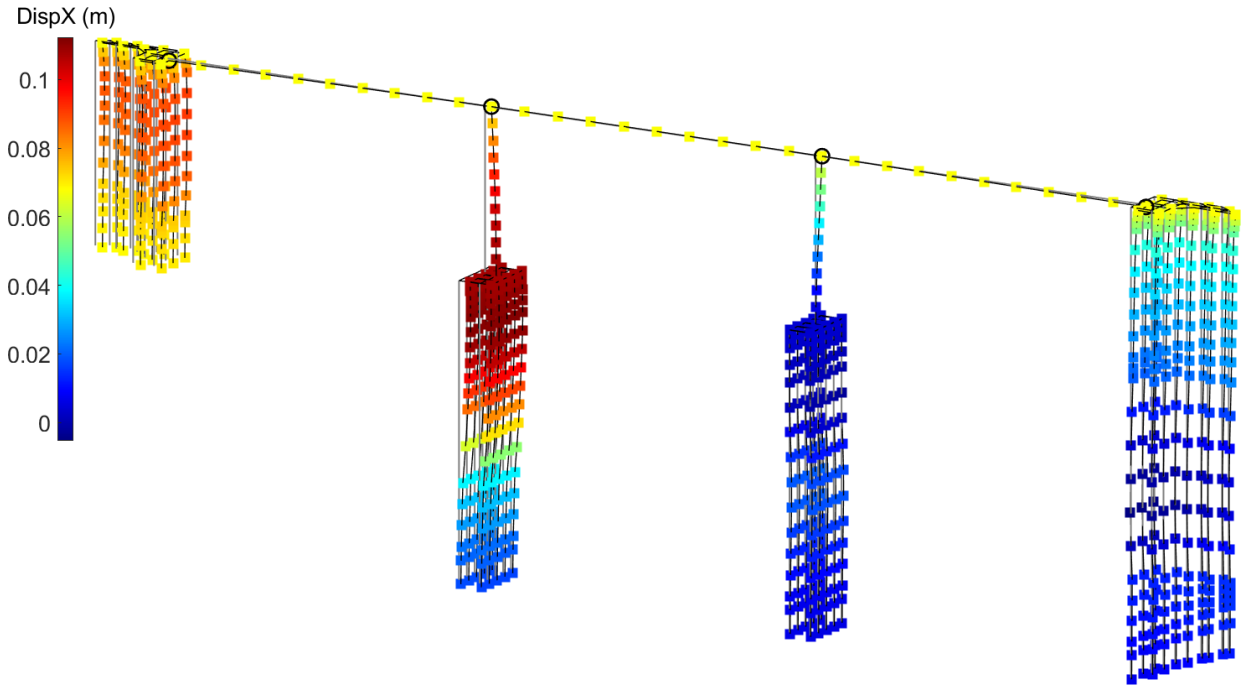

(b)

Figure 8.20 Deformed FE mesh of bridge under reversed input motion at max deck displacement: (a) Contour; (b) Structure (factor = 10)

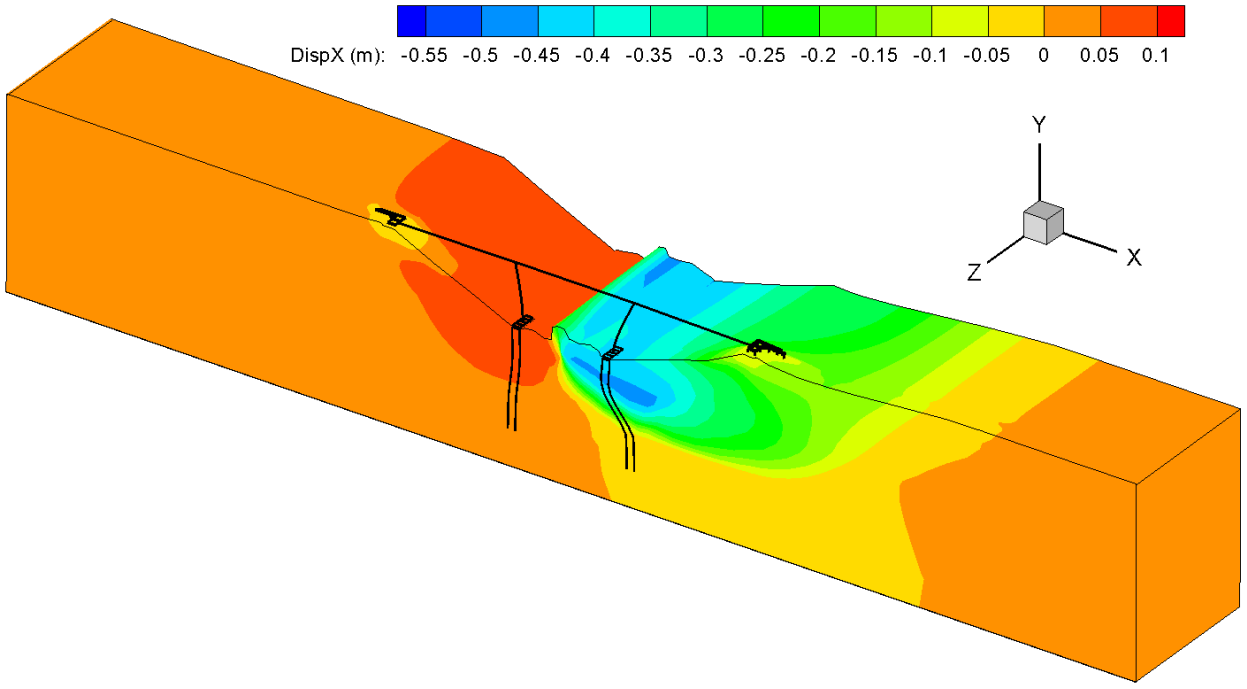

(a)

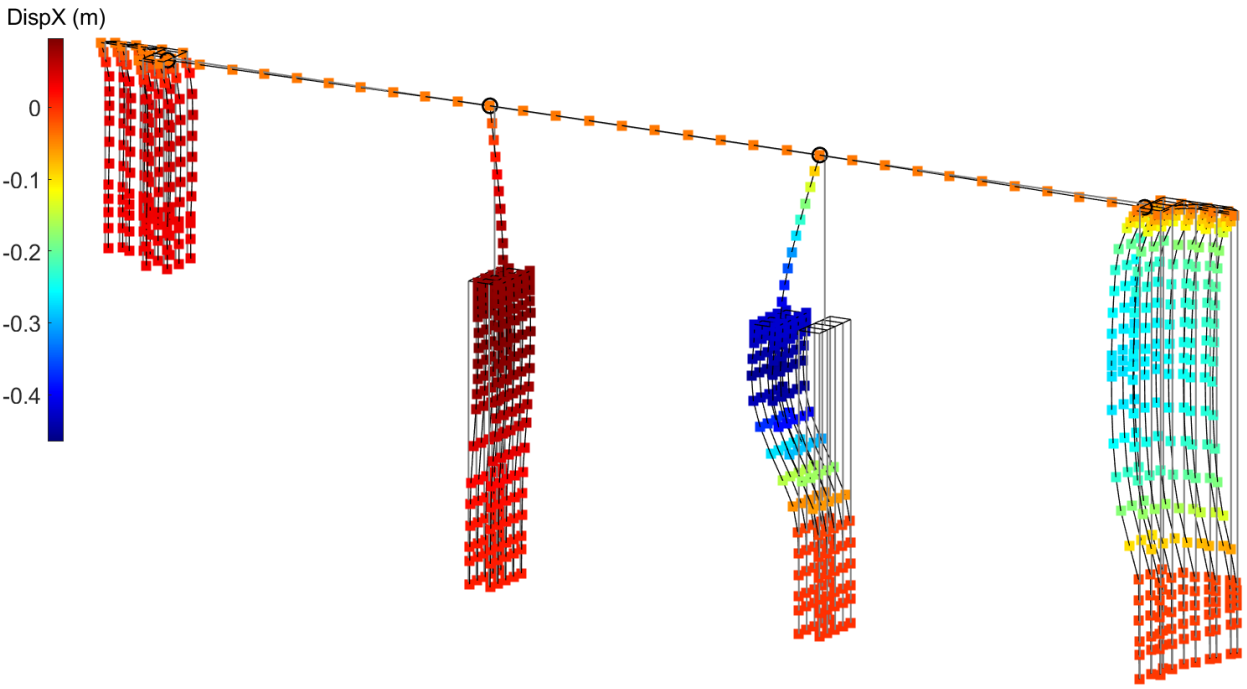

(b)

Figure 8.21 Deformed FE mesh of bridge under reversed input motion at end of shaking; (a) Contour; (b) Structure (factor = 10)

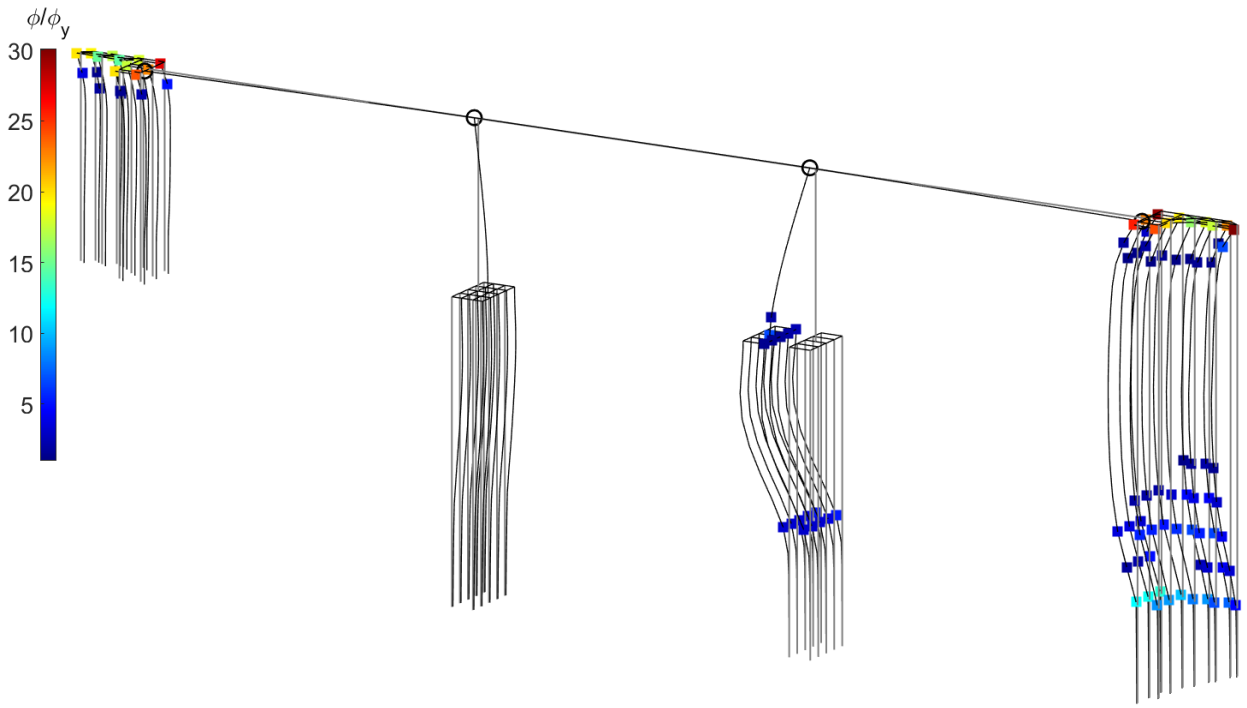

(a)

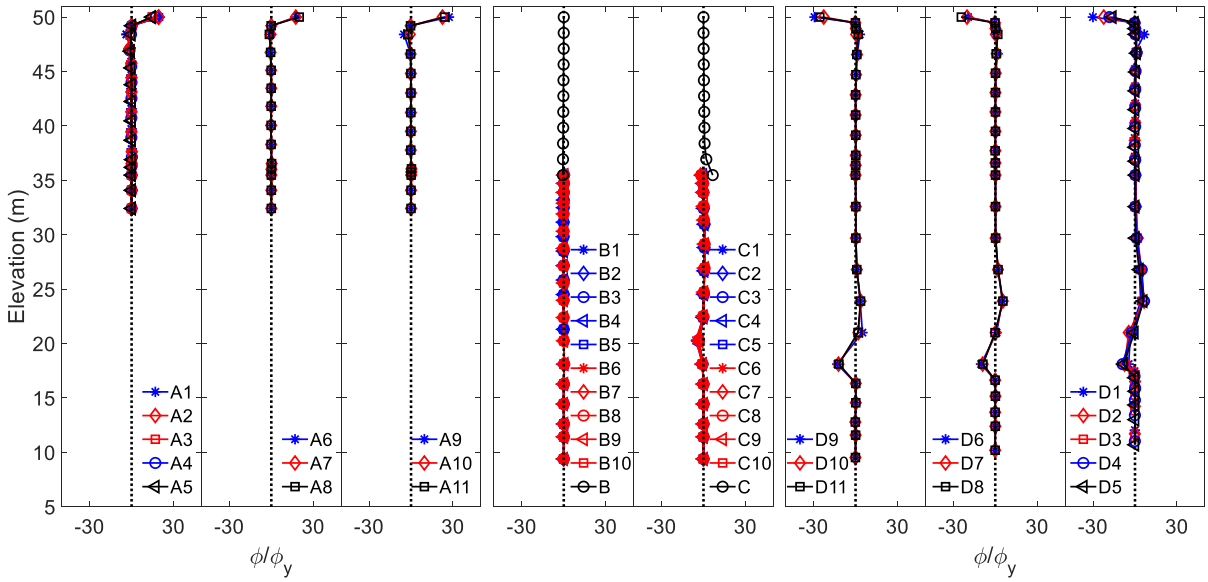

(b)

Figure 8.22 Ductility demand under reversed input motion at end of shaking: (a) Ratio ϕ/ϕ_y; (b) Profile (grey represents original configuration; values < 1 are not shown for clarity; factor = 10)

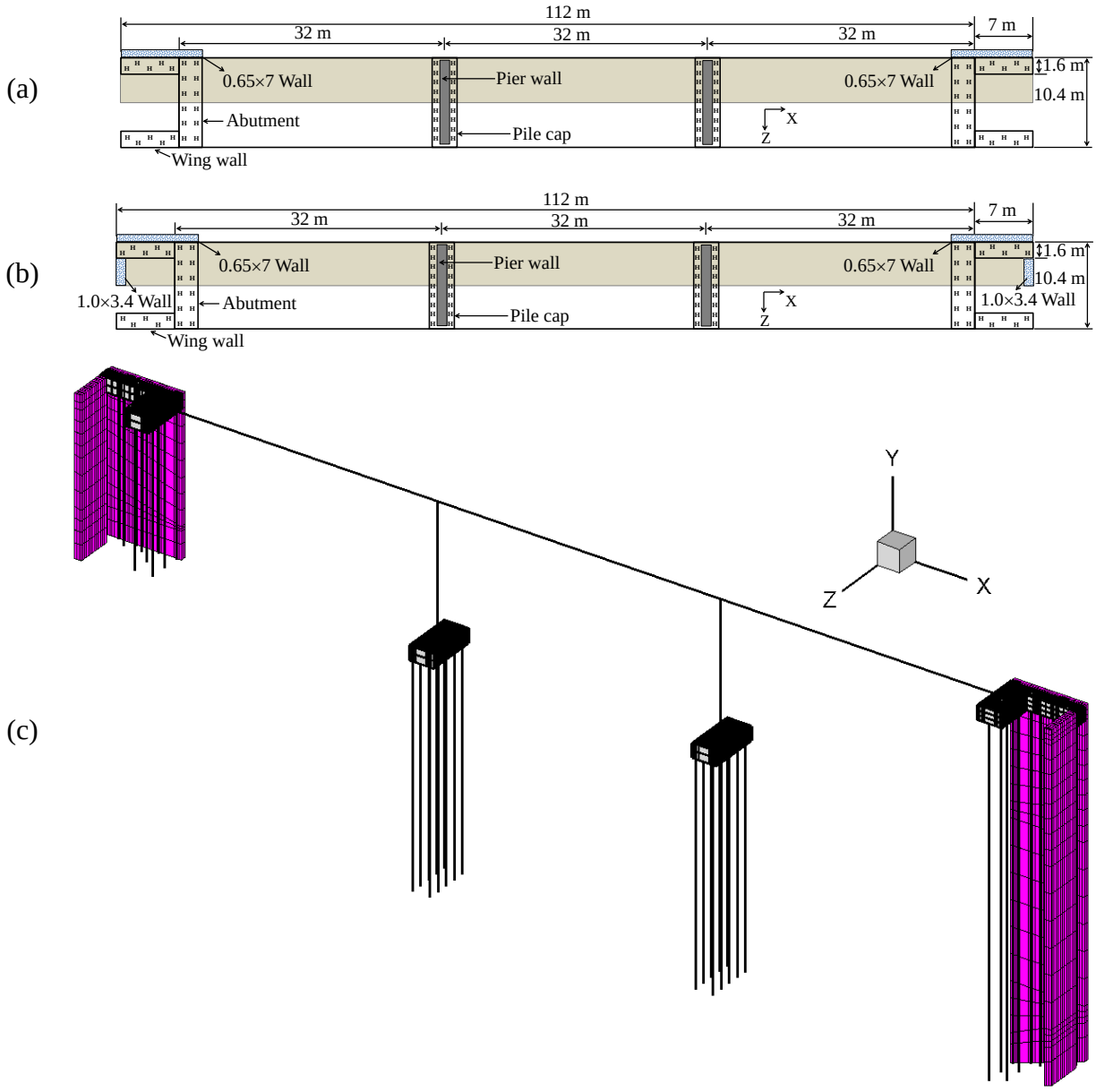

Figure 8.23 Retrofit analysis: (a) Scenario 1 by adding two 0.65 m × 7 m walls; (b) Scenario 2 by adding additional two 1.0 m × 3.4 m walls; (c) Bridge structure of Scenario 2

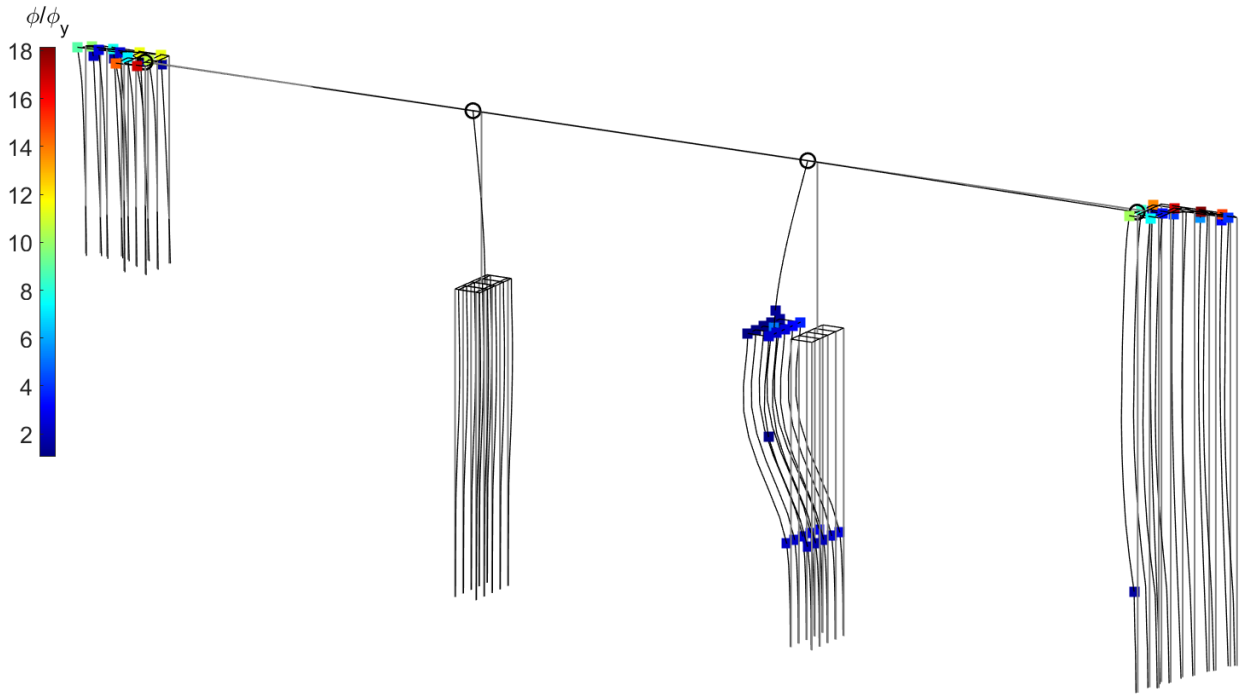

(a)

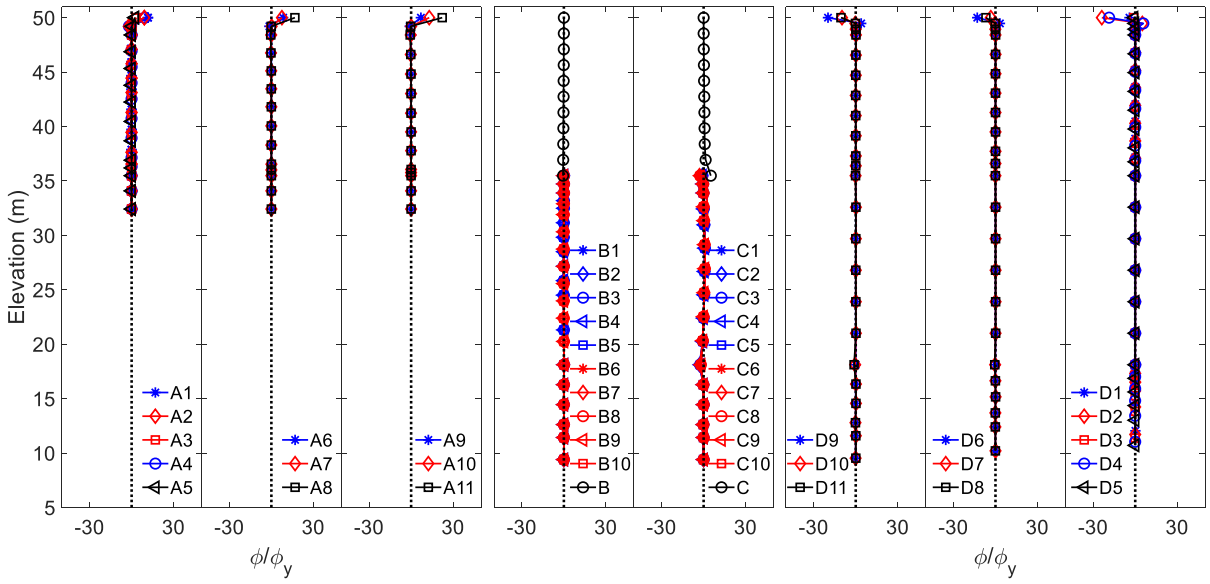

(b)

Figure 8.24 Ductility demand for retrofit analysis of Scenario 1: (a) Ratio ϕ/ϕ_y; (b) Profile (grey represents original configuration; values < 1 are not shown for clarity; factor = 10)

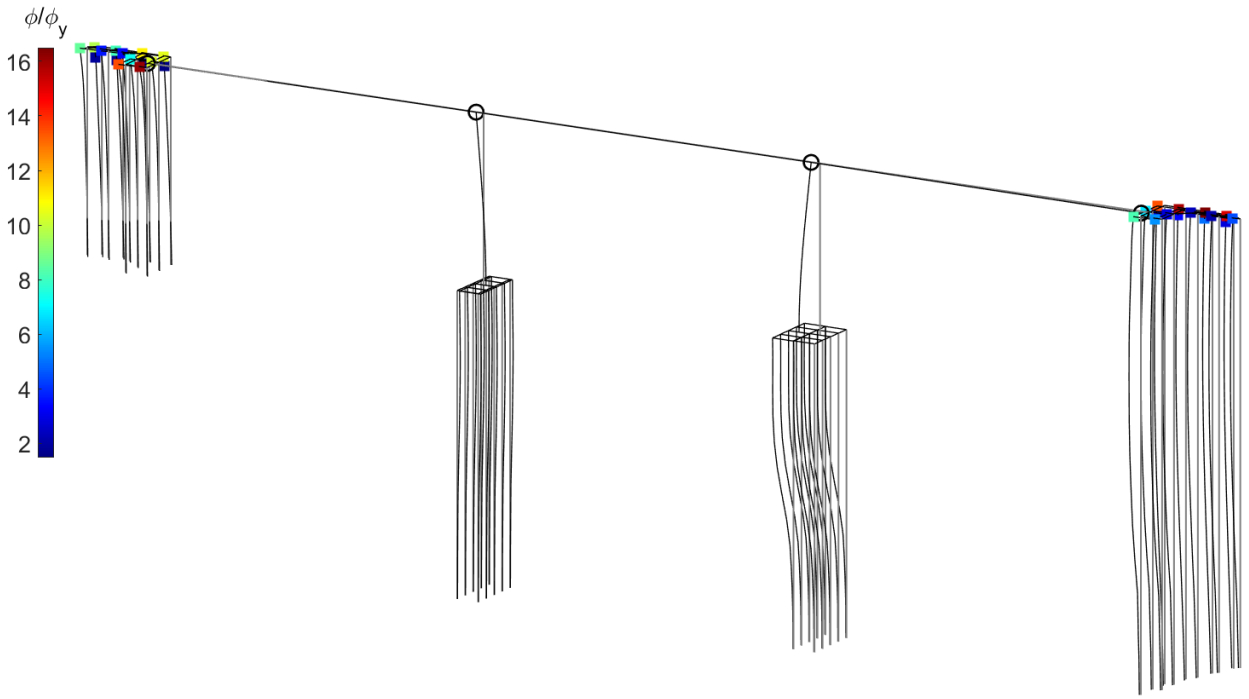

(a)

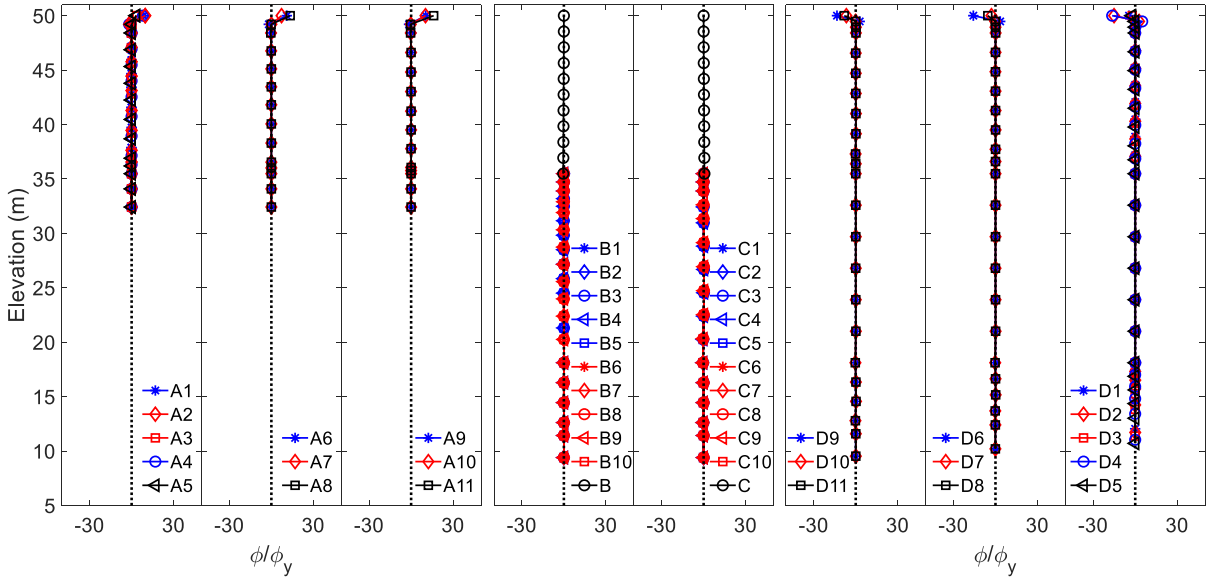

(b)

Figure 8.25 Ductility demand for retrofit analysis of Scenario 2: (a) Ratio ϕ/ϕ_y; (b) Profile (grey represents original configuration; values < 1 are not shown for clarity; factor = 10)

Chapter 9. Arch Bridge Configuration for Mitigation of Liquefaction-Induced Lateral Deformations

9.1. Abstract

An arch bridge configuration is proposed as a structural system to mitigate the consequences of potential liquefaction-induced lateral deformations. Where applicable in terms of the underlying canyon geometry, such a configuration might offer beneficial outcomes as discussed in this study. For that purpose, a full three-dimensional (3D) Finite Element (FE) computational simulation is conducted to highlight these benefits. The restraining effect of the superstructure (acting as a strut) on the liquefaction-induced ground deformation is illustrated. In this FE model, a realistic multi-layer soil profile is considered with interbedded liquefiable/non-liquefiable strata. The calibrated OpenSees material PressureDependMultiYield03 is employed to simulate the essential characteristics of pressure sensitive soil response. Finally, recommendations are included for practical implementation.

9.2. Introduction

Recent earthquakes (Arduino et al 2010; Wotherspoon et al. 2011; Ledezma et al. 2012; Verdugo et al. 2012; Cubrinovski et al. 2011, 2014) continue to demonstrate the detrimental effects of liquefaction on bridge abutments, supporting columns and pier foundations. A schematic illustration of such damage (Cubrinovski et al. 2014a, b) for pile-supported bridges is shown in Figure 9.1a. Due to seismic excitation, liquefied soil layers may result in substantial accumulated permanent deformation of the sloping ground near the abutments, causing severe damage to the pile foundations (Youd 1993; Hamada et al. 1996; Tokimatsu and Asaka 1998; Berrill et al. 2001; Arduino et al. 2010; Ledezma et al. 2012; Verdugo et al. 2012; Wotherspoon et al 2011; Turner et al. 2016).

In order to reduce damage to the abutments and the conventional deep foundations (Figure 9.1a), an arch bridge configuration is proposed as the structural system (Figure 9.1b). This arch bridge configuration (Figure 9.1b) is to be supported on an essentially rigid relatively shallow foundation, precluding possible damage to the conventional deep foundation alterative (Figure 9.1). In essence, such an arch bridge configuration stands to offer the following advantages: i) own weight of the bridge exerts restoring lateral earth pressure forces that stabilize the canyon sloping ground and reduce the extent of potential lateral deformations, ii) the relatively rigid bridge deck superstructure acts as a strut between both sides of the underlying canyon, providing a self-reacting mechanism, with lateral loads on both ends of the bridge providing restoring forces, iii) absence of conventional bridge columns and underlying foundations cause potential lateral ground deformations to have no detrimental influence on the bridge superstructure, and iv) after a strong earthquake, potential retrofit is fast and economical, as the bridge structure naturally conforms to the surrounding deformed ground configuration, and only relatively minor grading or re-levelling work might be needed.

In order to illustrate these beneficial response mechanisms, a full three-dimensional (3D) FE model motivated by the details of an actual bridge-ground system was developed. In this model, a realistic multi-layer soil profile is considered with interbedded liquefiable/non-liquefiable strata. On this basis, the following sections of this chapter outline the: 1) computational framework, 2) specifics and model properties of the bridge-ground system, 3) details of the employed FE modeling techniques, 4) conducted numerical simulations and salient bridge system response mechanisms, and 5) insights derived from the study. Finally, a number of conclusions are presented and discussed.

9.3. Computational Framework

The Open System for Earthquake Engineering Simulation (OpenSees, McKenna 2011, http://opensees.berkeley.edu) framework was employed to conduct the nonlinear bridge-ground system analysis subjected to seismic excitation. OpenSees is developed by the Pacific Earthquake Engineering Research (PEER) Center, and it is widely used for simulation of geotechnical systems and soil-structure interaction applications (Yang and Elgamal 2002; Lu et al. 2011; Su et al. 2017). The OpenSees elements and materials used in this FE model are briefly described below.

Three-dimensional solid-fluid brick elements (i.e., bbarBrickUP element in OpenSees) following the *u-p* formulation (Chan 1988) were employed for simulating saturated soil response, where *u* is displacement of the soil skeleton and *p* is pore-water pressure. Implementation of this *u-p* element is based on the following assumptions: 1) small deformation and rotation; 2) solid and fluid density remain constant in time and space; 3) porosity is locally homogeneous and constant with time; 4) soil grains are incompressible; 5) solid and fluid phases are accelerated equally. Hence, the soil layers represented by these effective stress fully coupled elements account for deformations and changes in pore-water pressure during seismic excitation.

The OpenSees soil material PressureDependMultiYield03 (typically used with the solid-fluid fully coupled brick elements, Khosravifar et al. 2018) is employed to simulate the liquefaction-induced shear strain accumulation mechanism in cohesionless soils (Yang and Elgamal 2002; Elgamal et al. 2003; Yang et al. 2003; Yang et al. 2008). In order to more closely capture the established guidelines concerning triggering of liquefaction (Idriss and Boulanger 2008), the PressureDependMultiYield03 material has been recently updated (Khosravifar et al. 2018). In addition, the PressureIndependMultiYield material (Elgamal 2008; Yang et al. 2008; Lu et al. 2011) is employed for simulating elasto-plastic undrained clay-type shear response.

The FE matrix equation of the bridge-ground system is integrated in time using a single-step predictor multi-corrector scheme of the Newmark type (Chan 1988; Parra 1996) with integration parameters $\gamma = 0.6$ and $\beta = 0.3025$. The equation is solved using the modified Newton-Raphson approach with Krylov subspace acceleration (Carlson and Miller 1998; Mazzoni et al. 2009). A relatively low level of stiffness proportional viscous damping was used to enhance numerical stability (coefficient = 0.003), with the main damping emanating from the soil nonlinear shear stress-strain hysteresis response (Su et al. 2017; Qiu et al. 2020).

9.4. Finite Element Model

Figure 9.2 depicts the proposed arch bridge-ground configuration. For the purposes of this study, seismic response is addressed only in the longitudinal direction (i.e., no transverse-direction shaking imparted). The modeled reinforced concrete bridge is approximately 96 m long and 10 m wide. On this basis, a 3D bridge-ground FE mesh (half mesh due to symmetry) is generated comprising 31,376 nodes, 27,840 brick elements. All structural components including the reinforced concrete deck (linear self-weight q as shown in Figure 9.3) were modeled using 3D linear elastic beam-column elements. Along both side mesh boundaries (Figure 9.2), 2D plane strain soil columns of large size and depth (not shown) are included (Su et al. 2017; Qiu et al. 2020). These soil columns, at an adequate distance away from the bridge structure (Figure 9.2) to minimize boundary effects (around 100 m, i.e., the same length of bridge structure), efficiently reproduce the desired shear beam free-field response at these locations. In the transverse direction, 40 m of the soil domain is included to capture ground response away from the bridge structure.

9.4.1. Ground Configuration

The overall ground configuration is shown in Figure 9.3, based on existing boring data and site conditions (Caltrans 2017). In general, the subsurface conditions (Figure 9.3) encountered at

the site consisted of Artificial Fill (Q1), Medium Dense Sand (Q2), Soft Clay (Q3) and Monterey Formation Bedrock (TM). The water table was prescribed at an elevation of 30 m located at the top of Layer Q2 as shown in Figure 9.3. Table 9.1 and Table 9.2 list the saturated medium dense sand and clay (PIMY in OpenSees) model parameters, respectively. For illustration, the soil model responses for clay and sand (Table 9.1 and Table 9.2) under undrained monotonic loading conditions (confinement = 100 kPa or 1 atmosphere) are presented in Figure 9.4. As shown in Figure 9.4b, shear strength of the saturated medium dense sand (Q2) increases under monotonic loading due to the dilative tendency as defined in Table 9.1.

9.4.2. Boundary and Loading Conditions

As mentioned above, both lateral mesh boundaries (X = 0 m and X = 300 m) are located away from the bridge structure (Figure 9.2 and Figure 9.3). Along the 40.0 m apart longitudinal symmetry planes (Figure 9.2), no out of plane motion is allowed. Loading was implemented in a staged fashion (Su et al. 2017; Qiu et al. 2020) as follows:

1) Gravity was applied to activate the initial static state for the soil domain only with: i) linear elastic properties (Poisson's ratio of 0.47 for all layers), ii) nodes on both lateral boundaries of the model were fixed against longitudinal translation, iii) nodes were fixed along the base against vertical translation, iv) pore pressure degree of freedoms were fixed at and above 30 m to specify the water table (Figure 9.2). At the end of this step, the static soil state is imposed and displacements under own-weight application is re-set to zero using the OpenSees command InitialStateAnalysis.

2) Soil properties were switched from linear elastic to plastic (Table 9.1 and Table 9.2).

3) The 3D elastic beam-column elements of reinforced concrete deck and foundation were added. The mat foundation nodes were connected to the soil nodes using the OpenSees EqualDOF constraint (for the three translations). Thereafter, self-weight of the bridge structure was applied.

In this study, the base of the computational soil domain is located at a depth of 50 m from the ground surface (Figure 9.3), about 35 m away from the bridge foundations. Lateral response of the soil strata below this 50 m depth was represented by the Lysmer-Kuhlemeyer (Lysmer and Kuhlemeyer 1969) dashpot boundary, applied along the base of the FE model (base *Vs* = 600 m/s, in the range of soft rock, slightly higher than stiffness of the overlying stratum), so as to avoid spurious wave reflections. As such, two dashpots are activated in the x and z directions at each node along the base, and the incident seismic wave excitation is defined by dynamic equivalent nodal forces (Zhang et al. 2008 and Elgamal et al. 2008).

For the shaking phase (purely in the longitudinal direction), seismic motion (Figure 9.5) was simply taken as that of the 1994 Northridge earthquake ground surface Rinaldi Receiving Station record (Component S48W), scaled down to a peak amplitude of 0.3 g. For the purpose of this study, deconvolution was employed as a simple approach (using Shake91 by Idriss and Sun), to derive an incident earthquake motion (Figure 9.5), imparted (Elgamal et al. 2008) thereafter along the base of the FE model (elevation 0.0 m in Figure 9.3). In this representation, free-field motion along both the lateral side mesh boundaries is generated by the included soil columns mentioned above.

9.5. Computed Response

9.5.1. Longitudinal Ground Deformation at End of Shaking

Figure 9.6 depicts the longitudinal relative displacement contours at end of shaking. At the left and right boundaries, deformation of the TM soil canyon was minimal, only reaching about

0.01 m (Figure 9.6). Within the canyon, the left and right downslope deformations are seen to interact, pushing against each other. Away from the bridge (Z = 0 m), downslope crest displacements were about -0.37 m at R0, compared to +0.04 m only at L0. At Z = 40 m, the bridge through its deck and foundations acted as a strut that reduced deformations from the R0 -0.37 m to R1 of about -0.13 m, with resistance mobilized from the left side slope whose downslope deformation was reversed from the L0 of +0.04 m (downslope) to the L1 of -0.13 m (Figure 9.6-Figure 9.9).

Figure 9.7 displays the longitudinal displacement profile along the slope top (from Z = 0 m to 40 m at both sides). The downslope displacements accumulated significantly upon passage of the main shaking pulse at about 3 seconds and continued to accumulate until the end of shaking. Figure 9.8 and Figure 9.9 provide clearer pictures of the accumulated longitudinal displacement at different elevations on both side slopes (Locations L0, L1, R0 and R1). With the bridge deck connecting both sides, slope crest R1 displacement is lower than R0, restrained by resistance from the left side where L1 displacement became larger than L0.

Figure 9.10 depicts the longitudinal displacement of the bridge superstructure and the axial force along the deck at end of shaking. It can be seen that the large right-side downslope deformation forced the entire bridge to move leftwards (about -0.13 m), pushing into the left-side slope as an additional restraining mechanism. As such, compressive axial forces were imposed on the deck (Figure 9.10c).

9.5.2. Vertical Ground Deformation at End of shaking

Figure 9.11 displays the vertical relative displacement contours at end of shaking. Peak settlement occurred near the right-side slope (location R2) and showed slumping of as much as 0.3 m (Figure 9.11b). For this relatively narrow canyon geometry, the interaction of both slopes

(Figure 9.12) resulted in the central section experiencing upward ground heave reaching of about 0.45 m (Figure 9.11). Finally, settlement is lower at Z = 40 m (Figure 9.12 and Figure 9.13), due to presence of the bridge's structural system (Locations R1, R3 compared to R0, R2).

The vertical settlement (Figure 9.14) is also seen to be much larger at the right embankment (0.23 m) compared to its left counterpart. In this case, relatively minor grading work might be needed, with minimal to no damage sustained by the bridge structure.

9.5.3. Liquefaction and Permanent Shear Strain

Figure 9.15 shows time histories of effective confinement p' divided by the initial value p'_0 (before shaking) at locations of M0 and M1 (Figure 9.3). The ratio p'/p'_0 reaching 0 indicates loss of effective confinement due to liquefaction. With the medium dense Q2 sand at the elevation range of about 18.1-29.1 m, it is noted that the ratio p'/p'_0 at Z = 0.0 m decreased slightly faster than that at Z = 40 m closer to the bridge. Upon liquefaction, Q2 at both locations M2 and M3 attains its low specified residual shear strength of 2 kPa (Figure 9.15a and Table 9.1) at zero p'/p'_0. In light of the large deformations of the right-side slope (Figure 9.6), accumulated shear strains in this Q2 stratum and in the soft Q3 (Figure 9.15-Figure 9.17) are seen to be quite high. Away from the bridge (Z = 0 m), larger shear strains are noted within Q3 and the base of the liquefied Q2 (Figure 9.15-Figure 9.17).

From the overall picture of shear strains γ_{xy} at the end of shaking (Figure 9.16), it may be noted that:

1. At the left and right boundaries of the ground domain, shear strain is relatively small reaching only about 0.5 %, mainly due to the high shear strength afforded by the stiff canyon Q1 and TM strata (Figure 9.3 and Table 9.2).

2. At the right-side slope (Locations M2 and M3), downslope shear strains were accumulated, reaching peak values of about 18 % near the base of the liquefied sand Q2 layer. In Figure 9.16b, the overall shear strain at Location M3 (Z = 40 m close to the bridge) is about 2.5 % less than that at Location M2 (Z = 0 m away from the bridge), due to restraining effects of the bridge's structural system.

9.5.4. Acceleration

Figure 9.18 and Figure 9.19 show acceleration response at various locations of the bridge-ground configuration. In general, amplitudes are amplified closer to the ground surface. Motion along the ground surface appears to be rather similar, in view of the stiff TM ground formation that surrounds the canyon (Figure 9.3). Since there is a larger extent of softer soils at the right-side slope compared to that at the left, peak spectral acceleration at R0 is significantly lower than that at L0. Nevertheless, the relatively small difference in acceleration along the bridge deck and its abutments denotes influence of the connectivity exerted by the bridge structure (Figure 9.18 and Figure 9.19).

9.6. Retrofit Analysis

Strictly for the purpose of illustration, potential use of the numerical model to conduct retrofit studies is addressed briefly in this section. For that purpose, an additional numerical simulation was conducted with larger shallow foundations resting on both side slopes (Figure 9.20). As such, this extended foundation, aims to further help in containing the laterally spreading slope materials on both sides.

Figure 9.21 displays the deformed mesh at end of shaking with retrofitted shallow foundations. It can be seen that the movement of right-side slope are significantly restrained by the larger shallow foundation. Furthermore, vertical displacement of the right-side slope and the

bridge superstructure (Figure 9.22) are lower when compared to the original results (Figure 9.11-Figure 9.13). Even better outcomes might result from additionally extending the foundation vertically as well as laterally. As such, further analyses are warranted.

9.7. Summary and Conclusions

A full 3D FE analysis framework was presented to study a number of salient features associated with the liquefaction-induced seismic response of a proposed arch bridge-ground system. For that purpose, a 3D FE model was developed, motivated by the details of an actual bridge-ground configuration. The bridge-ground system and details of the corresponding numerical analysis were discussed. Furthermore, the bridge's favorable response as dictated by its proposed structural configuration is illustrated.

Specific observations and conclusions include:

1) The arch bridge superstructure provides a mechanism to exert a significant restraining effect on lateral ground deformations. Such restraining effects stem from: i) own weight of the bridge exerting restoring lateral earth pressure forces at the abutments, and ii) the bridge acting as a strut and providing restraint due to the lateral deformations of both slopes counter-reacting each other.

2) Absence of bridge columns and underlying foundations cause potential lateral ground deformations to have no detrimental influence of the bridge superstructure.

3) After an earthquake: i) potential retrofit is economical with no need to address costly deep foundation challenges, and ii) the bridge structure naturally conform to the surrounding deformed ground configuration, where relatively minor grading or re-levelling work might be needed, with minimal to no damage to the bridge structure.

9.8. Acknowledgements

Chapter 9, in full, is currently being prepared for submission for publication of the material as it may appear in the following journal publication (The dissertation author was the primary investigator and author of this paper):

Qiu, Z., Elgamal, A. and Ebeido, A. "Arch Bridge Configuration for Mitigation of Liquefaction-Induced Lateral Deformations."

Table 9.1 Sand (Figure 9.1) model parameters (Khosravifar et al. 2018)

Model Parameters (PressureDependMultiYield03)		Q2
Reference mean effective pressure, p'_r (atm)		2.0
Mass density, ρ (t/m^3)		1.89
Maximum shear strain at reference pressure, $\gamma_{max,r}$		0.1
Low-strain shear modulus at reference pressure, G_r (MPa)		73.8
Stiffness dependence coefficient d, $G = G_r(\frac{\boldsymbol{P'}}{\boldsymbol{P'_r}})^{\boldsymbol{d}}$		0.5
Poisson's ratio v for dynamics		0.4
Shear strength at zero confinement, c (kPa)		2.0
Friction angle ϕ, with resulting shear strength defined as $p'\sin\phi$		35°
Phase transformation angle		29°
Contraction coefficient, c_1		0.035
Contraction coefficient, c_2		3.0
Contraction coefficient, c_3		0.2
Dilation coefficient, d_1		0.15
Dilation coefficient, d_2		3.0
Dilation coefficient, d_3		0.2
Additional contraction parameters	b_1	0.2
	b_2	20
	b_3	0.0
	b_4	0.001

Table 9.2 Clay (Figure 9.1) model parameters

Model parameters (PressureIndependMultiYield)	Q1	Q3	TM
Mass density, ρ (t/m^3)	1.92	1.84	2.16
Shear modulus, G (MPa)	139	75.2	293
Poisson's ratio for dynamics, v	0.4	0.4	0.4
Cohesive strength, c (kPa)	108	53	400
Shear strain at which the maximum shear strength is reached	0.1	0.1	0.1

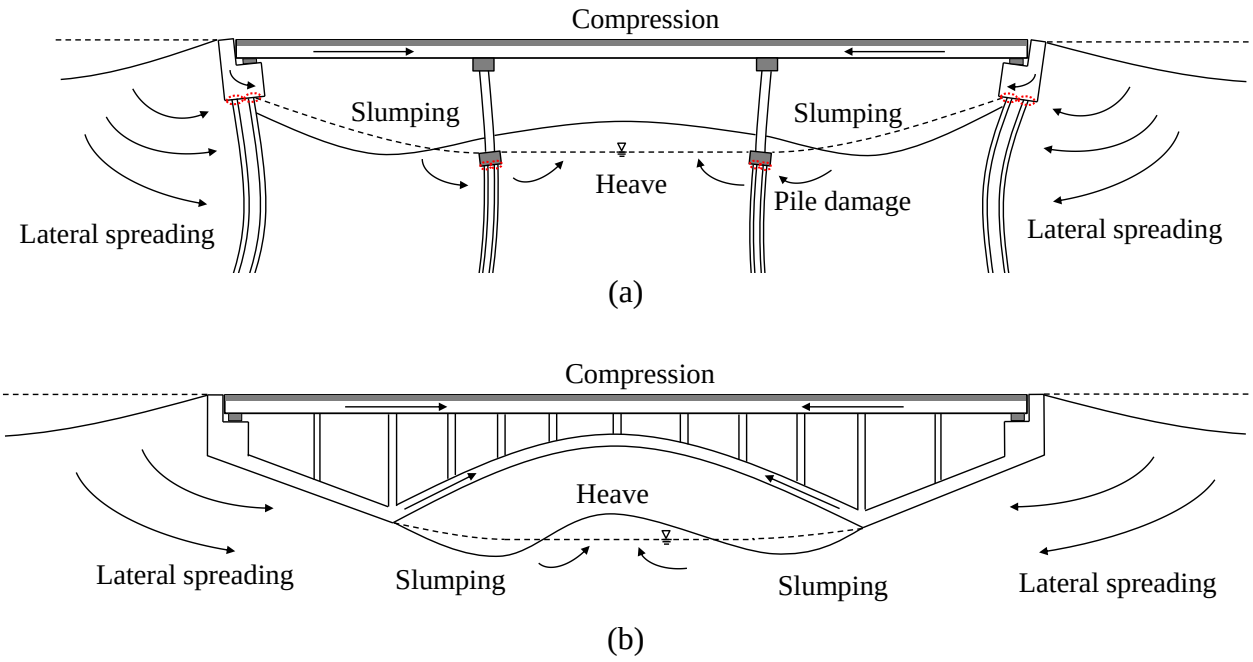

Figure 9.1 Schematic illustration of typical spreading-induced damage mechanism: (a) Pile-supported bridge; (b) Arch bridge

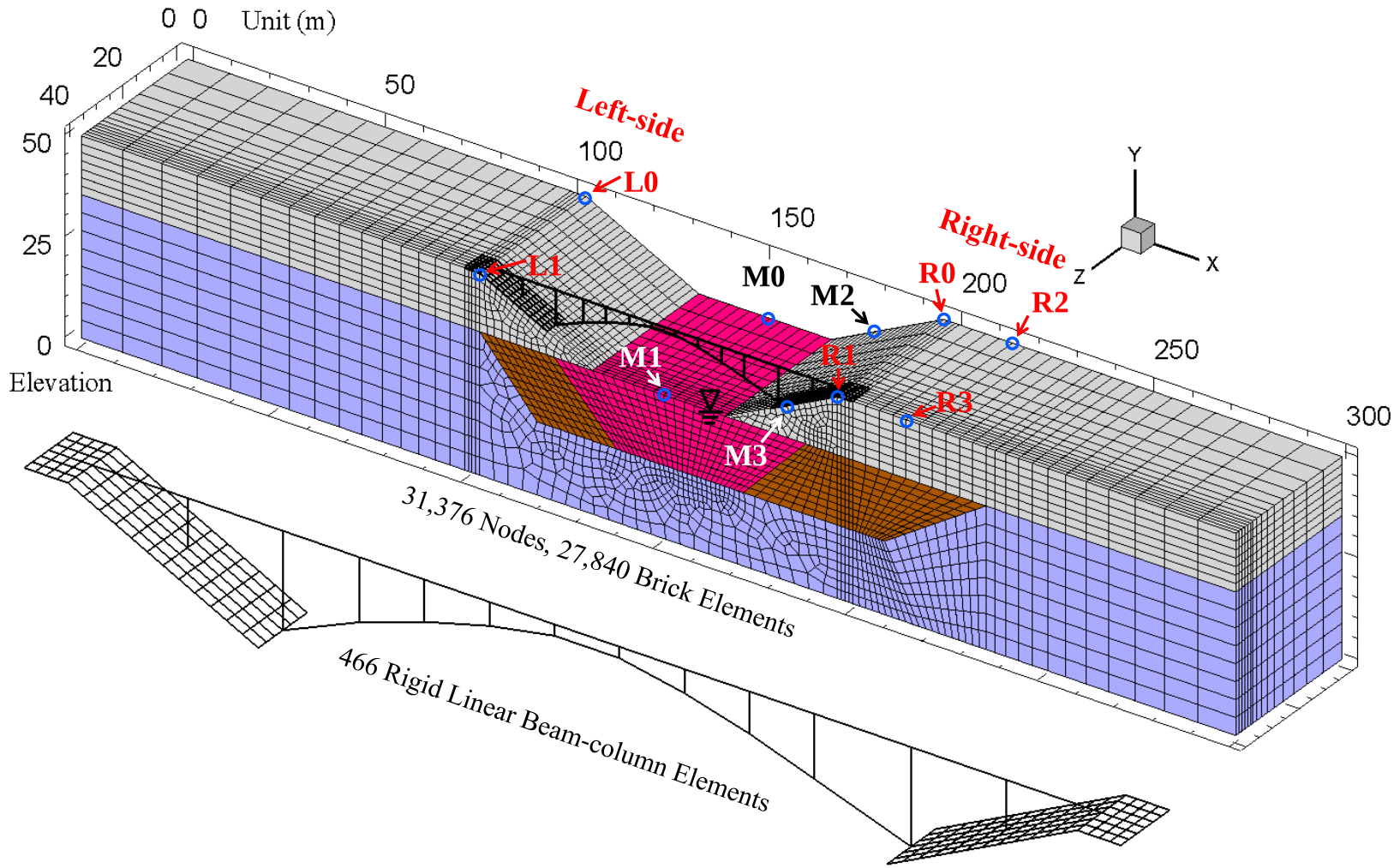

Figure 9.2 3D FE model (half mesh due to symmetry)

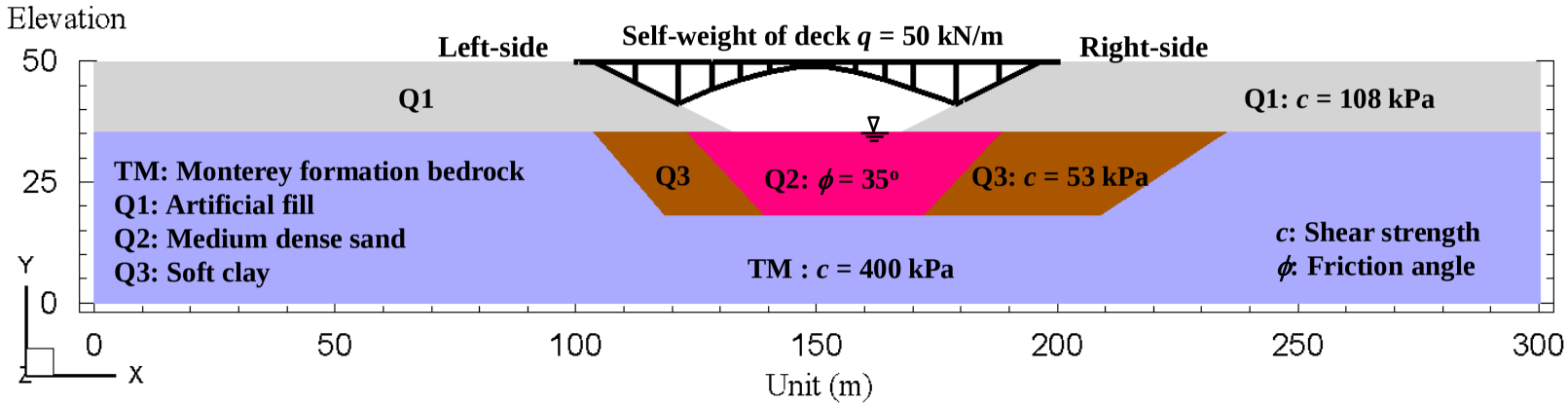

Figure 9.3 Groud configuration

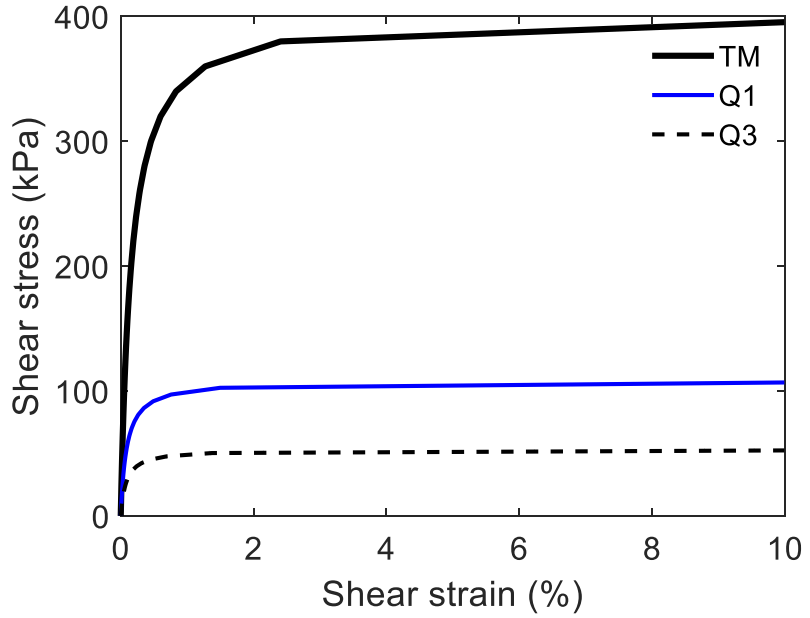

(a)

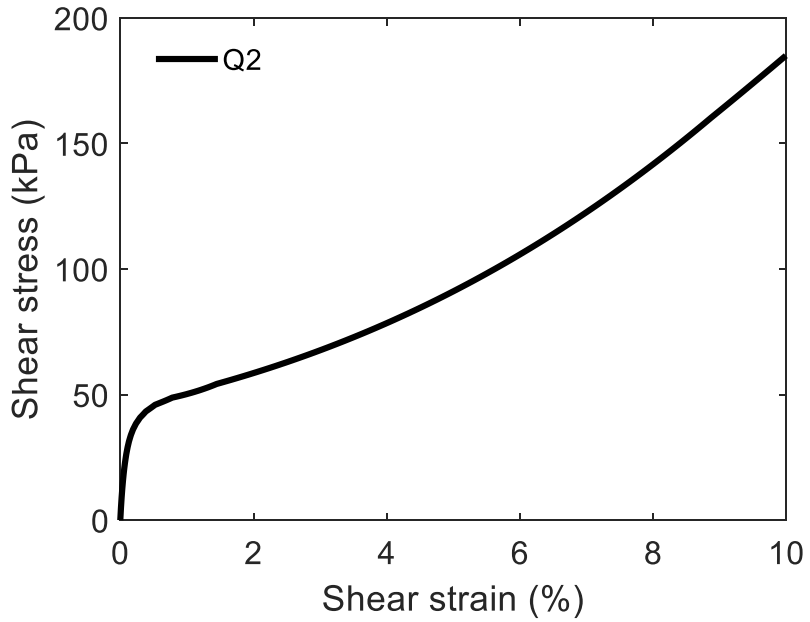

(b)

Figure 9.4 Soil model response: (a) Clay PIMY; (b) Sand model under undrained condition (Table 9.1 and Table 9.2)

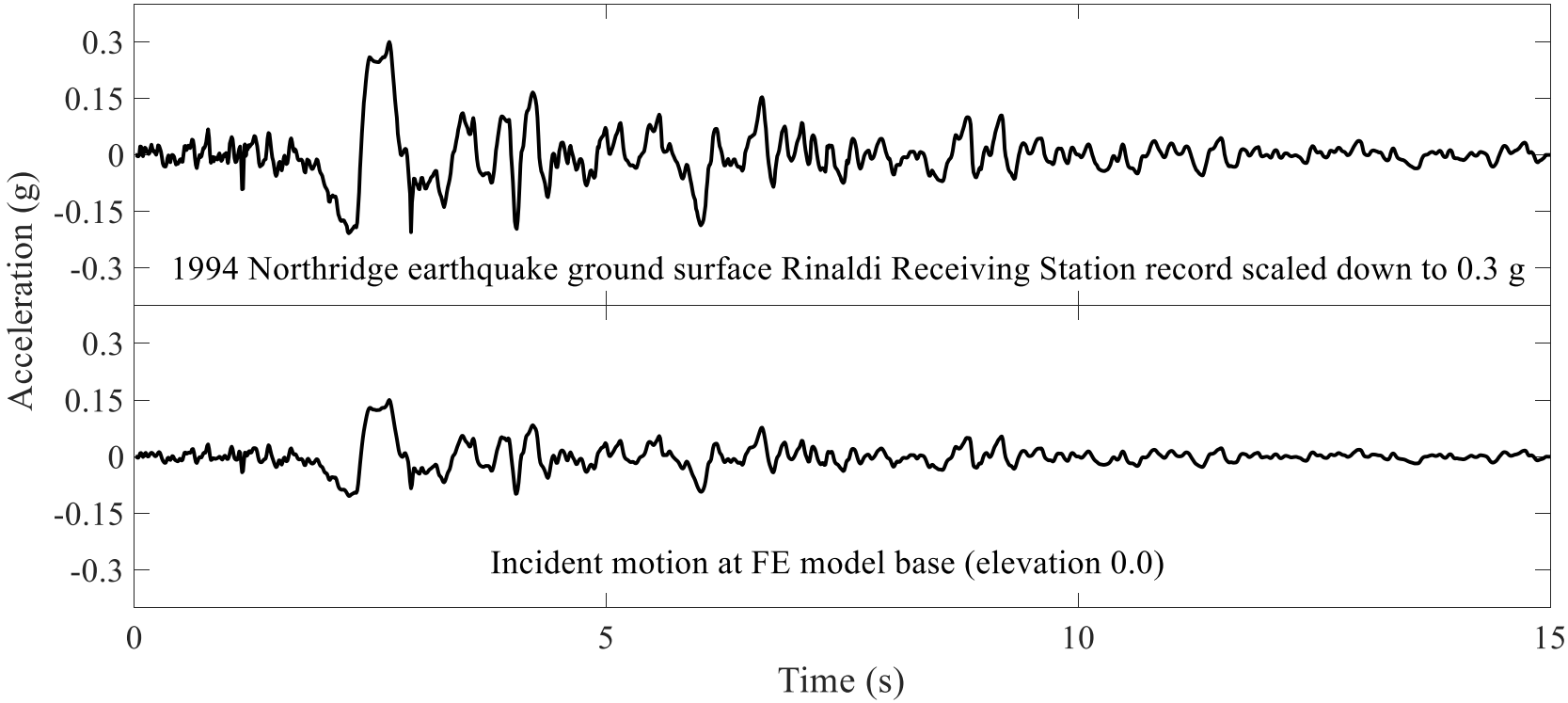

Figure 9.5 Input motion

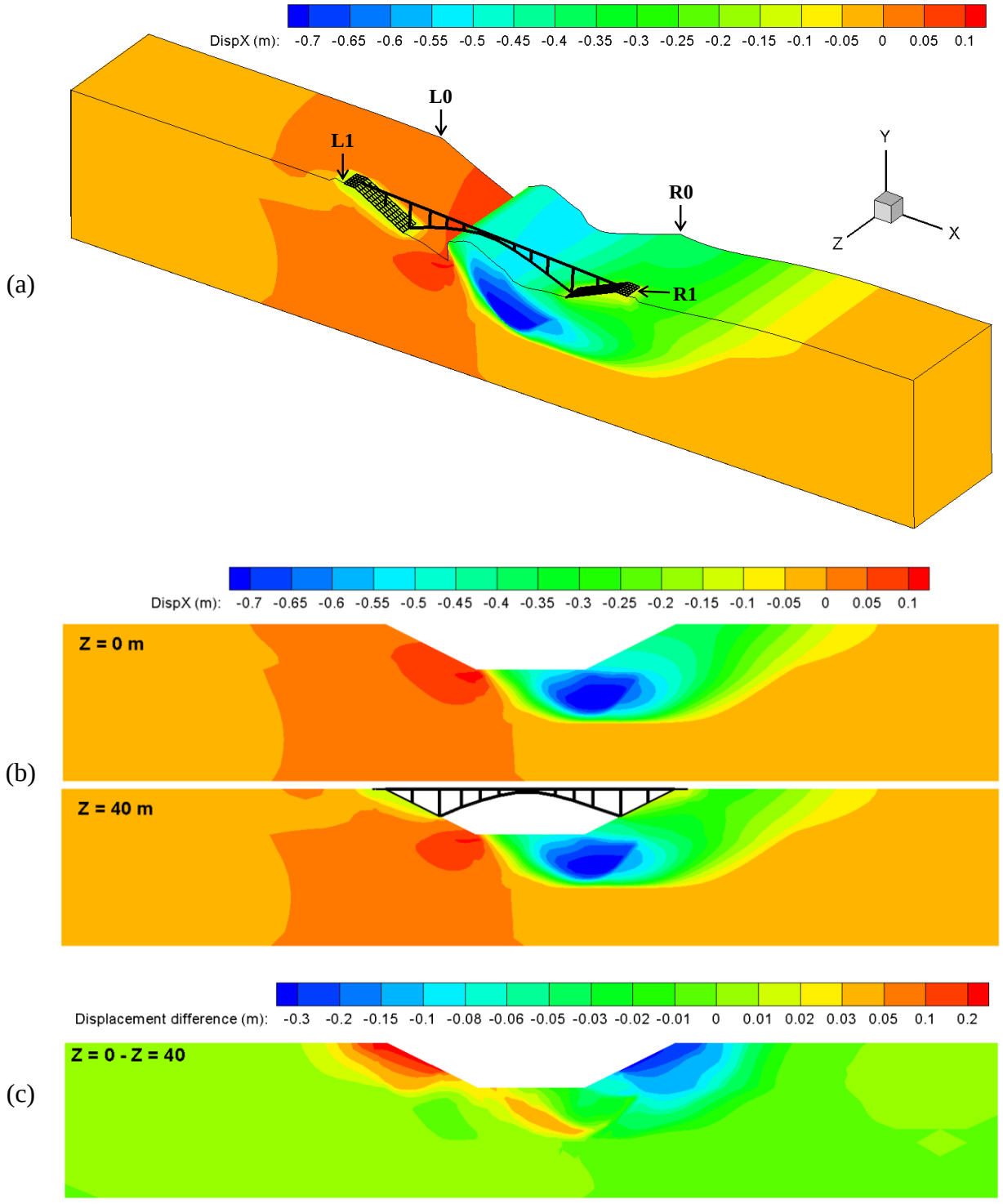

Figure 9.6 Longitudinal displacement contours at end of shaking (factor = 10): (a) Isometric view; (b) Side views at Z = 0 m and 40 m; (c) Difference between Z = 0 m and Z = 40 m

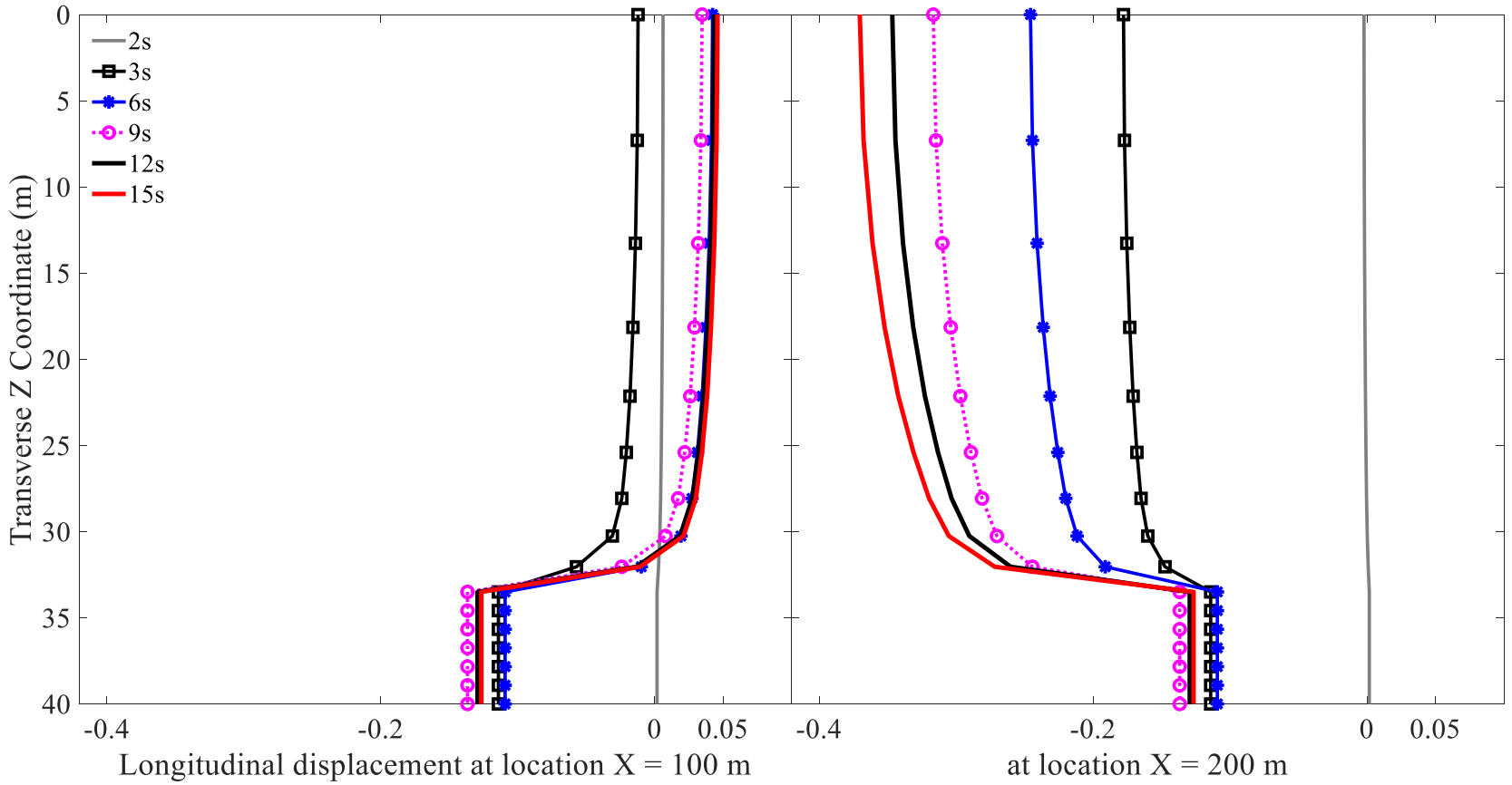

Figure 9.7 Longitudinal displacement profile of slope top along transverse Z direction at locations X = 100 m (L0-L1) and X = 200 m (R0-R1)

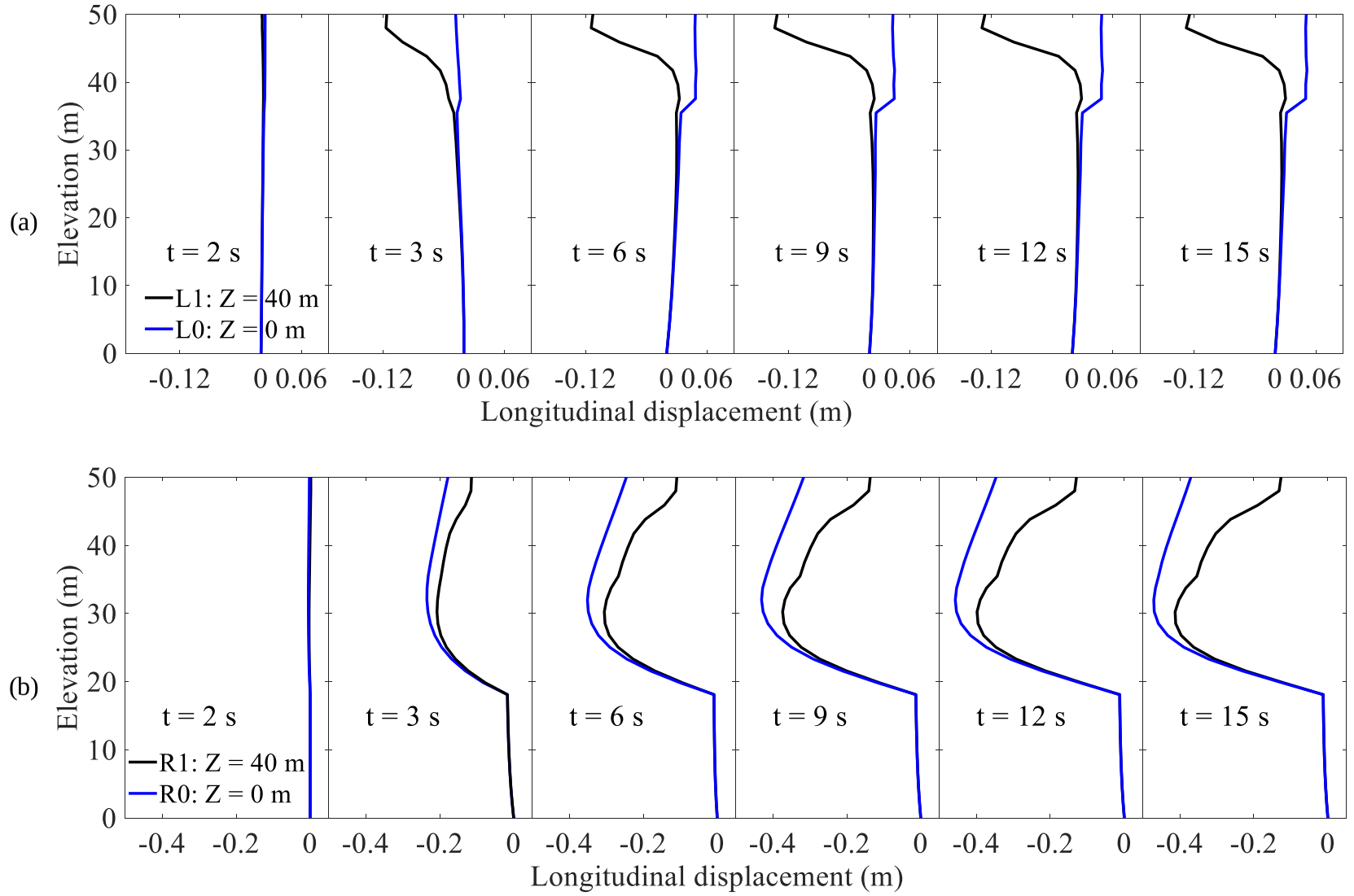

Figure 9.8 Longitudinal displacement profile along depth: (a) Locations X = 100 m (L0 and L1); (b) Locations X = 200 m (R0 and R1)

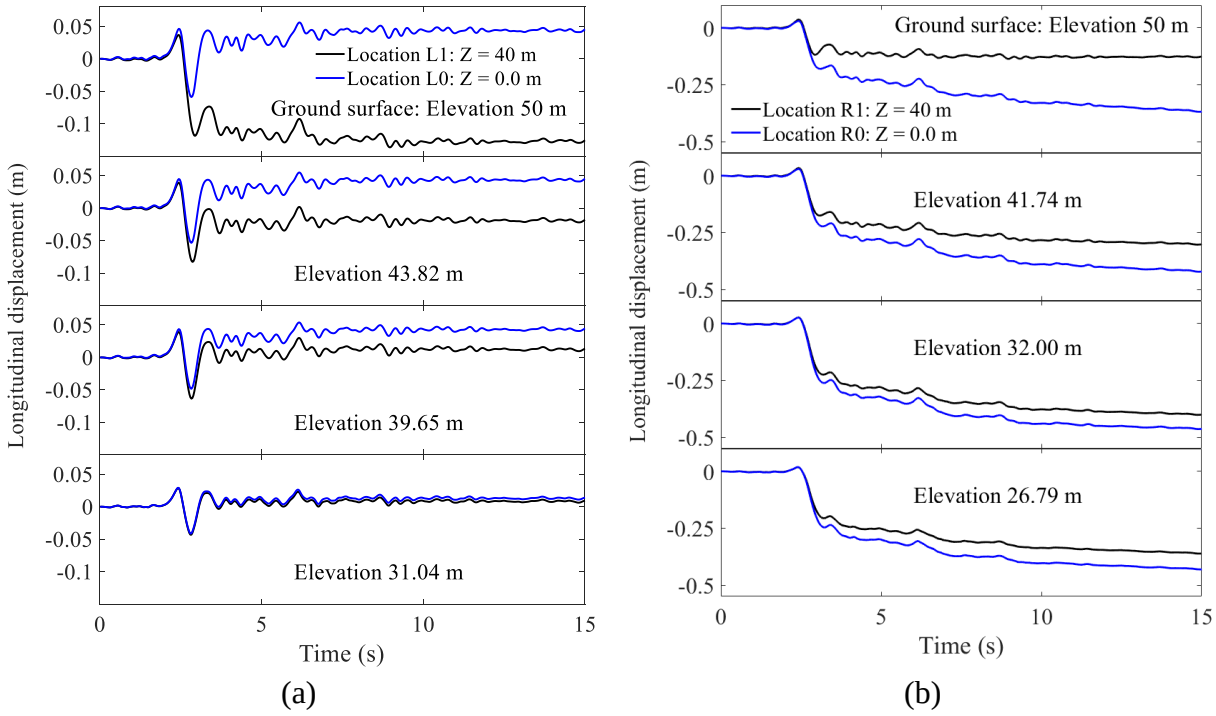

(a) (b)

Figure 9.9 Computed lateral displacement time histories: (a) Locations L0 and L1; (b) Locations R0 and R1

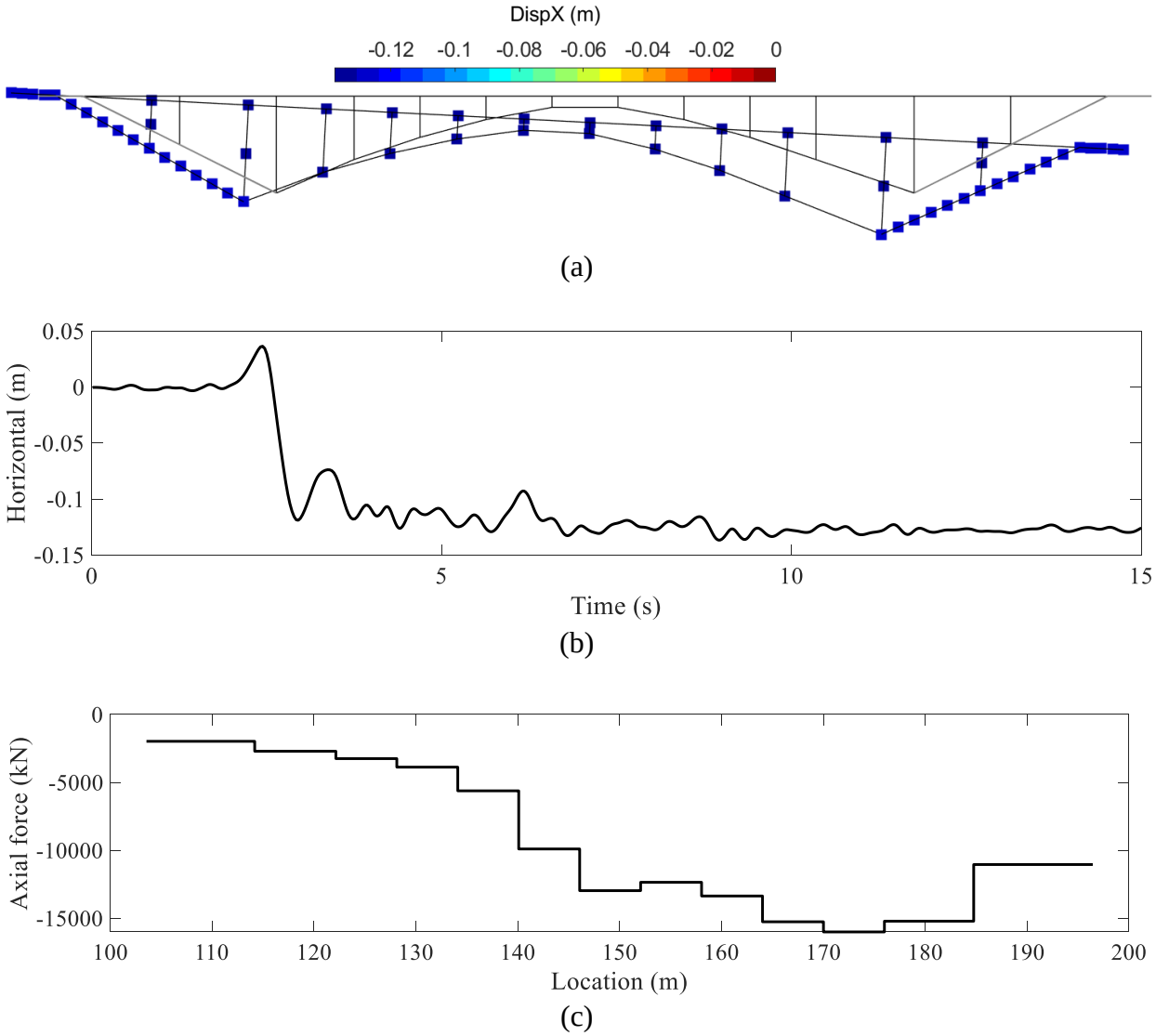

Figure 9.10 Deck response: (a) Longitudinal displacement contour; (b) Time history; (c) Axial force (factor = 10)

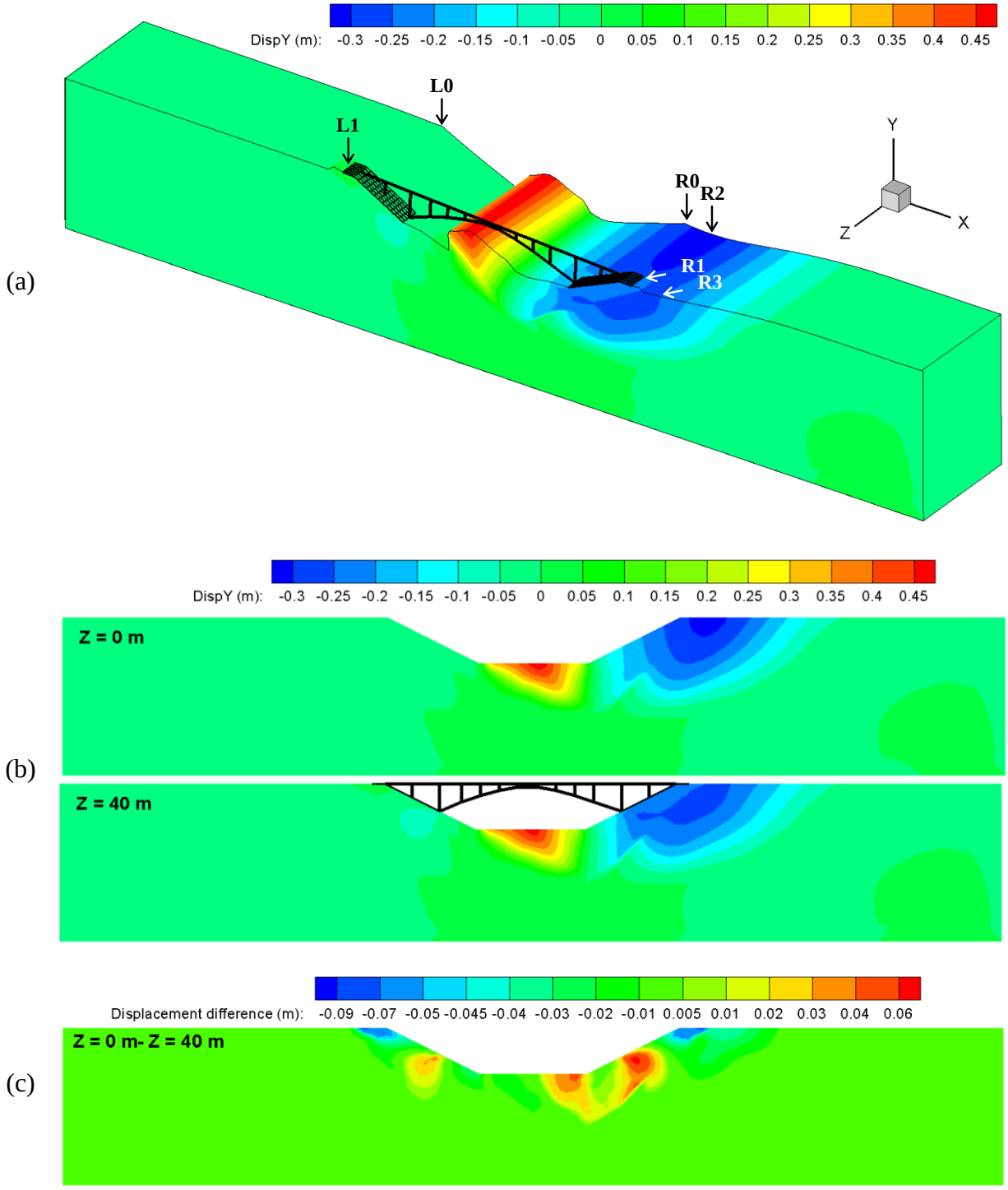

Figure 9.11 Vertical displacement contours at end of shaking (factor = 10): (a) Isometric view; (b) Side views at Z = 0 m and 40 m; (c) Difference between Z = 0 m and Z = 40 m

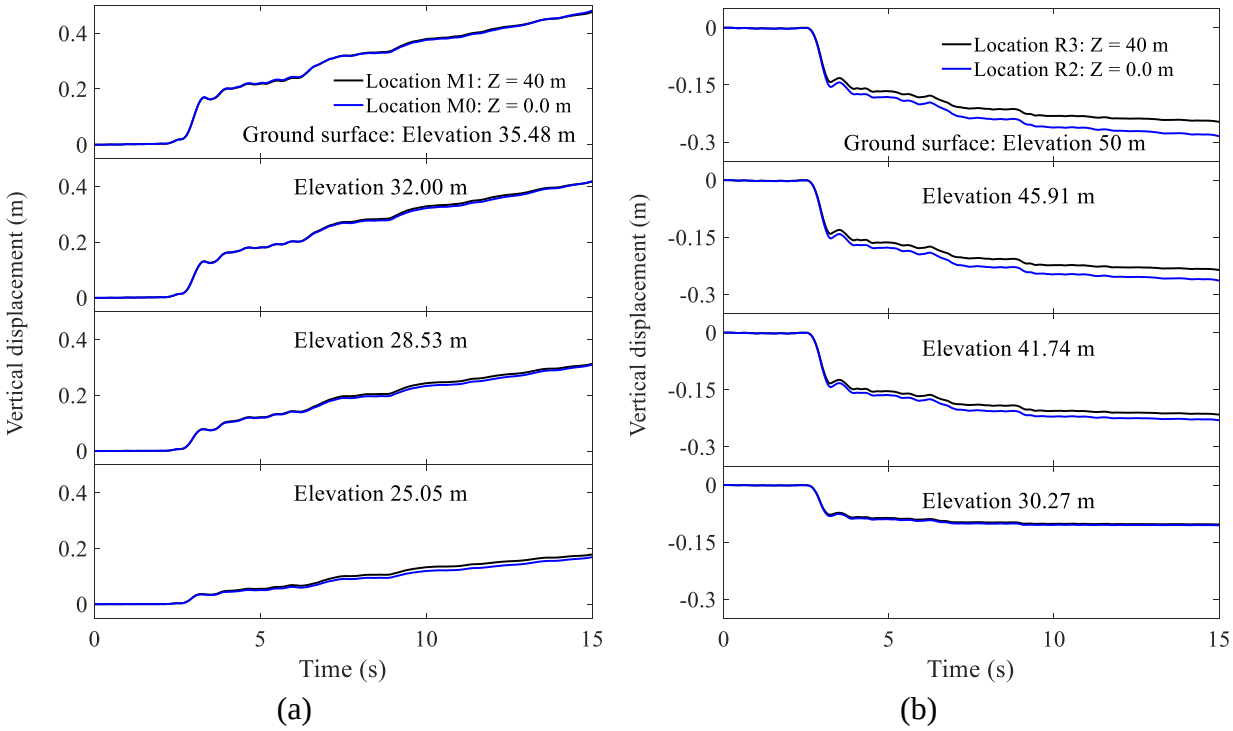

Figure 9.12 Computed vertical displacement time histories: (a) Locations M0 and M1; (b) Locations R2 and R3

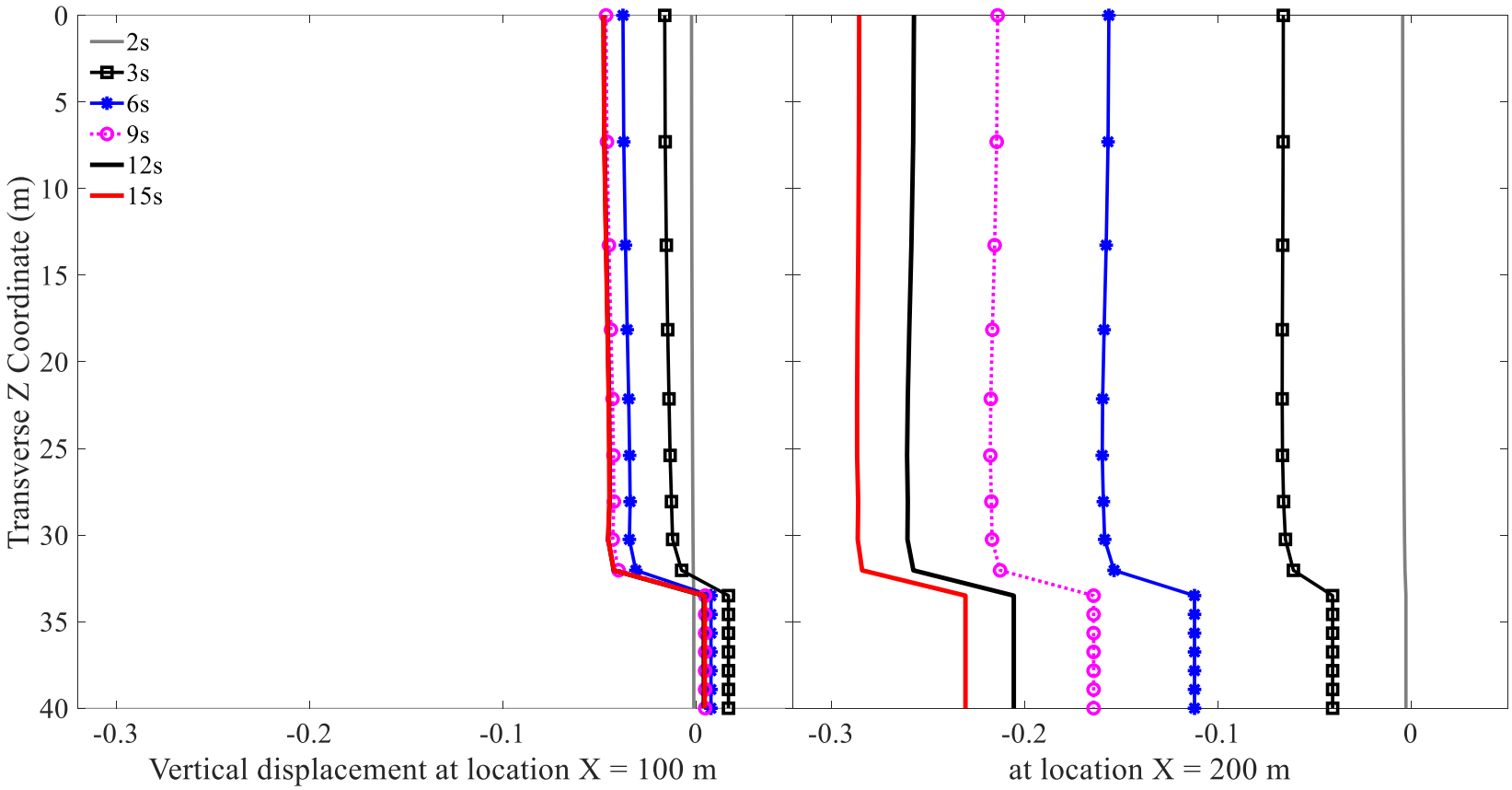

Figure 9.13 Vertical displacement profile of slope top along transverse Z direction at locations X = 100 m (L0-L1) and X = 200 m (R0-R1)

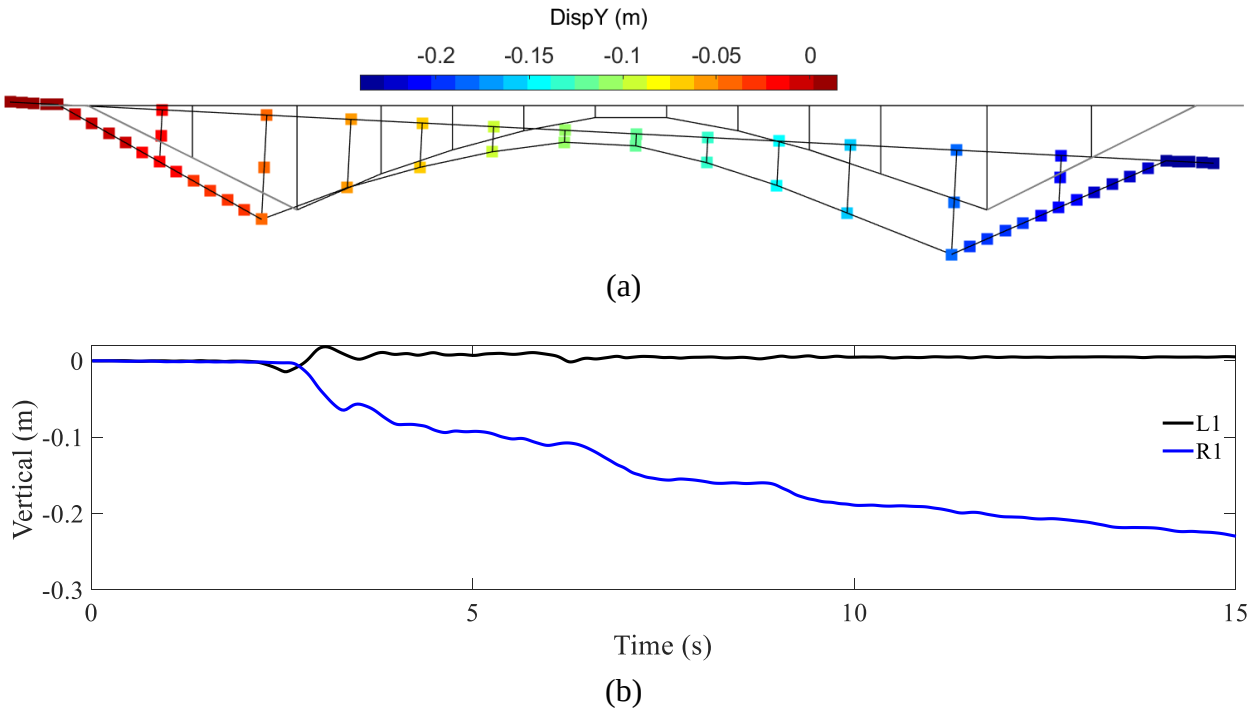

Figure 9.14 Vertical displacement of deck: (a) Contour; (b) Time history

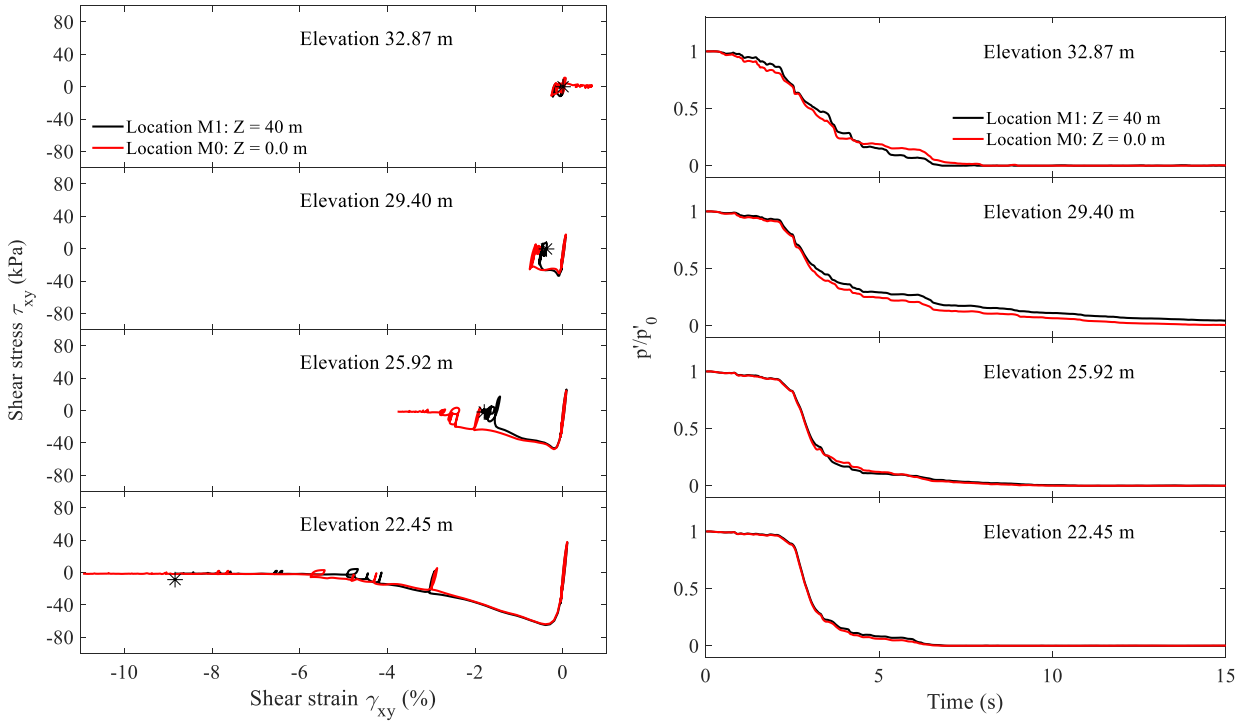

Figure 9.15 Soil response in Layer Q2 at Locations M0, M1: (a) Shear stress-strain; (b) Time histories for ratio of confinement and initial confinement

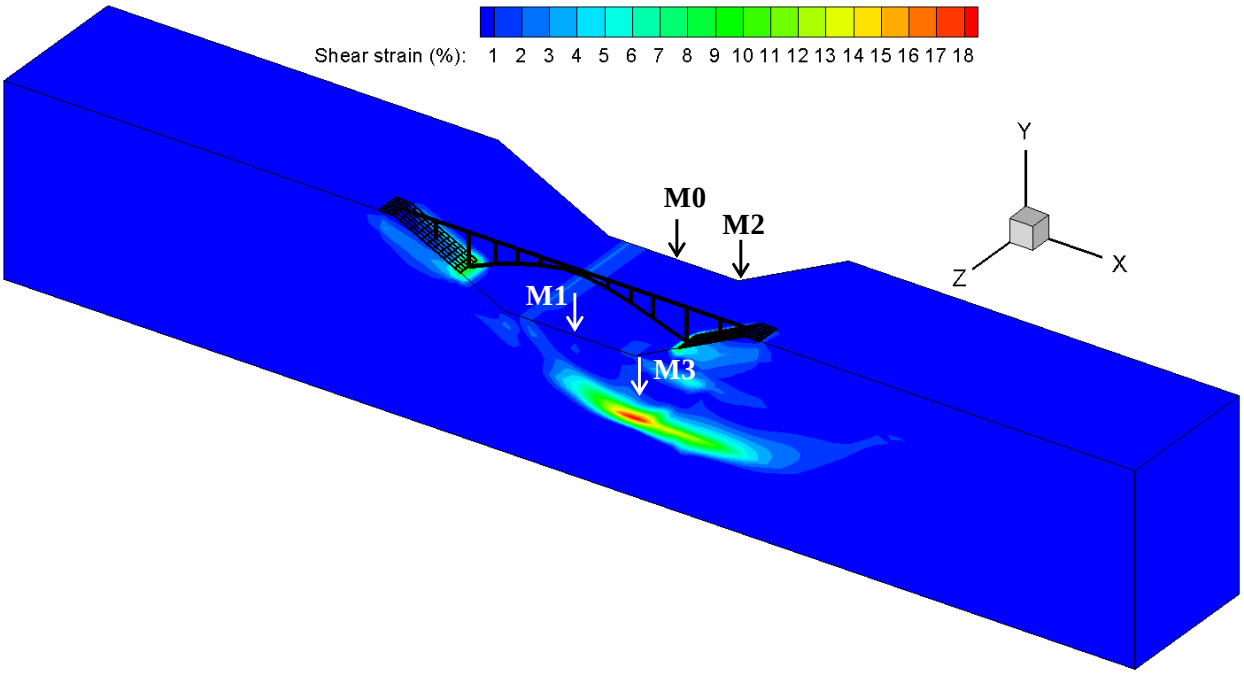

(a)

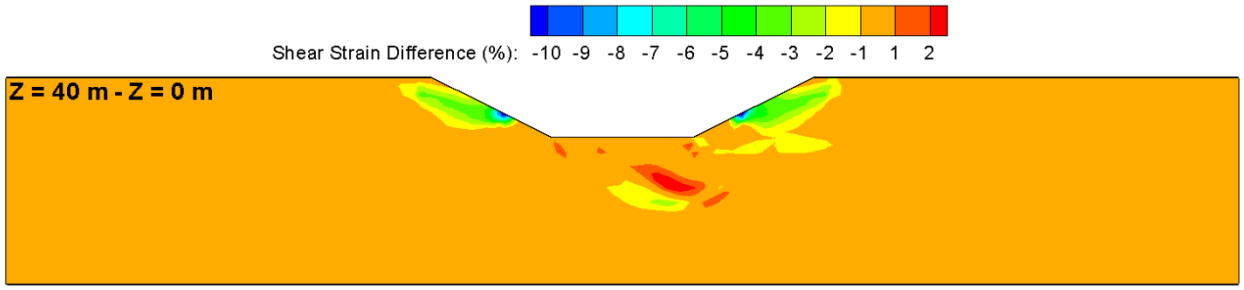

(b)

Figure 9.16 Shear strain γ_{xy} contours: (a) Isometric view at end of shaking; (b) Difference between Z = 0 m and Z = 40 m

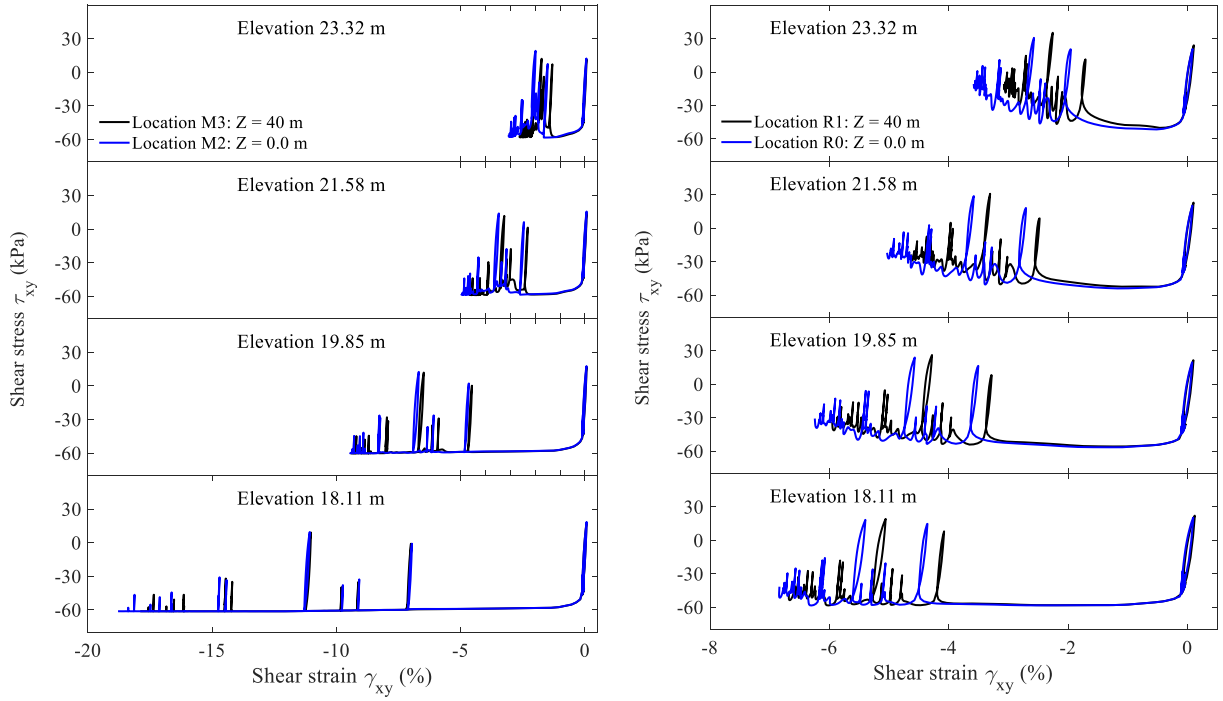

(a) (b)

Figure 9.17 Shear stress-strain in clay Q3 Layer: (a) Locations M2 and M3; (b) Locations R0 and R1

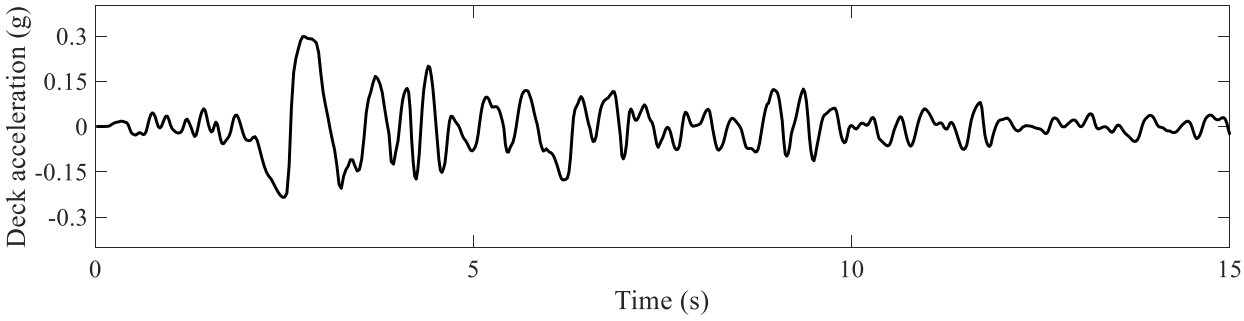

(a)

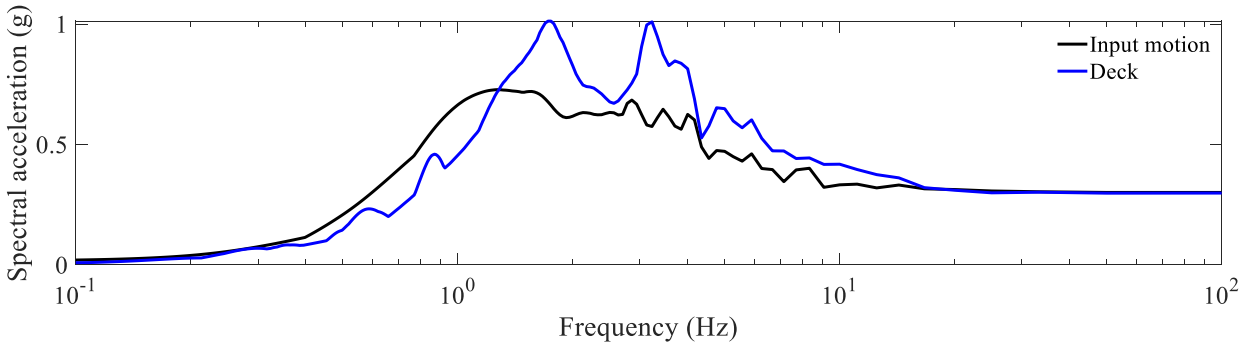

(b)

Figure 9.18 Deck acceleration: (a) Time history; (b) Spectral (5 % damped)

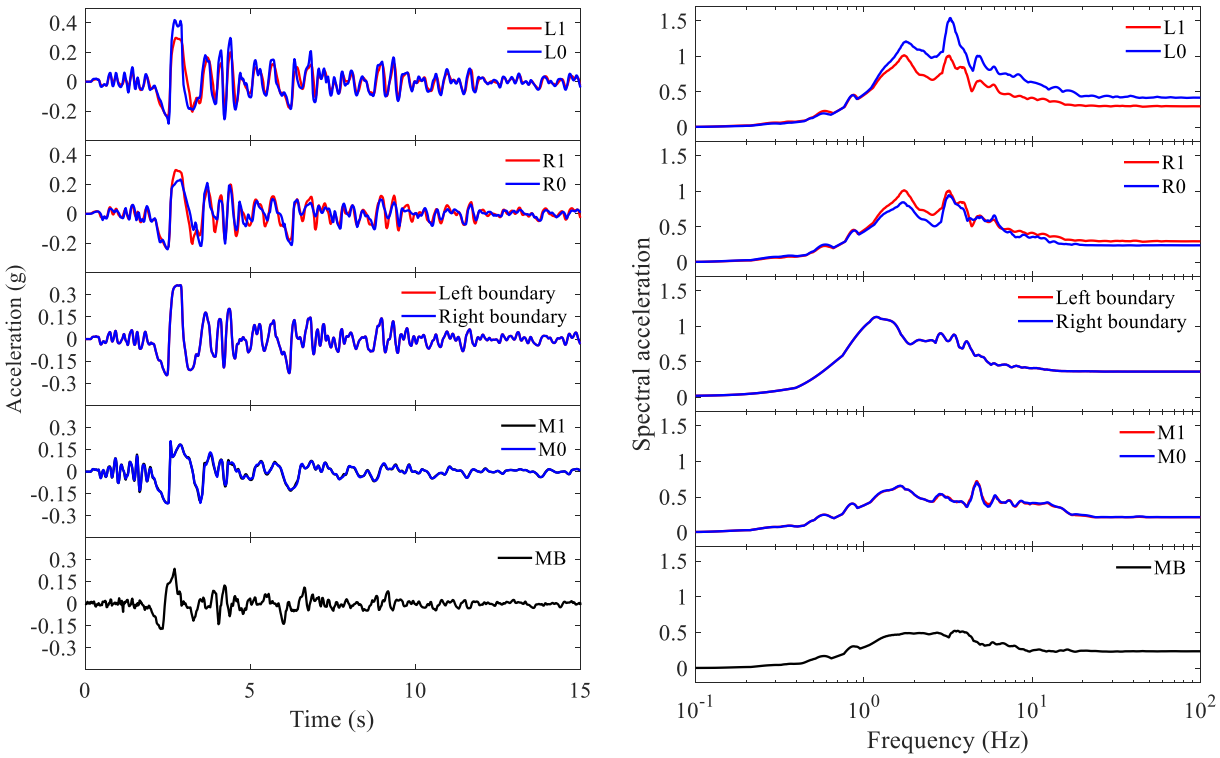

(a) (b)

Figure 9.19 Acceleration response along the bridge-ground configuration (Figure 9.3): (a) Time histories; (b) Spectra (5 % damped)

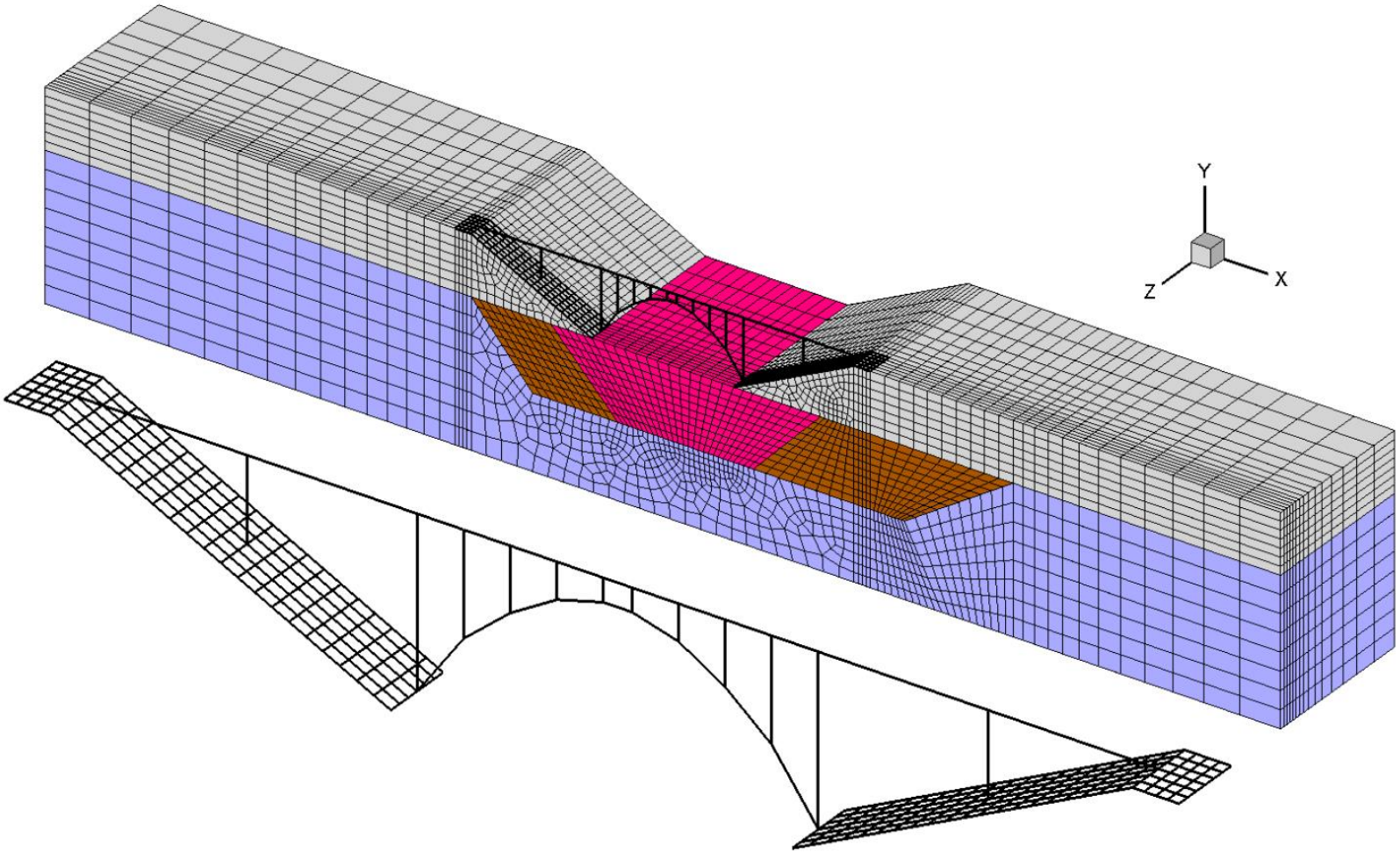

Figure 9.20 3D FE model with larger shallow foundations resting on both side slopes

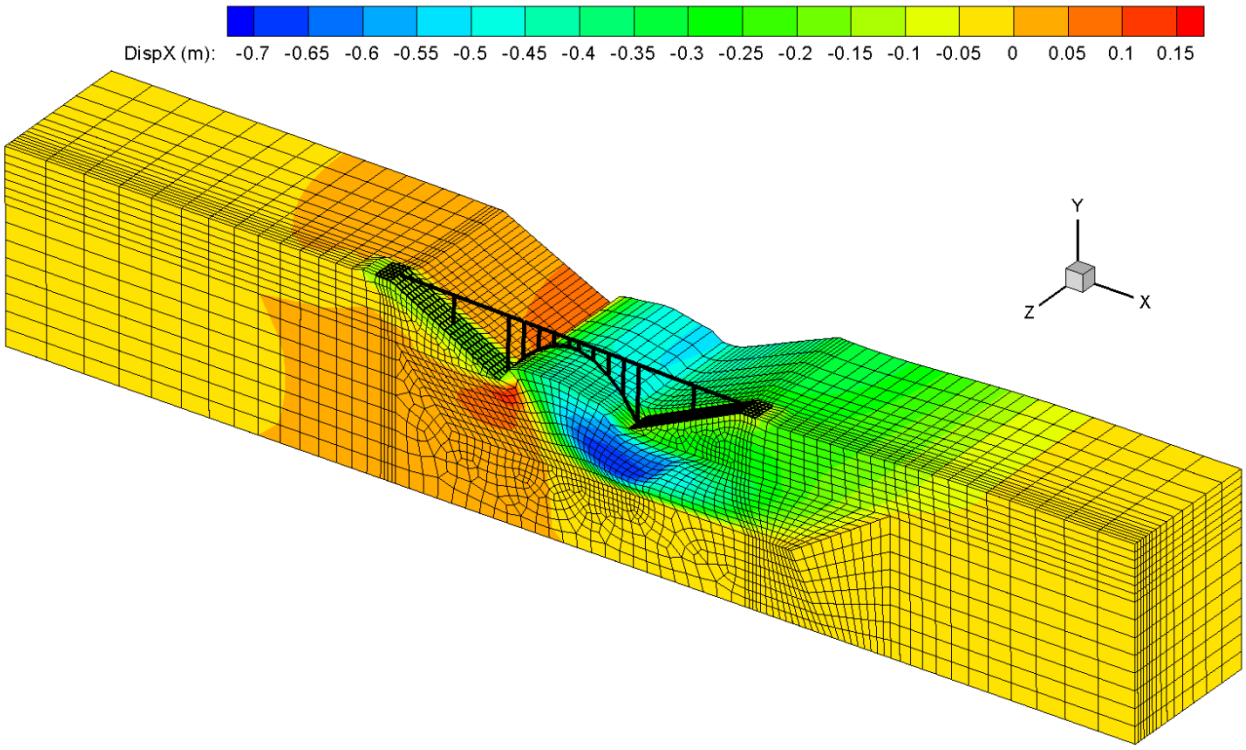

(a)

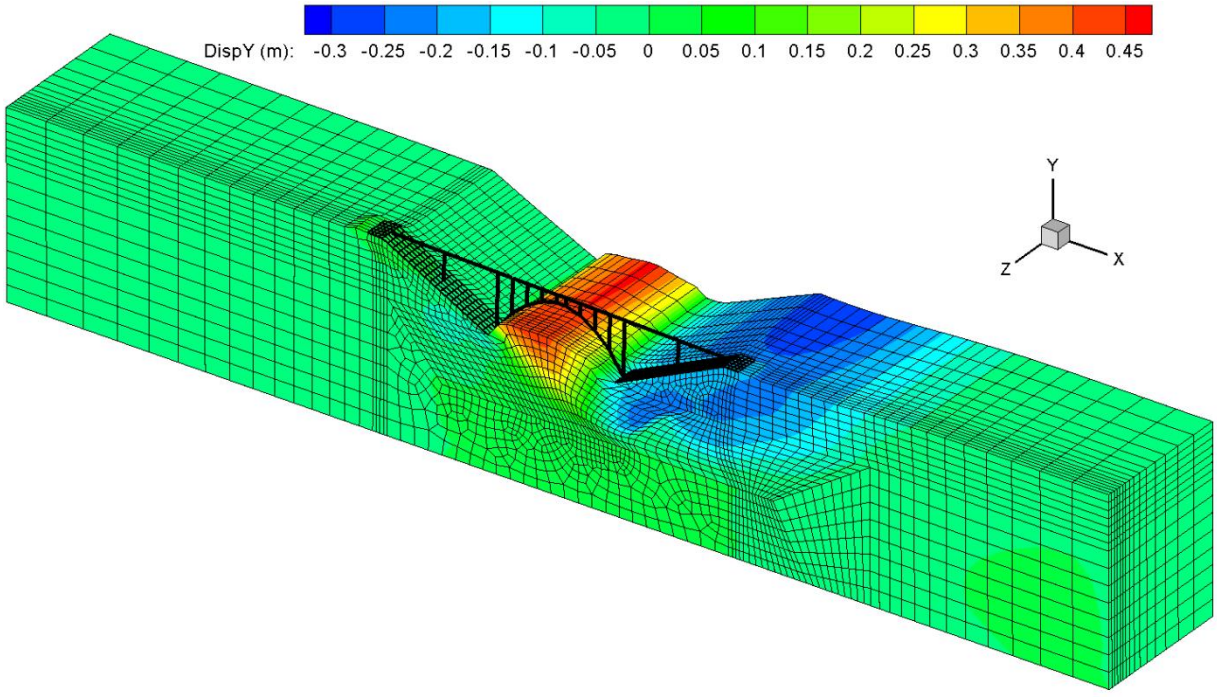

(b)

Figure 9.21 Displacement contours at end of shaking (factor = 10): (a) Longitudinal; (b) Vertical

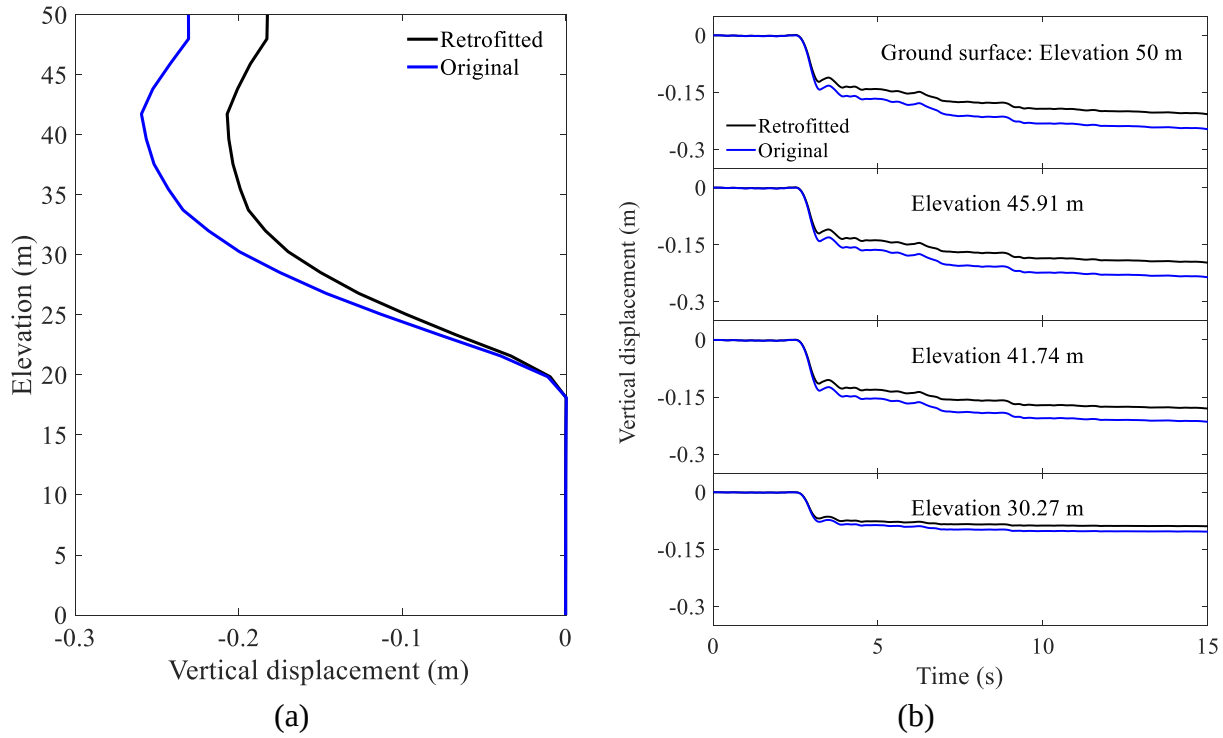

Figure 9.22 Vertical displacement: (a) Profile at Location R1; (b) Time histories at Location R3

Chapter 10. Canyon Effects on Seismically-Induced Liquefaction and Lateral Deformations

10.1. Introduction

The geometry of canyon-shaped configurations might play a significant role in dictating the extent of liquefaction and related lateral deformations. Due to the interaction of both side slopes, a state of higher lateral confinement may be prevalent in the central sections of the canyon. This elevated state of confinement might in turn increase the resistance to liquefaction at such locations. In addition, the zones undergoing downslope lateral deformation on both sides might overlap and result in reduced values. In this regard, a finite element (FE) framework with three different geometric configurations is developed to investigate such effects. The computed results are directly compared with those obtained from corresponding 1D soil columns.

All FE simulations are conducted using the OpenSees Framework for earthquake engineering simulation. Overall, the derived insights are of significance for assessment of liquefaction-induced ground deformations, particularly in narrower canyons. The following sections of this chapter outline: i) specifics of the canyon configurations and soil model properties, ii) details of the employed FE modeling techniques, iii) results of the numerical simulations, and iv) insights derived from the study. Finally, a number of conclusions are presented and discussed.

10.2. Computational Framework

The Open System for Earthquake Engineering Simulation (OpenSees, http://opensees.berkeley.edu, McKenna 2011) framework was employed to conduct the nonlinear canyon analyses subjected to seismic excitation. OpenSees is developed by the Pacific Earthquake Engineering Research (PEER) Center and is widely used for simulation of geotechnical systems

and soil-structure interaction applications (Yang and Elgamal. 2002; Lu et al. 2001; Su et al. 2017). The OpenSees elements and materials used in this FE model are briefly described below.

Two-dimensional four-node quadrilateral elements (OpenSees quadUP) following the *u-p* formulation (Chan 1988) were employed for simulating saturated soil response, where *u* is displacement of the soil skeleton and *p* is pore-water pressure. Implementation of this *u-p* element is based on the following assumptions: 1) small deformation and rotation; 2) solid and fluid density remain constant in time and space; 3) porosity is locally homogeneous and constant with time; 4) soil grains are incompressible; 5) solid and fluid phases are accelerated equally. Hence, the soil layers represented by these effective stress fully coupled elements account for deformations and changes in pore-water pressure during seismic excitation.

The employed soil constitutive model (Yang and Elgamal. 2002; Parra 1996; Yang 2000; Elgamal et al. 2003) was developed based on the multi-surface plasticity theory (Iwan 1967; Prevost 1985). In this model, the shear stress-strain backbone curve is represented by the hyperbolic relationship. As such, soil is simulated by the implemented OpenSees material PressureDependMultiYield02.

The FE matrix equation of the bridge-ground system is integrated in time using a single-step predictor multi-corrector scheme of the Newmark type (Chan 1998; Parra 1996) with integration parameters $\gamma = 0.6$ and $\beta = 0.3025$. The equation is solved using the modified Newton-Raphson approach with Krylov subspace acceleration (Carlson and Miller 1998; McKenna 2011). A relatively low level of stiffness proportional viscous damping was used to enhance numerical stability (coefficient = 0.003), with the main damping emanating from the soil nonlinear shear stress-strain hysteresis response (Su et al. 2017).

10.3. Finite Element Model

10.3.1. Ground and Canyon Configuration

Figure 10.1 displays the 2D FE canyon models with various inclination angles including 2:1, 4:1 and 8:1. These FE models are 500 m long and 43 m high. The width and height of the middle channel are 20 m and 25 m, respectively. All the 2D FE models are comprised of 3746 nodes and 3600 quad elements. For simplicity, the water table was assumed at elevation = 25 m. Along both the lateral mesh boundaries (Figure 10.1), soil columns of large size (not shown) are included (Nielsen 2014; Su et al. 2017; Qiu et al. 2020). These soil columns, at an adequate distance (100-200 m) away from the crest of the canyon slopes to minimize boundary effects (Løkke and Chopra 2017, 2018), efficiently reproduce the desired free-field response at these locations.

To investigate the conventional liquefaction of the central canyon sections, a 1D soil column model was generated (Figure 10.1d) with the same number of quad elements. In this regard, the computed results of this 1D model are directly compared with those obtained from the 2D FE canyon models.

In these FE models, a saturated sand layer was studied based on Nevada Sand properties at a medium relative density (D_r) of approximately 40 % (Elgamal et al. 2003; Yang et al. 2003). The main modeling parameters included standard dynamic soil properties, such as low-strain shear modulus and friction angle (Table 10.1), as well as parameters to control the dilatancy effects (phase transformation angle, contraction, and dilation). For illustration, an example of undrained cyclic shear stress-controlled response with cyclic stress ratio (CSR) = 0.18 under the effective confining stress of 100 kPa is displayed in Figure 10.2. As can be seen in this figure, the model starts accumulation of cycle-by-cycle shear deformations as the soil liquefied at about 9 seconds.

10.3.2. Boundary and Loading Conditions

As mentioned above, both lateral mesh boundaries are located away from the slope (Figure 10.1). Loading was implemented in a staged fashion as follows:

1) Gravity was applied to activate the initial static state with: i) linear elastic properties (Poisson's ratio of 0.47 to lower the initial locked shear stress), ii) nodes on both side boundaries (vertical faces) of the FE model were fixed against longitudinal translation, iii) nodes were fixed along the model base, iv) water table was specified with fixed pore pressure degree of freedom for nodes at elevation = 25 m and above. At the end of this step, the static soil state (Figure 10.3-Figure 10.5) was imposed and displacements under own-weight application were re-set to zero using the OpenSees command InitialStateAnalysis.

2) Soil properties were switched from elastic to plastic (Table 10.1) and the internal variables of the soil consitutive model were adjusted to this stress state (before shaking).

3) Dynamic analysis was conducted by applying an acceleration time history (Figure 10.1e) to the base of the FE model. For simplicity, seismic motion (Figure 10.1e) was simply taken as that of the 1994 Northridge earthquake ground surface Rinaldi Receiving Station record (Component S48W), scaled down to a peak amplitude of 0.3 g.

10.4. Computed Response

10.4.1. Deformation

Figure 10.6-Figure 10.7 display the horizontal and vertical ground deformations at end of shaking. Due to the interaction of both slopes, the downslope movement of one side was significantly restrained by the other. The level of interference becomes more significant in narrower canyons with steeper inclinations (Figure 10.6 and Figure 10.8). Finally, vertical

displacement of the center section is larger with the increase in inclination angle (Figure 10.7 and Figure 10.9).

Figure 10.10 illustrates the shear strain γ_{xy} contours at end of shaking. As seen in this figure, permanent shear strain γ_{xy} occurred near the bottom and the value was higher in the steeper inclinations.

Computed displacements of these 2D canyon models are directly compared with those obtained from 1D shear beam results under the same input motion scenario (Figure 10.1e). As seen in Figure 10.8 and Figure 10.9, peak horizontal displacement of the 1D models was higher than those of the 2D canyon models. In addition, vertical displacements of 1D model were significantly lower compared to the 2D canyon models (Figure 10.9). Obviously, the upward heave of the 2D models does not occur at all in the 1D model response.

10.4.2. Excess Pore Pressure

Figure 10.11 and Figure 10.12 show excess pore pressure u_e and excess pore pressure ratio $r_u = u_e/\sigma'_v$ at end of shaking, where σ'_v denotes initial mean effective stress. The soil liquefaction is conventionally defined by the value of r_u reaching a maximum of 1.0. As seen from Figure 10.11 and Figure 10.12, the sand layer was liquefied at end of shaking ($r_u = 1$) except within the channel zone in the center of the canyon. The r_u time histories of the 1D shear beam model and 2D canyon models are displayed in Figure 10.13. As seen in this figure, the 1D model ($r_u = 1$) was fully liquefied shortly after about 6 seconds. However, the values of r_u in the center sections of the 2D canyon models were far below 1.0, demonstrating that the conventional 1D liquefaction assessment techniques may significantly over-estimate the risk due to liquefaction and associated lateral deformation.

10.4.3. Soil Response

Figure 10.14-Figure 10.16 show the vertical, horizontal, and mean effective stress contours at end of shaking. Overall, vertical effective stress in the 2D models was reduced to a relatively low level (Figure 10.17). However, a state of higher lateral confinement (Figure 10.18 and Figure 10.19) was induced in the center of the canyon due to the interaction of both slopes. This mechanism in turn would potentially increase the liquefaction resistance at such locations (e.g., potential reduction of excess pore pressure in Figure 10.12 and Figure 10.13).

To further illustrate the involved mechanism, the shear stress-strain and mean effective stress-shear stress curves are displayed in Figure 10.20 and Figure 10.21. It can be seen that the confinement of the 1D model was reduced to zero soil faster during the shaking event (Figure 10.19), and the shear stress reached the residual state.

10.5. Post-Shaking Excess Pore Pressure Ratio

Post-shaking excess pore pressure ratio time histories are shown in Figure 10.22. It can be seen that the values of r_u in the center of 2D canyon models were increased after shaking at shallower depth until about 500 seconds, mainly due to migration of higher pore pressures from both side slopes.

10.6. Two-Dimensional Slope Model with Various Inclinations

To further illustrate the canyon effects on the liquefaction-induced ground deformation, three additional FE simulations were performed with only one side slope (Figure 10.23). Unlike the canyon configuration, downslope ground movement is not restrained (no interaction from the other side). Figure 10.24 and Figure 10.25 display the horizontal and vertical displacement contours at end of shaking. It can be seen that both horizontal and vertical displacements were higher when compared to the 2D canyon models (Figure 10.6 and Figure 10.7).

10.7. Summary and Conclusions

A 2D FE framework with three different geometric configurations is developed to investigate the effects of canyon geometry on liquefaction and downslope ground deformations. The computed results are directly compared with those obtained from corresponding 1D shear beam models. Furthermore, canyon effects on the post-shaking excess pore pressure dispassion are investigated. All FE simulations are conducted in the open system for earthquake engineering simulation framework (OpenSees).

Specific observations and conclusions include:

1) Geometric configuration of the sloping canyon might play a significant role in dictating the extent of liquefaction and its consequences. Due to the interaction of both slopes, a state of higher lateral confinement may be induced in the central sections of canyon. This mechanism might in turn increase the liquefaction resistance at such locations.

2) Particularly for relatively narrow canyons, soil in the central sections will experience a significant tendency for upward heave with associated possible reduction in excess pore pressure due to dilation and the relatively low soil permeability (during seismic excitation).

3) It was demonstrated that the conventional one-dimensional liquefaction assessment techniques may significantly over-estimate the risk due to liquefaction and associated lateral deformation.

4) Post-shaking excess pore pressure dissipation can be affected by the canyon geometric configuration.

5) An interference pattern in the sloping canyon showed that downslope movement of one side can be significantly restrained by the other. The level of interference becomes more significant in narrower canyons with steeper inclinations.

10.8. Acknowledgements

Chapter 10, in full, is currently being prepared for submission for publication of the material as it may appear in the following journal publication (The dissertation author was the primary investigator and author of this paper):

Qiu, Z. and Elgamal, A. "Canyon Effects on Seismically-Induced Liquefaction and Lateral Deformations."

Table 10.1 Sand model parameters

Model Parameters (PressureDependMultiYield02)	Loose (D_r = 40 %)
Reference mean effective pressure, p'_r (kPa)	100.0
Mass density ρ (t/m^3)	1.8
Maximum shear strain at reference pressure, $\gamma_{max,r}$	0.1
Shear modulus at reference pressure, G_r (MPa)	90.0
Stiffness dependence coefficient n, defined in $G = G_r(\frac{\boldsymbol{P'}}{\boldsymbol{P'_r}})^{\boldsymbol{n}}$	0.5
Poisson's ratio in dynamic analysis, v	0.4
Shear strength at zero confinement, c (kPa)	2.0
Friction angle, ϕ (degree)	32.0
Phase transformation angle, ϕ_{PT} (degree)	26.0
Contraction coefficient, c_1	0.067
Contraction coefficient, c_2	5.0
Contraction coefficient, c_3	0.23
Dilation coefficient, d_1	0.06
Dilation coefficient, d_2	3.0
Dilation coefficient, d_3	0.27
Damage coefficient, Liq_1	1.0
Damage coefficient, Liq_2	0.0
Permeability (m/s)	1.0×10^{-5}

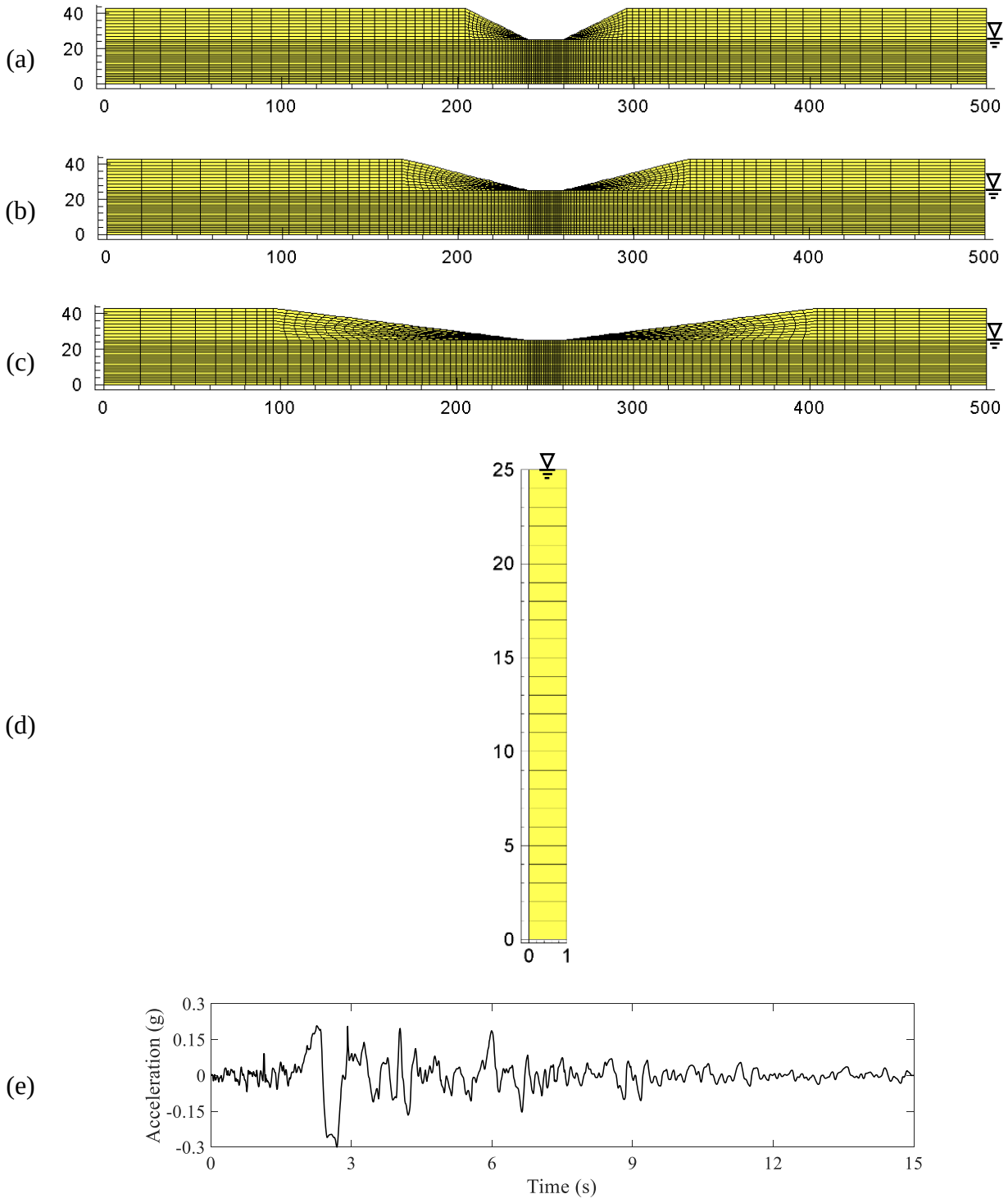

Figure 10.1 FE canyon model with various inclination angles: (a) 2:1; (b) 4:1; (c) 8:1; (d) 1D shear beam; (e) Input motion

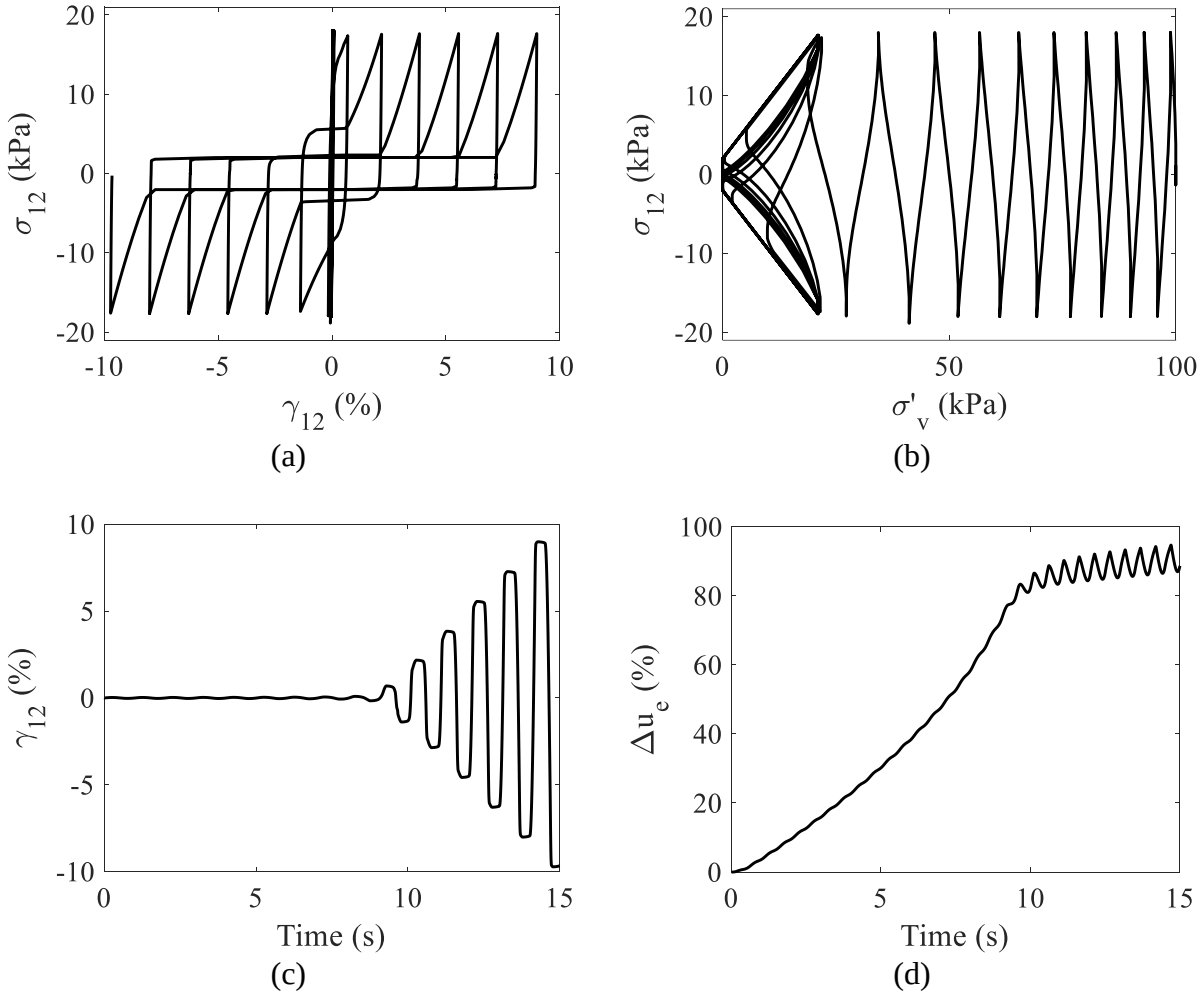

Figure 10.2 Sand model response: (a) Shear stress-strain; (b) Mean effective stress-shear stress; (c) Shear strain; (d) Excess pore pressure

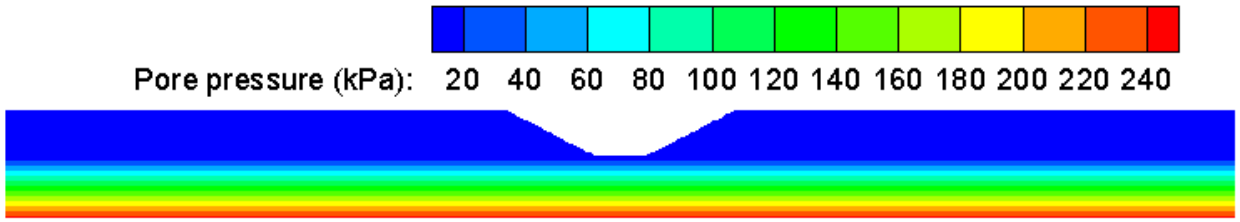

(a)

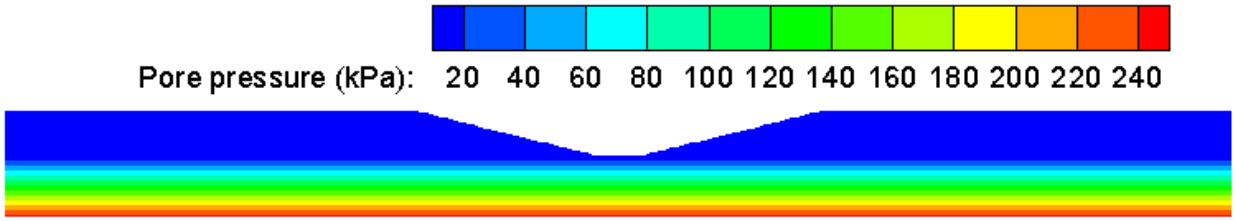

(b)

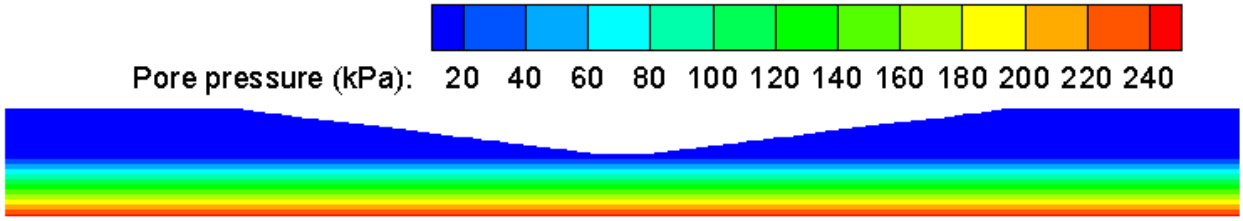

(c)

Figure 10.3 Pore pressure contour before shaking: (a) Inclination 2:1; (b) Inclination 4:1; (c) Inclination 8:1

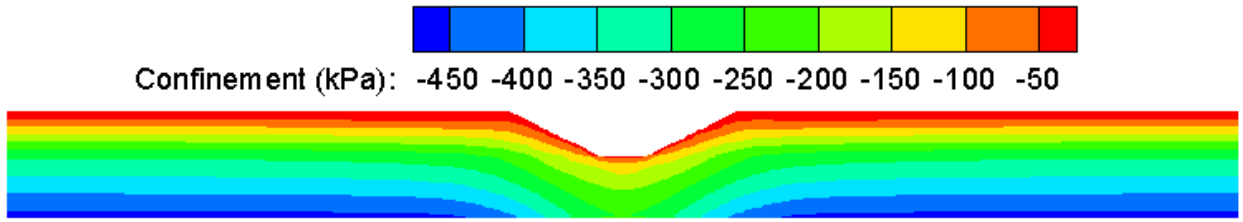

(a)

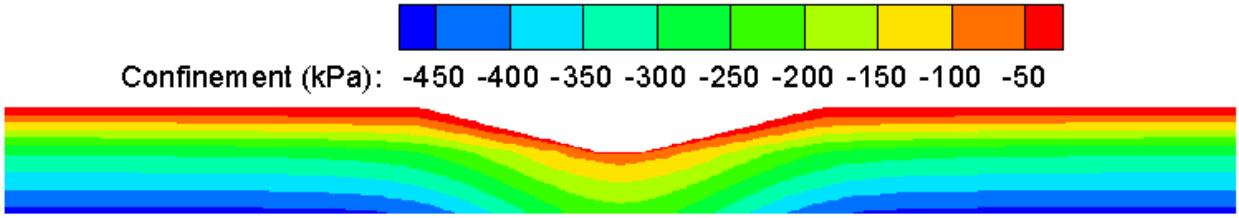

(b)

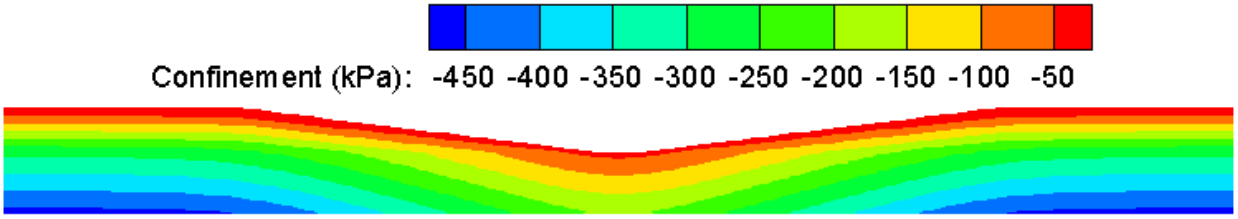

(c)

Figure 10.4 Mean effective stress contour before shaking: (a) Inclination 2:1; (b) Inclination 4:1; (c) Inclination 8:1

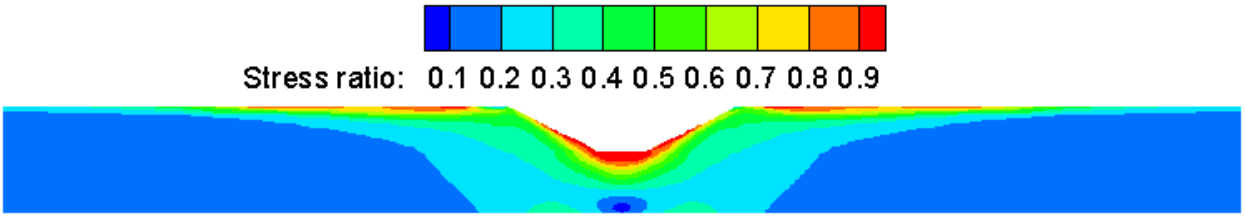

(a)

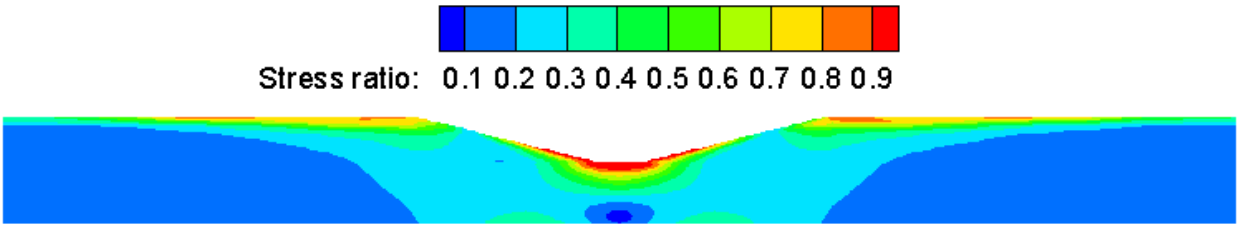

(b)

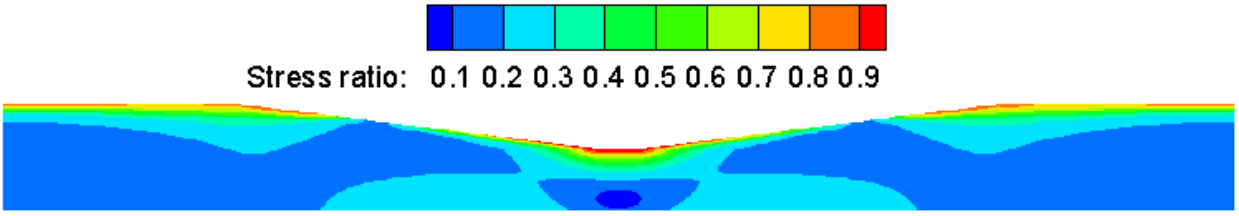

(c)

Figure 10.5 Shear stress ratio contour before shaking: (a) Inclination 2:1; (b) Inclination 4:1; (c) Inclination 8:1

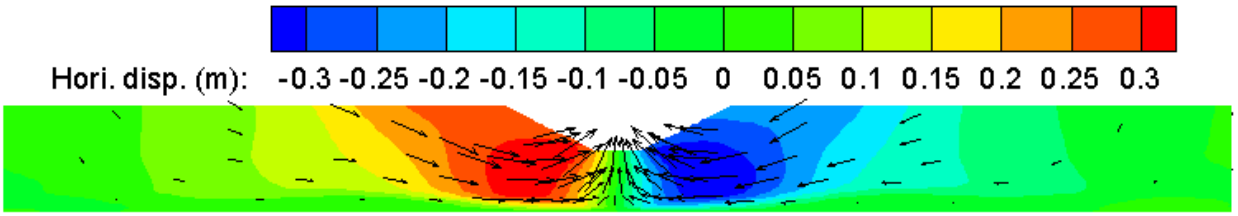

(a)

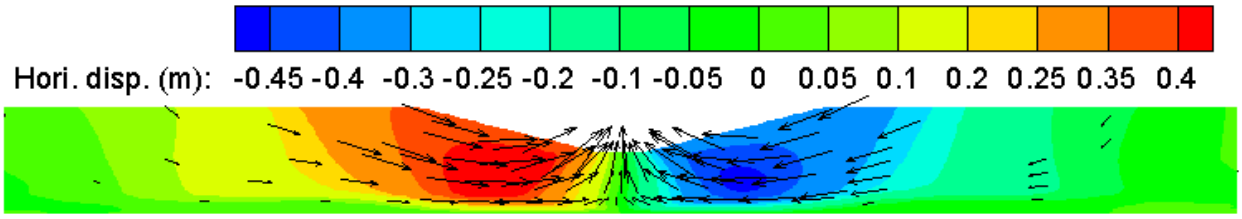

(b)

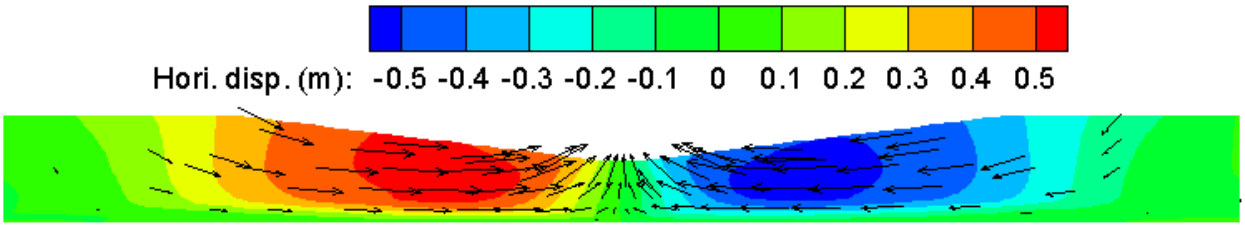

(c)

Figure 10.6 Horizontal displacement contour at end of shaking: (a) Inclination 2:1; (b) Inclination 4:1; (c) Inclination 8:1 (arrows displaying the direction of ground movement)

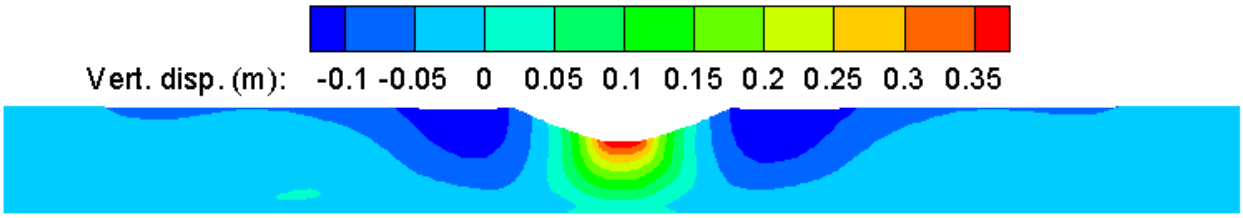

(a)

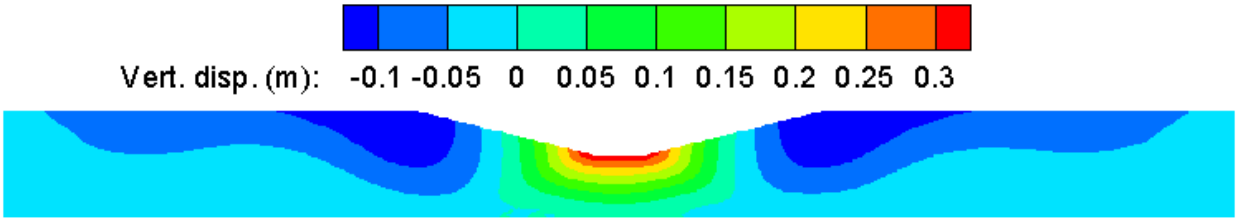

(b)

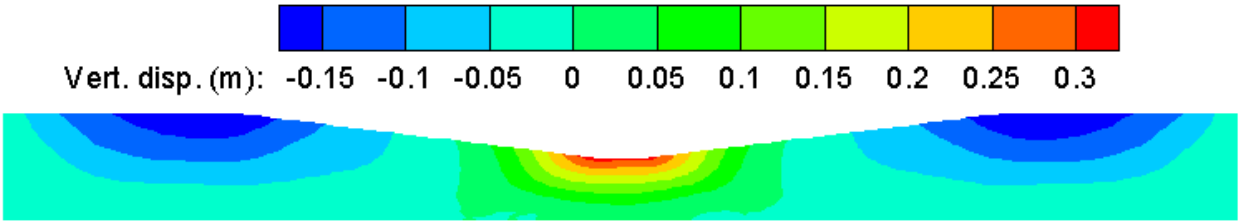

(c)

Figure 10.7 Vertical displacement contour at end of shaking: (a) Inclination 2:1; (b) Inclination 4:1; (c) Inclination 8:1

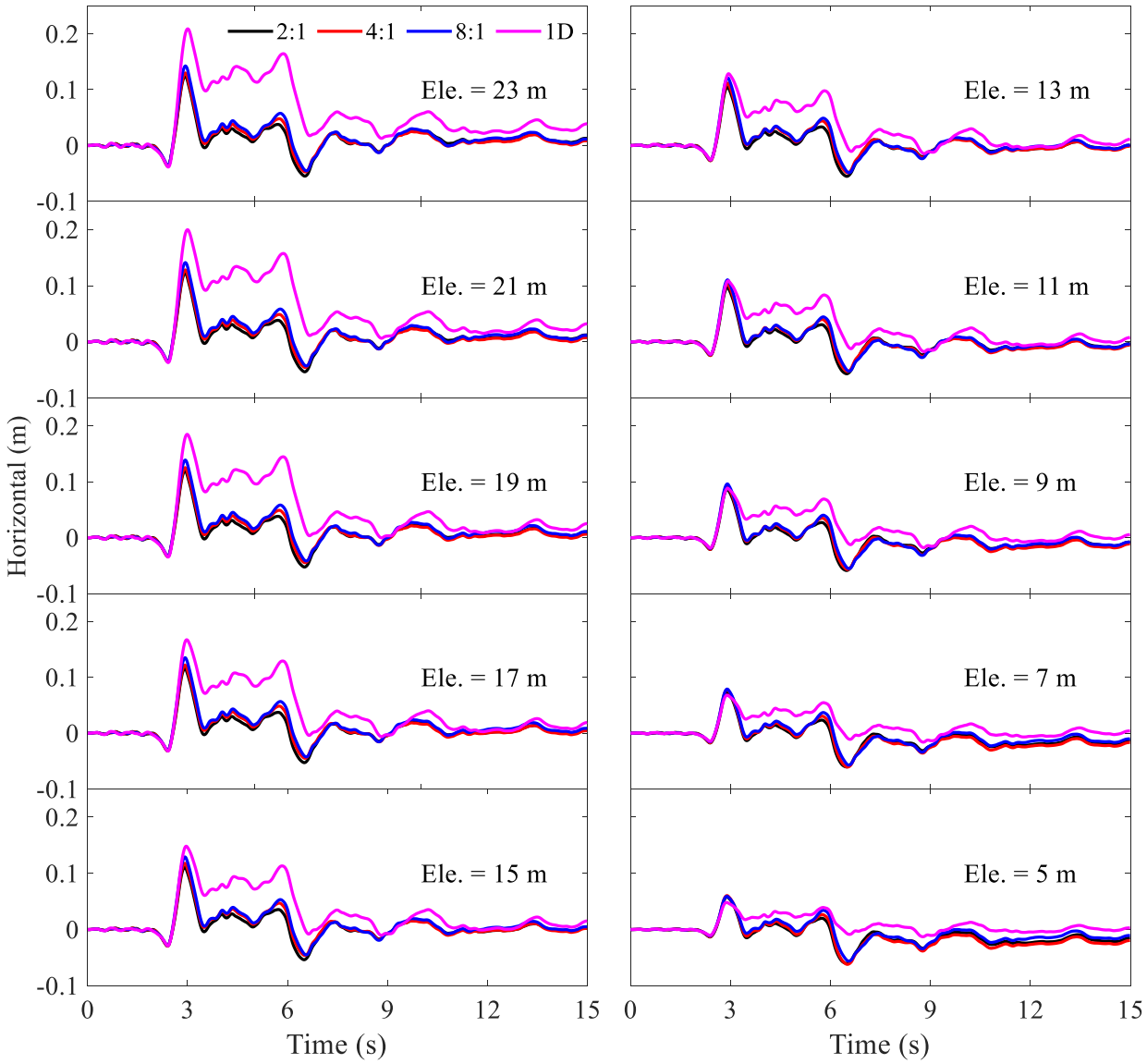

Figure 10.8 Horizontal displacement time histories

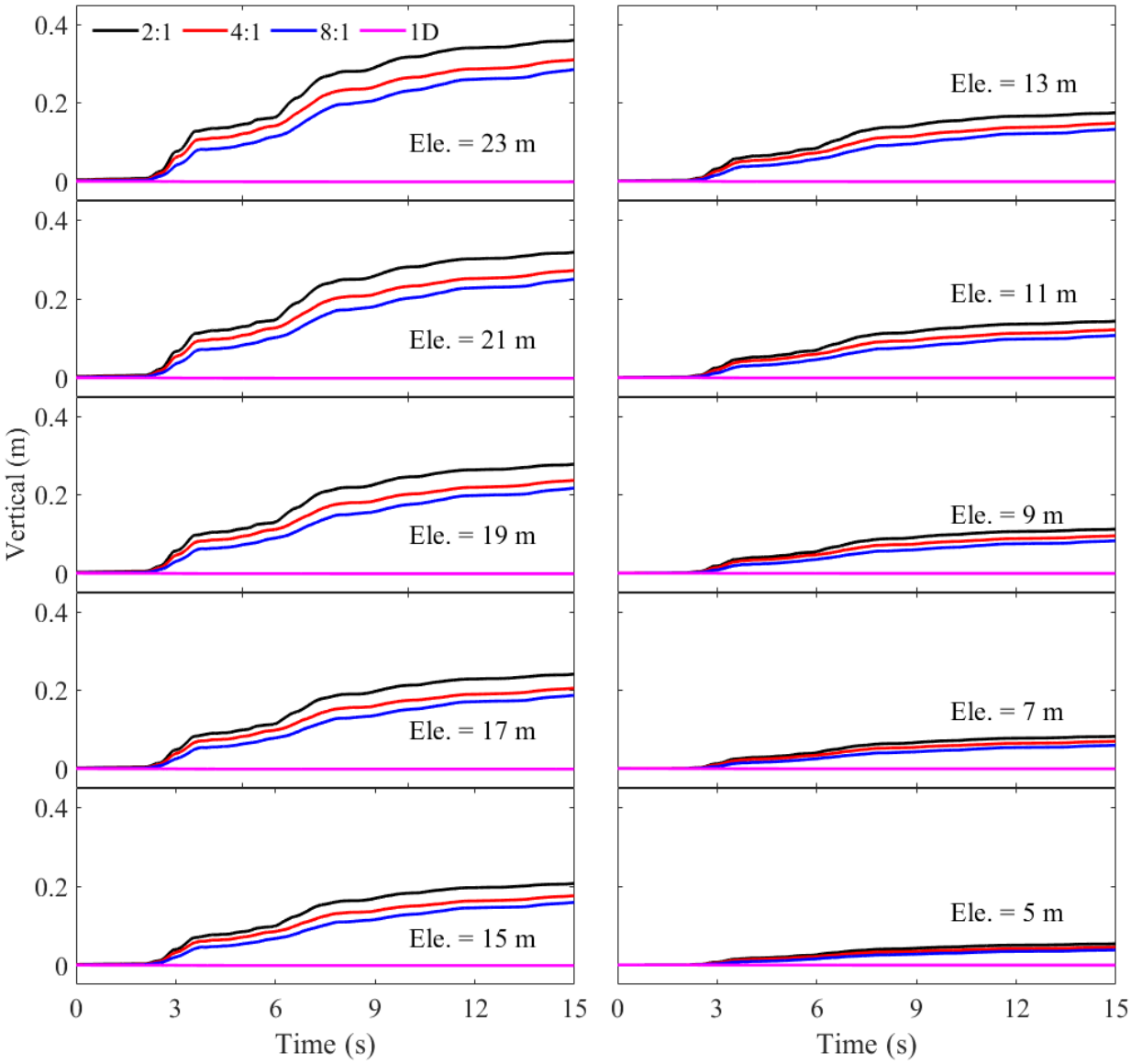

Figure 10.9 Vertical displacement time histories

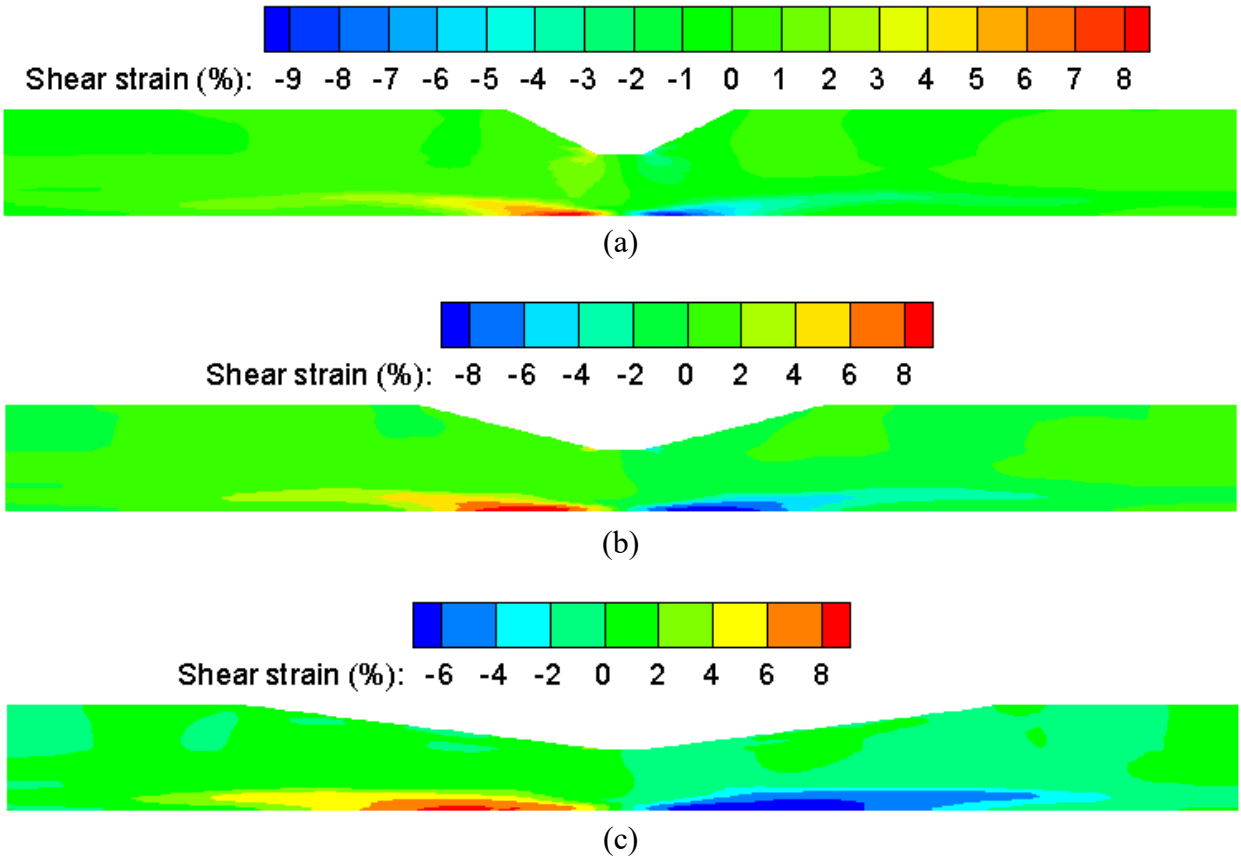

Figure 10.10 Shear strain contour at end of shaking: (a) Inclination 2:1; (b) Inclination 4:1; (c) Inclination 8:1

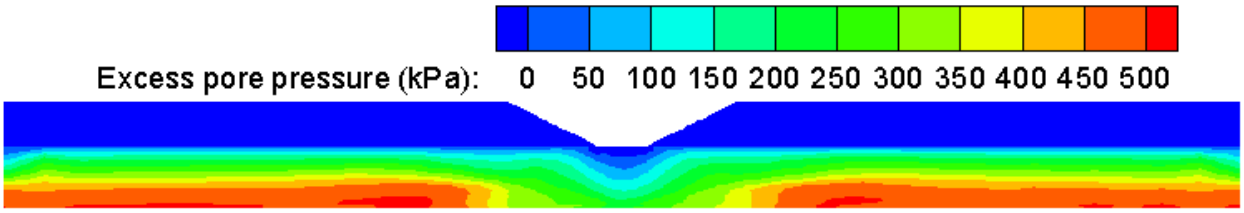

(a)

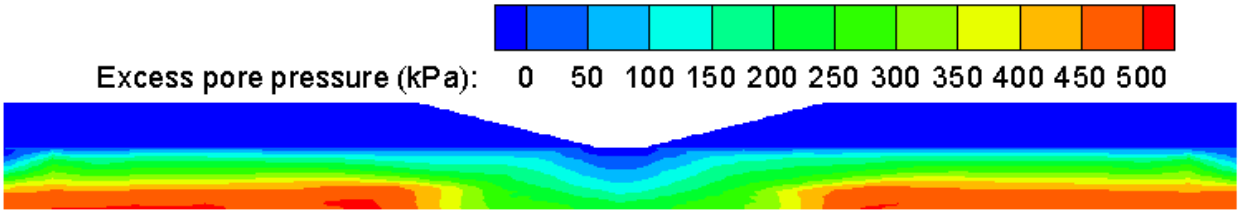

(b)

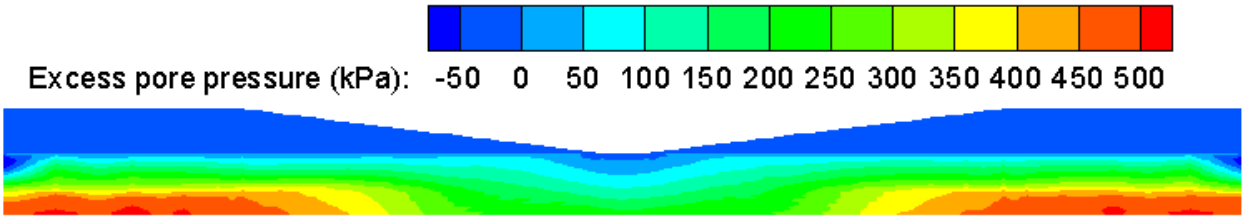

(c)

Figure 10.11 Excess pore pressure contour at end of shaking: (a) Inclination 2:1; (b) Inclination 4:1; (c) Inclination 8:1

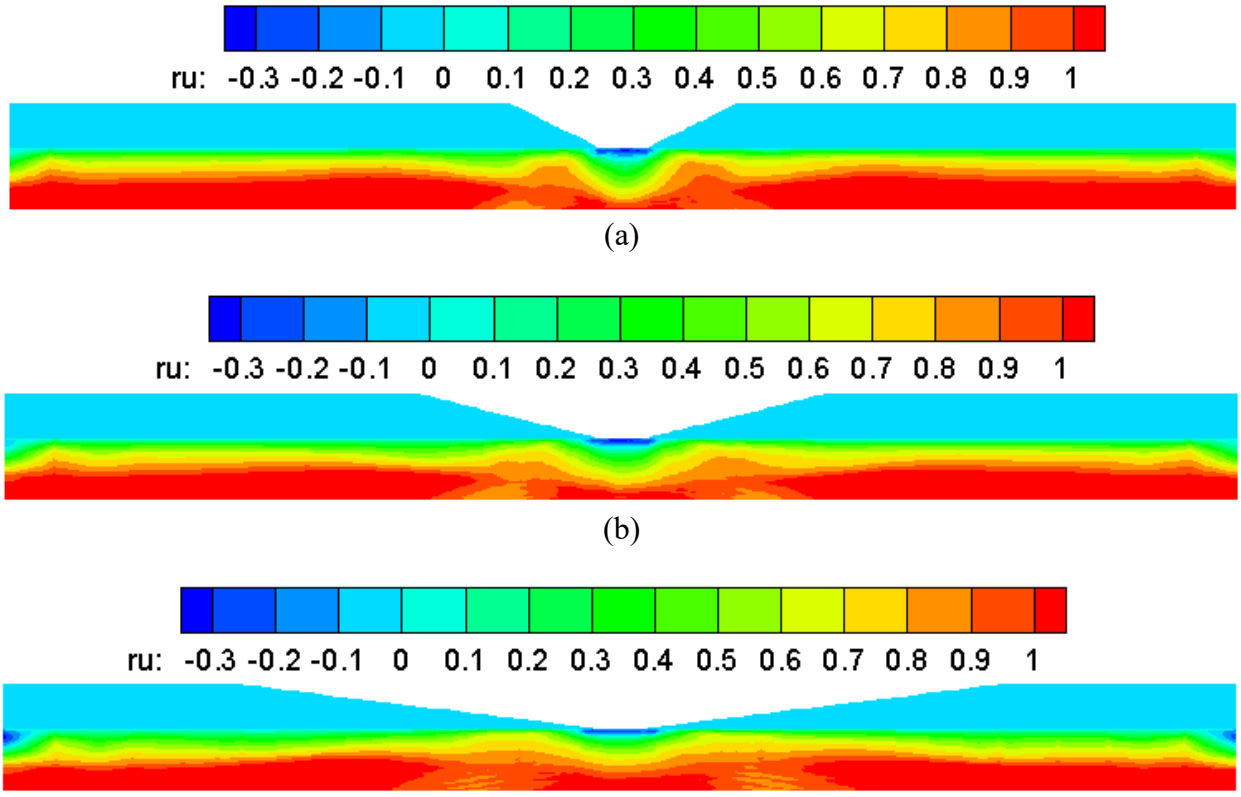

Figure 10.12 Excess pore pressure ratio contour at end of shaking: (a) Inclination 2:1; (b) Inclination 4:1; (c) Inclination 8:1

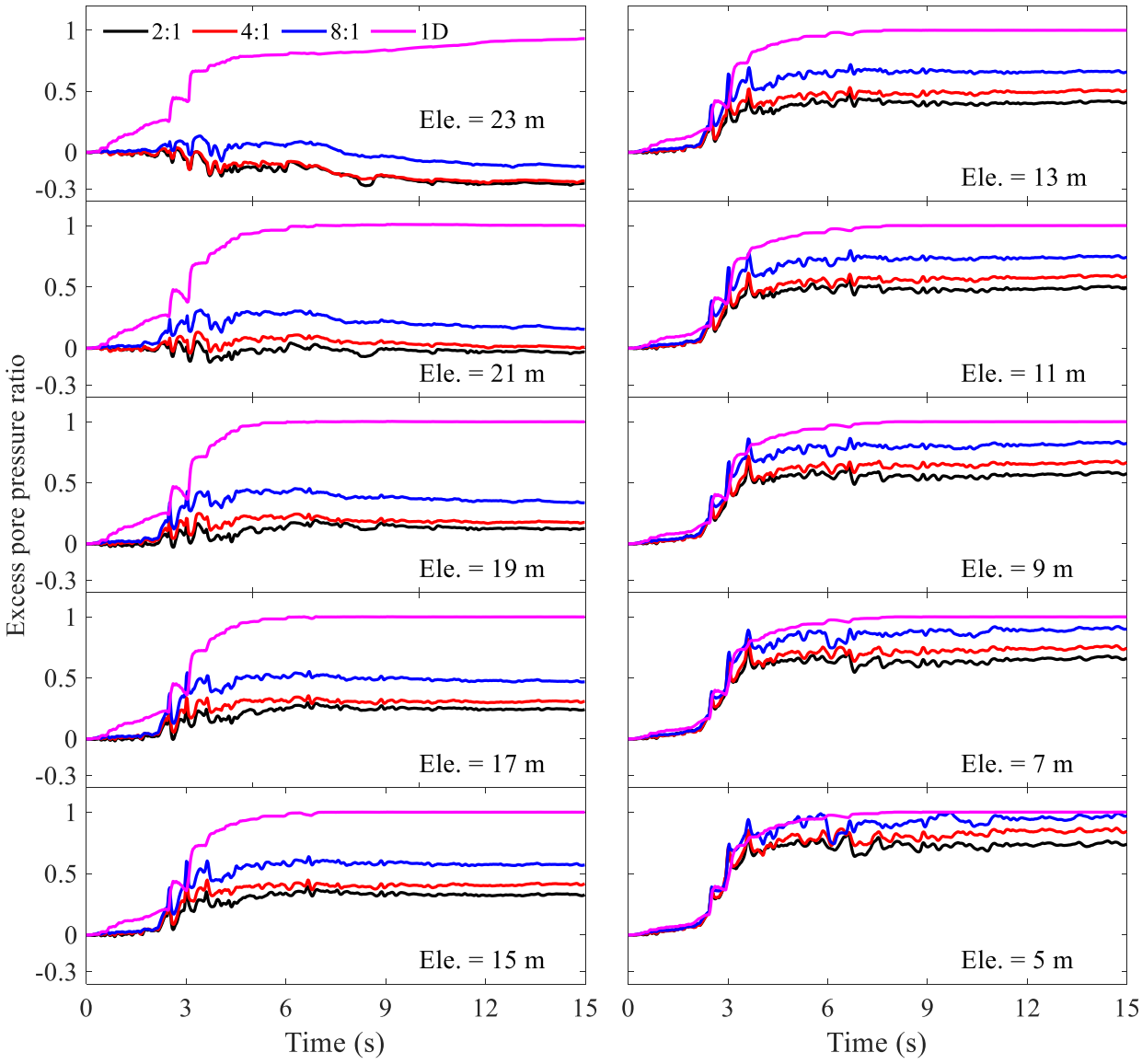

Figure 10.13 Excess pore pressure ratio time histories

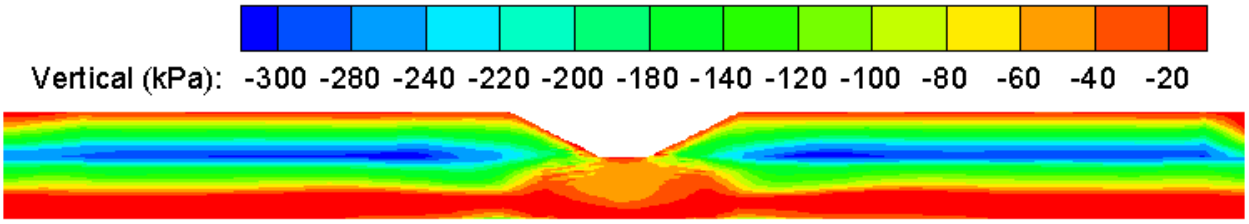

(a)

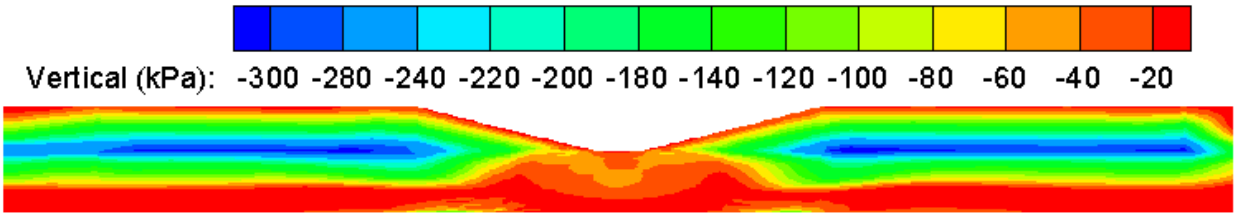

(b)

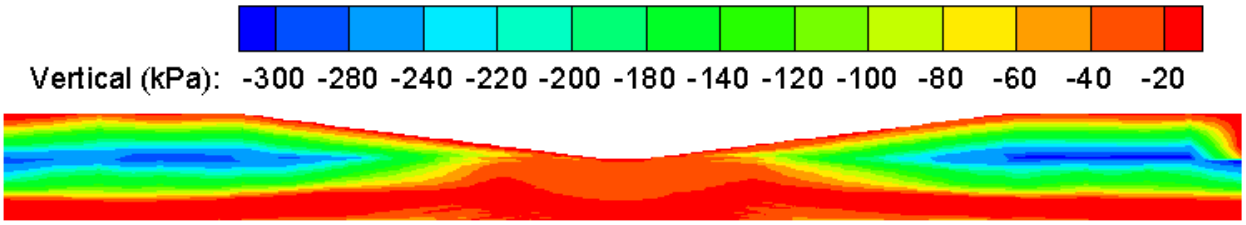

(c)

Figure 10.14 Vertical effective stress contour at end of shaking: (a) Inclination 2:1; (b) Inclination 4:1; (c) Inclination 8:1

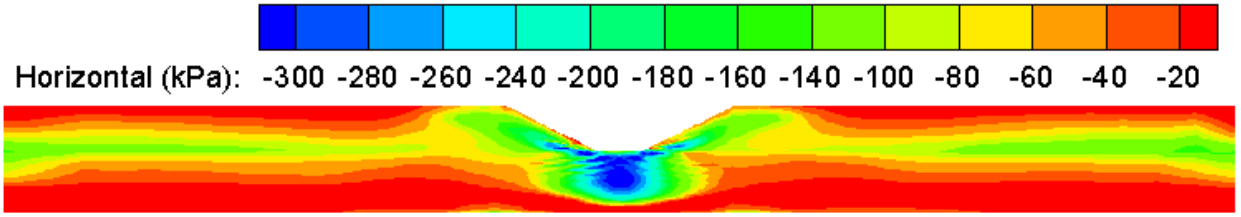

(a)

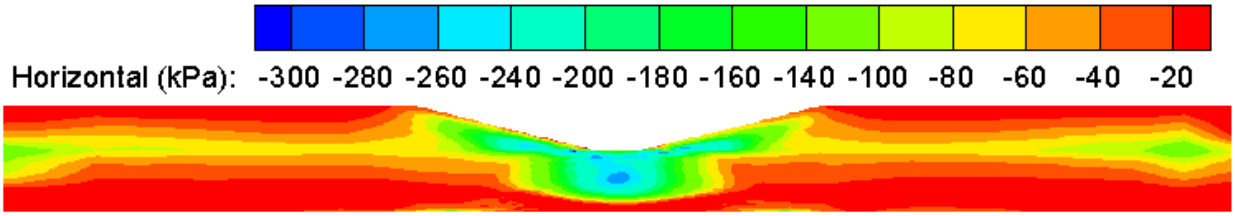

(b)

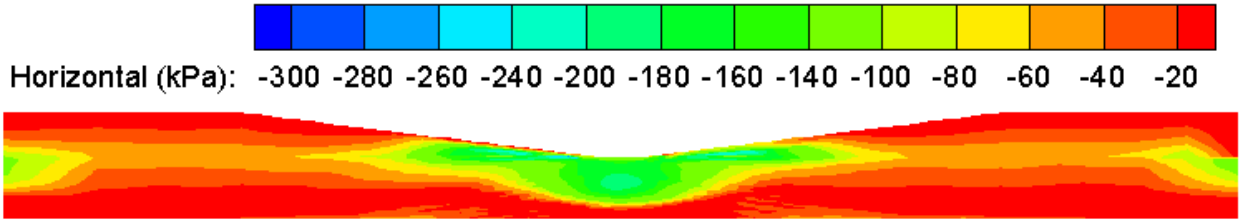

(c)

Figure 10.15 Horizontal effective stress contour at end of shaking: (a) Inclination 2:1; (b) Inclination 4:1; (c) Inclination 8:1

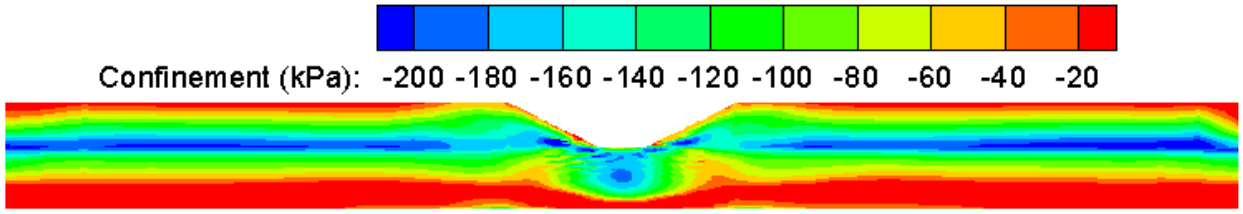

(a)

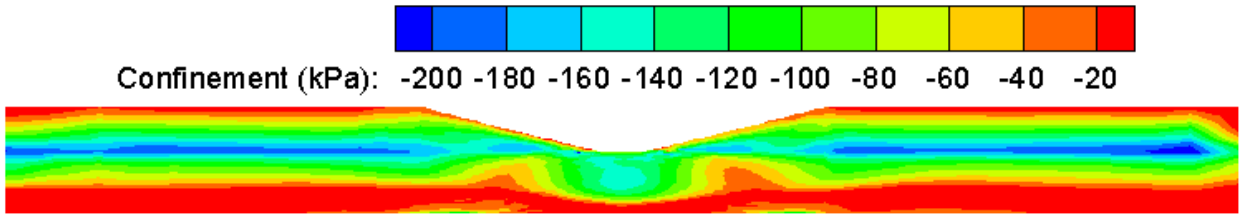

(b)

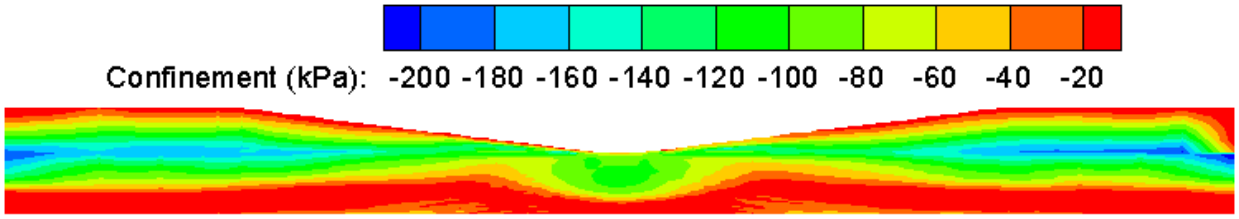

(c)

Figure 10.16 Mean effective stress contour at end of shaking: (a) Inclination 2:1; (b) Inclination 4:1; (c) Inclination 8:1

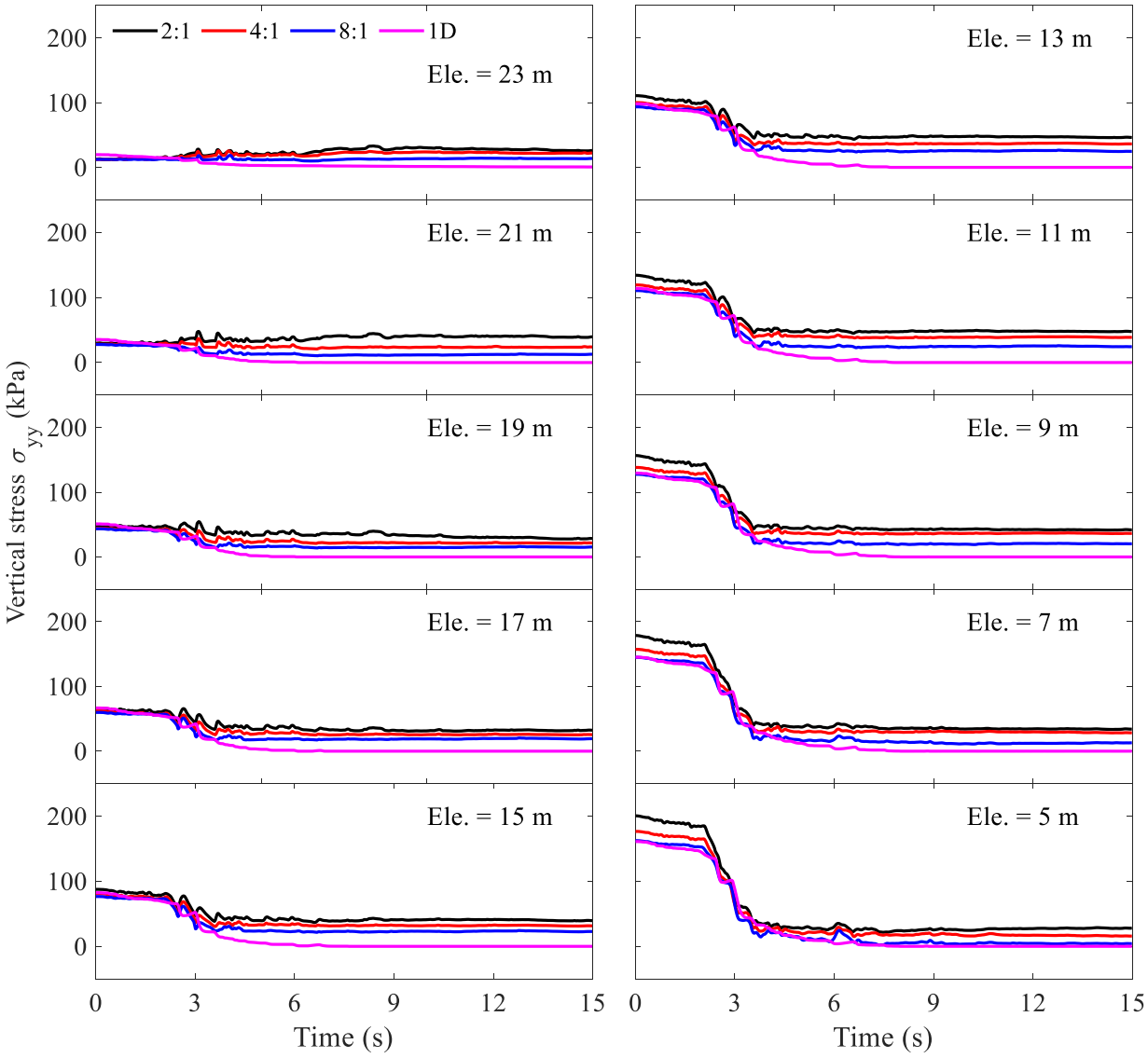

Figure 10.17 Vertical effective stress time histories

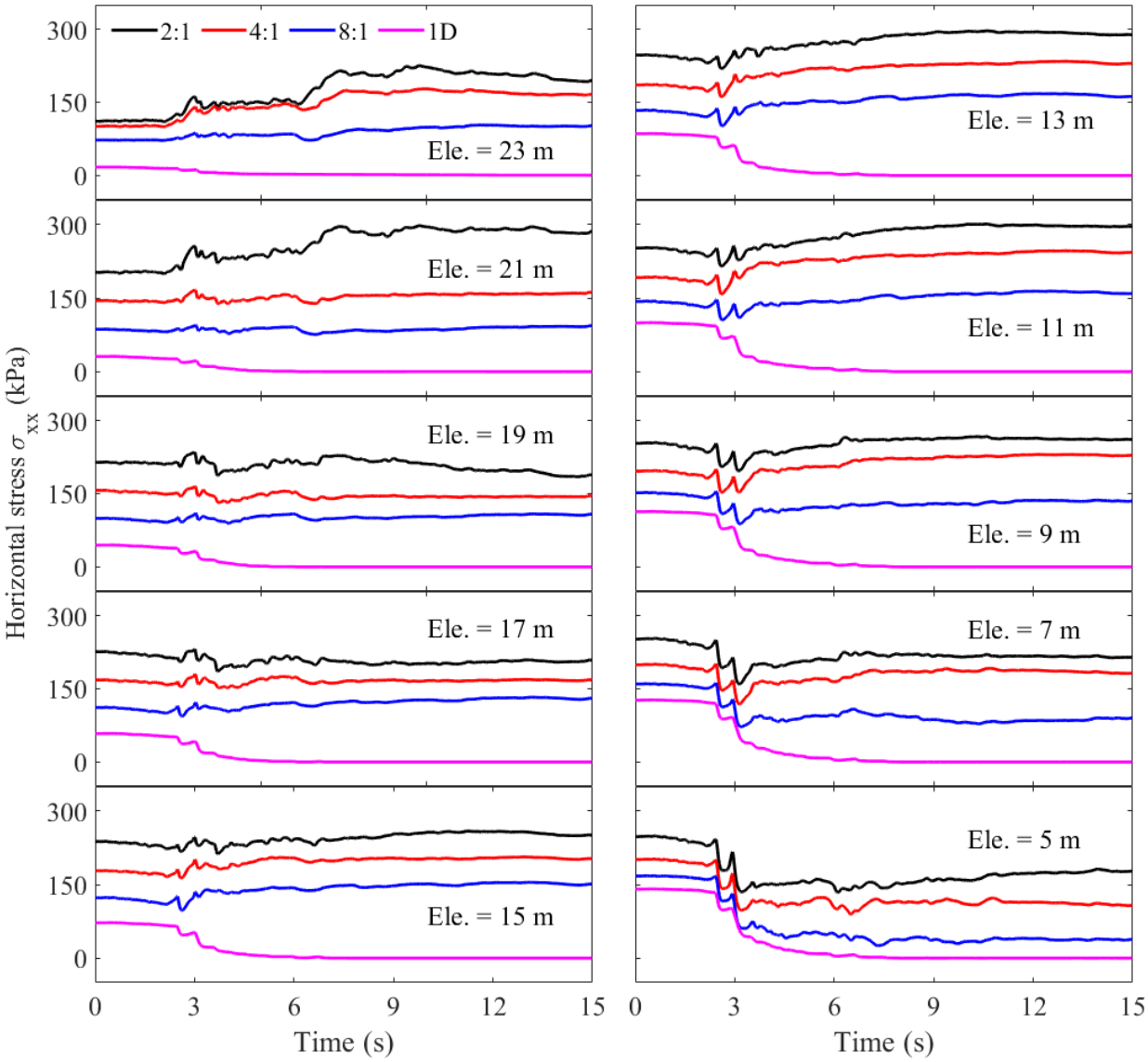

Figure 10.18 Horizontal effective stress time histories

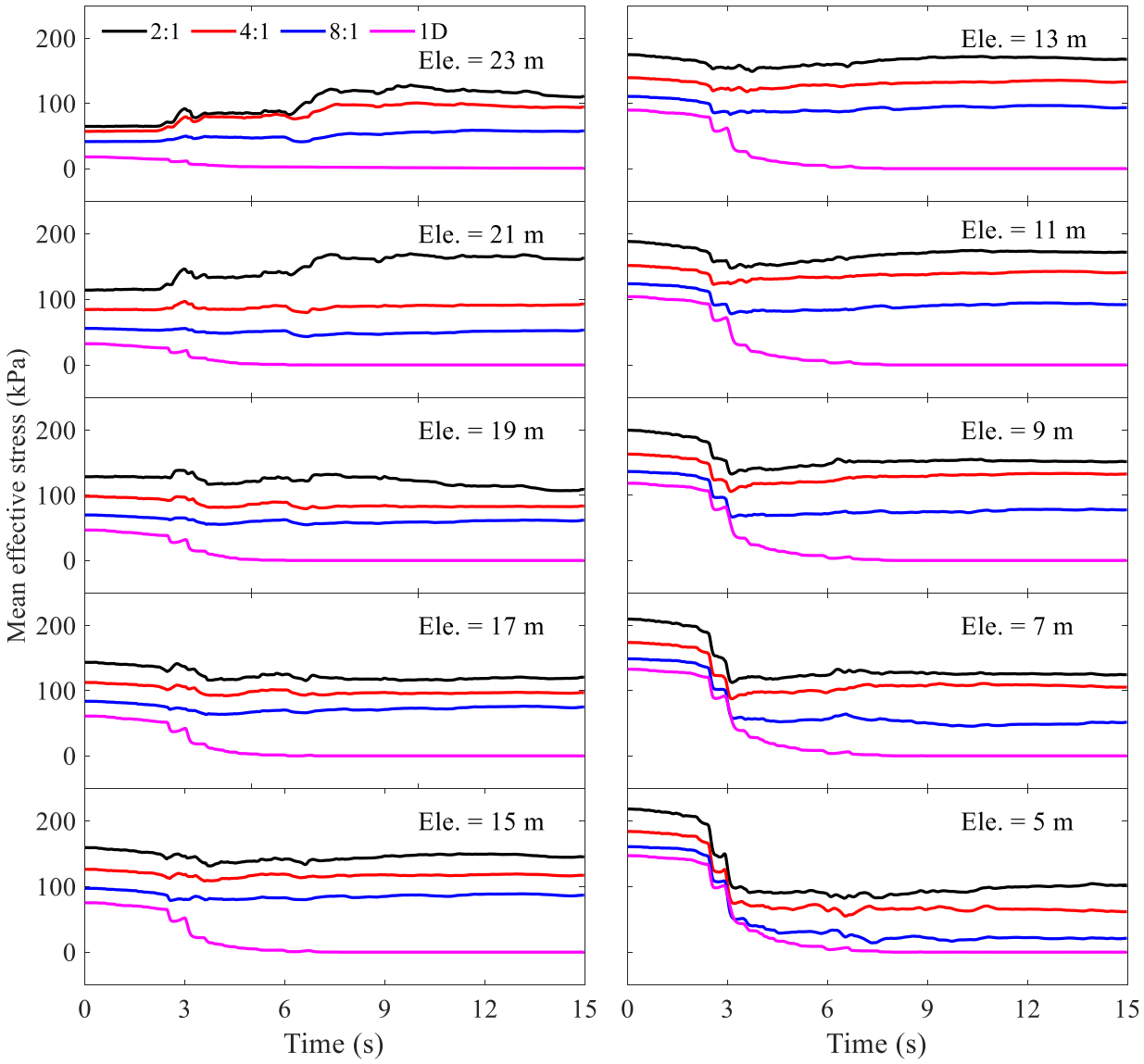

Figure 10.19 Mean effective stress time histories

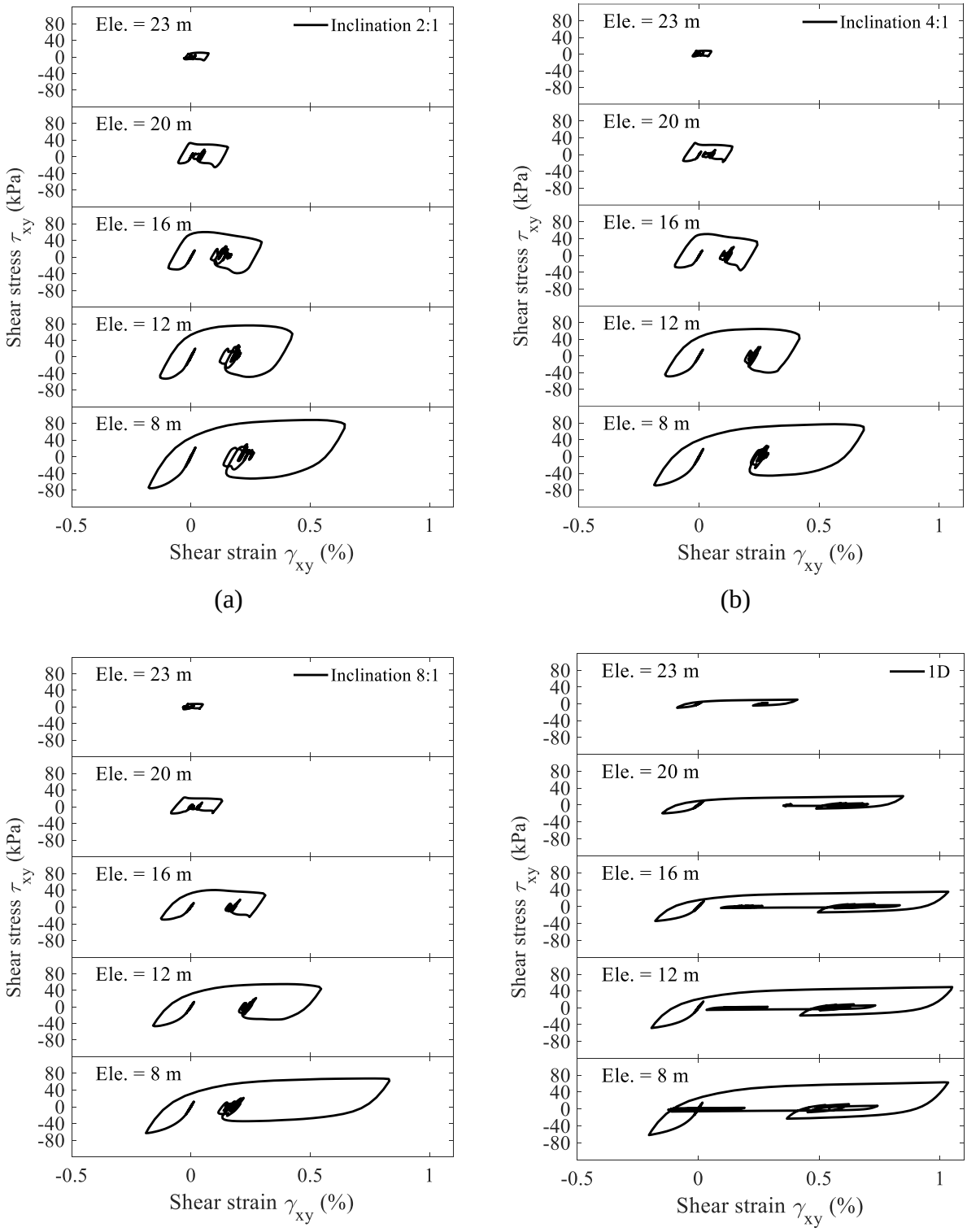

Figure 10.20 Shear stress-strain: (a) Inclination 2:1; (b) Inclination 4:1; (c) Inclination 8:1; (d) 1D shear beam

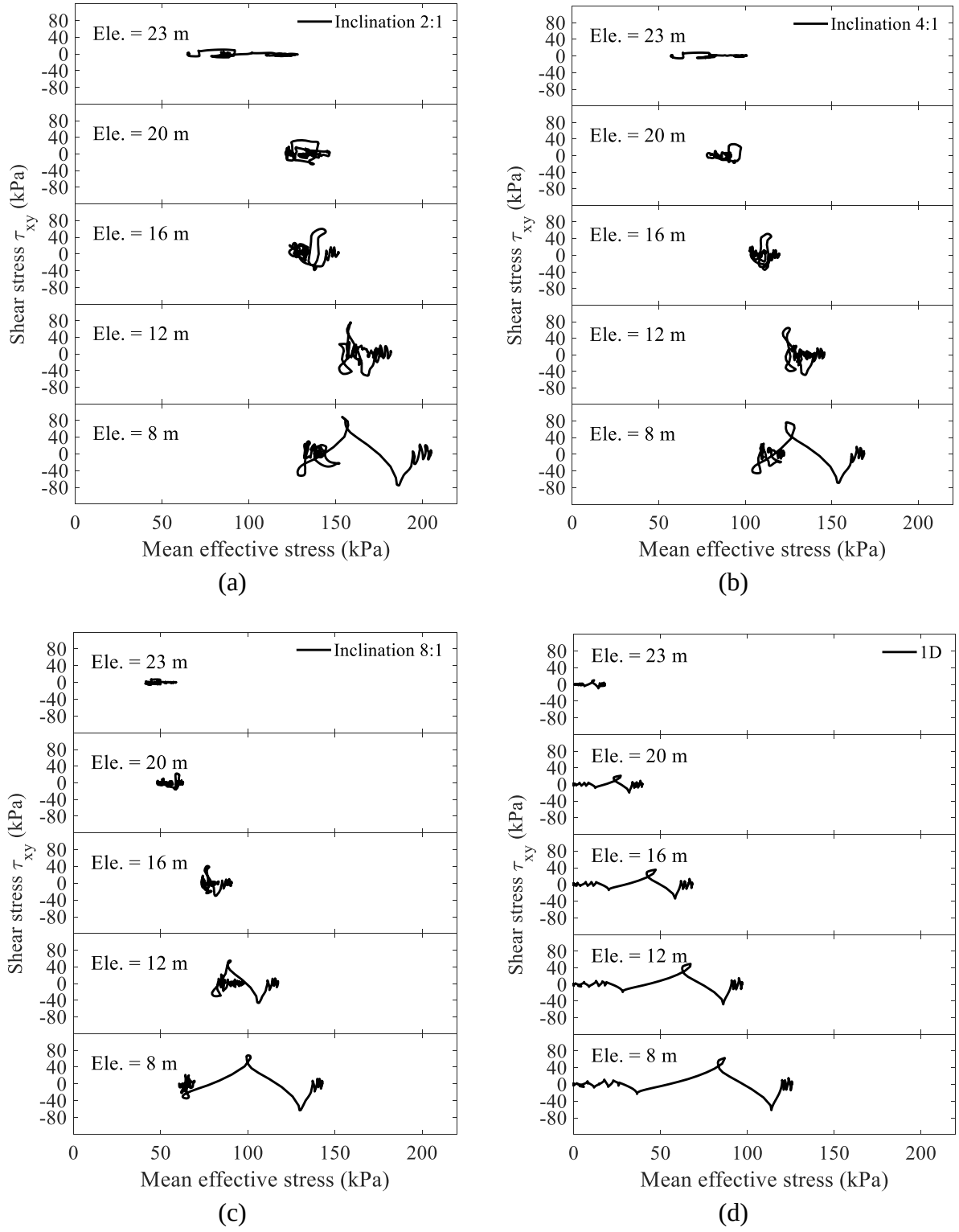

Figure 10.21 Mean effective stress-shear stress: (a) Inclination 2:1; (b) Inclination 4:1; (c) Inclination 8:1; (d) 1D shear beam

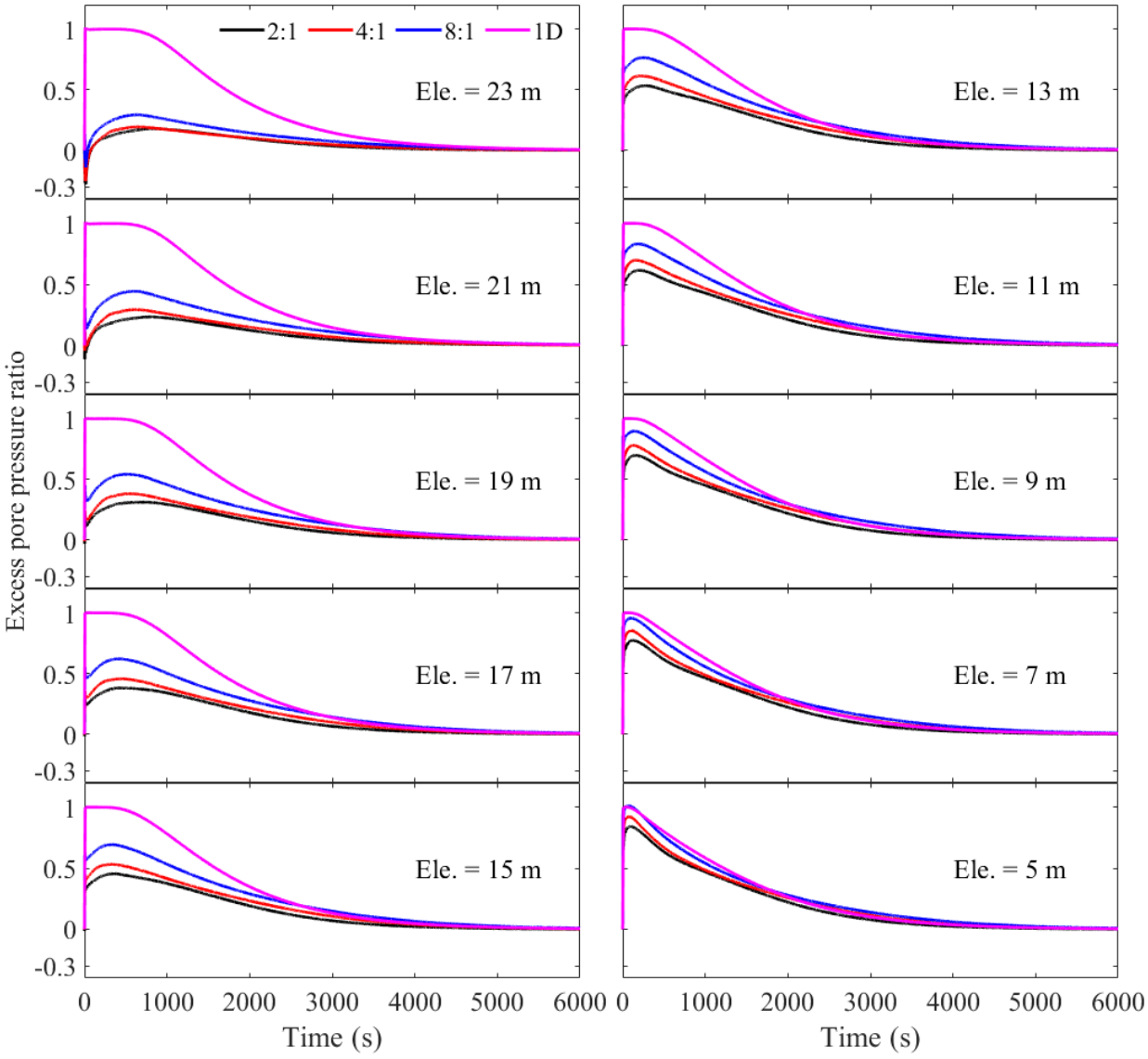

Figure 10.22 Post-shaking excess pore pressure ratio

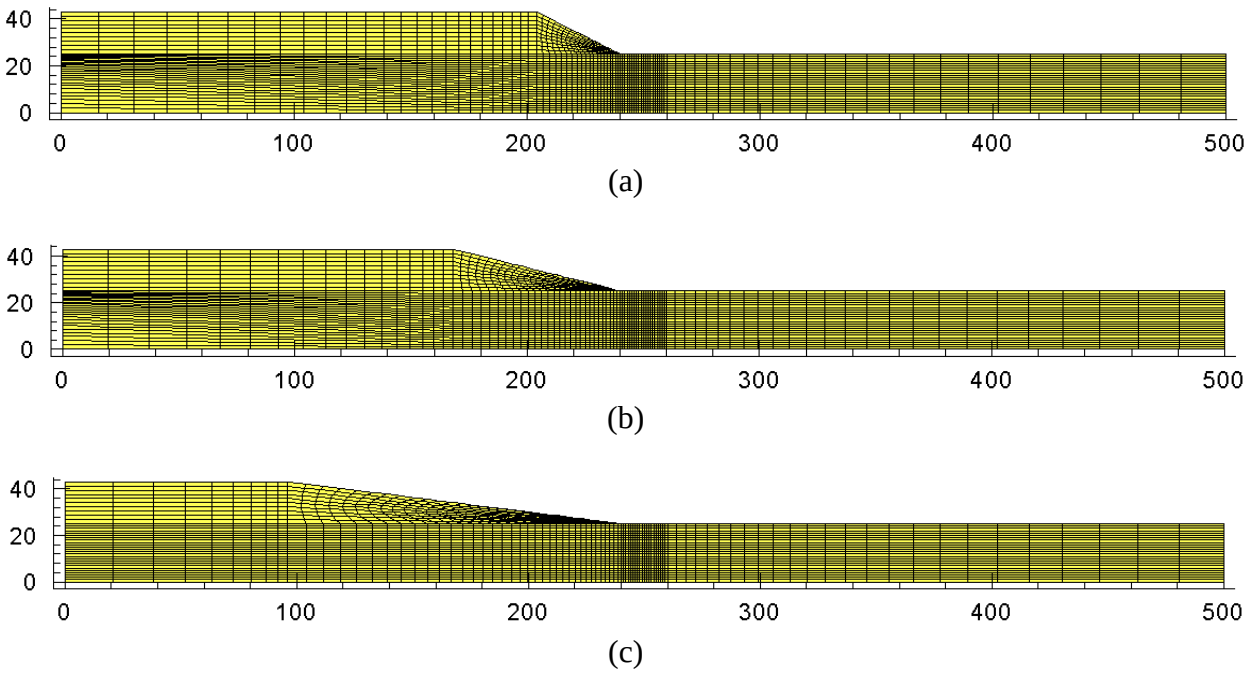

Figure 10.23 FE slope model with various inclination angles: (a) 2:1; (b) 4:1; (c) 8:1

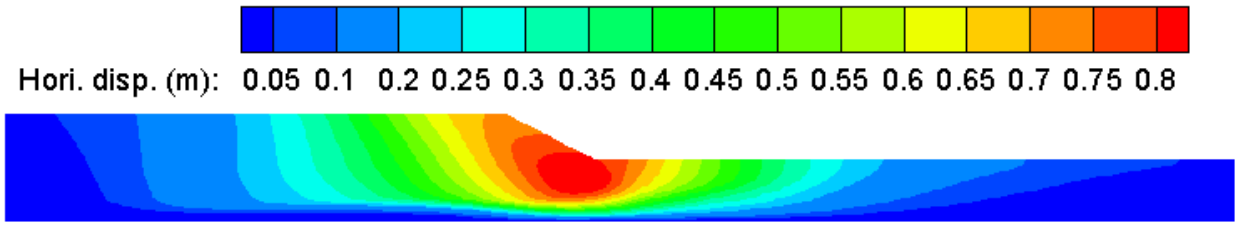

(a)

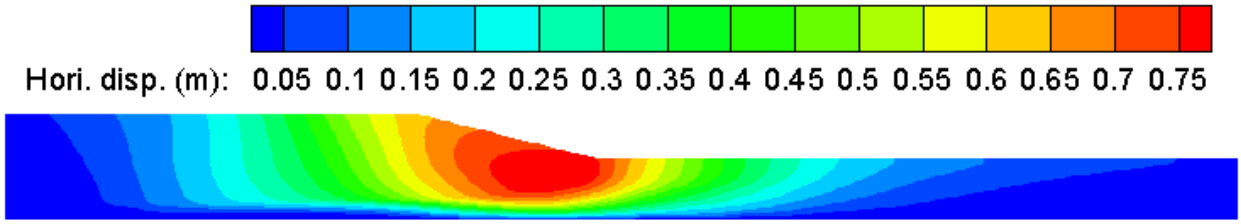

(b)

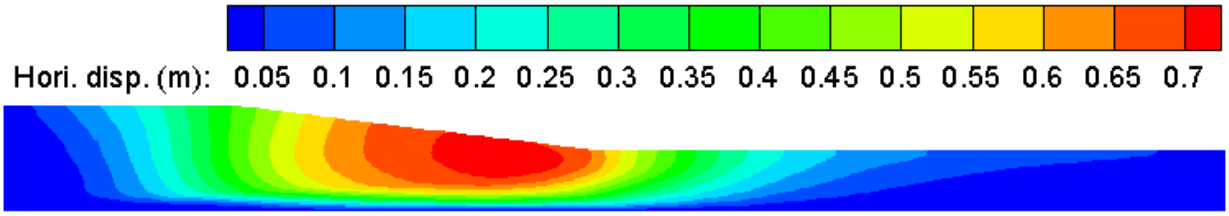

(c)

Figure 10.24 Horizontal displacement contour at end of shaking: (a) Inclination 2:1; (b) Inclination 4:1; (c) Inclination 8:1

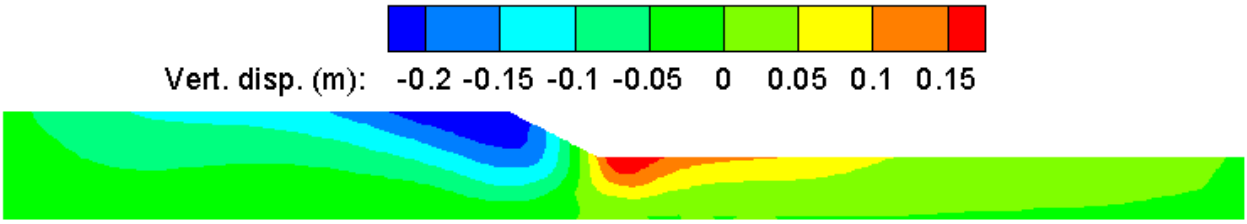

(a)

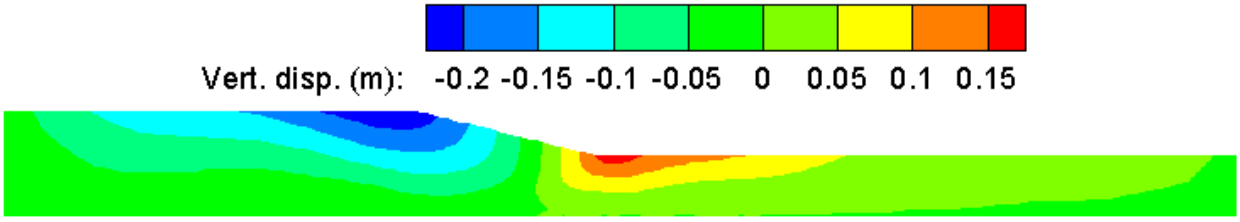

(b)

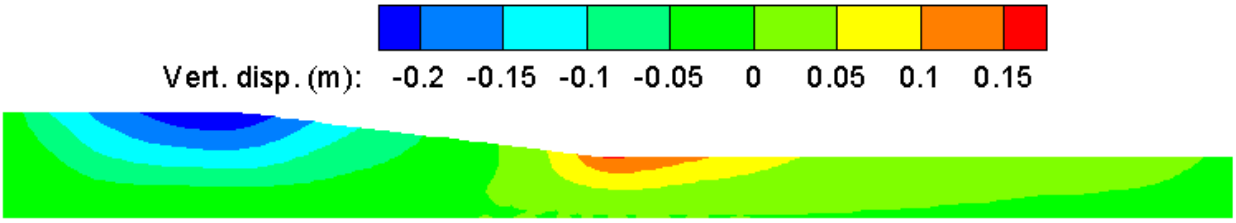

(c)

Figure 10.25 Vertical displacement contour at end of shaking: (a) Inclination 2:1; (b) Inclination 4:1; (c) Inclination 8:1

Chapter 11. Liquefaction-Induced Excess Pore Pressure beyond Vertical Effective Stress and Potential Consequences

11.1. Abstract

Liquefaction is conventionally defined by the excess pore-pressure ratio r_u reaching 1.0. For a class of practical applications, liquefaction might result in r_u exceeding 1.0 by a large margin, with potential detrimental consequences. As such, liquefaction-induced excess pore pressures that exceed the effective vertical stress, referred to herein as super-liquefaction scenarios ($r_u > 1$), are discussed. The underlying mechanism is presented, along with simple representative experimental and numerical simulations. The results demonstrate a potential for this mechanism to play an important role in a number of ground/structure configurations of practical significance. Conceptually, similar response might have contributed to the observed soil deformations in some documented case histories. For such situations, closer attention is needed to further quantify the main factors that influence this mechanism and its consequences.

11.2. Introduction

Conventionally (e.g., NRC 1985; Idriss and Boulanger 2008), liquefaction is addressed mainly based on 1-dimensional (1D) site response considerations, with a uniform horizontal ground surface, and horizontally stratified soil layers. In this scenario, seismically-induced excess pore pressures can reach a maximum dictated by the initial effective vertical stress σ_v' due to the overlying soil strata. As such, excess pore pressure u_e due to liquefaction can eventually reach a maximum of σ_v', with the corresponding excess pore-pressure ratio r_u (= u_e/σ_v') reaching a maximum of 1.0 (also known as initial liquefaction). At this point, the critical hydraulic gradient (driving the upward water flow relative to the soil particles) defined as $i_c = (\rho_{sat}-\rho_w)/\rho_w$ will reach a value of about 1, where ρ_{sat} and ρ_w are mass densities of saturated soil and water respectively.

For liquefaction scenarios that deviate from the above 1D level-ground configuration (Figure 11.1), excess pore pressure u_e throughout the entire spatial domain will be influenced by the highest attained value (liquefied location with the highest effective vertical confinement). In particular, r_u reaching 1.0 at a location where initial effective confinement is high (Figure 11.1), might eventually result in a u_e that far exceeds confinement at a neighboring location of shallower depth. At these shallow locations, hydraulic gradients might far exceed the critical value (i_c) with increased potential for piping (sand boil), heave, uplift, or slope stability failure.

In the following sections, i) a brief summary of related literature is provided as general background, ii) the super-liquefaction mechanism is described, iii) representative experimental and numerical results are shown, and iv) conclusions are drawn with suggestions for future research.

11.3. Mechanism of Super-Liquefaction

The mechanism may be simply illustrated in the context of the 2-dimensional scenarios shown schematically in Figure 11.1. Upon liquefaction, these geometric configurations result in:

1. Levels of excess pore pressure u_e are dictated by pore pressure build-up in the zone of greater height (H).

2. Depending on the characteristics of pore pressure migration towards the zone of lower height (h), this zone might experience excess pore pressures equivalent to that of the (H) zone.

3. As such, a piping/sand boil mechanism might be promoted in the lower zone (h), further contributing to the overall lateral and vertical deformations.

11.4. Numerical Simulation

In order to present a simple illustration, a U-shaped configuration (height = 9 m) is studied as shown in Figure 11.2a. The OpenSees FE framework is employed (as discussed below). In this configuration, (H) is taken as 9 m and (h) as 4 m. For further focus on the mechanism, only the 9

m side of this configuration (as a 1D shear beam) is subjected to the base excitation shown in Figure 11.2b. As such, no external seismic loading is applied on the (h) = 4 m side.

11.4.1. Computational Framework

The Open System for Earthquake Engineering Simulation (OpenSees, McKenna 2011) framework was employed to conduct the analysis subjected to seismic excitation. OpenSees is developed by the Pacific Earthquake Engineering Research (PEER) Center, and is widely used for simulation of geotechnical systems and soil-structure interaction applications (Yang and Elgamal 2002; Lu et al. 2011; Su et al. 2017). The OpenSees elements and materials used in this FE model are briefly described below.

Two-dimensional four-node quad elements with two-phase material following the *u-p* (Chan 1988) formulation were employed for simulating saturated soil response, where *u* is the displacement of the soil skeleton and *p* is the pore water pressure. Implementation of the *u-p* element is based on the following assumptions: 1) small deformation and rotation; 2) solid and fluid density remain constant in time and space; 3) porosity is locally homogeneous and constant with time; 4) soil grains are incompressible; 5) solid and fluid phases are accelerated equally. Hence, the soil layers represented by these effective stress fully coupled brick *u-p* elements are capable of accounting for soil deformations and the associated changes in pore water pressure.

The employed soil constitutive model (Parra 1996; Yang 2000; Yang and Elgamal 2002; Elgamal et al. 2003) was developed based on the multi-surface-plasticity theory (Mroz 1967; Iwan 1967; Prevost 1978, 1985). In this employed model, the shear-strain backbone curve was represented by the hyperbolic relationship with the shear strength based on simple shear (reached at a octahedral shear strain of 10 %). As such, soil is simulated by the implemented OpenSees materials PressureDependMultiYield02.

The FE matrix equation of the soil system is integrated in time using a single-step predictor multi-corrector scheme of the Newmark type (Chan 1988; Parra 1996) with integration parameters $\gamma = 0.6$ and $\beta = 0.3025$. The equation is solved using the modified Newton-Raphson method, i.e., Krylov subspace acceleration (Carlson and Miller 1998; Mazzoni et al. 2009) for each time step. A relatively low level of stiffness proportional viscous damping was used to enhance numerical stability (coefficient = 0.003), with the main damping emanating from the soil nonlinear shear stress-strain hysteresis response (Su et al. 2017).

11.4.2. Soil Response

Figure 11.3a shows the stress path near locations L1 and L2. Confinement is gradually reduced to zero as pore pressure builds up (Figure 11.3b). As seen in Figure 11.3b, the excess pore pressure u_e at locations L1 and L2 reached the initial overburden effective stress σ_v' = 60 kPa and 80 kPa at around 2 seconds, leading to a value of $r_u = 1$ (liquefaction), respectively. Thereafter, excess pore pressure u_e stays constant. Due to the higher hydraulic conductivity (permeability = 10^{-2} m/s) of the porous material which connects the two zones, excess pore pressures at locations R1 and R2 increases until 8 seconds and then stay constant. Since there was no seismic excitation imparted to the right-side column, the increase of excess pore pressure u_e at R1 and R2 are solely due to migration of high pore pressure from the left-side column. As seen in Figure 11.3b, peak excess pore pressure u_e at locations R1 and R2 are 21 kPa and 64 kPa, about two times of initial overburden effective stress σ_v' = 10 kPa and 30 kPa, respectively. As such, the corresponding r_u = 2 is noticeably higher than the conventional value of 1.0.

11.4.3. Hydraulic Gradient

In accordance with the excess pore pressure, Figure 11.4 shows the hydraulic gradient i between locations L1-L2, and R1-R2, respectively. As seen in this figure, the hydraulic gradient

between locations L1 and L2 satisfied the conventional liquefaction condition and reached a value of about 1 after 2 seconds. In addition, the hydraulic gradient between locations R1 and R2 was increasing steadily and reached a peak value of 2.2 at about 3 seconds.

To further illustrate the hydraulic gradient (Appendix A) variation during and the post shaking phase, Figure 11.5 depicts the contours with arrows in element center showing the direction of pore pressure migration at different time instants. From Figure 11.4 and Figure 11.5, it can be seen that:

1. In left-side soil column, the higher pore pressure at deeper depth travelled vertically to lower pore pressure at shallower depth, and the peak value of hydraulic gradient reached about 1.

2. Upon liquefaction, the hydraulic gradient at the bottom of left column (Element A) reached a maximum value of 3.8 (thereafter reduced and attained a low value at about 2.5 seconds), due to the high pore pressure migrating to the right column through the bottom porous material.

3. In right-side column, the hydraulic gradient of Element B reached a maximum value of about 4 at 2.5 seconds and then reduced to about 2 when the hydraulic gradient of Element C (at top of right-side column) reached its maximum value of 2 at about 8 seconds.

11.4.4. Flow Velocity

The flow velocity of the fluid travelling through the soil is conveniently defined as $v = k \times i$, where k denotes the permeability (Table 11.1) and i is the hydraulic gradient (Figure 11.4 and Figure 11.5). As such, Figure 11.6 depicts the flow velocity contours with arrows in element center showing the direction of water flow at various time constants. As seen in Figure 11.6, the flow velocity in the porous material at the bottom is relatively high, pointing horizontally toward to the right-side column.

11.4.5. Vertical Displacement

Figure 11.7 shows the vertical displacement at locations L1, L2, R1 and R2. Due to the high pore pressure and the corresponding upward high pressure in right-side column, the vertical displacements of locations R1 and R2 are positive (moving upward), indicating a tendency for the soil to be washed out in right-side column. Meanwhile, as expected, locations L1 and L2 were settling with negative vertical motion (Figure 11.7).

11.5. Sand Boil Formation in Layered Soils

As highlighted in earlier physical studies (Liu and Qiao 1984; Elgamal et al. 1989; Fiegel and Kutter 1994), high hydraulic gradient might occur if the overlaying soil is relatively impervious. In this regard, an additional FE simulation with a relatively impervious (clay permeability = 10^{-7} m/s) layer was performed to investigate the high hydraulic gradient in such layered soils. As seen in Figure 11.8, a clay layer was added to the top of right-side column in the U-shaped tube. Boundary and loading conditions are unchanged and mentioned above.

Figure 11.9 shows the excess pore pressure at locations of L1-L3 and R1-R2. Due to the presence of the overlaying relatively impervious clay layer, the excess pore pressure at locations R1 and R2 continued increasing even after the end of shaking, until it reached the same value as that of location L3.

Figure 11.10 displays the hydraulic gradients at locations L1-L2 and R1-R2, respectively. Due to the impervious clay layer in right-side column, excess pore pressure of locations R1 and R2 reached the same value after end of shaking. As a result, the post-shaking hydraulic gradient between locations R1 and R2 was decreased to 0.

Figure 11.11 and Figure 11.12 show the hydraulic gradient and flow velocity contours with arrows in element center displaying the direction of fluid flow. It can be seen that the peak

hydraulic gradient occurred below the clay layer, but the flow velocity of right-side column was minimal due to its low permeability.

11.6. Centrifuge Test Illustration

Figure 11.14 shows the centrifuge test (Zeghal et al. 2019) on a sheet pile retaining wall with recorded excess pore pressure ratio (PD, PFW, PFWB) as presented in Chapter 5. It can be seen clearly that the excess pore pressure ratio in downstream (PFW, PFWB) reached a peak value by as much as 4 (Figure 11.14). To further illustrate this underlaying mechanism of super liquefaction, Figure 11.15 displays the computed hydraulic gradient contours of test RPI-9 with arrows in element center showing the direction of pore pressure migration at different time constants. From this figure, it can be seen that:

1) Away from the structure, excess pore pressure travelled vertically to the ground surface with a hydraulic gradient value of about 1.

2) High hydraulic gradient (about 7) occurred at the base of the sheet-pile due to soil-structure interaction. As such, the dense sand near the base of structure drew in water from the surrounding soils.

3) Due to soil liquefaction in land-side section, the higher pore pressure migrated from the landside to the water-side sections through the bottom. As a result, the soil response of water-side sections would be significantly influenced by the higher pore pressure induced by the land-side section.

11.7. Discussion

The mechanism discussed above was shown to potentially generate very high excess pore pressures, hydraulic gradients, and water flow velocities. Such response mechanisms would promote the potential occurrence of piping (laterally and vertically), associated reduction in shear

strength, and sediment transport in the form of sand boils. Nevertheless, much quantification is needed to identify the main parameters and influence in terms of the detrimental outcomes and potential influence on undesirable large soil deformations. Those parameters include:

1) amount of water released by the liquefied soil causing the high excess pore-pressures,

2) rate of flow of this water towards the vulnerable low excess pore-pressure zone,

3) influence of soil layering and heterogeneity on this mechanism in terms of rate of water release, localization of potential drainage paths, resulting localized loss of shear resistance, and sand boil formation with resulting sediment transport,

4) potential extent and rate of soil dilation in the lower excess pore presure zone, leading to partial accommodation of the high excess pore pressure zone released water, helping to reduce the hydraulic gradients.

Further research in this area is deemed of much significance. Indeed, the well-known failure configuration of the San Fernando Dam (Seed et al. 1973, 1975) might have been influenced to some degree by this mechanism, warranting a closer analysis. In addition to the back calculated failure configuration (Seed et al. 1973, 1975), the reported location of excessive sand soil activity (Bardet and Davis 1996), are generally in the low excess pore-pressure zone near the toe of the upstream slope.

Along with the physical quantification aspects of this mechanism, development of numerical tools that directly address and account for the associated response aspects are needed. These include, quantity and migration paths of the released water, hydraulic gradients, flow velocities, impacts on piping and heave, stratification leading to evolution of free water flow conduits (Yang and Elgamal 2002), changes in permeability due to void redistribution, and modeling of potential large deformations.

11.8. Summary and Conclusions

A mechanism described as super-liquefaction is presented and explored. A simple FE configuration was employed to illustrate this mechanism. In this regard, FE analyses for a U-shaped tube filled with sandy soils under seismic excitation are carried out to quantitatively study the high excess pore pressure ratio and transient hydraulic gradient due to super-liquefaction. The simulated results demonstrate this mechanism of fluid flow that is possibly consistent with observations from experiments and filed observations.

11.9. Acknowledgements

Chapter 11, in full, is currently being prepared for submission for publication of the material as it may appear in the following journal publication (The dissertation author was a primary investigator and author of this paper):

Elgamal, A., Qiu, Z. and Luo, L. "Liquefaction-Induced Excess Pore Pressure beyond Vertical Effective Stress and Potential Consequences."

Table 11.1 Sand model parameters

Model Parameters (PressureDependMultiYield02)	Value
Reference mean effective pressure, p'_r (kPa)	101.0
Mass density, ρ (t/m^3)	2.0
Maximum shear strain at reference pressure, γ	0.1
Shear modulus at reference pressure, G_r (MPa)	60.0
Stiffness dependence coefficient n, $G = G_r(\frac{\boldsymbol{P'}}{\boldsymbol{P'_r}})^{\boldsymbol{n}}$	0.5
Poisson's ratio v for dynamics	0.33
Shear strength at zero confinement, c (kPa)	2.0
Friction angle ϕ	31°
Phase transformation angle, ϕ_{PT}	31°
Contraction coefficient, c_1	0.087
Contraction coefficient, c_2	5.0
Contraction coefficient, c_3	0.18
Dilation coefficient, d_1	0.0
Dilation coefficient, d_2	0.0
Dilation coefficient, d_3	0.0
Damage parameter, Liq_1	1.0
Damage parameter, Liq_2	0.0
Permeability (m/s)	1×10^{-5}

(a)

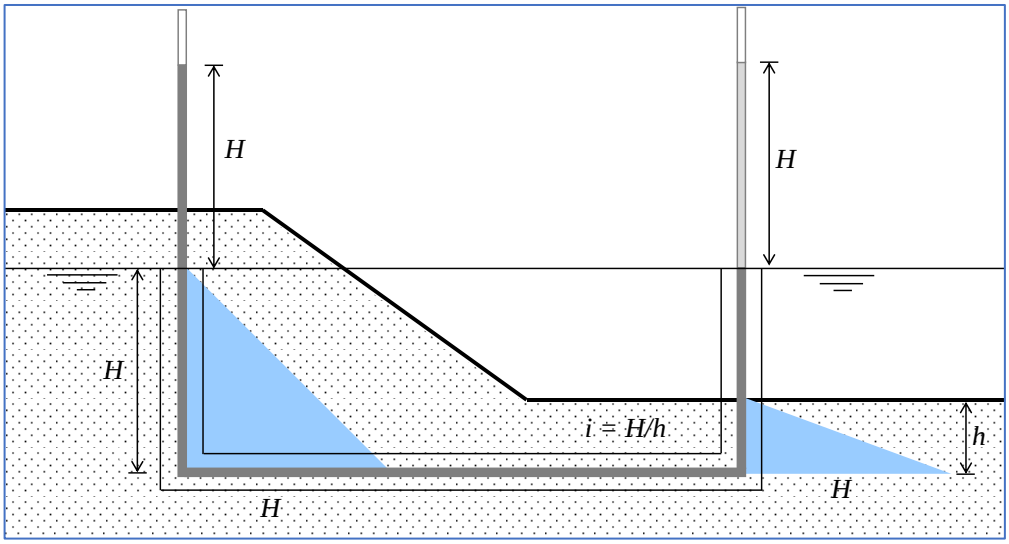

(b)

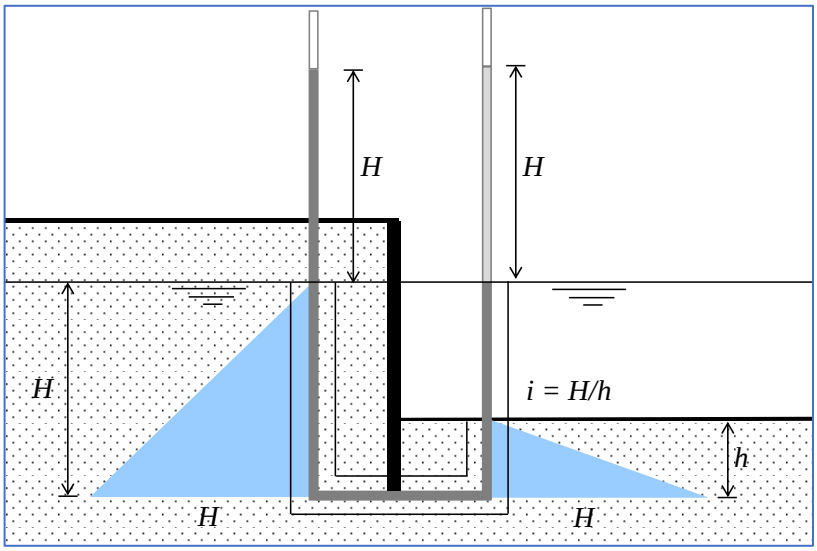

(c)

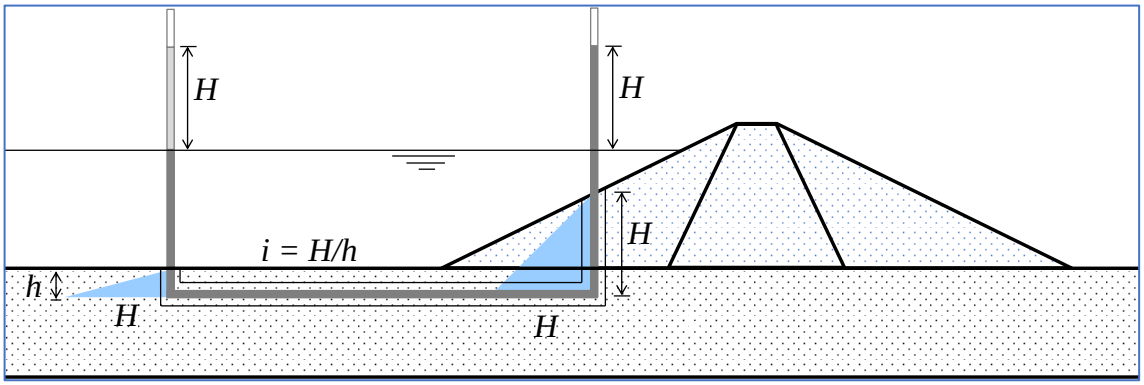

Figure 11.1 Mechanism of super-liquefaction: (a) Ground slope or river canyon; (b) sheet-pile retaining wall; (c) Earth dam

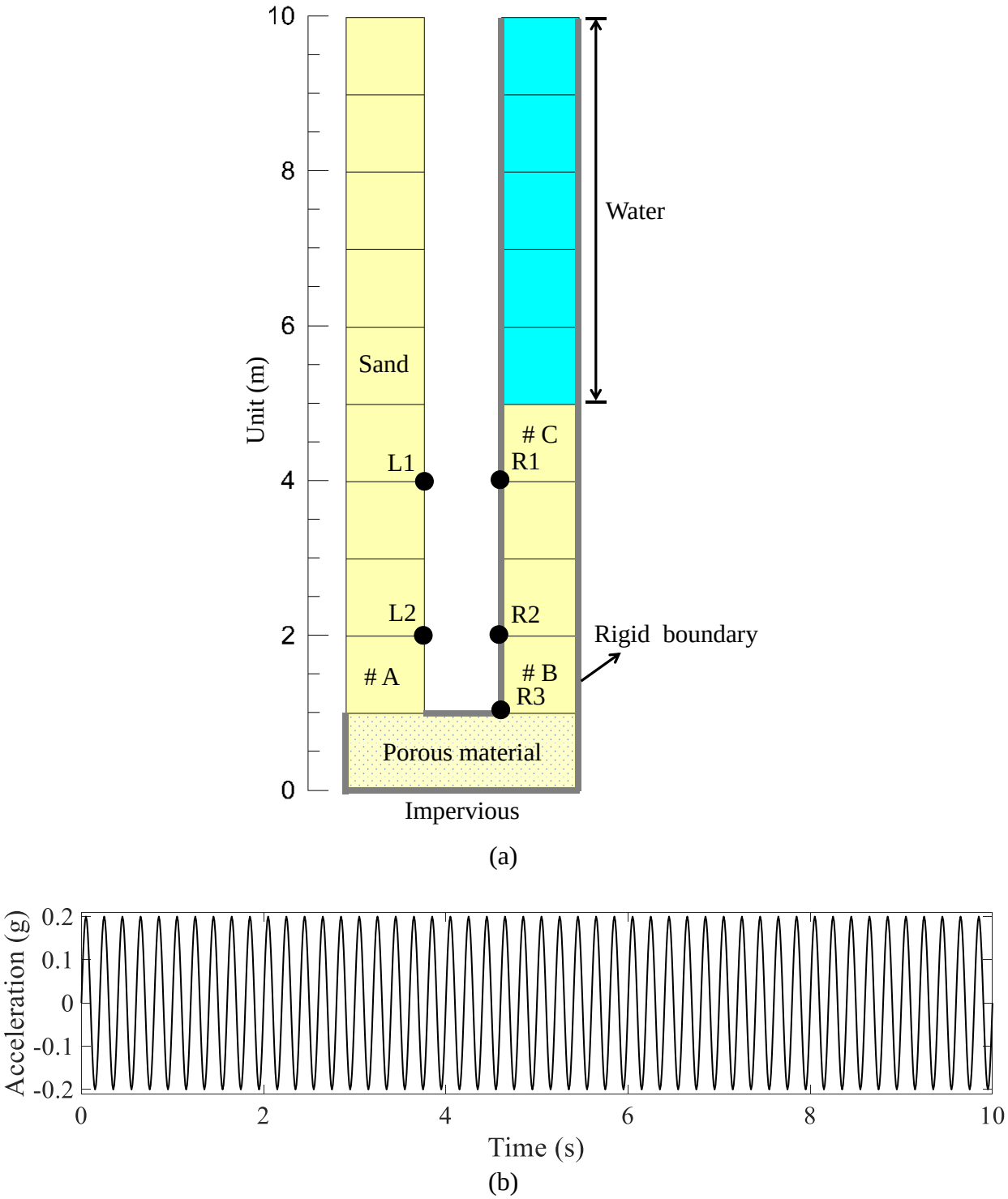

Figure 11.2 Numerical example: (a) U-shaped tube; (b) Input motion

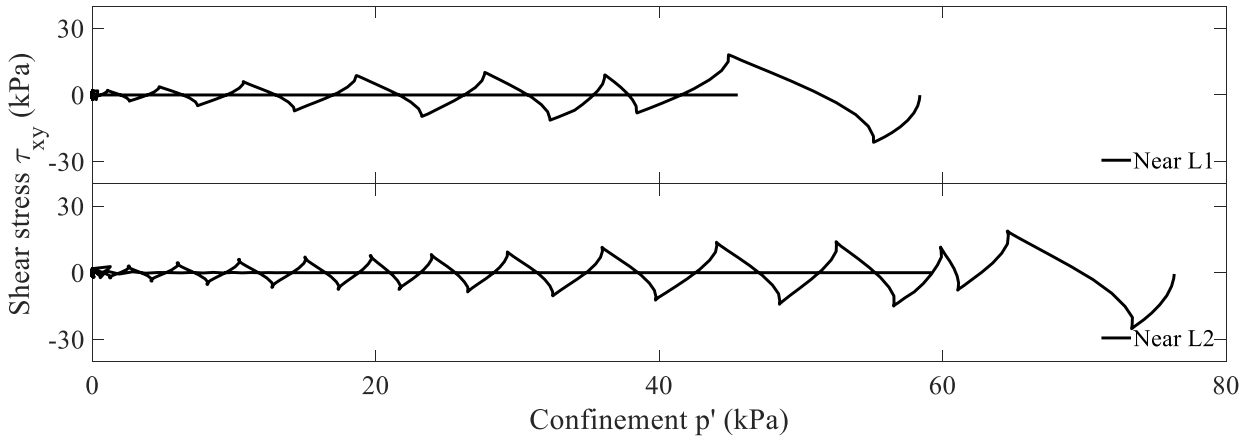

(a)

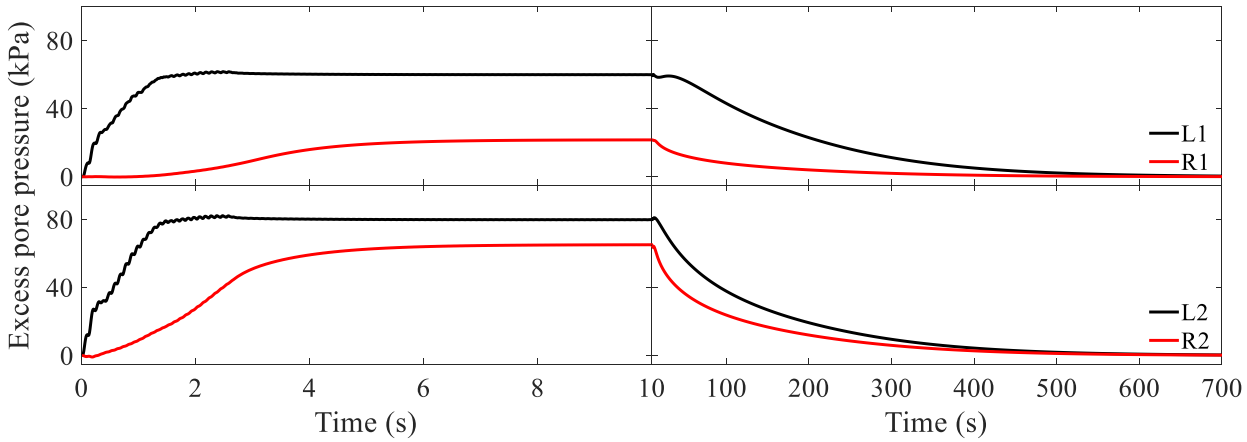

(b)

Figure 11.3 Soil response: (a) Shear stress-confinement; (b) Excess pore pressure

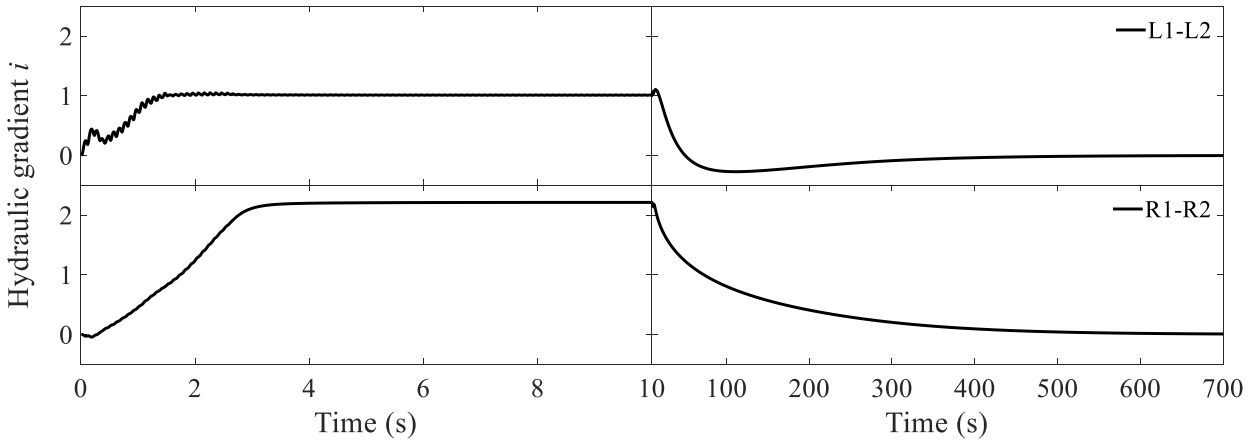

(a)

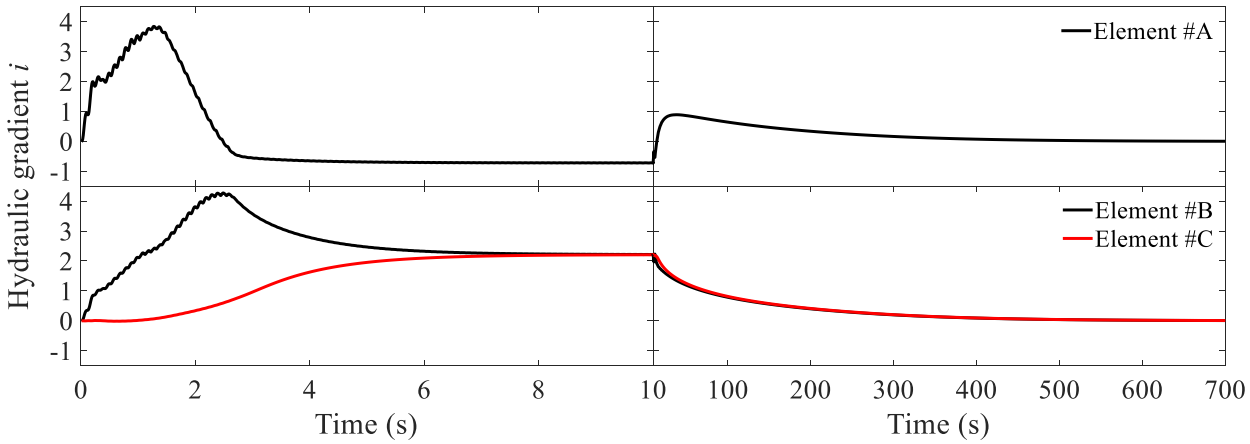

(b)

Figure 11.4 Hydraulic gradient time history: (a) L1-L2 and R1-R2; (b) Elements A, B, C

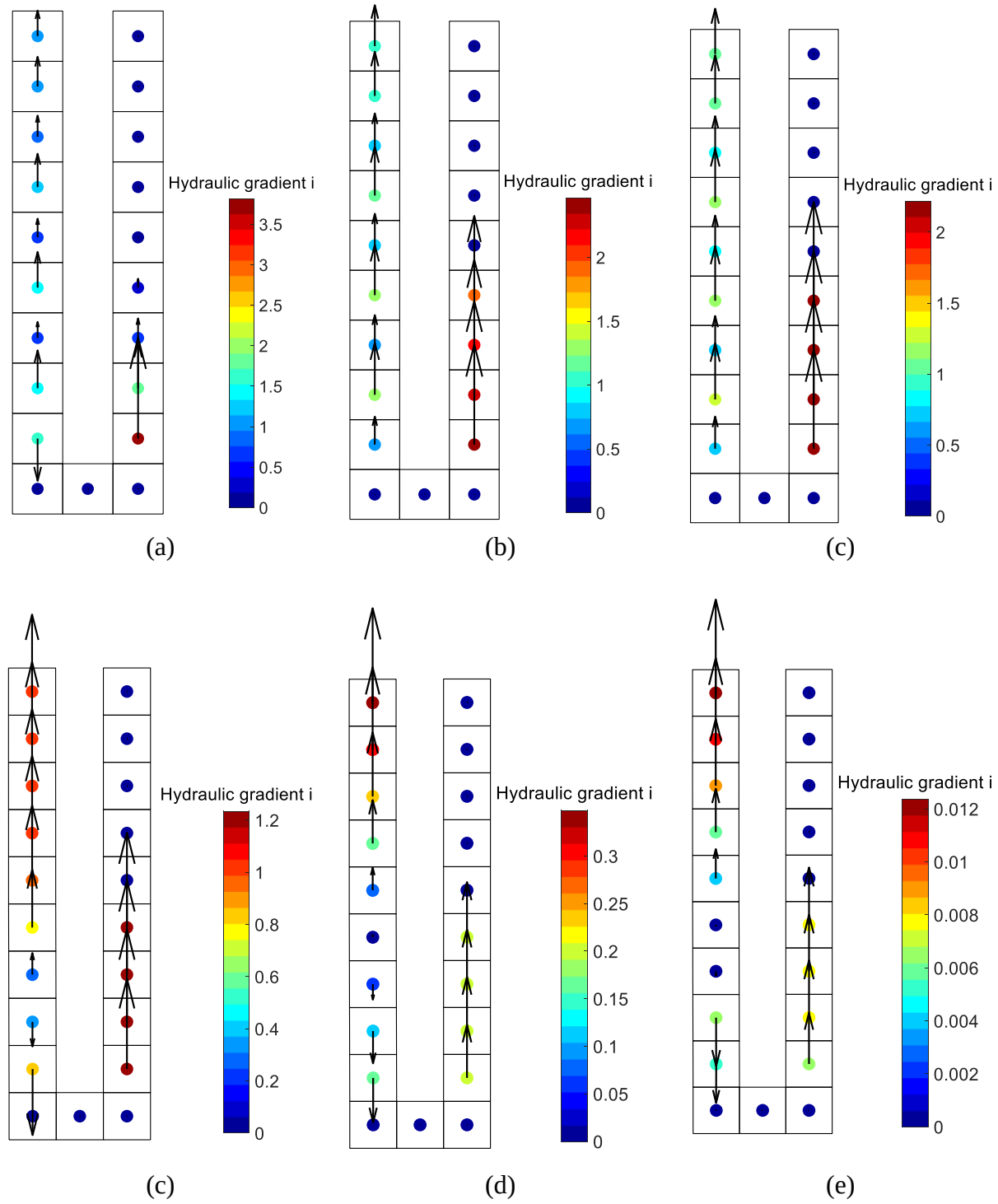

Figure 11.5 Hydraulic gradient contour at: (a) 2 seconds; (b) 5 seconds; (c) 10 seconds; (d) 50 seconds; (e) 300 seconds; (f) 700 seconds

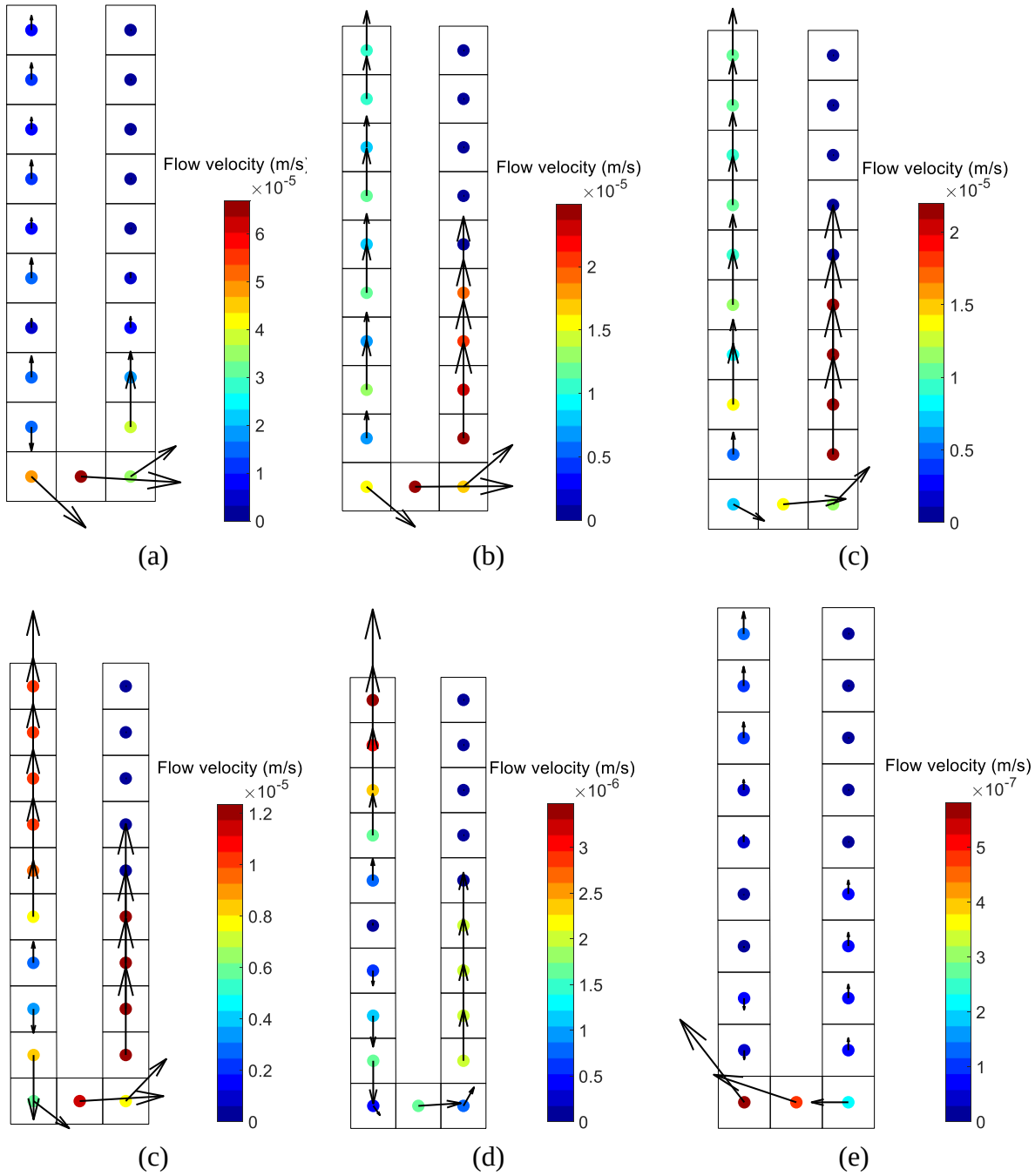

Figure 11.6 Flow velocity contour at: (a) 2 seconds; (b) 5 seconds; (c) 10 seconds; (d) 50 seconds; (e) 300 seconds; (f) 700 seconds

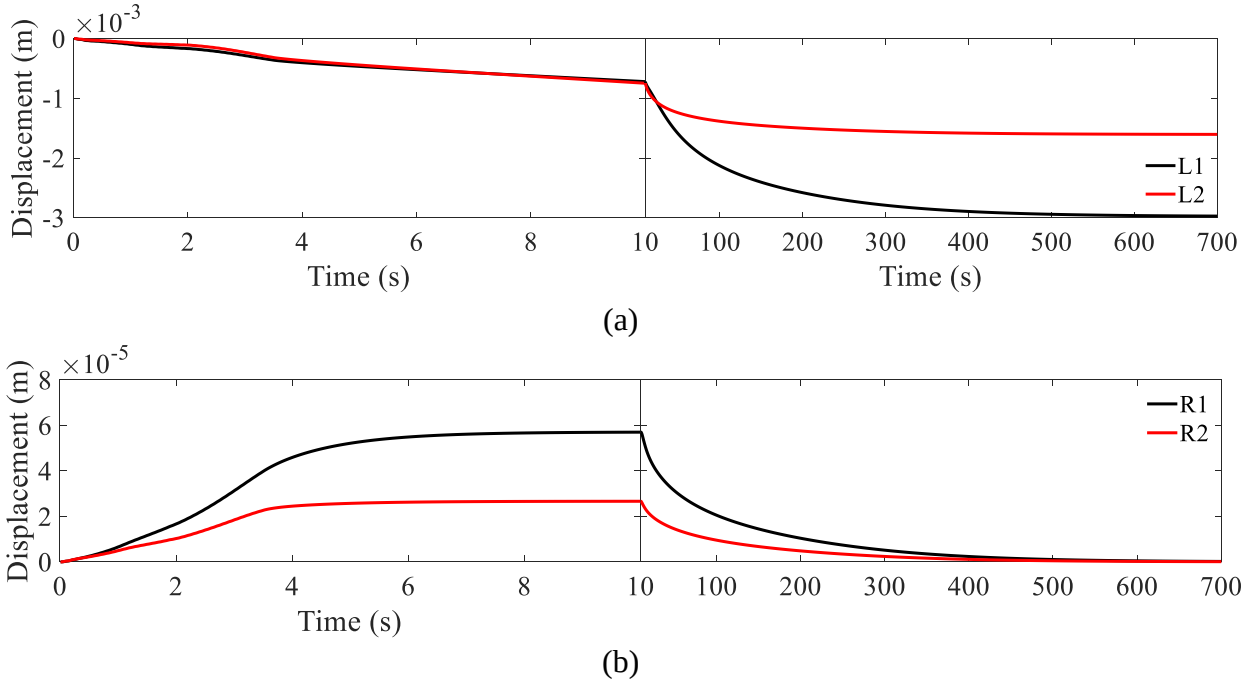

Figure 11.7 Vertical displacement time history: (a) L1, L2; (b) R1, R2

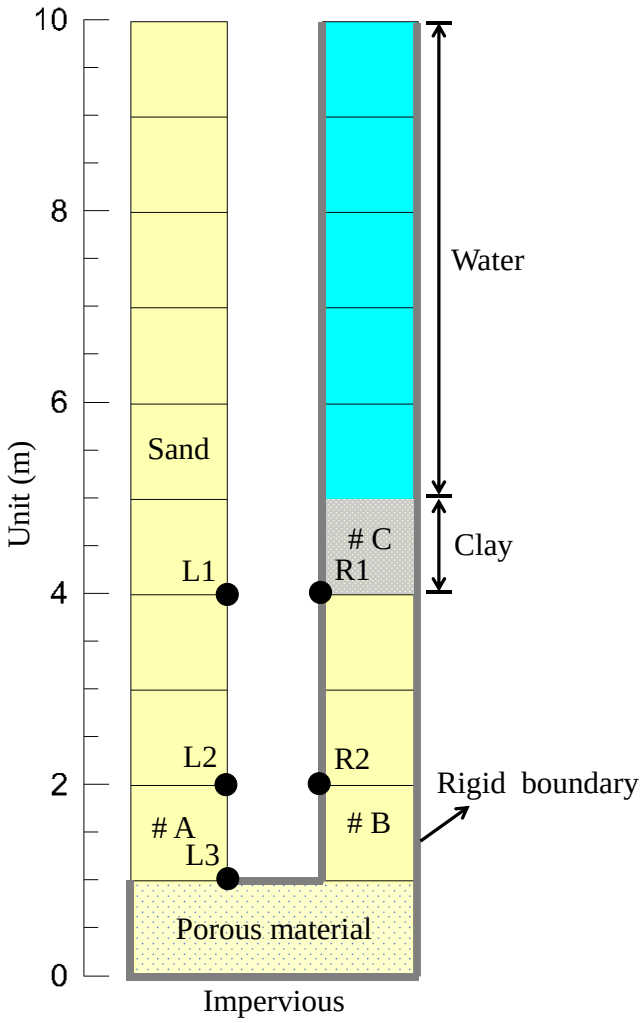

Figure 11.8 A U-Shaped tube with layered soils

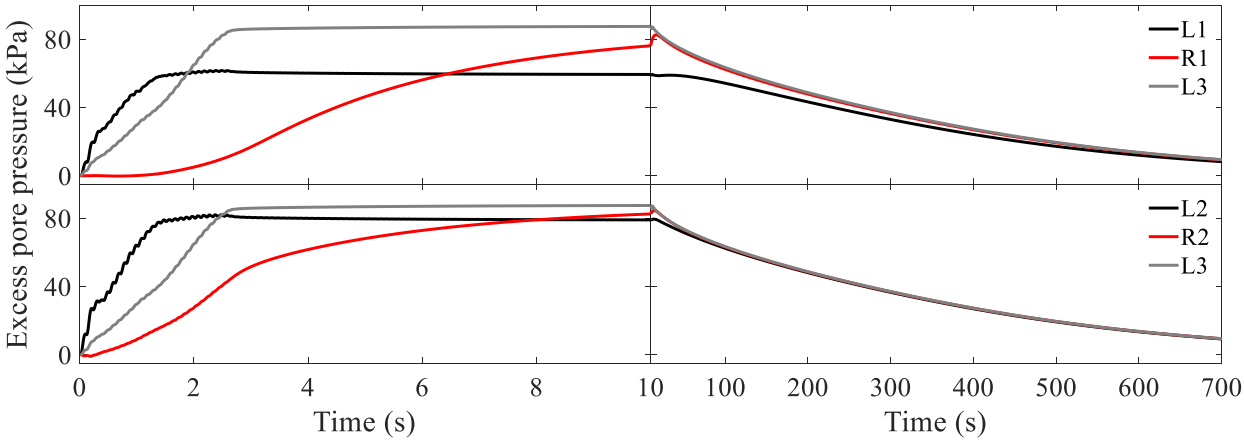

Figure 11.9 Excess pore pressure time history

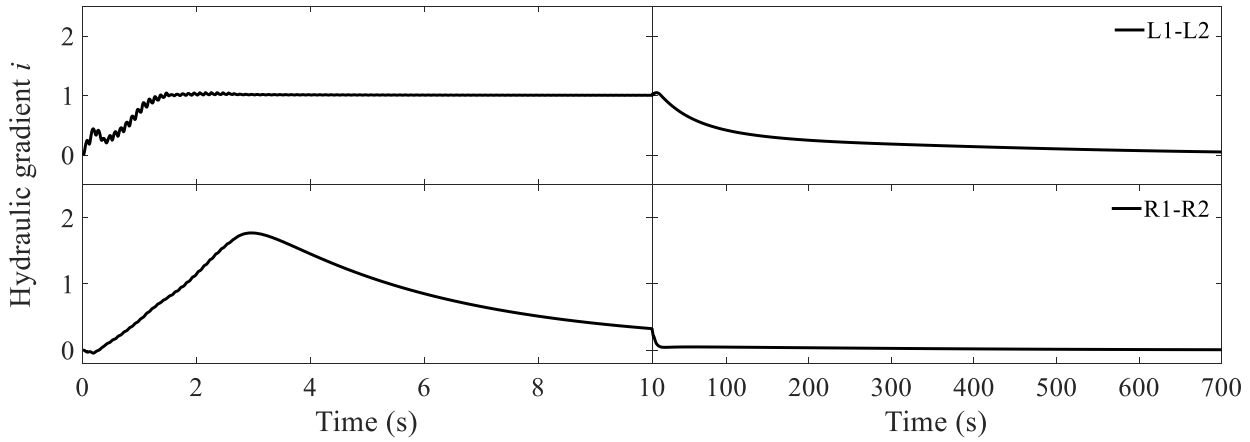

(a)

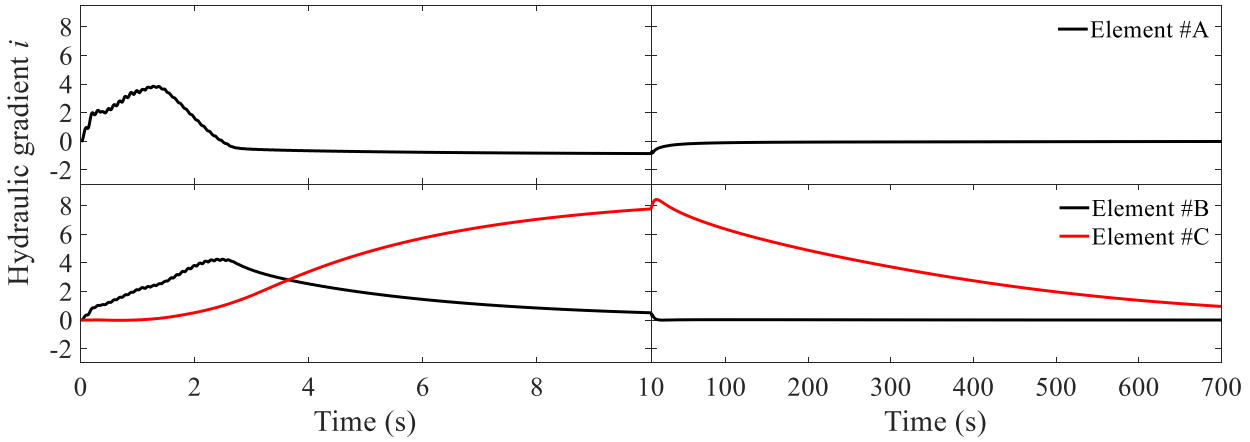

(b)

Figure 11.10 Hydraulic gradient time history: (a) L1-L2 and R1-R2; (b) Elements A, B, C

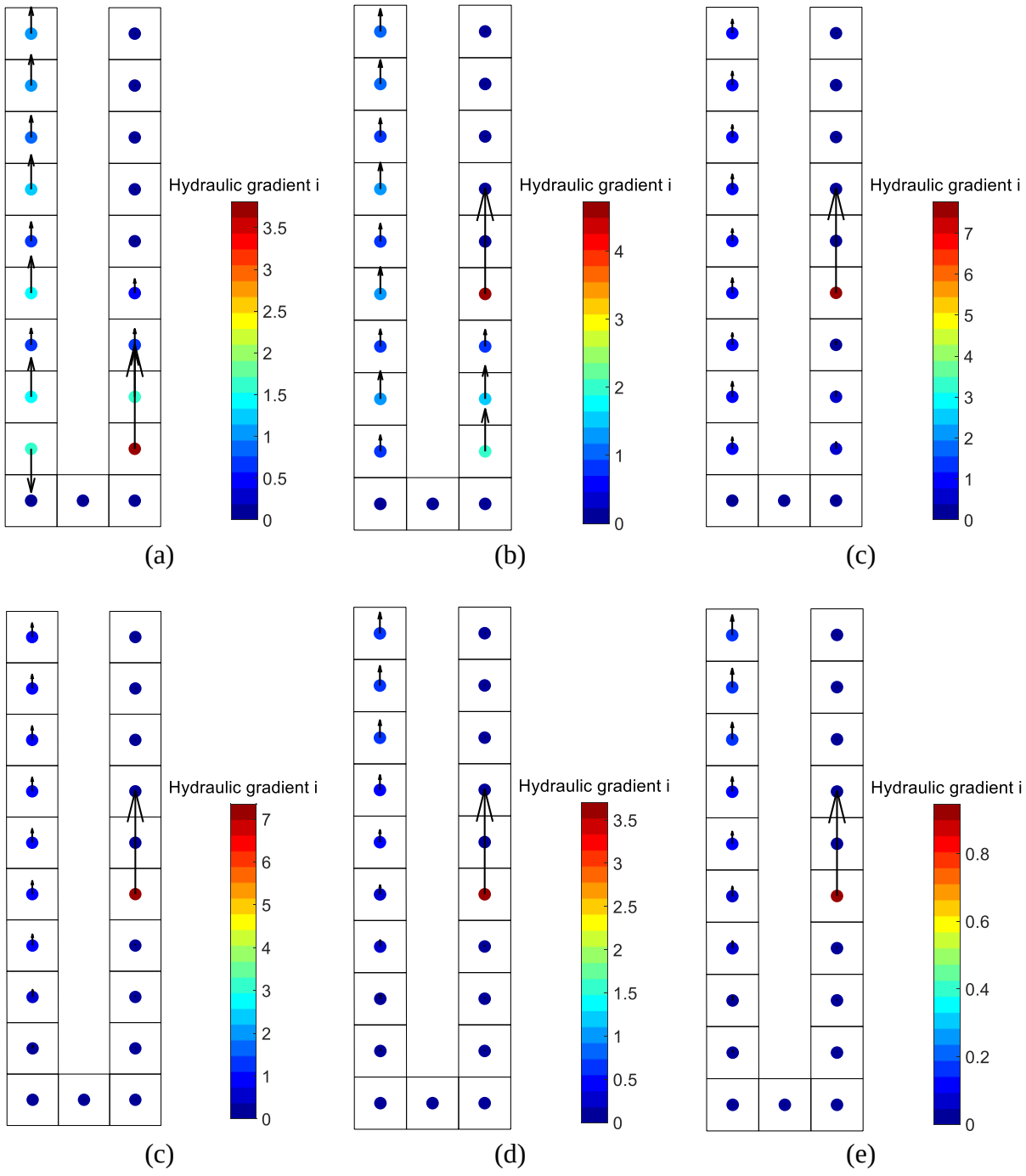

Figure 11.11 Hydraulic gradient contour with layered soils at: (a) 2 seconds; (b) 5 seconds; (c) 10 seconds; (d) 50 seconds; (e) 300 seconds; (f) 700 seconds

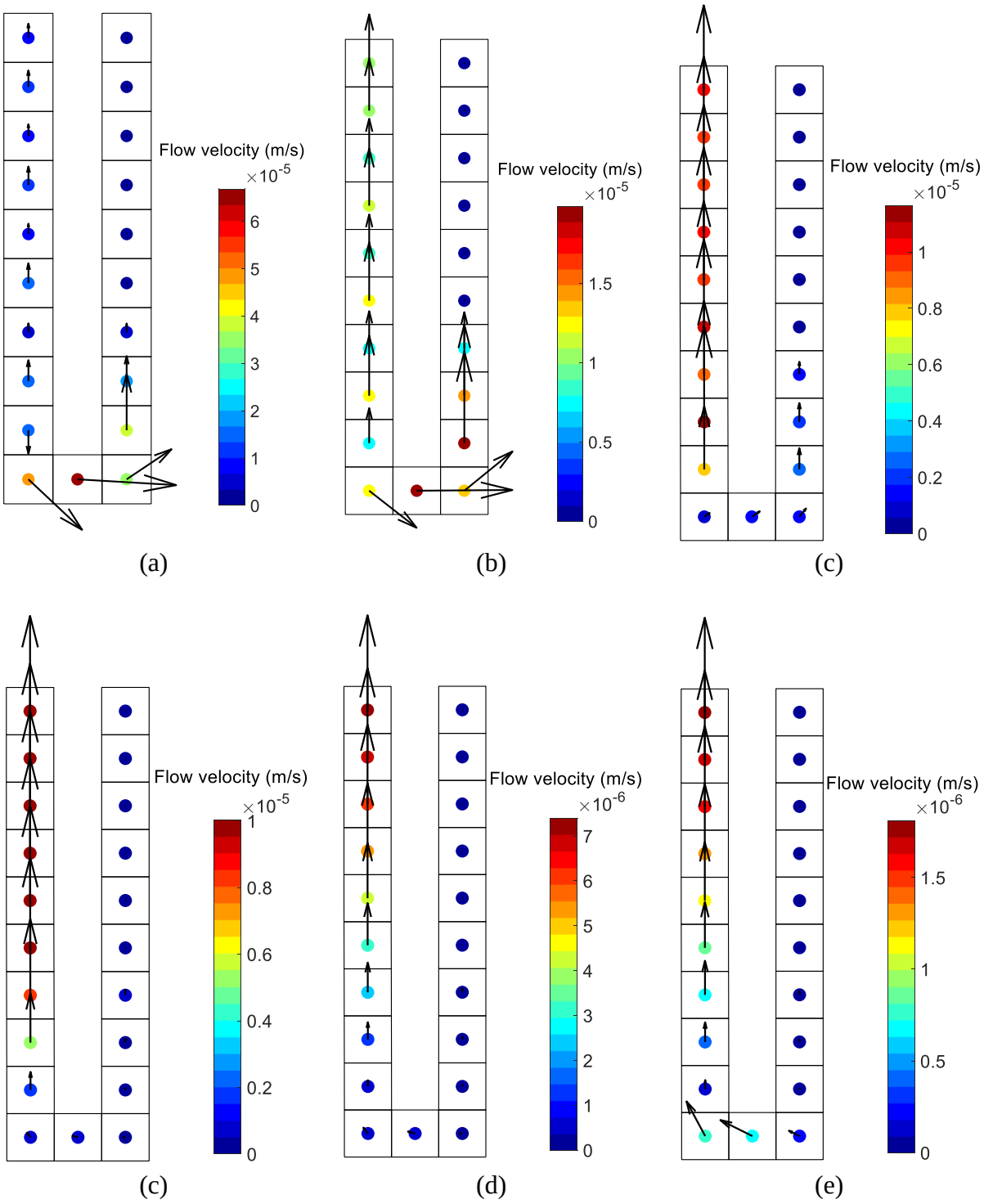

Figure 11.12 Flow velocity contour with layered soils at: (a) 2 seconds; (b) 5 seconds; (c) 10 seconds; (d) 50 seconds; (e) 300 seconds; (f) 700 seconds

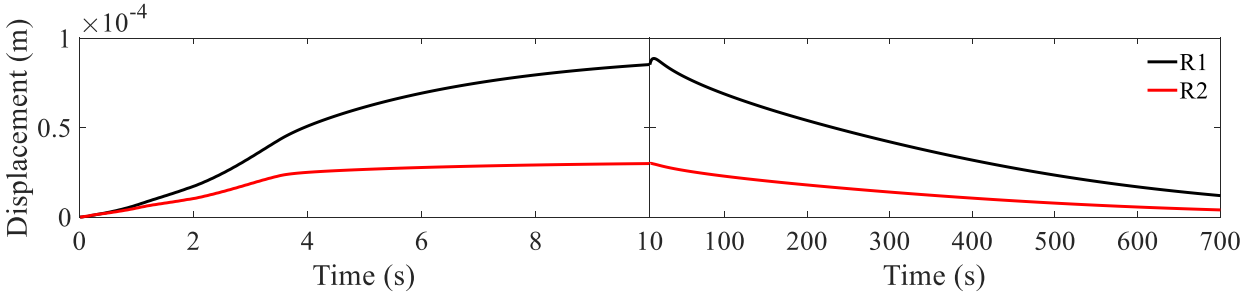

(a)

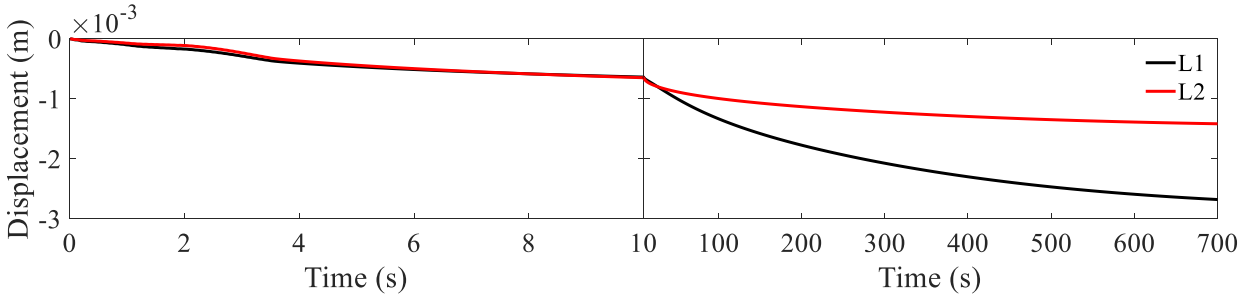

(b)

Figure 11.13 Vertical displacement time history: (a) R1, R2; (b) L1, L2

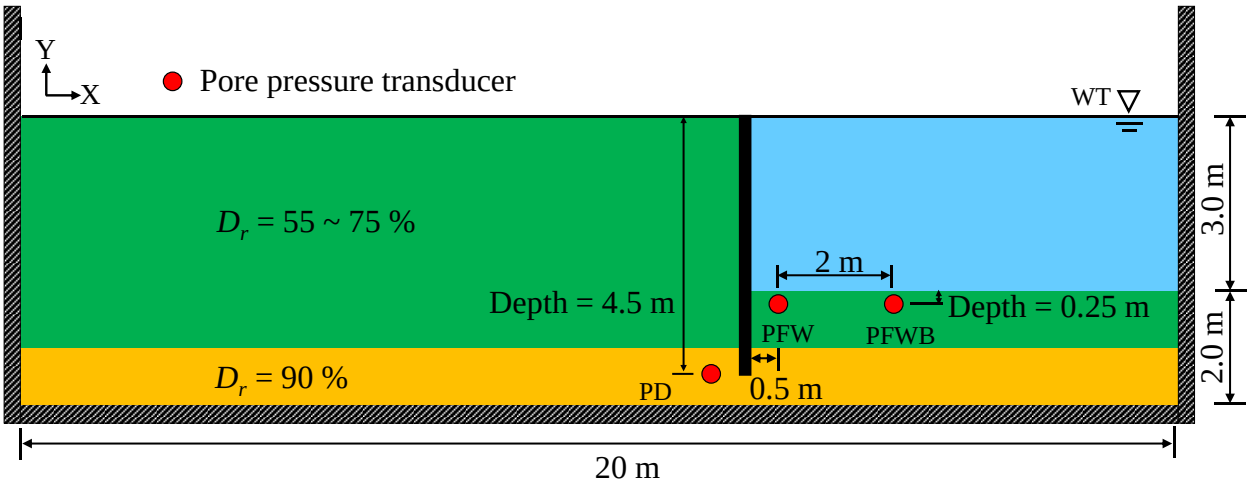

(a)

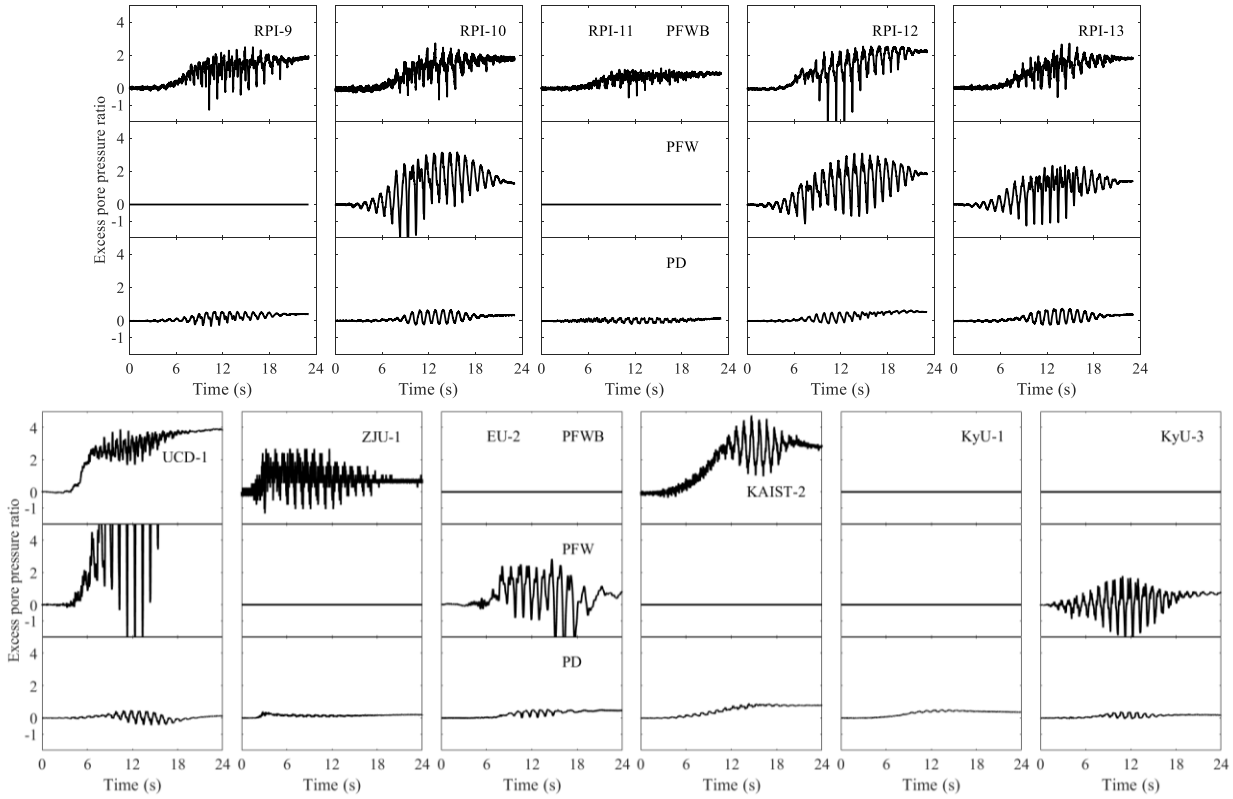

(b)

Figure 11.14 Centrifuge test illustration (data from Zeghal et al. 2019): (a) Schematic representation; (b) Excess pore pressure ratio at locations of PD, PFW, PFWB

(a)

(b)

(c)

(d)

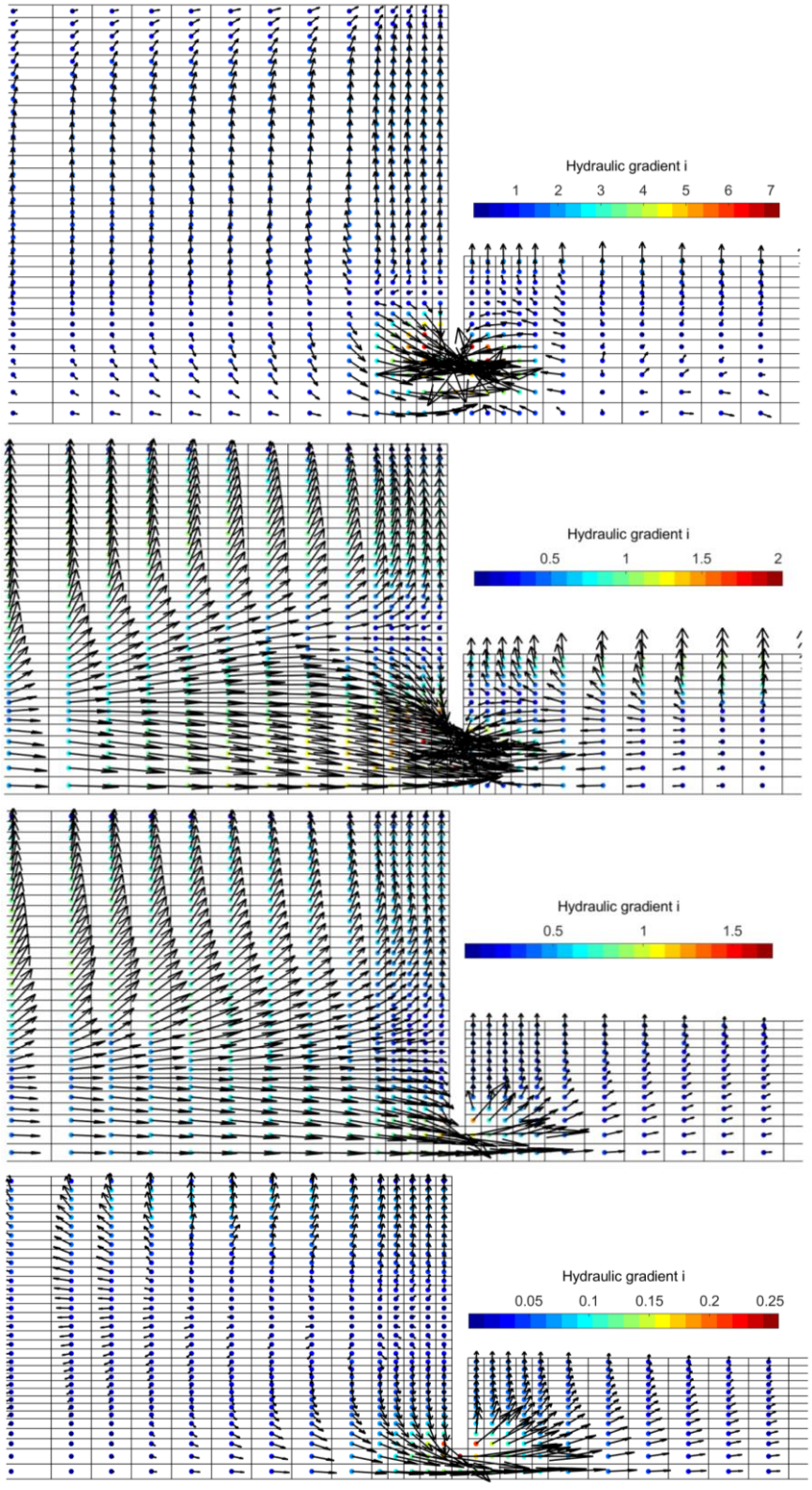

Figure 11.15 Computed hydraulic gradient of RPI-9 test (Zeghal et al. 2019) at: (a) 12 seconds; (b) 20 seconds; (c) 24 seconds; (d) 100 seconds

Chapter 12. Meshfree Framework for Seismic Response of Earth Systems

12.1. Abstract

An effort is proposed to bring the capabilities and advantages of the meshfree method within a dedicated open-source framework for use in earthquake engineering applications. Meshfree is a class of numerical methods designed to inherit the main advantages of the Finite Element Method (FEM), while at the same time overcoming the main disadvantages caused by mesh dependency. As such, it more accurately allows for capabilities such as large deformations, high gradients, crack propagation, and multi-scale strain localization phenomena. All of these capabilities are of much relevance to Performance-Based-Earthquake-Engineering (PBEE) assessment frameworks under conditions of strong excitation. For that purpose, the open-source code RKPM2D for solving PDEs under the reproducing kernel particle method (RKPM)-based meshfree computational framework is employed, with the extended capabilities of nonlinear dynamic (seismic) analysis. For illustration, results of an earth embankment subjected to seismic loading are presented and discussed. Overall, the employed computational framework has the potential to evaluate the seismic performance of soil system subjected to earthquake loading, with large deformation and solid-fluid coupled formulation developments currently underway.

12.2. Introduction

The Reproducing Kernel Particle Method (RKPM, Chen et al. 2013, 2017a, b; Chen and Belytschko 2015) has achieved great success as an advanced numerical approach to solve partial differential equations. Compared to conventional mesh-based numerical methods such as the Finite Element Method (FEM), the reproducing kernel approximations are constructed based on a set of scattered points without any mesh connectivity, and thus the strong tie between the quality

of the discretization and the quality of approximation in conventional mesh-based methods is relaxed. This “meshfree” feature makes RKPM well-suited for solving nonlinear mechanics and multiphysics problems where FEM suffers from mesh-distortion or element entanglement.

Based on the above, an open-source RKPM-based meshfree (Chen et al. 2013, 2017a, b; Chen and Belytschko 2015) computational framework (Huang et al. 2019) for linear static analysis (https://data.mendeley.com/datasets/prfxg9cbrx/2, RKPM2D) was developed by JS Chen and co-workers. Currently, the RKPM2D is being extended to conduct nonlinear dynamic analysis. As such, a representative simulation of earth embankment subjected to earthquake loading is presented to demonstrate the computational capabilities of this extended RKPM open-source code. From the computed results, this RKPM2D computational framework has the potential to evaluate seismic performance of earth systems, for scenarios that will eventually include large-deformation, localization, and soil liquefaction.

To this end, further research work will be addressing: i) development of a large-strain analysis module, and ii) adaptation and implementation of the UCSD OpenSees incremental-plasticity seismic soil response models (Parra, 1996; Yang, 2000; Yang and Elgamal 2002; Elgamal et al. 2003; Yang et al. 2003; Khosravifar et al. 2018; Elgamal et al. 2020 https://opensees.berkeley.edu/wiki/index.php/UCSD_Soil_References). As such, a wide range of practical applications will benefit greatly from this initial effort and potential future developments. For instance, the meshfree approach widens the user-base and horizon of applications for large-displacement and/or large-strain seismic response as depicted by the recent pioneering simulations of Profs. Soga, Seed and co-workers (e.g., Chowdhury et al. 2018, 2019; Wang et al. 2019; Islam et al. 2018). Facilitated by the meshfree large-displacement and deformation response characteristics, more accurate consequences of strong shaking are paramount for performance-

based engineering (PBE) assessments. In general, this domain of simulation has been generally receiving much attention from recognized entities such as the National Academies of Sciences, Engineering, and Medicine (e.g., http://dels.nas.edu/resources/static-assets/besr/miscellaneous/Open-Session-Materials/COGGE/NAE-Webinar-Soga-Original.mp4).

12.3. Reproducing Kernel Approximation for Ground Systems

In RKPM, the numerical approximation is constructed based upon a collection of scattered points or nodes (Chen et al. 2013, 2017a, b; Chen and Belytschko 2015). For finite dimensional solutions of PDEs, the domain is discretized by a set of nodes as shown in Figure 12.1 and Figure 12.2. As seen in Figure 12.2, circular kernel support coverage is employed with the compact size $\alpha = ch$, where c is the normalized support size (taken as 2 for illustration), and h is the nodal spacing.

Domain integration (Chen et al. 2013, 2017a, b; Chen and Belytschko 2015; Hillman and Chen, 2016; Huang et al. 2019) plays an important role in controlling the solution errors of meshfree methods. Unlike FEM which utilizes the element topology for integration, quadrature domains for meshfree methods can be chosen either as background cells that are independent from numerical discretization, or associated with the nodal representative domains (Huang et al. 2019). The former scheme is commonly adopted in conjunction with the Gauss quadrature scheme and the latter naturally leads to nodal integration schemes, both of which have been implemented in the open-source code RKPM2D. In the following simulation, modified stabilized nodal integration (Huang et al. 2019) is employed for eliminating spurious low-energy modes.

12.4. Gravity Analysis

Before shaking, gravity was applied first to activate an initial static state (Figure 12.3) with linear elastic properties for the earth embankment model shown above. All nodes were fixed along

the base where input ground excitation is imparted subsequently (Figure 12.4a). The soil response (Figure 12.4b) is represented by a strain softening plasticity model and the material parameters are presented in Qiu and Elgamal 2020a. Figure 12.3 shows the initial vertical/horizontal effective stress state and shear stress ratio (initial shear stress τ/shear strength τ_{max}).

12.5. Dynamic Analysis

After the gravity analysis phase, the soil properties were switched from elastic to plastic. Dynamic analysis is conducted by applying an acceleration time history (Figure 12.4a) to the base of the model. Herein, this seismic input motion (Figure 12.4a) was simply taken as that of the 1994 Northridge earthquake ground surface Rinaldi Receiving Station record (Component S48W). Explicit integration is used with the load time step Δt = 0.0005s. A relatively low level of updated stiffness proportional damping (coefficient = 0.003) was used to enhance numerical stability of the ground system response.

Figure 12.5 shows the computed displacement contours at end of shaking. As shown (Figure 12.5), the right slope of the earth embankment deformed laterally in the downslope direction, reaching a maximum horizontal displacement of about 1.6 m (arrows displaying the direction of ground deformation). The displacement time histories of points M and A-C are depicted in Figure 12.5. It can be seen that the horizontal displacement accumulated significantly immediately after the negative peak value of base input motion and continued to accumulate until the end of shaking. Vertical displacement of the embankment is also seen (Figure 12.6), reaching about 0.5 m.

Figure 12.7 shows the shear strain contour at end of shaking. Permanent shear strain occurred near the bottom of the right slope, reaching about 60 %. Representative nodal shear stress-strain response of point D is shown in Figure 12.7b. As seen in this figure, the computational model

reproduces cycle-by-cycle accumulation of permanent deformation towards the down-slope direction. Ultimately, the shear stress reached its residual state (Figure 12.7b).

12.6. Computed Response without Strain Softening

To assess influence of strain softening effect, an additional numerical simulation of the above earth embankment model was conducted using the PressureIndependMultiYield material (Elgamal et al. 2008; Lu et al. 2011). Figure 12.8 shows the horizontal and vertical displacement contours at end of shaking. Compared to the strain softening scenario (Figure 12.5), permanent horizontal and vertical displacements using the PressureIndependMultiYield material are significantly lower (Figure 12.8). In addition, the shear strains are much reduced (Figure 12.9) compared to their strain softening counterpart (Figure 12.7).

12.7. Conclusions

An effort is proposed to bring the capabilities and advantages of the meshfree method within a dedicated open-source framework for use in earthquake engineering applications. As such, the open-source code RKPM2D for solving PDEs under the reproducing kernel particle method (RKPM)-based meshfree computational framework is employed, with the extended capabilities of nonlinear dynamic (seismic) analysis. For illustration, results of an earth embankment subjected to seismic loading are presented and discussed. Overall, the employed computational framework has the potential to evaluate seismic performance of soil systems subjected to earthquake loading. Further research is underway towards: i) development of a large-strain analysis module, and ii) adaptation and implementation of the UCSD OpenSees incremental-plasticity seismic soil response models. As the developments continue, a wide range of practical applications will benefit greatly from this effort and potential future developments.

12.8. Acknowledgements

The author is extremely grateful for the help and support of Professor JS Chen and his research group. This research would not have been possible without Professor Chen's earlier extensive work in this area, his willingness to share his computer codes, and his unwavering support throughout.

Chapter 12, in part, has been submitted for publication of the material as it may appear in the following conference publication (The dissertation author was the primary investigator of this paper):

Elgamal, A., Chen, J., Qiu, Z., Huang T., Wei, H., and Lu, J. (2020). "Meshfree framework for seismic response of earth systems." In 16th International Conference of IACMAG International Association for Computer Methods and Advances in Geomechanics, Torino, Italy. 3-4 May.

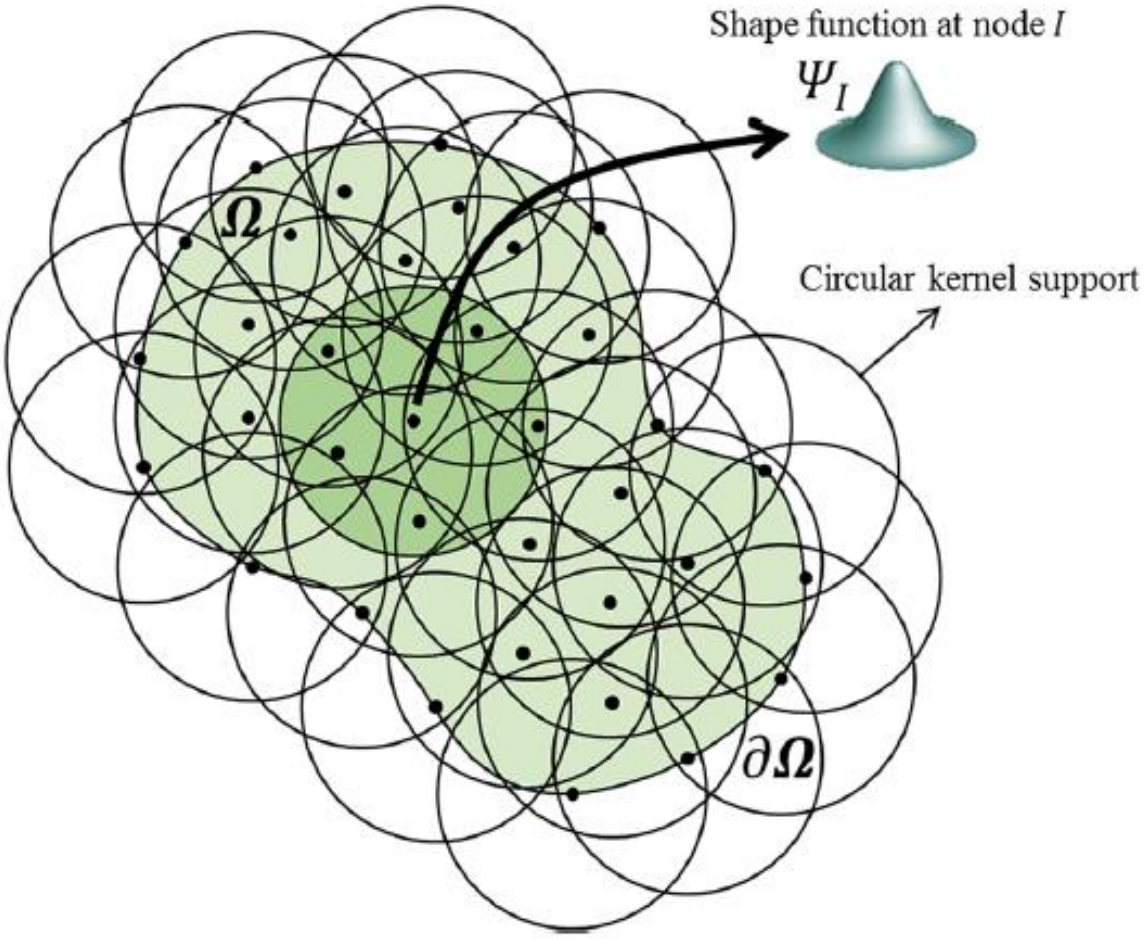

Figure 12.1 Illustration of a 2D RK discretization: support coverage and nodal shape function with circular kernel (after Chen et al. 2013, 2017a, b)

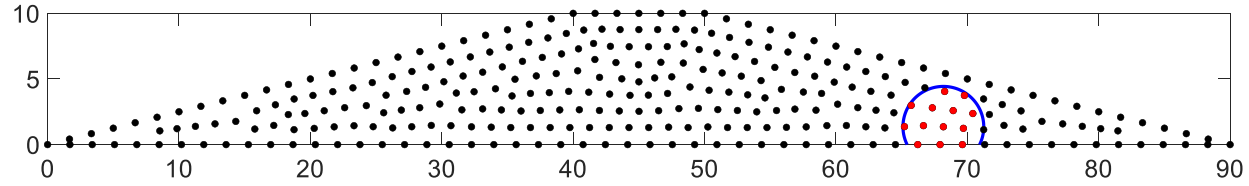

(a)

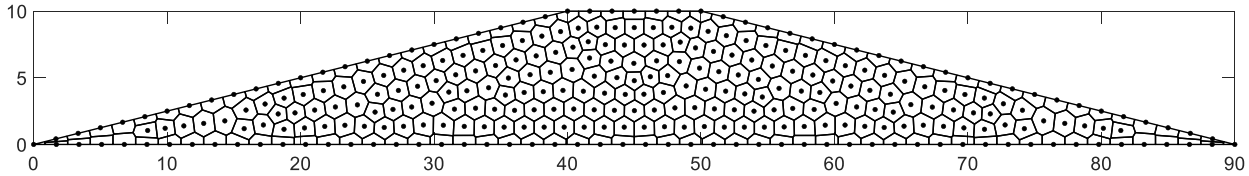

(b)

Figure 12.2 An earth embankment configuration: (a) Illustration of 2D RK discretization; (b) Illustration of nodal integration cells (unit: m)

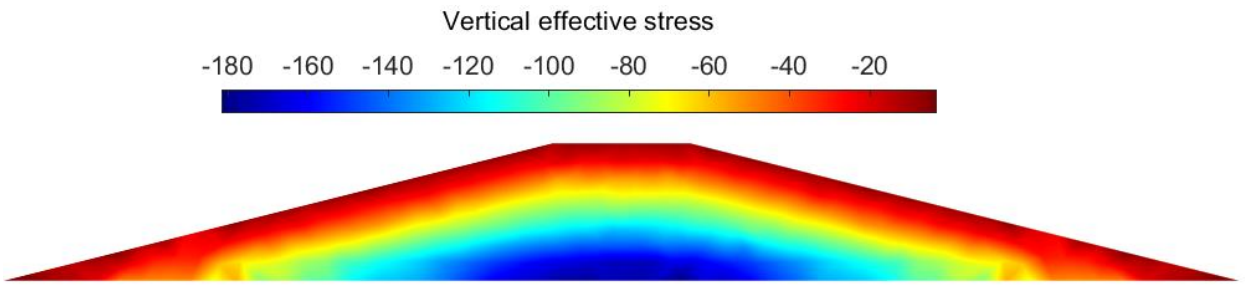

(a)

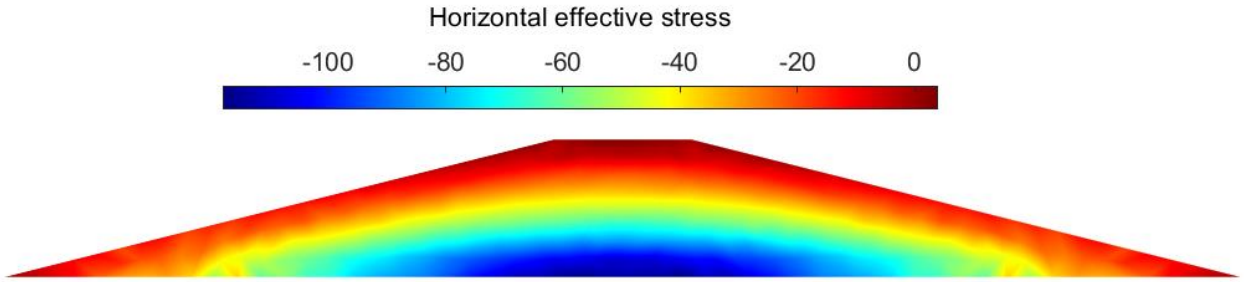

(b)

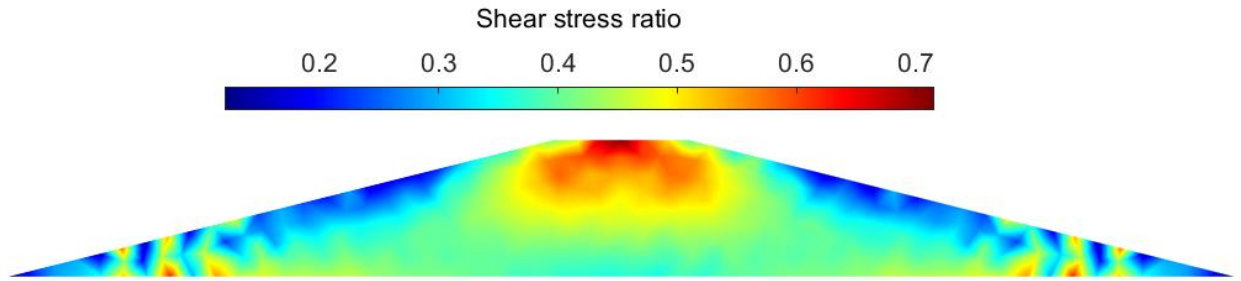

(c)

Figure 12.3 Initial state of soil: (a) Vertical effective stress; (b) Horizontal effective stress; (c) Shear stress ratio

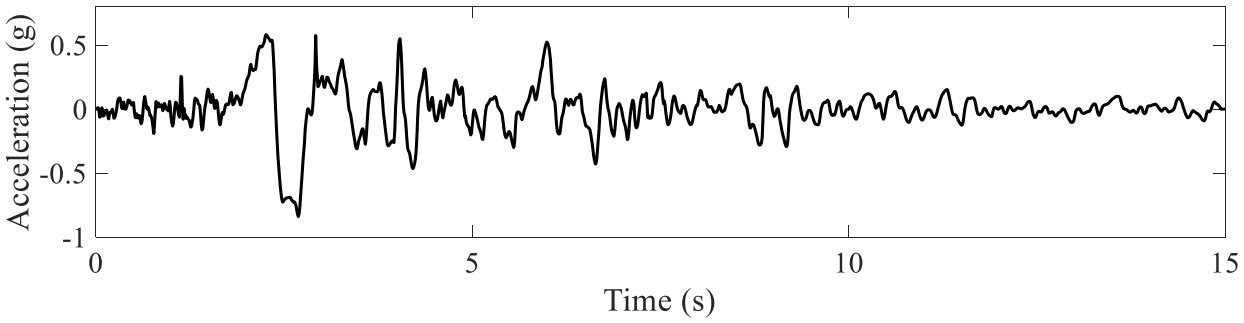

(a)

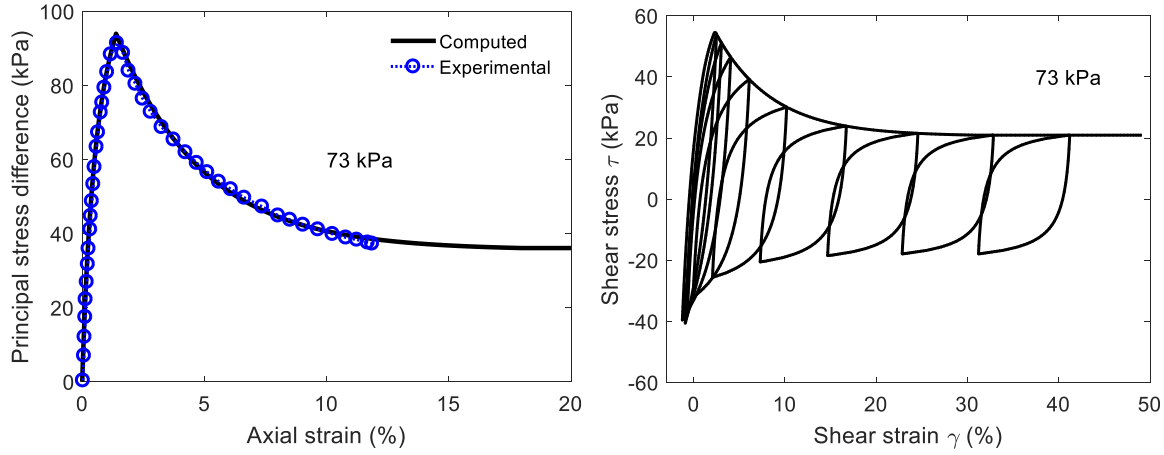

(b)

Figure 12.4 Input motion and model response of strain softening model: (a) 1994 Northridge earthquake ground surface Rinaldi Receiving Station record; (b) Calibrated quick Tiller clay (Gylland et al. 2014) and the cyclic model response

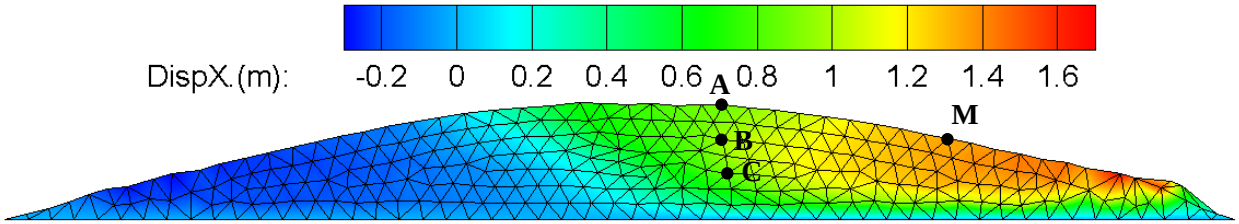

(a)

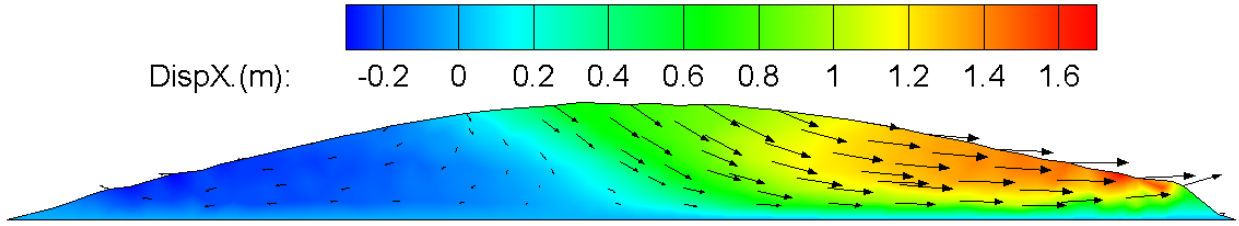

(b)

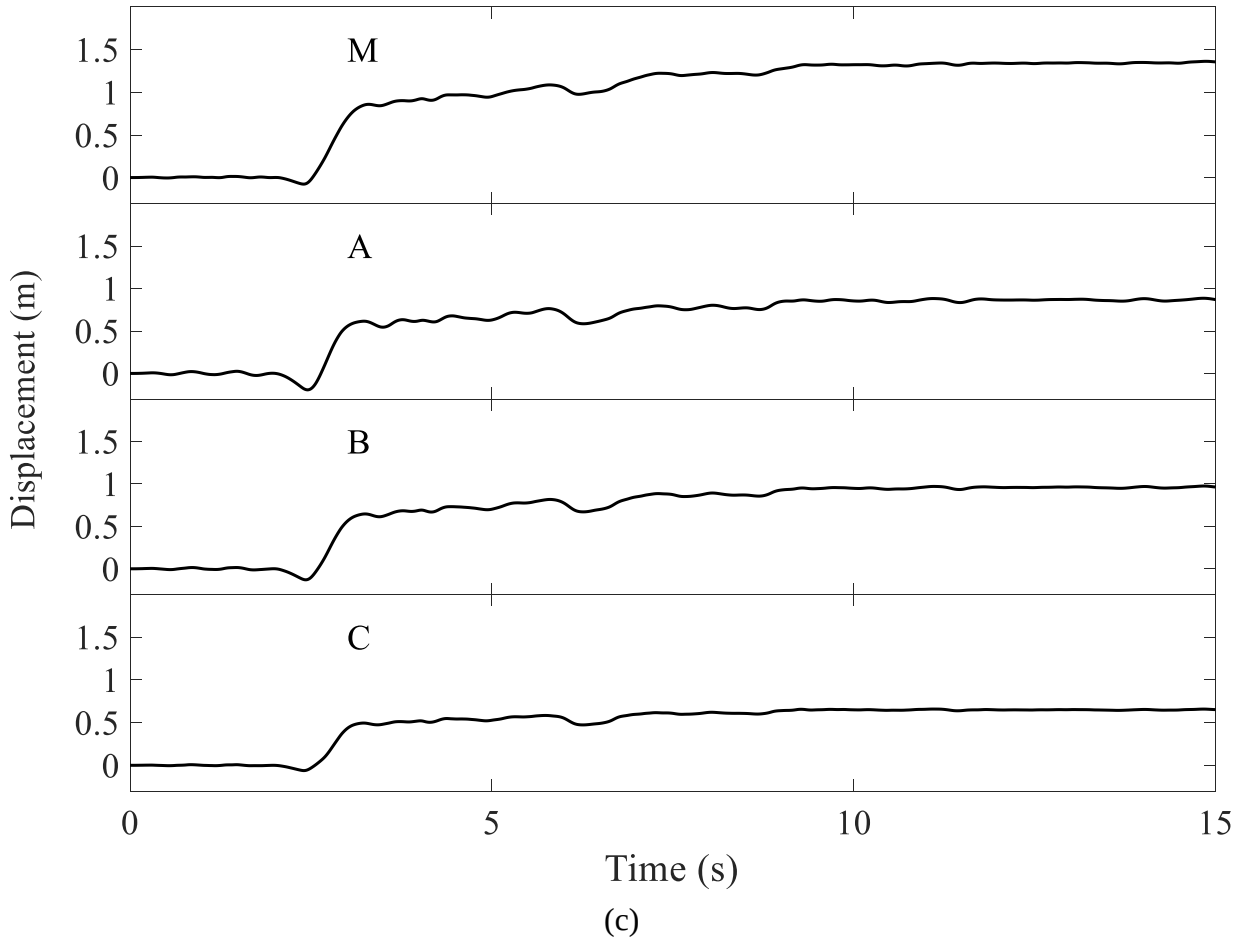

(c)

Figure 12.5 Horizontal displacement: (a) Deformed mesh at end of shaking; (b) Contour with arrows showing the direction of ground movement; (c) Time histories

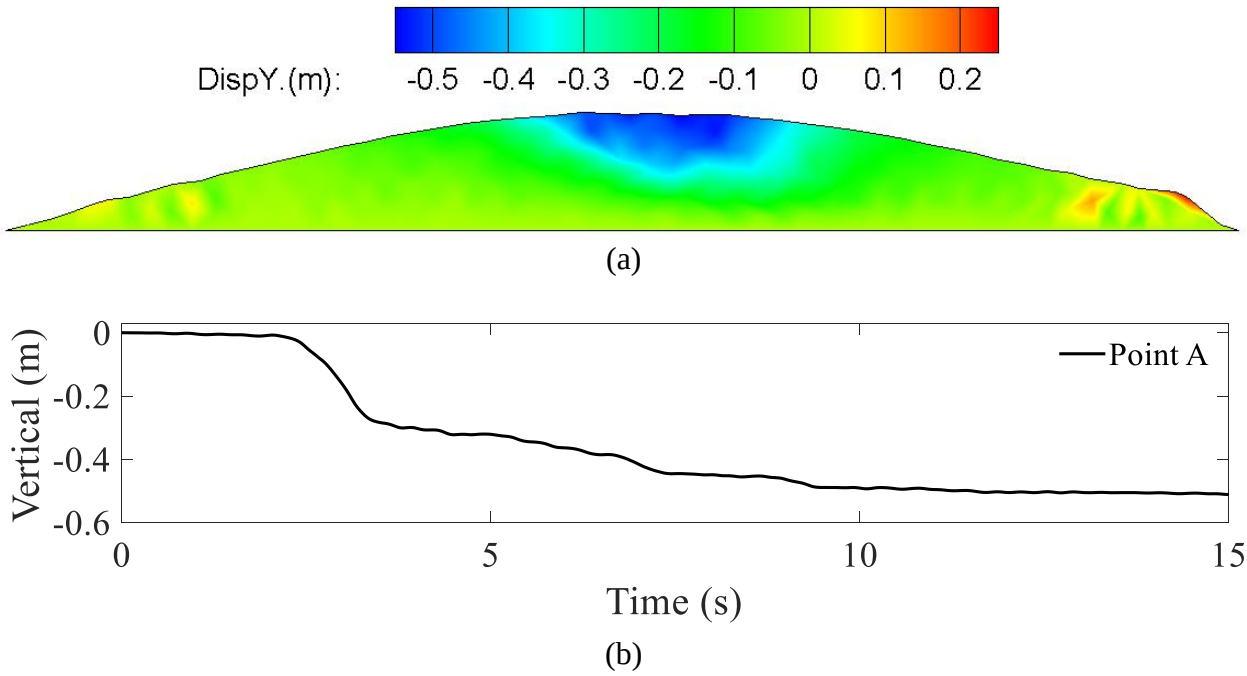

Figure 12.6 Vertical displacement: (a) Contour at end of shaking; (b) Time histories

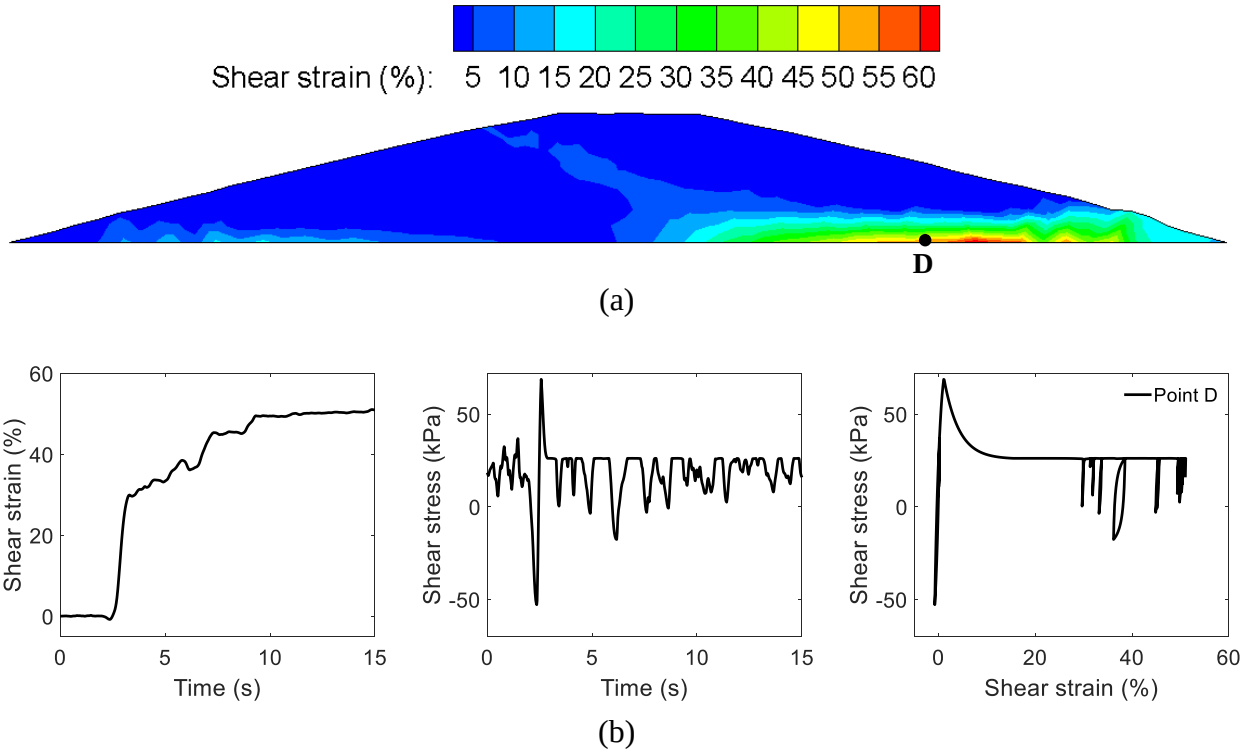

Figure 12.7 Shear strain: (a) Contour; (b) Shear stress-strain at point D

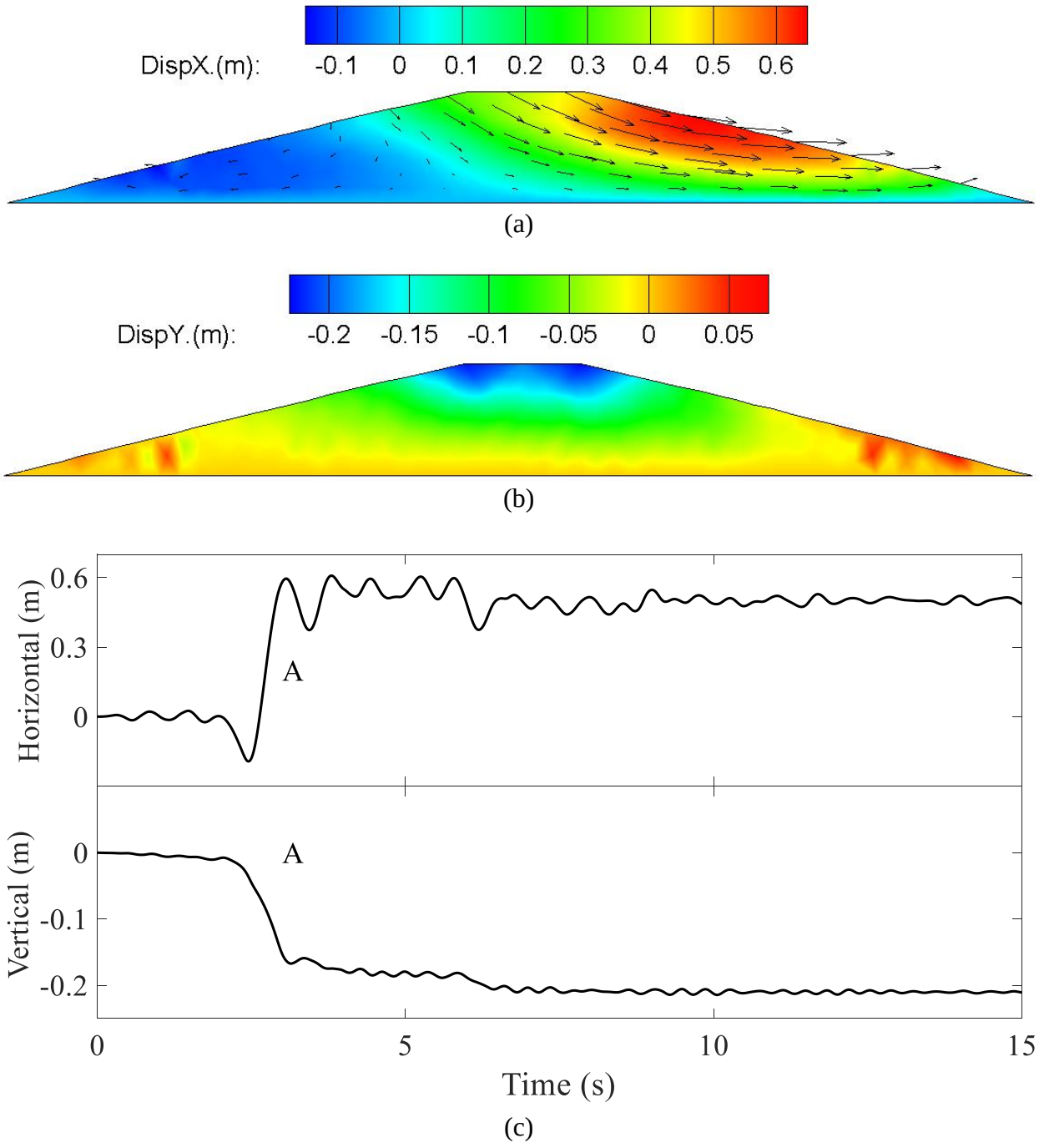

Figure 12.8 Displacement without strain softening: (a) Horizontal displacement contour at end of shaking; (b) Vertical displacement contour at end of shaking; (c) Point A (Figure 12.5)

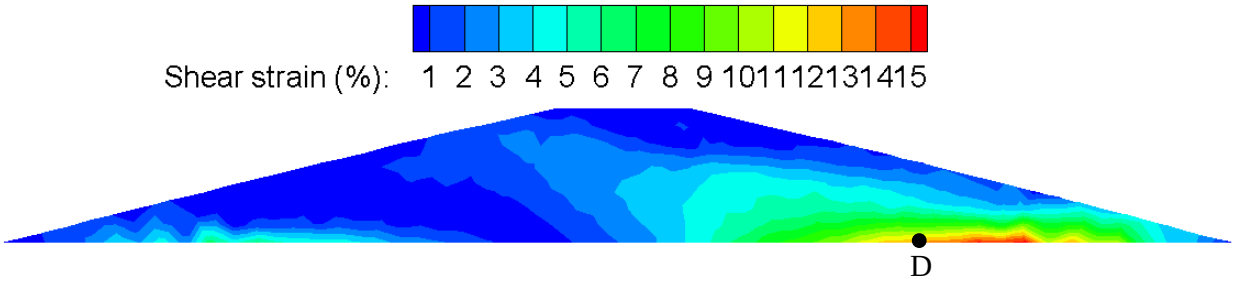

(a)

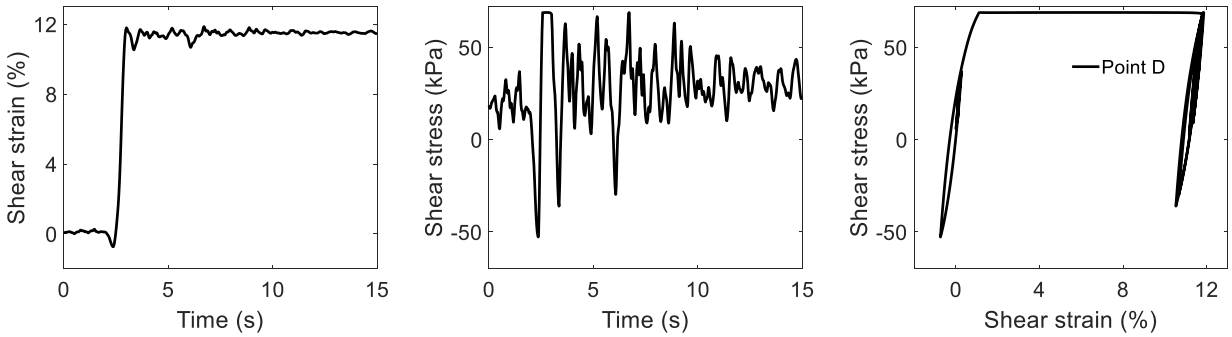

(b)

Figure 12.9 Shear strain without strain softening: (a) Contour; (b) Shear stress-strain at point D

Chapter 13. Conclusions and Future Work

13.1. Summary

This dissertation provides a wide range of studies in soil constitutive modeling, calibrations of experiments, and computational modeling of three-dimensional (3D) large-scale bridge-ground systems. In order to reproduce salient response characteristics of soil seismic response, three plasticity constitutive models were discussed and implemented into the employed computational framework OpenSees, including a pressure-dependent sand model with Lode angle effect, a 3D strain softening model and a practical 3D cyclic softening model. Furthermore, for calibration purposes, finite element (FE) numerical simulations of a series of experiments were conducted to investigate the underlying mechanisms of liquefaction-induced ground deformation and sheet pile system response. The overall experimental data were reasonably captured by the conducted FE simulations, demonstrating that the employed constitutive models as well as the computational framework have the potential to realistically evaluate the performance of ground-structure systems when subjected to seismically-induced liquefaction.

In addition, a FE analysis framework was presented to study a number of salient features associated with the liquefaction-induced seismic response of large-scale bridge-ground systems. For that purpose, 3D FE models were developed, motivated by the details of actual bridge-ground configurations including a multi-span bridge, a short-span bridge in a relatively narrow canyon, and a newly proposed arch bridge configuration. In each case, the bridge-ground system and details of the corresponding numerical analysis were discussed. Displacement, moment, shear, axial forces, and ductility demand of the structure, resulting from the liquefaction-induced ground deformations were explored. In addition, the bridge's restraining influence on downslope deformations, effect of input motion polarity, and potential for retrofit studies were investigated.

The numerical framework and the insights derived from this study are of general relevance to bridge-ground seismic response scenarios.

Finally, exploratory studies were presented about: i) liquefaction scenarios where excess pore-pressure might exceed the initial effective vertical stress, and ii) use of meshfree methodologies in geotechnical earthquake engineering, to more accurately account for large deformations, and eventually to incorporate crack propagation logics.

13.2. Conclusions

13.2.1. Three-Dimensional Strain Softening Model

1. Strength and stiffness degradation due to the strain softening mechanism might play a substantial role in terms of accumulated deformations and its effect on the resulting ground acceleration and extent of permanent displacement.
2. Incorporation of strain softening where applicable, is an important consideration for a wide range of ground scenarios involving sensitive clays, cemented soils, over-consolidated clays, very dense sands, and frozen soils among others.
3. Additional experimental data sets are needed in order to further quantify degradation of strength and stiffness due to cyclic loading (post-peak behavior). As such new data sets become available, the gained insights may be introduced into the presented softening framework.

13.2.2. Multi-Span Bridge-Ground Seismic Response

1. As highlighted in earlier studies (Cubrinovski et al. 2014; McGann and Arduino 2015; Shin et al. 2008; Zhang et al. 2008), response is highly dependent on the bridge-ground system as an integral global entity. Connectivity provided by the bridge deck, soil profile variability along the bridge length, and geometric configuration of the slopes are all factors

that can significantly influence the outcome.

2. Particularly for pulse-type seismic motions, local slope deformations may be superposed on an overall global pattern of permanent lateral ground motion, which might contribute to higher demands due to the combined outcome of both.
3. The bridge structure and its foundations exerted a significant restraining effect on lateral ground deformations. Such restraining effects partially stem from the bridge-ground global connectivity characteristics, which can be of considerable influence.
4. Peak demands for some of the piers and/or piles might occur due to the combined inertial and kinematic load during the shaking event. In simplified analyses, both inertial as well as kinematic load cases should be considered.
5. Moments and curvatures in the piers depend on relative displacement between the deck and the pile foundations. In this regard, some of the observed peak demand values were near the center of the bridge, where the pile foundations did not move appreciably in either direction.
6. Significant tensile forces might evolve in pile group configurations, and further attention to potential consequences is suggested.
7. Polarity of the input motion may influence the outcomes, and further attention to this matter is warranted from the seismological point of view.
8. Further studies may be conducted to assess sensitivity of the numerical results to the salient modeling idealizations including the employed geometric configuration, material models and properties, as well as input motions and characteristics of the associated transmitting boundary. Higher demands resulting from 3D modeling with full 3D seismic excitation might be also explored, albeit requiring a significantly greater effort.

13.2.3. Short-Span Bridge-Ground Seismic Response

1. For relatively narrow canyon geometries, soil in the central sections can experience a significant tendency for upward heave and may induce a state of higher lateral confinement of the ground. These mechanisms might in turn increase the liquefaction resistance at such locations.
2. As highlighted in earlier studies (Shin et al. 2008; Zhang et al. 2008; Cubrinovski et al. 2014, McGann and Arduino 2015), response is highly dependent on the soil ground system as an integral global entity. Connectivity provided by the bridge deck, soil profile and its variation along the bridge length, and geometric configuration of the slopes and the underlying water channel are all factors that can significantly influence the outcome.
3. Substantial pile deformations may occur at the pile-abutment connection due to rotation as observed and presented by Cubrinovski et al. (2014). In addition, the piles could be strained at the interfaces between liquefiable and non-liquefiable or soft clay and stable soil strata.
4. The bridge structure and its foundations act as a strut that might exert a significant added restraint to the slope deformations on both sides. These restraining effects partially stem from the bridge's global connectivity and the corresponding abutment-to-abutment interaction, which can be of much influence.
5. Peak demands for some of the piles might occur due to the combined inertial and kinematic load during the shaking event. In a simplified analysis, both inertial as well as kinematic load cases should be considered.

13.2.4. Proposed Arch Bridge-Ground Seismic Response

1. An arch bridge superstructure provides a mechanism to exert a restraining effect on downslope lateral ground deformations. Such restraining effects stem from: i) own weight

of the bridge exerting lateral earth pressure forces at the abutments, and ii) the bridge global connectivity characteristics, reacting against the tendency for downslope deformations on both sides of the canyon.

2. Absence of bridge columns and underlying foundations cause potential lateral ground deformations to have minimal detrimental influence of the bridge superstructure.
3. After an earthquake: i) potential retrofit is economical with no need to address costly deep foundation challenges, and ii) the bridge structure naturally conforms to the surrounding deformed ground configuration, where relatively minor grading or re-leveling work might be needed, with minimal to no damage to the bridge structure.

13.3. Future Work

1. Inherent anisotropy (Yoshimine et al. 1998; Abelev and Lade 2004) shows the soil contractive tendency becoming more stronger with the increase of maximum principal stress and intermediate principal stress. As such, implementation of an inherent anisotropy effect into the into the OpenSees material LadeDuncanMultiYield material is important to more accurately capture this salient characteristic of soil response.

2. Performance-based earthquake engineering (PBEE) assessment of the full 3D bridge-ground systems due to liquefaction-induced lateral spreading. The PBEE methodology (Mackie et al. 2011, 2012) can implemented with repair cost and down-time estimates to achieve the desired performance objectives. Additional research is needed to extend this PBEE framework to handle 3D bridge-ground system response, subjected to liquefaction-induced lateral spreading, In this regard, the parallel version of OpenSees (OpenSeesSP) can be used to efficiently complete all individual shaking event simulations simultaneously by using the computation cluster DesignSafe-CI (https://www.designsafe-ci.org/).

3. Additional effort is needed to bring the capabilities and advantages of the meshfree method within a dedicated open-source framework RKPM2D for use in earthquake engineering applications. As such, this method more accurately allows for capabilities such as large deformations, high strain gradients and strain localization, crack propagation, and multi-scale strain localization phenomena, all being mechanisms of much relevance to PBEE assessment frameworks under conditions of strong excitation.

4. Implementation of state variables in the pressure-dependent multi-surface plasticity models would further streamline the analyses and help in terms scenarios such as that of void redistribution. In this regard, the soil might undergo a substantial change in its relative density during the seismic loading process, and a seamless process to handle this matter would be beneficial.

References

Abuhajar, O., El Naggar, M.H. and Newson, T. (2010). "Review of Available Methods for Evaluation of Soil Sensitivity for Seismic Design." *Fifth International Conference on Recent Advances in Geotechnical Earthquake Engineering and Soil Dynamics*, MAY, San Diego, CA.

Al Atik, L. and Sitar, N. (2010). "Seismic Earth Pressures on Cantilever Retaining Structures." *Journal of Geotechnical and Geoenvironmental Engineering*, 136(10), 1324-1333.

Almutairi, A., Lu, J., Elgamal, A. and Mackie, K. (2018). "MSBridge: OpenSees Pushover and Earthquake Analysis of Multi-span Bridges - User Manual." Structural Systems Research Project Report No. SSRP-16/05, University of California at San Diego, La Jolla.

Arduino, P., Ashford, S., Assimaki, D., Bray, J., Eldridge, T., Frost, D., Hashash, Y., Hutchinson, T., Johnson, L., Kelson, K. and Kayen, R. (2010). "Geo-engineering Reconnaissance of the 2010 Maule, Chile Earthquake." GEER Association Report No. GEER-022, 1.

Armstrong, R.J. (2018). "Numerical Analysis of LEAP Centrifuge Tests Using a Practice-based Approach." *Soil Dynamics and Earthquake Engineering*, 113, 793-803.

Asgari, A., Oliaei, M. and Bagheri, M. (2013). "Numerical Simulation of Improvement of a Liquefiable Soil Layer Using Stone Column and Pile-pinning Techniques." *Soil Dynamics and Earthquake Engineering*, 51, 77-96.

Ashford, S.A., Boulanger, R.W., Brandenberg, S.J. and Shantz, T. (2009). "Overview of Recommended Analysis Procedures for Pile Foundations in Laterally Spreading Ground." *In TCLEE 2009: Lifeline Earthquake Engineering in a Multihazard Environment*, 1-8.

Ashford, S.A., Boulanger, R.W. and Brandenberg, S.J. (2011). "Recommended Design Practice for Pile Foundations in Laterally Spreading Ground." Pacific Earthquake Engineering Research Center. University of California, Berkeley, Calif. PEER Rep, (2011/04).

Anagnostopoulos, A.G., Kalteziotis, N., Tsiambaos, G.K. and Kavvadas, M. (1991). "Geotechnical Properties of the Corinth Canal Marls." *Geotechnical & Geological Engineering*, 9(1), 1-26.

Andersson-Sköld, Y., Torrance, J.K., Lind, B., Odén, K., Stevens, R.L. and Rankka, K. (2005). "Quick Clay-A Case Study of Chemical Perspective in Southwest Sweden." *Engineering Geology*, 82(2), 107-118.

Aygün, B., Dueñas-Osorio, L., Padgett, J.E. and DesRoches, R. (2009). "Seismic Vulnerability of Bridges Susceptible to Spatially Distributed Soil Liquefaction Hazards." *In Structures Congress 2009: Don't Mess with Structural Engineers: Expanding Our Role*, 1-10.

Aygün, B., Dueñas-Osorio, L., Padgett, J.E. and DesRoches, R. (2010). "Efficient Longitudinal Seismic Fragility Assessment of a Multispan Continuous Steel Bridge on Liquefiable Soils." *Journal of Bridge Engineering*, 16(1), 93-107.

Bagheri, F. and El Naggar, M.H. (2015). "Effects of Installation Disturbance on Behavior of Multi-helix Piles in Structured Clays." *DFI Journal-The Journal of the Deep Foundations Institute*, 9(2), 80-91.

Bardet, J.P. and Davis, C.A. (1996). "Performance of San Fernando Dams During 1994 Northridge Earthquake." *Journal of Geotechnical Engineering,* 122(7), 554-564.

Bastidas, A.M.P. (2016). Ottawa F-65 Sand Characterization. University of California, Davis.

Berrill, J.B., Christensen, S.A., Keenan, R.P., Okada, W. and Pettinga, J.R. (2001). "Case Study of Lateral Spreading Forces on a Piled Foundation." *Geotechnique,* 51(6), 501-517.

Bowers, M.E. (2007). "Seismic Fragility Curves for a Typical Highway Bridge in Charleston, SC Considering Soil-structure Interaction and Liquefaction Effects." PhD Thesis, Clemson University.

Bray, J. and Frost, D. (2010). Geo-engineering reconnaissance of the 2010 Maule, Chile earthquake. Report No. GEER-022 of the NSF Sponsored GEER Association Team, 1.

Brooks, G.R. (2013). "A Massive Sensitive Clay Landslide, Quyon Valley, Southwestern Quebec, Canada, and Evidence for a Paleoearthquake Triggering Mechanism." *Quaternary Research,* 80(3), 425-434.

Boulanger, R.W. and Idriss, I.M. (2006). "Liquefaction Susceptibility Criteria for Silts and Clays." *Journal of Geotechnical and Geoenvironmental Engineering,* 132(11), 1413-1426.

Boulanger, R.W. and Idriss, I.M. (2007). "Evaluation of cyclic softening in silts and clays." *Journal of Geotechnical and Geoenvironmental Engineering,* 133(6), 641-652.

Boulanger, R.W. and Ziotopoulou, K. (2015). "PM4Sand (Version 3): A Sand Plasticity Model for Earthquake Engineering Applications." Center for Geotechnical Modeling Report No. UCD/CGM-15/01, Department of Civil and Environmental Engineering, University of California, Davis, Calif.

Boulanger, R.W., Chang, D., Brandenberg, S.J., Armstrong, R.J. and Kutter, B.L. (2007). "Seismic Design of Pile Foundations for Liquefaction Effects." *In Earthquake Geotechnical Engineering,* 277-302. Springer, Dordrecht.

Burland, J.B. (1990). "On the Compressibility and Shear Strength of Natural Clays." *Géotechnique,* 40(3), 329-378.

Burland, J.B., Rampello, S., Georgiannou, V.N. and Calabresi, G. (1996). "A Laboratory Study of the Strength of Four Stiff Clays." *Géotechnique,* 46(3), 491-514.

Caltrans (2017). Personal Communications.

Carlson, N.N. and Miller, K. (1998). "Design and Application of a Gradient-weighted Moving Finite Element Code II: in Two Dimensions." *SIAM Journal on Scientific Computing,* 19(3): 766-798.

Chan, A.H.C. (1988). "A Unified Finite Element Solution to Static and Dynamic Problems in Geomechanics." PhD Thesis, University College of Swansea.

Chang, D., Boulanger, R., Brandenberg, S. and Kutter, B. (2013). "FEM Analysis of Dynamic Soil-pile-structure Interaction in Liquefied and Laterally Spreading Ground." *Earthquake Spectra,* 29(3), 733-755.

Chang, G. and Mander, J. (1994). "Seismic Energy Based Fatigue Damage Analysis of Bridge Columns: Part I – Evaluation of Seismic Capacity." NCEER Technical Report 94-0006.

Chang, B.J. and Hutchinson, T. C. (2013). "Experimental Investigation of Plastic Demands in Piles Embedded in Multi-layered Liquefiable Soils," *Soil Dynamics and Earthquake Engineering*, 49, 146-156.

Chen, W.F. and Mizuno, E. (1990). Nonlinear Analysis in Soil Mechanics, Theory and Implementation, Elsevier, New York, NY.

Chen, W. and Qiu, T. (2014). "Simulation of Earthquake-Induced Slope Deformation Using SPH Method." *International Journal for Numerical and Analytical Methods in Geomechanics*, 38(3), 297-330.

Chen, J.S., Hillman, M. and Rüter, M. (2013) "An Arbitrary Order Variationally Consistent Integration Method for Galerkin Meshfree Methods." *International Journal for Numerical Methods in Engineering*, 95, 387-418.

Chen, J.S. and Belytschko, T. (2015). "Meshless and Meshfree Methods." *Encyclopedia of Applied and Computational Mathematics*. Springer, Berlin, 886-894.

Chen, J.S., Hu, W., Puso, M.A., Wu, Y. and Zhang, X. (2007). "Strain Smoothing for Stabilization and Regularization of Galerkin Meshfree Methods." *In Meshfree Methods for Partial Differential Equations III (57-75)*. Springer, Berlin, Heidelberg

Chen, J.S., Liu, W.K., Hillman, M.C., Chi, S.W., Lian, Y. and Bessa, M.A. (2017a). Reproducing Kernel Particle Method for Solving Partial Differential Equations. *Encyclopedia of Computational Mechanics Second Edition*, 1-44.

Chen, J.S., Hillman, M. and Chi, S.W. (2017b). "Meshfree Methods: Progress Made After 20 Years." *Journal of Engineering Mechanics*. 143(4), 04017001.

Chowdhury, K., Seed, R. B., Dreger, D. S., Perlea, V., Beaty, M., Ma, F. and Wang, Z. L. (2018). "Re-Evaluation of the Lower San Fernando Dam: A Seismic Performance Case History Involving Liquefaction Flow Failure Conditions." *In Geotechnical Earthquake Engineering and Soil Dynamics V: Liquefaction Triggering, Consequences, and Mitigation*. Reston, VA: American Society of Civil Engineers, 502-517.

Chowdhury, K., Seed, R. B., Perlea, V., Beaty, M., Ma, F. and Hu, G. (2019). "Lessons Learned from Re-Evaluation of the Upper and Lower San Fernando Dams Using Current State of Practice in Numerical Modeling." *USSD Conference and Exhibition*, at Chicago, IL.

Conte, E., Silvestri, F. and Troncone, A. (2010). "Stability Analysis of Slopes in Soils with Strain-softening Behaviour." *Computers and Geotechnics*, 37(5), 710-722.

Crawford, C.B. (1968). "Quick clays of eastern Canada." *Engineering Geology*, 2(4), 239-265.

Cubrinovski, M., Bradley, B., Wotherspoon, L., Green, R., Bray, J., Wood, C., Pender, M., Allen, J., Bradshaw, A., Rix, G. and Taylor, M. (2011). "Geotechnical Aspects of the 22 February 2011 Christchurch Earthquake." *Bulletin of the New Zealand Society for Earthquake Engineering*, 44(4), 205-226.

Cubrinovski, M., Winkley, A., Haskell, J., Palermo, A., Wotherspoon, L., Robinson, K., Bradley, B., Brabhaharan, P. and Hughes, M. (2014). "Spreading-Induced Damage to Short-Span Bridges in Christchurch, New Zealand." *Earthquake Spectra*, 30(1), 57-83.

Dafalias, Y. Manzari, M. and Papadimitriou, A. (2006). "SANICLAY: Simple Anisotropic Clay Plasticity Model." *International Journal for Numerical and Analytical Methods in Geomechanics*, 30(12), 1231-1257.

Das, B.M. (2019). Advanced Soil Mechanics. CRC Press.

De Borst, R. and Pamin, J. (1996). "Gradient Plasticity in Numerical Simulation of Concrete Cracking." *European Journal of Mechanics Series A Solids*, 15, 295-320.

De Borst, R., Pamin, J., Peerlings, R.H.J. and Sluys, L.J. (1995). "On Gradient-enhanced Damage and Plasticity Models for Failure in Quasi-brittle and Frictional Materials." *Computational Mechanics*, 17(1-2), 130-141.

Demers, D., Robitaille, D., Locat, P. and Potvin, J. (2014). "Inventory of Large Landslides in Sensitive Clay in the Province of Quebec, Canada: Preliminary Analysis." *In Landslides in Sensitive Clays* (77-89). Springer, Dordrecht.

Dey, R., Hawlader, B., Phillips, R. and Soga, K. (2015). "Large Deformation Finite-element Modeling of Progressive Failure Leading to Spread in Sensitive Clay Slopes." *Géotechnique*, 65(8) 657-668.

Dey, R., Hawlader, B.C., Phillips, R. and Soga, K. (2016). "Numerical Modelling of Submarine Landslides with Sensitive Clay Layers." *Géotechnique*, 66(6), 454-468.

Dodd, L. and Restrepo-Posada, J. (1995). "Model for Predicting Cyclic Behavior of Reinforcing Steel." *Journal of Structural Engineering*, 121(3), 433-445.

Ebeido, A., Elgamal, A., Tokimatsu, K. and Abe, A. (2019). "Pile and Pile-Group Response to Liquefaction-Induced Lateral Spreading in Four Large-Scale Shake-Table Experiments." *Journal of Geotechnical and Geoenvironmental Engineering*, 145(10), 04019080.

Elgamal, A. (1991). "Shear Hysteretic Elasto-plastic Earthquake Response of Soil Systems." *Earthquake Engineering & Structural Dynamics*, 20(4), 371-387.

Elgamal, A., Yang, Z., Parra, E. and Ragheb, A. (2003). "Modeling of cyclic mobility in saturated cohesionless soils." *International Journal of Plasticity*, 19(6), 883-905.

Elgamal, A., Dobry, R. and Adalier, K. (1989). "Study of Effect of Clay Layers on Liquefaction of Sand Deposits Using Small-Scale Models." *In Proc., 2nd U.S.-Japan Workshop on Soil Liquefaction*, Buffalo, NY, NCEER Report No. 89-0032, O'Rourke, T.D. and Hamada, M., eds., 233-245, September.

Elgamal, A., Yan, L., Yang, Z. and Conte, J.P. (2008). "Three-dimensional Seismic Response of Humboldt Bay Bridge-foundation-ground System." *Journal of Structural Engineering*, 134(7), 1165-1176.

Elgamal, A. and Lu, J. (2009). "A Framework for 3D Finite Element Analysis of Lateral Pile System Response." *In Contemporary Topics in In Situ Testing, Analysis, and Reliability of Foundations*, ASCE GSP 186, 616-623.

Elgamal, A., Lu, J. and Forcellini, D. (2009). "Mitigation of Liquefaction-induced Lateral Deformation in a Sloping Stratum: Three-dimensional Numerical Simulation." *Journal of Geotechnical and Geoenvironmental Engineering*,135(11), 1672-1682.

Elgamal, A., Lu, J. and Mackie, K. (2014). "MSBridge: OpenSees Pushover and Earthquake Analysis of Multi-span Bridges-User Manual." Structural Systems Research Project SSRP-14/03, University of California at San Diego, La Jolla.

Elgamal, A., Lu, J., Almutairi, A. and Mackie, K (2017). "MSBridge: OpenSees Pushover and Earthquake Analysis of Multi-span Bridges-User Manual, Beta 1.0." University of California at San Diego, La Jolla.

Elgamal, A., Qiu, Z., Lu, J. and Almutairi, A. (2020). "Nonlinear Seismic Response of Ground-Structure Systems: Developments and Challenges." *In 16th International Conference of IACMAG International Association for Computer Methods and Advances in Geomechanics*, Torino, Italy. 3-4 May.

El Ghoraiby, M.A., Park, H. and Manzari, M.T. (2017). "LEAP 2017: Soil Characterization and Element Tests for Ottawa F65 Sand." Report by George Washington University, Washington, DC, 14th March.

El Ghoraiby, M., Park, H. and Manzari, M.T. (2020). "Physical and Mechanical Properties of Ottawa F65 Sand." *In Model Tests and Numerical Simulations of Liquefaction and Lateral Spreading* (45-67). Springer, Cham.

Fei, W. and Yang, Z.J. (2019). "Modeling Unconfined Compression Behavior of Frozen Fairbanks Silt Considering Effects of Temperature, Strain Rate and Dry Density." *Cold Regions Science and Technology*, 158, 252-263.

Fiegel, G.L. and Kutter, B.L. (1994). "Liquefaction Mechanism for Layered Soils." *Journal of Geotechnical Engineering*,120(4), 737-755.

Geertsema, M. and Torrance, J.K. (2005). "Quick Clay from the Mink Creek Landslide near Terrace, British Columbia: Geotechnical Properties, Mineralogy, and Geochemistry." *Canadian Geotechnical Journal*, 42(3), 907-918.

Ghofrani, A., McGann, C. R. and Arduino, P. (2016). "Influence of Modeling Decisions on Three-dimensional Finite Element Analysis of Two Existing Highway Bridges Subjected to Lateral Spreading." *Transportation Research Record*, 2592(1), 143-150.

Ghofrani, A. and Arduino, P. (2018). "Prediction of LEAP Centrifuge Test Results Using a Pressure-dependent Bounding Surface Constitutive Model." *Soil Dynamics and Earthquake Engineering*, 113, 758-770.

Gregersen, O. (1981). "The Quick Clay Landslide in Rissa, Norway." *NGI Publication*, 135, 1-6.

Gu, Q., Conte, J.P., Elgamal, A. and Yang, Z. (2009). "Finite Element Response Sensitivity Analysis of Multi-yield-surface J_2 Plasticity Model by Direct Differentiation Method." *Computer Methods in Applied Mechanics and Engineering*, 198(30-32), 2272-2285.

Gu, Q., Conte, J.P., Yang, Z. and Elgamal, A. (2011). "Consistent Tangent Moduli for Multi-yield-surface J_2 Plasticity Model." *Computational Mechanics*, 48(1), 97-120.

Gu, Q., Qiu, Z. and Huang, S. (2015). "A Modified Multi-yield-surface Plasticity Model: Sequential Closest Point Projection Method." *Computers and Geotechnics*, 69, 378-395.

Gylland, A.S. and Jostad, H.P. (2010). “Effect of Updated Geometry in Analyses of Progressive Failure.” *In Proceedings of the 7th European Conference on Numerical Methods in Geotechnical Engineering*, Trondheim, Norway (2-4).

Gylland, A.S., Jostad, H.P. and Nordal, S. (2014). “Experimental Study of Strain Localization in Sensitive Clays.” *Acta Geotechnica*, 9(2), 227-240.

Hamada, M., Isoyama, R. and Wakamatsu, K. (1996). “Liquefaction-induced Ground Displacement and Its Related Damage to Lifeline Facilities.” *Soils and Foundations*, 36(Special), 81-97.

Hamada, M. (2000). “Performance of Foundations Against Liquefaction-induced Permanent Ground Displacement.” *Proceedings of the 12th World Conference on Earthquake Engineering, Auckland, New Zealand*, Paper No. 1754.

Hashash, Y.M., Dashti, S., Romero, M.I., Ghayoomi, M. and Musgrove, M. (2015). “Evaluation of 1-D Seismic Site Response Modeling of Sand Using Centrifuge Experiments.” *Soil Dynamics and Earthquake Engineering*, 78, 19-31.

He, L., Ramirez, J., Lu, J., Tang, L., Elgamal, A. and Tokimatsu, K. (2017). “Lateral Spreading Near Deep Foundations and Influence of Soil Permeability.” *Canadian Geotechnical Journal*, 54(6), 846-861.

He, L., Elgamal, A., Abdoun, T., Abe, A., Dobry, R., Hamada, M., Meneses, J., Sato, M., Shantz, T. and Tokimatsu, K. (2009). “Liquefaction-Induced Lateral Load on Pile in a Medium D_r Sand Layer.” *Journal of Earthquake Engineering*, 13(7), 916-938.

Hillman, M. and Chen, J. S. (2016). “An Accelerated, Convergent and Stable Nodal Integration in Galerkin Meshfree Methods for Linear and Nonlinear Mechanics.” *International Journal for Numerical Methods in Engineering*, 107, 603-630.

Horpibulsuk, S., Miura, N. and Bergado, D.T. (2004). “Undrained Shear Behavior of Cement Admixed Clay at High Water Content.” *Journal of Geotechnical and Geoenvironmental Engineering*, 130(10), 1096-1105.

Horpibulsuk, S., Liu M.D, Liyanapathirana, D.S. and Suebsuk, J. (2010). “Behaviour of Cemented Clay Simulated Via the Theoretical Framework of the Structured Cam Clay Model.” *Computers and Geotechnics*, 37(1-2), 1-9.

Huang, T.H., Wei, H., Chen, J.S. and Hillman, M.C. (2019). “RKPM2D: An Open-source Implementation of Nodally Integrated Reproducing Kernel Particle Method for Solving Partial Differential Equations.” *Computational Particle Mechanics*, 1-41.

Idriss, I.M., Dobry, R. and Sing, R.D. (1978). “Nonlinear Behavior of Soft Clays During Cyclic Loading.” *Journal of Geotechnical and Geoenvironmental Engineering*, 104 (ASCE 14265).

Idriss, I.M. and Sun, J.I. (1993). “User’s manual for SHAKE91: A Computer Program for Conducting Equivalent Linear Seismic Response Analyses of Horizontally Layered Soil Deposits.” Center for Geotechnical Modeling, Dept. of Civil and Environmental Engineering, University of California Press, Davis, CA.

Idriss, I.M. and Boulanger, R.W. (2008). Soil Liquefaction During Earthquakes. Earthquake Engineering Research Institute.

Ilankatharan, M. and Kutter, B. (2008). “Numerical Simulation of a Soil Model-model Container-Centrifuge Shaking Table System.” *In Geotechnical Earthquake Engineering and Soil Dynamics IV,* 1-10.

Ilankatharan, M. and Kutter, B. (2010). “Modeling Input Motion Boundary Conditions for Simulations of Geotechnical Shaking Table Tests.” *Earthquake Spectra,* 26(2), 349-369.

Ishibashi, I., Kawamura, M. and Bhatia, S.K. (1985). “Effect of Initial Shearing on Cyclic Drained and Undrained Characteristics of Sand.” *Geotechnical Engineering Report*, 85-2.

Ishihara, K. (1996). Soil Behavior in Earthquake Geotechnics. Oxford: Clarendon Press.

Islam, N., Hawlader, B., Wang, C. and Soga, K. (2018). “Large-deformation Finite-element Modelling of Earthquake-induced Landslides Considering Strain-softening Behaviour of Sensitive Clay.” *Canadian Geotechnical Journal*, (999), 1-16.

Iwan, W.D. (1967). “On a Class of Models for the Yielding Behavior of Continuous and Composite Systems.” *Journal of Applied Mechanics,* ASME, 34, 612-617.

Jehel, P., Léger, P. and Ibrahimbegovic, A. (2014). “Initial Versus Tangent Stiffness-based Rayleigh Damping in Inelastic Time History Seismic Analyses.” *Earthquake Engineering & Structural Dynamics*, 43(3), 467-484.

Karimi, Z. and Dashti, S. (2015). “Numerical and Centrifuge Modeling of Seismic Soil-foundation–structure Interaction on Liquefiable Ground.” *Journal of Geotechnical and Geoenvironmental Engineering*, 142(1), 04015061.

Karimi, Z. and Dashti, S. (2016). “Seismic Performance of Shallow Founded Structures on Liquefiable Ground: Validation of Numerical Simulations Using Centrifuge Experiments.” *Journal of Geotechnical and Geoenvironmental Engineering*, 142(6), 04016011.

Kasama, K., Ochiai, H. and Yasufuku, N. (2000). “On the Stress-strain Behaviour of Lightly Cemented Clay Based on an Extended Critical State Concept.” *Soils and Foundations*, 40(5), 37-47.

Kavvadas, M. and Amorosi, A. (2000). “A Constitutive Model for Structured Soils.” *Geotechnique*, 50(3), 263-273.

Kaynia, A.M. (2012). “QUIVER-slope–numerical Code for One-dimensional Seismic Response of Slopes with Strain Softening Behaviour.” *NGI Rapport*, 20071851-00.

Kaynia, A.M. and Saygili, G. (2014). “Predictive Models for Earthquake Response of Clay and Sensitive Clay Slopes.” *In Perspectives on European Earthquake Engineering and Seismology*, (557-584). Springer, Cham.

Keefer, D.K. (1984). “Landslides Caused by Rarthquakes.” *Geological Society of America Bulletin*, 95(4), 406-421.

Kent, D.C. and Park. R. (1971) “Flexural Members with Confined Concrete.” *Journal of the Structural Division,* No ST7, Proc Paper 8243, 97(11), 1969-1990.

Kerr, P.F. and Drew, I.M. (1968). “Quick-clay Slides in the USA.” *Engineering Geology*, 2(4), 215-238.

Khosravifar, A., Elgamal, A., Lu, J. and Li, J. (2018). "A 3D Model for Earthquake-induced Liquefaction Triggering and Post-liquefaction Response." *Soil Dynamics and Earthquake Engineering*, 110: 43-52.

Kokusho, T. and Mimori, Y. (2015). "Liquefaction Potential Evaluations by Energy-based Method and Stress-based Method for Various Ground Motions." *Soil Dynamics and Earthquake Engineering*, 75, 130-146.

Kokusho, T. (2017). "Liquefaction Potential Evaluations by Energy-based Method and Stress-based Method for Various Ground Motions: Supplement." *Soil Dynamics and Earthquake Engineering*, 95, 40-47.

Kourkoulis, R., Anastasopoulos, I., Gelagoti, F. and Gazetas, G. (2010). "Interaction of Foundation−Structure Systems with Seismically Precarious Slopes: Numerical Analysis with Strain Softening Constitutive Model." *Soil Dynamics and Earthquake Engineering*, 30(12),1430-1445.

Kovacevic, N., Hight, D.W. and Potts, D.M. (2007). "Predicting the Stand-up Time of Temporary London Clay Slopes at Terminal 5, Heathrow Airport." *Géotechnique*, 57(1), 63-74.

Kramer, S.L. (1996). Geotechnical Earthquake Engineering, Prentice Hall, Upper Saddle River, N.J.

Kutter, B.L., Manzari, M.T., Zeghal, M., Zhou, Y.G. and Armstrong, R.J. (2014). "Proposed Outline for LEAP Verification and Validation Processes." *Safety and Reliability: Methodology and Applications*, 99.

Kutter, B.L., Carey, T.J., Hashimoto, T., Manzari, M.T., Vasko, A., Zeghal, M. and Armstrong, R.J. (2015). "LEAP Databases for Verification, Validation, and Calibration of Codes for Simulation of Liquefaction." *In Sixth International Conference on Earthquake Geotechnical Engineering*, Christchurch, New Zealand.

Kutter, B.L., Carey, T.J., Hashimoto, T., Zeghal, M., Abdoun, T., Kokkali, P., Madabhushi, G., Haigh, S.K., d'Arezzo, F.B., Madabhushi, S. and Hung, W.Y. (2018a). "LEAP-GWU-2015 Experiment Specifications, Results, and Comparisons." *Soil Dynamics and Earthquake Engineering*, 113, 616-628.

Kutter, B.L., Zeghal, M. and Manzari, M.T. (2018b) "LEAP-UCD-2017 Experiments (Liquefaction Experiments and Analysis Projects)", DesignSafe-CI [publisher], Dataset, doi:10.17603/DS2N10S.

Kutter, B.L., Manzari, M.T. and Zeghal, M. (2020a) "Model Tests and Numerical Simulations of Liquefaction and Lateral Spreading." *LEAP-UCD-2017 Proceedings*, Springer.

Kutter, B.L., Manzari, M.T., Zeghal, M., Arduino, P., Barrero, A.R., Carey, T.J., Chen, L., Elgamal, A., Ghofrani, A., Montgomery, J. and Ozutsumi, O., Qiu, Z., Taiebat, M., Tobita, T., Travasarou, T., Tsiaousi, D., Ueda, K., Ugalde, J., Yang, M., Zheng, B. and Ziotopoulou, K. (2020b). "Chapter 11 Numerical Sensitivity Study Compared to Trend of Experiments for LEAP-UCD-2017." *In B. Kutter et al. (Eds.), Model Tests and Numerical Simulations of Liquefaction and Lateral Spreading: LEAP-UCD-2017*. New York: Springer.

Kutter, B.L., Carey, T.J., Stone, N., Zheng, B., Gavras, A., Manzari, M., Zeghal, M., Abdoun, T., Korre, E., Escoffier, S., Haigh, S., Madabhushi, G., Madabhushi, S.S. C., Hung, W.Y., Liao,

T.W., Kim, D.S., Kim, S.N., Ha, J. G., Kim, N.R., Okamura, M., Sjafuddin, A. N., Tobita, T., Ueda, K., Vargas, R., Zhou, Y. and Liu, K. (2020c). "LEAP-UCD-2017 comparison of centrifuge test results." *In B. Kutter et al. (Eds.), Model Tests and Numerical Simulations of Liquefaction and Lateral Spreading: LEAP-UCD-2017*. New York: Springer.

Kutter, B.L., Carey, T.J., Stone, N., Bonab, M.H., Manzari, M., Zeghal, M., Escoffier, S., Haigh, S., Madabhushi, G., Hung, W. Y., Kim, D.S., Kim N. R., Okamura, M., Tobita, T., Ueda, K. and Zhou, Y. (2020d). "LEAP-UCD-2017 V. 1.01 Model Specifications." *In B. Kutter et al. (Eds.), Model Tests and Numerical Simulations of Liquefaction and Lateral Spreading: LEAP-UCD-2017*. New York: Springer.

Kvalstad, T.J., Nadim, F., Kaynia, A.M., Mokkelbost, K.H. and Bryn, P. (2005). "Soil Conditions and Slope Stability in the Ormen Lange Area." *Marine and Petroleum Geology*, 22(1-2), 299-310.

Kwon, O.S., Sextos, A. and Elnashai, A. (2009). "Seismic Fragility of a Bridge on Liquefaction Susceptible Soil." *In 10th international conference on seismic safety and reliability*,13-17.

Kwon, O.S. and Elnashai, A.S. (2008). "Seismic Analysis of Meloland Road Overcrossing Using Multiplatform Simulation Software Including SSI." *Journal of Structural Engineering*, 134(4), 651-660.

Lacy, S. (1986). Numerical Procedures for Nonlinear Transient Analysis of Two-phase Soil System. Ph.D. dissertation, Princeton University, New Jersey.

Lade, P.V. and Duncan, J.M. (1975). "Elastoplastic Stress-strain Theory for Cohesionless Soil." *Journal of Geotechnical and Geoenvironmental Engineering*, 101(ASCE# 11670 Proceeding).

Lai, Y., Jin, L. and Chang, X. (2009). "Yield Criterion and Elasto-plastic Damage Constitutive Model for Frozen Sandy Soil." *International Journal of Plasticity*, 25(6), 1177-1205.

Lasry, D. and Belytschko, T. (1988). "Localization Limiters in Transient Problems." *International Journal of Solids and Structures*, 24(6), 581-597.

Law, H.K. and Lam, I.P. (2001). "Application of Periodic Boundary for Large Pile Group." *Journal of Geotechnical and Geoenvironmental Engineering*, 127(10), 889-892.

Lee, K.L. and Seed, H.B. (1967). "Drained Strength Characteristics of Sands." *Journal of Soil Mechanics & Foundations Div*.

Lee, K., Chan, D. and Lam, K. (2004). "Constitutive Model for Cement Treated Clay in a Critical State Framework." *Soils and Foundations*, 44(3), 69-77.

Ledezma, C. and Bray, J. (2010). "Probabilistic Serformance-based Procedure to Evaluate Pile Foundations at Sites with Liquefaction-induced Lateral Displacement." *Journal of Geotechnical and Geoenvironmental Engineering*, 136(3), 464-476.

Ledezma, C., Hutchinson, T., Ashford, S.A., Moss, R., Arduino, P., Bray, J., Olson, S., Hashash, Y.M., Verdugo, R., Frost, D. and Kayen, R. (2012). "Effects of Ground Failure on Bridges, Roads, and Railroads." *Earthquake Spectra*, 28(S1), S119-S143.

Lefebvre, G., Leboeuf, D., Hornych, P. and Tanguay, L. (1992). "Slope Failures Associated with the 1988 Saguenay Earthquake, Quebec, Canada." *Canadian Geotechnical Journal*, 29(1): 117-130.

L'Heureux, J.S. (2012). "A Study of the Retrogressive Behaviour and Mobility of Norwegian Quick Clay Landslides." *Landslide and Engineered Slopes: Protecting Society through Improved Understanding*. Taylor & Francis Group, London, 981-988.

Liu, M.D. and Carter, J.P. (2002). "A Structured Cam Clay Model." *Canadian Geotechnical Journal*, 39(6), 1313-1332.

Liu, H. and Qiao, T. (1984). "Liquefaction Potential of Saturated Sand Deposits Underlying Foundation of Structure", *Proceedings, 8th World Conference on Earthquake Engineering*, San Francisco, California, 199-206.

Locat, A., Jostad, H.P. and Leroueil, S. (2013). "Numerical Modeling of Progressive Failure and Its Implications for Spreads in Sensitive Clays." *Canadian Geotechnical Journal*, 50(9), 961-978.

Locat, A., Locat, P., Demers, D., Leroueil, S., Robitaille, D. and Lefebvre, G. (2017). "The Saint-Jude Landslide of 10 May 2010, Quebec, Canada: Investigation and Characterization of the Landslide and Its Failure Mechanism." *Canadian Geotechnical Journal*, 54(10), 1357-1374.

Løkke A and Chopra AK. (2017). "Direct Finite Element Method for Nonlinear Analysis of Semi-unbounded Dam–water–foundation Rock Systems." *Earthquake Engineering & Structural Dynamics*, 46(8): 1267-1285.

Løkke, A. and Chopra, A.K. (2018). "Direct Finite Element Method for Nonlinear Earthquake Analysis of 3-dimensional Semi-unbounded Dam–water–foundation Rock Systems." *Earthquake Engineering & Structural Dynamics*, 47(5):1309-1328.

Longva, O., Janbu, N., Blikra, L. H. and Bøe, R. (2003). "The 1996 Finneidfjord Slide; Seafloor Failure and Slide Dynamics." *In Submarine Mass Movements and Their Consequences*, 531-538, Springer, Dordrecht.

Loria, A.R., Frigo, B. and Chiaia, B. (2017). "A Non-linear Constitutive Model for Describing the Mechanical Behaviour of Frozen Ground and Permafrost." *Cold Regions Science and Technology*, 133, 63-69.

Lu, J. (2006). Parallel Finite Element Modeling of Earthquake Site Response and Liquefaction. Ph.D. thesis, Department of Structural Engineering, Univ. of California, San Diego.

Lu, J., Elgamal, A., Yan, L., Law, K.H. and Conte, J.P. (2011). "Large-scale Numerical Modeling in Geotechnical Earthquake Engineering." *International Journal of Geomechanics*, 11(6), 490-503.

Lu, J., Kamatchi, P. and Elgamal, A. (2019). "Using Stone Columns to Mitigate Lateral Deformation in Uniform and Stratified Liquefiable Soil Strata." *International Journal of Geomechanics*, 19(5), 04019026.

Lysmer, J. and Kuhlemeyer, R.L. (1969). "Finite Dynamic Model for Infinite Media." *Journal of Engineering Mechanics Division*, 95, 859-878.

Mackie, K.R., Lu, J. and Elgamal, A. (2012). "Performance-based Earthquake Assessment of Bridge Systems Including Ground-foundation Interaction." *Soil Dynamics and Earthquake Engineering*, 42, 184-196.

Mander J.B., Priestley M.J. and Park R. (1988). "Theoretical Stress-strain Model for Confined Concrete." *Journal of Structural Engineering*, 114(8), 1804-1826.

Manzari, M.T., Kutter, B.L., Zeghal, M., Iai, S., Tobita, T., Madabhushi, S.P.G., Haigh, S.K., Mejia, L., Gutierrez, D.A., Armstrong, R.J. and Sharp, M.K. (2014). "LEAP Projects: Concept and Challenges." *In Proceedings, 4th International Conference on Geotechnical Engineering for Disaster Mitigation and Rehabilitation*, 109-116.

Manzari, M.T., El Ghoraiby, M., Kutter, B.L., Zeghal, M., Abdoun, T., Arduino, P., Armstrong, R.J., Beaty, M., Carey, T., Chen, Y. and Ghofrani, A. (2018). "Liquefaction Experiment and Analysis Projects (LEAP): Summary of Observations from the Planning Phase." *Soil Dynamics and Earthquake Engineering*, 113, 714-743.

Manzari, M.T., El Ghoraiby, M., Zeghal, M., Kutter, B.L., Arduino, P., Barrero, A.R., Bilotta, E., Chen, L., Chen, R., Chiaradonna, A., Elgamal, A., Fasano, G., Fukutake, K., Fuentes, W., Ghofrani, A., Haigh, S., Hung, W.-Y., Ichii, K., Kim, D. S., Kiriyama, T., Lascarro, C.,Madabhushi, M. S. P., Mercado, V., Montgomery, J., Okamura, M., Ozutsumi, O., Qiu, Z., Taiebat, M., Tobita, T., Travasarou, T., Tsiaousi, D., Ueda, K., Ugalde, J., Wada, T., Wang, R., Yang, M., Zhang, J., Zhou, Y. and Ziotopoulou, K. (2020a). "LEAP-2017: Chapter 10 Comparison of the Type-B Numerical Simulations with Centrifuge Test Results." *In B. Kutter et al. (Eds.), Model Tests and Numerical Simulations of Liquefaction and Lateral Spreading: LEAP-UCD-2017*. New York: Springer.

Manzari, M.T., El Ghoraiby, M., Zeghal, M., Kutter, B.L., Arduino, P., Barrero, A.R., Bilotta, E., Chen, L., Chen, R., Chiaradonna, A., Elgamal, A., Fasano, G., Fukutake, K., Fuentes, W., Ghofrani, A., Haigh, S., Hung, W.-Y., Ichii, K., Kim, D. S., Kiriyama, T., Lascarro, C.,Madabhushi, M. S. P., Mercado, V., Montgomery, J., Okamura, M., Ozutsumi, O., Qiu, Z., Taiebat, M., Tobita, T., Travasarou, T., Tsiaousi, D., Ueda, K., Ugalde, J., Wada, T., Wang, R., Yang, M., Zhang, J, Zhou, Y. and Ziotopoulou, K. (2020b). "LEAP-2017: Chapter 9 Simulation Exercise: Calibration of Constitutive Models and Simulation of the Element Tests." *In B. Kutter et al. (Eds.), Model Tests and Numerical Simulations of Liquefaction and Lateral Spreading: LEAP-UCD-2017*. New York: Springer.

Masing, G. (1926). "Eigenspannumyen und verfeshungung beim messing." *In Proc. Inter. Congress for Applied Mechanics*, 332-335.

Matasović, N. and Vucetic, M. (1995). "Generalized Cyclic-degradation-pore-pressure Generation Model for Clays." *Journal of Geotechnical Engineering*, 121(1), 33-42.

Mazzoni, S., McKenna, F., Scott, M. H. and Fenves, G. L. (2009). "Open System for Earthquake Engineering Simulation, User Command-Language Manual." Pacific Earthquake Engineering Research Center, University of California, Berkeley, OpenSees version 2.0, May.

McGann, C.R. and Arduino, P. (2014). "Numerical Assessment of Three-dimensional Foundation Pinning Effects During Lateral Spreading at the Mataquito River Bridge." *Journal of Geotechnical and Geoenvironmental Engineering*, 140(8), 04014037.

McGann, C.R. and Arduino, P. (2015). "Numerical Assessment of the Influence of Foundation Pinning, Deck Resistance, and 3D Site Geometry on the Response of Bridge Foundations to Demands of Liquefaction-induced Lateral Soil Deformation." *Soil Dynamics and Earthquake Engineering*, 79, 379-390.

McKenna, F. (2011). "OpenSees: A Framework for Earthquake Engineering Simulation." *Computing in Science & Engineering*, 13(4), 58-66.

Mohammadi, S. and Taiebat, H.A. (2013). "A Large Deformation Analysis for the Assessment of Failure Induced Deformations of Slopes in Strain Softening Materials." *Computers and Geotechnics*, 49, 279-288.

Motamed, R., Towhata, I., Honda, T., Tabata, K. and Abe, A. (2013). "Pile Group Response to Liquefaction-induced Lateral Spreading: E-Defense Large Shake Table Test," *Soil Dynamics and Earthquake Engineering*, 51, 35-46.

Mroz, Z. (1967). "On the Description of Anisotropic Work Hardening." *Journal of the Mechanics and Physics of Solids*, 15(3), 163-175.

National Research Council (NRC). (1985). Liquefaction of Soils During Earthquakes, National Academy Press, Washington, D.C.

National Academies of Sciences, Engineering, and Medicine (2016). State of the Art and Practice inthe Assessment of Earthquake-Induced Soil Liquefaction and Its Consequences. Washington, DC:The National Academies Press.

Newmark, N.M. (1965). "Effects of Earthquakes on Dams and Embankments." *Geotechnique*, 15(2), 139-160.

Nguyen, L. and Fatahi, B. (2016). "Behaviour of Clay Treated with Cement & Fibre While Capturing Cementation Degradation and Fibre Failure-C3F Model." *International Journal of Plasticity*, 81, 168-195.

Nielsen, A.H. (2014). "Towards a Complete Framework for Seismic Analysis in Abaqus." *Proceedings of the ICE-Engineering and Computational Mechanics*, 167(1), 3-12.

Padgett, J.E., Ghosh, J. and Dueñas-Osorio, L. (2013). "Effects of Liquefiable Soil and Bridge Modelling Parameters on the Seismic Reliability of Critical Structural Components." *Structure and Infrastructure Engineering*, 9(1), 59-77.

Park, R. (1988). "Ductility Evaluation from Laboratory and Analytical Testing." *In Proceedings of the 9th world conference on earthquake engineering*, Tokyo-Kyoto, Japan, 8, 605-616.

Park, D.S. and Kutter, B.L. (2015). "Static and Seismic Stability of Sensitive Clay Slopes." *Soil Dynamics and Earthquake Engineering*, 79, 118-129.

Park, D.S. and Kutter, B.L. (2016). "Sensitive Bounding Surface Constitutive Model for Structured Clay." *International Journal for Numerical and Analytical Methods in Geomechanics*, 40(14), 1968-1987.

Parra, E. (1996). Numerical Modeling of Liquefaction and Lateral Ground Deformation Including Cyclic Mobility and Dilation Response in Soil Systems. PhD Thesis. Rensselaer Polytechnic Institute.

Perret, D., Mompin, R., Demers, D., Lefebvre, G. and Pugin, A.J.M. (2013). "Two Large Sensitive Clay Landslides Triggered by the 2010 Val-Des-Bois Earthquake, Quebec (Canada) Implications for Risk Management." *In Proceedings of the 1st International Workshop on Landslides in Sensitive Clays (IWLSC)*, Quebec City, Quebec.

Petrini, L., Maggi, C., Priestley, M.N. and Calvi, G.M. (2008). "Experimental Verification of Viscous Damping Modeling for Inelastic Time History Analyzes." *Journal of Earthquake Engineering*, 12(S1), 125-145.

Prevost, J.H. and Hoeg, K. (1975). "Soil Mechanics and Plasticity Analysis of Strain Softening." *Geotechnique*, 25(2), 279-297.

Prevost, J.H. (1977). "Mathematical Modelling of Monotonic and Cyclic Undrained Clay Behaviour." *International Journal for Numerical and Analytical Methods in Geomechanics*, 1(2), 195-216.

Prevost, J.H. (1978). "Plasticity Theory for Soil Stress-strain Behavior." *Journal of the Engineering Mechanics Division*, 104(5): 1177-1194.

Prevost, J.H. (1985). "A Simple Plasticity Theory for Frictional Cohesionless Soils." *Soil Dynamics and Earthquake Engineering*, 4(1): 9-17.

Priestley, M.J.N. and Grant, D.N. (2005). "Viscous Damping in Seismic Design and Analysis." *Journal of Earthquake Engineering*, 9(spec02), 229-255.

Qiu, Z., Lu, J., Elgamal, A., Su, L., Wang, N. and Almutairi, A. (2019). "OpenSees Three-Dimensional Computational Modeling of Ground-Structure Systems and Liquefaction Scenarios." *Computer Modeling in Engineering & Sciences*, 120(3), 629-656.

Qiu, Z. and Elgamal, A. (2020a). "Three-Dimensional Modeling of Strain-Softening Soil Response for Seismic-Loading Applications." *Journal of Geotechnical and Geoenvironmental Engineering*, 146(7), 04020053.

Qiu, Z., Ebeido, A., Almutairi, A., Lu, J., Elgamal, A., Shing, P.B. and Martin, G. (2020). "Aspects of bridge-ground seismic response and liquefaction-induced deformations." *Earthquake Engineering & Structural Dynamics*, 49(4), 375-393.

Qiu, Z. and Elgamal, A. (2020b). "Numerical Simulations of LEAP Dynamic Centrifuge Model Tests for Response of Liquefiable Sloping Ground." *In Model Tests and Numerical Simulations of Liquefaction and Lateral Spreading*, 521-544. Springer, Cham.

Qiu, Z. and Elgamal, A. (2020c). "Numerical Simulations of LEAP Centrifuge Tests for Seismic Response of Liquefiable Sloping Ground." *Soil Dynamics and Earthquake Engineering*, 139, 106378.

Quinn, P.E., Diederichs, M.S., Rowe, R.K. and Hutchinson, D.J. (2011). "A New Model for Large Landslides in Sensitive Clay Using a Fracture Mechanics Approach." *Canadian Geotechnical Journal*, 48(8), 1151-1162.

Quinn, P.E., Diederichs, M.S., Rowe, R.K. and Hutchinson, D.J. (2012). "Development of Progressive Failure in Sensitive Clay Slopes." *Canadian Geotechnical Journal*, 49(7), 782-795.

Rayamajhi, D., Nguyen, T.V., Ashford, S.A., Boulanger, R.W., Lu, J., Elgamal, A. and Shao, L. (2013). "Numerical Study of Shear Stress Distribution for Discrete Columns in Liquefiable Soils." *Journal of Geotechnical and Geoenvironmental Engineering*, 140(3), 04013034.

Rayamajhi, D., Ashford, S.A., Boulanger, R.W. and Elgamal, A. (2016a). "Dense Granular Columns in Liquefiable Ground. I: Shear Reinforcement and Cyclic Stress Ratio Reduction." *Journal of Geotechnical and Geoenvironmental Engineering*, 142(7), 04016023.

Rayamajhi, D., Boulanger, R.W., Ashford, S.A. and Elgamal, A. (2016b). "Dense Granular Columns in Liquefiable Ground. II: Effects on Deformations." *Journal of Geotechnical and Geoenvironmental Engineering,* 142(7), 04016024.

Rodrıguez, C.E., Bommer, J.J. and Chandler, R.J. (1999). "Earthquake-induced Landslides: 1980–1997." *Soil Dynamics and Earthquake Engineering,* 18(5), 325-346.

Scott, M. and Fenves, G. (2006). "Plastic Hinge Integration Methods for Force-based Beam-column Elements." *Journal of Structural Engineering,* 132(2), 244-252.

Scott, M. and Ryan, L. (2013). "Moment-rotation Behavior of Force-based Plastic Hinge Elements." *Earthquake Spectra,* 29(2), 597-607.

Seed, H.B. and Wilson, S.D. (1967). "The Turnagain Heights Landslide in Anchorage, Alaska. Dept. of Civil Engineering, Institute of Transportation and Traffic Engineering." University of California, Berkeley.

Seed, H.B. (1970). "Soil Moduli and Damping Factors for Dynamic Response Analysis." EERC.

Seed, H.B., Wong, R.T., Idriss, I.M. and Tokimatsu, K. (1986). "Moduli and Damping Factors for Dynamic Analyses of Cohesionless Soils." *Journal of Geotechnical Engineering,* 112(11), 1016-1032.

Seed, H.B., Lee, K.L., Idriss, I.M. and Makdisi, F. (1973). Analysis of the Slides in the San Fernando Dams During the Earthquake of Feb. 9, 1971. College of Engineering, University of California.

Seed, H.B., Lee, K.L., Idriss, I.M. and Makdisi, F.I. (1975). "The Slides in the San Fernando Dams during the Earthquake of February 9, 1971." ASCE, *Journal of the Geotechnical Engineering Division,* GT7, 651-688

Sharma, S.S. and Fahey, M. (2003a). "Degradation of Stiffness of Cemented Calcareous Soil in Cyclic Triaxial Tests." *Journal of Geotechnical and Geoenvironmental engineering,* 129(7), 619-629.

Sharma, S.S. and Fahey, M. (2003b). "Evaluation of Cyclic Shear Strength of Two Cemented Calcareous Soils." *Journal of Geotechnical and Geoenvironmental Engineering,* 129(7), 608-618.

Sharma, S.S. and Fahey, M. (2004). "Deformation Characteristics of Two Cemented Calcareous Soils." *Canadian geotechnical journal,* 41(6), 1139-1151.

Shelman, A., Tantalla, J., Sritharan, S., Nikolaou, S. and Lacy, H. (2014). "Characterization of Seasonally Frozen Soils for Seismic Design of Foundations." *Journal of Geotechnical and Geoenvironmental Engineering,* 140(7), 04014031.

Shin, H., Arduino, P. and Kramer, S.L. (2007). "Performance-based Evaluation of Bridges on Liquefiable Soils." *In Structural Engineering Research Frontiers,* 1-16.

Shin, H., Arduino, P., Kramer, S.L. and Mackie, K. (2008). "Seismic Response of a Typical Highway Bridge in Liquefiable Soil." *In Geotechnical Earthquake Engineering and Soil Dynamics IV,* 1-11.

Solberg, I.L., Long, M., Baranwal, V.C., Gylland, A.S. and Rønning, J.S. (2016). "Geophysical and Geotechnical Studies of Geology and Sediment Properties at a Quick-clay Landslide Site at Esp, Trondheim, Norway." *Engineering Geology*, 208, 214-230.

Soltanieh, S., Memarpour, M. M. and Kilanehei, F. (2019). "Performance Assessment of Bridge-soil-foundation System with Irregular Configuration Considering Ground Motion Directionality Effects." *Soil Dynamics and Earthquake Engineering*, 118, 19-34.

Stark, T.D. and Contreras, I.A. (1998). "Fourth Avenue Landslide During 1964 Alaskan Earthquake." *Journal of Geotechnical and Geoenvironmental engineering*, 124(2), 99-109.

Su, L., Lu, J., Elgamal, A. and Arulmoli, A.K. (2017). "Seismic Performance of a Pile-supported Wharf: Three-dimensional Finite Element Simulation." *Soil Dynamics and Earthquake Engineering*, 95, 167-179.

Su, L., Wan, H.P., Li, Y. and Ling, X.Z. (2018). "Soil-Pile-Quay Wall System with Liquefaction-Induced Lateral Spreading: Experimental Investigation, Numerical Simulation, and Global Sensitivity Analysis." *Journal of Geotechnical and Geoenvironmental Engineering*, 144(11), 04018087.

Suebsuk, J., Horpibulsuk, S. and Liu, M.D. (2011). "A Critical State Model for Overconsolidated Structured Clays." *Computers and Geotechnics*, 38(5), 648-658.

Sun, J.I., Golesorkhi, R. and Seed, H.B. (1988). "Dynamic Moduli and Damping Ratios for Cohesive Soils." Berkeley: Earthquake Engineering Research Center, University of California.

Taiebat, M., Kaynia, A.M. and Dafalias, Y.F. (2010). "Application of an Anisotropic Constitutive Model for Structured Clay to Seismic Slope Stability." *Journal of Geotechnical and Geoenvironmental Engineering*, 137(5), 492-504.

Tang, L., Cong, S., Ling, X., Lu, J. and Elgamal, A. (2015). "Numerical Study on Ground Improvement for Liquefaction Mitigation Using Stone Columns Encased with Geosynthetics." *Geotextiles and Geomembranes*, 43(2), 190-195.

Terzaghi, K., Peck, R.B. and Mesri, G. (1996). Soil Mechanics in Engineering Practice. John Wiley & Sons.

Todorovska, M.I. and Trifunac, M.D. (1991). "Amplitudes, Polarity and Time of Peaks of Strong Ground Motion During the 1994 Northridge, California, Earthquake." *Soil Dynamics and Earthquake Engineering*, 16(4),235-258.

Tokimatsu, K. and Asaka, Y. (1998). "Effects of Liquefaction-induced Ground Displacements on Pile Performance in the 1995 Hyogoken-Nambu Earthquake." *Soils and Foundations*, 38(Special), 163-177.

Tokimatsu, K. and Suzuki, H. (2004). "Pore Water Pressure Response Around Pile and Its Effects on *p-y* Behavior During Soil Liquefaction," *Soils and Foundations*, 44(6), 101-110.

Tokida, K., Iwasaki, H., Matsumoto, H. and Hamada, T. (1970). "Liquefaction Potential and Drag Force Acting on Piles in Flowing Soils. *WIT Transactions on The Built Environment*, 3.

Torabi, H. and Rayhani, M.T. (2014). "Three-dimensional Finite Element Modeling of Seismic Soil–structure Interaction in Soft Soil." *Computers and Geotechnics*, 60, 9-19.

Troncone, A. (2005). “Numerical Analysis of a Landslide in Soils with Strain-softening Behaviour.” *Geotechnique*, 55(8), 585-596.

Troncone, A., Conte, E. and Donato, A. (2014). “Two and Three-dimensional Numerical Analysis of the Progressive Failure that Occurred in an Excavation-induced Landslide.” *Engineering Geology*, 183, 265-275.

Tsai, C.C., Mejia, L.H. and Meymand, P. (2014). “A Strain-based Procedure to Estimate Strength Softening in Saturated Clays During Earthquakes.” *Soil Dynamics and Earthquake Engineering*, 66, 191-198.

Turner, B., Brandenberg, S.J. and Stewart, J.P. (2013). “Evaluation of Collapse and Non-collapse of Parallel Bridges Affected by Liquefaction and Lateral Spreading.” *In 10th International Conference on Urban Earthquake Engineering*, March 1-2, 2013, Tokyo Institute of Technology, Tokyo, Japan

Turner, B.J., Brandenberg, S.J. and Stewart, J.P. (2016). “Case Study of Parallel Bridges Affected by Liquefaction and Lateral Spreading.” *Journal of Geotechnical and Geoenvironmental Engineering*, 142(7), 05016001.

Ueda, K. and Iai, S. (2018). “Numerical Predictions for Centrifuge Model Tests of a Liquefiable Sloping Ground Using a Strain Space Multiple Mechanism Model Based on the Finite Strain Theory.” *Soil Dynamics and Earthquake Engineering*, 113, 771-792.

Ueda, K. (2018). LEAP-Asia-2018: Stress-strain Response of Ottawa Sand in Cyclic Torsional Shear Tests, DesignSafe-CI [publisher], Dataset, doi:10.17603/DS2D40H.

Ueda, K., Uratani, K. and Iai, S. (2019). “Influence of Inherent Anisotropy on the Seismic Behavior of Liquefiable Sandy Level Ground.” *Soils and Foundations*, 59(2), 458-473.

Vasko, A. (2015). An Investigation into the Behavior of Ottawa Sand through Monotonic and Cyclic Shear Tests. The George Washington University.

Vasko A., El Ghoraiby, M.A. and Manzari, M.T. (2018). Charaterization of Ottwa Sand. DesignSafe, https://doi.org/10.17603/DS2TH7Q.

Verdugo, R., Sitar, N., Frost, J.D., Bray, J., Candia, G., Eldridge, T., Hashash, Y., Olson, S.M. and Urzua, A. (2012) “Seismic Performance of Earth Structures During the February 2010 Maule, Chile, Earthquake: Dams, Levees, Tailings Dams, and Retaining Walls.” *Earthquake Spectra*, 28(S1), S75-S96.

Vucetic, M. and Dobry, R. (1988). “Degradation of Marine Clays under Cyclic Loading.” *Journal of Geotechnical Engineering*, 114(2), 133-149.

Vucetic, M. (1988). “Normalized Behavior of Offshore Clay under Uniform Cyclic Loading.” *Canadian Geotechnical Journal*, 25(1), 33-41.

Wang, Z., Dueñas-Osorio, L. and Padgett, J.E. (2013a). “Seismic Response of a Bridge–soil–foundation System under the Combined Effect of Vertical and Horizontal Ground Motions.” *Earthquake Engineering and Structural Dynamics*, 42(4), 545-564.

Wang, Z., Padgett, J.E. and Dueñas-Osorio, L. (2013b). “Influence of Vertical Ground Motions on the Seismic Fragility Modeling of a Bridge-soil-foundation System.” *Earthquake Spectra*, 29(3), 937-962.

Wang, C., Hawlader, B. and Perret, D. (2016). “Finite Element Simulation of the 2010 Saint-Jude Landslide in Quebec.” *In Proceedings of the 69th Canadian Geotechnical Conference*, Quebec City, Quebec, Canada.

Wang, C., Hawlader, B., Islam, N. and Soga, K. (2019). “Implementation of a Large Deformation Finite Element Modelling Technique for Seismic Slope Stability Analyses.” *Soil Dynamics and Earthquake Engineering*, 127, 105824.

Whittle, A.J. and Kavvadas, M.J. (1994). “Formulation of MIT-E3 Constitutive Model for Overconsolidated Clays.” *Journal of Geotechnical Engineering*, 120(1), 173-198.

Wilson, P. and Elgamal, A. (2015). “Shake Table Lateral Earth Pressure Testing with Dense *c-ϕ* Backfill.” *Soil Dynamics and Earthquake Engineering*, 71, 13-26.

Wotherspoon, L., Bradshaw, A., Green, R., Wood, C., Palermo, A., Cubrinovski, M. and Bradley, B. (2011). “Performance of Bridges During the 2010 Darfield and 2011 Christchurch earthquakes.” *Seismological Research Letters*, 82(6), 950-964.

Yang, Z., Elgamal, A. and Parra, E. (2003). “Computational Model for Cyclic Mobility and Associated Shear Deformation.” *Journal of Geotechnical and Geoenvironmental Engineering*, 129(12), 1119-1127.

Yang, Z. (2000). Numerical Modeling of Earthquake Site Response Including Dilation and Liquefaction. PhD Thesis, Columbia University.

Yang Z. and Elgamal A. (2002). “Influence of Permeability on Liquefaction-induced Shear Deformation.” *Journal of Engineering Mechanics*, 128(7), 720-729.

Yang, Z.J., Still, B. and Ge, X. (2015). “Mechanical Properties of Seasonally Frozen and Permafrost Soils at High Strain Rate.” *Cold regions science and technology*, 113, 12-19.

Yang, Z. and Elgamal, A. (2008). “Multi-surface Cyclic Plasticity Sand Model with Lode Angle Effect.” *Geotechnical and Geological Engineering*, 26(3), 335-348.

Yang, Z., Lu, J. and Elgamal, A. (2008). “OpenSees Soil Models and Solid-fluid Fully Coupled Elements: User's Manual.” Department of Structural Engineering, University of California, San Diego

Yao, Y., Gao, Z., Zhao, J. and Wan, Z. (2012). “Modified UH Model: Constitutive Modeling of Overconsolidated Clays Based on a Parabolic Hvorslev Envelope.” *Journal of Geotechnical and Geoenvironmental Engineering*, 138(7), 860-868.

Youd, T.L. (1993). “Liquefaction-induced Damage to Bridges.” *Transportation Research Record*, 1411, 35-41.

Yoshimine, M., Ishihara, K. and Vargas, W. (1998). “Effects of Principal Stress Direction and Intermediate Principal Stress on Undrained Shear Behavior of Sand.” *Soils and Foundations*, 38(3), 179-188.

Zeghal, M. (2019). LEAP-RPI 2020, Version 0.91 Model Specifications.

Zeghal, M., Goswami, N., Kutter, B.L., Manzari, M.T., Abdoun, T., Arduino, P., Armstrong, R., Beaty, M., Chen, Y.M., Ghofrani, A. and Haigh, S. (2018). “Stress-strain Response of the LEAP-2015 Centrifuge Tests and Numerical Predictions.” *Soil Dynamics and Earthquake Engineering*, 113, 804-818.

Zergoun, M. and Vaid, Y.P. (1994). “Effective Stress Response of Clay to Undrained Cyclic Loading.” *Canadian Geotechnical Journal*, 31(5), 714-727.

Zhang, Y., Yang, Z., Liu, J. and Fang, J. (2017). “Impact of Cooling on Shear Strength of High Salinity Soils.” *Cold Regions Science and Technology*, 141, 122-130.

Zhang, Y., Conte, J.P., Yang, Z., Elgamal, A., Bielak, J. and Acero, G. (2008). “Two-dimensional Nonlinear Earthquake Response Analysis of a Bridge-foundation-ground System.” *Earthquake Spectra*, 24(2), 343-386.

Zienkiewicz, O.C., Chan, A.H.C., Pastor, M., Paul, D.K. and Shiomi, T. (1990). “Static and Dynamic Behaviour of Soils: A Rational Approach to Quantitative Solutions. I. Fully Saturated Problems.” *Proceedings of the Royal Society of London. Series A, Mathematical and Physical Sciences*, 285-309.

Ziotopoulou, K. (2018). “Seismic Response of Liquefiable Sloping Ground: Class A and C Numerical Predictions of Centrifuge Model Responses.” *Soil Dynamics and Earthquake Engineering*, 113, 744-757.

Zhou, Y., Chen, J., She, Y., Kaynia, A.M., Huang, B. and Chen, Y. (2017). “Earthquake Response and Sliding Displacement of Submarine Sensitive Clay Slopes.” *Engineering geology*, 227, 69-83.

Zhu, Y. and Carbee, D.L. (1984). “Uniaxial Compressive Strength of Frozen Silt under Constant Deformation Rates.” *Cold regions Science and Technology*, 9(1), 3-15.

Appendix A. Hydraulic Gradient

The hydraulic gradient is defined as $i = \frac{1}{\rho g}\frac{\Delta u_e}{\Delta h}$, where Δu_e is the difference of excess pore pressure between two locations, ρ is the mass density of water, g is the gravitational acceleration and Δh is the difference in height. As such, the hydraulic gradient is obtained below.

A.1. Two-Dimensional Hydraulic Gradient

The excess pore pressure u_e in a quadrilateral element is given by:

$$u_e(x,y) = N_1(\xi,\eta)u_{1,e} + N_2(\xi,\eta)u_{2,e} + N_3(\xi,\eta)u_{3,e} + N_4(\xi,\eta)u_{4,e} = \sum_{j=1}^{4} N_j(\xi,\eta)u_{j,e} \qquad (1)$$

where, $u_{1,e}$ to $u_{4,e}$ are excess pore pressures at four corner nodes of a quadrilateral element and N_1 to N_4 are bilinear shape function:

$$\begin{aligned} N_1(\xi,\eta) &= \frac{1}{4}(1-\xi)(1-\eta),\ N_2(\xi,\eta) = \frac{1}{4}(1+\xi)(1-\eta) \\ N_3(\xi,\eta) &= \frac{1}{4}(1+\xi)(1+\eta),\ N_4(\xi,\eta) = \frac{1}{4}(1-\xi)(1+\eta) \end{aligned} \qquad (2)$$

By the definition above, the hydraulic gradient in an element is obtained by:

$$i = \begin{bmatrix} i_x \\ i_y \end{bmatrix} = \begin{bmatrix} \frac{\partial u_e(x,y)}{\partial x} \\ \frac{\partial u_e(x,y)}{\partial y} \end{bmatrix} = \begin{bmatrix} \frac{\partial N_1}{\partial x} & \frac{\partial N_2}{\partial x} & \frac{\partial N_3}{\partial x} & \frac{\partial N_4}{\partial x} \\ \frac{\partial N_1}{\partial y} & \frac{\partial N_2}{\partial y} & \frac{\partial N_3}{\partial y} & \frac{\partial N_4}{\partial y} \end{bmatrix} \begin{bmatrix} u_{1,e} \\ u_{2,e} \\ u_{3,e} \\ u_{4,e} \end{bmatrix} \qquad (2)$$

For simplicity, $\xi = 0$ and $\eta = 0$ are used in computation of i representing the hydraulic gradient in the center of a quadrilateral element.

A.2. Three-Dimensional Hydraulic Gradient

The excess pore pressure u_e in a brick element is given by:

$$u_e(x,y,z) = N_1(\xi,\eta,\zeta)u_{1,e} + N_2(\xi,\eta,\zeta)u_{2,e} + N_3(\xi,\eta,\zeta)u_{3,e} + N_4(\xi,\eta,\zeta)u_{4,e}$$
$$+ N_5(\xi,\eta,\zeta)u_{5,e} + N_6(\xi,\eta,\zeta)u_{6,e} + N_7(\xi,\eta,\zeta)u_{7,e} + N_8(\xi,\eta,\zeta)u_{8,e} = \sum_{j=1}^{8} N_j(\xi,\eta,\zeta)u_{j,e} \quad (4)$$

where, $u_{1,e}$ to $u_{8,e}$ are excess pore pressures at eight corner nodes of a brick element and N_1 to N_8 are:

$$N_1(\xi,\eta,\zeta) = \frac{1}{8}(1-\xi)(1-\eta)(1-\zeta),\ N_2(\xi,\eta,\zeta) = \frac{1}{8}(1+\xi)(1-\eta)(1-\zeta)$$

$$N_3(\xi,\eta,\zeta) = \frac{1}{8}(1+\xi)(1+\eta)(1-\zeta),\ N_4(\xi,\eta,\zeta) = \frac{1}{8}(1-\xi)(1+\eta)(1-\zeta)$$

$$N_5(\xi,\eta,\zeta) = \frac{1}{8}(1-\xi)(1-\eta)(1+\zeta),\ N_6(\xi,\eta,\zeta) = \frac{1}{8}(1+\xi)(1-\eta)(1+\zeta) \quad (5)$$

$$N_7(\xi,\eta,\zeta) = \frac{1}{8}(1+\xi)(1+\eta)(1+\zeta),\ N_8(\xi,\eta,\zeta) = \frac{1}{8}(1-\xi)(1+\eta)(1+\zeta)$$

By the definition above, the hydraulic gradient in an element is obtained by:

$$i = \begin{bmatrix} i_x \\ i_y \\ i_z \end{bmatrix} = \begin{bmatrix} \dfrac{\partial u_e(x,y,z)}{\partial x} \\ \dfrac{\partial u_e(x,y,z)}{\partial y} \\ \dfrac{\partial u_e(x,y,z)}{\partial z} \end{bmatrix}$$

$$\frac{\partial u_e(x,y,z)}{\partial x} = \frac{\partial N_1}{\partial x}u_{1,e} + \frac{\partial N_2}{\partial x}u_{2,e} + \frac{\partial N_3}{\partial x}u_{3,e} + \frac{\partial N_4}{\partial x}u_{4,e} + \frac{\partial N_5}{\partial x}u_{5,e} + \frac{\partial N_6}{\partial x}u_{6,e} + \frac{\partial N_7}{\partial x}u_{7,e} + \frac{\partial N_8}{\partial x}u_{8,e} \quad (6)$$

$$\frac{\partial u_e(x,y,z)}{\partial y} = \frac{\partial N_1}{\partial y}u_{1,e} + \frac{\partial N_2}{\partial y}u_{2,e} + \frac{\partial N_3}{\partial y}u_{3,e} + \frac{\partial N_4}{\partial y}u_{4,e} + \frac{\partial N_5}{\partial y}u_{5,e} + \frac{\partial N_6}{\partial y}u_{6,e} + \frac{\partial N_7}{\partial y}u_{7,e} + \frac{\partial N_8}{\partial y}u_{8,e}$$

$$\frac{\partial u_e(x,y,z)}{\partial z} = \frac{\partial N_1}{\partial z}u_{1,e} + \frac{\partial N_2}{\partial z}u_{2,e} + \frac{\partial N_3}{\partial z}u_{3,e} + \frac{\partial N_4}{\partial z}u_{4,e} + \frac{\partial N_5}{\partial z}u_{5,e} + \frac{\partial N_6}{\partial z}u_{6,e} + \frac{\partial N_7}{\partial z}u_{7,e} + \frac{\partial N_8}{\partial z}u_{8,e}$$

In computation of 3D hydraulic gradient, $\xi = 0$, $\eta = 0$ and $\zeta = 0$ are used to represent the hydraulic gradient in the center of a brick element. For illustration, the same 3D U-shaped configurations as in Figure 11.2 and Figure 11.8 are presented. Figure B.1 and Figure B.2 show the hydraulic gradient at end of shaking. It can be seen that the hydraulic gradient values in Figure B.1 and Figure B.2 are identical to those in Figure 11.5 and Figure 11.10.

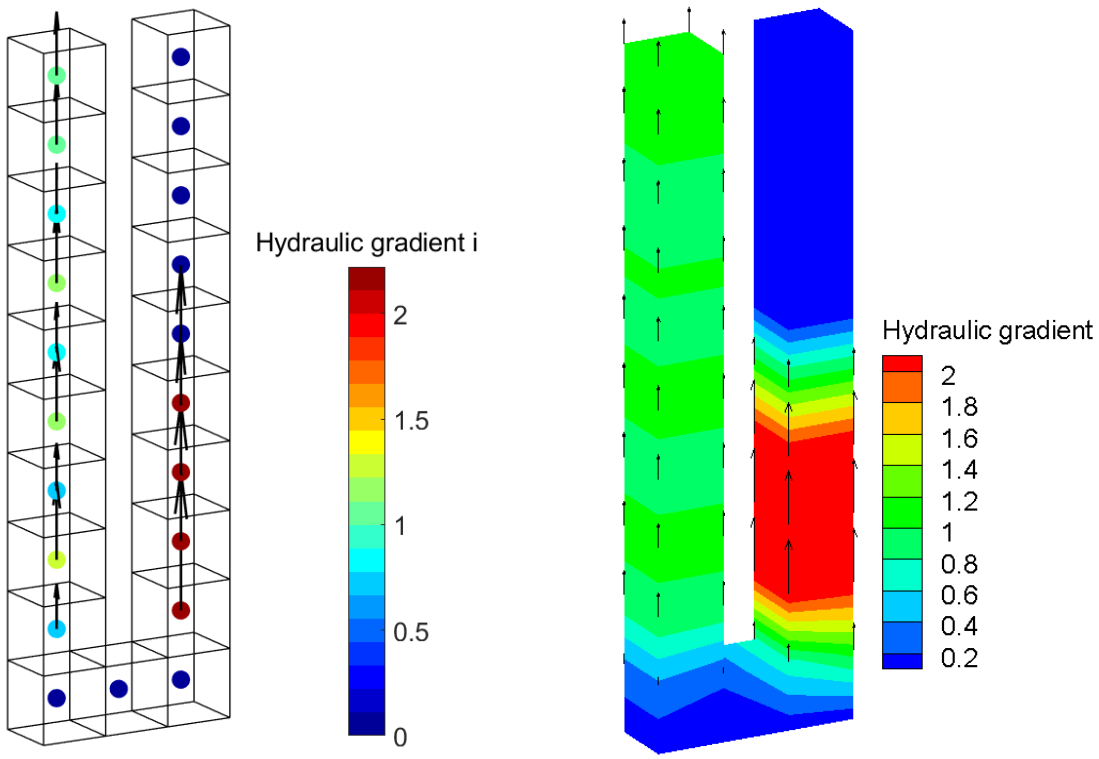

Figure A.1 Hydraulic gradient at end of shaking

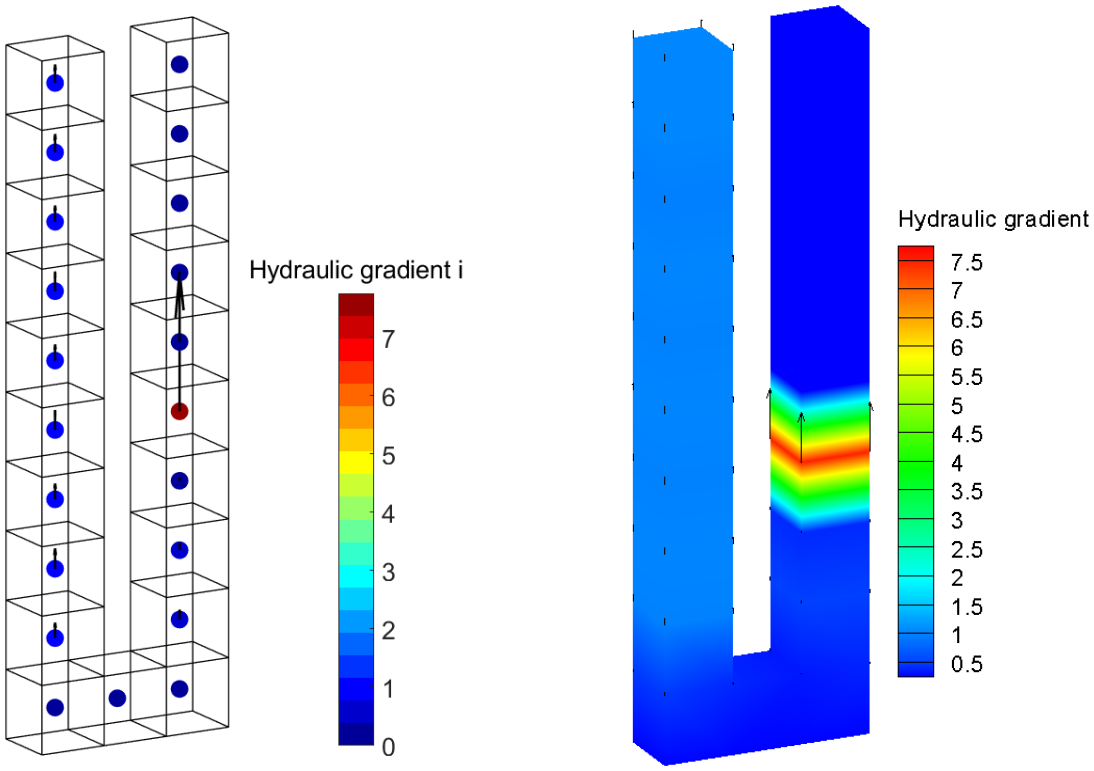

Figure A.2 Hydraulic gradient of layered soils at end of shaking